Generation of Millimetre-Wavelength Orbital Angular Momentum

A thesis submitted to The University of Manchester for the degree of

Doctor of Philosophy

in the Faculty of Engineering and Physical Sciences

2014

Peter Schemmel

School of Physics and Astronomy

Contents

List of Figures

List of Tables

Abstract

Generation of Millimetre-Wavelength Orbital Angular Momentum

Peter Schemmel

A thesis submitted to the University of Manchester for the degree of Doctor of Philosophy, 2014.

Studying the orbital angular momentum (OAM) of light has become rather fashionable in the 21st century. Yet, most of major advances in OAM related research have been conducted in the visible regime of light. A significant portion OAM research revolves around using OAM radiation to perform some function that is deemed useful. Examples of this are optical trapping, micro-machine manipulation and the development of advanced communication systems. Photon entanglement measurements also make use of OAM radiation. Interest in probing radiation for naturally generated OAM is far less popular. For example, interest in building OAM sensitive telescopes was sparse at the beginning of this thesis, however the first reported detection of astrophysical OAM was published in 2013. This thesis aims to tackle these two areas of sparse research by developing the components and understanding in order to build OAM sensitive millimetre-wavelength telescopes. Spiral phase plates (SPPs) are the device of choice. The majority of the thesis sets out to test three different SPPs, in order to compare and contrast different methods for their manufacture and design. Electromagnetic theory of OAM and its generation is reviewed first. Then, each SPP is modelled numerically followed by in-depth modelling of each plate by using the computational electromagnetic package FEKO. Finally, each plate is measured with a three dimensional field scanner developed as part of this thesis. Development of a new modular SPP design concludes this thesis.

Declaration

No portion of the work referred to in the thesis has been submitted in support of an application for another degree or qualification of this or any other university or other institute of learning.

Copyright Statement

(i) The author of this thesis (including any appendices and/or schedules to this thesis) owns certain copyright or related rights in it (the "Copyright") and s/he has given The University of Manchester certain rights to use such Copyright, including for administrative purposes.

(ii) Copies of this thesis, either in full or in extracts and whether in hard or electronic copy, may be made **only** in accordance with the Copyright, Designs and Patents Act 1988 (as amended) and regulations issued under it or, where appropriate, in accordance with licensing agreements which the University has from time to time. This page must form part of any such copies made.

(iii) The ownership of any certain Copyright, patents, designs, trade marks and other intellectual property (the "Intellectual Property") and any reproductions of copyright works in the thesis, for example graphs and tables ("Reproductions"), which may be described in this thesis, may not be owned by the author and may be owned by third parties. Such Intellectual Property and Reproductions cannot and must not be made available for use without the prior written permission of the owner(s) of the relevant Intellectual Property and/or Reproducitons.

(iv) Further information on the conditions under which disclosure, publication and commercialisation of this thesis, the Copyright and any Intellectual Property and/or Reporductions described in it may take place is available in the University IP Policy (see http://documents.manchester.ac.uk/DocuInfo.aspx?DocID=487), in any relevant Thesis restriction declarations deposited in the University Library, The University Library's regulations
(see http://manchester.ac.uk/library/aboutus/regulations) and in The University's policy on Presentation of Theses.

Bazinga

Sheldon Cooper

Dedication

For those who always believed.

Mom, Dad, Will and Saima.

Acknowledgements

As you know, Im not comfortable with prolonged good-byes and maudlin displays of emotion, so I prepared this short [transcript]. - Sheldon

Numerous people have supported the creation of this thesis, and to thank them all would require far too many pages. However, I would like to thank a few specific people here. To start I would like to thank my family, Susan, John, Will and Saima. They have always been there to support me... emotionally and financially! Despite living 3,806 miles from my parents and brother, watching a few episodes of Everybody Loves Raymond brought them right into the hot zone.

My mom and dad have always provided me with a wonderful environment to grow, and never stopped me from believing that I could do anything I put my mind to. Without that naivet I would not have taken so many chances in life, nor would I have moved to the UK, and I certainly would never have become a physicist. Thank you mom for teaching me how to not be too serious and to enjoy life. Thank you dad for always being there when things got tough and knowing what to do to fix it. I'm also appreciative of my brother Will, who makes me laugh and is living proof that I should not consider a career in music. Good thing this physics thing worked out. He once gave me a wedgie that tore my boxers, and for that he has earned much respect. Finally, I'd like to thank my better half Saima. Without her I wouldn't know how wonderful curry is, ride the Magic Bus or endure the agony of RyanAir. I'm glad she was there to take care of me when I was sick and that she has a car to drive me to A&E (That's ER for my American friends). She is my travel companion, best friend, and my inspiration. With her life is full of colour, and almost as important, without her I would have to scratch my own back and that's just no fun. Thank you Saima for always knowing what to say to raise my spirits, for our weekend walks and talks over coffee.

I'd also like to thank three people who had a pronounced impact on my life. First

is Bill Barrett who taught everything there is to know about building motorcycles. He didn't have to let a thirteen year old kid into his shop, but he did and I wouldn't be here today without his help. Next up is Mr. Ty Tiejen, despite the fact that he is a Minnesota Vikings fan. Mr. Tiejen showed me that math isn't scary, which came in handy when I started to study physics. Finally, I'd like to thank Mr. Kent Anderson, who let me join his AP American History class. He pushed me to always work hard, taught me that there is no such thing as number two, just number one and number three. Finally, he showed me that shooting rubber bands at people in class is something you never have to grow out of.

I would also like to thank Prof. Tom Irving for employing me as an undergraduate and allowing me to explore his optics lab. The work I conducted during those four years certainly put me on my current career path, and I'm extremely appreciative of his mentorship. I also have enormous gratitude for Dr. Yurii Shylnov who spent a year tutoring me in topology, group theory and quantum mechanics. Not only was he a magnificent mentor but he was also a great friend. Enough thanks can not be bestowed upon my thesis supervisors Dr. Bruno Maffei and Dr. Giampaolo Pisano. Their friendship and guidance were paramount to my research. They have enabled my research ambitions and most importantly they showed me how to be a professional academic. Sorry Bruno, for all the homework I gave you!

Finally I'd like to thank some of my friends and colleagues; Fahri, Stefania, Mareike, Ho Ting, Stephen and Matthew. Thanks for all the fun times.

Peter

Supporting Publications

M. D. Gray, G. Pisano, S. Maccalli and **P. Schemmel**, *"Amplification of OAM Radiation by Astrophysical Masers ,"* submitted to Royal Astronomical Society June (2014).

P. Schemmel, G. Pisano and B. Maffei, *"A modular spiral phase plate design for orbital angular momentum generation at millimetre wavelengths,"* Optics Express, Vol. 22, Iss. 112, 14712 - 14726, (2014).

G. Pisano, G. Maffei, M. W. Ng, V. Haynes, I. Mohamed, **P. Schemmel** and S. Maccalli, *"Development of Millimetre-Wave Quasi-Optical Devices Based on the Mesh Technology,"* Proc. 8th Eur. Conf. Antennas Propag., (2014).

P. Schemmel, S. Maccalli, G. Pisano, B. Maffei, and M.W. Ng, *"Three Dimensional Measurements of a Millimetre Wave Orbital Angular Momentum Vortex,"* Optics Letters, Vol. 39, 626-629, (2014).

P. Schemmel , S. Maccalli, B. Maffei, F. Ozturk, G. Pisano, and M.W. Ng, *"A Near Field 3D Scanner for Millimetre Wavelengths,"* in Proceedings of the 35th ESA Antenna Workshop on Antenna and Free Space RF Measurements, (2013).

B. Maffei, S. Legg, M. Robinson, F. Ozturk, M.W. Ng, **P. Schemmel** and G. Pisano, *"Implementation of a Quasi-Optical Free-Space S-Parameters Measurement System"* in Proceedings of the 35th ESA Antenna Workshop on Antenna and Free Space RF Measurements, (2013).

S. Maccalli, G. Pisano, **P. Schemmel**, S. Colafrancesco, B. Maffei, M.W. Ng, M. Gray, *"Intensity and Phase Profile Measurements of Vortex Beams at Millimetre Wavelengths"* Poster presented at Photon12, conference, Durham, UK, (2012).

1

Introduction and Motivation

1.1 What is Orbital Angular Momentum?

Over several centuries there has been a debate over whether light is a particle or a wave. Each side fought vigorously against the other, and it wasn't until the advent of modern physics that light was decided to be both. Quantum mechanics captures the nature of duality, by describing particles with wave functions. However, for most cases in the quantum world, things are more or less visualised as particles. In classical electrodynamics light is viewed as a wave. Yet, in 1992 Allen *et al.* [1] discovered that light waves with an azimuthal phase dependance carry orbital angular momentum (OAM), which had quantised values of $L = l\hbar$. Suddenly, the wave and particle nature of light clashed again. Not only did the quantum number l define the total OAM, it also defined the number of helically wrapped phase fronts of the propagating wave (Fig. 1.1) [2]. Yet, it was also shown that single photons can have OAM [3]. Even electrons have been shown to be capable of carrying OAM [4, 5]. Now, the once distinct line between wave and particle descriptions of light has been blurred.

Coupling between the wave and particle nature of light is just one of many interesting facets of OAM analysis. In 1936 Beth conducted experiments [6] to show that light with spin angular momentum (SAM) could rotate a quarter wave plate. An analogous

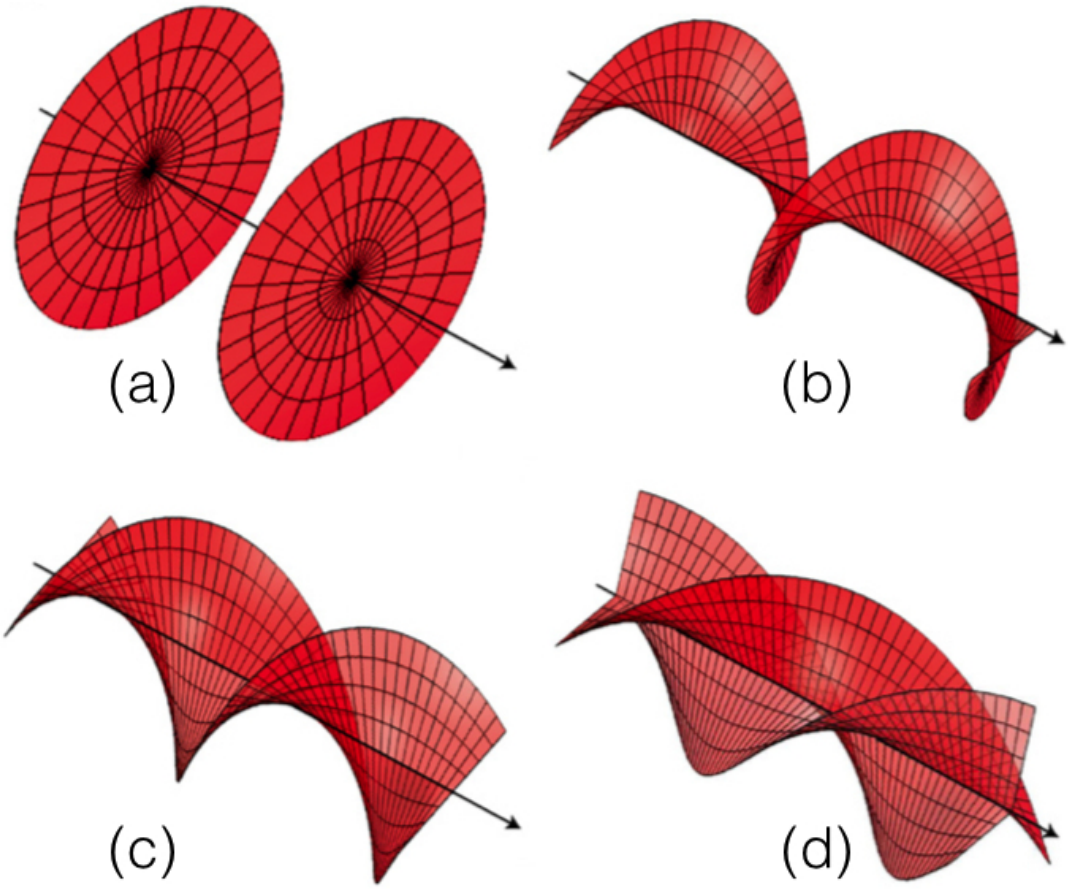

Figure 1.1: Helical wave fronts of light beams with $l = 0, +1, +2, +3$*, (a, b, c, d). Adapted from [2].*

experiment was completed in 2014 to show that light with OAM could rotate a suspended metal ring [7]. This property of OAM radiation has been used for trapping atoms and particles and driving micro-machines [8].

Beams with OAM are sometimes called optical vortices because the field's momentum orbits around the propagation axis [2]. In such beams, a phase singularity or dislocation exists along the propagation axis, causing a central intensity null and annular intensity pattern [9]. Each phase singularity represents a topological defect in the propagating phase front [10]. Phase structures of OAM beams provide an avenue for experimental research into topological features of radiation. Singularities in OAM

beams have even been shown to loop [11] and knot [12] (Fig. 1.2). Singularities can even interact with each other [13].

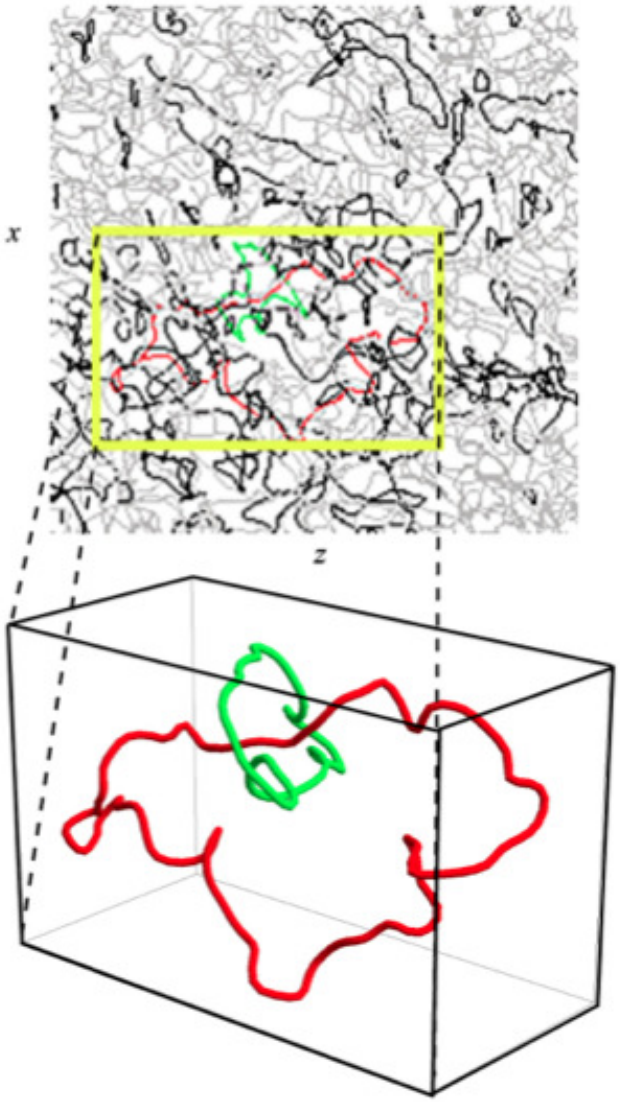

Figure 1.2: Computational phase singularities in a volume, much like experimental laser speckle patterns, showing how loops and knots are created. The upper portion of the image is a two-dimensional slice of the three-dimensional volume below. Knotted vortex lines are highlighted in red and green. Adapted from [10].

In addition to the interesting use of OAM in topological studies or to rotate and

trap objects, OAM has also become a useful tool for quantum entanglement studies and communications [8, 9]. Both of these applications are made possible by the difference between spin and orbital momentum. Spin angular momentum, or circular polarisation, only has two possible states, left and right. These have been routinely exploited to explore photon entanglement and to boost the carrying capacity of communication systems. Unlike spin however, there are a theoretically doubly infinite number of OAM states. This is because the mode number l can have values between negative and positive infinity. Photons with the capability to occupy so many states are of interests to entanglement experimenters, and provide the possibility of extremely large bandwidth communication systems.

1.2 Millimetre Wavelength OAM and Astronomy: Thesis Motivation

Despite a few exceptions, the majority of OAM research has been conducted in the optical regime. This is partly due to the ease of manipulating OAM modes with spatial light modulators, which are only available for optical wavelengths [2]. Very little work with OAM has been undertaken in the radio regime, and even fewer publications exists in which the operating wavelengths were either millimetre or sub-millimetre. In addition to this lack of OAM research at millimetre wavelengths, there has been a subsequent lack of research in OAM astronomy. There have been some suggestions of looking for OAM radiation from astrophysical sources, [14]. Over the course of writing this thesis, more people have become interested in OAM astrophysicists. There was even a detection of photons with OAM from stars embedded in turbulent media [15]. Yet, the number of OAM astrophysics remains extremely small. Despite this, observations of OAM from astrophysical sources could lead to insights into their generating mechanisms. More importantly, OAM measurements represents uncharted waters to the astrophysics community. Observations of OAM have the potential to spark new discoveries of objects

and processes that have not been considered before.

This thesis aims to help develop the tools necessary to conduct OAM astrophysics in the millimetre and sub-millimetre regimes. It is believed that the lack of OAM research in this area is mainly due to the lack of simple methods to manipulate OAM modes. Unlike optical systems that utilise CCD detectors, feed antenna are typically used to detect millimetre wavelength radiation. This limits typical experimental systems to just a single pixel. Furthermore, OAM beams do not couple to feed antenna due to a mismatch between the electromagnetic fields. In order to detect millimetre wavelength OAM, a device must be used to switch between OAM and non-OAM (nOAM) states in an efficient and known manner.

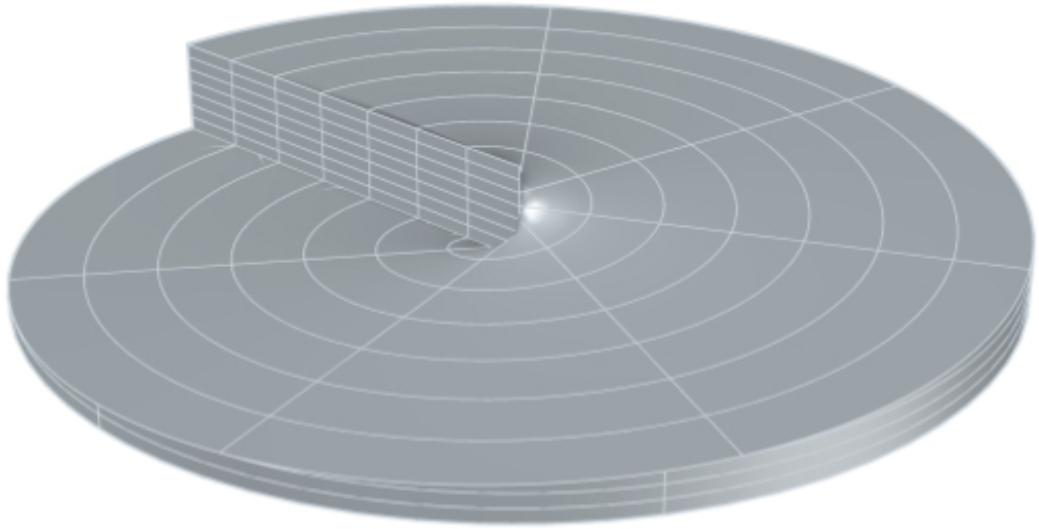

Figure 1.3: A CAD model of a SPP for OAM manipulation at millimetre wavelengths.

Spiral phase plates (SPPs) are the simplest device known to convert OAM and nOAM states, which is also practical for millimetre wavelength systems (Fig. 1.3). It should be noted that the measurements in this thesis convert nOAM into OAM, i.e. the reverse process of what would happen in an astronomical telescope. This was done for practicality and simplicity reasons. For example, multiple SPPs and a more complicated optical path would be required to conduct OAM to nOAM measurements. However the

process of converting nOAM to OAM and visa versa are interchangeable. This thesis focuses on designing, modelling and testing various SPPs. It is hoped that developing a deep understanding of these devices will enable future researchers to incorporate them into millimetre wavelength telescopes and receiver systems.

Radio telescopes fitted with SPPs could be called phase modulating telescopes or PMTs. A PMT functions as follows. First, consider nOAM radiation (fundamental Gaussian beams) entering a radio telescope. In a normal telescope, this radiation reflects off of the dish surface and enters the feed antenna at the focus. However, in a PMT, the radiation reflects off of the dish surface and passes through a SPP. Here, the initial nOAM radiation is converted to OAM radiation by the SPP. This OAM radiation reaches the focal point, but does not couple to the feed antenna due to the mismatch between the relative fields. This results in a minimum signal level.

Now consider an incident OAM beam. This beam reflects off of the dish surface and intersects the SPP. If the SPP mode number is equal but opposite to the incident OAM mode, the initial OAM radiation is converted to nOAM radiation. This new nOAM radiation then propagates to the focal point and couples to the feed antenna. This results in a maximum signal level.

Of course this is a simplistic model, and practical systems are more complicated. To begin with, SPPs are not pure mode converters. This means that they do not switch all nOAM radiation into OAM and visa versa. However, characterisation of SPPs, such as the work in this thesis, can provide astronomers with the necessary information to account for this. Secondly, practical receiver systems experience noise caused by several sources including stray radiation entering the feed via the antenna side lobes, receiver noise temperature and others. If all these background sources are well understood, they may be removed from the recorded data.

Constructing a PMT is fairly straightforward and there are several possible PMT configurations (Fig. 1.4 - 1.6). The simplest PMT configuration is a primary focus reflecting dish telescope, which has a SPP placed in front of the feed antenna (Fig. 1.4). There are two main advantages of this type of system. First is its simplicity. Here a SPP

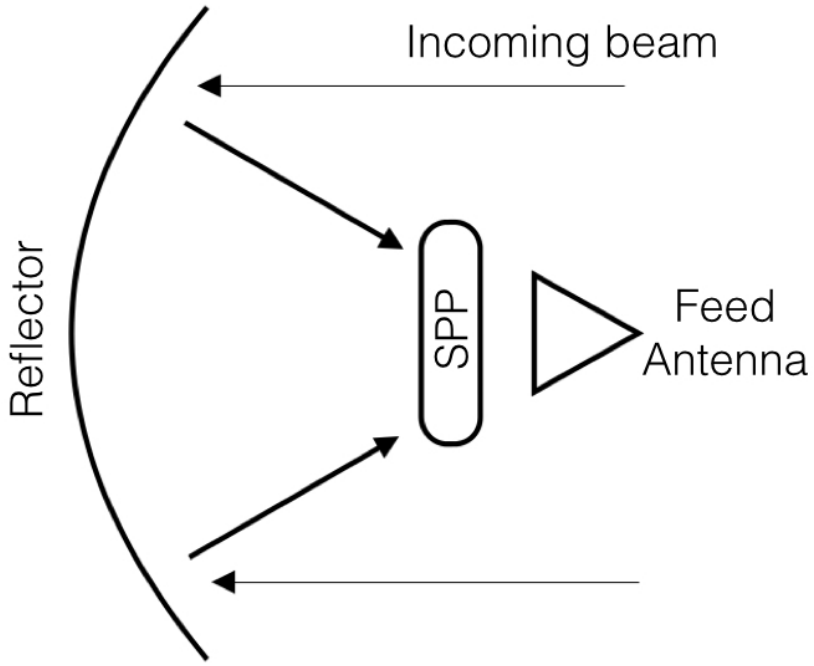

Figure 1.4: The simplest PMT configuration, where a SPP is placed in front of the feed antenna in a primary focus reflection dish telescope.

can be directly mounted in front of the feed antenna. The second primary advantage is that several of these types of radio telescopes already exist. However, this PMT design suffers from inflexibility. Only one SPP may be mounted at a time, without utilising complex devices to exchange SPPs, which may also increase blockage. This means that primary focus PMTs are only sensitive to one OAM mode at a time.

Cassegrain focus PMTs offer an alternative to primary focus PMTs (Fig. 1.5). The advantage of such a system is that a device that moves several SPPs in and out of the propagation axis of the feed antenna may be employed without increasing telescope blockage. This allows the PMT to be sensitive to multiple OAM modes.

A Cassegrain focus PMT can be improved upon by developing an OAM spectrum analyser for millimetre and radio wavelengths (Fig. 1.6). Such an analyser would have a simple optical path, where beam splitters are used to divert the incident radiation to several SPPs. This is advantageous because such a PMT would be capable of monitoring

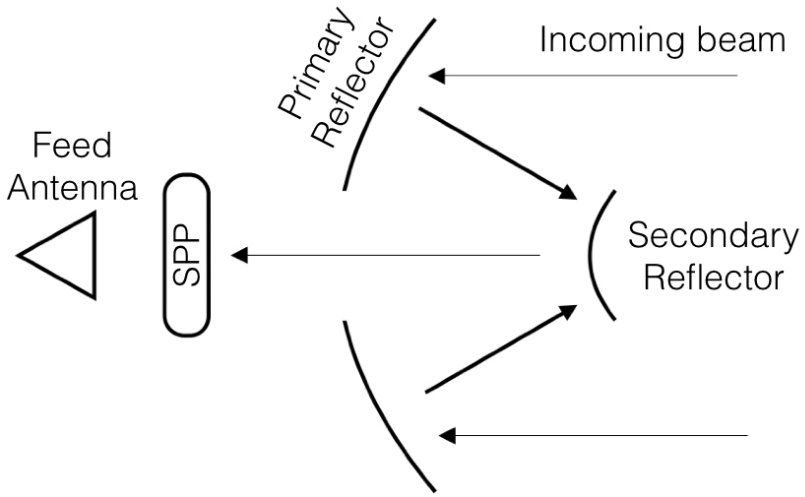

Figure 1.5: Cassegrain focus telescope with a SPP placed in front of the feed antenna.

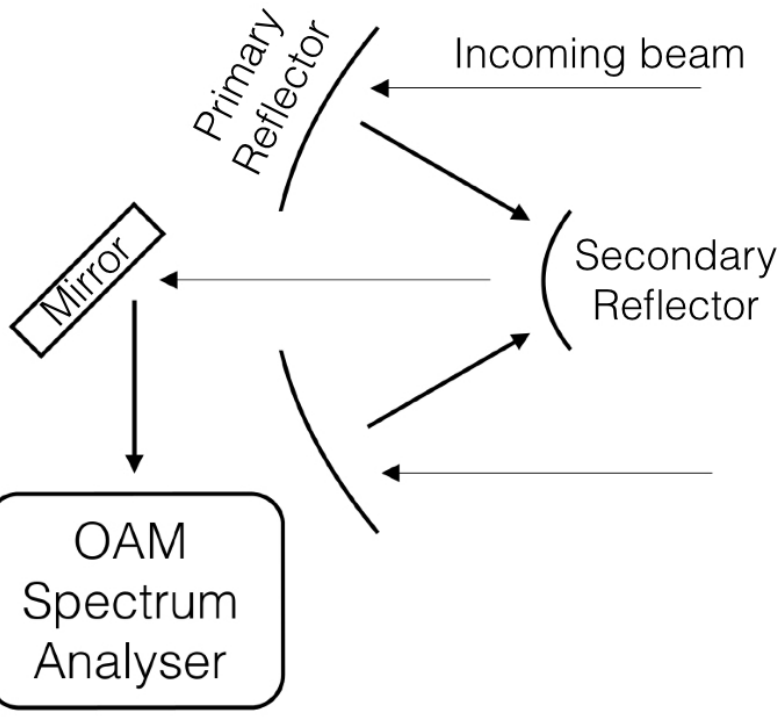

Figure 1.6: An advanced Cassegrain focus telescope with a mirror reflecting radiation into an OAM spectrum analyser.

several OAM modes at once. However, it does have a drawback with regards to signal strength. OAM signals are expected to be low [15], depending on the source. Splitting the incident beam multiple times lowers the signal strength at the receiver. If the incident beam is split too many times, the signal strength at the receiver could be below the noise level, and no signal would be detected.

1.3 Thesis Outline

Clearly, there is a need for the development of OAM sensitive radio and millimetre wavelength telescopes. SPPs have been shown to be the simplest method for turning standard telescope systems into PMTs. However, a deep understanding of how SPPs generate and manipulate OAM modes at millimetre wavelengths has yet to be achieved. This thesis sets out to fill this gap in knowledge, and to design, model and test millimetre wavelength SPPs. In the second chapter of this thesis, the theoretical foundations for OAM and higher order Gaussian beams will be discussed. It will be shown that higher order Gaussian beams carry OAM, and that they are simply described by Laguerre Gaussian modes. The following chapter details several ways to generate beams with OAM. These include natural mechanisms, with particular interest paid to turbulent media. A review of synthetic, or laboratory, generated OAM is also conducted. Holographic diffraction gratings and Q-plates are reviewed before an in depth analysis of SPP functionality is conducted. While the earlier section of this thesis were largely a review of the current state of OAM research, the following sections encapsulate my personal contributions to the thesis. First it is shown how SPPs generate OAM. Secondly, it is shown that SPPs are not pure mode converters. Various SPP designs are reviewed followed by a demonstration of SPP bandwidth characteristics and vortex generation. My significant, personal contributions in chapter three include demonstrating that SPPs are impure mode converters due to a mismatch in the angular momentum mode number in phase and amplitude, a new modular SPP design, using Gaussian beam mode analysis to model the frequency response of an SPP, and developing a toy model to visualise

vortex generation by a SPP. The fourth chapter of this work focuses on analytical and computational modelling of SPPs. To the best of my knowledge this is the first time such work has been done. First, simple numerical models are conducted in order to understand the basics of SPP functionality. Following this is a fairly complete study of SPPs using the software package FEKO. Three SPP designs are modelled using several source types. The fifth chapter reviews the characterisation of a near field scanning system developed to measure beams generated by SPPs. While 3D scanners are not new measurement facilities, I personally constructed the device, wrote its control and analysis software, and conducted characterisation measurements to confirm its functionality. Following this chapter is a presentation of data recorded from the three manufactured SPP designs. Two separate sources were used to generate incident beams, which in turn produced transmitted OAM beams with several differences. One source type represented a more practical telescope optical path, while the second source type was less realistic, but allowed for a better analysis of the generated phase singularities. Although not the first millimetre wavelength measurements of OAM, this resulted in a published journal paper, which showed step change improvements over previous measurements. Following these measurements is a chapter devoted to the design, modelling and testing of a modular SPP. Such a design has never been built or tested before, and I was the leading contributor[1]. The thesis ends with a conclusion and review of the presented work and an outlook on future projects.[2]

[1] I would like to thank Dr. Giampaolo Pisano for his extremely helpful discussions while the modular SPP was being developed, and Dr. Bruno Maffei for discussing the measurement methodology

[2] Appendix C contains several terms, definitions and OAM field features, which the reader may not be familiar with.

2

Energy, Momentum and Higher Order Gaussian Beams

2.1 Introduction

This chapter, in conjunction with Appendix A and Appendix B, develops the form of the fundamental beam used in antenna analysis and quasi-optical (QO) design, starting from the core of classical electrodynamics. First, this chapter develops the plane wave solution to the Helmholtz wave equation and uses this solution to discuss the energy and momentum of electromagnetic fields. Appendix A derives the Helmholtz wave equation, in detail, starting from electro- and magnetostatics. Appendix B reviews the procedure used to describe arbitrary functions by an orthonormal expansion. Following the initial description of linear, spin angular and orbital angular momentum the fundamental Gaussian beam solution to the Helmholtz equation is derived. Gaussian beams are the foundation of optical system design. Finally higher order Gaussian modes are presented, and it is shown that these higher order modes carry orbital angular momentum (OAM).

Since the foundations of this initial work are typically contained in available texts, references will be given here while in text references will be left for specific details of the theoretical work. Content from Sec. 2.2 through 2.3.6 refers to [16–18], while Sec.

2.4 through 2.5 refers to [19]. As a supplement also see, [20].

2.2 Plane Wave Solutions to the Helmholtz Wave Equation

In this section, the simplest solution to the Helmholtz equation will be derived. The process begins with the Helmholtz equation,

$$\left(\nabla^2 + k^2\right)\Psi = 0 \tag{2.1}$$

Here, ∇^2 is the Laplacian, k is the wavenumber and Ψ is the vector field (See Appendix A).Using (B.3), Ψ can be expressed as a superposition of orthogonal functions. For plane wave solutions, the field changes only along the propagation axis. Therefore, the problem reduces to one dimensional geometry, so sines and cosines can be used to expand Ψ (Table B.1). Using the complex number identity,

$$e^{i\theta} = cos\,(\theta) + i sin\,(\theta) \tag{2.2}$$

Equation (2.1) becomes,

$$\Psi = \sum_n a_n e^{i\theta} \tag{2.3}$$

where θ is the phase of Ψ such that,

$$\theta = kz - \omega t \tag{2.4}$$

with,

$$k = \frac{2\pi}{\lambda} \tag{2.5}$$

and

$$\omega = kc \tag{2.6}$$

If Ψ is considered to be a single plane wave mode then there is only one term in (2.3). Therefore,

$$\Psi = A_0 e^{i\theta} \tag{2.7}$$

and then,

$$E = E_0 e^{i\theta} \tag{2.8}$$

For plane waves in free space, $\nabla \cdot \boldsymbol{E} = 0$ and $\nabla \cdot \boldsymbol{B} = 0$. So,

$$E_{0_z} = B_{0_z} = 0 \tag{2.9}$$

This shows that the electric and magnetic fields are perpendicular to the axis of propagation. Equations for the x- and y-components are recovered by working out the curl of the electric field (See Appendix A for more information),

$$\begin{gathered} \nabla \times \boldsymbol{E} = -\frac{\partial \boldsymbol{B}}{\partial t} \\ \left(\frac{\partial E_z}{\partial y} - \frac{\partial E_y}{\partial z}\right)\hat{x} + \left(\frac{\partial E_x}{\partial z} - \frac{\partial E_z}{\partial x}\right)\hat{y} + \left(\frac{\partial E_y}{\partial x} - \frac{\partial E_x}{\partial y}\right)\hat{z} = -\frac{\partial \boldsymbol{B}}{\partial t} \\ \left(\frac{\partial E_y}{\partial x} - \frac{\partial E_x}{\partial y}\right)\hat{z} = -\frac{\partial \boldsymbol{B}}{\partial t} \end{gathered} \tag{2.10}$$

The y-component of the electric field is,

$$\begin{aligned} \frac{\partial E_y}{\partial x} &= \frac{-\partial \boldsymbol{B}}{\partial t} \\ \partial E_y &= -\frac{\partial x}{\partial t}\partial B_x \\ E_y &= -cB_x \\ E_y &= -\frac{\omega}{c}B_x \end{aligned} \tag{2.11}$$

and the x-component is,

$$\begin{aligned} \frac{\partial E_x}{\partial y} &= \frac{\partial \boldsymbol{B}}{\partial t} \\ \partial E_x &= \frac{\partial x}{\partial t}\partial B_y \\ E_x &= cB_y \\ E_x &= \frac{\omega}{c}B_y \end{aligned} \tag{2.12}$$

Equations (2.11) and (2.12) can be simplified into the single equation,

$$\boldsymbol{B_0} = \frac{k}{\omega}\left(\hat{z} \times \boldsymbol{E_0}\right) \tag{2.13}$$

The amplitudes of the electric and magnetic field are related by,

$$B_0 = \frac{1}{c}E_0 \tag{2.14}$$

2.3 Energy and Momentum

2.3.1 Conservation of Energy

In order to understand how electromagnetic fields carry energy and momentum, it is necessary to understand the forces applied to charged particles by the fields. This is because momentum is the time derivative of the work done by a system, work is the integral of the force applied over a path and the change in energy of a system is equal to the work done on the system. We begin by finding the work energy theorem for electrodynamics. Firstly, the force applied to a charge q is,

$$\boldsymbol{F} = q\left(\boldsymbol{E} + \boldsymbol{v} \times \boldsymbol{B}\right) \tag{2.15}$$

The work done, dW by an electromagnetic field acting the charge in an time interval dt is,

$$\begin{aligned} dW = \boldsymbol{F} \cdot dl &= q\left(\boldsymbol{E} + \boldsymbol{v} \times \boldsymbol{B}\right) \cdot \boldsymbol{v} dt \\ &= q\boldsymbol{E} \cdot \boldsymbol{v} dt + q\boldsymbol{v} \times \boldsymbol{B} \cdot \boldsymbol{v} dt \\ &= q\boldsymbol{E} \cdot \boldsymbol{v} dt + 0\, dt \\ &= q\boldsymbol{E} \cdot \boldsymbol{v} dt \end{aligned} \tag{2.16}$$

Equation (2.16) may be rewritten using the following definitions,

$$\begin{aligned} q &= \rho d\tau \\ \boldsymbol{J} &= \rho \boldsymbol{v} \end{aligned} \tag{2.17}$$

Equation (2.16) then becomes,

$$dW = \rho d\tau \boldsymbol{E} \cdot \boldsymbol{v} dt \tag{2.18}$$

Moving the dt to the left hand side the momentum of the EM field is found to be,

$$\frac{dW}{dt} = \int_V \boldsymbol{E} \cdot \boldsymbol{J} d\tau \tag{2.19}$$

To find $\boldsymbol{E} \cdot \boldsymbol{J}$ we use (See Appendix A for more information),

$$\nabla \times \boldsymbol{B} = \mu_0 \boldsymbol{J} + \mu_0 \epsilon_0 \frac{\partial \boldsymbol{E}}{\partial t} \tag{2.20}$$

and solve for the current density $\boldsymbol{J}$,

$$\boldsymbol{J} = \frac{1}{\mu_0}\left(\nabla \times \boldsymbol{B} - \mu_0 \epsilon_0 \frac{\partial \boldsymbol{E}}{\partial t}\right) \tag{2.21}$$

Applying $(\boldsymbol{E}\cdot)$ to each side yields,

$$\boldsymbol{E} \cdot \boldsymbol{J} = \frac{1}{\mu_0} \boldsymbol{E} \cdot (\nabla \times \boldsymbol{B}) - \epsilon_0 \boldsymbol{E} \cdot \frac{\partial \boldsymbol{E}}{\partial t} \tag{2.22}$$

The following product identity can be used to find $\boldsymbol{E} \cdot (\nabla \times \boldsymbol{B})$.

$$\nabla \cdot (\boldsymbol{E} \times \boldsymbol{B}) = \boldsymbol{B} \cdot (\nabla \times \boldsymbol{E}) - \boldsymbol{E} \cdot (\nabla \times \boldsymbol{B}) \tag{2.23}$$

The second term $\nabla \times \boldsymbol{E}$ is known to be (See Appendix A for more information),

$$\nabla \times \boldsymbol{E} = -\frac{\partial \boldsymbol{B}}{\partial t} \tag{2.24}$$

Then,

$$\boldsymbol{E} \cdot (\nabla \times \boldsymbol{B}) = -\boldsymbol{B} \cdot \frac{\partial \boldsymbol{B}}{\partial t} - \nabla \cdot (\boldsymbol{E} \times \boldsymbol{B}) \tag{2.25}$$

$$\boldsymbol{B} \cdot \frac{\partial \boldsymbol{B}}{\partial t} = \frac{1}{2}\frac{\partial}{\partial t}\left(\boldsymbol{B}^2\right) \tag{2.26}$$

$$\boldsymbol{E} \cdot \frac{\partial \boldsymbol{E}}{\partial t} = \frac{1}{2}\frac{\partial}{\partial t}\left(\boldsymbol{E}^2\right) \tag{2.27}$$

Substituting these results into (2.22) leaves,

$$\begin{aligned} \boldsymbol{E} \cdot \boldsymbol{J} &= \frac{1}{\mu_0}\left(-\boldsymbol{B} \cdot \frac{\partial \boldsymbol{B}}{\partial t} - \nabla \cdot (\boldsymbol{E} \times \boldsymbol{B})\right) - \epsilon_0 \boldsymbol{E} \cdot \frac{\partial \boldsymbol{E}}{\partial t} \\ &= \frac{-1}{2}\frac{\partial}{\partial t}\left(\epsilon_0 \boldsymbol{E}^2 + \frac{1}{\mu_0}\boldsymbol{B}^2\right) - \frac{1}{\mu_0}\nabla \cdot (\boldsymbol{E} \times \boldsymbol{B}) \end{aligned} \tag{2.28}$$

Finally,

$$\frac{dW}{dt} = \frac{-d}{dt}\int_{\mathcal{V}} \frac{1}{2}\left(\epsilon_0 \boldsymbol{E}^2 + \frac{1}{\mu_0}\boldsymbol{B}^2\right) d\tau - \frac{1}{\mu_0}\oint_{\mathcal{S}} (\boldsymbol{E} \times \boldsymbol{B}) \cdot da \tag{2.29}$$

The left integral is the total energy in the electromagnetic field, while the right integral is the rate that energy leaves the volume $\mathcal{V}$ through the surface $\mathcal{S}$. Equation (2.29) can be simplified by defining the Poynting vector, which has units of energy per unit time per unit area.

$$\boldsymbol{S} \equiv \frac{1}{\mu_0}(\boldsymbol{E} \times \boldsymbol{B}) \tag{2.30}$$

The Poynting vector is the energy flux density, and $\boldsymbol{S} \cdot da$ is the energy flux. The total energy stored in the field can be defined as

$$U_{em} \equiv \int_V u_{em}\, d\tau = \int_V \frac{1}{2}\left(\epsilon_0 \boldsymbol{E}^2 + \frac{1}{\mu_0}\boldsymbol{B}^2\right) d\tau \tag{2.31}$$

Then,

$$\boxed{\frac{dW}{dt} = \frac{-\partial U_{em}}{\partial t} - \oint \boldsymbol{S} \cdot da} \tag{2.32}$$

Equation (2.32) is the work energy theorem for electrodynamics. It states that the work done on a charge q is equal to the loss of electromagnetic field energy plus the loss of any energy that flowed out of the boundary surface.

2.3.2 Conservation of Momentum and the Maxwell Stress Tensor

If instead of manipulating the total force $\boldsymbol{F}$ on a charge q, we look at the force per unit volume $\boldsymbol{f}$, the conservation of momentum of electrodynamics will emerge. Consider a charge distribution ρ. Equation (2.15) becomes,

$$\boldsymbol{F} = \int_V (\rho \boldsymbol{E} + \boldsymbol{J} \times \boldsymbol{B})\, d\tau \tag{2.33}$$

The force per unit volume is then,

$$\boldsymbol{f} = \rho \boldsymbol{E} + \boldsymbol{J} \times \boldsymbol{B} \tag{2.34}$$

Using Maxwell's equations (Appendix A), ρ and $\boldsymbol{J}$ are replaced so that the force per unit volume $\boldsymbol{f}$ becomes,

$$\boldsymbol{f} = \epsilon_0 (\nabla \cdot \boldsymbol{E})\, \boldsymbol{E} + \left(\frac{1}{\mu_0}\nabla \times \boldsymbol{B} - \epsilon_0 \frac{\partial \boldsymbol{E}}{\partial t}\right) \times \boldsymbol{B} \tag{2.35}$$

We now must find out what $\partial \boldsymbol{E}/\partial t \times \boldsymbol{B}$ is. This can be accomplished by using the product rule on $\boldsymbol{E} \times \boldsymbol{B}$,

$$\frac{\partial}{\partial t}(\boldsymbol{E}\times\boldsymbol{B}) = \left(\frac{\partial \boldsymbol{E}}{\partial t}\times\boldsymbol{B}\right) + \left(\boldsymbol{E}\times\frac{\partial \boldsymbol{B}}{\partial t}\right) \tag{2.36}$$

and Faraday's Law,

$$\frac{\partial \boldsymbol{B}}{\partial t} = -\nabla\times\boldsymbol{E} \tag{2.37}$$

The previously unknown product $\partial\boldsymbol{E}/\partial t\times\boldsymbol{B}$ is,

$$\frac{\partial \boldsymbol{E}}{\partial t}\times\boldsymbol{B} = \frac{\partial}{\partial t}(\boldsymbol{E}\times\boldsymbol{B}) + \boldsymbol{E}\times(\nabla\times\boldsymbol{E}) \tag{2.38}$$

which means that the force per unit volume becomes,

$$\boldsymbol{f} = \epsilon_0\left[(\nabla\cdot\boldsymbol{E})\,\boldsymbol{E} - \boldsymbol{E}\times(\nabla\times\boldsymbol{E})\right] - \frac{1}{\mu_0}\left[\boldsymbol{B}\times(\nabla\times\boldsymbol{B})\right] - \epsilon\frac{\partial}{\partial t}(\boldsymbol{E}\times\boldsymbol{B}) \tag{2.39}$$

The term $(\nabla\cdot\boldsymbol{B})\,\boldsymbol{B}$ is added to either side of $\boldsymbol{f}$ since, $\nabla\cdot\boldsymbol{B} = 0$. Also,

$$\begin{aligned}\nabla^2\boldsymbol{E} &= 2(\boldsymbol{E}\cdot\nabla)\,\boldsymbol{E} + 2\boldsymbol{E}\times(\nabla\times\boldsymbol{E})\\ \boldsymbol{E}\times(\nabla\times\boldsymbol{E}) &= \frac{1}{2}\nabla\boldsymbol{E}^2 - (\boldsymbol{E}\cdot\nabla)\,\boldsymbol{E}\end{aligned} \tag{2.40}$$

Now,

$$\begin{aligned}\boldsymbol{f} =& \epsilon_0\left[(\nabla\cdot\boldsymbol{E})\,\boldsymbol{E} + (\boldsymbol{E}\cdot\nabla)\,\boldsymbol{E}\right] + \frac{1}{\mu_0}\left[(\nabla\cdot\boldsymbol{B})\,\boldsymbol{B} + (\boldsymbol{B}\cdot\nabla)\,\boldsymbol{B}\right]\\ &- \frac{1}{2}\nabla\left(\epsilon_0\boldsymbol{E}^2 + \frac{1}{\mu_0}\boldsymbol{B}^2\right) - \epsilon\frac{\partial}{\partial t}(\boldsymbol{E}\times\boldsymbol{B})\end{aligned} \tag{2.41}$$

To simplify this expression the Maxwell Stress Tensor is defined,

$$T_{ij} \equiv \epsilon_0\left(\boldsymbol{E}_i\boldsymbol{E}_j - \frac{1}{2}\delta_{i,j}\boldsymbol{E}^2\right) + \frac{1}{\mu_0}\left(\boldsymbol{B}_i\boldsymbol{B}_j - \frac{1}{2}\delta_{i,j}\boldsymbol{B}^2\right) \tag{2.42}$$

where $\delta_{i,j}$ is the Kronecker delta, which is equal to one if ($i = j$) and is equal to zero otherwise. Then,

$$\boldsymbol{f} = \nabla \cdot T_{ij} - \epsilon_0 \mu_0 \frac{\partial \boldsymbol{S}}{\partial t} \tag{2.43}$$

Finally, the total force on charges in a volume $\mathcal{V}$ is

$$\boldsymbol{F} = \oint T_{ij} \cdot da - \epsilon_0 \mu_0 \frac{\partial}{\partial t} \int_V \boldsymbol{S} d\tau \tag{2.44}$$

2.3.3 Conservation of Momentum

Since the total force on the charges q in the volume $\mathcal{V}$ is known in terms of the Poynting vector, the total momentum of the system may be described. According to mechanics, the force applied to an object is equal to the time derivative of the momentum of the object. Therefore,

$$\boldsymbol{F} = \frac{\partial \boldsymbol{P}_{\boldsymbol{Mech}}}{\partial t} = \oint T_{ij} \cdot da - \epsilon_0 \mu_0 \frac{\partial}{\partial t} \int_{\mathcal{V}} \boldsymbol{S} d\tau \tag{2.45}$$

The second integral is equal to the momentum of the electromagnetic field $\boldsymbol{P}_{\boldsymbol{em}}$, while the first integral is the rate of momentum flowing through the boundary surface.

$$\boldsymbol{P}_{\boldsymbol{em}} = \epsilon_0 \mu_0 \frac{\partial}{\partial t} \int_{\mathcal{V}} \boldsymbol{S} d\tau \tag{2.46}$$

The electromagnetic field momentum density is,

$$\boldsymbol{\rho}_{\boldsymbol{em}} = \epsilon_0 \mu_0 \boldsymbol{S} \tag{2.47}$$

2.3.4 Linear Momentum

Consider a monochromatic plane wave (2.8). The field is said to be linearly polarised (Fig. 2.1) if E_0 is real and constant. Linearly polarised fields carry linear momentum. Substituting in the form of the electric and magnetic fields into the equation for the Poynting vector (2.30)

$$S = \frac{1}{\mu_0} E_0 \times \frac{1}{c} E_0 cos^2 (kz - \omega t)\, \hat{z} \tag{2.48}$$

Taking the time average value and using $\epsilon_0 = \left(\mu_0 c^2\right)^{-1}$,

$$\langle S \rangle = \frac{1}{2} c \epsilon_0 E_0^2 \hat{z} \tag{2.49}$$

From (2.49), it is clear that momentum is being carried directly along the Z-Axis.

2.3.5 Spin Angular Momentum

Now consider a left circularly polarised electric field (Fig. 2.1) with the form,

$$E = E_0 (\hat{x} + i\hat{y})\, exp\, [i (kz - \omega t)] \tag{2.50}$$

Such a field has a constant electric field vector at a point. However, the electric field vector rotates in a plane perpendicular to the propagation axis, with an angular frequency of ω. Such fields carry spin angular momentum, or SAM. The Poynting vector of a field with SAM continues to point along the propagation axis. Yet, because the electric field rotates in the XY plane, the Poynting vector spins along its longitudinal axis.

2.3.6 Orbital Angular Momentum

If we return to the definition of the momentum density of an electromagnetic wave,

$$\boldsymbol{\rho_{em}} = \epsilon_0 \mu_0 \boldsymbol{S} = \epsilon_0 (\boldsymbol{E} \times \boldsymbol{B}) \tag{2.51}$$

we may define the orbital angular momentum. From classical mechanics it is know that an object that orbits some point in space has some orbital angular momentum (OAM). For an electromagnetic field to have OAM it too must orbit some point in space. In electrodynamics momentum density ρ may be considered the "object." Therefore,

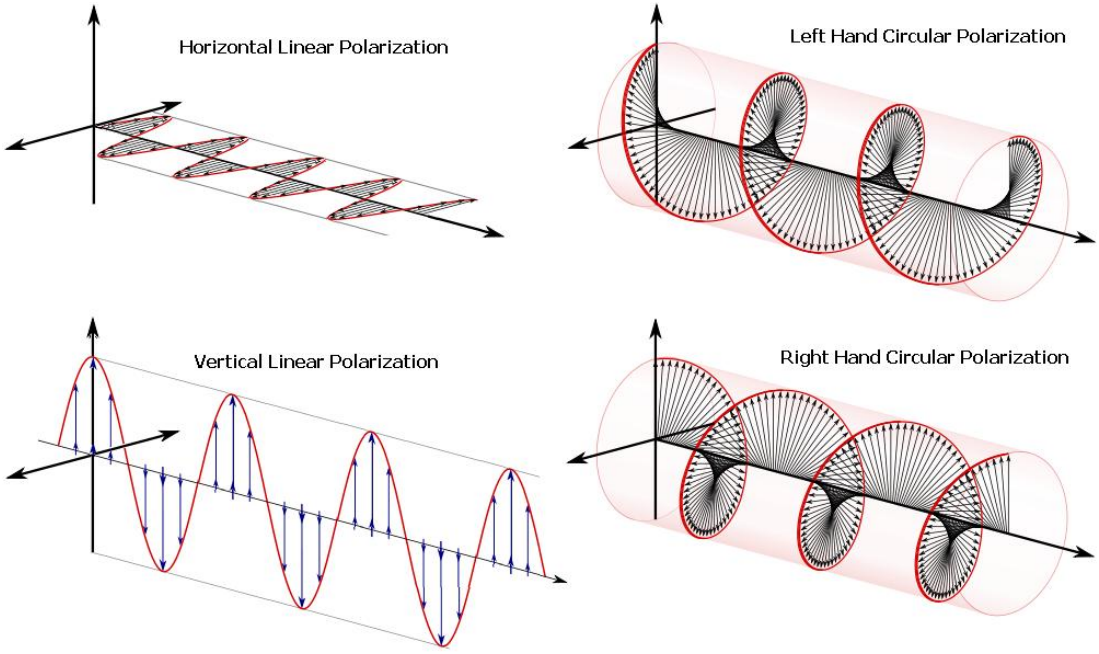

Figure 2.1: Linear and circular polarisation of the electric field. Linear polarised fields carry linear momentum, while circular polarised fields carry spin angular momentum [21].

the cross product between a radial vector from an arbitrary point in space and the momentum density vector defines the OAM.

$$\boldsymbol{l}_{em} = \boldsymbol{r} \times \boldsymbol{\rho}_{\boldsymbol{em}} = \epsilon_0 \left[\boldsymbol{r} \times (\boldsymbol{E} \times \boldsymbol{B})\right] \tag{2.52}$$

For electromagnetic beams, the reference point is often taken to be the propagation axis ($r = 0$).

2.4 Fundamental Gaussian Beam Solution to the Helmholtz Wave Equation

Time dependent plane wave solutions to the Helmholtz equation (2.1) have the form,

$$E(x, y, z, t) = E(x, y, z)\, e^{i\omega t} \tag{2.53}$$

Dropping the time dependence and replacing the electric field by an amplitude function $u(x, y, z)$ leaves,

$$E(x, y, z) = u(x, y, z)\, e^{-ikz} \tag{2.54}$$

which is a plane wave in z if the amplitude $u(x, y, z) = 1$. Non-plane wave solutions to the Helmholtz equation may be found by allowing $u(x, y, z) \neq 1$. Expanding the Helmholtz equation in cartesian coordinates gives,

$$\frac{\partial^2 E}{\partial x^2} + \frac{\partial^2 E}{\partial y^2} + \frac{\partial^2 E}{\partial z^2} + k^2 E = 0 \tag{2.55}$$

To solve this differential equation, the first and second derivatives of equation (2.54) with respect to z and the second derivative of equation (2.54) with respect to x and y must be found. The second derivative of (2.54) respect to z is,

$$\begin{aligned}
\frac{\partial^2}{\partial z^2}\left(ue^{-ikz}\right) &= \frac{\partial}{\partial u}\left(\frac{\partial}{\partial u}e^{-ikz}\right) \\
&= \frac{\partial}{\partial u}\left(u_z e^{-ikz} + (-ik)\, u^{-ikz}\right) \\
&= u_z z e^{-ikz} + (-ik)\, u_z e^{-ikz} + (-ik)\, u_z e^{-ikz} + (-ik)^2\, u e^{-ikz} \\
&= u_z z e^{-ikz} + (-2ik)\, u_z e^{-ikz} + (-ik)^2\, u e^{-ikz}
\end{aligned} \tag{2.56}$$

where the partial derivative signs have been replaced by subscripts for brevity. The second derivative of (2.54) with respect to x is,

$$\frac{\partial^2 u(x, y, z)\, e^{-ikz}}{\partial x^2} = e^{-ikz} u_{xx} \tag{2.57}$$

Repeating the differentiation for y gives a similar result. Substituting these results into equation (2.53) leaves,

$$u_{xx}e^{-ikz} + u_{yy}e^{-ikz} + u_{zz}e^{-ikz} - (2ik)\, u_z e^{-ikz} - k^2 u e^{i} ikz + k^2 u e^{i} ikz = 0 \tag{2.58}$$

Eliminating the term $exp\,(-ikz)$ and simplifying leaves the "reduced wave equation,"

$$\frac{\partial^2 u\,(x,y,z)}{\partial x^2}+\frac{\partial^2 u\,(x,y,z)}{\partial y^2}+\frac{\partial^2 u\,(x,y,z)}{\partial z^2}-2ik\frac{\partial u\,(x,y,z)}{\partial z}=0 \tag{2.59}$$

Equation (2.59) may be further simplified by the so called "paraxial approximation," which assumes that the variation of the amplitude $u\,(x,y,z)$ with respect to the propagation along z is small.

$$\left[\frac{\Delta\partial u/\partial z}{\Delta z}\right]\lambda \ll \frac{\partial u}{\partial z} \tag{2.60}$$

If the paraxial approximation is true then,

$$\frac{\partial^2 u}{\partial z^2} \ll \frac{\partial u}{\partial z} \tag{2.61}$$

The paraxial wave equation is then,

$$\frac{\partial^2 u\,(x,y,z)}{\partial x^2}+\frac{\partial^2 u\,(x,y,z)}{\partial y^2}-2ik\frac{\partial u\,(x,y,z)}{\partial z}=0 \tag{2.62}$$

In cylindrical coordinates this becomes,

$$\frac{\partial^2 u\,(r,\phi,z)}{\partial r^2}+\frac{1}{r}\frac{\partial u\,(r,\phi,z)}{\partial r}+\frac{1}{r}\frac{\partial^2 u\,(r,\phi,z)}{\partial \phi^2}-2ik\frac{\partial u\,(r,\phi,z)}{\partial z}=0 \tag{2.63}$$

To get the fundamental solution to (2.63) the additional assumption that $\partial^2 u\,(r,\phi,z)\,/\partial\phi^2 = 0$ is made. This results in the "axially symmetric paraxial wave equation,"

$$\frac{\partial^2 u\,(r,\phi,z)}{\partial r^2}+\frac{1}{r}\frac{\partial u\,(r,\phi,z)}{\partial r}-2ik\frac{\partial u\,(r,\phi,z)}{\partial z}=0 \tag{2.64}$$

From the plane wave solution, it is known that the solution should have an exponential in z. Further, (2.64) contains the first and second derivative of the wave amplitude $u\,(x,y,z)$ with respect to r. These facts imply a trial solution of,

$$u\,(r,z)=A\,(z)\,exp\left(-ikr^2/q\,(z)\right) \tag{2.65}$$

where $A(z)$ and $q(z)$ are parameters that will be found by solving the axially symmetric paraxial wave equation. The first and second derivative of (2.65) with respect to r and the first derivative of (2.65) with respect to z are needed to solve the reduced wave equation (2.64) using (2.65) . The first derivative with respect to r is,

$$\frac{\partial u}{\partial r} = \frac{-ikr}{q(z)} A(z)\, exp\left(-ikr^2/q(z)\right) \tag{2.66}$$

The second derivative with respect to r is,

$$\begin{aligned} \frac{\partial^2 u}{\partial r^2} &= \frac{\partial}{\partial r}\left(\frac{-ikr}{q(z)} A(z)\, exp\left(\frac{-ikr^2}{q(z)}\right)\right) \\ &= A(z)\, exp\left(\frac{-ikr^2}{q(z)}\right)\left[\frac{-ik}{q(z)} - \frac{k^2 r^2}{q^2(z)}\right] \end{aligned} \tag{2.67}$$

Finally, the first derivative with respect to z is,

$$\frac{\partial u}{\partial z} = \frac{dA(z)}{dz} exp\left(\frac{-ikr^2}{q(z)}\right) + A(z)\left[\frac{d}{dz} exp\left(\frac{-ikr^2}{q(z)}\right)\right] \tag{2.68}$$

To solve the right hand side of (2.68) the quantity $a/q(z)$ is substituted as,

$$\begin{aligned} u &= \frac{a}{q(z)} \\ a &= \frac{-ikr^2}{2} \end{aligned} \tag{2.69}$$

Then,

$$\begin{aligned} \frac{d}{dz} exp\left(\frac{a}{q(z)}\right) &= \frac{d}{dz}\frac{du}{du} exp(u) = \frac{d}{du} exp(u)\frac{du}{dz} \\ &= exp(u)\frac{du}{dz} = exp\left(\frac{a}{q(z)}\right)\frac{d}{dz}\frac{a}{q(z)} \end{aligned} \tag{2.70}$$

Using the substitution,

$$v = q(z) \tag{2.71}$$

It is found that,

$$\begin{aligned} \frac{d}{dz}\frac{a}{q(z)} &= a\frac{d}{dv}\frac{1}{v}\frac{dv}{dz} = \frac{-a}{v^2}\frac{dv}{dz} \\ &= \frac{-a}{q^2(z)}\frac{dq(z)}{dz} = exp\left(\frac{a}{q(z)}\right)\left(\frac{-a}{q^2(z)}\right)\frac{dq(z)}{dz} \\ &= exp\left(\frac{a}{q(z)}\right)\left(\frac{ikr^2}{2q^2(z)}\right)\frac{dq(z)}{dz} \end{aligned} \tag{2.72}$$

The first derivative of the amplitude $u(x, y, z)$ with respect to z is finally,

$$\frac{\partial u}{\partial z} = \frac{A(z)}{dz}exp\left(\frac{-ikr^2}{2q(z)}\right) + A(z)\,exp\left(\frac{-ikr^2}{q(z)}\right)\left(\frac{ikr^2}{2q^2(z)}\right)\frac{dq(z)}{dz} \tag{2.73}$$

Combining the previous results and substituting into the axially symmetric wave equation (2.63) leaves,

$$\begin{aligned} \left[\frac{-ik}{q(z)} - \frac{k^2r^2}{q^2(z)}\right]A(z) - \frac{ik}{q(z)}A(z) - 2ik\left[\frac{dA(z)}{dz} + \frac{ikr^2}{2q^2(z)}A(z)\frac{dq(z)}{dz}\right] &= 0 \\ \frac{-2ikA(z)}{q(z)} - \frac{k^2r^2A(z)}{q^2(z)} - 2ik\frac{dA(z)}{dz} + \frac{k^2r^2}{q^2(z)}A(z) &= 0 \end{aligned} \tag{2.74}$$

Simplifying (2.74) gives,

$$-2ik\left[\frac{A(z)}{q(z)} + \frac{dA(z)}{dz}\right] + \frac{k^2r^2A(z)}{q^2(z)}\left[\frac{dq(q(z))}{dz} - 1\right] = 0 \tag{2.75}$$

The left side of (2.75) depends on z, while the right side depends on r and z. Therefore each side must be equal to zero in order to satisfy (2.75). This leaves two differential equations to solve, the first of which is,

$$\frac{dq(z)}{dz} = 1 \tag{2.76}$$

Integrating over dz,

$$\int_{z_0}^{z} dq(z) = \int_{z_0}^{z} dz$$

$$q(z) - q(z_0) = z - z_0 \tag{2.77}$$

$$q(z) = q(z_0) + (z - z_0)$$

For simplicity $q(z)$ is written,

$$\frac{1}{q(z)} = \left(\frac{1}{q(z)}\right)_R - i\left(\frac{1}{q(z)}\right)_I \tag{2.78}$$

This implies,

$$exp\left(\frac{-ikr^2}{2q(z)}\right) = exp\left[\frac{-ikr^2}{2}\left(\frac{1}{q(z)}\right)_R - \frac{kr^2}{2}\left(\frac{1}{q(z)}\right)_I\right] \tag{2.79}$$

The imaginary term represents the phase variation produced by a wave front in the paraxial limit. Since $u(r) = u_0\, exp(irk)$ we postulate that,

$$\left(\frac{1}{q(z)}\right)_R = \frac{1}{R} \tag{2.80}$$

This may be checked by geometrical considerations (Fig. 2.2).

To find the phase variation $\phi(r)$ between the reference plane and spherical phase front we note that the phase is equal to the wave number multiplied by the physical separation distance between the two.

$$\phi(r) = kD \tag{2.81}$$

From Fig (2.2) the following geometrical relations are evident.

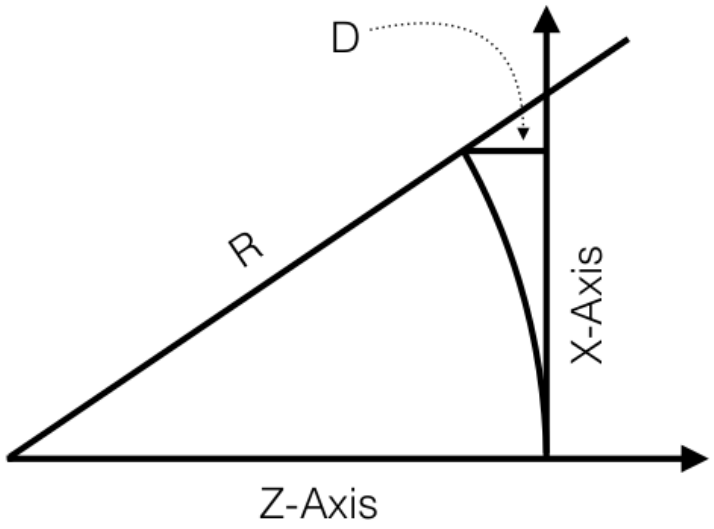

Figure 2.2: Geometry used to calculate the phase difference between a reference plane (X-Axis) and a spherical phase front.

$$\begin{aligned} R &= x + D \\ x &= Rcos\,(\theta) \\ sin\,(\theta) &= \frac{r}{R} \\ \theta &= \frac{r}{R} \end{aligned} \tag{2.82}$$

To find $\phi\,(r)$ the small angle approximations in (2.83) are used.

$$\begin{aligned} cos\,(\theta) &\approx 1 - \frac{\theta^2}{2} \\ sin\,(\theta) &\approx \theta \end{aligned} \tag{2.83}$$

The physical distance D between the reference plane and spherical phase front is found from R,

$$R = Rcos(\theta) + D$$

$$\begin{aligned} D &= R(1 - cos(\theta)) \\ &= R\left(1 - 1 + \frac{\theta^2}{2}\right) \\ &= R\frac{\theta^2}{2} \\ &= \frac{r^2}{2R} \end{aligned} \tag{2.84}$$

This results in a phase variation of,

$$\phi(r) = kD = \frac{kr^2}{2R} \tag{2.85}$$

The two phase terms may be equated, which results in the conclusion that the real part of the complex beam parameter $q(z)$ being equal to the reciprocal to the radius of curvature.

$$exp\left[\frac{-ikr^2}{2}\frac{1}{q(z)_R}\right] = exp\left[-i\phi(r)\right]$$

$$\begin{aligned} \frac{kr^2}{2}\frac{1}{q(z)_R} &= \frac{kr^2}{2R} \\ \frac{1}{q(z)_R} &= \frac{1}{R} \end{aligned} \tag{2.86}$$

To find the physical meaning of the imaginary part of the complex beam parameter $q(z)$ we note a that Gaussian distribution is known to have the form,

$$f(r) = f(0)\,exp\left(-\left(\frac{r}{r_0}\right)^2\right) \tag{2.87}$$

We can then equate

$$exp\left(-\frac{r}{r_0}^2\right) = exp\left(-\frac{kr^2}{2}\frac{1}{q(z)_I}\right) \tag{2.88}$$

So,

$$\frac{r^2}{r_0^2} = \frac{kr^2}{2}\left(\frac{1}{q(z)}\right)_I \tag{2.89}$$

where r_0 denotes the $(1/e)$ amplitude level of the beam. The beam radius $\omega(z)$ is then defined,

$$r_0 \equiv \omega(z) \tag{2.90}$$

Substituting (2.83) into (2.88) shows that,

$$\left(\frac{1}{q(z)}\right)_I = \frac{2}{kr_0^2} = \frac{2}{k\omega^2(z)} \tag{2.91}$$

The final form of $q(z)$ may then be written as,

$$\frac{1}{q(z)} = \frac{1}{R} - \frac{i\lambda}{\pi\omega^2(z)} \tag{2.92}$$

At $z = 0$,

$$u(r,0) = A(0)\,exp\left(\frac{-ikr^2}{2q(0)}\right) \tag{2.93}$$

and,

$$\omega(0) = \sqrt{\frac{\lambda q(0)}{i\pi}} \tag{2.94}$$

The exponential containing the complex beam parameter may be rewritten in terms of the beam radius so that,

$$\begin{aligned} exp\left(\frac{-ikr^2}{2q\left(0\right)}\right) &= exp\left(\frac{-i2\pi r^2}{2\lambda q\left(0\right)}\right) \\ exp\left(\frac{-i\pi r^2}{\lambda q\left(0\right)}\right) &= exp\left(\frac{-r^2}{\omega_0^2}\right) \end{aligned} \tag{2.95}$$

Combining (2.93) with the result from (2.95).

$$u\left(r,0\right) = A\left(0\right) exp\left(\frac{-r^2}{\omega_0^2}\right) \tag{2.96}$$

This matches the Gaussian distribution form of (2.87). To find the form of $\omega\left(z\right)$ we can rewrite $q\left(z\right)$ as,

$$q\left(z\right) = \frac{i\pi\omega_0^2}{\lambda} + z \tag{2.97}$$

Taking the real part gives,

$$\begin{aligned} \left(\frac{1}{q\left(z\right)}\right)_R &= \left(\frac{\lambda}{i\pi\omega_0^2 + z\lambda}\right)_R \\ \left[\frac{\lambda\left(-i\pi\omega_0^2 + z\lambda\right)}{i\pi\omega_0^2 + z\lambda}\right]_R &= \left[\frac{z\lambda^2 - i\pi\lambda\omega_0^2}{\pi^2\omega_0^4 + z^2\lambda^2}\right]_R \\ \frac{1}{R} &= \frac{z\lambda^2}{\pi^2\omega_0^4 + z^2\lambda^2} \end{aligned} \tag{2.98}$$

$$R = \frac{\pi^2\omega_0^4 + z^2\lambda^2}{z\lambda^2} = z + \frac{\pi^2\omega_0^2}{z\lambda^2}$$

Leaving [22],

$$\boxed{R\left(z\right) = z + \frac{1}{z}\left(\frac{\pi\omega_0^2}{\lambda}\right)^2} \tag{2.99}$$

The imaginary part of the complex beam parameter gives,

$$\left(\frac{1}{q(z)}\right)_I = \frac{\pi\omega_0^2\lambda}{\pi^2\omega_0^2 + z^2\lambda^2} = \frac{\lambda}{\pi\omega}$$

$$\frac{\pi\omega_0^2\omega^2}{\pi^2\omega_0^2 + z^2\lambda^2} = 1 \tag{2.100}$$

$$\pi^2\omega_0^2\omega = \pi^2\omega_0^4 + z^2\lambda^2$$

$$\omega^2 = \omega_0^2 + \frac{z^2\lambda^2}{\pi^2\omega_0^2}$$

Giving [22],

$$\boxed{\omega(z) = \omega_0\left[1 + \left(\frac{z\lambda}{\pi\omega_0^2}\right)^2\right]} \tag{2.101}$$

The second differential equation from (2.75) is,

$$\frac{\partial A(z)}{\partial z} = \frac{-A(z)}{q(z)}$$

$$\frac{dA(z)}{A(z)} = \frac{-dz}{q(z)} \tag{2.102}$$

Substituting in the definition of the complex beam parameter from (2.77),

$$\frac{dA(z)}{A(z)} = \frac{-dq(z)}{q(z)}$$

$$\int \frac{dA(z)}{A(z)} = \int \frac{-dq(z)}{q(z)} \tag{2.103}$$

$$ln(A(z)) - ln(A(0)) = -[ln(q(z)) - ln(q(0))]$$

$$ln\left(\frac{A(z)}{A(0)}\right) = ln\left(\frac{q(0)}{q(z)}\right)$$

Then, using the definition of the complex beam parameter from (2.97)

$$\frac{A(z)}{A(0)} = \frac{q(0)}{q(z)} = \frac{i\pi\omega_0^2}{\lambda\left(i\pi\omega_0^2/\lambda + z\right)}$$

$$= \frac{i\pi\omega_0^2}{i\pi\omega_0^2 + z\lambda} \cdot \frac{-i\pi\omega_0^2 + z\lambda}{-i\pi\omega_0^2 + z\lambda}$$

$$= \frac{\pi^2\omega_0^4 + i\pi\omega_0^2 z\lambda}{\pi^2\omega_0^4 + z^2\lambda^2} \cdot \frac{1/\pi^2\omega_0^4}{1/\pi^2\omega_0^4} \tag{2.104}$$

$$\frac{A(z)}{A(0)} = \frac{1 + iz\lambda/\pi\omega_0^2}{1 + \left(z\lambda/\pi\omega_0^2\right)^2}$$

Using the following trigonometric substitution,

$$tan(\phi_0) = \frac{z\lambda}{\pi\omega_0^2} \tag{2.105}$$

we find that,

$$\frac{A(z)}{A(0)} = \frac{1 + i\,tan(\phi_0)}{1 + i\,tan^2(\phi_0)}$$

$$= \frac{1 + i\,sin(\phi_0)/cos(\phi_0)}{1 + i\,sin^2(\phi_0)/cos^2(\phi_0)}$$

$$= \frac{(cos(\phi_0) + i\,sin(\phi_0))/cos(\phi_0)}{(cos^2(\phi_0) + i\,sin^2(\phi_0))/cos^2(\phi_0)} \tag{2.106}$$

$$\frac{A(z)}{A(0)} = cos(\phi_0)(cos(\phi_0) + i\,sin(\phi_0)) = cos(\phi_0)\,exp(i\phi_0)$$

Since $\phi_0 = tan^{-1}\left(\lambda z/\pi\omega_0^2\right)$,

$$cos\left(\phi_0\right) = \frac{1}{sec\left(\phi_0\right)} = \frac{1}{\sqrt{1 + tan^2\left(\phi_0\right)}} = \frac{1}{\sqrt{1 + \phi_0^2}}$$

$$= \frac{1}{\sqrt{1 + \left(\lambda z / \pi\omega_0^2\right)^2}} \tag{2.107}$$

$$cos\left(\phi_0\right) = \frac{\omega_0}{\omega}$$

Finally, the complex beam amplitude is,

$$u\left(r, z\right) = \frac{\omega_0}{\omega} exp\left(-\frac{r^2}{\omega^2} - \frac{i\pi r^2}{R} + i\phi_0\right) \tag{2.108}$$

and the electric field is,

$$E\left(r, z\right) = \frac{\omega_0}{\omega} exp\left(-\frac{r^2}{\omega^2} - ikz - \frac{i\pi r^2}{R} + i\phi_0\right) \tag{2.109}$$

To normalise the electric field we set,

$$\int |E|^2 \cdot 2\pi r dr = 1$$

$$\int \left(E^* \cdot E\right) \cdot 2\pi r dr = 1$$

$$\int A\left(z\right)^2 \frac{\omega_0^2}{\omega} exp\left(-2r^2/\omega\right) 2\pi r dr = 1$$

$$\frac{A^2\omega_0^2}{\omega^2} 2\pi \left[\frac{-1}{4}\omega^2 exp\left(-2r^2/\omega^2\right)\right]_0^\infty = 1 \tag{2.110}$$

$$\frac{-A^2\omega^2\pi}{2}\left(0 - 1\right) = 1$$

$$A^2 = \frac{2}{\pi\omega_0^2}$$

The normalisation constant is then,

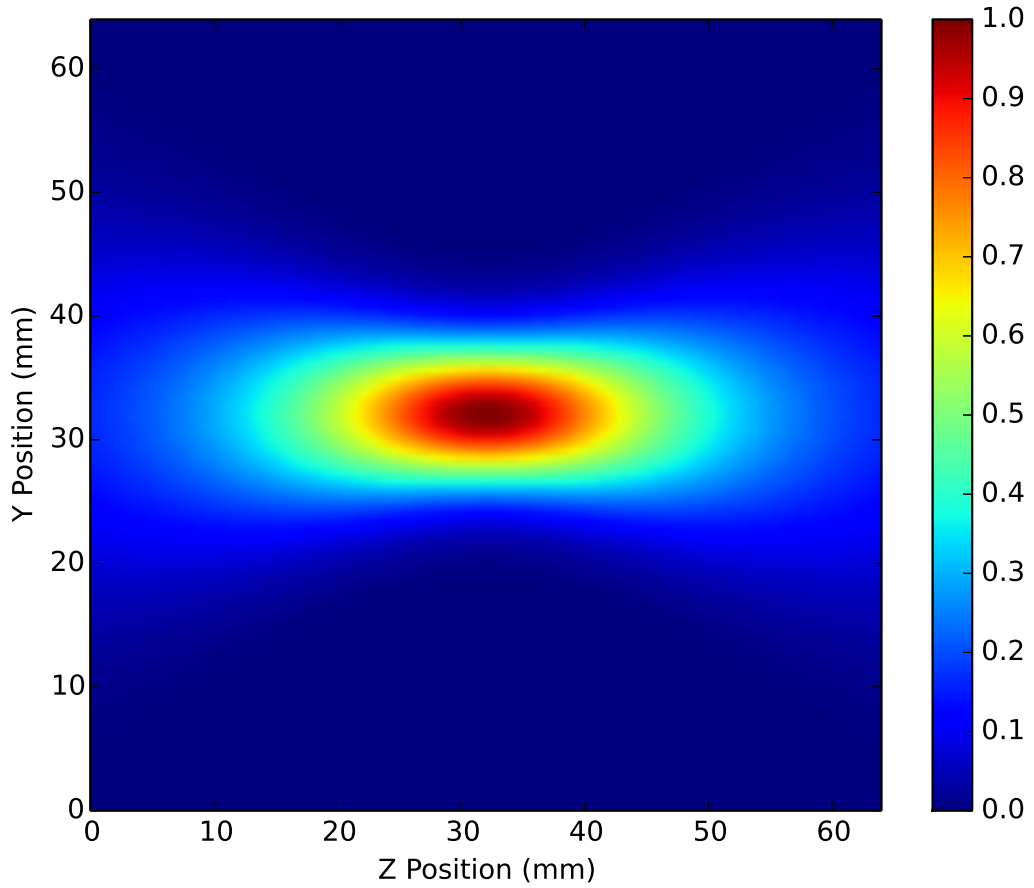

Figure 2.3: A Gaussian beam profile in the YZ plane showing divergence characteristics and the central beam waist.

$$A = \sqrt{\frac{2}{\pi\omega_0^2}} \tag{2.111}$$

The normalised fundamental beam solution to the axially symmetric paraxial beam equation is then (Fig. 2.3),

$$\boxed{\begin{aligned} E(r,z) &= A\left(\frac{\omega_0}{\omega}\right) exp\left(-\frac{r^2}{\omega^2} - ikz - \frac{i\pi r^2}{R} + i\phi_0\right) \\ E(r,z) &= \sqrt{\frac{2}{\pi\omega}} exp\left(-\frac{r^2}{\omega^2} - ikz - \frac{i\pi r^2}{R} + i\phi_0\right) \end{aligned}} \tag{2.112}$$

2.5 Higher Order Modes in Cylindrical Coordinates

A general solution to the Helmholtz equation must allow for variations as a function of the radius r and in the azimuthal angle ϕ. Knowing this, a different trial solution for the Helmholtz equation is,

$$u(r,\phi,z) = A(z)\, exp\left[\frac{-ikr^2}{2q(z)}\right] S(r)\, exp\left[i\, l\phi\right] \tag{2.113}$$

where $exp\left[i\, l\phi\right]$ is an azimuthal phase variation and $S(r)$ is a radial amplitude function. The form of $S(r)$ may be solved for via the paraxial wave equation. When completed, the form of $S(r)$ is,

$$S(r) = \left(\frac{\sqrt{2}r}{\omega(z)}\right)^{l} L_{\rho,l}\left(\frac{2r^2}{\omega^2(z)}\right) \tag{2.114}$$

where $L_{\rho,l}$ denotes the Laguerre polynomials. Here, l **represents the azimuthal mode number**. It will be shown in Sec. 2.6 that any beam with a non zero azimuthal mode number carries orbital angular momentum. The number ρ **corresponds to the number of radial nodes in the beam, and therefore is known as the radial mode number**. The electric field is given by,

$$\begin{aligned} E_{\rho,l}(r,\phi,z) = &\left[\frac{2\rho!}{\pi(\rho+l)!}\right]^{0.5} \frac{1}{\omega(z)}\left[\frac{\sqrt{2}r}{\omega(z)}\right]^{l} L_{\rho,l}\left(\frac{2r^2}{\omega^2(z)}\right) \\ &exp\left[\frac{-r^2}{\omega^2(z)} - ikz - \frac{i\pi r^2}{\lambda R(z)} - i(2\rho+l+1)\phi_0(z) + i\, l\phi\right] \end{aligned} \tag{2.115}$$

Equation (2.115) shows that higher order modes, also called Laguerre Gaussian (LG) modes (Fig. 2.4) after the inclusion of the Laguerre polynomials, are characterised by a beam radius and curvature just as is the case with the fundamental mode. However, the radial profile of high order LG beams exceeds that of the fundamental mode. The radius of the maximum intensity, r_{max} in a higher order mode with $\rho = 0$ is [23],

$$r_{max} = \sqrt{l\frac{\omega^2(z)}{2}} \tag{2.116}$$

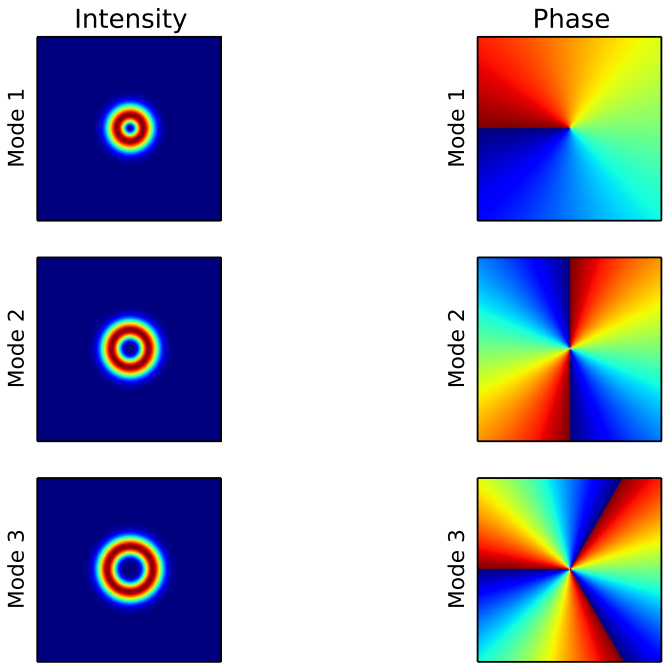

Figure 2.4: Intensity and phase of the first three Laguerre Gaussian modes with rho = 0.

and the spot size is,

$$\sigma(z)_{\rho,l} = \omega(z)\sqrt{2\rho + l + 1} \tag{2.117}$$

While both azimuthal (l) and radial (ρ) mode numbers can influence the size of a LG beam, it should be remembered that OAM is only associated with the azimuthal mode number.

2.6 Orbital Angular Momentum

To show that LG beams carry OAM, we follow the important results presented in [1]. For a linearly polarised LG beam, the momentum density is,

$$P = \frac{1}{c^2}S = \frac{1}{c}\left[\frac{rz}{z^2 + z_r^2}\hat{r} + \frac{l}{kr}\hat{\phi} + \hat{z}\right]\left|U_{l,\rho}\right|^2 \tag{2.118}$$

where $U_{l,\rho}$, is the found by removing the propagation phase factor from (2.115). The angular momentum is found by taking $\epsilon_o r \times S$.

$$L = \left[\frac{-l}{\omega}\frac{z}{r}\hat{r} + \frac{r}{c}\left(\frac{z^2}{z^2 + Z_r^2} - 1\right)\hat{\phi} + \frac{l}{\omega}\hat{z}\right]\left|U_{l,\rho}\right|^2 \tag{2.119}$$

The z-component of L is then, [1]

$$L_z = \frac{cPl}{\omega} = \frac{2\pi c\hbar l}{\lambda\omega} = \frac{ck\hbar l}{ck} = l\hbar \tag{2.120}$$

where P is the z-component of the linear momentum (2.118). This proves that LG beams carry a quantised angular momentum in the z-direction equal to $l\hbar$.

2.7 Conclusion

In this chapter the Helmholtz wave equation was initially solved with a plane wave solution. This allowed for the analysis of energy and momentum in electrodynamics, and led to the definition of the Poynting vector. It was also shown that plane wave solutions can carry angular momentum. It was then shown that the Helmholtz equation also supports non-planar solutions. Using the paraxial wave equation approximation to the Helmholtz wave equation, and by assuming no azimuthal dependence of the solution, the fundamental Gaussian beam was derived. Higher order modes were then described using cylindrical co-ordinates, by allowing for a radial amplitude function and azimuthally dependent phase. Finally, it was demonstrated that higher order Gaussian beams carry quantised OAM.

[1] It should be noted that the L denoting orbital angular momentum is different and distinct from $L_{l\rho}$ that are the Laguerre Polynomials

3

Generating Beams with Orbital Angular Momentum

3.1 Introduction

Electromagnetic (EM) fields can garner OAM through natural or synthetic (laboratory generated) mechanisms. In either case there are three general ways that an EM field can be forced into an OAM state. The simplest way for an EM field to gain OAM is by transmission through a medium that applies an azimuthal phase shift. Spiral Phase Plates (SPPs) [24–28], atmospheric turbulence [29–44], and astrophysical turbulent assemblages of molecules or atoms (TAMA) [15] all work via induced phase shifts. Conservation of momentum is a second method by which OAM may be imparted onto a traveling EM field. For linear systems, the total angular momentum J of the field may be represented as the sum of the spin and orbital momentum components,[1]

$$J = L + S \tag{3.1}$$

Conservation of momentum states that the value of J, for a system, must not change over time. However, the values of spin S and orbital L momentum may change. Q-plates

[1] Total angular momentum J should not be confused with the J representing current used in Chapter 2

are devices that are designed to take advantage of the freedom to exchange momentum between spin and orbital states [45, 46]. A third mechanism for OAM generation is through coherent interference. An example of this is the diffractive hologram [47], often encoded on spatial light modulators (SLMs) to impart OAM onto laser beams. Other examples of such systems are phased antenna arrays [48, 49], spherical wave interference [50] and laser beam arrays [51].

3.2 Natural Generation

This section will explore some of the natural mechanisms that can impart OAM states onto EM fields. Several possible astrophysical sources that have been proposed, will be discussed. In addition, the use of a SPP as a chronograph will be reviewed, which could possibly have produced the first detection of OAM modes from an astrophysical source. A summary of a significant series of papers produced by D. Sanchez and D. Oesch will follow. Their work begins by theoretically showing that OAM states may be generated by turbulence in the Earth's atmosphere. The theoretical work is then supported by laboratory experiments and finally by actual observations.

3.2.1 Astrophysical Mechanisms

The concept of probing astrophysical sources for OAM radiation was recently introduced by M. Harwit [14]. Literature in the subject area is sparse, primarily due to the respective young age of the OAM astrophysics field. Additionally, the technology required to make observations is still in the research and development phase. *The primary purpose of this thesis is to advance OAM technology to allow astronomers the opportunity to make astrophysical OAM observations.* Several possible sources were put forward in [14] including masers, luminous point sources, Kerr black holes and the Cosmic Microwave Background (CMB) radiation. Masers are a particularly interesting source, which could generate OAM through a Q-plate like mechanism [52]. Orbital angular momentum

signals in a maser can also be amplified through standard maser amplification processes [53]. Recently, OAM was detected from luminous point sources imbedded in TAMA regions [15]. Harwit also suggested that radiation scattering from a Kerr, or rotating, black hole could absorb some of the black hole's angular momentum. This was discussed in more detail in [54], which showed that as light passed through spacetime wrapping around a black hole, it acquired a non-zero OAM mode spectrum. Harwit's final suggestion was that the CMB could be a source of OAM radiation. Specifically, gravitational discontinuities on the last scattering surface of the CMB would impart a discontinuity to the emitted radiation. Measurements of an OAM spectrum from the CMB would yield information on the type and strength of gravitational discontinuities on the last scattering surface. In addition laser pumped high order atomic transitions have been shown to facilitate OAM generation [55–58]. Stationary and rotating plasma vortices also radiate OAM [59]. Finally, Compton backscattering of photons [60–63] induces OAM while electron beams with OAM may radiate photons with OAM under certain conditions [4, 64].

Clearly there is a growing interest in detecting OAM radiation from astrophysical sources. Yet, the field is in its infancy and developing instruments and techniques is currently the most prominent challenge. Determining exactly what scientific parameters will be made measurable by OAM observations is difficult to predict. The most promising work on this subject is detailed in the next subsection on "Atmospheric and Astrophysical Turbulence." There, researchers are able to measure the number of turbulent atmospheric layers, their vertical separation and relative velocities by measuring optical OAM generated by passing through the medium. It is easy to imagine extending this type of measurement to more distant sources. Perhaps measurements of OAM from interstellar media or nebula, for example, could lead to a deeper understanding of the physical structure and flow characteristics of the media. Like any other measurement, observations of OAM will allow astronomers to calculate characteristic parameters of the generating mechanisms. If OAM is generated by the CMB, this could lead to a determination of the fluctuations on the last scattering surface. Another example

would be measurements of OAM generated by plasma vortices, which would lead to measurements of the rotational flow. Furthermore, synchrotron generated OAM could lead to measurements of electron velocities and trajectories. In the end, the most important measurements of astrophysical OAM are the ones that we have not predicted.

3.2.2 Atmospheric and Astrophysical Turbulence

In a significant series of papers [29–44], researchers from the United States Air Force Research Labs showed that turbulent mediums can create measurable OAM.

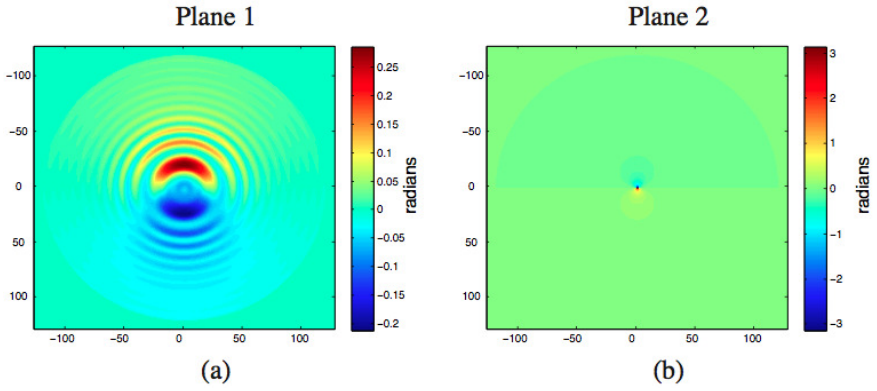

Figure 3.1: Numerical example of the precursor (a) and generated (b) phase a branch point separation of $\delta = 3$ (arbitrary units), and a Fresnel number of $N_F = 31$. Adapted from [41].

The group begin by theoretically showing that under the right conditions a beam from a monochromatic point source passing through a turbulent medium will contain branch points (BPs), or 2π circulations in phase (Fig. 2.4). It was found that the strength of the turbulence determines the average propagation distance, from the turbulent surface, at which BPs are generated. As the beam continues to propagate, the number of BPs increases until a saturation level is reached. Additionally, BPs must be created in pairs of opposite mode number in order to conserve momentum. Measurements of inter and intra- BP pair separation allows for measurements of the number, velocity, separation and strength of the layers comprising the turbulent medium. (Inter-BP-pair

separation (δ) is defined as the radial distance between the positive and negative BPs, which make up a BP pair.) This is accomplished by measuring the BP phase enabling a calculation of the precursor, or generating phase structure (Fig. 3.1), through a Fresnel transform [41]. The fresnel number is defined as $N_F = R^2/(L\lambda)$, where R is the largest radius in the optical system and L is the propagation distance. In [41], R is taken to be the radius of the propagating optical wave in which BPs will be created.

These theoretical predictions were confirmed with indoor (Fig. 3.2) and outdoor experiments at a U.S. Air Force optical testing range. This body of work is important and relevant because it demonstrates that radiation with OAM may be generated by natural means. Furthermore, measurements of OAM can be used to calculate physical characteristics of the generating medium. Recently, the group also measured OAM signals from stars embedded in turbulent medium [15], representing the first claimed measurement of OAM from astrophysical sources.

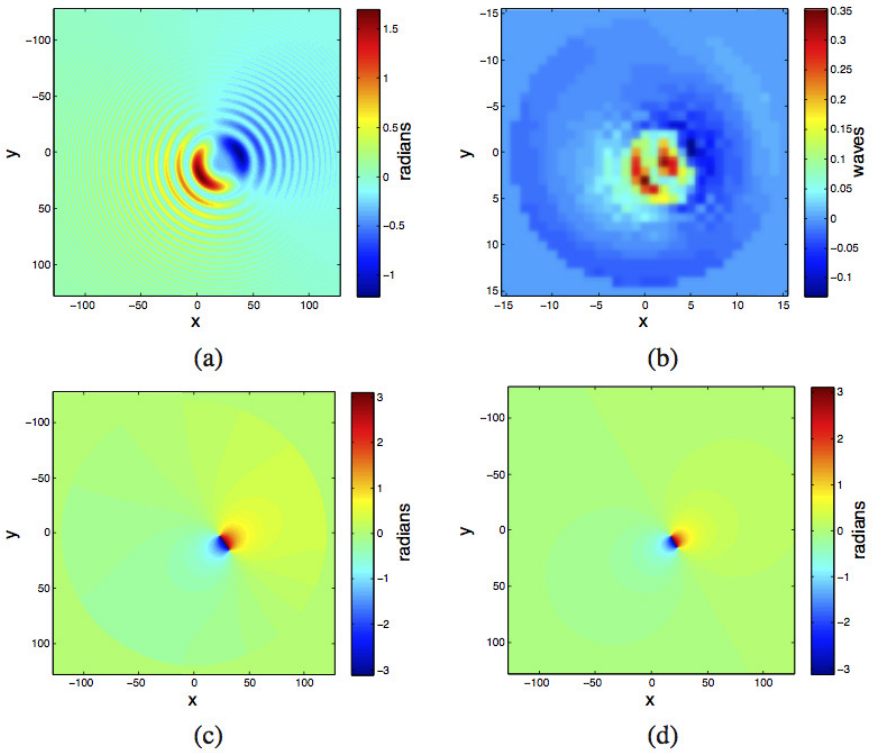

Figure 3.2: Numerically calculated precursor phase (a) and desired BP phase (d) for experimental validation. The desired BP phase was created by sending phase commands to an adaptive optics system (b), which resulted in a measured phase (d) at a wave front sensor plane. This experiment showed that measurement of a BP pair can be used to calculate the form of the generating phase plane. Adapted from [41].

3.3 Synthetic Generation and Phase Modulating Devices

The most common method for manipulating OAM states is through the use of a phase modulating device (PMD). There are three main categories of PMDs. The first are known as holograms, which are specially designed diffraction gratings with a centrally located singularity. A second type of PMD is known as a Q-plate. Q-plates are inhomogeneous and anisotropic dielectric slabs of material with a surface geometry that utilises the conservation of momentum to induce a change in SAM (See Sec: 2.3.5), thereby generating OAM. The third type of PMD, which this thesis focuses on, is the spiral phase plate (SPP). An SPP is a dielectric slab of material that has a helically

machined surface. Radiation passing through the SPP experiences an azimuthal phase shift. If the phase shift is an integer multiple l of 2π, the outgoing radiation occupies an OAM state equal to l.

3.3.1 Holograms

Holograms are diffraction gratings with a forked singularity in their centre [47, 65] (Fig.3.3). Holograms are typically generated on spatial light modulators[2] (SLMs). The profile of a hologram is the interference pattern of a tilted plane wave and the desired output beam. In order to generate a beam with OAM, the desired output beam must have an $exp\,(il\phi)$ phase dependence. When the hologram is illuminated by a plane wave the desired OAM beam is produced. If a mode l OAM beam illuminates the hologram a plane wave is generated. The hologram profile can be defined mathematically by the hologram transfer function,

$$H = |\Psi_1 + \Psi_2|^2 = \left|e^{ik_x x} + e^{il\phi}\right|^2 = 2\left[1 + cos\,(kx - l\phi)\right] \tag{3.2}$$

where k_x is the wave number in the propagation direction, and $\phi = tan^{-1}\,(y/x)$ is the azimuthal angle.

The intensity pattern produced by a hologram is the Fourier transform of the product of the input beam and (3.2) (Fig. 3.4).

$$I = \mathcal{F}\left[e^{-(r/\omega)^2}\left|e^{ik_x x} + e^{il\phi}\right|^2\right] \tag{3.3}$$

where $r = \sqrt{x^2 + y^2}$ and ω is the beam radius.

In addition to being able to program holograms to SLMs displays, holograms may be manufactured via lithographic techniques or by printing of the hologram transfer function (3.2) to transparencies [65]. Furthermore, holograms are advantageous because they sort OAM modes according to the azimuthal mode number (Eq. 3.2). This lends holograms to be perfect devices for separating superimposed OAM modes, especially at

[2]SLMs are programable liquid crystal displays

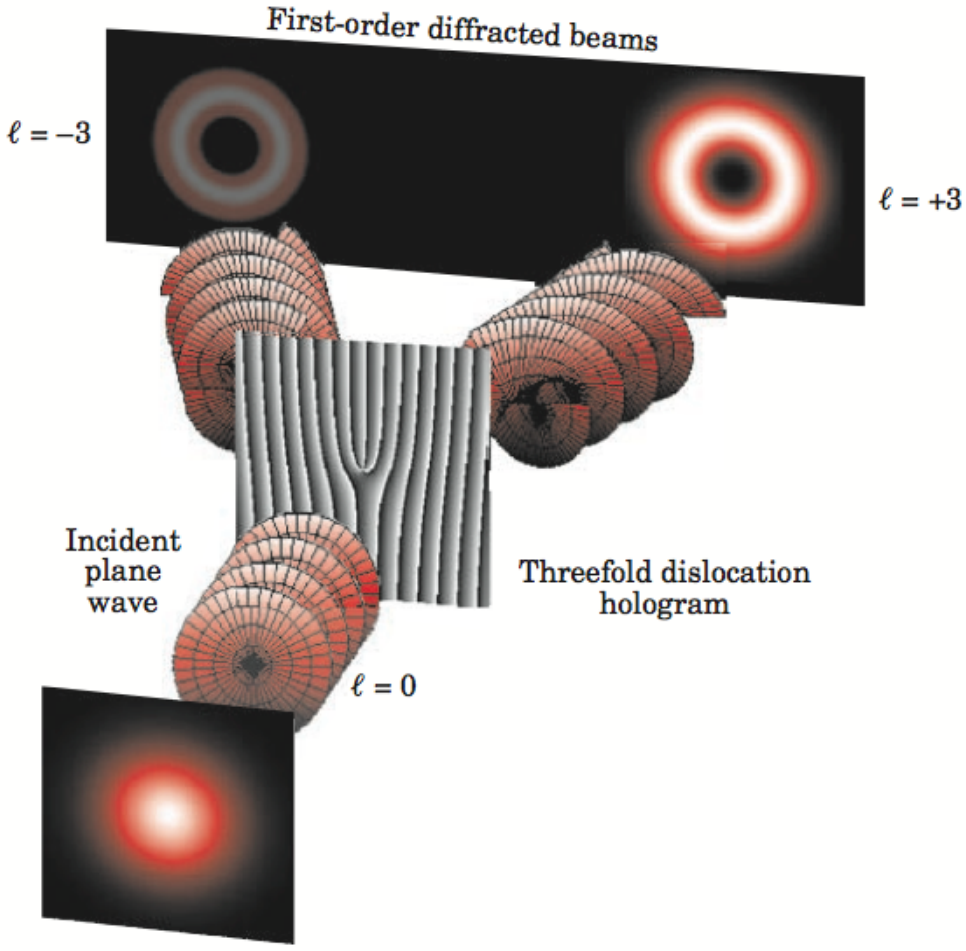

Figure 3.3: The generation of beams with OAM by passing a Gaussian beam through a hologram [2]. An incident Gaussian beam $l = 0$ passes through a $\Delta l = 3$ hologram and is split into two $l = -3$ and $l = 3$ beams.

optical wavelengths [66, 67]. SLM holograms have also been used to in OAM adaptive optics-like systems [68]. Finally, some work has also be done to construct holograms for millimetre wavelength beams [69, 70].

3.3.2 Q-Plates

Q-plates are specialised dielectric gratings, which are inhomogeneous and anisotropic. Inhomogeneity implies that the plate is not uniform, or that one point on the plate will

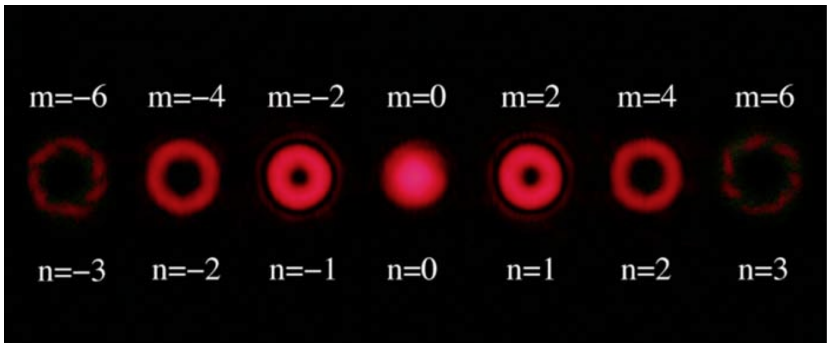

Figure 3.4: Holographic diffraction pattern generated by passing a Gaussian beam through a $\Delta l = 2$ computer generated hologram [65]. The OAM state m of each diffraction order n is multiplied by Δl.

be characterised differently than another (Fig 3.5). Anisotropic implies that the plate will have different properties along two different vectors having the same origin. Spin only momentum transfer occurs in anisotropic materials such as wire grid polarisers. Orbital only momentum transfer occurs in inhomogeneous isotropic materials such as a SPP. Since a Q-plate is both inhomogeneous and anisotropic, spin to orbit momentum conversion is possible. Q-plates convert one SAM state into the other, and in the process generates an OAM state through the conservation of momentum. Rotationally symmetric surface gratings lead to momentum conversion only between the input and output fields, while non-rotationally symmetric geometries result in some OAM transfer to the Q-plate itself.

The surface grating geometry is defined by the optical axis, which forms an angle with the X-Axis given by (Fig. 3.6) [45],

$$\alpha\left(r,\phi\right) = q\phi + \alpha_0 \tag{3.4}$$

where the parameters q and α_0 are constants.

The relation between the input and output field is described by the use of the Jones matrix,

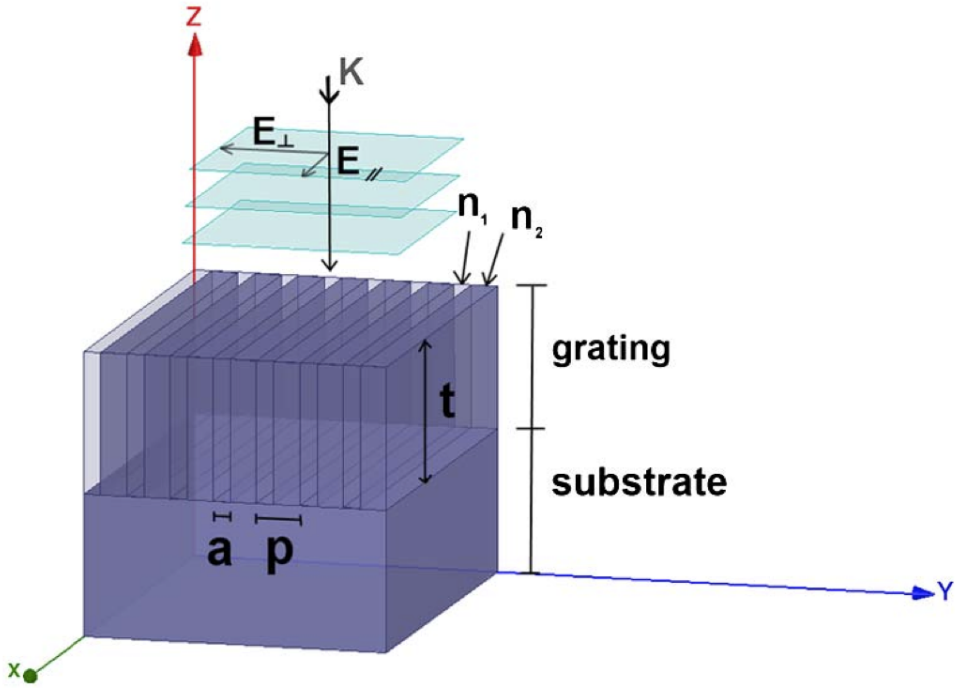

Figure 3.5: Q-plate dielectric grating structure with index of refraction n_2 (n_1 is the index of refraction of air) [46].

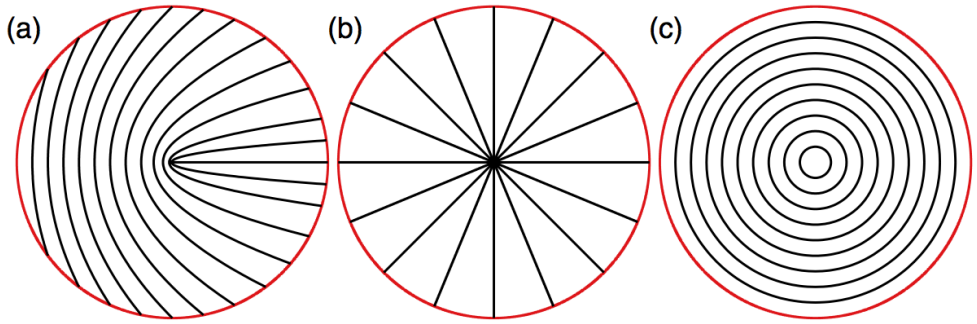

Figure 3.6: Three Q-plate geometries (a) $q = 1/2$ and $\alpha_0 = 0$ for $l = \pm 1$ generation, (b) $q = 1$ and $\alpha_0 = 0$ for $l = \pm 2$ generation and (c) $q = 1$ and $\alpha_0 = \pi/2$ for $l = \pm 2$ generation. (b) and (c) are rotationally symmetric, eliminating momentum transfer to the Q-plate. Adapted from [45].

$$M = \mathbf{R}(-\alpha) \cdot \begin{pmatrix} 1 & 0 \\ 0 & -1 \end{pmatrix} \cdot \mathbf{R}(\alpha) = \begin{pmatrix} cos(2\alpha) & sin(2\alpha) \\ sin(2\alpha) & -cos(2\alpha) \end{pmatrix} \tag{3.5}$$

For a left circularly polarised input wave $E_{in} = E_0 \times [1, i]$ the output wave is,

$$E_{out} = M \cdot E_{in} = E_0 e^{i2\alpha} \begin{bmatrix} 1 \\ i \end{bmatrix} = E_0 e^{i2q\phi} e^{i2\alpha_0} \begin{bmatrix} 1 \\ -i \end{bmatrix} \tag{3.6}$$

where α has been replaced by (3.4). Equation (3.6) shows that the initial left circularly polarised beam was converted to a right circularly polarised beam. This confirms the statement that Q-plates exchange SAM states. However, (3.6) also shows that the field gained a phase factor of $exp[i2(q\phi + \alpha_0)]$. Equating the Q-plate phase factor with the OAM phase $exp(il\phi)$ shows that $l = 2q$. Switching the input field from left circular to right circular adds a minus sign to the Q-plate phase factor such that $l = -2q$. Therefore, the input SAM state determines the sign of the output OAM state.

A Q-plate has been designed to work at 100 GHz by Maccalli et al, and the results are presented in [46]. Here, a Q-plate with a geometry defined by $q = 1$ and $\alpha_0 = \pi/2$ was manufactured out of nylon ($n \approx 1.73$). The grating parameters necessary to induce the proper birefringence to generate OAM are described in [71]. The level of birefringence is $\Delta n_B = n_{\parallel} - n_{\perp}$, while the grating thickness is $t = \lambda/(2\Delta n_B)$ and the periodicity P must obey $P \ll \lambda/2$ in order to not induce diffraction. Both indices of refraction are found by [71],

$$n_{\parallel} = \sqrt{n_1^2\sigma + n_2^2(1-\sigma)} \tag{3.7}$$

and

$$n_{\perp} = \frac{1}{\sqrt{\frac{1}{n_1^2}\sigma + \frac{1}{n_2^2}(1-\sigma)}} \tag{3.8}$$

where σ is the ratio of opening to period. Using $n_1 = 1$ and $n_2 = 1.73$ while choosing $\sigma = 0.5$ results in a birefringence of $\Delta n_B = 0.189$. From this the grating

thickness can be calculated. For this example the required thickness is $t = 7.94\,\text{mm}$. Finally, be choosing an opening length of 0.5 mm, and with $\sigma = 0.5$, a periodicity of 1.0 mm is calculated. Maccalli et al. started with these calculated parameters and optimised them using the software package HFSS. The modified Q-plate parameters are displayed in Table 1 of [46].

3.3.3 Spiral Phase Plates

Perhaps the simplest PMD is the SPP. SPPs are dielectric materials that vary in thickness as a function of the azimuthal angle [72]. Radiation passing through the plate experiences an azimuthal dependent phase shift, producing OAM (Fig. 3.7).

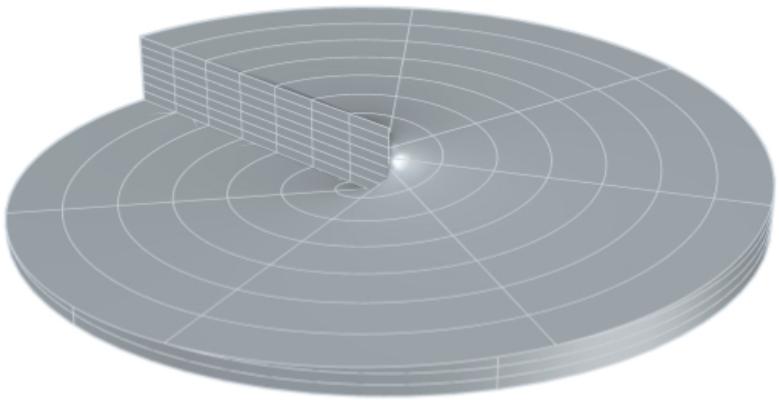

Figure 3.7: A CAD drawing of an $\Delta l = \pm 1$ spiral phase plate.

A simple ray optics calculation shows how a SPP generates beams with quantised OAM. The phase of a wave in SPP material is,

$$\Phi = kx(\phi, r) = \frac{2\pi}{\lambda} x(\phi, r) \tag{3.9}$$

where k is the wave number, λ is the wavelength and x is the optical thickness of the SPP at a specified azimuthal angle ϕ and radius r. The optical thickness is defined as,

$$x(\phi, r) = n_1 d(\phi, r) \tag{3.10}$$

where n_1 is the index of the refraction of the SPP material and d is the physical thickness of the SPP at a point (ϕ, r). The unwrapped SPP profile (A plot of h versus ϕ for some specific radius.) is used to determine the functional representation of $d(\phi, r)$ (Fig. 3.8) .

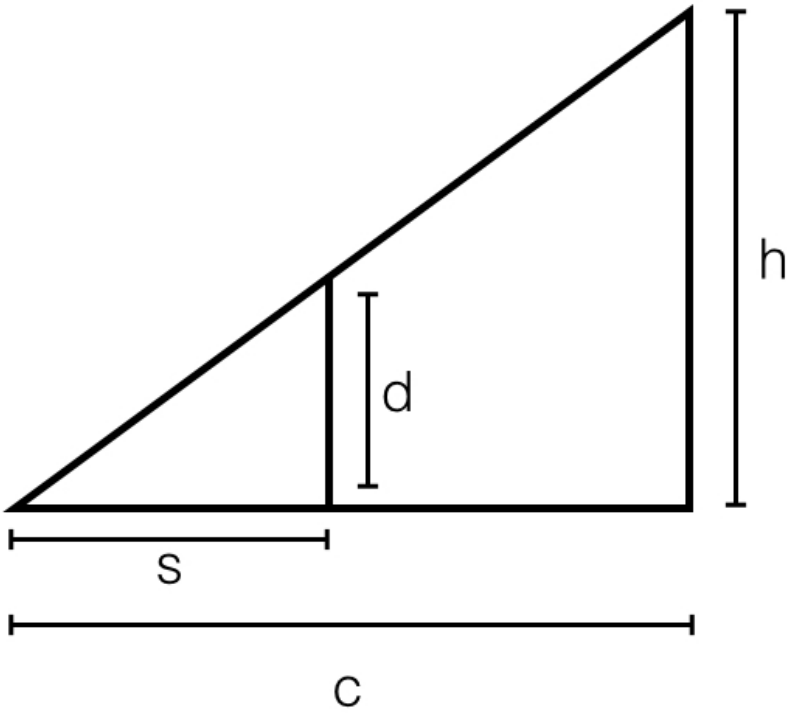

Figure 3.8: Unwrapped SPP profile.

In Fig. 3.8, s is the arc length subtended by the angle ϕ at r, while c is the circumference of the SPP. The tangent of the triangular SPP profile is constant leading to the relation,

$$tan(\theta) = \frac{d}{s} = \frac{h}{c} \tag{3.11}$$

Substituting in the definitions $s = \phi r$ and $c = 2\pi r$ gives,

$$d = \frac{hs}{c} = \frac{h\phi r}{2\pi r} = \frac{h\phi}{2\pi} \tag{3.12}$$

The optical thickness (3.10) becomes,

$$x = \frac{n_1 h\phi}{2\pi} \tag{3.13}$$

The phase (3.9) is then,

$$\Phi_1 = \frac{2\pi}{\lambda}\frac{n_1 h\phi}{2\pi} = \frac{n_1 h\phi}{\lambda} \tag{3.14}$$

The phase of a second wave passing through the same region of space without the SPP is,

$$\Phi_2 = \frac{n_2 h\phi}{\lambda} \tag{3.15}$$

where n_2 is the new index of refraction. The phase shift induced by the SPP is the difference between Φ_1 and Φ_2.

$$\Delta\Phi = \frac{n_1 h\phi}{\lambda} - \frac{n_2 h\phi}{\lambda} = (n_1 - n_2)\frac{h\phi}{\lambda} = \Delta n\frac{h\phi}{\lambda} \tag{3.16}$$

For the SPP to produce a LG mode, the total phase shift must be an integer multiple of 2π. This implies that,

$$2\pi\, l = \Delta n\frac{h\phi}{\lambda} \tag{3.17}$$

Solving for h and substituting $\phi = 2\pi$ at h gives the well known equation for the step height of an SPP,

$$h = \frac{l\lambda}{\Delta n} \tag{3.18}$$

The SPP imparts the same phase shift independent of the input mode number l. Therefore, the azimuthal mode number in (3.18) may be rewritten as $\Delta\, l$ to make explicit that the mode of the input and output beams are different but not restricted to an input

of $l = 0$. Finally, the change in mode number of an input beam with wavelength λ for a given SPP material and design will experience a shift in l equal to Δl where,

$$\Delta l = \frac{\Delta n\, h}{\lambda} \tag{3.19}$$

This approximation is only valid for low divergent beams and small step heights. Snell's Law may be applied to show that the resulting OAM is quantised. Snell's Law states that,

$$n_2\, sin\,(\theta + \alpha) = n_1\, sin\,(\theta) \tag{3.20}$$

where θ is the pitch of the SPP surface and α is the refraction angle of a transmitted ray. Using the small angle approximation and solving for the product $n_2\,\alpha$, Snell's Law becomes,

$$\begin{gathered} n_2\,(\theta + \alpha) = n_1\theta \\ \\ n_2\theta + n_2\alpha = n_1\theta \\ \\ n_2\alpha = (n_1 - n_2)\,\theta = \Delta n\theta \end{gathered} \tag{3.21}$$

The linear momentum in the SPP is[3],

$$p = n_2 \frac{2\pi\,\hbar}{\lambda} \tag{3.22}$$

Using the small angle approximation and the result from (3.21), the linear momentum in the azimuthal direction due to the SPP is,

$$p_\phi = n_2 \frac{2\pi\,\hbar}{\lambda} \sin(\alpha) \approx n_2 \frac{2\pi\,\hbar}{\lambda}\alpha = \frac{2\pi\Delta n\theta\hbar}{\lambda} \tag{3.23}$$

The total angular momentum is then,

[3]The linear momentum is not written in its usual form with Planck's constant, but instead with $2\pi\,\hbar$. This is simply to avoid confusion by using h for both Planck's constant and the step height of the SPP.

$$L = rp_\phi = \frac{2\pi r \Delta n \theta \hbar}{\lambda} \tag{3.24}$$

Substituting $h = \Delta l \lambda / \Delta n$ and $\theta \approx h/2\pi r$ shows that the OAM transferred to radiation via a SPP is quantised.

$$L = \frac{\Delta n \hbar}{\lambda} \frac{l\lambda}{\Delta n} = l\hbar \tag{3.25}$$

3.3.4 Beam Mode Decompositions

Due to the additional $exp\,(il\phi)$ phase factor induced by SPPs, the resulting beam is not a pure LG mode. This is because the total azimuthal phase term becomes,

$$exp\left[i\left(l_{pmd} + l_{LG}\right)\phi\right] = exp\,(il_{out}\phi) \tag{3.26}$$

However, $l_{out} \neq l_{LG}$, while l_{LG} remains the l used in the amplitude terms contained in (2.115). Therefore, SPPs are not pure mode converters [24, 26, 73]. The output beam generated by a SPP can however, be described using Gaussian Beam Mode Analysis (GBMA) [19, 74, 75], when the input beam divergence and SPP step height h are small [24]. The output beam may be represented as a superposition of LG modes (B.3),

$$U_m^n\,(r, \phi, z) = \sum_{l=-\infty}^{\infty} \sum_{\rho=0}^{\infty} A_{\rho,m}^{l,n} U_\rho^l\,(r, \phi, z) \tag{3.27}$$

where, U_ρ^l are the LG modes if a cylindrical coordinate system is adopted. The mode coefficients $A_{\rho,m}^{l,n}$ are,

$$A_{\rho,m}^{l,n} = \left\langle U_\rho^l | U_m^n \right\rangle \tag{3.28}$$

Here the brackets denote an integration on the plane perpendicular to the propagation axis z (This is the (r, ϕ) plane in cylindrical coordinates). An arbitrary phase shift may be introduced into the system by multiplying the input field by $exp\,(-i\Phi)$ [76]. For SPPs, the function Φ is required to induce an azimuthal phase shift of Δl, found using

(3.18). Therefore, the phase shift term for a SPP is $exp\,(-i\Delta l\phi)$ [24]. Introducing the phase shift term to (3.27) gives,

$$U_m^n\,(r,\phi,z) = \sum_{l=-\infty}^{\infty}\sum_{\rho=0}^{\infty} A_{\rho,m}^{l,n} U_\rho^l\,(r,\phi,z)\,exp\,(-i\Delta l\phi) \tag{3.29}$$

which then implies,

$$A_{\rho,m}^{l,n} = \left\langle U_\rho^l\,|exp\,(-i\Delta l\phi)|\,U_m^n \right\rangle \tag{3.30}$$

A mode spectrum, or fraction of power of the input field U_ρ^l contained in each mode U_m^n is found by calculating the normalised coupling coefficient for each mode.

$$\left|C_{\rho,m}^{l,n}\right|^2 = \frac{\left|\left\langle U_\rho^l\,|exp\,(-i\Delta l\phi)|\,U_m^n \right\rangle\right|^2}{\left|\left\langle U_m^n|U_m^n\right\rangle\right|^2} \tag{3.31}$$

3.3.5 SPP Designs

Practical SPP designs can differ greatly from the phase-only altering theoretical $exp\,(il\phi)$ form, and the degree to which designs differ from functional description partly depends on the manufacturing process. At millimetre wavelengths, SPPs are typically manufactured from a single slab of dielectric material [27]. Two notable exceptions is a reflecting SPP [77] and a flat teflon plate with holes drilled into the surface, thereby adjusting the effective index of refraction and inducing a phase shift [78]. Common low-loss dielectrics are polypropylene and nylon. Centre regions of smooth surfaced SPPs are particularly difficult to manufacture due to the undefined phase required at $r = 0$. In addition smooth surfaced SPPs require a significant amount of machining time. For these reasons, smooth surfaced millimetre wave SPPs (Fig. 3.9a) are typically stepped [26], or machined in discrete step height sections (7.1).

A comparison between smooth and stepped SPPs is conducted in Sec. 3.3.6. Please note that an in-depth analysis of the SPP designs used in this thesis is conducted in Chapter 4. Analysis conducted in this chapter is only to introduce SPP functionality.

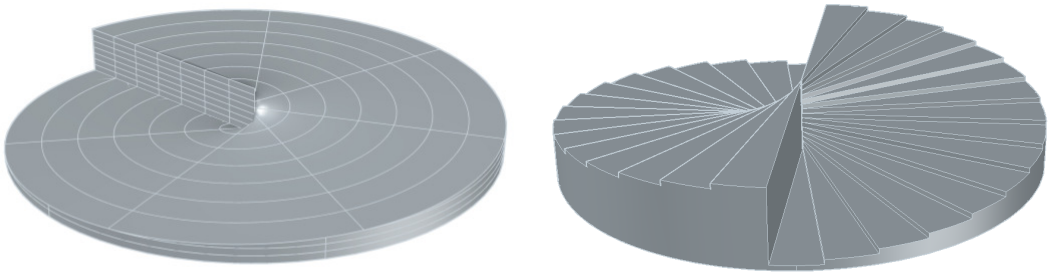

(a) Smooth surfaced SPP *(b) Stepped SPP in a split configuration*

Figure 3.9: A CAD model of a smooth surfaced $\Delta l = \pm 1$ *SPP for use at* $100\,GHz$ *(a). A CAD model of a "split stepped," SPP. Here two* $\Delta l = \pm 1$ *SPPs were compressed from an angular range of* $[0, 2\pi]$ *to* $[0, \pi]$ *and pushed together in order to generate an* $l = \pm 2$ *LG beam (b).*

Stepped SPPs also suffer from reduced accuracy near their centre. However, this is due to the finite size of the machining tools available. In addition to being stepped, SPPs with $|\Delta l| > 1$ can be placed in a split configuration. Split configurations allow for smaller total step heights h by compressing some number $b = |l|$ mode one SPPs into an angular region of $\Theta_b = 2\pi/b$ (Fig. 7.1). A combination of a stepped and split SPP design has been developed in [28]. Here, a third type of SPP, a modular configuration, is developed. This modular SPP (Fig. 7.2a) is comprised of several interlocking, individual stepped mode one SPPs, machined on the top and bottom surfaces.

3.3.6 Modal Analysis of SPP Designs

Mode spectra for various SPP designs may be calculated numerically using (3.31). (These calculations are taken from Schemmel et al. [28]) Such calculations can include smooth or stepped SPPs in standard or split configurations. Additionally, individual step thicknesses may be varied by a set, or a random amount, in order to simulate manufacturing errors. Other effects such as transmission through the dielectric, inhomogeneities of the index of refraction, the finite size of the SPP or variations in step heights as a function of radius can also be included. In these numerical calculations

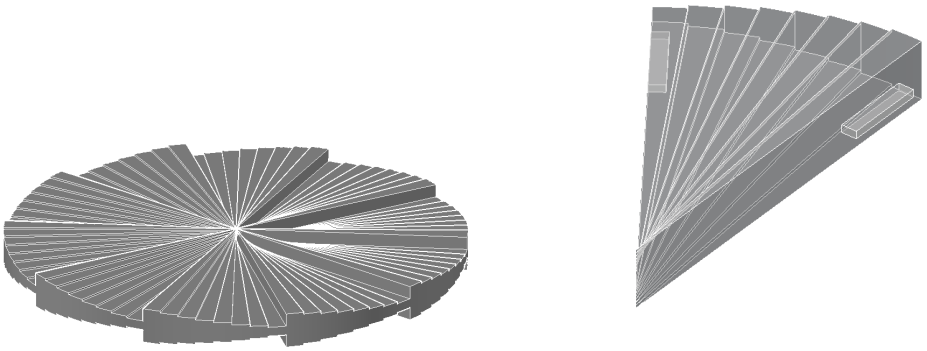

(a) Full $\Delta l = \pm 10$ SPP *(b) A single module of the full SPP*

Figure 3.10: A CAD rendering of a full $\Delta l = \pm 10$ SPP (a). A single module from the full SPP. The tongue, which is used to attached the next section, is visible on the right hand side, while the groove is visible on the left (b).

SPPs are represented by a grid of points, each indicating the applied phase shift to that (x, y) point. For a smooth SPP, this grid is defined by $exp\,(i\Delta l\phi)$, while stepped SPPs are represented by discretising the smooth SPP grid.

To compare the affect of a stepped versus a smooth SPP, numerical simulations of a $\Delta l = 1$ SPP illuminated with a U_0^0 Gaussian beam were conducted on a field eight times the input beam width on a grid of 200×200 points. The stepped SPP was comprised of sixteen steps without random variations in thickness. Decomposition results (Table 3.1) for both the smooth and stepped SPP show that all of the initial Gaussian power was converted into a LG beam with $l = 1$. However, since the SPP is not a pure mode converter, radial modes with $\rho \neq 0$ are also present. Note that these results are valid independent of the incident wavelength, as long as the SPP step height is chosen appropriately. It should also be pointed out that the mode content for each (l, ρ) pair generated by the sixteen stepped SPP is lower than for the smooth SPP. This is a result of leakage from modes containing a large fraction of the incident power, to modes containing less power. Analysis of each mode in Table 3.1 shows that there is

Table 3.1: Mode content, in percentages, of a U_0^0 beam passed through a smooth and a sixteen stepped $\Delta l = 1$ SPP.

Smooth	$l = 1$	78.545	9.820	3.684	1.919	1.176	0.794
Stepped	$l = 1$	76.353	9.537	3.576	1.862	1.141	0.770
	$\rho =$	0	1	2	3	4	5

roughly a 2.8 to 3.0 percent drop in power in each mode. Finally, because the mode content is normalised to the input power (3.31), the value of each coupling coefficient is independent upon the number of modes the beam is decomposed over. Taking the smooth $\Delta l = 1$ SPP in Table 3.1 as an example, only 95.938% of the input beam's power is represented in the first six radial modes. Decomposing over additional modes will not change the calculated coefficient values. Instead, it would show that remaining $\approx 4\%$ of the input beam power lies in the additional radial modes.

3.3.7 SPP Bandwidth

Although SPPs are designed for use at a single frequency, they will still attempt to impart an incident beam with some amount of OAM [79] according to,

$$\Delta l = \frac{h\Delta n}{\lambda} \tag{3.32}$$

Broadband characteristics of an SPP may be simulated by generating a SPP for use at a particular frequency, while simulating over several incident frequencies. To show this, a smooth $\Delta l = 1$ SPP, designed for use at 100 GHz, was simulated across the W-Band (75 − 110 GHz). Figure 3.11 shows the maximum mode content as a function of the input frequency. As expected, there is a peak in the maximum mode content at 100 GHz, the design frequency. As the incident frequency moves away from this point, the maximum mode content decreases, implying that the plate becomes less efficient.

Peaks in the maximum mode content are visible by expanding the simulation

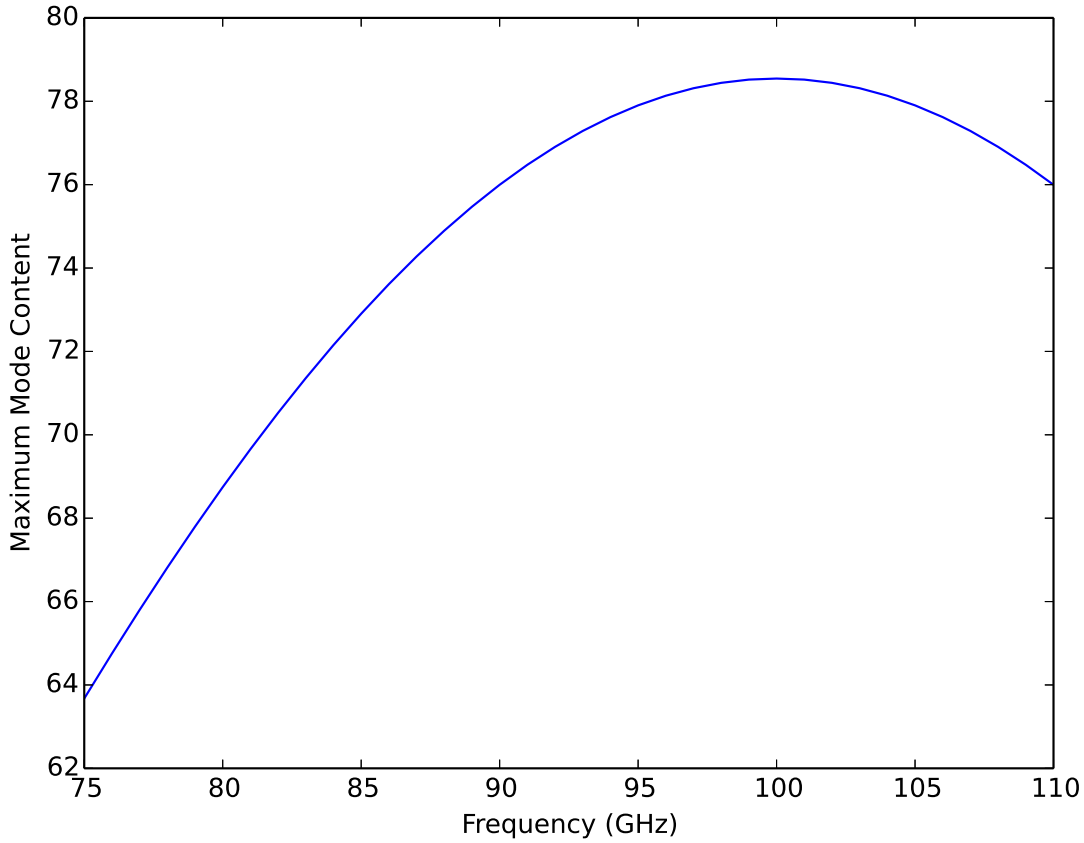

Figure 3.11: Maximum mode content as a function of input frequency for a $\Delta l = \pm 1$ *SPP designed for use at* 100 *GHz, across the W-Band.*

frequency range from $1 - 300$ GHz (Fig.3.12a). These peaks may be explained by analysing the maximum mode content's azimuthal (Fig. 3.12b) and radial (Fig. 3.12c) mode numbers, as a function of frequency. It is clear that the local minima in Fig. 6.1c correspond to jumps in the azimuthal mode number, while the radial mode number remains at $\rho = 0$ across all frequencies.

The relation between SPP design parameters h and Δn and functional parameters λ and Δl is needed in order to understand why these changes in azimuthal mode number exist. When designing an SPP, the index of refraction and primary step height are defined. As an example, a $|\Delta l| = 1$ polypropylene SPP has,

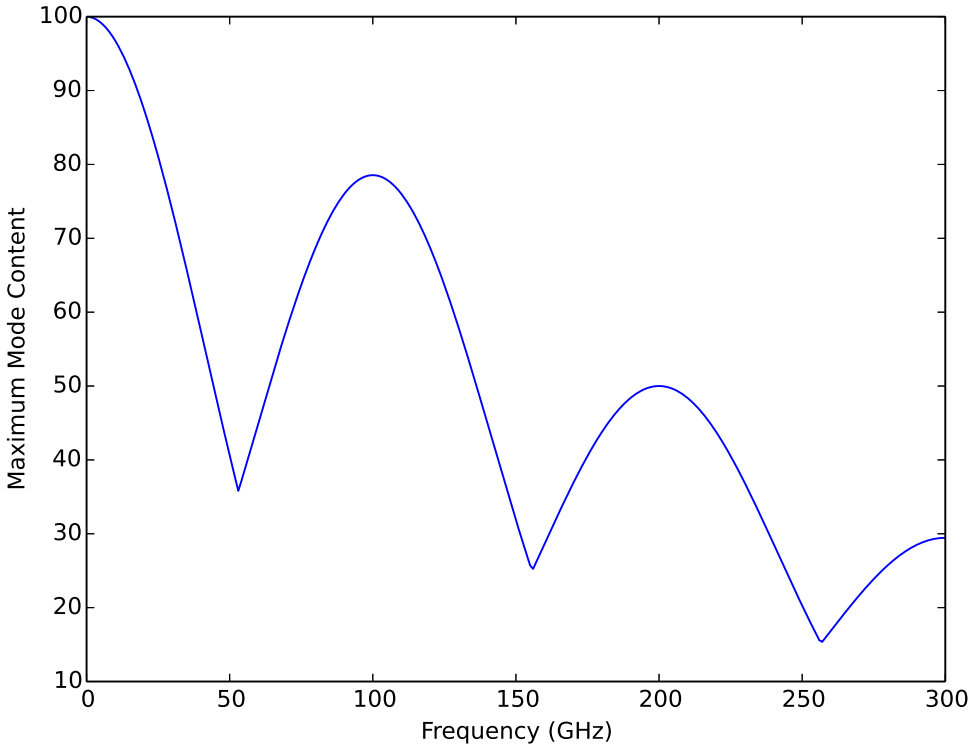

(a) Maximum mode content as a function of input frequency.

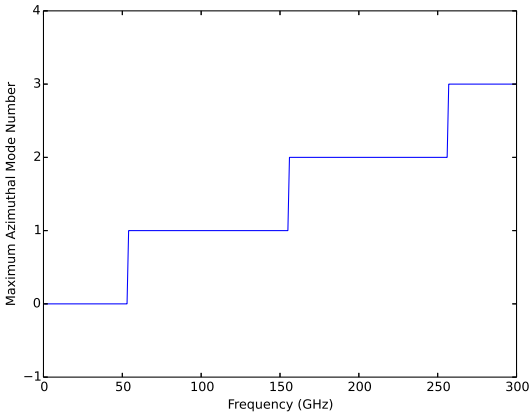

(b) Azimuthal mode number of maximised mode content.

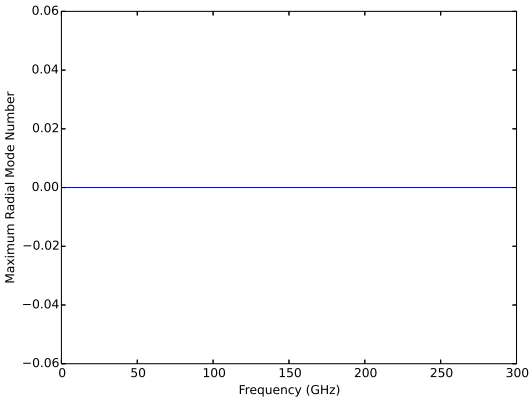

(c) Radial mode number of maximised mode content.

Figure 3.12: Maximum mode content as a function of input frequency for a $\Delta l = \pm 1$ *SPP designed for use at* $100\,GHz$*, simulated between* $1-300\,GHz$ *(a). Between* $50-150\,GHz$ *the SPP generates mostly* $l = 1$ *radiation, with a peak at the design frequency. Below* $50\,GHz$*, the mode content is primarily the* $l = 0$*, while above the mode content is primarily* $l = 2$*.*

$$h\,\Delta n = 6\text{mm} * (1.5 - 1) = 3\text{mm} \tag{3.33}$$

This implies that the change in mode number is,

$$\Delta l = \frac{h\,\Delta n}{\lambda} = \frac{3\text{mm}}{\lambda} = \frac{3\text{mm}}{3\text{mm}} = 1 \tag{3.34}$$

at 100 GHz. Yet, Fig. 3.12 shows that an $l = 2$ beam is generated at 200 GHz ($\lambda = 1.5$ mm). By rewriting (3.34),

$$\lambda = \frac{h\,\Delta n}{\Delta l} = \frac{3\text{mm}}{2} = 1.5\text{mm} \tag{3.35}$$

which is exactly where the second peak is observed. Therefore, these peaks may be interpreted as modal harmonics. Jumps in the maximum content's azimuthal mode number may also be analysed. They occur between 53 − 54 GHz, 155 − 156 GHz and 256 − 257 GHz. The residual change in Δl for each case may be calculated by,

$$\begin{aligned} \Delta l_{53} - l_{initial} &= \frac{3\text{mm}}{5.66\text{mm}} - 0 = 0.530 \\ \Delta l_{54} - l_{initial} &= \frac{3\text{mm}}{5.55\text{mm}} - 0 = 0.541 \end{aligned} \tag{3.36}$$

$$\begin{aligned} \Delta l_{155} - l_{initial} &= \frac{3\text{mm}}{1.94\text{mm}} - 1 = 0.546 \\ \Delta l_{156} - l_{initial} &= \frac{3\text{mm}}{1.92\text{mm}} - 1 = 0.5463 \end{aligned} \tag{3.37}$$

$$\begin{aligned} \Delta l_{256} - l_{initial} &= \frac{3\text{mm}}{1.17\text{mm}} - 2 = 0.564 \\ \Delta l_{257} - l_{initial} &= \frac{3\text{mm}}{1.16\text{mm}} - 2 = 0.586 \end{aligned} \tag{3.38}$$

This reveals two interesting features. First, the azimuthal mode number does not change around 0.50 as apparently was naively expected. Secondly, the residual change in Δl increases with an increase in frequency! This is a peculiar yet exciting result, and the exact reasoning for this is still unknown.

3.3.8 Progressive Vortex Generation

An interesting question arises around the use of SPPs. Just how does a fundamental beam transform into a higher order mode? This can be studied with a toy model using the computational electromagnetics software package FEKO [80]. In this toy model, a $\Delta l = \pm 1$ SPP is illuminated by a Gaussian beam generated by a corrugated feed horn antenna (Fig. 3.13). Although this model was never measured, the methodology it uses has been validated in Chapter 5. There, similar FEKO methodology was used to model a corrugated feed horn. This horn was then measured, and the resulting data corresponds well with the predicted results using FEKO's Multi-Fast Method of Moments (MLFMM), which is a subset of the Method of Moments (MoM). MoM and MLFMM describe surface current densities on user defined geometry by a superposition of basis functions. MoM calculates the interaction between each basis function. This leads to memory requirements which scale as N^2 and CPU time requirements of N^3 [80]. This makes it difficult to calculate fields from electrically large objects. MLFMM was developed to help solve this problem. MLFMM calculates the interaction between groups of basis functions. This leads to memory requirements which scale as $N\,(\log\ N)^2$ and CPU time as N^2 [80]. Electric fields are then propagated via the basis functions and may be plotted along a line, on a surface, or in a volume using FEKO [81].

As the radius of the SPP is made smaller and smaller the incident Gaussian beam begins to over illuminate the SPP and the OAM content of the transmitted beam is decreased. When the SPP is very small, it intersects only a small portion of the incident beam, leaving a large portion of the radiation without a modified phase. Figures 3.14 to 3.25 show what happens to the near field of the SPP as this process takes place. Each plotted surface is 300 mm from the SPP, and the analysed wavelength was $\lambda = 3.00$ mm.

In Fig. 3.14, the very small radius of the SPP generates very little OAM in the transmitted beam. Very little intensity modulation is visible and the phase remains spherical.

A small increase in the SPP radius (Fig. 3.15) changes very little in the modelled

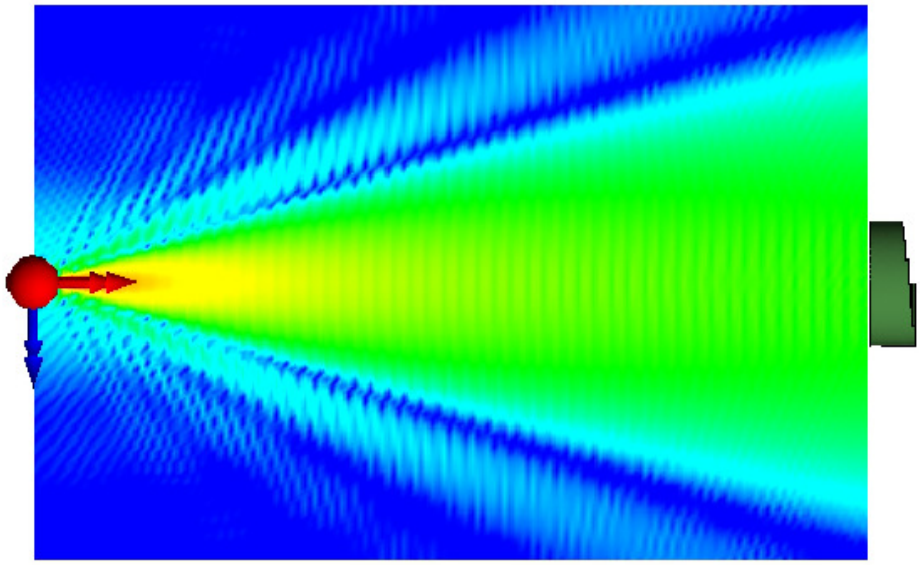

Figure 3.13: Incident field generated by a corrugated feed horn as it approaches the SPP. The SPP is increased in size, effectively increasing the percent of OAM in the transmitted Gaussian beam.

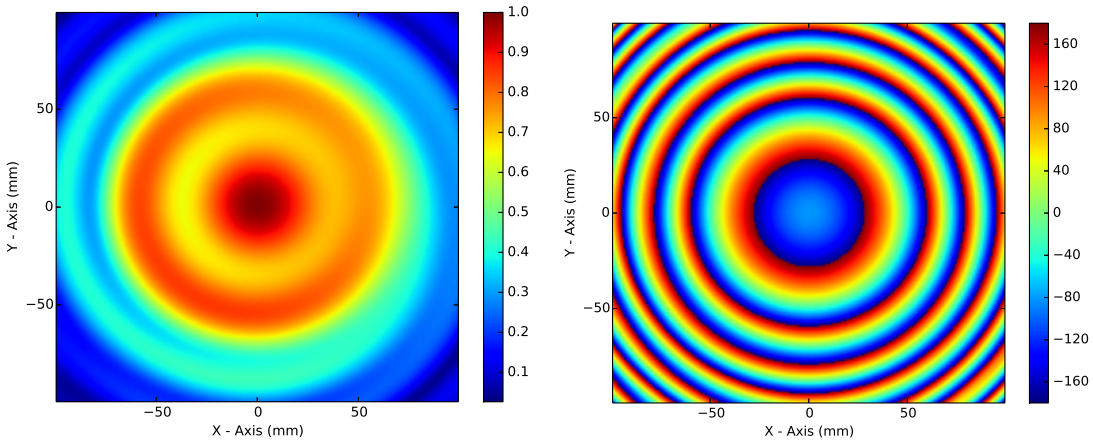

(a) Linear Intensity *(b) Phase (Degrees)*

Figure 3.14: SPP Radius 4 *mm* (1.33λ)

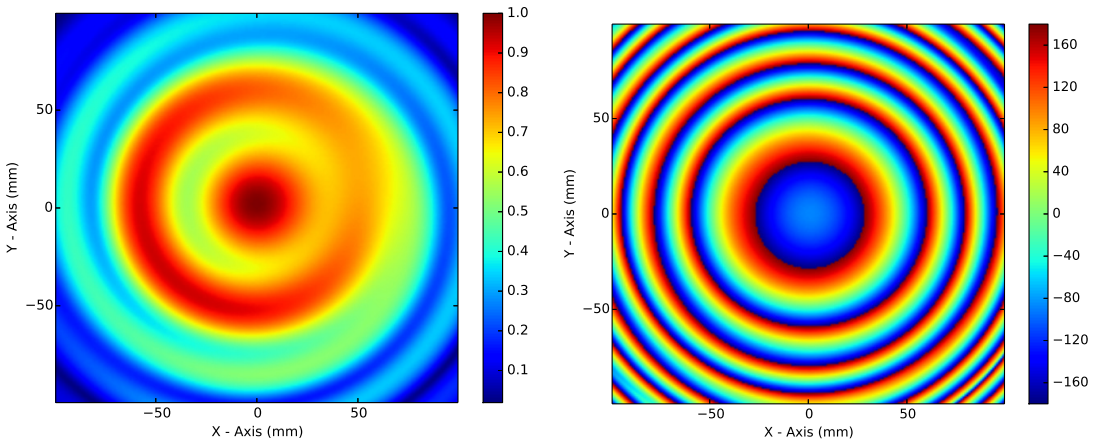

(a) Linear Intensity *(b) Phase (Degrees)*

Figure 3.15: SPP Radius 5 mm (1.67λ)

phase, however a slight asymmetry in intensity starts to grow. Surprisingly, the intensity is more sensitive to these increase in OAM content then the phase. However, it should be remembered that this is just a toy model, and perhaps this hyper-sensitivity is a result of diffraction from the SPP circumference.

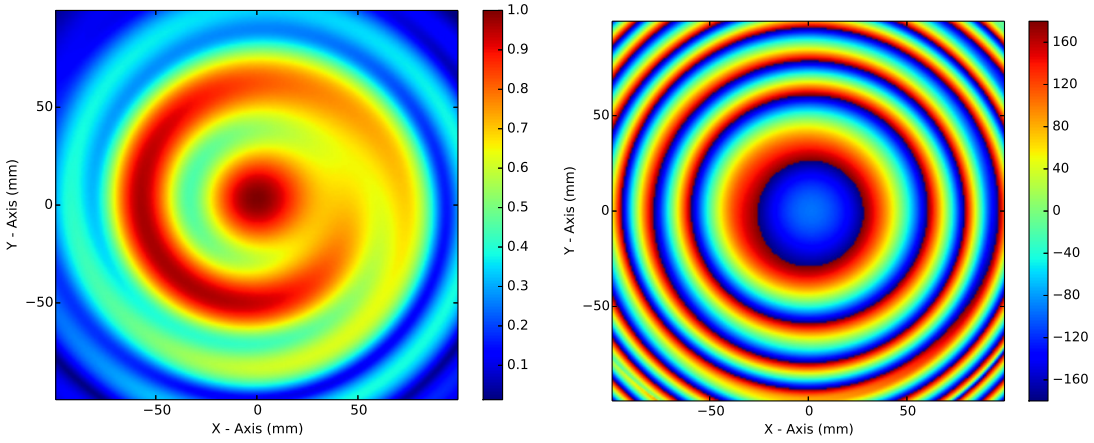

(a) Linear Intensity *(b) Phase (Degrees)*

Figure 3.16: SPP Radius 6 mm (2λ)

A further increase in the SPP radius (Fig. 3.16) starts to show a spiral intensity pattern, and a small distortion in the centre of the phase pattern.

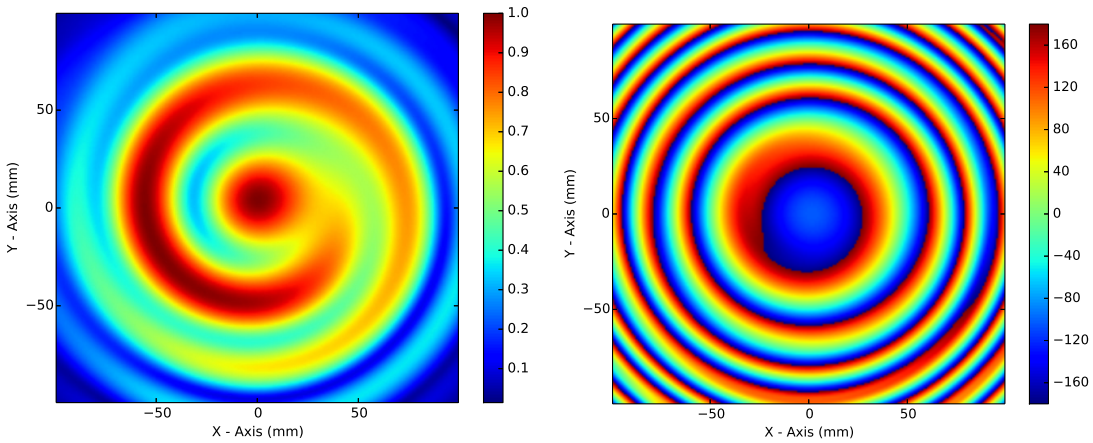

(a) Linear Intensity *(b) Phase (Degrees)*

Figure 3.17: SPP Radius 7 *mm* (2.33λ)

Phase variations finally become visible when the SPP radius is 7 mm (2.33λ) (Fig. 3.17). In addition, the intensity pattern maintains its spiral pattern.

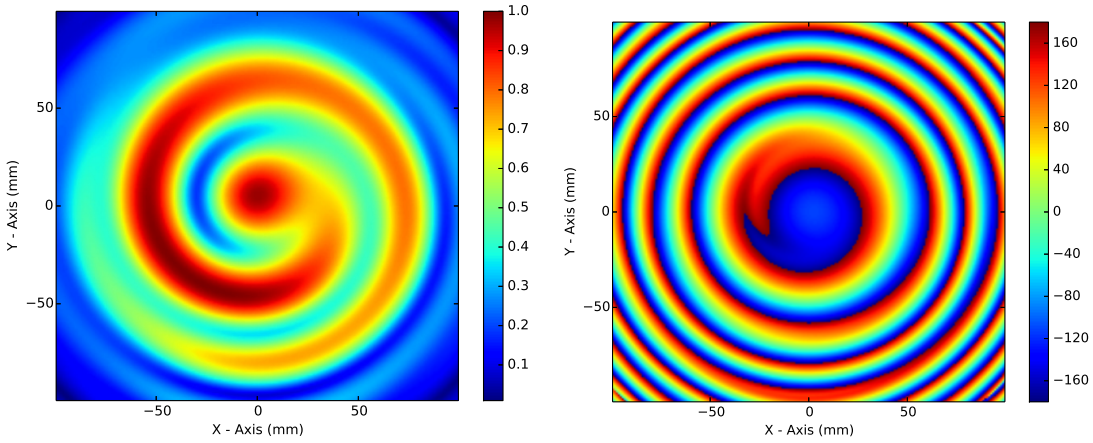

(a) Linear Intensity *(b) Phase (Degrees)*

Figure 3.18: SPP Radius 8 *mm* (2.67λ)

A slight increase in the SPP radius from 7 mm to 8 mm (2.33λ to 2.67λ) shows little change in the intensity pattern. However, a cusp has been created in the phase. This cusp will eventually become the phase dislocation.

As the SPP radius is increased further (Fig. 3.19) the intensity pattern begins to

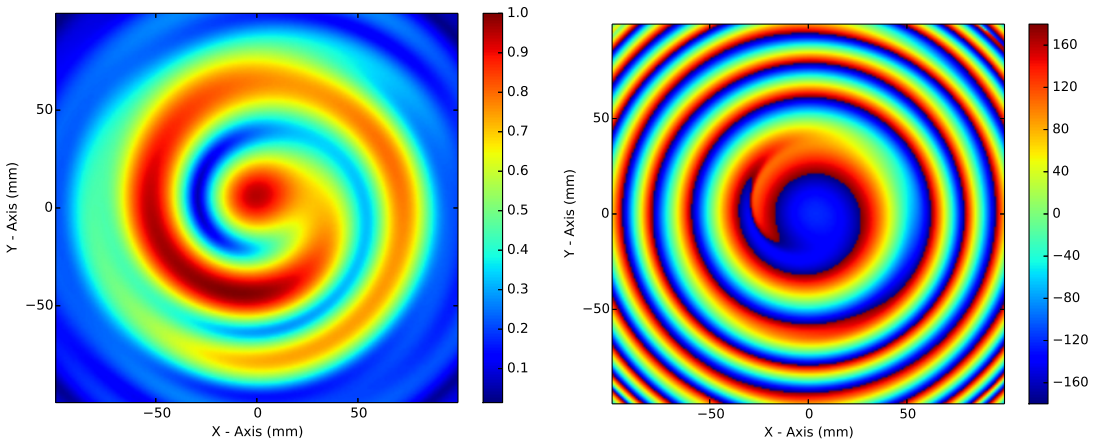

(a) Linear Intensity *(b) Phase (Degrees)*

Figure 3.19: SPP Radius 9 mm (3λ)

form an even clearer spiral. A cusp in the phase continues to deepen.

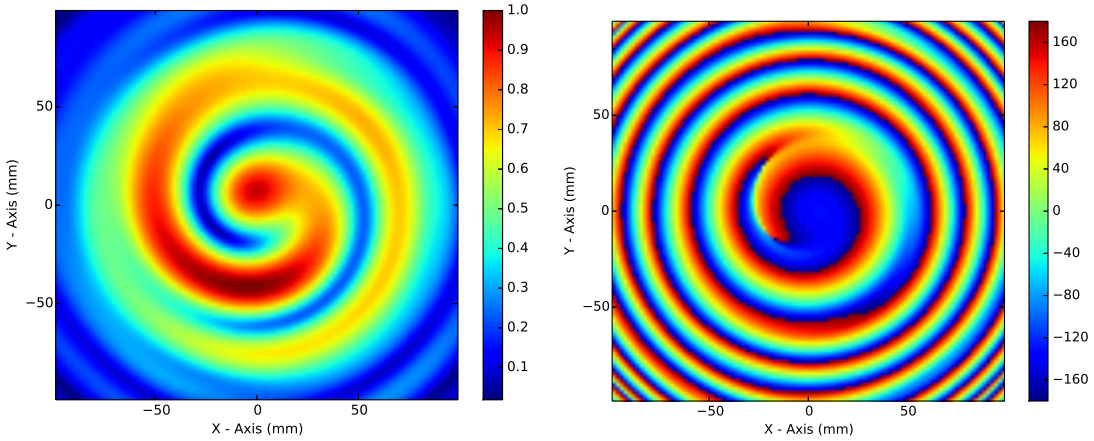

(a) Linear Intensity *(b) Phase (Degrees)*

Figure 3.20: SPP Radius 10 mm (3.33λ)

Increasing the SPP radius to 10 mm (3.33λ) introduces enough OAM content to the incident beam that a phase dislocation is generated (Fig. 3.20). Here, the cusp in phase has grown too deep, and has broken apart. Little indication of this cataclysmic event is visible in the intensity however.

Close analysis of the intensity pattern in Fig. 3.21 shows a deep intensity null at the

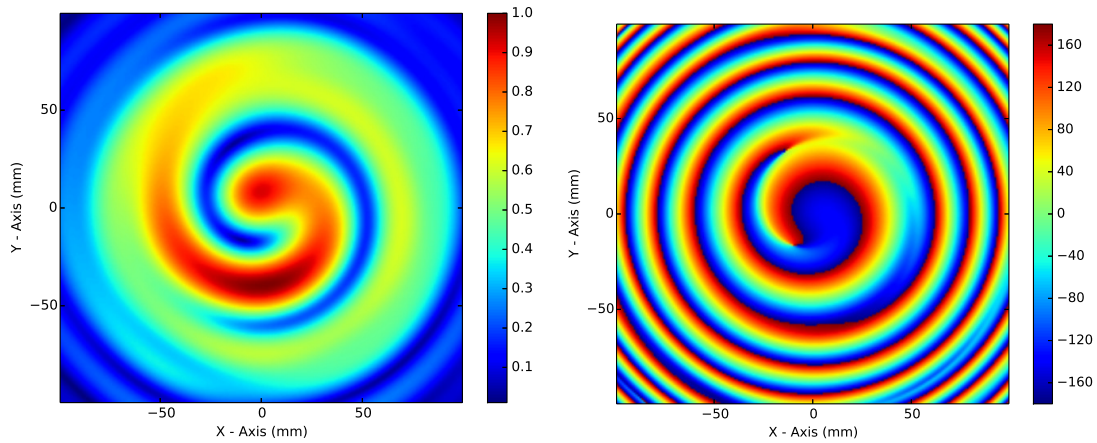

(a) Linear Intensity *(b) Phase (Degrees)*

Figure 3.21: SPP Radius 11 *mm* (3.67λ)

same location of the two newly generated phase discontinuities.

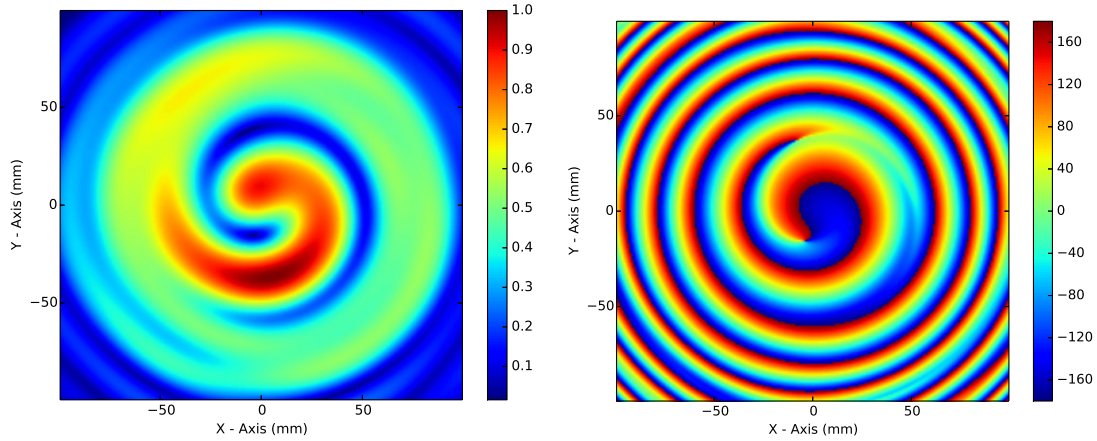

(a) Linear Intensity *(b) Phase (Degrees)*

Figure 3.22: SPP Radius 12 *mm* (4λ)

As the SPP radius increases further (Fig. 3.22), the intensity starts to wrap around the central intensity null. This is the beginning of the expected annular ring pattern.

The annular intensity ring starts to become very apparent in Fig. 3.23. The central intensity null has moved with the central phase dislocation, further towards the propagation axis. The phase dislocation line continues to move towards the outer spherical

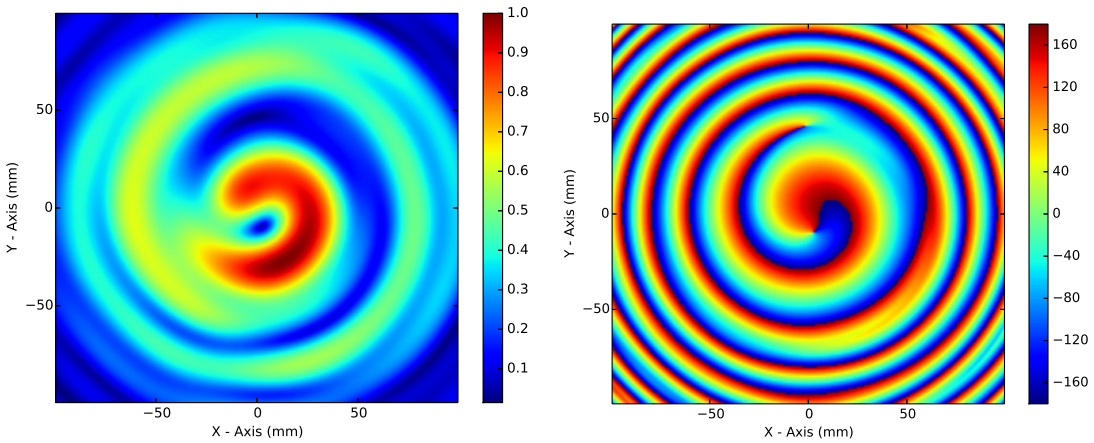

(a) Linear Intensity *(b) Phase (Degrees)*

Figure 3.23: SPP Radius 15 *mm* (5λ)

phase lines.

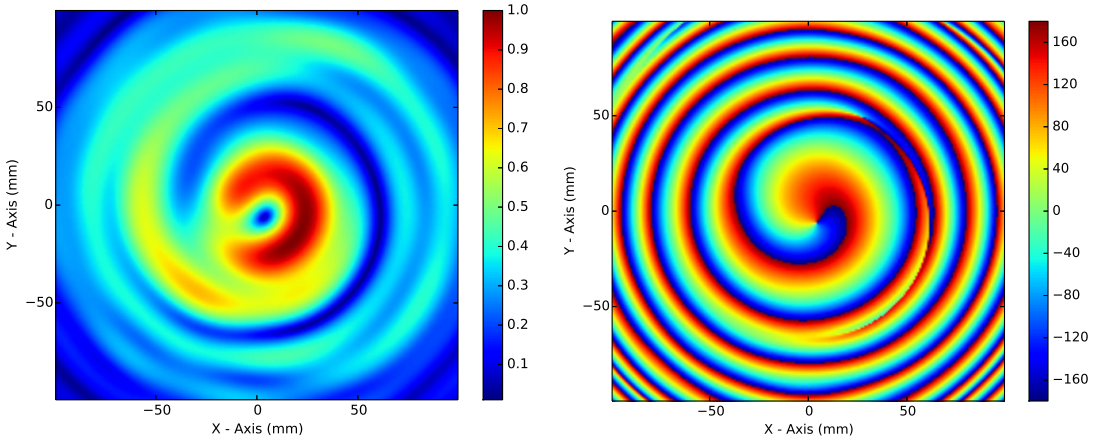

(a) Linear Intensity *(b) Phase (Degrees)*

Figure 3.24: SPP Radius 17 *mm* (5.67λ)

With a SPP radius of 17 mm (5.67λ) (Fig. 3.24) the phase dislocation line has intersected the outer spherical phase lines and the intensity pattern continues to form a closed annular ring pattern.

A further jump to a SPP radius of 20 mm (6.67λ) (Fig. 3.25) shows the intensity pattern enclosing the central intensity null. In addition the phase dislocation line

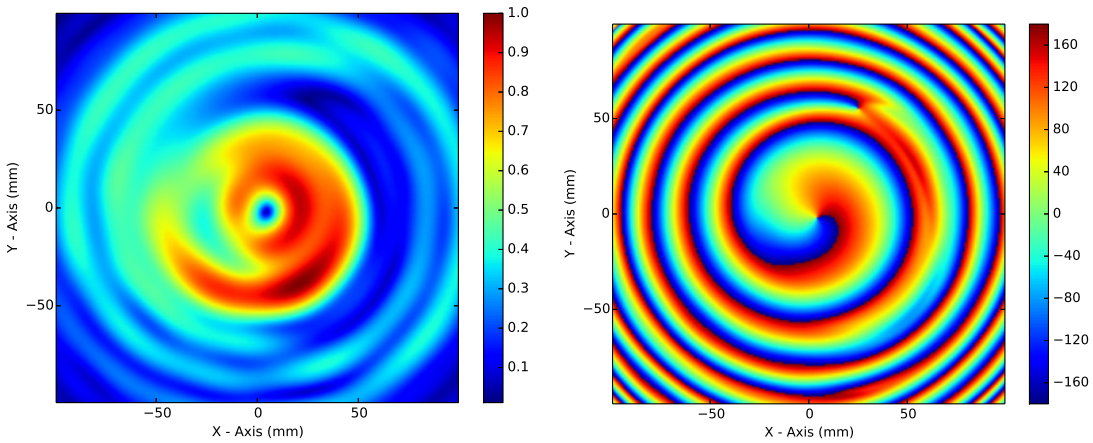

(a) Linear Intensity *(b) Phase (Degrees)*

Figure 3.25: SPP Radius 20 *mm* (6.67λ)

continues to intersect and join with the outer spherical phase lines.

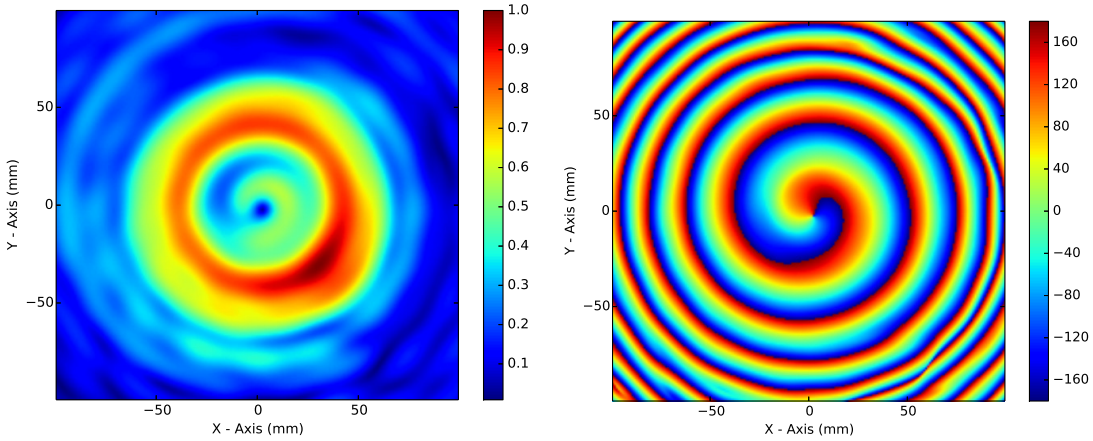

(a) Linear Intensity *(b) Phase (Degrees)*

Figure 3.26: SPP Radius 30 *mm* (10λ)

Finally, with a SPP radius of 30 mm (10λ), the full annular intensity pattern has developed and the spiralling phase discontinuity has fully merged with the spherical phase lines. This toy model provides valuable insight into how Gaussian beams are transformed into optical vortices, or beams carrying OAM. As the OAM content of the beam is increased, the spherical wavefronts of the Gaussian beam slowly start to

collapse. As this happens a cusp in the phase begins to form. Eventually, the cusp becomes too deep and the phase dislocates. Now, two termination points, or branch points (BPs), are generated. These are were the phase circulates by 2π around the end of the dislocation line. As more OAM content is added the phase dislocation line starts to spiral around the central BP, and diverges radially. With an even larger increase in the OAM content, the spiralling phase dislocation meets up with a spherical phase line. The two lines in phase start to interact, and as the OAM content is increased even further, they merge into one phase dislocation.

3.4 Some Applications of Synthetic OAM

OAM Coronagraphy

Spiral phase plates have been used successfully in coronagraph systems [82–85] and may be used to overcome the Rayleigh criterion in optical systems [86]. Coronagraphs are used to block light from a primary star, allowing fainter sources near the star to become observable. In such systems, a SPP is placed between the aperture and exit pupil of a telescope. By centring the optical axis on a bright star [87], the SPP will convert the primary non-OAM (nOAM)[4] radiation into an OAM state. This OAM state, with central intensity null, diffracts faster than a pure Gaussian beam and is captured by a Lyot stop inside the telescope. At the same time, secondary source beams pass through the SPP, but off axis. These beams only experience an overall phase shift, not the full $2\pi l$ phase circulation. As such, they remain Gaussian and pass through the Lyot stop and onto the detector. Contrast ratios of 99.8% were seen in laboratory settings [82] while a 97% was seen in [83] and [84] discovered an exoplanet using an OAM coronagraph.

[4]It should be noted that the referenced papers in this section have assumed that the primary stars produce no OAM. However, this is not always the case as is demonstrated in [15].

3.4.1 Communications

Perhaps the most highly researched application using OAM radiation is in the area of wireless communications. Current communication systems rely on orthogonal polarisation states, among other wave properties, to increase data transfer rates. However, these systems are limited to only two linear or two circular polarisation states. On the other hand, OAM modes are defined by the double infinite mode number l (2.115), each of which is orthogonal to all other states. Therefore, communication via OAM modes has a theoretical infinite data transfer rate over a single frequency. Several proof of concept experiments have been conducted in the optical [88–93] and a few in radio [94, 95].

3.4.2 Digital Spiral Imaging and Radar

Of particular interest to myself, is the concept of digital spiral imaging [96–98] (DSI) in conjunction with radar. DSI measures the reflected mode spectrum of objects illuminated with various LG modes. In such experiments, an object is illuminated with some known LG mode, and the reflected beam is captured and decomposed over several modes. The resulting mode spectrum is then analysed in order to determine features about the target object. Traditional polarimetry has only two possible orthogonal polarisation states to measure, OAM DSI has an infinite number of states. This expanded state space can carry new information, potentially leading to new ways to probe objects.

In the future, the author intends to explore the concept of using OAM in radar applications. It could be possible to use OAM radar in earth observing satellites to track weather patterns (The helical structure of hurricanes comes to mind), or other planetary satellites mapping surface topology. OAM radar could also be used in aircraft radar, potentially foiling some current aspects of stealth technology. Or perhaps, OAM radar could be used to probe the ionosphere, looking for various layer structures, much like the atmospheric turbulence experiments.

3.5 Conclusion

This chapter covered various ways that OAM may be generated. These included several natural sources such as atmospheric and astrophysical turbulent mediums, the CMB, masers and luminous point sources. Special attention was paid to turbulent mediums as a significant amount of theoretical, experimental and early observation work was conducted. In addition, measurements of BPs from turbulent mediums allow for the calculation of the number of turbulent layers, their relative velocities, the turbulence strength and various other parameters. Synthetic OAM generation via PMDs was also covered. Holograms, or diffraction gratings with a central singularity, and Q-plates, or inhomogeneous and anisotropic dielectric slabs were reviewed. A significant portion of work was devoted to SPPs. It was shown through a ray optics calculation that SPPs impart changes in the quantised OAM of incident radiation. It was also shown that SPPs are impure mode converters, and SPP output beams must be decomposed onto a set of LG modes. Several different SPP designs were presented, and their affects on the expected SPP mode spectrum was analysed. Then, a toy model was developed to understand how increases in the OAM content of a propagation field affects the intensity and phase patterns. Finally, some applications of OAM were covered. These included OAM coronagraphy, OAM based communication systems and OAM radar. The following chapter will detail the computational electromagnetic modelling of SPPs with several source types.

4

Device Modelling

4.1 Introduction

Manufacturing and testing devices can be expensive, take a significant amount of time to complete, is susceptible to errors, and in some circumstances is impossible to complete before final system assembly. It is often easier to model the device. Computational models allow the designer to test and alter components quickly and easily. This allows the designer to spot problems early and to find a solution without having to spend the time and money on manufacturing and testing each iteration of a device. However, the ease of modelling can often lead the designer down inaccurate paths. Simplified early models must always be validated before more complicated models may be trusted. The process of developing devices is then an interplay between modelling and testing, going back and forth between the two as much as possible. Initial models are validated and then increased in complexity. More intricate models are then tested, and the process continues until the final device is manufactured, or until the system becomes too complex to measure. In the latter case the previously validated versions of the model are used to support the untested system model.

As the back and forth between modelling and testing continues, the complexity of the modelling increases. Analytical modelling was initially used to develop SPPs.

First, Gaussian beams were passed through analytically perfect SPPs. This helped to develop an understanding for how the conversion of Gaussian to LG beams is expected to function theoretically. The complexity of the analytical model was then increased by converting the perfect SPP to a stepped SPP. This proved that stepped SPPs would still function as an analytically perfect SPP, with a corresponding lower efficiency. Further analytical testing, such as working with incident superpositions or non-standard SPP designs, can be carried out. At this point however, it's more advantageous to switch to a software tool designed specifically for computational electromagnetics. This work makes extensive use of FEKO [80] for these advanced models. Software such as FEKO aids the development process significantly, but the designer does not have complete control, or knowledge, of what the inner workings of the algorithms are doing. Therefore, it is important that the developer breaks up each model into its constituent components in order to understand how each one affects the results, and if those results are expected. For example, before testing SPP designs, three source (Aperture, Plane Wave and Gaussian) types were modelled in free space. Then, a SPP mount was inserted into the model and tested with each source type. Each model produced a slightly different diffraction pattern, some of which mimicked the annular OAM radiation pattern. Without testing the SPP mount on its own, this affect would not have been noticed, and the resulting abnormal OAM pattern would have been attributed to the plate design instead of the SPP mount. This is a prime example of why it is important to isolate and test each part of a model. It is not until the very end of this process that the SPP design was inserted into the model.

In this chapter analytic and computational SPP models are presented. The analytical models demonstrate the theoretical functionality of SPPs, while also showing that stepped SPPs should function in a similar manner to smooth surfaced SPPs. The SPP system is then modelled using FEKO. Aperture, Plane Wave and Gaussian sources are tested in free space, with the SPP mount only, and with the mount and SPP together. Intensity and phase results are presented for each case.

Table 4.1: SPP step height parameters for analytical modelling.

Δl	Configuration	Primary Step (mm)	Single Step (mm)
±1	Single - Smooth	6	-
	8 Steps	-	0.86
	16 Steps	-	0.40
±2	Single - Smooth	12	-
	16 Steps	-	0.39
±2	Split - Smooth	6	-
	16 Steps	-	0.39

4.2 SPP Design and Analytical Modelling

This section details the SPP designs used in this thesis, developed in conjunction with [99]. Initially, several designs were developed and eventually three designs were selected for manufacture. First, there was a sixteen stepped $\Delta l = \pm 1$ SPP. Two thirty-two stepped $\Delta l = \pm 2$ SPPs were also developed. One of these utilised a standard, single step configuration while the other was in a split step configuration. Polypropylene ($n \approx 1.5$) was the material of choice. Section 4.2.1 through Sec. 4.2.3 detail the design, expected mode content and analytically reconstructed beam for each plate. Each SPP measured 100 mm in diameter. As a reference, the representative SPP step height parameters used in the analytical modelling are presented in Table 4.1.

4.2.1 Mode One Stepped SPP

Before modelling SPP designs in FEKO, the mode content of several SPP variations were analysed, starting with designs for a $\Delta l = \pm 1$ SPP. Firstly, the mode content of a smooth SPP was compared to designs utilising sixteen (Fig. 4.1) and eight steps-per-mode (Table 4.2). As expected, increasing the number of steps leads to an improved approximation of the smooth SPP design. Minor differences between the sixteen and

Table 4.2: Mode content, in percentages, of a U_0^0 beam passed through a smooth, sixteen and eight stepped $\Delta l = 1$ SPP.

Smooth	$\Delta l = 1$	78.54	9.82	3.68	1.92	1.18	0.79
16 Steps	$\Delta l = 1$	76.35	9.54	3.58	1.86	1.14	0.77
8 Steps	$\Delta l = 1$	69.70	8.70	3.26	1.70	1.04	0.70
	$\rho =$	0	1	2	3	4	5

eight stepped designs exists for radial mode numbers greater then zero. However, there is a 6.65% difference between the respective $(l = 1, \rho = 0)$ pairs. Ultimately, the sixteen stepped SPP design was chosen due to $l \neq 1$ modal contributions seen in the eight step decomposition. In addition to the mode content displayed in Table 4.2, the eight stepped SPP design had a 1.72% contribution from $(l = 0, \rho = 0)$ and 1.13% from $(l = 2, \rho = 0)$. Although the impurities are small, they represent components of the mode spectrum with $l \neq 1$ and so the design was discarded.

In addition to testing the number of discrete steps to use, an analysis into the effects caused by surface deviations was conducted. Final manufactured SPPs show some amount of deviation from the expected step heights. To try and understand how this affects the generated mode content, each point of the SPP surface was allowed to vary randomly within a thickness range of ±0.25 mm (0.083λ). This is a rather large deviation from a machining perspective, so these results represent an upper limit to the effect and are intended to exaggerate mode content deviations. Ten simulations were run, and the average mode content and standard deviation were calculated. Table 4.3 compares the sixteen and eight stepped $\Delta l = \pm 1$ designs. In the $(l = 1, \rho = 0)$ pairing, the sixteen step design shows a decrease in mode content of 1.29% while the eight step design shows a decrease of 0.65%. Minimum changes in mode content were seen when $\rho = 5$ for the sixteen step design and $\rho = 2$ for the eight step design. The sixteen step design had a minimum mode content change of 0.01% and the eight step design had a minimum change of 0.33%. The average difference between the SPP designs with and

Table 4.3: Mode content, in percentages, of a U_0^0 beam passed through a sixteen and eight stepped $\Delta l = 1$ SPP, with a maximum randomised surface deviation of ±0.25 mm.

16 Steps	$\Delta l = 1$	75.06 ±0.05	9.38 ±0.02	3.52 ±0.01	1.83 ±0.01	1.12 ±0.01	0.76 ±0.01
8 Steps	$\Delta l = 1$	69.05 ±0.08	8.61 ±0.028	3.22 ±0.01	1.77 ±0.07	1.68 ±0.01	1.03 ±0.10
	$\rho =$	0	1	2	3	4	5

without surface deviation, across the first six radial mode numbers was 0.26% for the sixteen step design and 0.30% for the eight step design.

Figure 4.1: A polypropylene $\Delta l = \pm 1$ SPP.

Calculated modal content for the sixteen stepped $\Delta l = \pm 1$ SPP (Table 4.1) was used to reconstruct the SPP generated beam at a propagation distance of 166.7λ (500 mm) (Fig. 4.2). Each point on the SPP surface was allowed to varying randomly between ±0.25 mm (0.083λ), the incident beam waist was 8.3λ (25 mm) and the incident wave-

length was $\lambda = 3\,\text{mm}$. The reconstructed intensity shows a very slight asymmetry indicated by the larger region of maximum intensity on the right hand side of the vortex (Fig. 4.2a). This is expected, if there exists a superposition of different azimuthal mode numbers. Examining the mode content further, it was found the this beam contained $0.43 \pm 0.03\%$ $(l = 0, \rho = 0)$ and $0.23 \pm 0.01\%$ $(l = 2, \rho = 0)$. Other $l \neq 1$ modes were also present, but the maximum contributed power from the set of these modes was $0.08 \pm 0.01\%$. Furthermore, the phase wraps around the propagation axis (Fig. 4.2b) as expected.

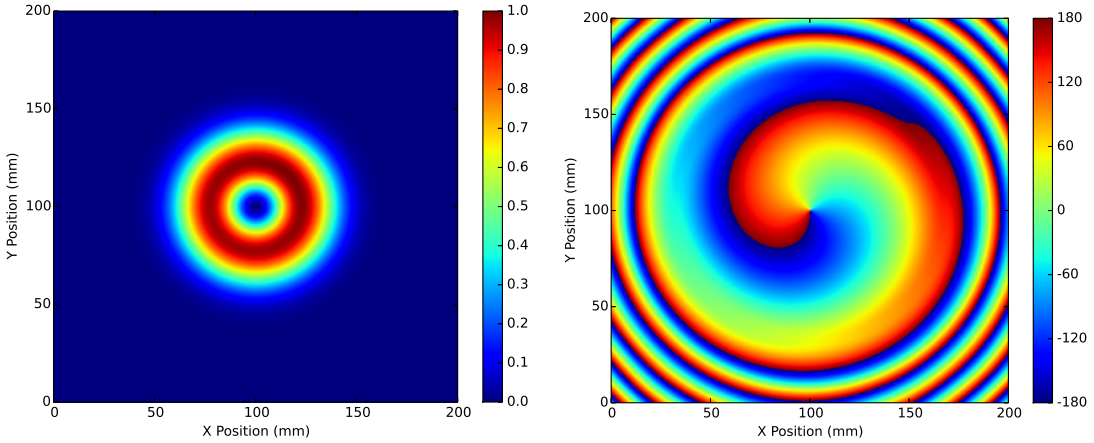

(a) Reconstructed Intensity *(b) Reconstructed Phase*

Figure 4.2: Reconstructed intensity and phase of a sixteen stepped $\Delta l = \pm 1$ *SPP with a randomly varying surface of* $\pm 0.25\,mm$ (0.83λ).

4.2.2 Mode Two Single Stepped SPP

A similar analysis was conducted for the $\Delta l = \pm 2$ in a single step configuration (Fig.4.3). Here, a smooth, thirty-two stepped and thirty-two stepped SPP with surface variations are compared. As with the $\Delta l = \pm 1$ mode spectra (Table 4.4), the smooth $\Delta l = \pm 2$ SPP has the most centralised mode content. Discretising the SPP lowers the $(l = 2, \rho = 0)$ from 50% to 48.69%, a change of 1.31%. Allowing the SPP surface to a randomly vary by $\pm 0.25\,\text{mm}$ lowers the $(l = 2, \rho = 0)$ mode content by a further 3.75%, a drop of

Table 4.4: Mode content, in percentages, of a U_0^0 beam passed through a smooth and a thirty-two single stepped $\Delta l = \pm 2$ SPP, with and without a maximum randomised surface deviation of ± 0.25 *mm.*

Smooth	$\Delta l = 2$	50.00	16.67	8.33	5.00	3.33	2.38
32 Steps	$\Delta l = 2$	48.69	16.23	8.11	4.87	3.25	2.32
Stepped and Deviation	$\Delta l = 2$	44.94	14.98	7.48	4.51	3.01	2.15
		±0.10	±0.04	±0.06	±0.03	±0.02	±0.02
	$\rho =$	0	1	2	3	4	5

5.06% from the smooth model.

Figure 4.3: A single step polypropylene $\Delta l = \pm 2$ SPP.

Modal content from Table 4.4 was then used to reconstruct the generated beam, at a propagation distance of 166.7λ (500 mm) (Fig. 4.3). In the reconstructed beam, two phase dislocations are visible, which wrap around the propagation axis. Again, the intensity pattern is slightly asymmetrical, with a higher peak in the upper right quadrant, due to $l \neq 2$ modes. The largest $l \neq 2$ mode was $(l = 1, \rho = 0)$, which contributed on average $0.28 \pm 0.03\%$ beam power, followed by $(l = 3, \rho = 0)$ contributing $0.12 \pm 0.01\%$

and finally the next largest $l \neq 2$ contribution was from differing modes but had an average value of $0.09 \pm 0.03\%$.

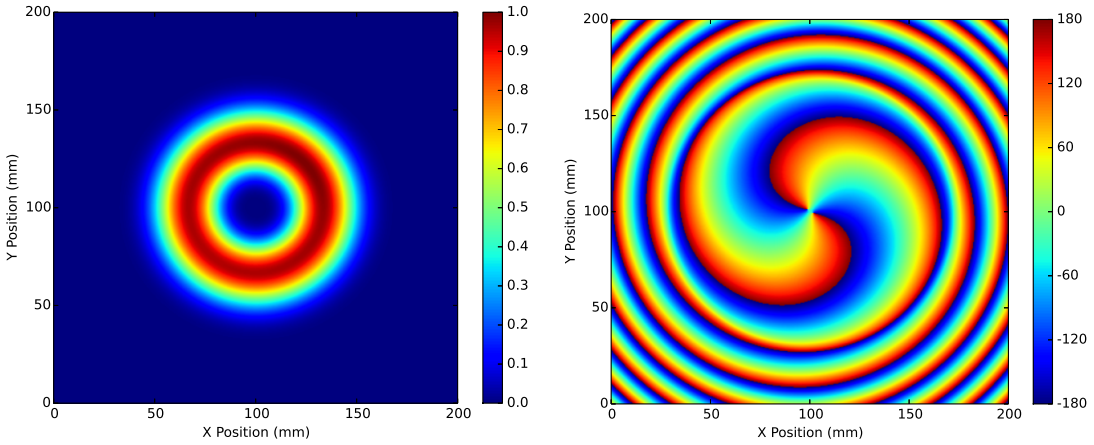

(a) Reconstructed Intensity *(b) Reconstructed Phase*

Figure 4.4: Reconstructed intensity and phase of a thirty-two stepped $\Delta 2 = \pm 1$ *SPP in a single step configuration, with a randomly varying surface of* $\pm 0.25\,mm$ (0.83λ).

4.2.3 Mode Two Split Stepped SPP

In this section the mode contents of a smooth, discretised, and randomly fluctuating surface $\Delta l = \pm 2$ SPP in a split configuration (Fig. 4.5) are compared. Mode content of the discretised split configuration (Table 4.4) is slightly lower compared to the discretised single step configuration (Table 4.5). As expected, allowing the surface to randomly vary lowers the mode content further. While the discretised single step configuration had a more concentrated mode content when compared to the split step configuration, the opposite was true if the surface was allowed to vary. This is due to the symmetry of the SPP, which is more resilient under improper phase shifts, while the single step configuration is not.

Table 4.5: Mode content, in percentages, of a U_0^0 beam passed through a smooth and a thirty-two split stepped $\Delta l = \pm 2$ SPP, with and without a maximum randomised surface deviation of ± 0.25 *mm.*

Smooth	$\Delta l = 2$	50.00	16.67	8.33	5.00	3.33	2.38
32 Steps	$\Delta l = 2$	48.68	16.23	8.12	4.87	3.25	2.32
Stepped and Deviation	$\Delta l = 2$	45.08	15.03	7.52	4.52	3.01	2.16
		±0.07	±0.05	±0.03	±0.02	±0.01	±0.01
	$\rho =$	0	1	2	3	4	5

Figure 4.5: A split stepped polypropylene $\Delta l = \pm 2$ SPP.

Finally, the generated modal content (Table 4.5) was used to reconstruct the intensity and phase (Fig. 4.6) of the split configuration $\Delta l = \pm 2$ SPP, at a propagation distance of 166.7λ (500 mm). As expected, two phase dislocations rotate about the propagation

axis. However, unlike the previously reconstructed beams, this intensity pattern exhibits mirror symmetry about the line $\phi = 135°$. To either side of this line, along the annular beam pattern the intensity increases to form a peak, and then decreases again. This is due to having a primary step on either side of the SPP. There were some $l \neq 2$ contributions to the mode content of the beam. The largest of these was $(l = 0, \rho = 0)$, which contributed $0.35 \pm 0.5\%$ to superposition, while $(l = 4, \rho = 0)$ contributed $0.06 \pm 0.00\%$. The next largest $l \neq 2$ contribution came from various modes but had an averaged value $0.05 \pm 0.01\%$.

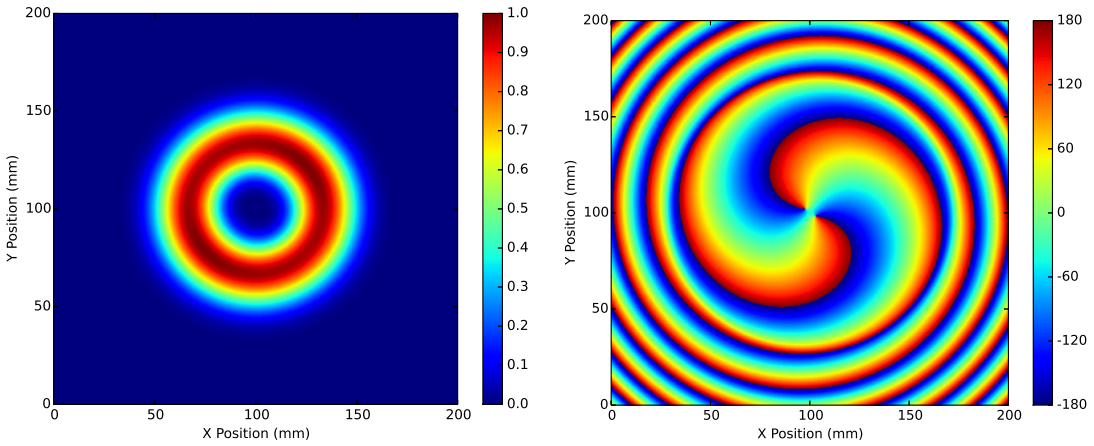

(a) Reconstructed Intensity *(b) Reconstructed Phase*

Figure 4.6: Reconstructed intensity and phase of a thirty-two stepped $\Delta l = \pm 2$ SPP in a split step configuration, with a randomly varying surface of $\pm 0.25\,mm$ (0.83λ).

4.2.4 RMS Intensity Error as a function of the number of steps-per-mode

It should be clear now that discretising the surface of an SPP alters the resulting intensity pattern. This effect has been discussed in [100], in which the minimum number of discrete SPP steps was found for a specific case by calculating the RMS error in intensity between a perfectly smooth and stepped SPP. Kotlyar and Kovalev [100], suggest that the RMS error in intensity must be below 2% to be considered acceptable.

Table 4.6: RMS Error (%) as a function of the number of steps-per-mode for three SPP designs.

Steps-per-mode	$\Delta l = 1$	$\Delta l = 2$	$\Delta l_{split} = 2$
4	7.38	8.16	7.96
8	1.29	1.80	1.08
16	0.29	0.43	0.22

Although there is no justification for the 2% level, it will be used as an upper bound for acceptability here. So, any RMS above 2% is unacceptable, anything below 2% is acceptable, however lower RMS is always desirable. Table 4.6 shows the RMS error in intensity, as a function of the number of steps-per-mode for all three SPP designs. As one would expect, increasing the steps-per-mode decreases the difference between the smooth and stepped SPP generated beams, thereby reducing the RMS error. Four steps-per-mode in any case is deemed unacceptable, while eight steps-per-mode is. Yet, because there is such a reduction in RMS error by using sixteen steps-per-mode, and because this step density is still easily machinable, the future SPPs manufactured for this thesis will use sixteen steps-per-mode.[1]

4.2.5 Analytical Conclusion

Analytical modelling of the $\Delta l = \pm 1$, $\Delta l = \pm 2$ and split configuration $\Delta l = \pm 2$ has given some insight into what to expect from actual measurements (Table 4.7. Table 4.2 showed that the mode spectra of a $\Delta l = \pm 1$ SPP became less concentrated as the number of steps used to approximate a smooth surface was decreased. Since smooth SPPs are known to be difficult to manufacture [27, 28], further analysis focused on stepped SPP designs. In particular, a sixteen and eight stepped $\Delta l = \pm 1$ was modelled with a point-wise surface variation of ± 0.25 mm (0.083λ), to mimic machining and surface

[1]This excludes Chapter 7, however a similar analysis was done for this new SPP design showing that the utilised steps-per-mode was still acceptable.

inaccuracies. Ten simulations were conducted and Table 4.3 shows the average mode content value with a one standard deviation value. These simulations resulted in an reconstructed intensity and phase plot (Fig. 4.2), showing an annular intensity pattern and spiralling phase dislocation, or branch cut (BC). A small amount of unwanted azimuthal modes results in an asymmetrical intensity pattern.

Two $\Delta l = \pm 2$ SPP designs were also studied. First, a single primary step $\Delta l = \pm 2$ SPP was simulated with a smooth, sixteen steps-per-mode, and sixteen steps-per-mode varying surface. Table 4.3 summarised the results of these simulations, and shows that mode content becomes less concentrated as the SPP continuously deviates from a smooth surface. An annular intensity and phase pattern was reconstructed from the simulated mode spectrum (Fig. 4.4). Two phase dislocations, or BCs were visible in the phase, while unwanted azimuthal modes contributed to a small asymmetry in the intensity pattern.

Next, a $\Delta l = \pm 2$ split configuration SPP was simulated in a similar manner to the single primary step $\Delta l = \pm 2$ SPP. Its mode spectrum is shown in Table 4.5. This split configuration SPP has an identical mode spectrum to the single primary step design, when both have a smooth surface. Both designs have nearly identical mode spectra when each SPP surface is stepped with sixteen steps-per-mode as well. However, the more realistic simulation, where the surface is allowed to vary, indicates that a split configuration is more stable. Under this scenario the mode spectrum of the split configuration is more concentrated when compared to the single primary step design. An intensity and phase pattern was also reconstructed for the split configuration (Fig. 4.6). It is difficult to determine if the intensity pattern is more or less symmetrical when compared to the single step SPP design. By reviewing the contribution of unwanted azimuthal modes, it is found that the split configuration has a higher $(l = 0, \rho = 0)$ contribution, but all other $l \neq 2$ contributions are lower, when compared to the single step SPP.

Finally, the steps-per-mode value chosen for the actual SPPs manufactured for this thesis was justified by calculating the RMS error between the intensity patterns of a

smooth SPP and a stepped SPP. A maximum value of 2% was required. It was found in Table 4.6 that four steps-per-mode was unacceptable in all cases, however eight steps-per-mode was acceptable. Yet, sixteen steps-per-mode was chosen for the SPPs used in this thesis, because the RMS error in all cases was below 0.5%.

Table 4.7: SPP step height parameters and mode spectra from numerical simulations.

Δl	Configuration	Primary Step (mm)	Single Step (mm)	$\rho = 0$	$\rho = 1$	$\rho = 2$	$\rho = 3$	$\rho = 4$	$\rho = 5$
±1	Single - Smooth	6	-	78.54	9.82	3.68	1.92	1.18	0.79
	8 Steps	-	0.86	69.70	8.70	3.26	1.70	1.04	0.70
	16 Steps	-	0.40	76.35	9.54	3.58	1.86	1.14	0.77
	8 Steps & Deviation	-	0.86 ± 0.25	69.05	8.61	3.22	1.77	1.68	1.03
	16 Steps & Deviation	-	0.40 ± 0.25	75.06	9.38	3.52	1.83	1.12	0.76
±2	Single - Smooth	12	-	50.00	16.67	8.33	5.00	3.33	2.38
	16 Steps	-	0.39	48.69	16.23	8.11	4.87	3.25	2.32
	16 Steps & Deviation	-	0.39 ± 0.25	44.94	14.98	7.48	4.51	3.01	2.15
±2	Split - Smooth	6	-	50.00	16.67	8.33	5.00	3.33	2.38
	16 Steps	-	0.39	48.68	16.23	8.12	4.87	3.25	2.32
	16 Steps & Deviation	-	0.39 ± 0.25	45.08	15.03	7.52	4.52	3.01	2.16

4.3 Modelling with FEKO

This section begins the analysis of the $\Delta l = \pm 1$ and $\Delta l = \pm 2$ SPPs through the use of the electromagnetic simulation software package FEKO. This section builds upon the previous analytical modelling section. There the basic properties of LG beams generated by SPPs was explored. Now, FEKO simulations will be conducted in order to explore the finer details of LG beam generation via SPPs. Each simulation is conducted at SPP design frequency of 100 GHz or $\lambda = 3$ mm. Only one frequency was simulated due to the computing time required. Recall that SPPs are designed to operate at one frequency and unmatched incident radiation will not be phase shifted as required (See Sec. 3.3.7). These simulations used the multi-level multipole method (MLFMM), a variation of method of moments analysis [81]. These simulations show the fine detail, especially in phase, of the generated LG beams. It is expected that these subtle effects will be visible in the measured fields (Chapter 6). In addition, these models may be adjusted in order to emphasise or remove certain phenomenological beam features. Therefore, these models can help experimentalists understand what electromagnetic field features correspond to what physical SPP feature.

4.3.1 Source Types

Three distinct source types will be analysed in this "Modelling with FEKO," section. They are a plane wave aperture source, a true plane wave and a Gaussian beam generated from a corrugated feed horn. There are multiple reasons to explore the affects of using each of these sources. Firstly, beams incident on SPPs are theoretically expected to be low divergent [24] and planar. For this reason, a true plane wave has been selected as a source. However, true plane waves are not realisable in experimental systems. Therefore, a plane wave leaving a square aperture has also been selected as a source. This has a second purpose as well. In Chapter 6, a compact test range antenna (CTRA) will be used to illuminate several SPPs. The CTRA is composed of two reflectors, which may be thought of as an aperture, which creates a quasi-planar phase front on

the resulting beam waist. Therefore, the aperture source used in the FEKO model is meant to mimic the CTRA field. Finally, a Gaussian beam generated by a corrugated feed horn was selected as the third source. Even though the Gaussian beam is not of low divergence, as the theoretical treatment of SPPs expects, it does represent more practical telescope systems. As discussed in Chapter 1, future millimetre wavelength PMTs will most likely be comprised of SPPs placed in front of the telescope feed antenna. Therefore, in a practical system, SPPs will be illuminated by highly divergent beams, and therefore the selection of the Gaussian beam source is justified.

4.3.2 Model Geometry

The configuration of each FEKO model utilises the geometry shown in Fig. 4.7. The configuration consists of three surfaces in the XY plane. Each surface is in the near field of the SPP. The three XY near fields are 10×10 cm in the x- and y-directions respectively and have a resolution of two points per millimetre. Near field 1 (closest to the SPP) is 6.7λ (20 mm) from the back surface of the plate. Near field 2 is 40λ (120 mm) from the back SPP surface, while near field 3 (furthest from the SPP) is 73.3λ (220 mm) from the back SPP surface. Each surface is made up of a grid of points spaced 0.5 mm apart[2]. The specific dimensions, resolutions and locations of each modelled near field were chosen so that measurements of the same surfaces were easily achievable with the system detailed in Chapter 5. Future sections mention the use of a modelled SPP mount. This mount (Fig. 4.7) is 175×175 mm with a 50 mm radius hole in the middle to accommodate the SPP. Radiation is allowed to propagation around the edges of the modelled mount, so as to mimic the actual SPP used in measurements.

4.3.3 Free Space Propagation of Sources

To fully understand the SPP model results, the effects of the SPP mount and source must be understood. Therefore, this first subsection examines the source beams in free

[2]The plotting functions used plot each individual point of the measurement file.

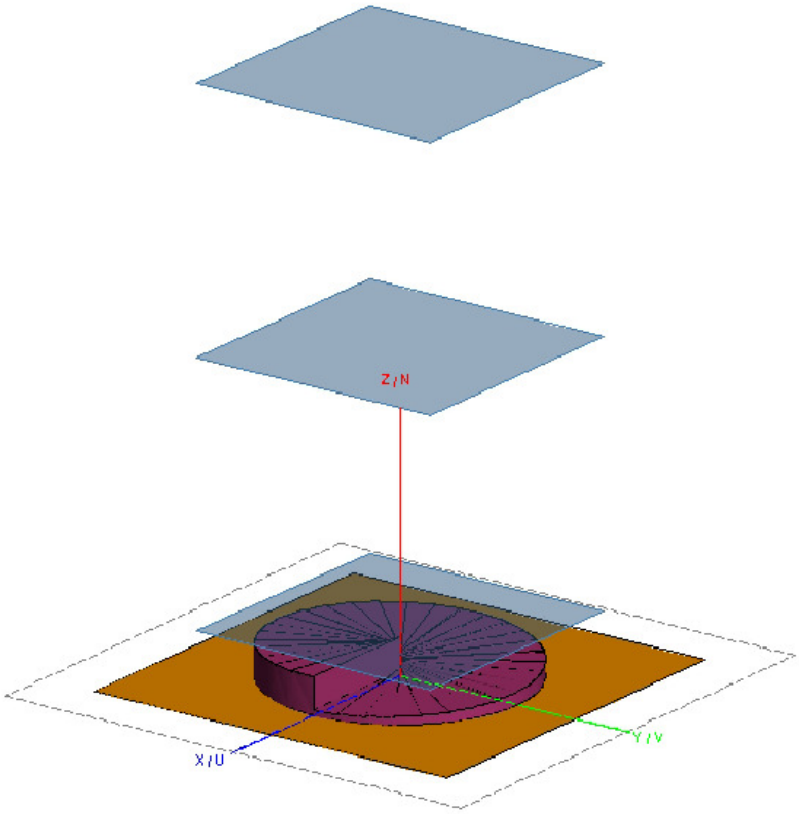

Figure 4.7: The FEKO configuration used in SPP modelling. The gold plate represents the SPP mount, the purple SPP is an $l = \pm 2$ stepped plate, the grey sheets are the locations of the modelled field.

space. The next subsection (4.3.4) explores the effect of the SPP mount on the source pattern.

Free Space Aperture Source

The aperture source used extended 55 mm from the centre of the beam propagation axis in both x- and y-directions. The source was made up of 111 source points in both directions, meaning there was one source point per millimetre. The phase of the first near field plane illuminated with an aperture source is shown in Fig. 4.8a, while the phase of the second and third planes are shown in Fig. 4.8b and Fig. 4.8c respectively.

Individual sources are visible in the first plane (Fig. 4.8a), while the beam starts

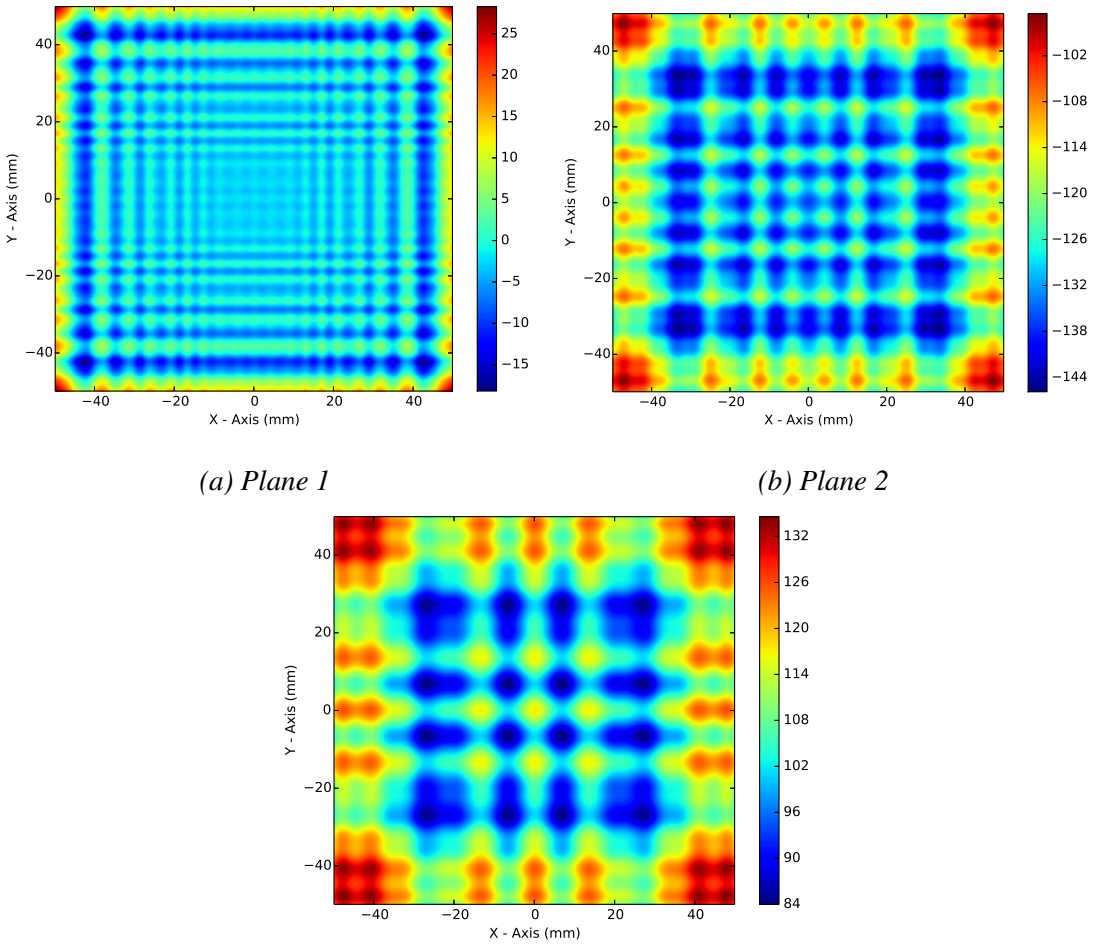

(a) Plane 1

(b) Plane 2

(c) Plane 3

Figure 4.8: Aperture source phase (Degrees) in free space.

to diverge as it reaches the second and third plane. Despite being made up of several independent sources, the aperture source creates a nearly planar phase front. This is especially true near the centre of the beam, between 50.0 mm and −50.0 mm in the x- and y-directions. The phase variation in this region was approximately 20°.

The phase pattern smoothed out further as the beam reached the third plane. Phase variations in the centre portion of the beam increased slightly from approximately 20° to 30°. Although the intensity around the edges of the plane are quite high, the intensity variation across the middle of the beam is low. The intensity peak in the centre of the plane is approximately 1.0 V/m, while the intensity minima in this region is

around 0.96 V/m. As the electric field from the free space aperture source is allowed to propagate, the individual source beams start to diverge and interfere, creating a more variant intensity pattern. The difference between the peak and minima intensity values in the centre of the beam shown in Fig. 4.9 is approximately 0.3 V/m. Intensity variations have started to smooth by the time the beam has reached the final modelling plane (Fig. 4.9e and 4.9f). The peak to peak variation in the centre of the beam is around 0.2 V/m.

Free Space Gaussian Source

A far field pattern of a compact corrugated W-Band horn (Known to have a beam that is 98% fundamental Gaussian.) was used to as a free space Gaussian source. This was done because the particular horn was implemented to create the incident Gaussian beam used to illuminate the SPPs during measurement. In addition the horn model had been validated previously (See Sec. 5.6).The phase of the Gaussian beam pattern on the 6.7λ (20 mm) plane is shown in Fig. 4.10a. The phase pattern is axially symmetric, while sidelobes are partially visible at the very extreme edge of the plot near ($x = \pm 40, y = \pm 40$). These should not affect future measurements since the SPP mount inner radius is 55.5 mm.

Phase was also modelled on the 40λ (120 mm) (Fig. 4.10b) and 73.3λ (220 mm) (Fig. 4.10c) planes. Both figures show a smooth phase pattern, with no distortions.

Modelled intensity patterns of the corrugated feed horn antenna are shown in Fig. 4.11. Each intensity pattern shows high levels of azimuthal symmetry. Additionally, the divergent property of the beam is visible by observing how the beam radius increases with propagation.

Free Space Plane Wave Source

A true plane wave was also modelled using FEKO. Since the plane wave formalism used by FEKO does not include any perturbations, phase and intensity of the wave are

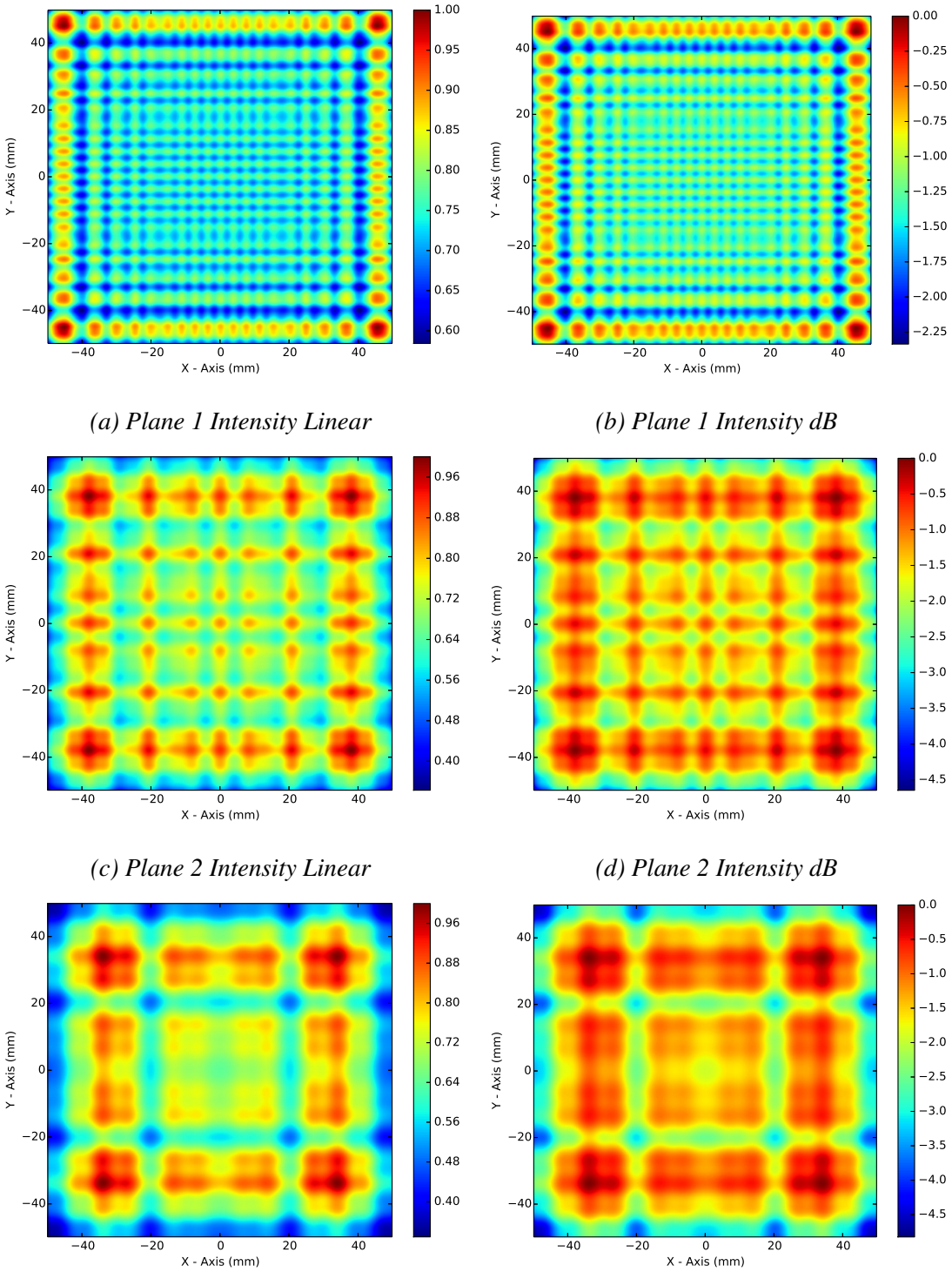

(a) Plane 1 Intensity Linear

(b) Plane 1 Intensity dB

(c) Plane 2 Intensity Linear

(d) Plane 2 Intensity dB

(e) Plane 3 Intensity Linear

(f) Plane 3 Intensity dB

Figure 4.9: Aperture source intensity modelled in free space

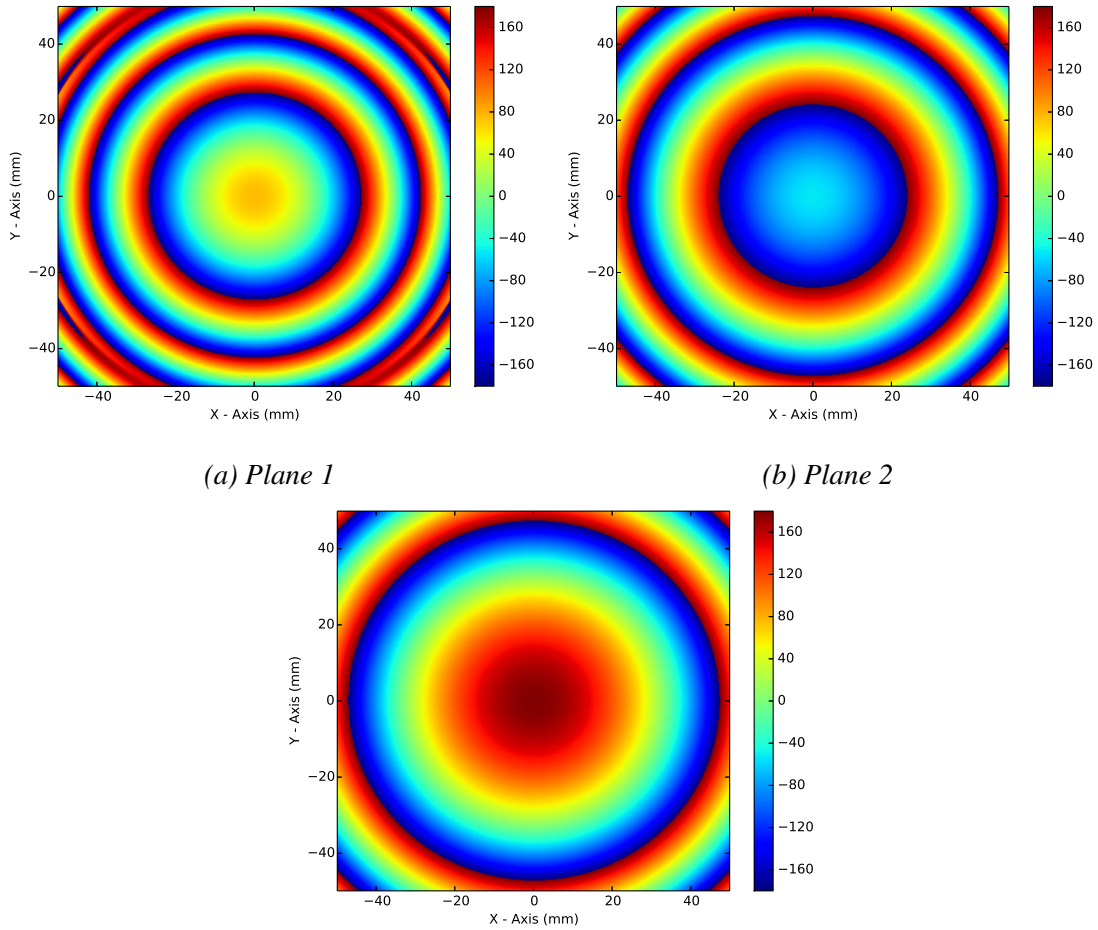

(a) Plane 1

(b) Plane 2

(c) Plane 3

Figure 4.10: Modelled phase (Degrees) of a free space Gaussian beam.

constant over all modelled planes.

4.3.4 Systematics Analysis

In this section, diffraction effects from the SPP mount are studied by illuminating the mount with the aperture, plane wave and Gaussian sources. These will be used to help determine, which beam features are due to the SPP and OAM and which features are due to SPP mount diffraction.

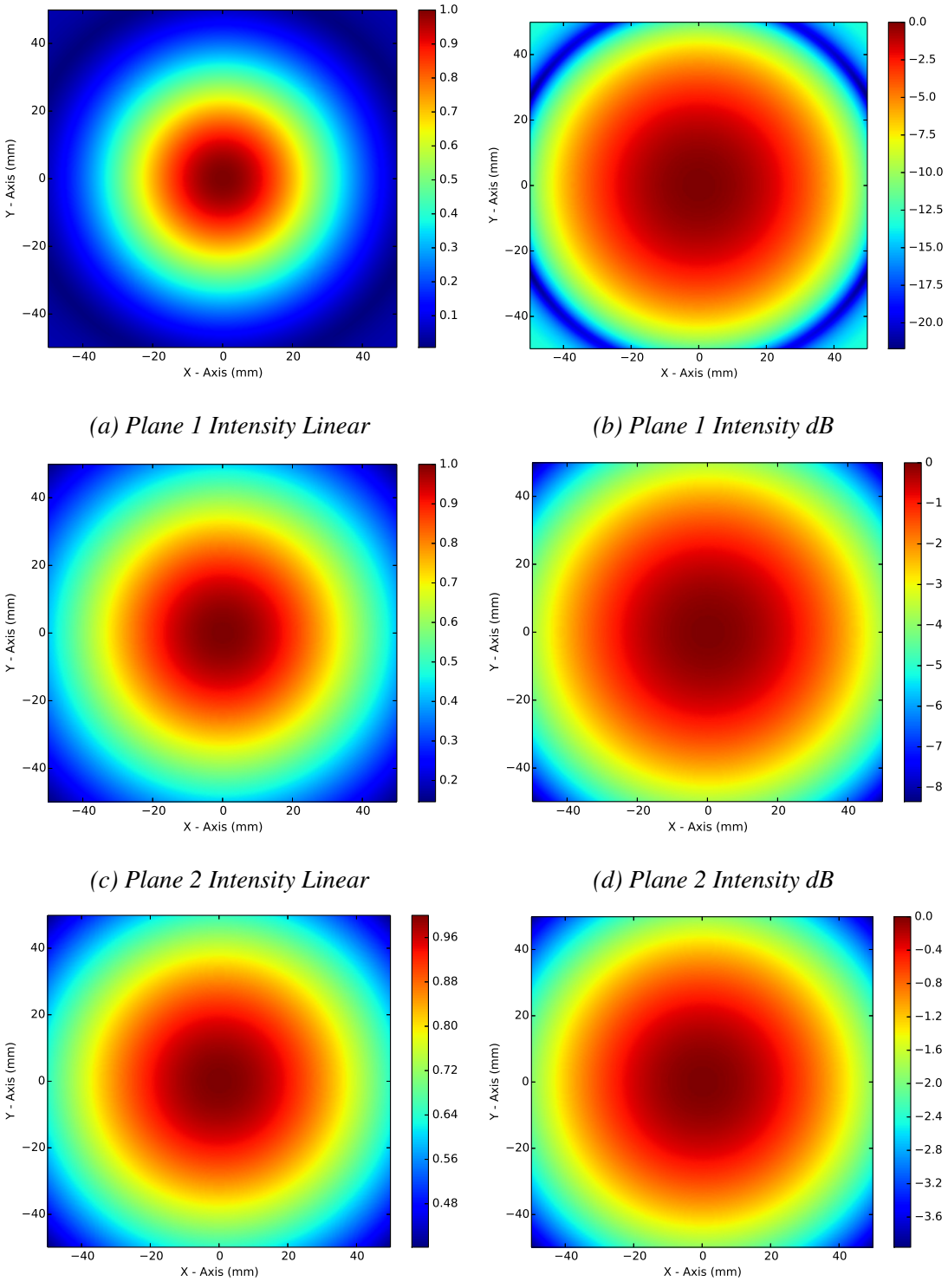

(a) Plane 1 Intensity Linear

(b) Plane 1 Intensity dB

(c) Plane 2 Intensity Linear

(d) Plane 2 Intensity dB

(e) Plane 3 Intensity Linear

(f) Plane 3 Intensity dB

Figure 4.11: Modelled intensity of a free space Gaussian beam.

Aperture source incident on SPP mount

Minute phase variations are visible on the first model plane (Fig. 4.12a). Individual sources are no longer visible, although multiple concentric rings in phase are. Additionally, phase variations along the Y-Axis and the line $x = 0.0$ mm, are slightly more defined than the variations in the x-direction.

Phase variations continued to be small after propagation to the 40λ (120 mm) plane (Fig. 4.12b). However, diffractive effects start to become relevant. There is a low phase peak ($\approx -80°$) at a radial distance of approximately 40 mm. There is also a second ($\approx -80°$) but smaller (in radial size) peak at a radial distance of approximately at 20 mm.

Phase variations in the third plane (Fig. 4.12c) are similar in location, but stronger in magnitude compared to the second plane (Fig. 4.12b). There is a peak, compared to the beam centre, of nearly 60°, comprised of two concentric rings at a radial distance of approximately 40 mm. The second phase peak at a radial distance of approximately 20 mm in Fig. 4.12b has become a phase trough in Fig. 4.12c, but remains at a radial distance of 20 mm.

Linear and dB scaled intensity patterns of the aperture source incident on the SPP mount, are presented in Fig. 4.13. Figure 4.13a and 4.13b are largely affected by the discretisation of the aperture source. A distinct cross pattern can be seen running along the lines $x = 0.0$ mm and $y = 0.0$ mm. Radial dependence of the intensity is also visible. As the beam propagates to the second modelling plane (Fig. 4.13c and 4.13d), three distinct intensity rings develop. These result from diffraction caused by the SPP mounting surface. In addition to these rings there is a strong intensity peak on the propagation axis. The intensity pattern is reorganised into two rings at the third modelling plane (Fig. 4.13e and 4.13f). Despite the discretised incident aperture source beam, the intensity on the 73.3λ (220 mm) plane is smooth and continuous.

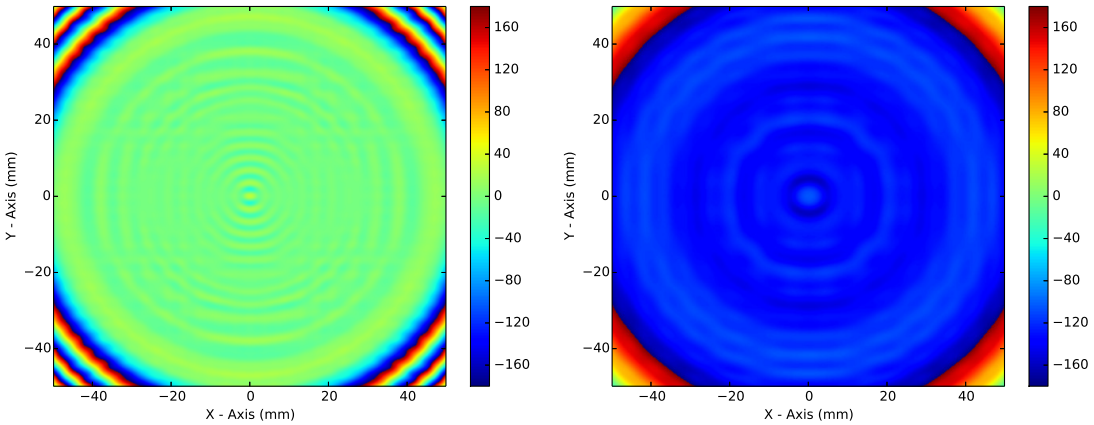

(a) Plane 1

(b) Plane 2

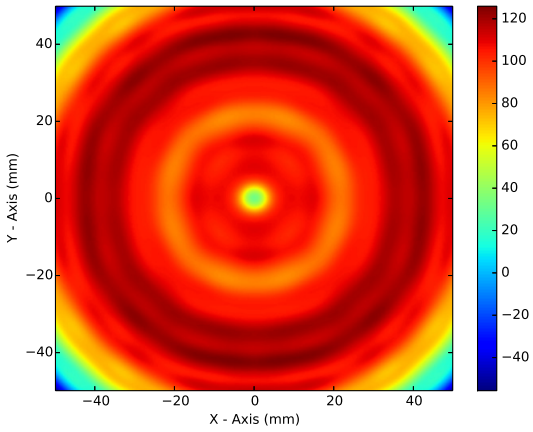

(c) Plane 3

Figure 4.12: Phase (Degrees) of an aperture source beam incident on the SPP mount.

Plane Wave source incident on SPP mount

A true plane wave incident on the SPP mount was also modelled. Multiple diffraction rings are visible in the first plane (Fig. 4.14a). However, the phase variation along the X-Axis, centred on the Y-Axis, is small. The 6.7λ (20 mm) phase plane is similar to the aperture source illuminated modell (Fig. 4.12a).

Unlike the aperture source illuminated 40λ (120 mm) plane (Fig. 4.12b), illumination by a plane wave is far more uniform. Small ring variations in phase are visible, but the peak variation is only approximately 40°.

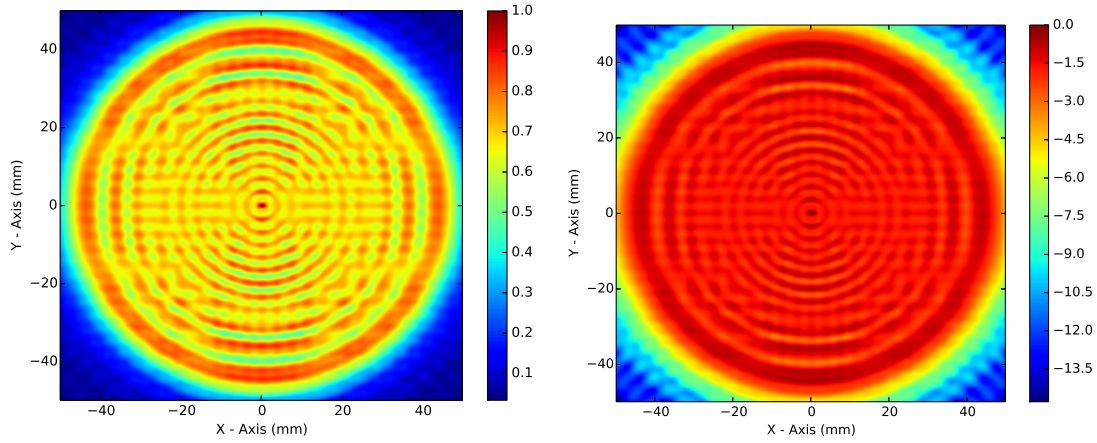

(a) Plane 1 Intensity Linear *(b) Plane 1 Intensity dB*

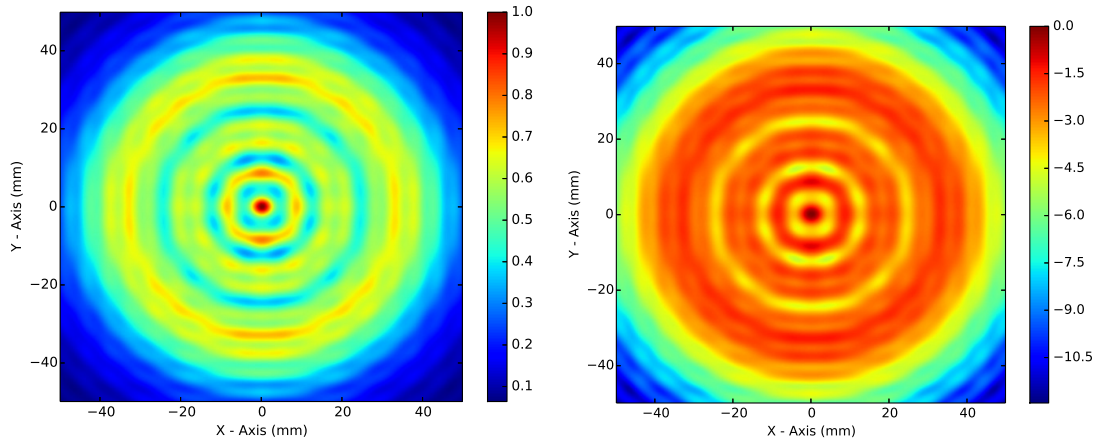

(c) Plane 2 Intensity Linear *(d) Plane 2 Intensity dB*

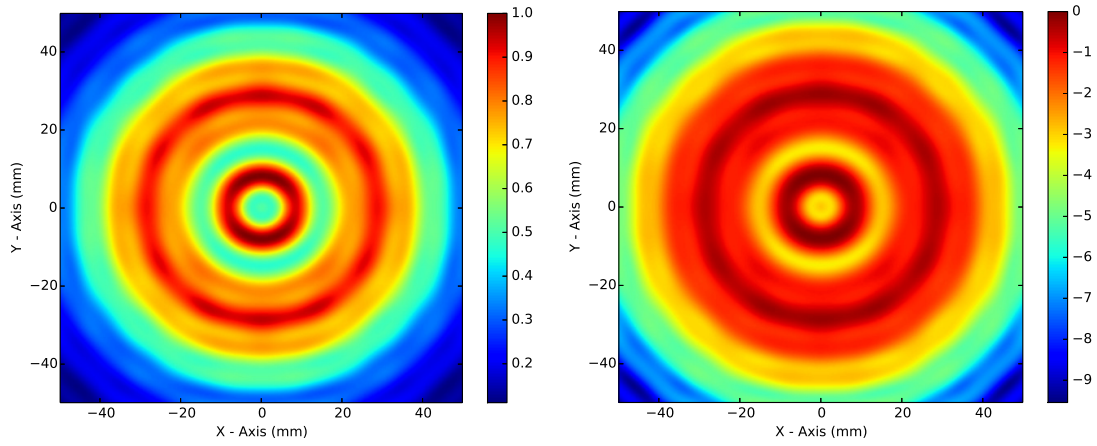

(e) Plane 3 Intensity Linear *(f) Plane 3 Intensity dB*

Figure 4.13: Intensity of an aperture source beam incident on the SPP mount.

Phase on the 73.3λ (220 mm) plane is even more uniform. There is a small phase jump in the centre of the beam, but only one diffraction ring is visible. Variations are small and the number of diffraction rings are fewer, but there is still some structure to the phase plane. Specifically there is an interference cross along the centre of the X- and Y-Axis.

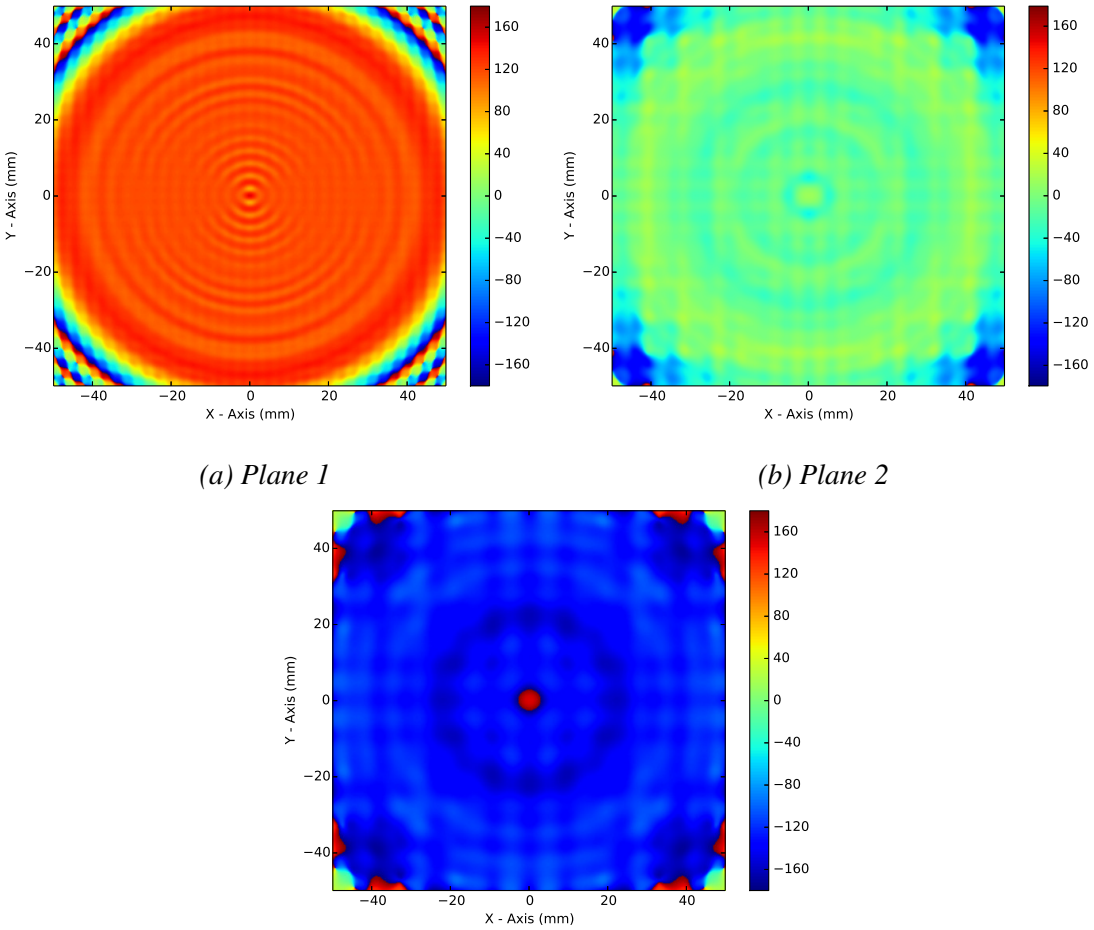

(a) Plane 1

(b) Plane 2

(c) Plane 3

Figure 4.14: Phase (Degrees) of an plane wave incident on the SPP mount.

Like the intensity patterns generated with the aperture source (Fig. 4.13a and 4.13b), the plane wave generated intensity (Fig. 4.15a and 4.15b) is radially dependent, and dominated by mount induced diffraction. Figure 4.15c and 4.15d show the generated intensity pattern on the second modelling plane. Just as in the aperture case, three

intensity rings are present accompanied by a strong on axis intensity peak. However, these patterns are highly discretised and discontinuous. The discontinuities persist to the third modelling plane (Fig. 4.15e and 4.15f). Two intensity rings are visible and prominent features along the $\phi = 45^\circ$ and $\phi = 135^\circ$ radials are present.

Gaussian source incident on SPP mount

Diffractive effects of the SPP mount on the Gaussian beam source were also studied. The source antenna was placed 50λ (150 mm) behind the SPP so that the edge taper was minimal (−40 dB). This limits diffraction caused by the mounting surface. Modelling of the first phase plane (Fig. 4.16a) indicates that this placement worked as expected. Results on the 6.7λ (20 mm) plane showed small diffractive affects on the extreme edges of the model. The rest of the phase pattern remained smooth and continuous.

Phase of the 40λ (120 mm) plane (Fig. 4.16b) and 73.3λ (220 mm) plane (Fig. 4.16c) remain largely unchanged from the free space model (Fig. 4.10b and 4.10c). The phase remained continuous across the entire pattern, and was free of diffractive affects from the SPP mounting structure.

These results create a dilemma for the research. In short, the lack of diffractive effects implies that the Gaussian beam would perform as a good probe of SPP functionality. However, the Gaussian beam is strongly divergent. This will lead to branch point (BP) separation. BPs are points of undefined phase, which are associated with branch cuts (BCs). BCs are lines of dislocation in phase patterns. Such an effect might be acceptable in practical systems where a feed antenna is illuminating a dish, but might not be useful when studying the development of vortex beams from a purely physics perspective. Therefore, all three source types were modelled, so that each situation could be studied.

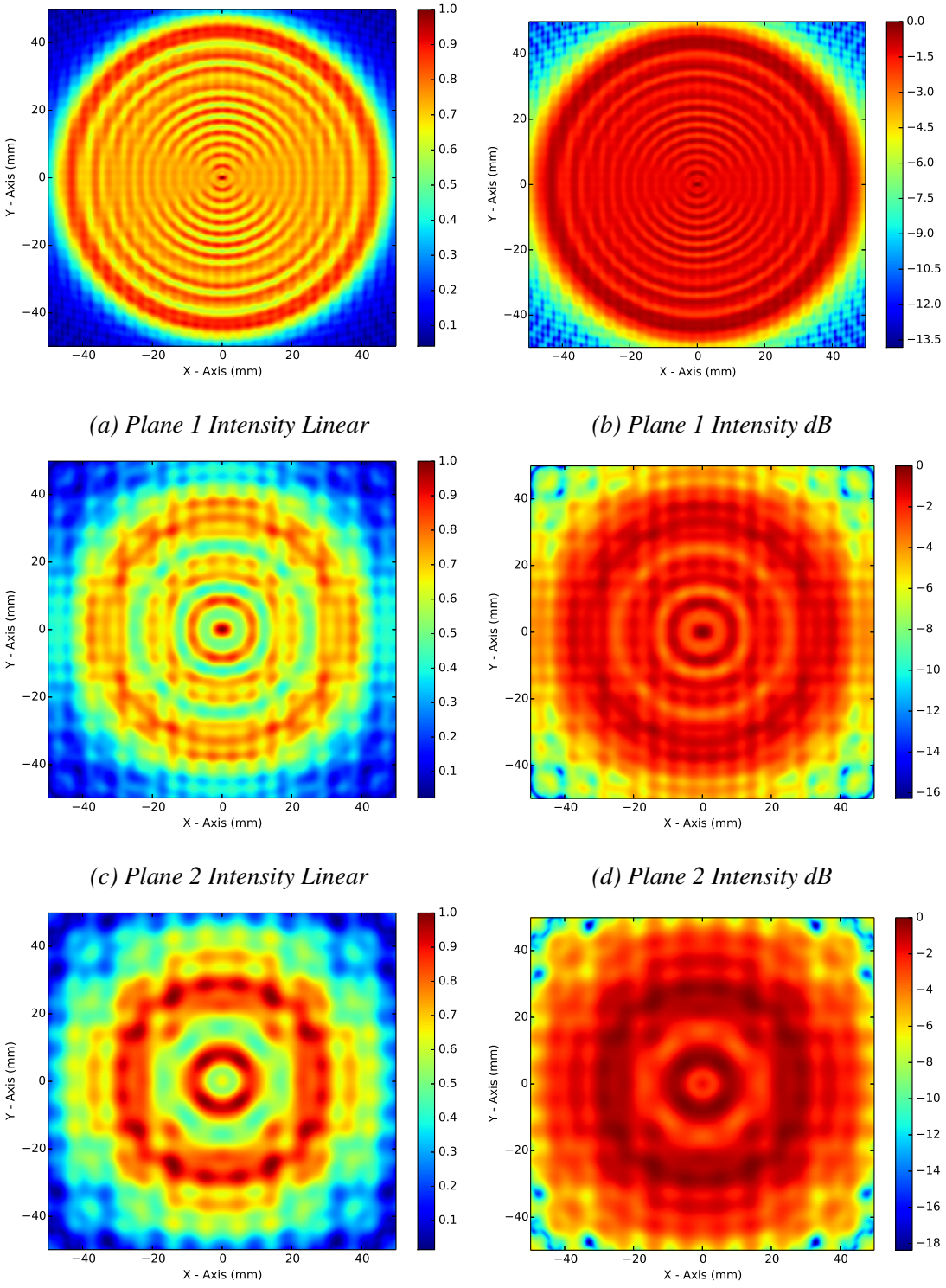

(a) Plane 1 Intensity Linear

(b) Plane 1 Intensity dB

(c) Plane 2 Intensity Linear

(d) Plane 2 Intensity dB

(e) Plane 3 Intensity Linear

(f) Plane 3 Intensity dB

Figure 4.15: Intensity of an plane wave incident on the SPP mount.

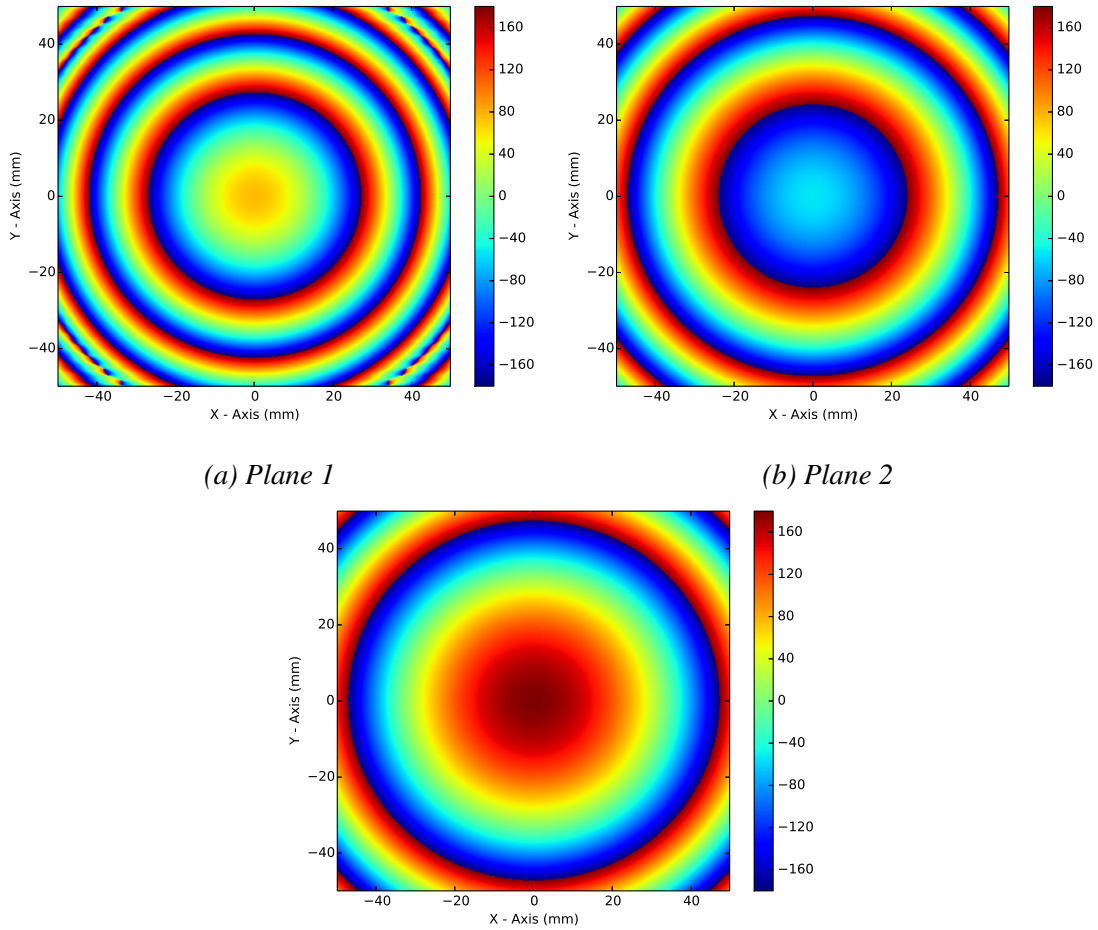

(a) Plane 1

(b) Plane 2

(c) Plane 3

Figure 4.16: Phase (Degrees) of a Gaussian beam incident on the SPP mount.

4.3.5 Systematics Analysis Conclusion

To review, the aperture and plane wave sources produce similar phase (Figs. 4.12 and 4.14) and intensity (Figs. 4.13 and 4.15) patterns. A large number of radial modes are present on the initial phase plane, while the number decreases with an increasing propagation distance. These radial modes are also visible in the intensity patterns. In addition, the intensity on the initial planes is polarisation dependent. The input polarisation of the fields in along the line $x = 0.00\,\text{mm}$, and it is along this line that the variations in intensity are best defined. Variations in the orthogonal direction are blurred, and out of focus. The Gaussian beam shows little deviation from the free space

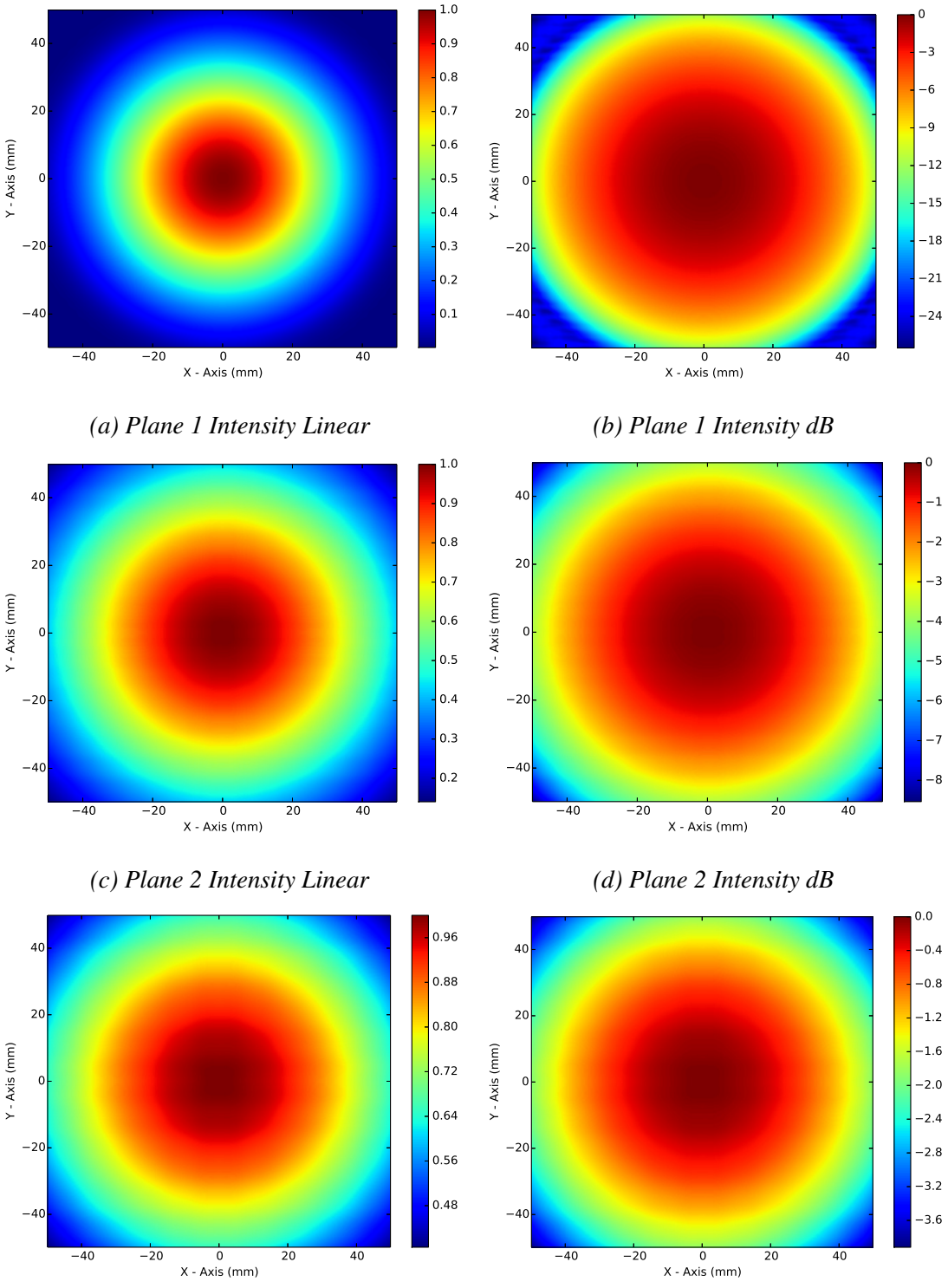

(a) Plane 1 Intensity Linear

(b) Plane 1 Intensity dB

(c) Plane 2 Intensity Linear

(d) Plane 2 Intensity dB

(e) Plane 3 Intensity Linear

(f) Plane 3 Intensity dB

Figure 4.17: Intensity of a Gaussian beam incident on the SPP mount.

Gaussian models. A small phase variation at the extreme edges of field are visible in Fig. 4.16a, but these are removed with an increase in propagation distance. Minimal diffraction effects were achieved by minimising the edge taper (−40 dB) at the SPP mount inner radius.

It is evident from this systematics study that the aperture and plane wave sources experience a great deal of mount induced diffraction. On the other hand, the Gaussian beam source experiences diffraction at a negligible level. However, the aperture and plane wave sources ensure low incident beam divergence. Not only is this required for the standard theoretical development of SPP functionality, but as it will be shown in the following section and in Chapter 6, low divergence beams allow for proper vortex development. This is in contrast to the Gaussian illuminated case, where the high divergence of the transmitted beam forces BPs to spread apart and not properly annihilate. Therefore, the full analysis of source, mount and SPP will be conducted for all three source types.

4.3.6 Full Analysis: Source, Mount and SPP

In this section, full analysis of a stepped $\Delta l = \pm 1$, a single stepped $\Delta l = \pm 2$ and a split stepped $\Delta l = \pm 2$ SPP design is conducted . Each plate was modelled according to the configuration depicted in Fig. 4.7. Phase, intensity in dB and intensity in linear scaling is presented for each plane. Additionally, an aperture feed, plane wave and Gaussian feed antenna were each used as sources for the models.

Aperture illuminated mode one single stepped SPP

Phase modulation generated by the $\Delta l = \pm 1$ SPP, at a distance of 6.7λ (20 mm) behind the plate surface is shown in Fig. 4.18. There is a clear phase dislocation line or BC, which begins at a BP, or location of undefined phase. The BC exhibits "phase dragging," or a back and forth "wiggling." Phase dragging is related to the ringed diffraction pattern also visible in the phase and is caused by the presence of several closely spaced

radial modes. These radial modes cause the BC to abruptly change direction, and when coupled with the expected rotation of the BC about the propagation axis, leads to phase dragging.

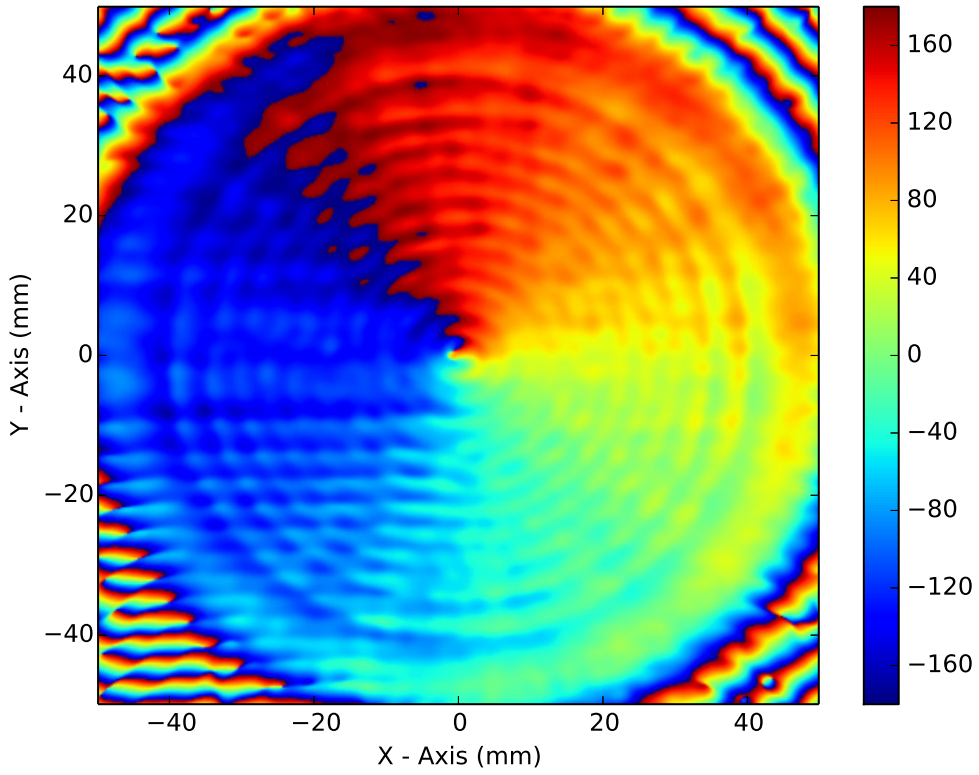

Figure 4.18: $\Delta l = \pm 1$ Aperture Source Plane 1 Phase.

Intensity on the 6.7λ (20 mm) plane is shown in dB (Fig. 4.19b) and linear (Fig. 4.19a) scaling, to emphasise structure at low and high signal levels respectively. Linear intensity resembles an image of the plate surface. Sixteen wedges are visible in the intensity map, along with the primary step along the positive X-Axis. Diffraction rings produced by the SPP mount are also visible in the pattern. Finally, the centre of the intensity pattern contains a circular region of low intensity. This is the intensity null generated by the undefined phase of the BP.

The same intensity pattern in dB scaling is shown in Fig. (4.19b). Decibel scaling forces variations at low signal levels to be more prevalent. Intensity structure around the centre of the beam vortex is more detailed when compared to the linear pattern.

Interestingly, the deepest portion of the vortex is not in line with the centre of the SPP, as indicated by the centre of the annular beam pattern being shifted to the right of the inner most diffraction ring. This is a result of impure mode generation. Although this SPP is designed to generate a $l = \pm 1$ LG beam, the SPP makes a superposition of LG beams. If a superposition is not rotationally symmetric, the surviving vortex is forced from the centre of the propagation axis.

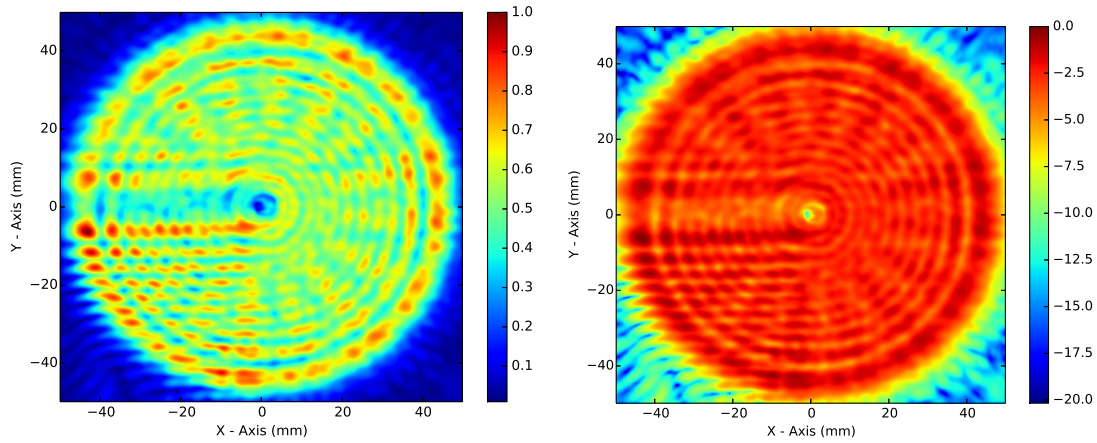

(a) Linear Intensity *(b) Intensity dB*

Figure 4.19: Aperture illuminated $\Delta l = \pm 1$ SPP intensity on Plane 1.

Phase on the second plane at 40λ (120 mm) (Fig. 4.20) continues to show a single BC and phase dragging. However, a new feature is visible. Around the centre of the propagation axis is a small "phase circulation." The BC associated with the central BP starts in the centre of the phase circulation, propagates outwardly, reaches the edge of the circulation, travels around the outer circulation circumference and finally propagates outwardly in a radial manner. This phase circulation is an indication of a strong radial node. The radial node is visible in the following intensity patterns (Fig. 4.21a and 4.21b).

Linear intensity shown in Fig. 4.21a shows a deep intensity null near the centre of the pattern. Intensity levels rise quickly, directly outside the null. However, an intensity trough follows soon after. This is the radial intensity null caused by the phase

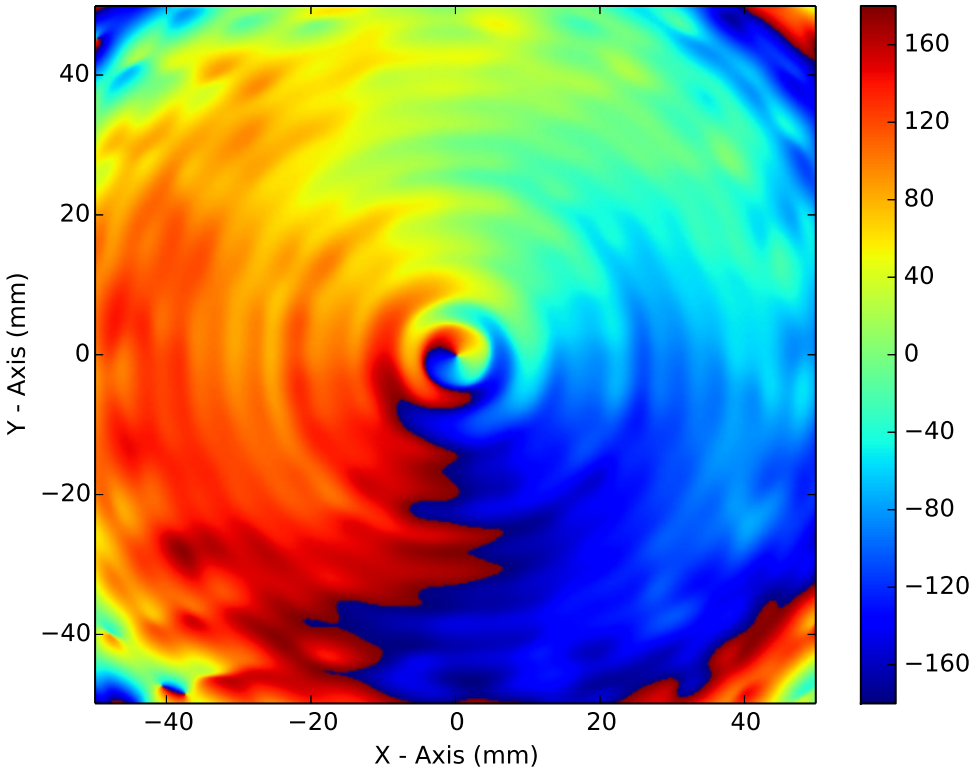

Figure 4.20: $\Delta l = \pm 1$ Aperture Source Plane 2 Phase.

circulation seen in Fig. 4.20. There are four intensity rings in total, though only the outer three can be attributed to diffraction from the SPP mount. The inner ring was originally the intensity peak seen in Figure 4.12b, but since there is a BP present in the centre of Fig. 4.20, the intensity peak becomes a ring.

Intensity in dB scaling shows two interesting features. First, there are sixteen isolated regions of intensity around the outer radius of the outer most intensity ring. These are caused by the stepped surface of the SPP. Additionally, there is a second but shallower intensity trough at a radial distance of approximately 25 mm from the beam centre. Upon reexamination of the phase in Fig. 4.20, a second phase circulation is barely visible at the same radial distance. This indicates the presence of another radial mode present in the superposition of LG beams, resulting in further mode contamination.

Phase on the 73.3λ (220 mm) plane (Fig. 4.22) has significantly smoothed out compared to the previous planes. Phase dragging persists, as well as the strong phase

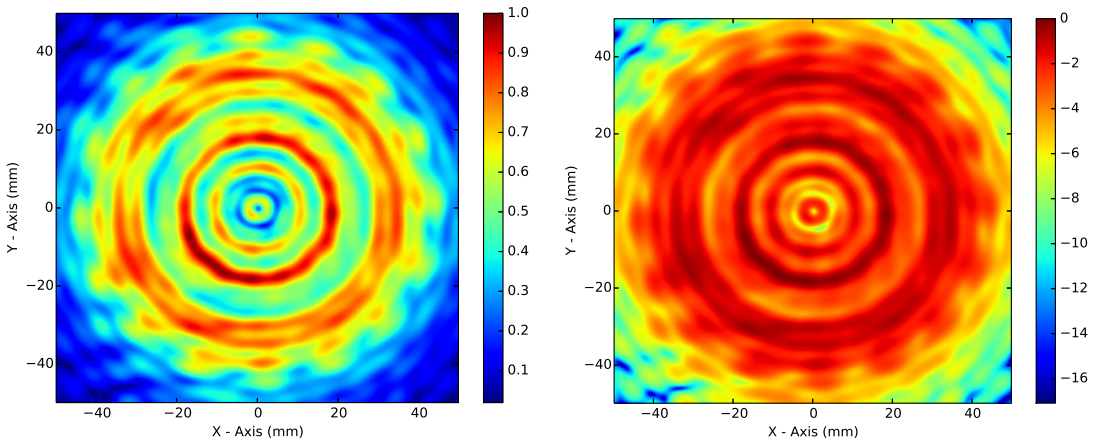

(a) Linear Intensity *(b) Intensity dB*

Figure 4.21: Aperture illuminated $\Delta l = \pm 1$ SPP intensity on Plane 2.

circulation in the centre of the pattern. Interestingly, the BC inside the initial phase circulation is straight, while outside the phase circulation the BC contains no clear straight segment. It appears that the phase circulation creates a boundary, which diffraction affects from the SPP mount can not penetrate. If so, a possible way to limit phase variations, and therefore improve mode purity, would be to enlarge the radius of the phase circulation.

Linear intensity on the third model plane is presented in Fig. 4.23a. Three intensity rings are visible, with a deep inner intensity trough due to the presence of a non zero radial mode number and a slightly weaker intensity trough at a larger radial distance from the propagation axis. Additionally, the vortex is seen to be slightly off centre. This can be visually deduced by observing that the inner intensity ring is not symmetrical. Instead, the intensity ring displays some ellipticity and contains an intensity peak in the lower left hand corner.

Ellipticity of the inner intensity ring is more pronounced by viewing the pattern in dB scaling (Fig. 4.23b). The inner most intensity trough, associated with a non zero radial mode number of the beam, is approximately -12 dB in an angular range of $[0, 3\pi/2]$. The intensity trough is significantly shallower (By approximately 3 dB) in an

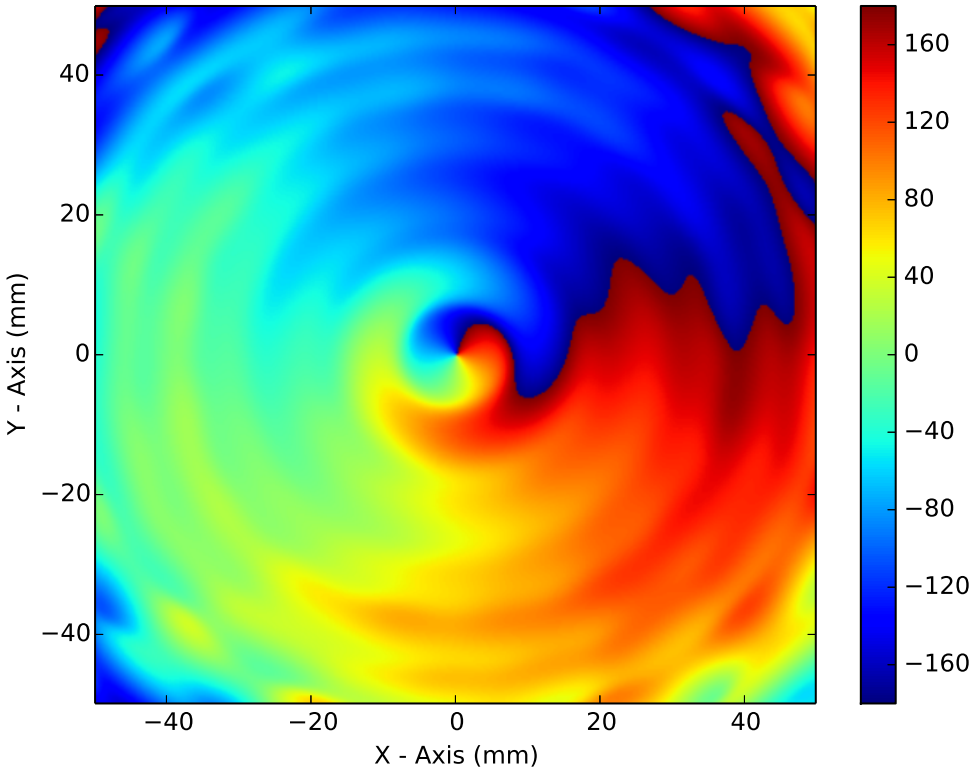

Figure 4.22: $\Delta l = \pm 1$ Aperture Source Plane 3 Phase.

angular range of $(3\pi/2, 2\pi)$.

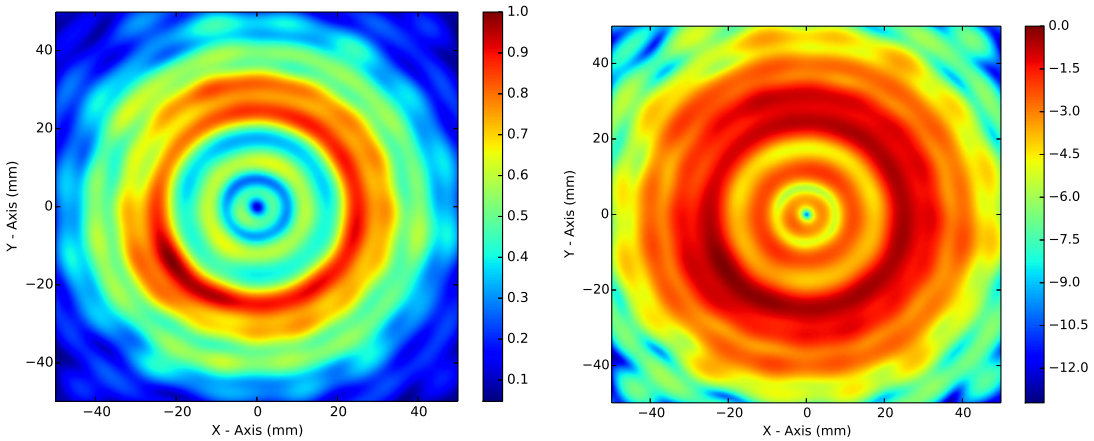

(a) Linear Intensity *(b) Intensity dB*

Figure 4.23: Aperture illuminated $\Delta l = \pm 1$ SPP intensity on Plane 3.

Plane wave illuminated mode one single stepped SPP

In order to compare FEKO source types, a true plane wave source was also modelled. Phase modelled on the 6.7λ (20 mm) plane is shown in Fig. 4.24. Phase dragging is visible along the BC. Again dragging is related to the concentric rings of phase variation. There is also some linear structure to the phase just above and below the line $y = 0.0$ mm. This is due to the primary SPP step.

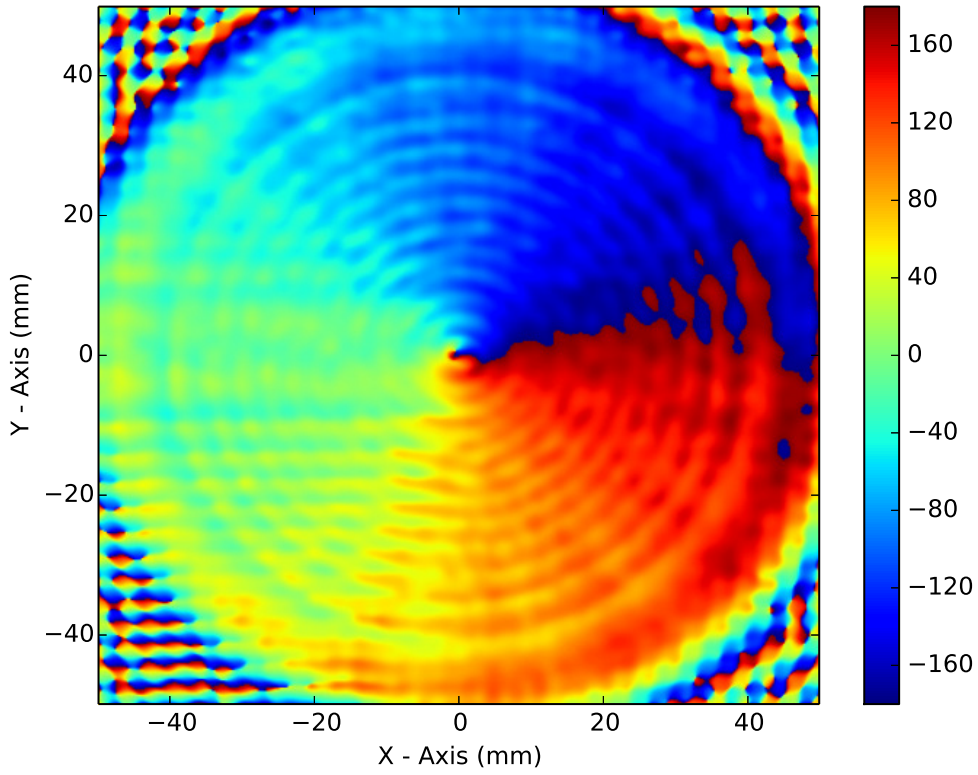

Figure 4.24: $\Delta l = \pm 1$ Plane Wave Source Plane 1 Phase.

Intensity modelled on the 6.7λ (20 mm) plane (Fig. 4.25a) resembles a near field image of the SPP surface. The intensity null in the centre of the pattern is caused by the BP associated with the single BC. The lower right quadrant of the field has a slightly higher intensity then the rest of the plate surface. This is attributed to a significant amount of diffraction from the primary step.

Intensity mapped to dB scaling confirms the presences of interference caused by

the largest SPP step. Linear variations in intensity are clearly visible parallel to the Y-Axis. Additionally, these variations are not visible in the first three quadrants of the SPP circumference. Here, only small radial variations in amplitude are present.

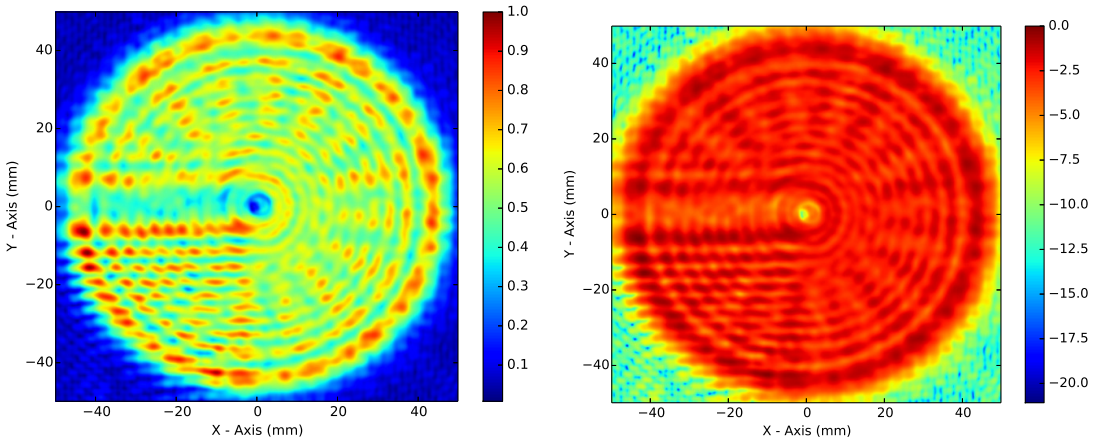

(a) Linear Intensity *(b) Intensity dB*

Figure 4.25: Plane Wave illuminated $\Delta l = \pm 1$ SPP intensity on Plane 1.

Phase modelled on the 40λ (120 mm) plane (Fig. 4.26) contains significant amounts of phase dragging in addition to the development of a phase circulation. The BC propagates in a straight line from the BP. It then reaches the boundary of the phase circulation, rotates about the circumference of the circulation and finally propagates outward with significant amounts of dragging.

Figure 4.27a shows the linear intensity pattern on the 40λ (120 mm) plane. The pattern is largely discontinuous, but still exhibits four intensity rings and a central intensity null. There is an intensity trough around the phase circulation, indicating the presence of a non zero radial mode number ρ. This mode contamination is caused by diffraction from the SPP mount.

The same intensity pattern in dB scaling (Fig. 4.27b) shows that the central intensity null and first intensity trough are approximately at the same intensity level (−15 dB). However, the second and third intensity troughs are at a much shallower level of approximately −8 dB.

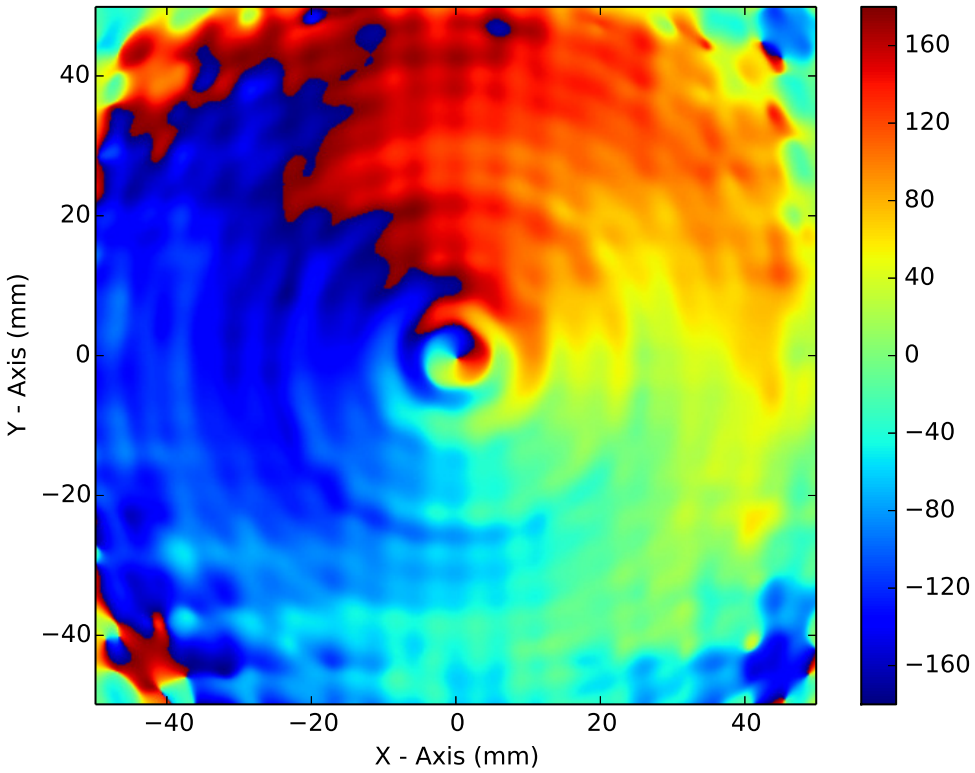

Figure 4.26: $\Delta l = \pm 1$ Plane Wave Source Plane 2 Phase.

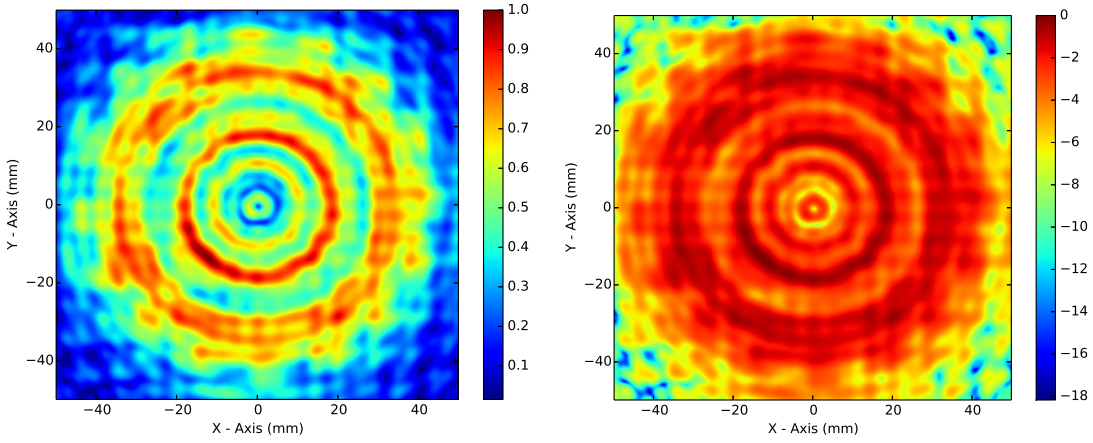

(a) Linear Intensity *(b) Intensity dB*

Figure 4.27: Plane Wave illuminated $\Delta l = \pm 1$ SPP intensity on Plane 2.

Interestingly, the phase on the final 73.3λ (220 mm) plane (Fig. 4.28) shows a BC wrapped around a phase circulation, but with phase dragging in a radial and azimuthal direction. It is still unclear as to what the primary cause of phase dragging in the radial direction is, since it is not seen in the corresponding plane illuminated by an aperture source (Fig. 4.22).

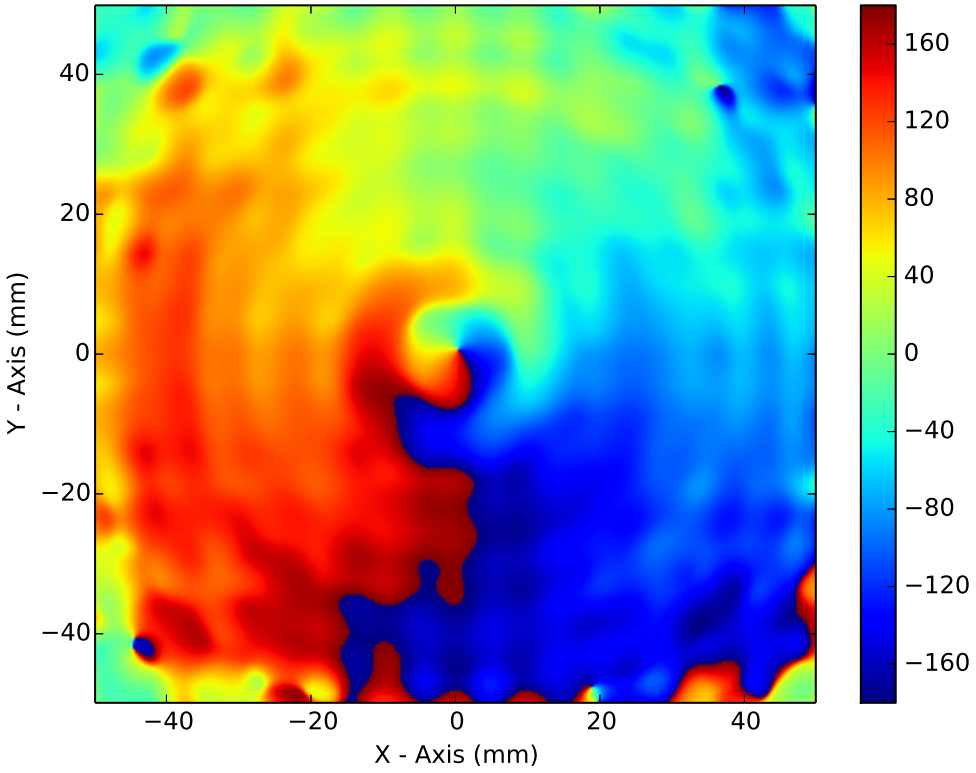

Figure 4.28: $\Delta l = \pm 1$ Plane Wave Source Plane 3 Phase.

Linear intensity on the 73.3λ (220 mm) plane (Fig. 4.29a) remains discontinuous. The second diffracted intensity ring has merged with the third. Beam divergence is low, confirmed by the outermost intensity ring's position. The central intensity null has grown, and the inner most intensity ring has lost structure. This appears to be due to the discontinuous nature prevalent in the proceeding plane wave illuminated models.

Decibel scaled intensity (Fig. 4.29b) gives little added insight, except to highlight that the intensity pattern is fairly symmetrical at this propagation distance and that the drop off between the outer most intensity ring and first intensity trough is abrupt and

sharp.

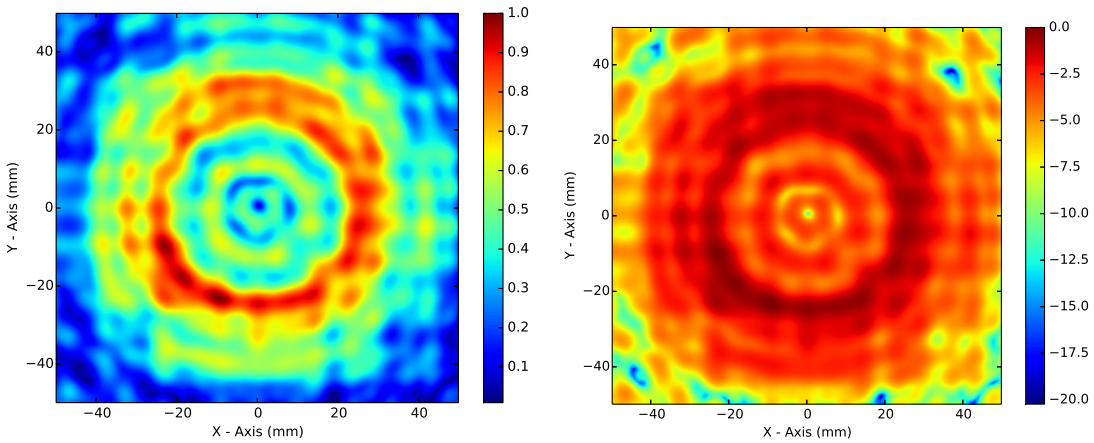

(a) Linear Intensity *(b) Intensity dB*

Figure 4.29: Plane Wave illuminated $\Delta l = \pm 1$ SPP intensity on Plane 3.

Gaussian beam illuminated mode one single stepped SPP

The $\Delta l = \pm 1$ stepped SPP was also modelled with an incident Gaussian beam generated by a corrugated feed horn antenna. The feed antenna was placed 50λ (150 mm) behind the SPP back surface to reduce the amount of diffraction from the SPP mount. This concept functioned well, as indicated by the phase on the 6.7λ (20 mm) plane shown in Fig. (4.30). Unlike phase planes modelled with an aperture or plane wave source, where the BC propagates radially, the phase pattern produced by the Gaussian source contains a BC that spirals around the propagation axis.

Interference in the lower right quadrant of the phase pattern was caused by diffraction from the primary step. Intensity leakage from the step is also pronounced in Fig. 4.31a. Lines of parallel high intensity regions propagate from the primary SPP step along the negative Y-Axis.

The intensity null, caused by the BP, is comparable in strength between all three source types. Although intensity in dB scaling shows some resemblance to the SPP surface structure, it is far less clear then when an aperture or plane wave source is used.

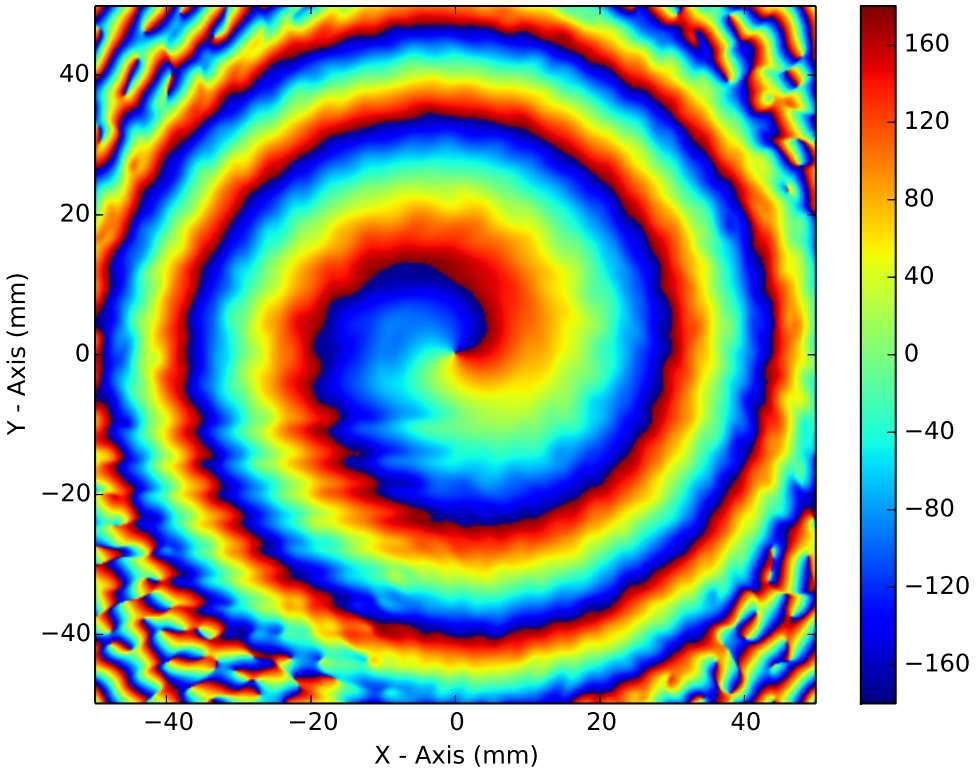

Figure 4.30: $\Delta l = \pm 1$ *Gaussian Source Plane 1 Phase.*

This can be attributed to the incident divergent beam, causesing an improper phase shift around the azimuthal angle of the plate.

Modelled phase on the second plane (Fig. 4.32 a distance of 40λ (120 mm) from the back SPP surface), is significantly smoother then the initial modelled phase. A BC spirals outwardly from the propagation axis, but the phase variations (Fig. 4.30) have largely been eliminated. Interestingly, there appears to be the possible initiation of a radial node, as indicated by the initial linear propagation of the phase dislocation out to a specific radius, which then initiates rotation.

Linear intensity modelled on the 40λ (120 mm) plane is presented in Fig. 4.33a. It is clear that the diffraction effects seen using an aperture or plane wave source have been removed. There is a single intensity ring, which is expected from the LG beam equation. The BP is not directly centred on the propagation axis. This is confirmed by the asymmetric intensity pattern, having a peak in the lower right hand quadrant.

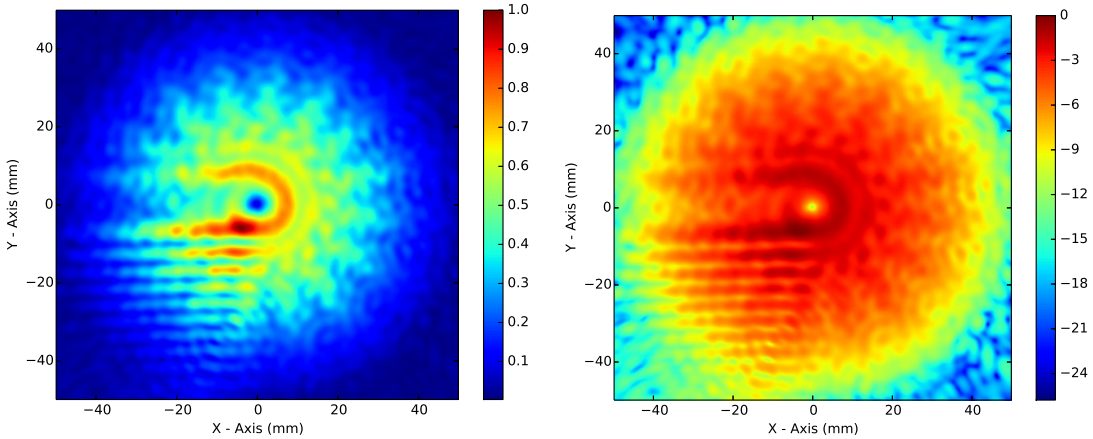

(a) Linear Intensity *(b) Intensity dB*

Figure 4.31: Gaussian illuminated $\Delta l = \pm 1$ SPP intensity on Plane 1.

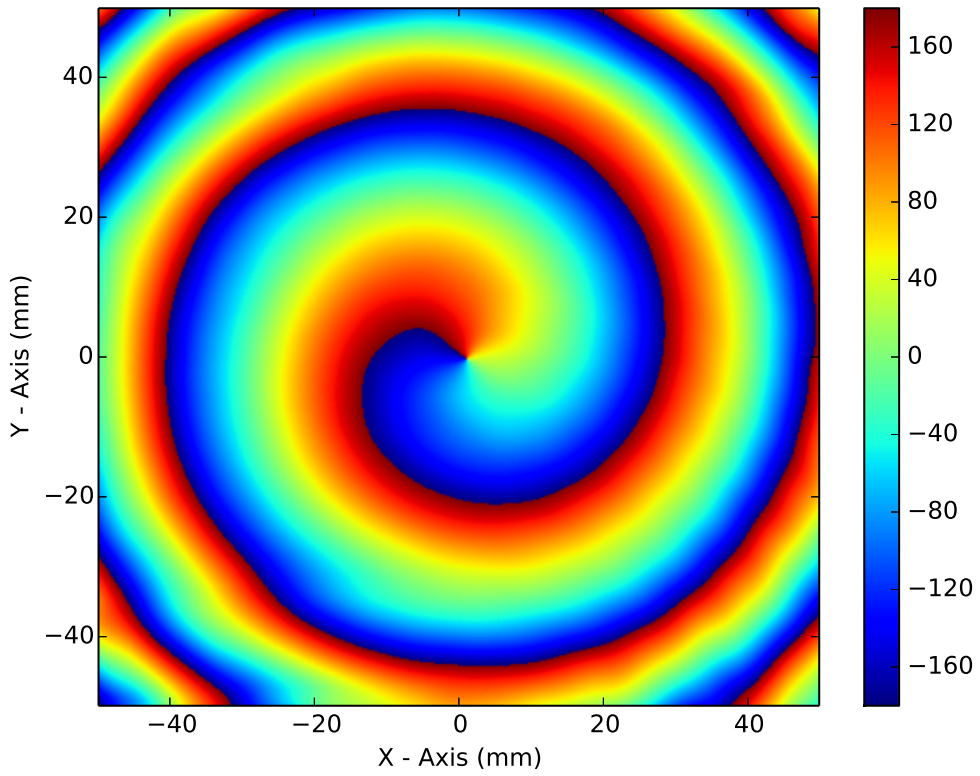

Figure 4.32: $\Delta l = \pm 1$ Gaussian Source Plane 2 Phase.

Intensity in dB scaling (Fig. 4.33b) shows that radiation leakage from the primary SPP step has not been completely removed. This is evident from the linear intensity segments at $y = \pm 40$ mm from $x = 0$ mm to $x = 40$ mm. However, beam divergence has caused the vortex to grow in radius, also improving the visible depth of the intensity null.

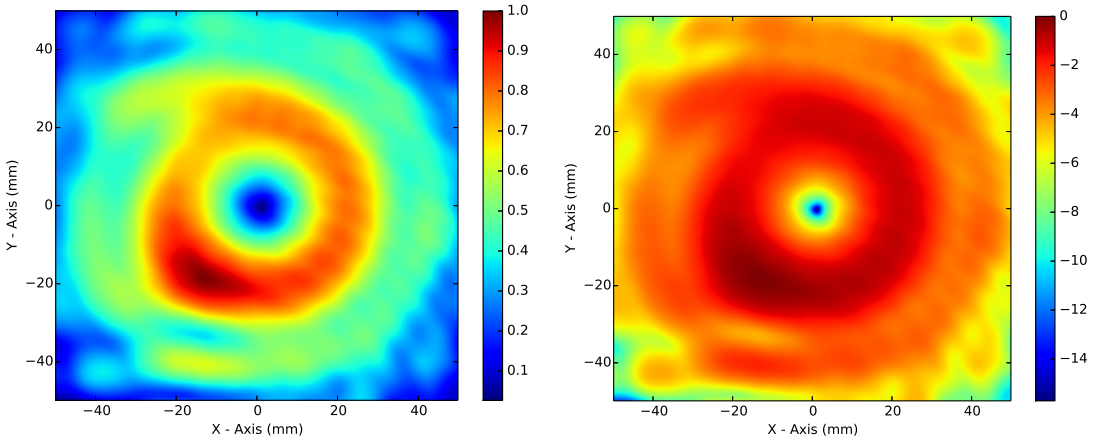

(a) Linear Intensity *(b) Intensity dB*

Figure 4.33: Gaussian illuminated $\Delta l = \pm 1$ SPP intensity on Plane 2.

Modelled phase on the final plane (Fig. 4.34, a distance of 73.3λ (220 mm) from the back surface of the SPP), shows continued smoothing of the BC. The BC spirals around the propagation axis, but the initial appearance of a radial node has disappeared. The initial straight segment of the BC, propagating from the BP is less pronounced.

Linear intensity modelled on the final 73.3λ (220 mm) plane (Fig. 4.35a) shows a further reduction in interference effects. However, the vortex continues to be off-centre and the intensity ring remains asymmetrical.

Intensity mapped onto dB scaling (Fig. 4.35b), indicates that the divergent Gaussian beam continues to pull the vortex apart with an increase in the propagation distance. Despite the BP not gaining in size (The point of undefined phase remains a point.), the intensity null continues to deepen and grow in radius.

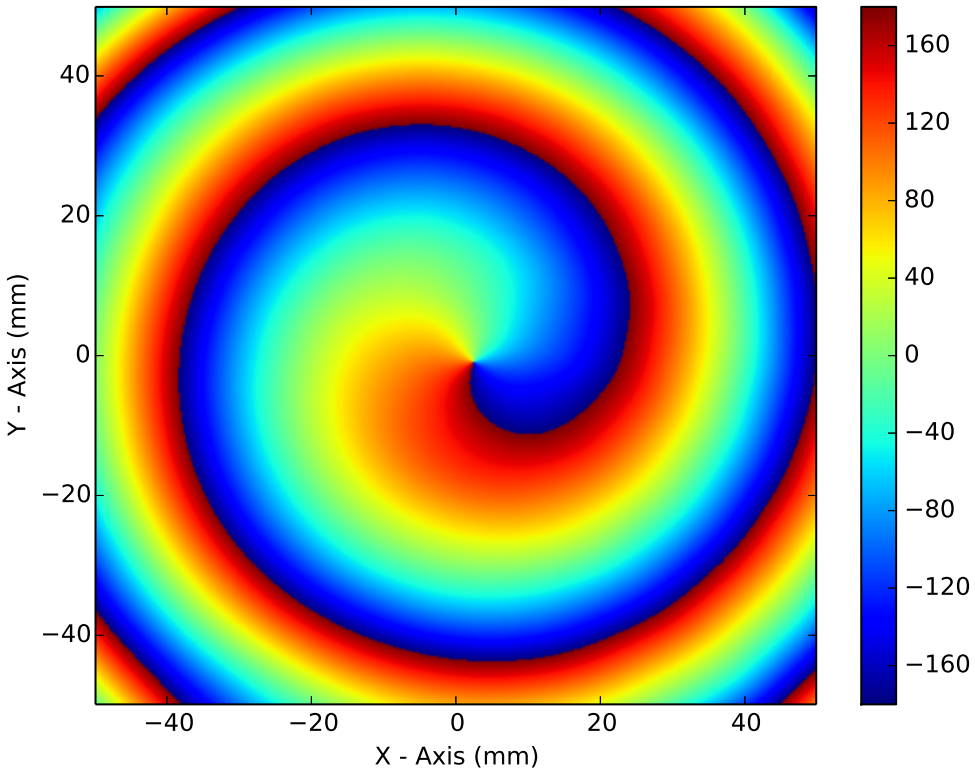

Figure 4.34: $\Delta l = \pm 1$ Gaussian Source Plane 3 Phase.

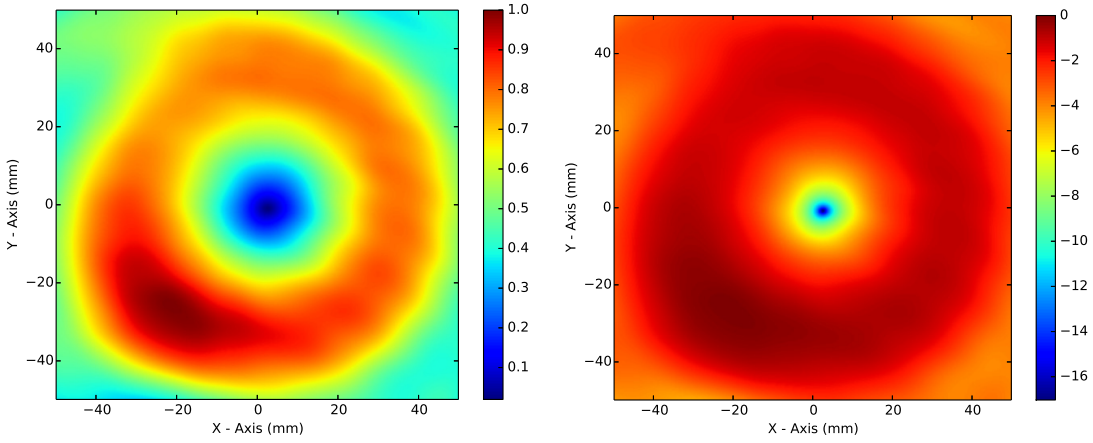

(a) Linear Intensity *(b) Intensity dB*

Figure 4.35: Gaussian illuminated $\Delta l = \pm 1$ SPP intensity on Plane 3.

$\Delta l = \pm 1$ FEKO modelling review

It is now a good point to review the various intensity and phase features seen by modelling a $\Delta l = \pm 1$ SPP with FEKO's MLFMM solver. Clearly the aperture and plane wave illuminated cases produce very similar results, especially when compared to Gaussian beam illumination. Disregarding phase dragging for the moment, the aperture and plane wave illuminated cases generated a BC that propagates radially outwards. On the other hand, Gaussian beam illumination creates a BC that spirals around the propagation axis. This is due to the difference between the incident quasi-planar and spherical phase surfaces. Additionally, aperture and plane wave illumination often resulted in the creation of strong phase radial nodes, or phase circulations. Aperture and plane wave illumination was not completely similar however. For example, aperture illumination resulted in phase dragging that carried in the azimuthal direction, while plane wave illumination produced radial and azimuthally dependent dragging. The reasoning for this difference is unknown. All three illumination cases showed interference from the primary SPP step. Gaussian beam illumination resulted in a single intensity ring, which is due to the optimised edge taper value. Aperture and plane wave illumination contained the expected OAM annular intensity ring plus mount induced diffraction rings. Finally, Gaussian illumination forced the central vortex to spread apart, while this was not visible in the other illumination cases.

Aperture illuminated mode two single stepped SPP

In addition to the $\Delta l = \pm 1$ SPP, two $\Delta l = \pm 2$ designs were modelled. The first design is a polypropylene single stepped SPP, comprised of thirty two discrete sections to maintain a steps-per-mode ratio of sixteen.

Phase modelled on the 6.7λ (20 mm) plane (Fig. 4.36) shows that the SPP has generated two BPs each with a corresponding BC. The BCs propagate outwardly, and exhibit a fair amount of phase dragging. Concentric rings of modulated phase are due to a large number of low power radial modes generated by mount induced diffraction.

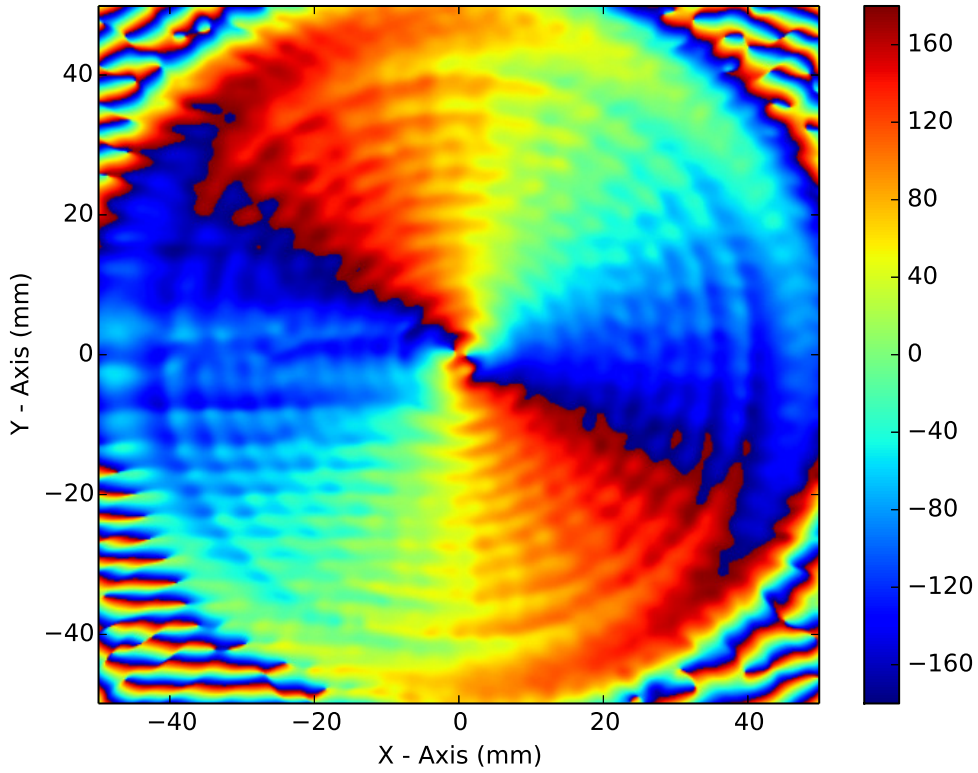

Figure 4.36: $\Delta l = \pm 2$ Single Stepped Aperture Source Plane 1 Phase.

Linear intensity modelled on the first plane (Fig. 4.37a) represents a near field image of the SPP. There is some visible interference in the lower right quadrant of the plate caused by the primary step. There is also a repeating concentric ring pattern, resulting from the rippling phase variations.

When plotted in dBs (Fig. 4.37b), the intensity pattern shows an interesting characteristic around the central intensity null, or vortex. The central portion of the null is circular. This corresponds to the undefined phase at the BP locations. However, the intensity null also has two sweeping teardrop shapes above and below the circular region. These seem to loosely be associated with the initial BC segment propagating away from the BPs.

BPs shown in Fig. 4.36 are also visible and remain in close proximity to each other on the second modelling plane (Fig. 4.38). Like the phase patterns seen with the $\Delta l = \pm 1$ SPP illuminated by an aperture or plane wave, the 40λ (120 mm) plane

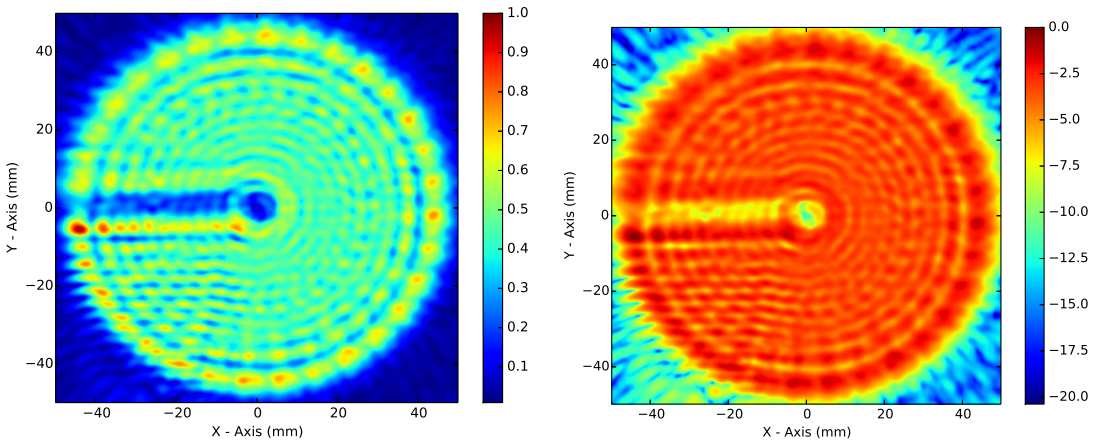

(a) Linear Intensity *(b) Intensity dB*

Figure 4.37: Aperture illuminated $\Delta l = \pm 2$ single stepped SPP intensity on Plane1.

contains a strong phase circulation. This is an indication of a radial node in the generated beam. Persistent phase dragging has smoothed slightly, but remains asymmetrical.

Linear intensity on the 40λ (120 mm) plane is made up of four ring structures. It is unclear whether a section of the the third intensity ring is partially detached, or if there is the possibility of an additional ring structure. The pattern shows a fair amount of symmetry, except for some linearities in the positive X-Axis portion of the plot.

Decibel scaled intensity (Fig. 4.39b) shows an axially symmetric structure. However, the central intensity null continues to show some ellipticity. In addition, the first intensity trough is roughly as deep as the intensity null, while the other intensity troughs associated with radial nodes, are relatively weak. This makes sense, as higher radial modes typically represent less power (Sec. 4.2).

The final modelling plane, located 73.3λ (220 mm) behind the back surface of the SPP, shows that the BPs have remained in close proximity to each other. Despite this, the radial extent of the phase circulation has increased. Phase dragging has continued to smooth itself, while the BCs remained on opposing sides of the phase circulation.

The corresponding linear intensity pattern is comprised of two clear ring structures, while there is a possibility of a distinct third ring. The most interesting part of this pattern

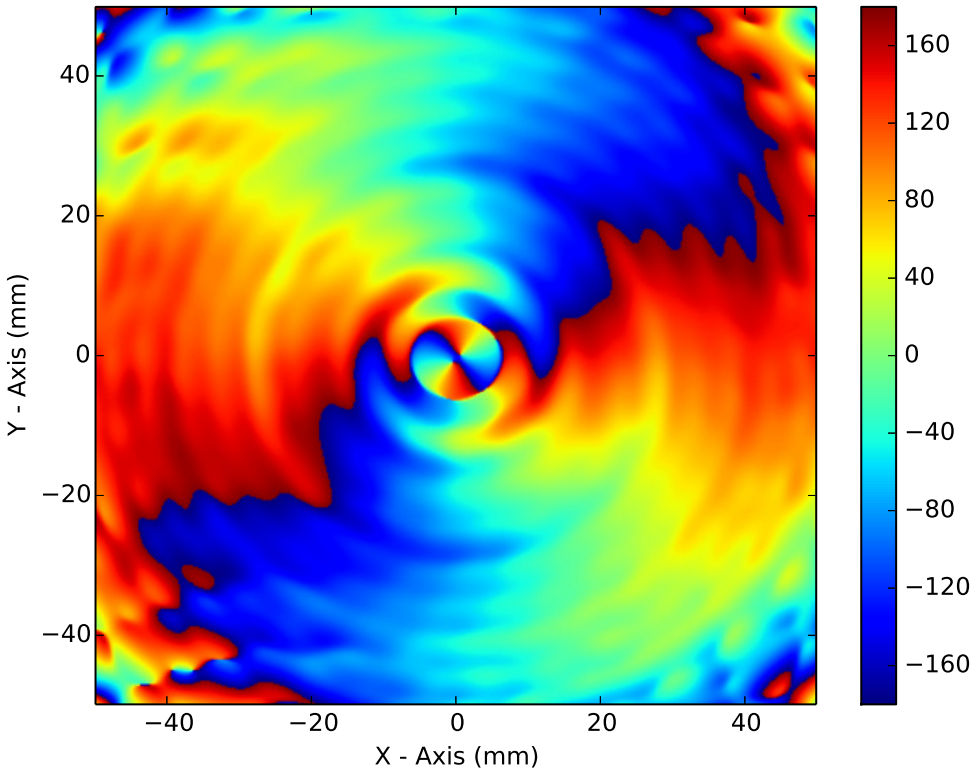

Figure 4.38: $\Delta l = \pm 2$ Single Stepped Aperture Source Plane 2 Phase.

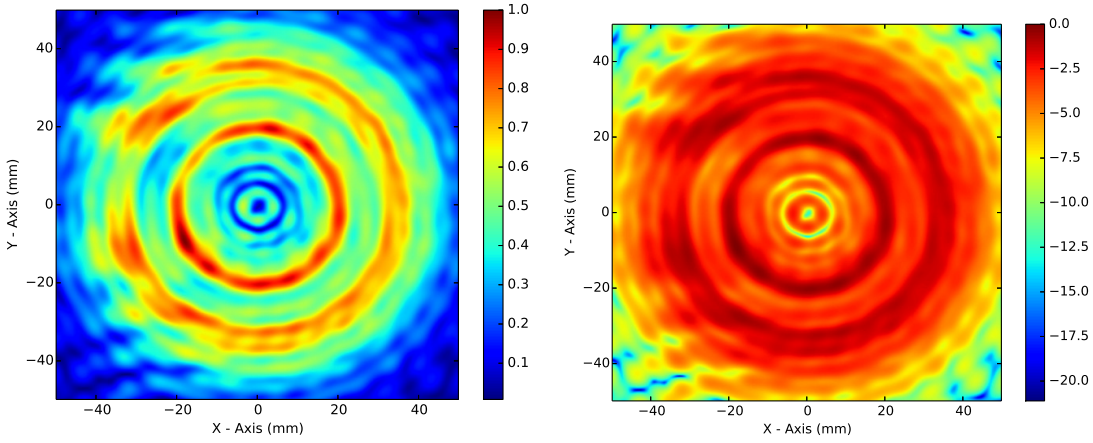

(a) Linear Intensity *(b) Intensity dB*

Figure 4.39: Aperture illuminated $\Delta l = \pm 2$single stepped SPP intensity on Plane 2.

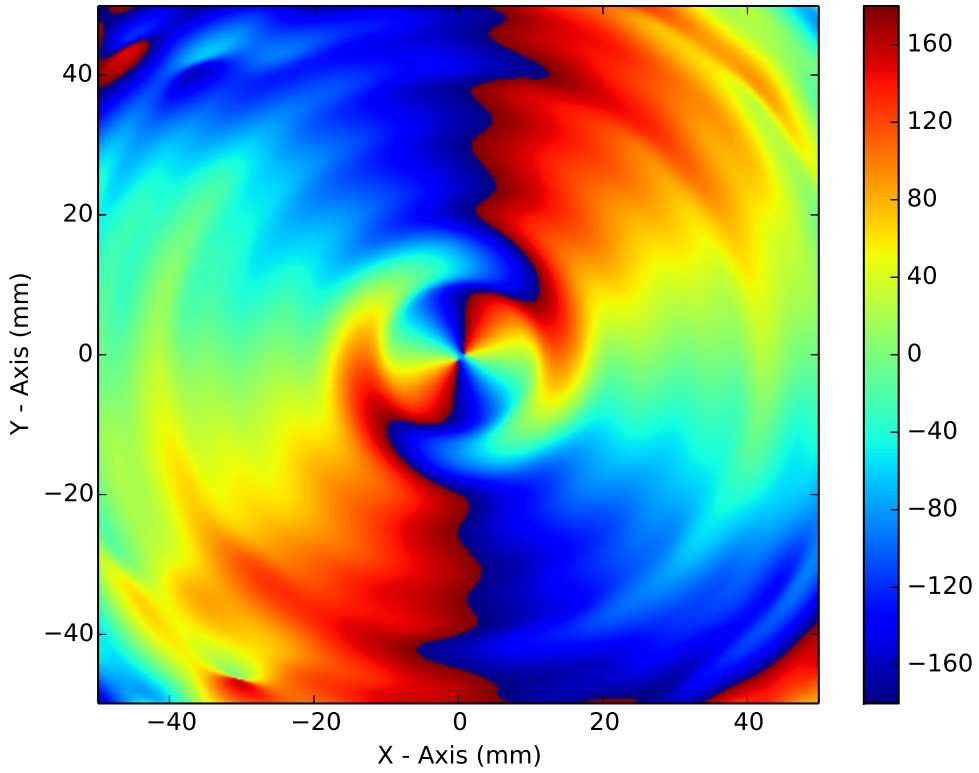

Figure 4.40: $\Delta l = \pm 2$ Single Single Stepped Aperture Source Plane 3 Phase.

is the asymmetry in both the inner most and outer most intensity rings. While both remain largely circular, the intensity is higher at an azimuthal angle of approximately $\phi = 350°$ to the positive X-Axis then the corresponding intensity at $\phi = 170°$. In addition, the intensity around $\phi = 10°$ is weaker then the apparent mean value for the ring. Radiation is being redirected from regions above the step ($\phi = 10°$ region) to the intensity peak below the step ($\phi = 350°$).

Decibel scaling shows that the central vortex has grown deeper. It also appears as if the central vortex is beginning to split into two separate vortices.

Plane wave illuminated mode two single stepped SPP

In order to asses the differences between various FEKO source types, a mathematically pure plane wave was used as a source for the $\Delta l = \pm 2$ single stepped SPP. Phase on the

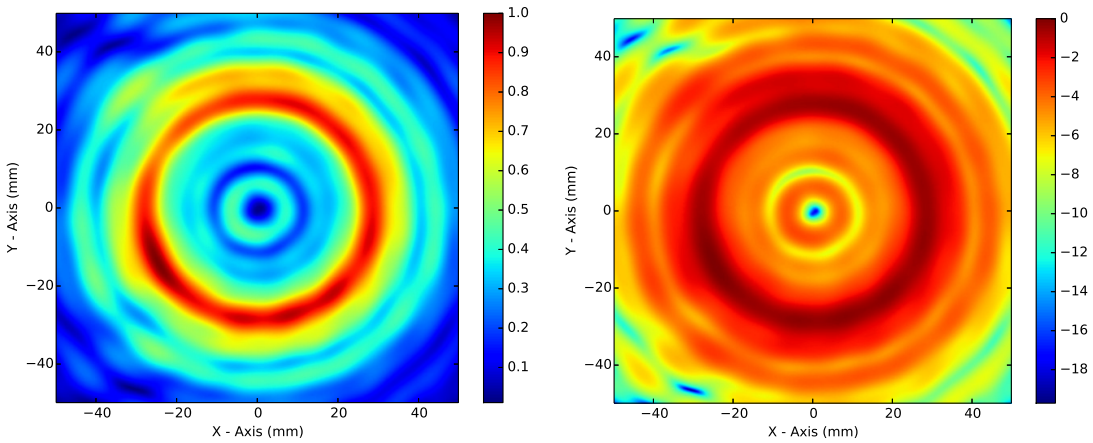

(a) Linear Intensity *(b) Intensity dB*

Figure 4.41: Aperture illuminated $\Delta l = \pm 2$ single stepped SPP intensity on Plane 3.

first model plane (Fig. 4.42), located 6.7λ (20 mm) from the back SPP surface, shows the existence of two BPs and the outwardly propagating BCs. Phase rippling is present, which is a result of diffraction from the circular SPP mount. The BCs are not perfectly parallel to each other, and appear to have an interior angle between them $< 180°$.

Linear intensity in Fig. 4.43a shows both the expected radial intensity variations caused by diffraction and the linear interference in the lower right quadrant of the SPP. These linear interference lines are a result of the transmitted field reflecting from the primary step. Decibel scaled intensity (Fig. 4.43b) shows the fine structure of the central vortex. The vortex centre is slightly misaligned to the propagation axis. It also contains a circular central section with swept teardrop shaped extensions. These extensions seem to be related to the initial BC segments closest to the BPs.

Like the previous examples, phase on the second plane has a strong phase circulation. In addition, phase rippling has collected into three major radial peaks. Phase dragging exists, and is jagged. Surprisingly, the interior angle between the BCs appears to remain unchanged.

Linear intensity (Fig. 4.45a) shows three ring structures, with the possibility of a fourth interior ring. The intensity rings are highly symmetric, excluding some linearity

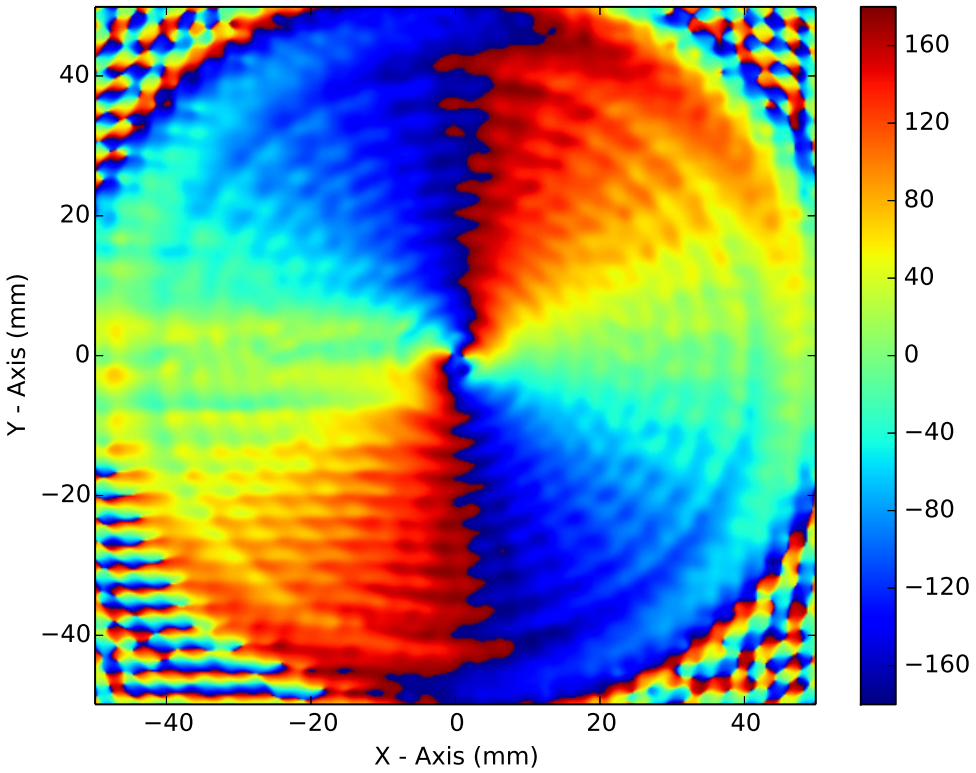

Figure 4.42: $\Delta l = \pm 2$ Single Stepped Plane Wave Source Plane 1 Phase.

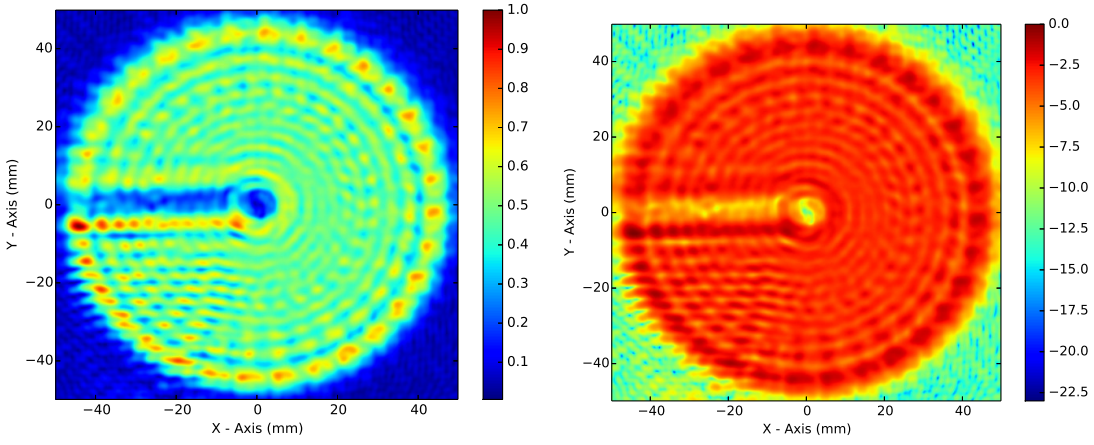

(a) Linear Intensity *(b) Intensity dB*

Figure 4.43: Plane Wave illuminated $\Delta l = \pm 2$single stepped SPP intensity on Plane 1.

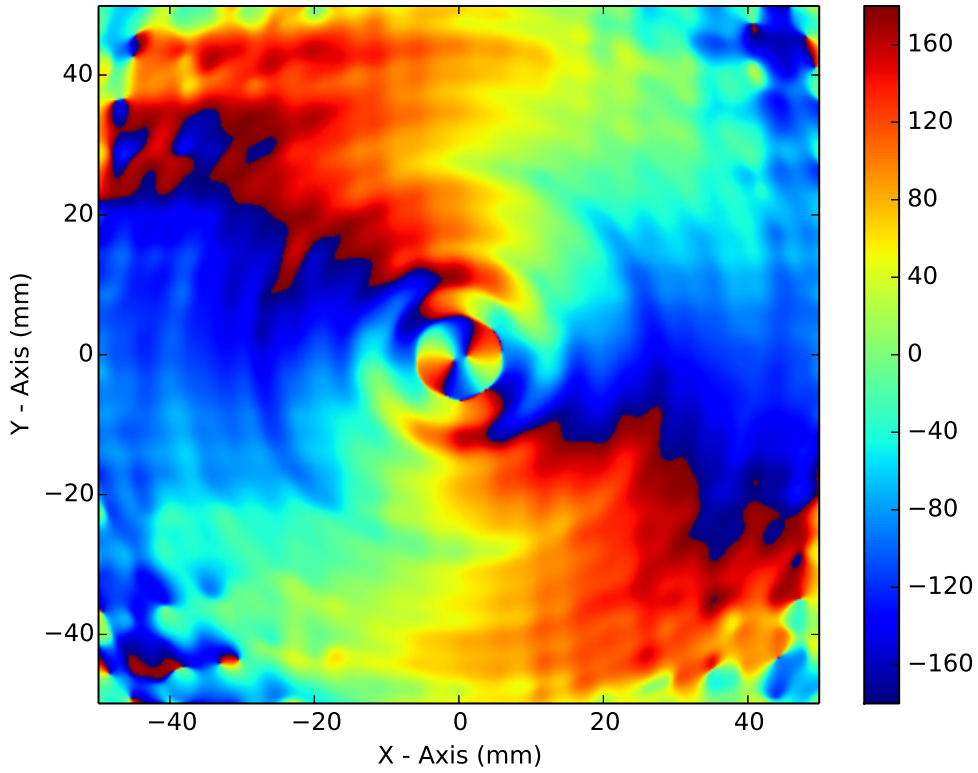

Figure 4.44: $\Delta l = \pm 2$ Single Stepped Plane Wave Source Plane 2 Phase.

in the pattern in the positive X-Axis region at $y = \pm 20$ mm. There is a slight increase in intensity along the $\phi = 350°$ radial. Figure 4.45b shows the intensity pattern in dB scaling. The central vortex has lost the swept wing tear drop extensions and now resembles two partially resolved circles.

The final modelled plane is located 73.3λ (220 mm) behind the back surface of the SPP. Phase data shown in Fig. 4.46. The two BPs have started to slowly move away from each other, due to the small divergence of the plane wave after passing through the SPP. The phase circulation that was prevalent in Fig. 4.44 is less evident. Phase dragging has smoothed slightly.

Linear intensity (Fig. 4.47a) shows two visible intensity rings. The intensity structures are highly symmetric, but the pattern is somewhat pixelated. Intensity scaled in dBs is slightly more interesting (See Fig. 4.47b). The inner vortex structure, which appeared as two joined circles in Fig. 4.45b is split into two very distinct circular

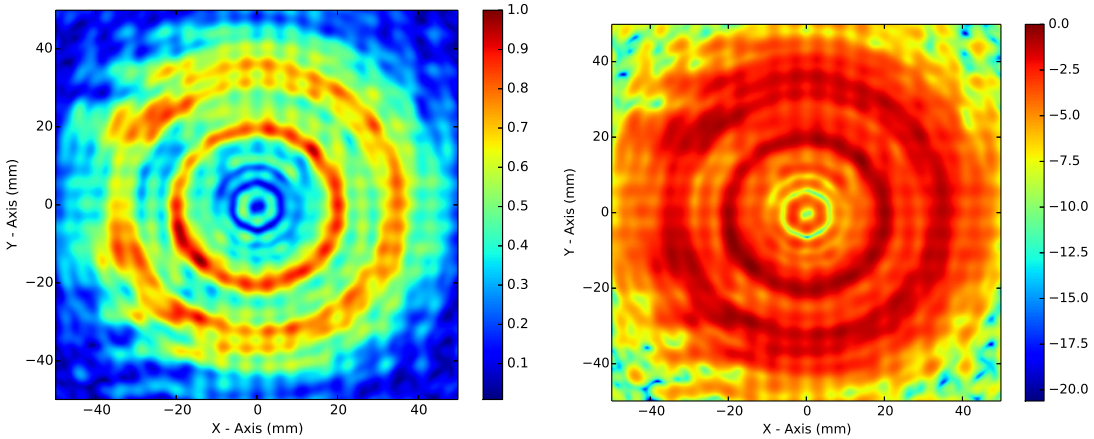

(a) Linear Intensity *(b) Intensity dB*

Figure 4.45: Plane Wave illuminated $\Delta l = \pm 2$ single stepped SPP intensity on Plane 2.

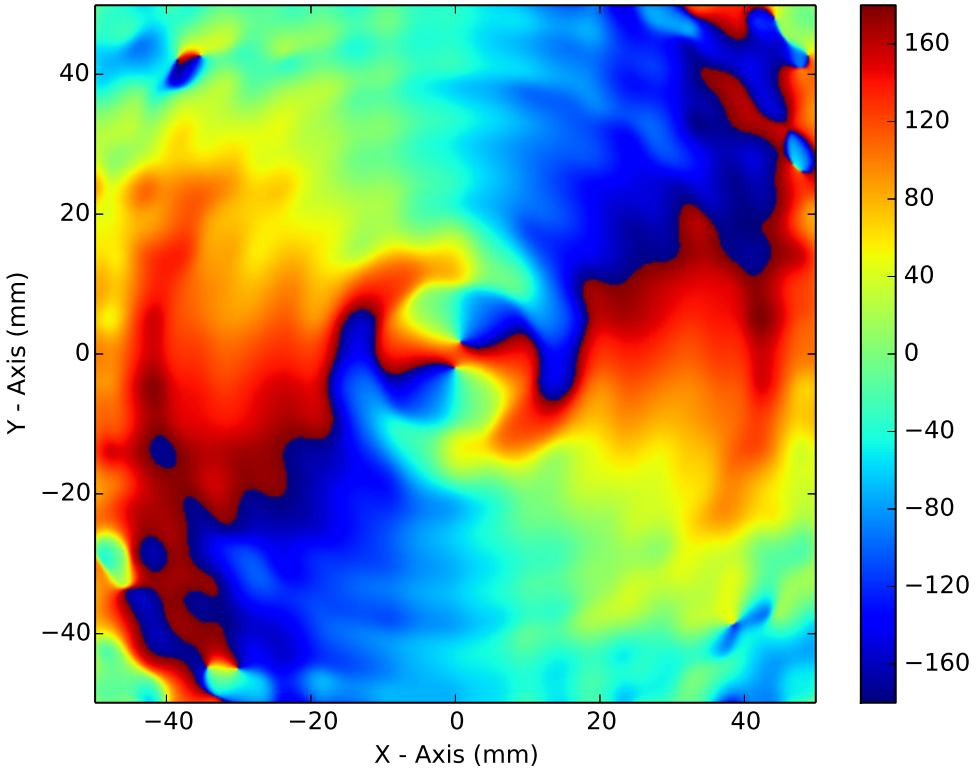

Figure 4.46: $\Delta l = \pm 2$ Single Stepped Plane Wave Source Plane 3 Phase.

vortices. This splitting is caused by the spreading the BP pair, in turn caused by the divergence of the generated beam.

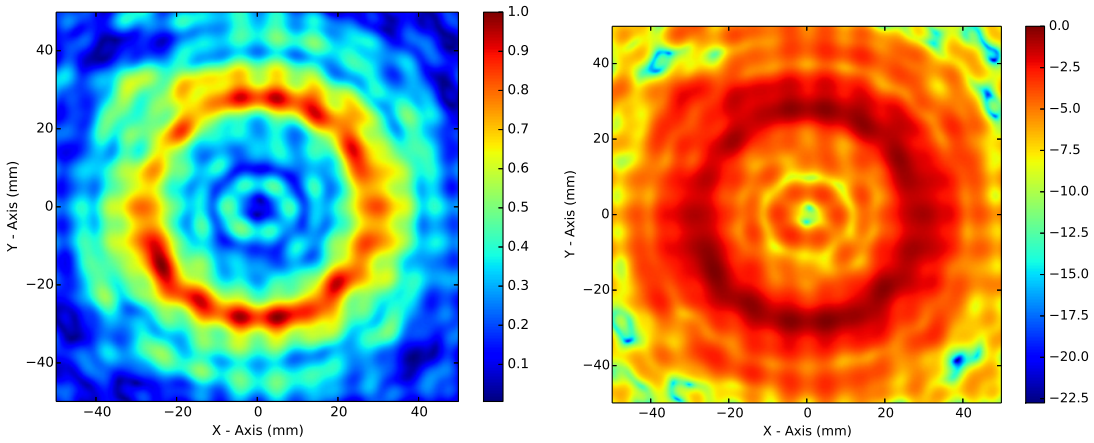

(a) Linear Intensity *(b) Intensity dB*

Figure 4.47: Plane Wave illuminated $\Delta l = \pm 2$ single stepped SPP intensity on Plane 3.

Gaussian beam illuminated mode two single stepped SPP

To understand what happens when SPPs are illuminated by highly divergent beams, a Gaussian beam generated by a corrugated feed antenna was modelled incident on the $\Delta l = \pm 2$ single stepped SPP. The 6.7λ (20 mm) modelled phase plane shows two BPs with associated BCs. Unlike the aperture and plane wave illuminated patterns, the BCs generated with a Gaussian beam, spiral around the propagation axis. Figure 4.48 also shows a large amount of interference caused by the primary SPP step, in the lower right hand quadrant of the SPP. This affect seems to be amplified by the divergence of the incident Gaussian beam.

Interference in the same location is also visible in the linear intensity pattern (Fig. 4.49a). In addition, the central vortex is quite large. Interestingly, the decibel scaled intensity (Fig. 4.49b), indicates that the central vortex has split into two separable circular regions. This didn't happen in aperture and plane wave illuminated models until the final model planes, Fig. 4.41b and Fig. 4.47b respectively.

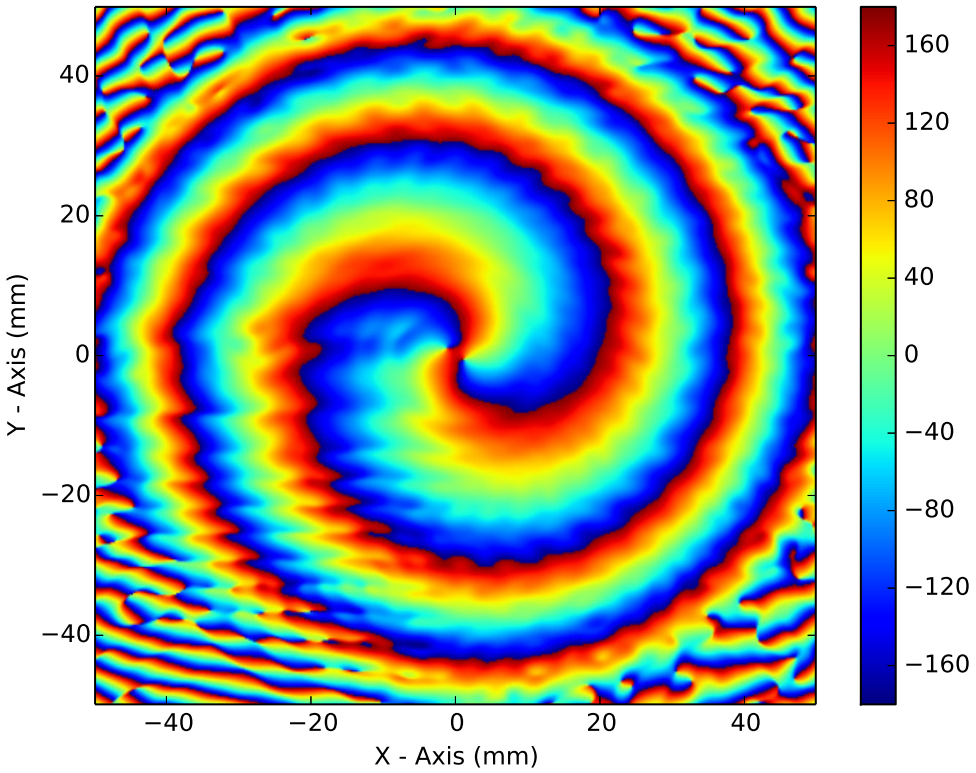

Figure 4.48: $\Delta l = \pm 2$ Single Stepped Gaussian Source Plane 1 Phase.

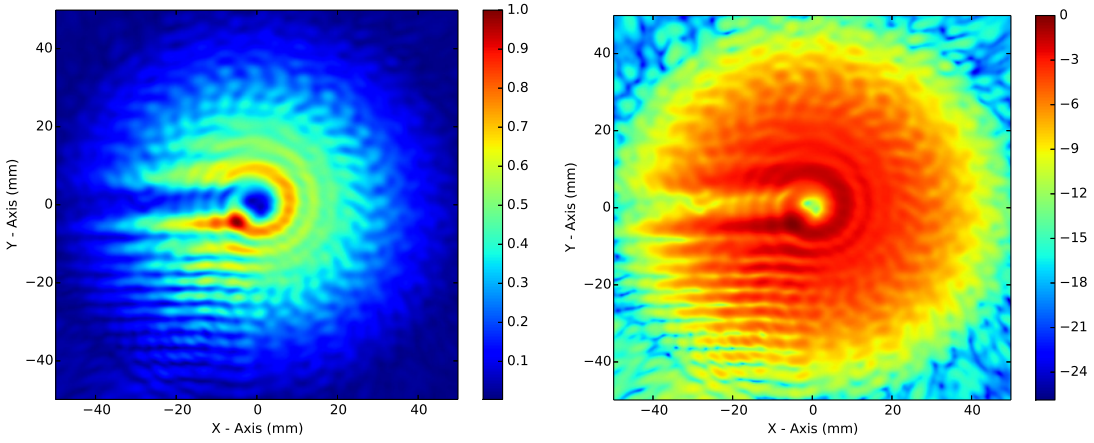

(a) Linear Intensity *(b) Intensity dB*

Figure 4.49: Gaussian illuminated $\Delta l = \pm 2$ single stepped SPP intensity on Plane 1.

Phase on the 40λ (120 mm) plane is shown in Fig. 4.50. The model shows two BPs separated by an increased distance compared to Fig. 4.48. In addition, the phase variations generated by the primary step have largely been smoothed out. However, there are a few variations on the positive X-Axis region around $y = \pm 30$ mm. Unlike the aperture and plane wave sources, no phase circulation is present.

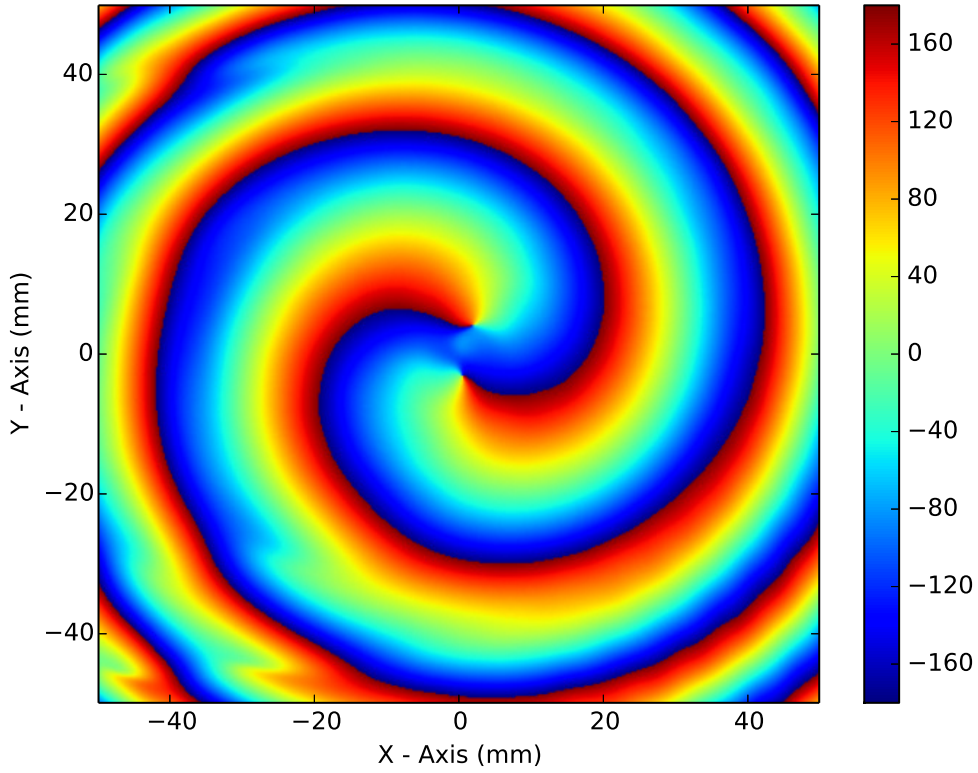

Figure 4.50: $\Delta l = \pm 2$ Single Stepped Gaussian Source Plane 2 Phase.

Linear intensity in Fig. 4.51a, shows a very large central null. Unlike the aperture and plane wave illuminated scenario, this Gaussian illuminated SPP produces a singular intensity ring. The left side of the intensity ring is smooth and continuous, while the right hand side has a discontinuity. This is produced by a mismatch in boundary conditions inside and outside of the primary step. This pushes intensity from the upper Y-Axis region to the lower Y-Axis region.

The central intensity vortex on the 40λ (120 mm), in dB scaling, has almost completely split into two separate vortices. It is of interest to note that the upper vortex runs

parallel to the $y = 0$ mm line, while the bottom vortex runs parallel to the line $x = 0$ mm.

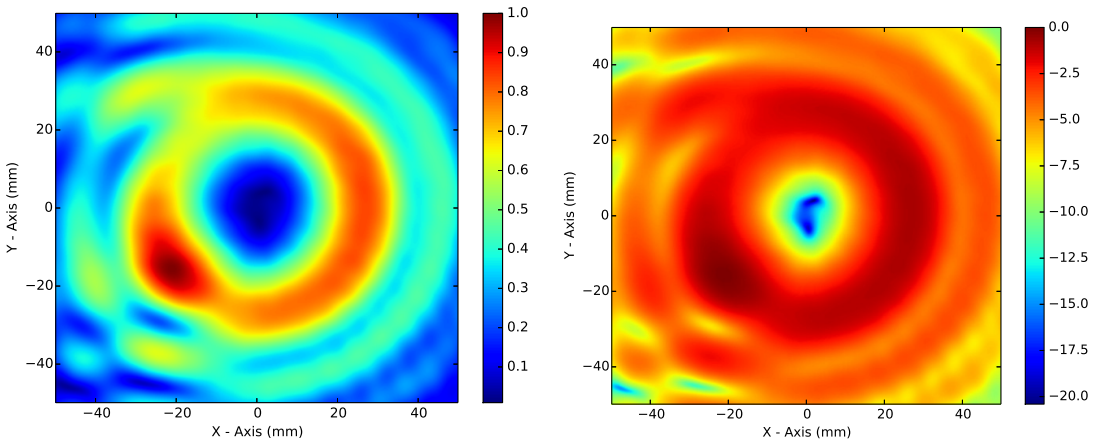

(a) Linear Intensity *(b) Intensity dB*

Figure 4.51: Gaussian illuminated $\Delta l = \pm 2$ single stepped SPP intensity on Plane 2.

The final model plane was placed 73.3λ (220 mm) from the back surface of the SPP. Phase modelled on this plane shows smoothly rotating BCs, which terminate at two separate BPs. BP separation distance has increased as a result of the divergence of the initial Gaussian beam. Phase variations resulting from the primary step have been smoothed, and are no longer visible.

Linear intensity in Fig. 4.53a continues to show the gradual divergence of the beam. The single intensity ring is smooth on the left hand side of the vortex, while the right hand side discontinuity continues to increase. As a result of the increased divergence, an isthmus of intensity has developed between the two nulls resulting from the undefined phase at each BP location.

Intensity in dB scaling (Fig. 4.53b) confirms the previous results. The important feature to notice is the increased separation of the intensity nulls. Additionally, the intensity nulls have lost their ellipticity. A small line of intensity separates them, and the vortex depth is lower compared to that of the 40λ (120 mm) plane (Fig. 4.51b).

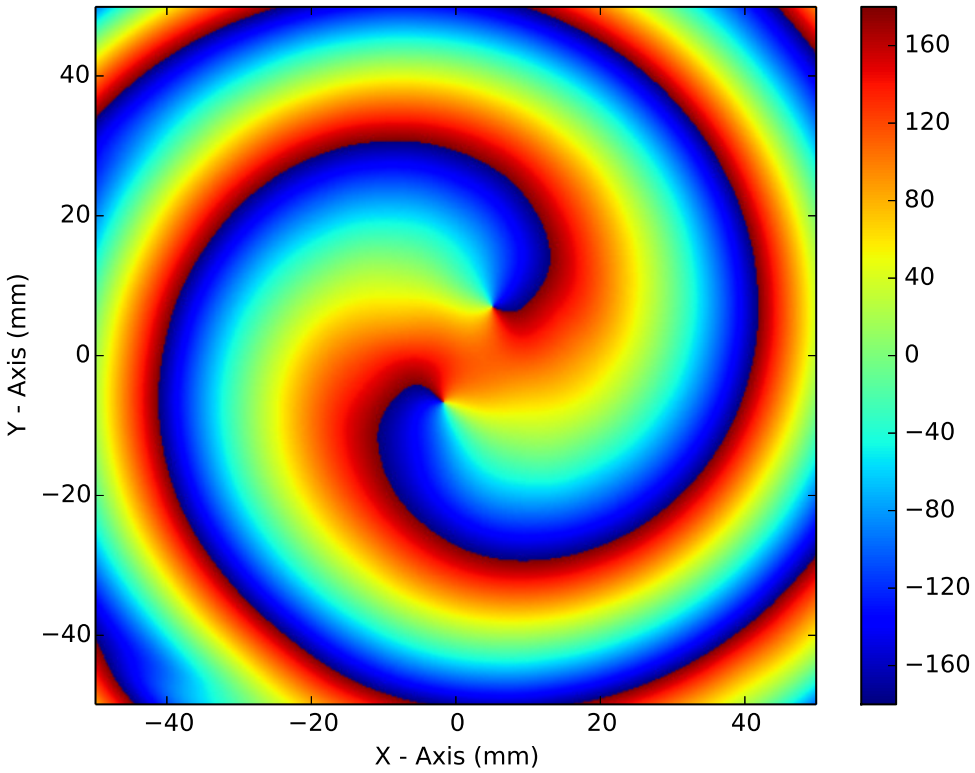

Figure 4.52: $\Delta l = \pm 2$ Single Stepped Gaussian Source Plane 3 Phase.

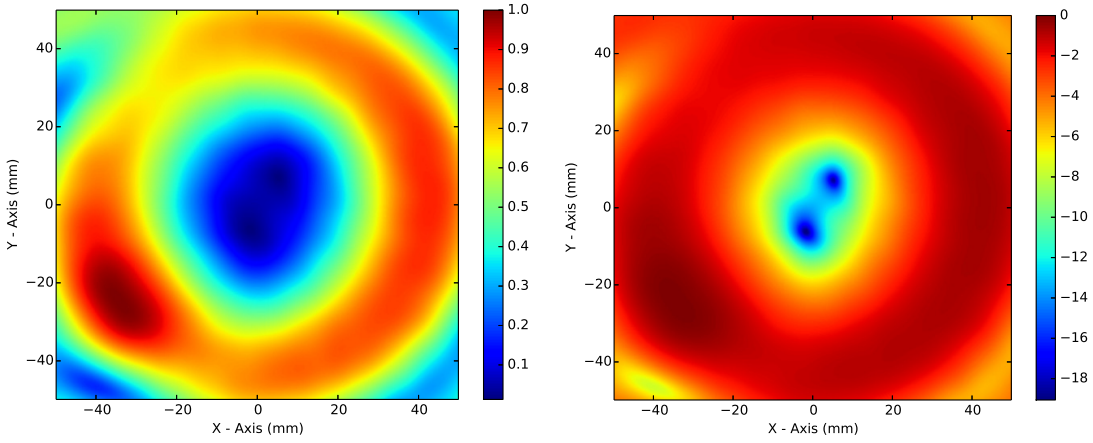

(a) Linear Intensity *(b) Intensity dB*

Figure 4.53: Gaussian illuminated $\Delta l = \pm 2$ single stepped SPP intensity Plane 3.

$\Delta l = \pm 2$ single stepped SPP review

Here, there will be a quick review of the $\Delta l = \pm 2$ single stepped SPP FEKO modelling results. Again, the aperture and plane wave illuminated models produced similar results, but with some interesting differences. On a qualitative level it was evident that the aperture fed SPP produced fewer low powered radial modes resulting in less phase dragging and smoother BCs. On the other hand, plane wave illumination produced rather jagged phase dragging patterns. Furthermore, BP separation distances under plane wave illumination were larger, compared to aperture illumination. Both of these source types produced a split vortex on the final modelling plane, while the vortex on the initial plane had teardrop shaped extensions. As was the case with the $\Delta l = \pm 1$ SPP, the Gaussian illuminated $\Delta l = \pm 2$ SPP produced a BC that spiralled around the propagation axis. The central vortex structure produced by the transmitted Gaussian beam showed new structural features. For example, intensity on the first modelling plane shows an overall vortex that is not circular symmetric, which contains two distinct regions of decreased intensity. Propagation to the second modelling plane resulted in separated vortices. Interestingly these seemed to show some incident beam polarisation dependence. One vortex was clearly aligned along the horizontal, while the other was unmistakably vertically aligned. Further propagation to the final modelling plane resulted in a complete separation of the vortices, which allowed radiation to fill into the space between them, forming an isthmus.

Aperture illuminated mode two split stepped SPP

A split $\Delta l = \pm 2$ was also modelled using FEKO. Such a design is more symmetrical then the single stepped $\Delta l = \pm 2$, and the total step height is smaller, resulting in less mode contamination. As with the other plate designs, the split step configuration was modelled using aperture, plane wave and Gaussian sources. Phase on the first model plane is shown in Fig. 4.54. Immediately noticeable is a peculiarity in the phase pattern around the BPs. Each BP is not a singular point. Instead, the BPs are comprised of

a phase circulation, which contains a total of two BCs and therefore, four BPs. It is unclear why these exist, but they are perhaps the most unexpected result in the entirety of this SPP modelling excersise.

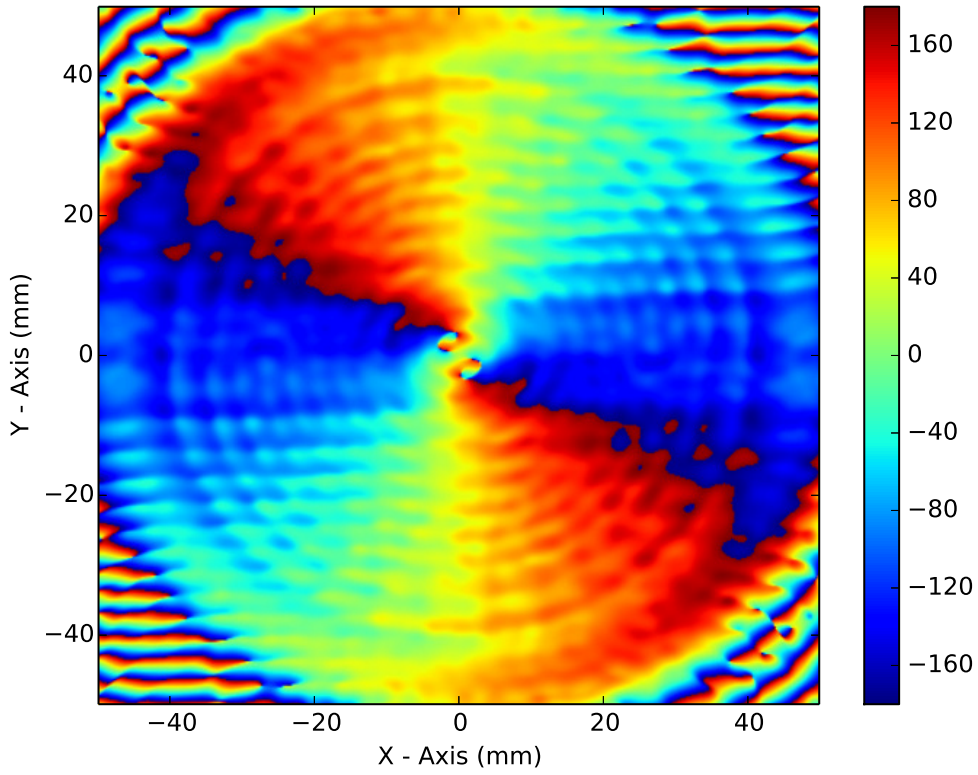

Figure 4.54: $\Delta l = \pm 2$ Split Stepped Aperture Source Plane 1 Phase.

Linear intensity in Fig. (4.55a) shows a radial dependence, corresponding to phase variations from diffraction of the mounting structure. There are visible high intensity regions in the lower right hand and upper left hand quadrants of the SPP image.

The central intensity null in Fig. 4.55b shows two distinct vortices associated with phase circulations at the expected BP locations in Fig. 4.54. Recall that the BPs were not singular points as anticipated, but instead were phase circulations containing four BPs each. This is the clear cause of the odd central intensity structure. Each vortex has a swept back teardrop shape with a small circular region of relatively lower intensity compared to the central region of the vortex. However, above and below each vortex there are two small intensity minima. These correspond to the two BPs at the end of

each BC in phase.

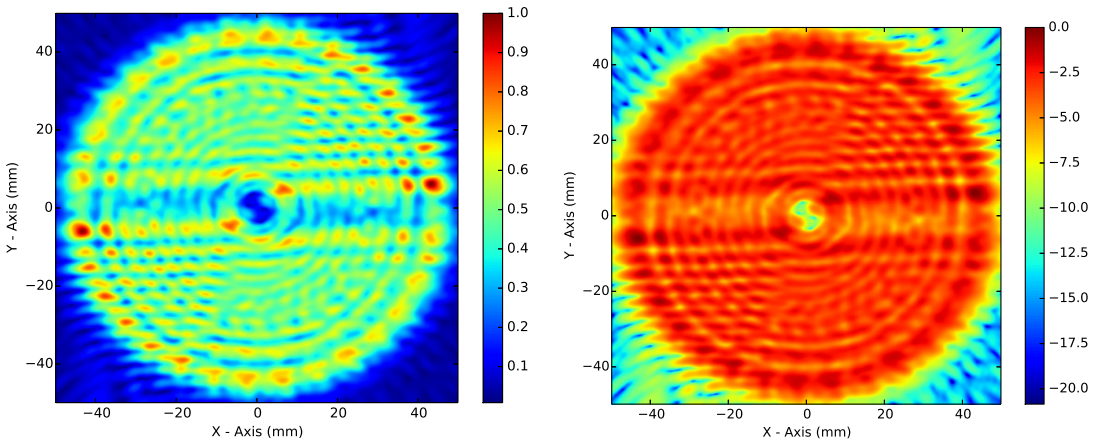

(a) Linear Intensity *(b) Intensity dB*

Figure 4.55: Aperture illuminated $\Delta l = \pm 2$ split stepped SPP intensity on Plane 1.

The initial oddities seen in first modelled phase plane (Fig. 4.54) have been removed by the time the LG beam reaches the second modelling plane, (Fig. 4.56). The phase pattern contains a strong central phase circulation, but now, only two BPs are present. This phase circulation, along with the other radially dependent phase variations are a result of diffraction of the beam from the SPP mounting surface. As was the case with all previous modelled phase planes, the phase in Fig. 4.56 shows dragging phenomena.

Figure 4.57a displays the linear intensity pattern on the second modelling plane. Four intensity rings are visible, with the third ring having the strongest intensity. The intensity pattern is mirror symmetric about X- and Y-Axis. Observing the third intensity ring, one can see that there are two peaked intensity regions, one approximately at $\phi = 135^\circ$ and $\phi = -45^\circ$. The second intensity ring also shows two peaked regions, but at different angular locations to the intensity peaks in the third ring. The second intensity ring peaks are approximately at $\phi = 100^\circ$ and $\phi = -80^\circ$ to the positive X-Axis. Finally, the inner most intensity ring also displays this asymmetrical intensity peaking. Again, the angular locations are different then any of the other rings. The inner intensity ring peaks are at angular location of $\phi = 0^\circ$ and $\phi = 180^\circ$ to the positive

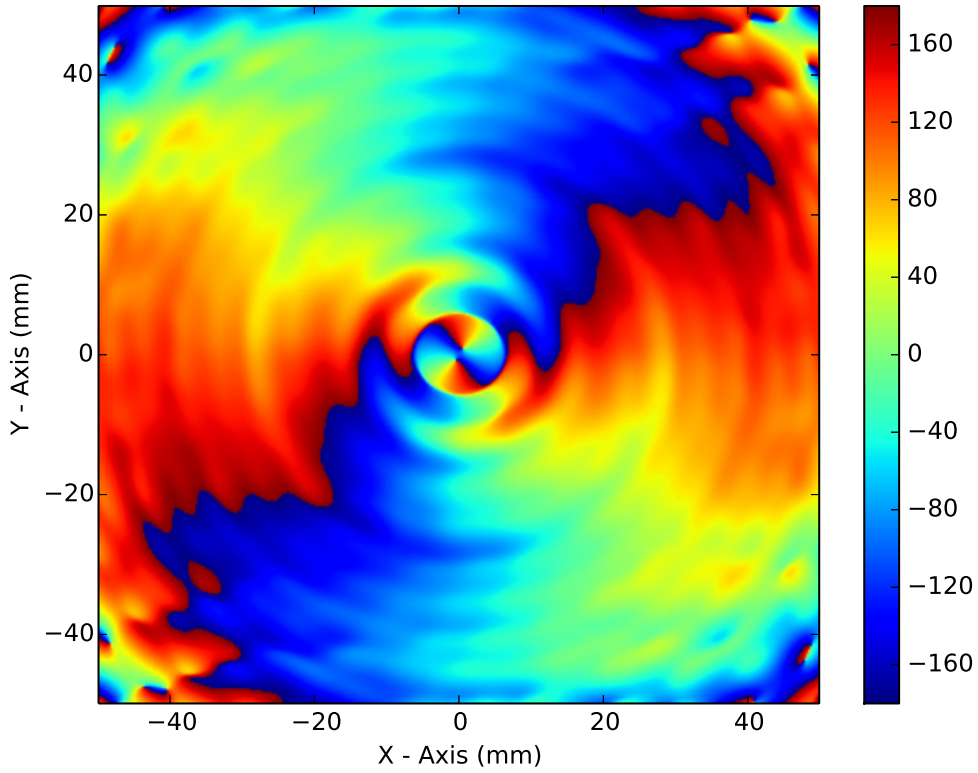

Figure 4.56: $\Delta l = \pm 2$ Split Stepped Aperture Source Plane 2 Phase.

X-Axis. Recollection of the phase (Fig. 4.56) shows that both BCs run through all of the intensity rings. Therefore, an integral of the phase around each intensity ring would show a phase shift of $2\pi\, l$, where $l = 2$.

Observation of the central intensity null in Fig. 4.57b shows that the odd structuring seen in Fig. 4.55b has been removed. This is a result of the restructuring of the phase (Fig. 4.56). Additionally, the central intensity null shows two semi-distinct intensity minima.

The final modelled phase plane (Fig. 4.58) shows further smoothing of the BCs. Observable phase dragging continues to be associated with radial phase variations. In addition, the BPs have remained extremely close to each other and inside the prominent phase circulation. What's most interesting here is the nearly 90° change in direction both BCs make when they reach the radial extent of the phase circulation.

Linear intensity, shown in Fig. 4.59a, displays two prominent intensity rings. Each

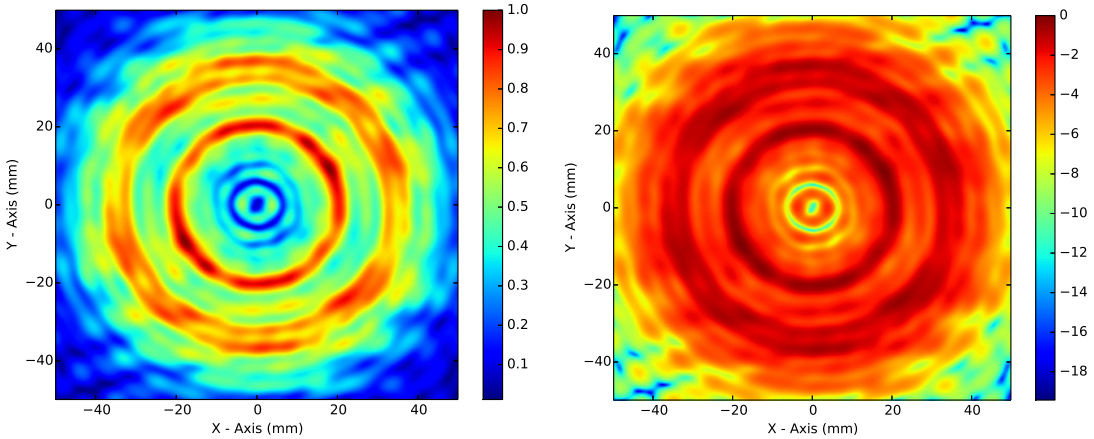

(a) Linear Intensity *(b) Intensity dB*

Figure 4.57: Aperture illuminated $\Delta l = \pm 2$ split stepped SPP intensity on Plane 2.

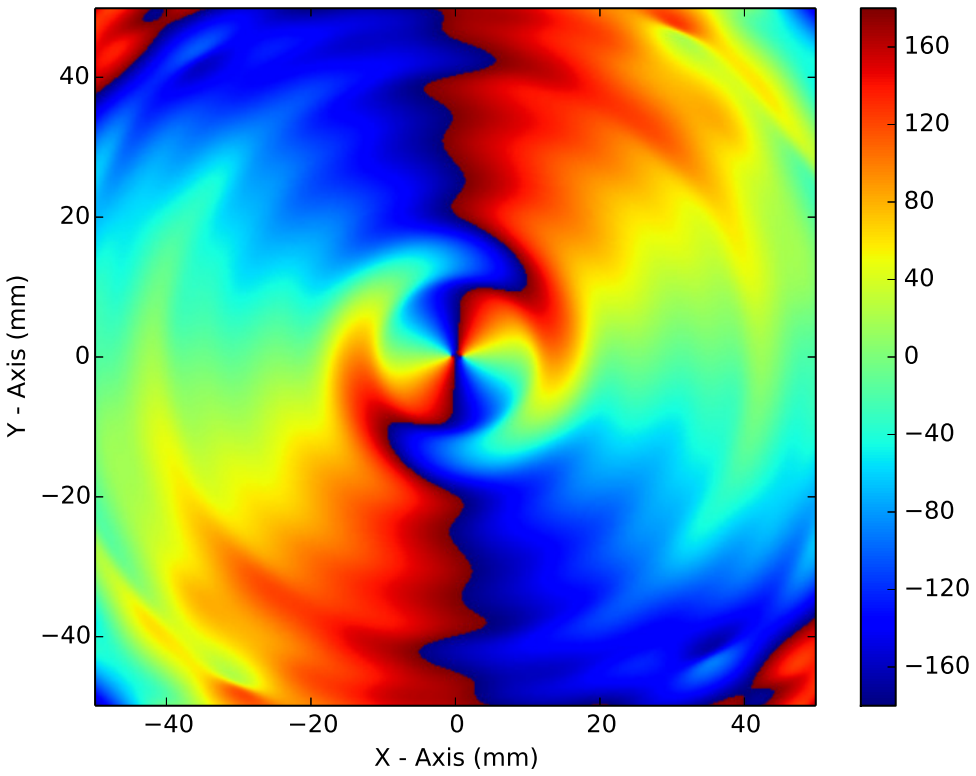

Figure 4.58: $\Delta l = \pm 2$ Split Stepped Aperture Source Plane 3 Phase.

ring is smooth and continuous, but display asymmetrical peaking at varying azimuthal angles. The outer most intensity ring has intensity peaking around $\phi = 135°$ and $\phi = -45°$. This is unchanged from the peak locations in Fig. 4.57a. The inner intensity ring also shows peaking at approximately $\phi = 100°$ and $\phi = -80°$.

Decibel scaled intensity (Fig. 4.59b) shows two additional features, not seen in the linearly scaled image (Fig. 4.59a). In Fig. 4.59b there is a pinching effect of the first radial node intensity trough. In addition, the central intensity vortex has become deeper, (approximately -32 dB), and is made up of two semi-distinct vortices, at $y = 0$ located on either side of of the line $x = 0$.

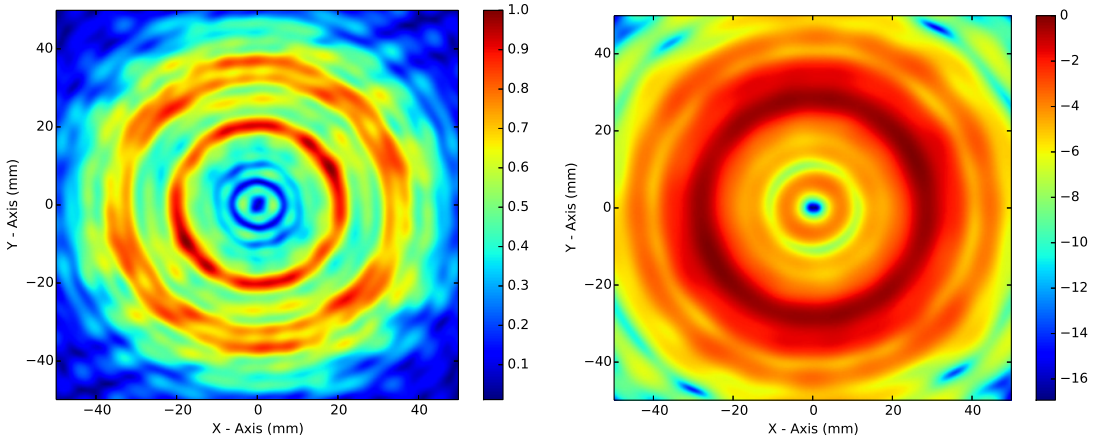

(a) Linear Intensity *(b) Intensity dB*

Figure 4.59: Aperture illuminated $\Delta l = \pm 2$ split stepped SPP intensity on Plane 3.

Plane wave illuminated mode two split stepped SPP

The odd phase structure generated by the aperture source illuminating the split $\Delta l = \pm 2$ SPP (Fig. 4.54) was also seen with plane wave illumination (Fig. 4.60). Phase circulations near the end of the BCs are not as clearly defined as was the case with aperture illumination, however a complex BP pairing is visible. It seems as through the BCs are starting to fold in on themselves, pinching off the phase dislocation to create two additional BP pairs, or are in the process of unfolding. An interference

pattern generated by both primary steps can also be seen in the lower right and upper left quadrants. Compare these regions to the upper right and lower left quadrants, and the interference is immediately visible. In the interference regions, phase is linear along the X-Axis, while the phase is random in the opposing corners.

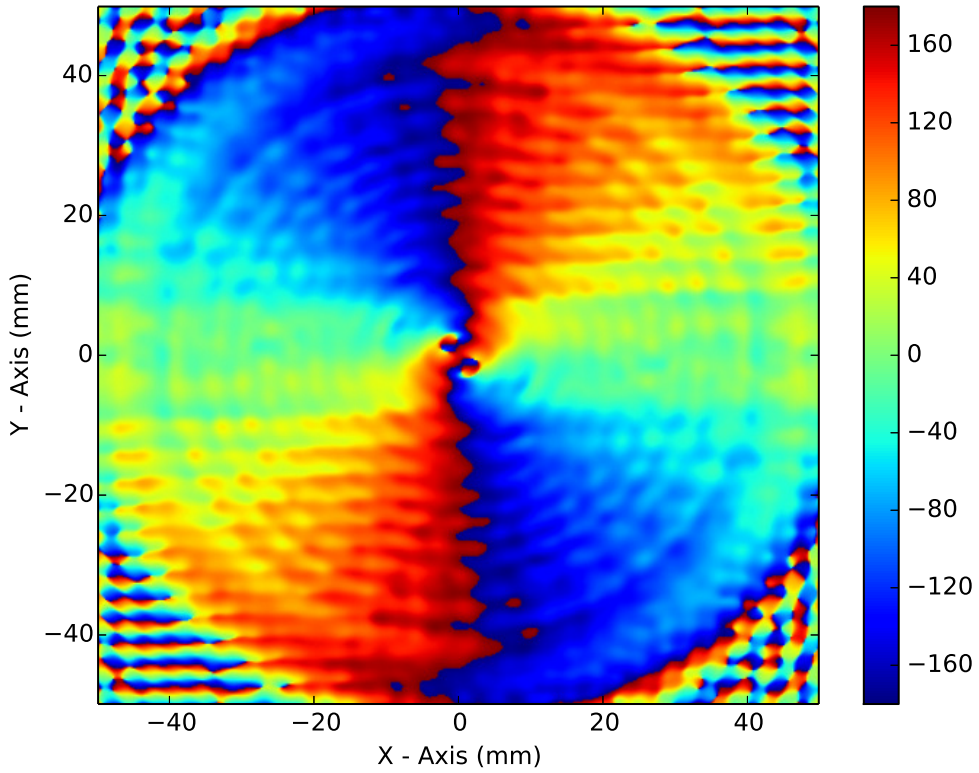

Figure 4.60: $\Delta l = \pm 2$ Split Stepped Plane Wave Source Plane 1 Phase.

Linear intensity modelling on the 6.7λ (20 mm) plane reinforces the premise that interference from the two primary SPP steps is occurring. Strong intensity variations with linear features along the X-Axis, are visible in the lower right and upper left quadrants. Opposing quadrants show predominantly radial variation inside the SPP surface extent. The central intensity null in Fig. 4.61b replicates the odd structure seen in Fig. 4.55b. There is a swept back teardrop shape to the intensity minima, with a small peak in the centre. The lowest intensity regions are associated with BP locations (Fig 4.60).

The 40λ (120 mm) modelled phase plane shows a restructuring of the BPs, so that

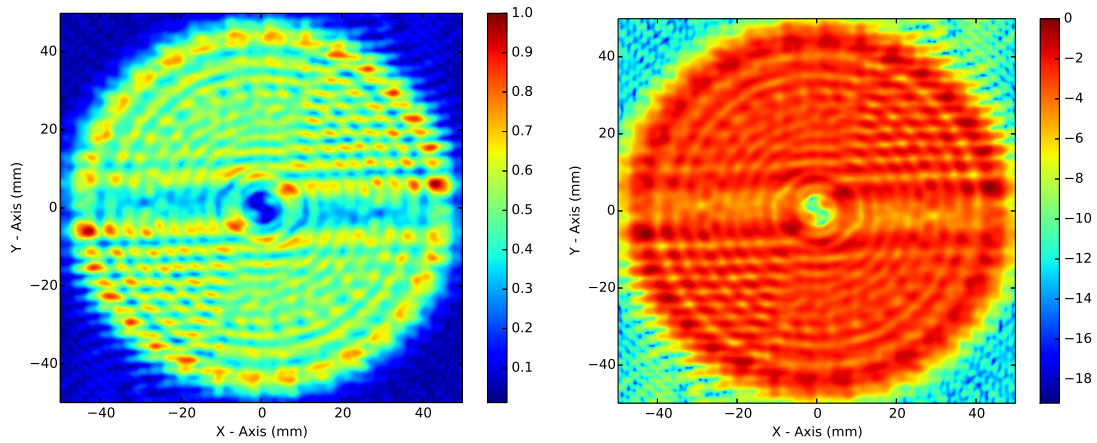

(a) Linear Intensity *(b) Intensity dB*

Figure 4.61: Plane Wave illuminated $\Delta l = \pm 2$ split stepped SPP intensity on Plane 1.

only two are present. A strong phase circulation has developed, and the BCs propagate outwardly from the BPs to the circulation boundary. At the boundary, the BCs quickly change direction and are then distorted by radially dependent phase dragging. Unlike the single stepped SPPs, phase dragging with the split step is highly symmetrical.

The linear intensity pattern (Fig. 4.63a) is comprised of four intensity rings. Each ring is slightly discontinuous, which is a result of plane wave illumination. Intensity peaking with an azimuthal dependence, similar to the aperture illuminated models, is visible. Decibel scaled intensity (Fig. 4.63b), shows a highly symmetric intensity trough with a central intensity null comprised of two circles associated with the BP locations.

Phase dragging of the BCs, (Fig 4.64) continues to be symmetrical. The phase circulation has weakened in relation to the second model plane (Fig 4.62). In addition, the BPs have started to drift apart.

Intensity in Fig. 4.65a has restructured itself into two primary rings. The intensity pattern remains largely discontinuous as a result of pure plane wave illumination. Decibel scaled intensity in Fig. 4.65b appears to have multiple numerical defects. The inner intensity ring is divided by three outwardly radial lines, resulting in six dislocated intensity peaks. The central intensity null is also split into two separate sections. A

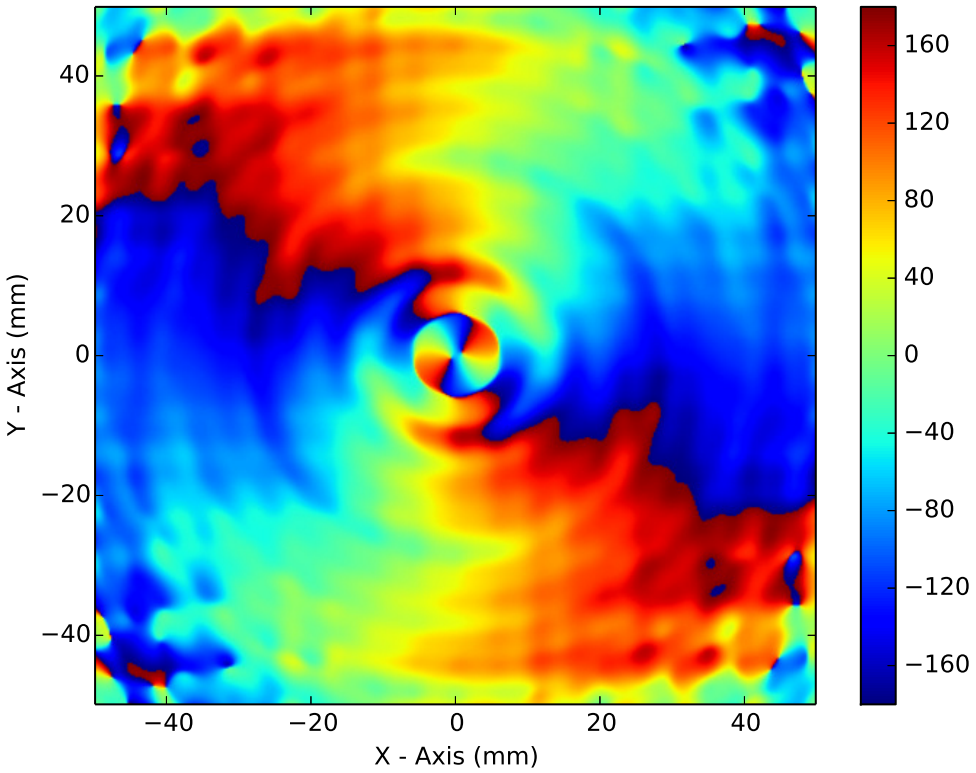

Figure 4.62: $\Delta l = \pm 2$ Split Stepped Plane Wave Source Plane 2 Phase.

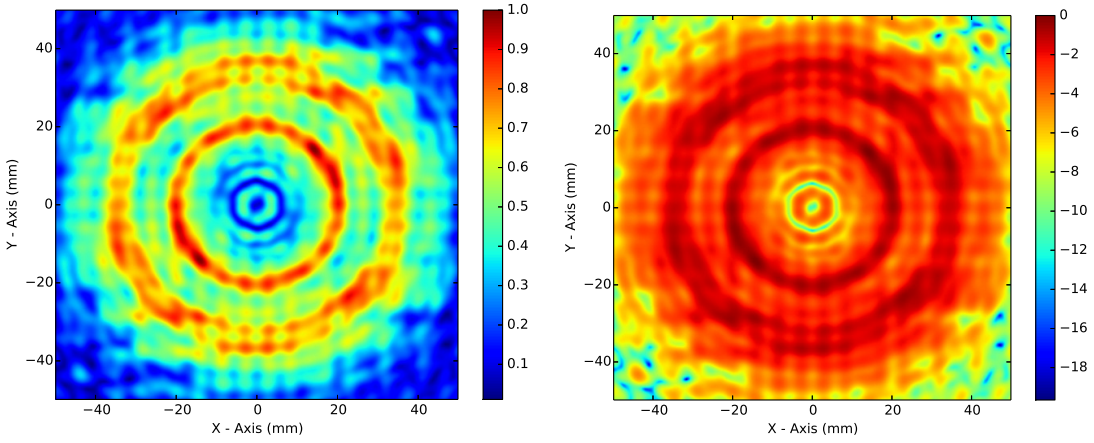

(a) Linear Intensity *(b) Intensity dB*

Figure 4.63: Plane Wave illuminated $\Delta l = \pm 2$ split stepped SPP intensity on Plane 2.

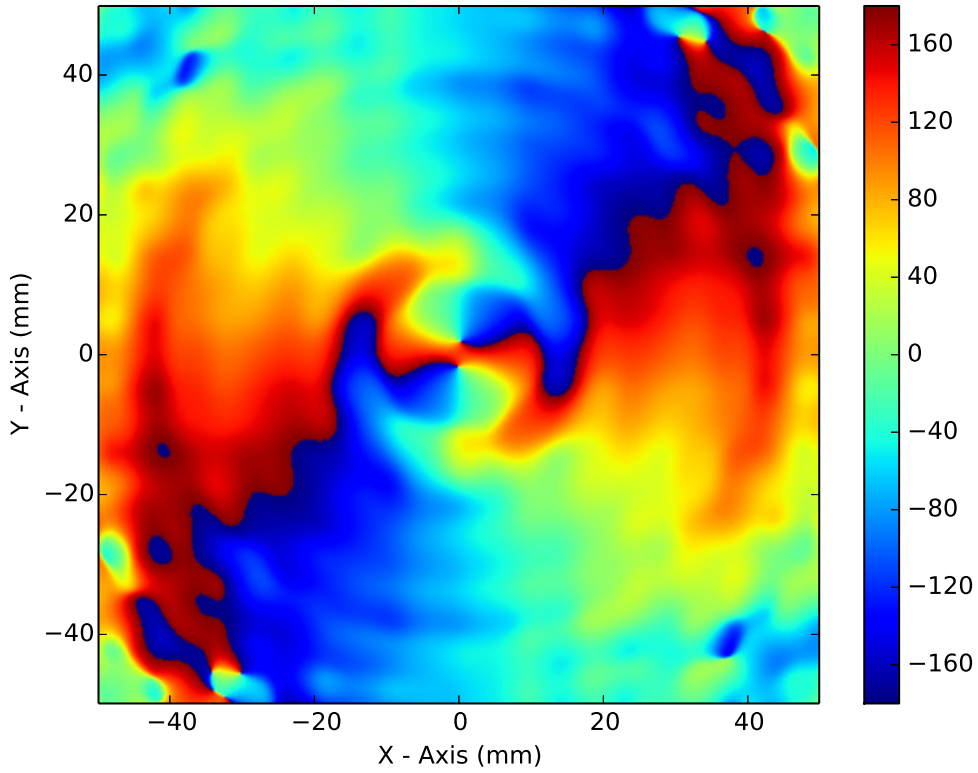

Figure 4.64: $\Delta l = \pm 2$ Split Stepped Plane Wave Source Plane 3 Phase.

cross pattern along the lines $x = 0\,\text{mm}$ and $y = 0\,\text{mm}$ is also visible.

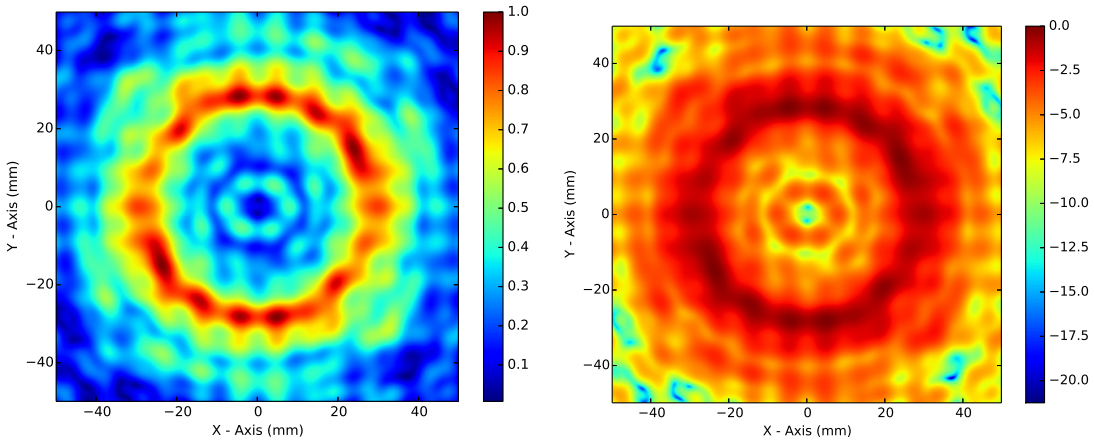

(a) Linear Intensity *(b) Intensity dB*

Figure 4.65: Plane Wave illuminated $\Delta l = \pm 2$ split stepped SPP intensity on Plane 3.

Gaussian illuminated mode two split stepped SPP

Finally, the split stepped $\Delta l = \pm 2$ SPP was illuminated by a Gaussian beam source, generated by a corrugated feed horn antenna. Recall that the feed was placed 50λ (150 mm) behind the SPP so that the first beam pattern nulls corresponded to the inner radius of the SPP mount. This was done in order to reduce diffraction affects inherent to the aperture and plane wave illuminated models. Phase modelled on the 6.7λ (20 mm) plane is displayed in Fig. 4.66. The phase pattern includes two BCs rotating around two BPs in the centre of the propagation axis. Interference from the primary SPP steps is visible in the lower right and upper left quadrants, as indicated by the linearity in the phase variations.

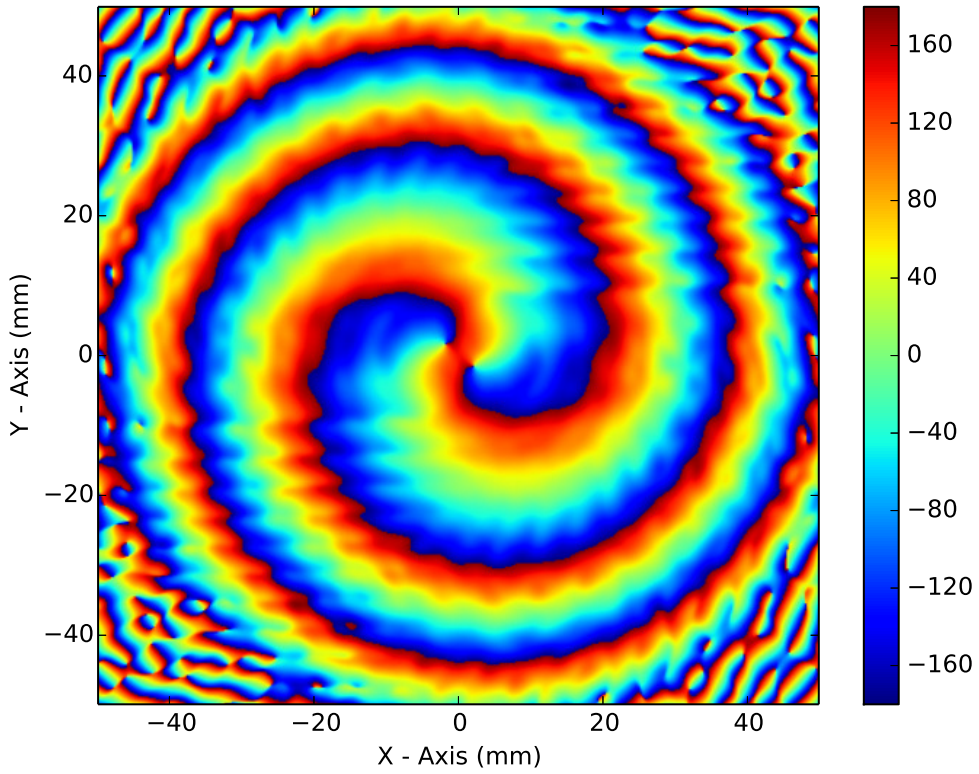

Figure 4.66: $\Delta l = \pm 2$Split Stepped Gaussian Source Plane 1 Phase.

High on-axis intensity peaks are visible (Fig. 4.67a). A linear structure to the intensity is also visible where the phase variations caused by leakage through the

primary SPP steps were positioned. The central intensity vortex is visible in dB scaling (Fig. 4.67b). Two distinct intensity minima are visible, which are located on top of the BP locations. Recall that the undefined phase at the BP location results in an undefined electric field, and therefore no intensity is expected. Due to the infinitesimal size of the BP, and the finite size of the modelling grid, the expected intensity nulls are only visible by the associated intensity minima in the neighbouring region of the BP locations.

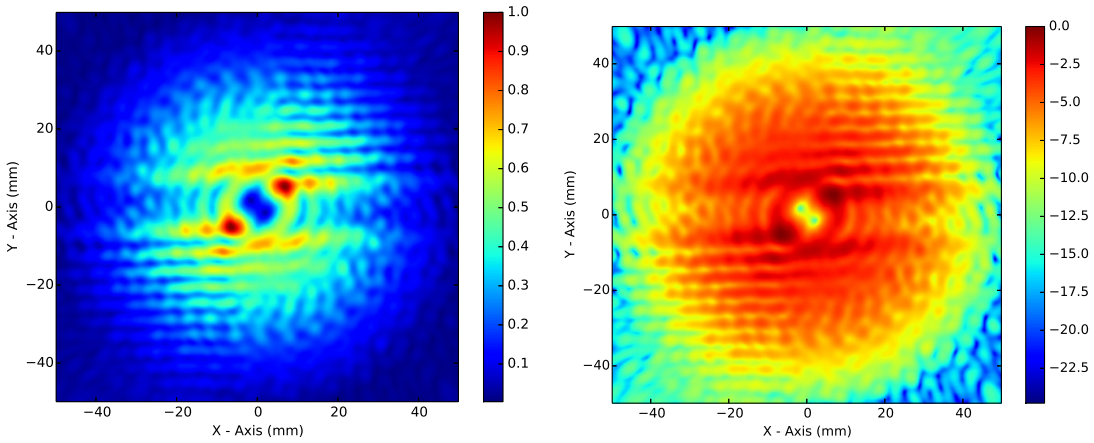

(a) Linear Intensity *(b) Intensity dB*

Figure 4.67: Gaussian illuminated $\Delta l = \pm 2$ split stepped SPP intensity on Plane 1.

Phase modelling of the second plane (Fig. 4.68) shows a substantial amount of smoothing compared to the initial model plane (Fig. 4.66). A 2π phase rotation around each BP is visible, and indicates that each BP has the same helicity. This is because the phase rotation, in relation to the BC as it enters the BP, increases from left to right.

Linear intensity in Fig. 4.69a is comprised of one primary intensity ring. Interestingly, the intensity ring shows an asymmetrical profile with azimuthal dependence. In the lower right quadrant, intensity is redirected from the positive Y-Axis region, which increases the intensity below the line $y = 0\,\text{mm}$ and decrease the intensity above it. The mirror image of this effect is visible in the upper left quadrant.

Splitting of the intensity vortices is visible when the intensity is scaled in dBs (Fig. 4.69b). Here, each BP generates an intensity null, which is visible as a circular region

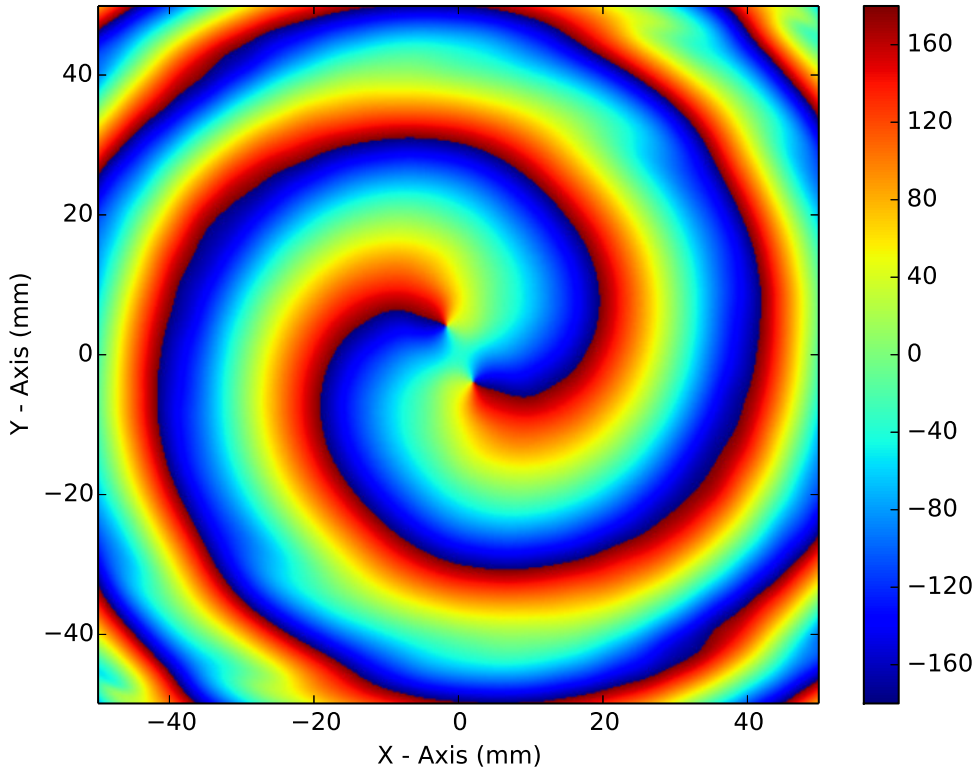

Figure 4.68: $\Delta l = \pm 2$ Split Stepped Gaussian Source Plane 2 Phase.

associated with an extreme dip in intensity (approximately −40 dB). However, since the incident Gaussian beam is divergent, the BPs have started to drift away from each other and a small isthmus of intensity has developed between them.

The final phase model (Fig. 4.70) on the 73.3λ (220 mm) plane shows two BCs rotating around their respective BPs, which have continued to diverge from their initial positions. In addition, the BP locations have rotated in relation to the phase on the second plane (Fig. 4.68). Finally, the BCs are beginning to indicate the very early onset of phase circulation. Here, each BC has begun to propagate away from its associated BP in a linear fashion. After a short propagation however, the BCs suddenly change direction, and begin to rotate about the propagation axis. This is the same behaviour associated with BCs leaving a phase circulation boundary.

Linear intensity is primarily one large intensity ring, but by the time the beam reaches the 40λ (120 mm) modelling plane (Fig. 4.71a). The asymmetrical intensity

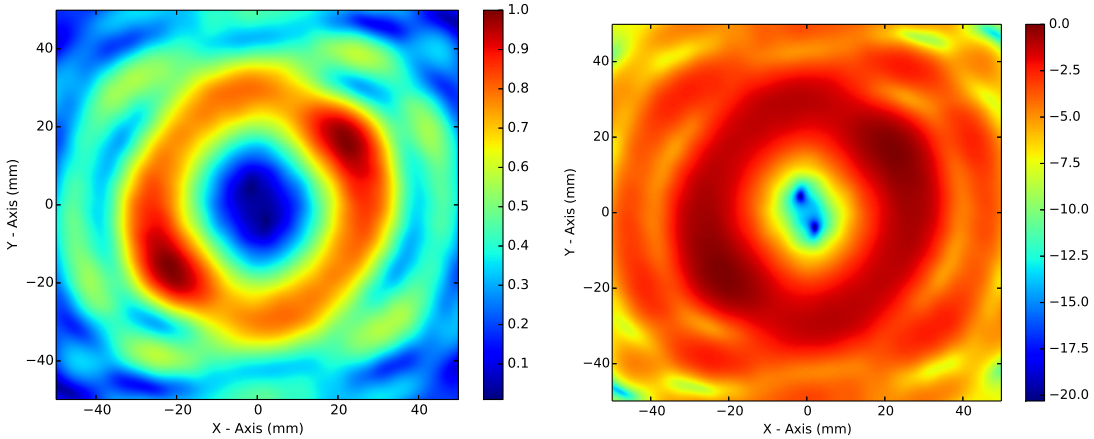

(a) Linear Intensity (b) Intensity dB

Figure 4.69: Gaussian illuminated $\Delta l = \pm 2$ split stepped SPP intensity on Plane 2.

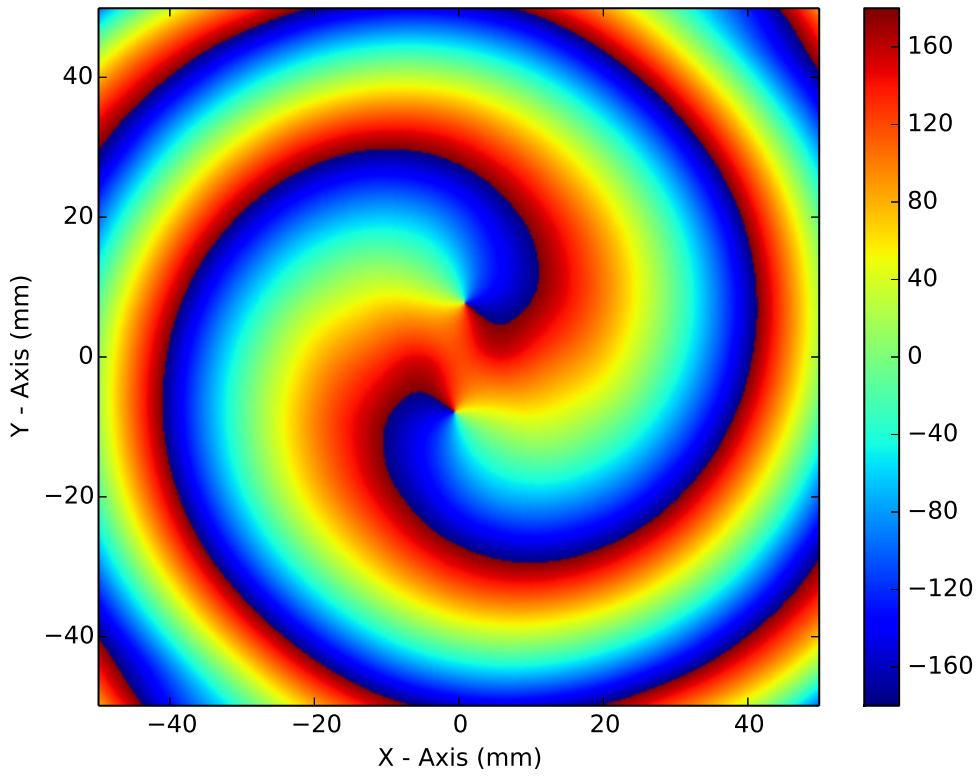

Figure 4.70: $\Delta l = \pm 2$ Split Stepped Gaussian Source Plane 3 Phase.

peaking, resulting from primary SPP step leakage, is visible.

The central intensity vortex detail is improved with dB scaling (Fig. 4.71b). Both primary vortices are clearly visible as circular regions with intensity levels below −40 dB. However, the intensity isthmus that was developing in Fig. 4.69b is no longer present. Instead, the intensity has dropped at the location where the BCs have abruptly change direction.

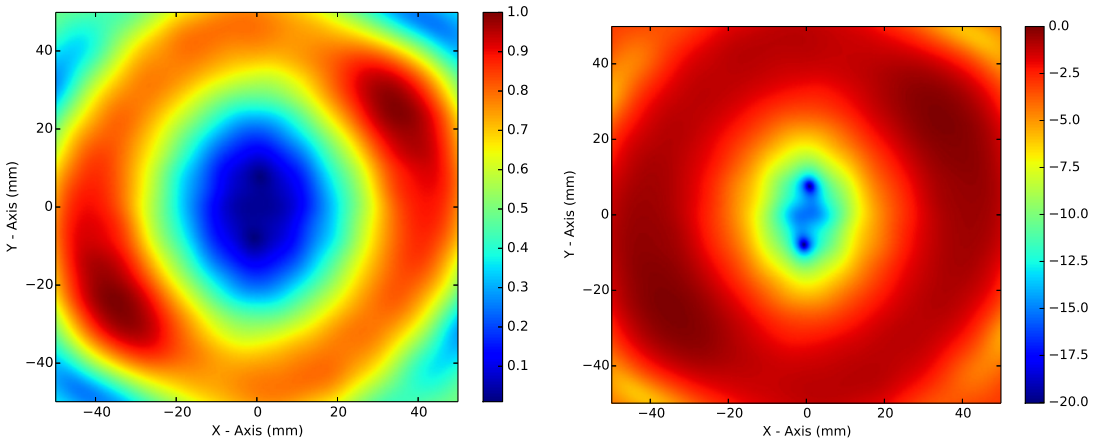

(a) Linear Intensity *(b) Intensity dB*

Figure 4.71: Gaussian illuminated $\Delta l = \pm 2$ split stepped SPP intensity on Plane 3.

$\Delta l = \pm 2$ split stepped SPP Review

Presented here is a review of the $\Delta l = \pm 2$ split stepped SPP FEKO modelling results. This specific SPP design produced the most interesting and unexpected modelling results. Both the aperture and plane wave sources generated two phase circulations at the termination points of both BCs. Typically, BPs exist at the end of BCs. However, these two sources produced phase circulations with two extra BCs and four extra BPs. This strange central phase structure produced intensity patterns with teardrop shaped vortices. The split step nature of this SPP design produced linear interference patterns in all three illumination cases, however interference in the Gaussian fed case was much less. Additionally, two intensity discontinuities are visible in on the first modelling

plane for all sources. This is due to a boundary condition mismatch between the field inside and outside the SPP step. The aperture source generated very little splitting of the BP pairing, while BP separation generated by the plane wave and Gaussian sources were relatively large. This split step design produced highly symmetrical phase dragging patterns. Finally, the third modelling plane generated by aperture illumination produced BCs that contained 90° changes in direction. These are believed to be indicators of a growing phase circulation.

4.4 Conclusion

To conclude, this chapter conducted analytical and computational modelling of three primary SPP designs, a $\Delta l = \pm 1$, a $\Delta l = \pm 2$ single step and a $\Delta l = \pm 2$ split step design. In the analytical modelling section, the mode content, or mode spectra, for each SPP was calculated. A comparison was made between a smooth, stepped and stepped with deviations surface. Smooth surfaces resulted in the most concentrated mode spectra, while stepped surfaces with random deviations from the design thickness produced the least concentrated mode spectra. However, these deviating surfaces best represent real world SPPs. From the calculated mode spectra, the intensity and phase at various propagation distances can be reconstructed. This was done for each SPP in order to determine what kind of electromagnetic field features should be expected. Finally, the analytical section concluded with a justification for the number of steps-per-mode chosen for the actual SPPs manufactured for use in this thesis. A review of all the SPP parameters can be found in Table 4.7.

Following the analytical modelling section was a comprehensive study of SPP generated beams via FEKO MLFMM modelling. Computational modelling of this type was used to develop and understanding of the more nuanced features of SPP generated beams. Three sources types were chosen. They were an aperture source, plane wave and a Gaussian beam generated by a corrugated feed antenna. Firstly, each source was modelled in free space to understand its respective propagation characteristics. Next,

each source was modelled in conjunction with the SPP mount, but without the SPP. This was done in order to understand what induced diffraction effects would be present. A relative large amount of diffraction was generated by the aperture and plane wave sources, while the Gaussian beam was produced very little diffraction. Finally, the full system, SPP and mount, were modelled. These models resulted in various field features. Some of these were, BCs and BP pairs, phase dragging, phase circulations, central intensity vortices, vortex splitting, teardrop shaped vortex structures and step interference. Measurements of actually SPPs will be presented in Chapter 6, and many of these characteristics will feature prominently.

5

Three Dimensional Near Field Scanning System Characterisation

5.1 Introduction

This chapter details the characterisation of a three dimensional field scanner, which will be used to measure LG beams produced by SPPs [101]. First, the concept of near field scanning is introduced. Near field scanning techniques are used to acquire the complex field parameters generated by the device under test (DUT). Near field scanning requires careful preparation and a deep understanding of the specific system being used, due to the many factors that influence measurement results. These include the probe shape, size and position, the DUT, the source size and shape, the optical path and the surrounding environment. Special care must be taken to minimise reflections between the source, DUT and probe, as these may greatly affect measurements. Particular interest is paid to the stability of the vector network analyser (VNA), which is used to make the field measurements. This is because large volume field scanning can take many hours depending on the scan area and requested resolution. Large fluctuations in VNA stability may therefore, introduce unwanted signal fluctuations into recorded data. A well known corrugated feed horn is then characterised, and the three dimensional

scanner measurements are compared to previously validated models. This will ensure that the scanning system functions properly. Finally, to prove that the scanning system can accurately measure real devices, a dielectric lens is measured and the results are compared to FEKO modelling and analytical Gaussian propagation predictions.

5.2 Near Field Scanning

Near field scanning is becoming increasingly important for millimetre wave systems including telecommunication and satellite qualifications [102, 103], radar diagnostics [104], very large antenna performance analysis [105] and various test ranges [106, 107]. Near field scanning offers several advantages compared to far field scanning such as a reduction in size and cost of testing facilities and increased accuracy [108]. The need for increased near field scanning techniques and facilities also coincides with the increased use of quasi optical (QO) components such as lenses, filters, polarisation modulators and various other devices [109–112]. These devices are used to increase the potential scientific return, or the technological capability of, satellites, telescopes or communication systems. It should be apparent however, that increasing the number of components in an optical system also increases the complexity of the system. Each QO component added to an optical system produces reflections between it and surrounding components. These reflections lead to standing waves, which interfere with the throughput signal, ultimately degrading system performance [113, 114]. When QO components are placed in the near field of other components, these reflections become much more difficult to model and predict. Therefore, it is extremely important to measure the near field of individual QO components to understand exactly what the incident wave on the next QO component will be. This information may be used in analysis of the modelling process to improve accuracy.

Additionally, some QO components can have very large minimum far field distances. Measuring the far field of these components directly requires large outdoor test ranges. These are often difficult to acquire and fund. There are also the added difficulties of

unknown interference sources and the weather. These limitations may be overcome by using analytical techniques to transform near field data into far field patterns with high degrees of accuracy. Near field scanning systems also offer more controlled and repeatable experiment environments.

Near field scanning of SPPs is advantageous for three reasons. First, measurements of the SPP beam patterns can be easily accomplished in three dimensions with a planar scanning system. Three dimensional measurements are desirable for OAM phase analysis, since the phase changes with propagation distance. Secondly, the near field SPP beam patterns are smaller in size than their respective far fields. Therefore, near field measurements allow for smaller measurement systems. Finally, the near field beam patterns generated by SPPs are of particular interest for purely physics-based reasons. Interesting phase and intensity patterns are generated in the near field, and close examination can lead to interesting measurements and results.

5.3 Field Scanner Description

A three dimensional field scanner has been developed to test various millimetre wave systems [101], and will be employed here to test the complex fields generated by SPPs. Before conducting measurements the scanner must be characterised and validated by measuring a known device. Scanned measurements of the known source are compared with previously accepted models in order to asses the system's performance. Poor performance may be due to several factors, however it is often related to interference through reflections or standing waves, a misalignment between the probe and DUT, a poor choice of probe or a lack of probe corrections.

The three dimensional scanner developed for these measurements consists of a square frame one metre high, seven hundred millimetres deep and eight hundred millimetres wide. Two coupled belt driven rails sit atop the frame and form the Z-Axis. Another belt driven rail sits perpendicularly atop the Z-Axis making the X-Axis of the scanner. A vertical screw driven rail is used for the Y-Axis and is attached to a movable

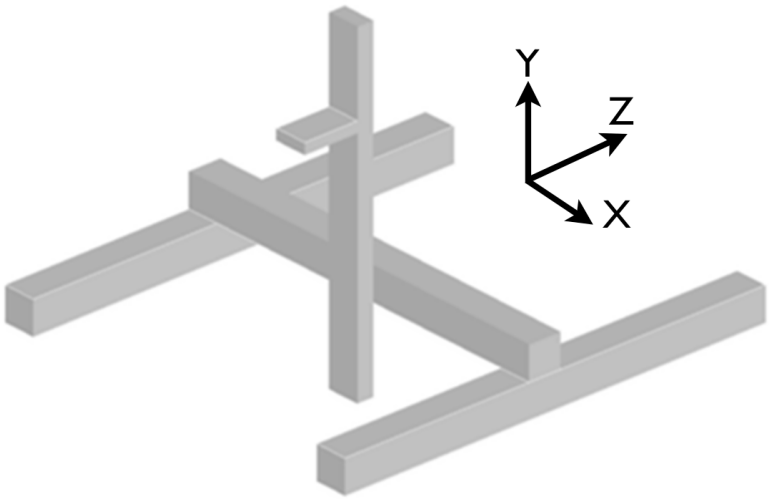

Figure 5.1: Rendering of the 3D Near Field Scanner. One X-Axis rail sits on top of two coupled Z-Axis rails. The Y-Axis rail rides along the X-Axis rail, and supports a movable carriage used to house the VNA frequency converter.

carriage on the X-Axis. A second movable carriage, which holds the probe, rides up and down the Y-Axis. The scanner has a working volume of 50 cm × 50 cm × 50 cm. Each axis is driven by a stepper motor supplied by "ondrives," [115]. Each motor is quoted as having a backlash of 0.006° and can easily be positioned within a micron of the desired location.

Figure 5.2: Rhodes & Schwarz ZVA-110 W-band frequency converter.

A Rhode & Schwarz RS ZVA-40 Vector Network Analyser (VNA), was used to measure the complex field parameters. Two RS ZVA-110 frequency converters (Fig. 5.2) were used to enable measurements across the W-band (75 − 110 GHz). One frequency converter was used to power the source port. A well known corrugated horn was used as a source for this characterisation [116]. A second frequency converter was used to measure the field captured by the probe.[1] For these measurements a circular WR-10 waveguide transition with a coaxial choke, was used as the probe. The probe had an opening diameter of 3 mm and a measured return loss of −34.4 dB at 100 GHz. 3D printed absorber [117] was placed around the probe to prevent reflections from the surrounding surfaces (Fig. 5.3). Since large scans may take many hours to days to complete, an analysis of the stability of the measurement system had to be completed before any scanning was done.

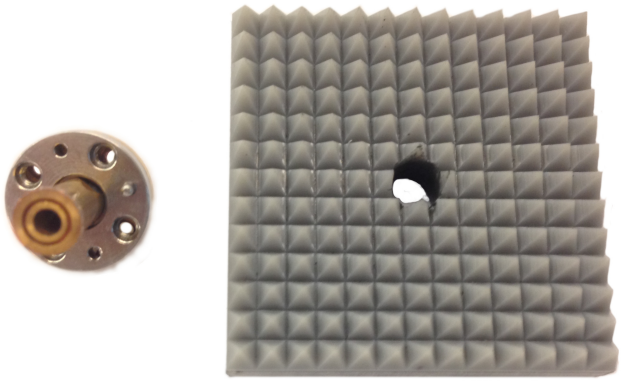

Figure 5.3: Circular waveguide transition with choke, used as a probe for the three dimensional field scanner (left) and 3D printed absorber used to suppress reflections (right).

[1] Although in these experiments one port was used exclusively as a the source while the other was used only as a probe, the VNA allows for the calculation of the field parameters in either direction.

5.4 Vector Network Analyser Operation

Vector network analysers (VNAs) are devices that measure the scattering characteristics, or S-parameters of an electrical network and are particularly suited to high frequency applications [118, 119].[2] S-parameter measurements conducted by a VNA allows for the calculation of both amplitude and phase of electrical networks, which in turn allows for the calculation of the network gain, loss and reflection and transmission coefficients. A two port network may be described by the four complex S-parameters S_{11}, S_{12}, S_{21} and S_{22} (Fig. 5.4).

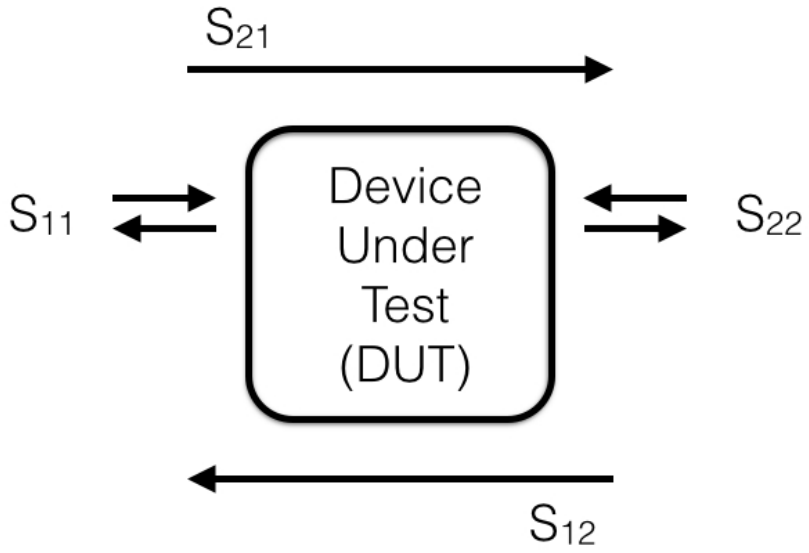

Figure 5.4: S-parameters for a two port network.

For simplicity, it is assumed that Port 2 is impedance matched to free space, for derivations of unmatched cases see [120]. Then, the S-parameters for a two port network are defined as,

$$S_{11} = \frac{V_1^{Reflected}}{V_1^{Transmitted}} \tag{5.1}$$

[2] A VNA alone can typically measure frequencies between approximately 500 MHz and 40 GHz, while the addition of frequency converts can allow VNAs to measure up to several hundred GHz.

$$S_{12} = \frac{V_1^{Reflected}}{V_2^{Transmitted}} \tag{5.2}$$

$$S_{21} = \frac{V_2^{Reflected}}{V_1^{Transmitted}} \tag{5.3}$$

$$S_{22} = \frac{V_2^{Reflected}}{V_2^{Transmitted}} \tag{5.4}$$

where, $V_1^{Transmitted}$ is the incident voltage to the DUT from port 1, $V_1^{Reflected}$ is the reflected voltage from the DUT at port 1, $V_2^{Transmitted}$ is the incident voltage on the DUT from port 2 and $V_2^{Reflected}$ is the reflected voltage from the DUT to port 2. If port 1 is considered to be the source and Port 2 the probe, the intensity gain of the DUT is simply

$$G = |S_{21}|^2 \tag{5.5}$$

while the transmitted phase ϕ is,

$$\phi = arctan\left[\frac{Im(S_{21})}{Re(S_{21})}\right] \tag{5.6}$$

This thesis makes extensive use of of both the gain and phase of two port networks, where a SPP takes the place of the DUT.

5.4.1 Vector Network Analyser Stability

Near field volume scans can take many hours, even days to complete. Any drift or variation in the S-parameters caused by the VNA itself can not be deemed negligible without investigation. Therefore, a series of stability tests were undertaken to understand the state of the VNA and frequency converters. Initial stability tests showed that the VNA had some internal electrical issues. As a result of the initial tests, the VNA power supplies and cabling were replaced. After the new hardware was acquired the location of the laboratory was moved from a shielded room with filtered power lines to an

unshielded room with unfiltered lines.[3] A second, and more thorough round of stability tests were conducted in the new laboratory. These showed that the new hardware had made an improvement on the VNA stability. However, the power lines into the new laboratory experienced load fluctuations during weekdays, approximately at 8:00 am and 6:00 pm. These fluctuations were visible in the stability test data. A third round of tests were conducted using a separate bench top power supply, itself powered by the building supply. This lowered the amplitude of the fluctuations but did not remove them. Stability testing continues, but major improvements to the scanner control software has allowed for an 83% decrease in scan times. Scans can now be conducted inside or outside of the load surges periods. Furthermore, private communication with Rhodes & Schwarz engineers [121] resulted in modifications to the VNA port power bias settings. Adjusting the port power bias levels increases the output power of each VNA port. This helps to offset power losses introduced by the RF cabling. This results in an increase in the power applied to the frequency converters amplifier circuits, helping to maintain their proper functionality. Finally, if the large jumps in phase and intensity are ignored, the remaining small noise variations are very small, and are acceptable for the SPP measurements to be conducted later. To conclude, the stability of the VNA was improved as much as possible by increasing the VNA port power bias, using a partially isolated bench top power supply and significantly decreasing the required scan time. As a result SPP measurements were conducted using the VNA and in this best possible state. A review of the stability tests follows.

Shielded laboratory with filtered power supply in free space

Initial stability tests were conducted in a shielded laboratory with filtered power supplies. In these tests the source horn and probe were separated by 300 mm. Phase and intensity of S_{21} data was taken for eighteen hours at one minute intervals. A single frequency sweep was used and no averaging was conducted. Measurements were taken with a 10

[3]This move was a result of a restructuring of the University of Manchester's Astronomy and Astrophysics Technology Group's facilities.

kHz bandwidth. Data was recorded at 90 GHz, 100 GHz and 110 GHz. Phase results are shown in Fig. 5.5.

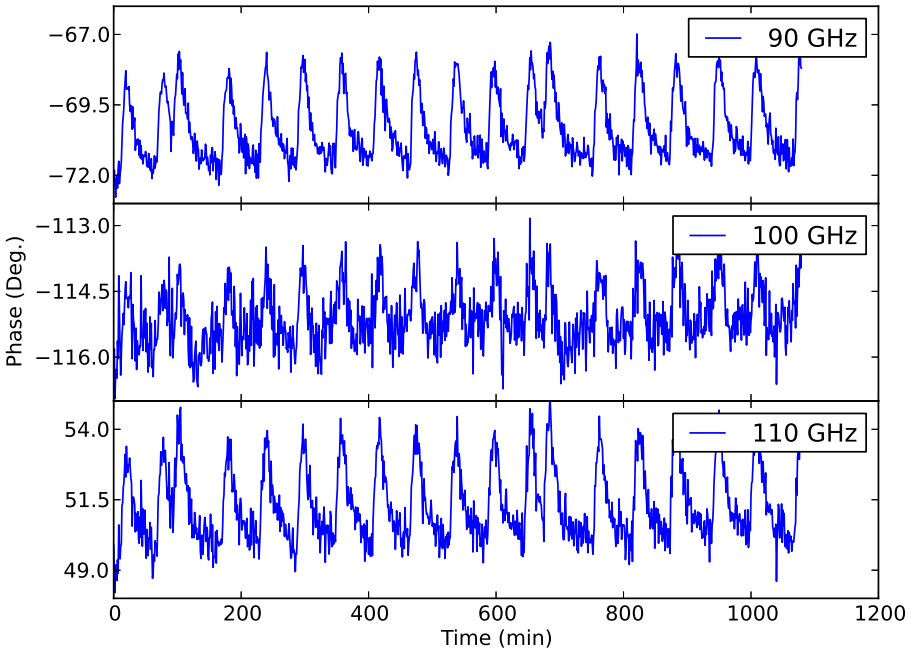

Figure 5.5: Initial phase stability test results conducted in the shielded lab. The sawtooth like pattern, with a one hour period, indicates that the source of the instability was electrical. As a result the power supplies and VNA cabling was replaced.

Analysis of Fig. 5.5 shows that there is a small upward drift in all of the phase traces. Further conversations with Rhodes & Schwarz engineers [121] revealed that this drift is most likely due to a gradual increase in temperature of the VNA and RF cabling. Minor changes in cable temperatures can increase the size of the RF cabling very slightly, which induces a change in measured phase. There is a peak to peak variation of approximately 5° , 3° and 5° at 90 GHz, 100 GHz and 110 GHz respectively. More concerning is the repeated saw tooth pattern in each trace. The pattern has a period of around one hour. This pattern shape and highly repetitive period seems to indicate that the variations are most likely due to a frequency converter amplifier fault as opposed to ventilation in the room or some other outside harmonic mechanical phenomena.

Intensity data was also taken using the same VNA settings and is shown in Fig. 5.6. There is a peak to peak variation of approximately 0.2 dB, 0.5 dB and 0.2 dB at 90 GHz, 100 GHz and 110 GHz respectively. Intensity data shows a similar saw tooth pattern to the phase data (Fig. 5.5) with a period of approximately one hour.

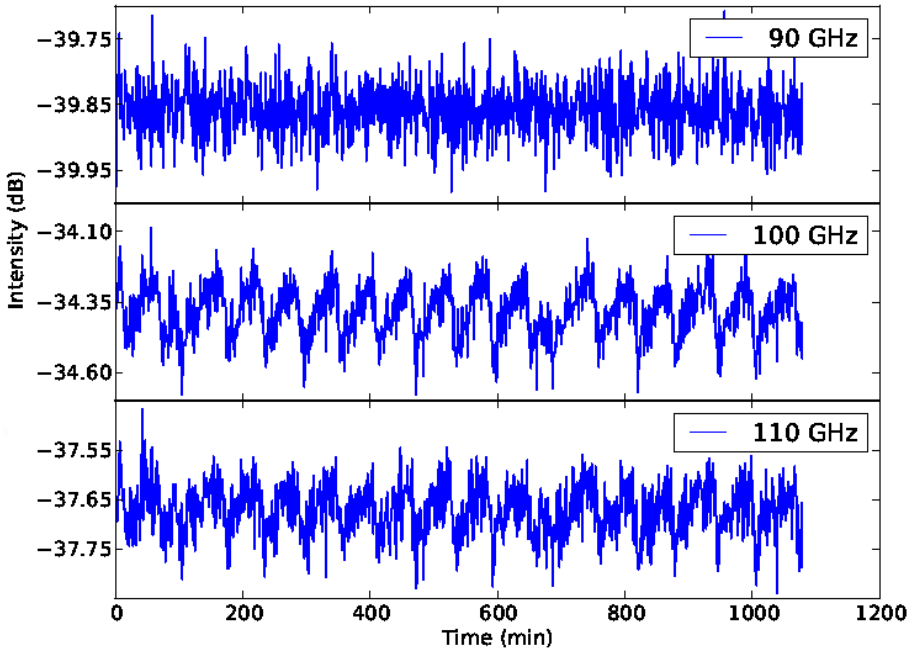

Figure 5.6: Initial intensity stability test results conducted in the shielded lab. As a result of these initial tests, the VNA power supplies and cabling were replaced.

Before the cause of these variations could be fully attributed to the VNA frequency converters, the power supplies and RF cabling had to be checked. During these checks it was found that movements of the RF cabling was introducing variations into S_{21} data, while one power supply was not working as efficiently as possible. In this light, new power supplies and cables were acquired. In the future, a directional coupler could be used to monitor the stability of the VNA, and to correct any measurements.

Un-Shielded laboratory RF cables only

After moving the VNA to a new laboratory and replacing the frequency converter power supplies and RF cabling, a second set of stability tests were conducted. The stability of the cables themselves were first tested, in order to rule them out if later tests still showed that the system was unstable. In these tests a cable was connected to Port 1 and Port 2 respectively. The ends of these cables were then connected to each other to complete a circuit. Again, no frequency converters were used in this test. The results of this cable to cable study are shown in Fig. 5.7 and 5.8. Data was taken between 500 MHz and 40 GHz, and used the same VNA set up parameters that were used in Sec. 5.4.1.

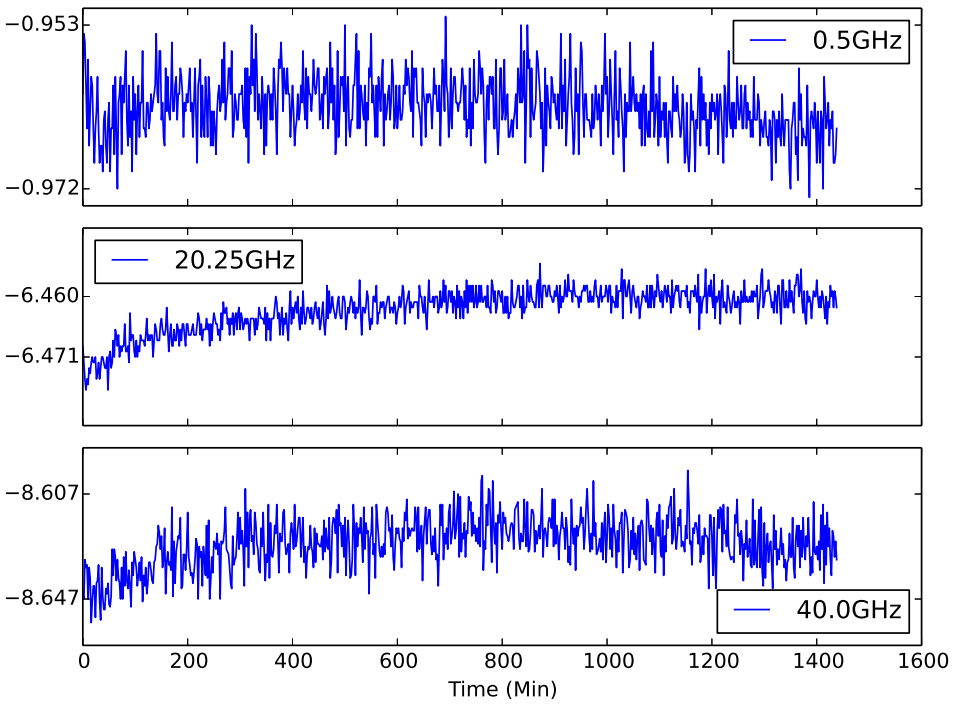

Figure 5.7: Cable to cable intensity stability test showing flat traces up to 40 *GHz. This indicates that the stability issue resides in the VNA frequency converters and not the VNA itself, or its cabling.*

Figure 5.7 indicates that there is a approximately a 0.02 dB peak to peak variation

in intensity at 500 MHz and 20.25 GHz, while there is a 0.04 dB variation at 40 GHz. There is a small visible drift in the first three hours of the 20.25 GHz and 40 GHz recorded signals. This can be attributed to the VNA electronics and cabling heating up and reaching a temperature equilibrium. Regardless, the variations are deemed to be acceptable for use. The corresponding phase data (Fig. 5.8) shows a similar drift in the 20.25 GHz and 40 GHz traces. However, there is no visible drift in the 500 MHz trace. It should be noted that these variations could be improved upon by averaging several VNA frequency sweeps and by changing the frequency sweep bandwidth.

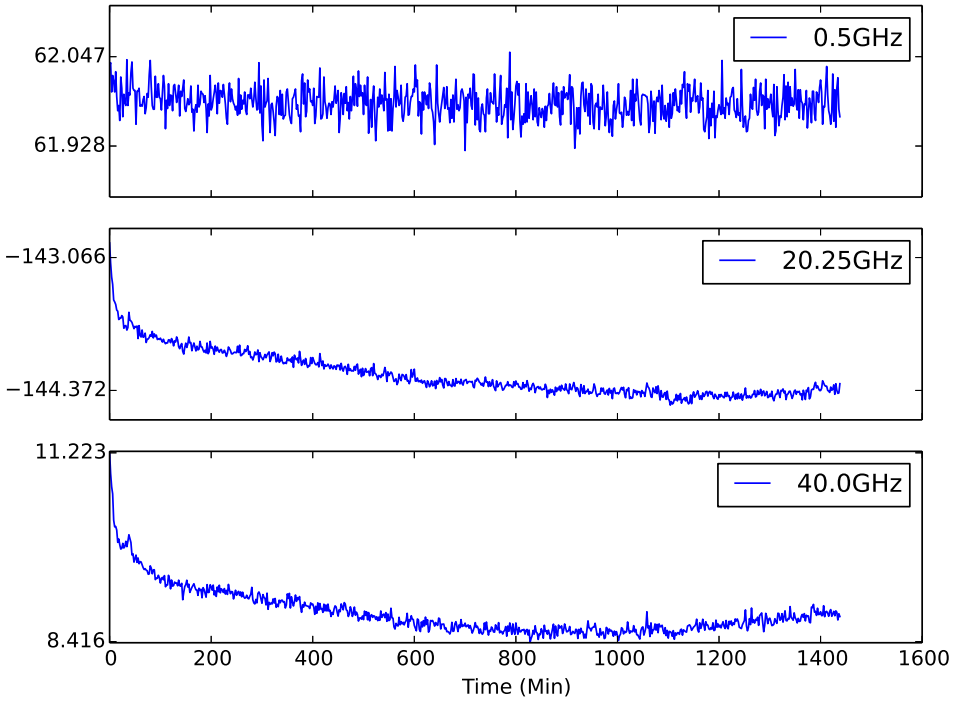

Figure 5.8: Cable to cable phase stability showing a small drift in higher frequencies as the VNA warmed. The phase remained stable after this initial period and confirms the assertion that the stability fault is being caused by the VNA frequency converter.

Un-Shielded laboratory frequency converts in closed circuit

Both W-Band frequency converters were tested since the previous cable to cable tests showed that the VNA and RF cabling were stable. For these tests the waveguides of both frequency converters were connected in order to create a closed circuit. The measurement bandwidth was 10 kHz while data was taken at 75 GHz, 92.5 GHz and 110 GHz. Intensity (Fig. 5.9) and phase (Fig. 5.10) traces show that there is some source of interference turning on approximately at 8:00am in the morning and shutting off at 6:00pm.

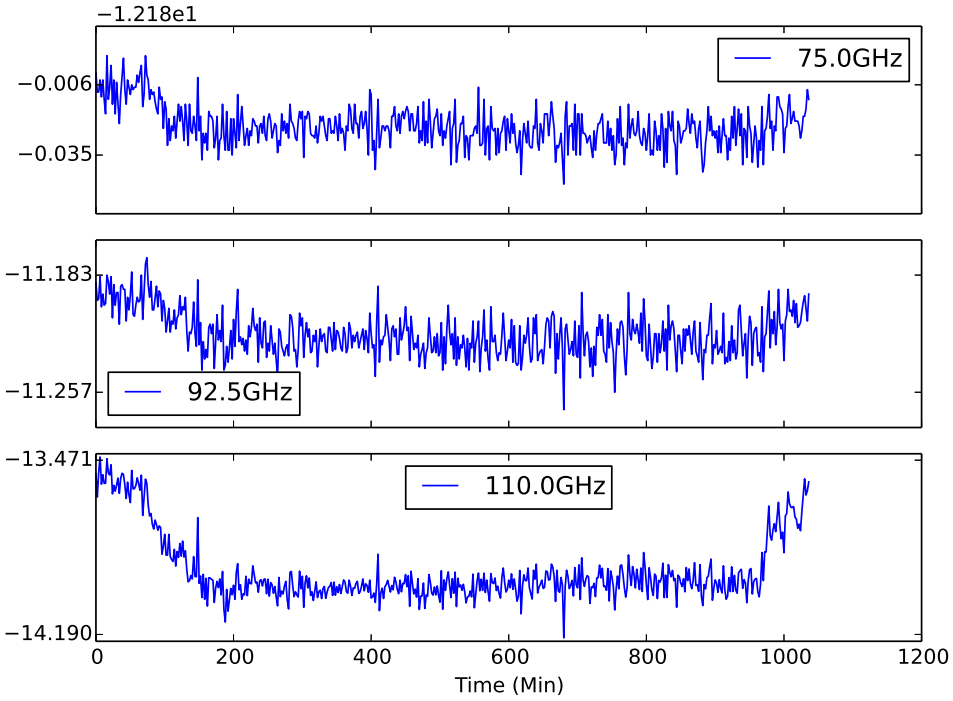

Figure 5.9: Weekday frequency converter intensity stability test. Large variations in amplitude are seen in the morning and evening.

Figure 5.9 indicates that there is approximately a 0.029 dB, 0.074 dB and 0.719 dB peak to peak variation in the recorded intensity values. This includes the large jumps caused by increased load on the building's power supply. The jumps in phase (Fig. 5.10), across all three traces, is not ideal. There is an approximate peak to peak variation

of 5.439°, 6.074° and 16.32° at 75 GHz, 92.5 GHz and 110 GHz respectively. Yet, disregarding the jumps in intensity and phase, the remaining variations are very small. Therefore, if the jumps in S_{21} data could be removed or greatly diminished, the VNA stability would be deemed acceptable for use.

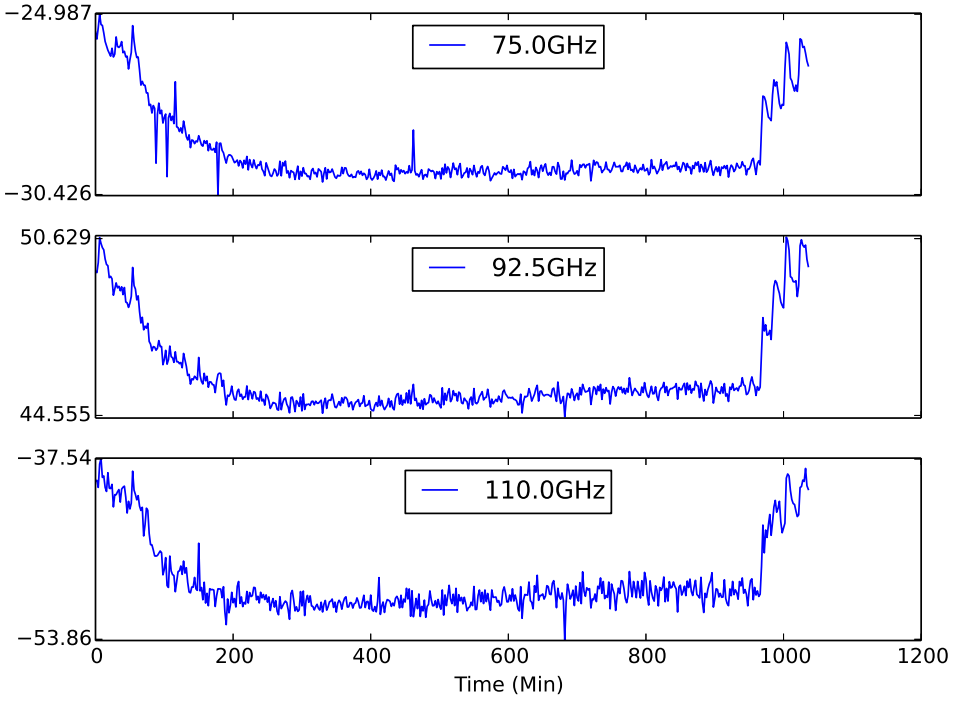

Figure 5.10: Weekday frequency converter phase stability test. Significant jumps in phase are clearly visible across the W-Band, in the morning and evening.

Un-Shielded laboratory frequency converts in closed circuit, weekend testing

Since the VNA and RF cabling only produced satisfactory results, while the inclusion of frequency converters did not, it was believed that small variations in the loading to the power circuit into the lab was initiating minor changes to the frequency converter amplifiers. These small changes induced base line shifts to the recorded S_{21} data, keeping however satisfactory noise variations. To further attempt to isolate the stability problem to the building's power supply, the initial frequency converter tests were carried

out over the weekend, when building electrical loads would be less. The results of these tests are shown in Fig. 5.11 and 5.12. VNA warmup can be seen in both the intensity and phase traces. However, the jumps in intensity and phase are clearly not visible. This implies that the root of the instability in Fig. 5.9 and 5.10, is related to the building power supply loads during the week.

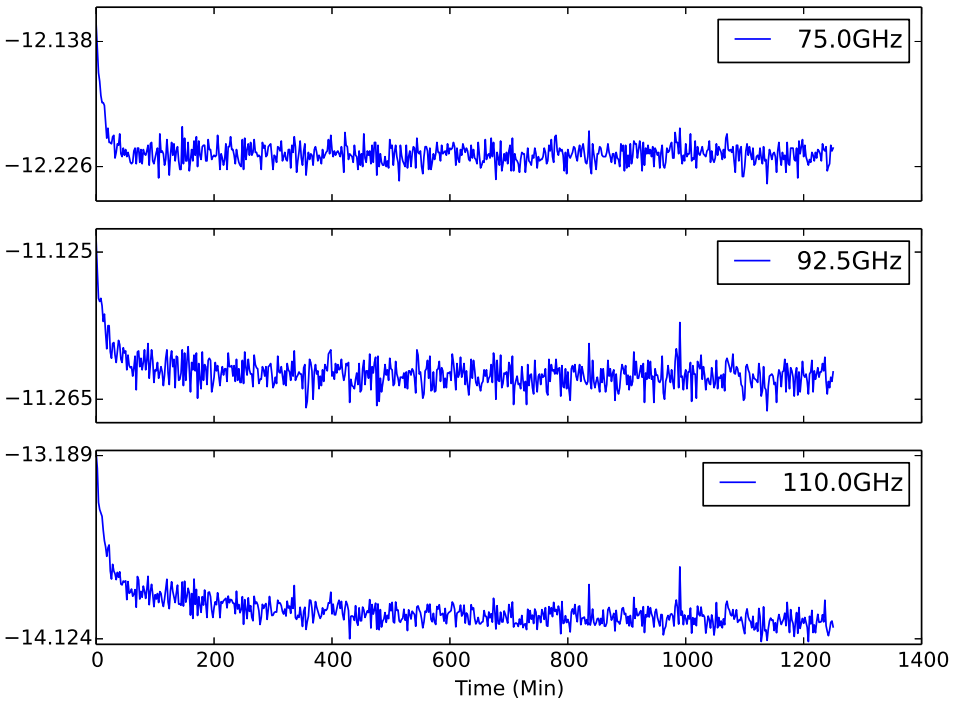

Figure 5.11: Weekend frequency converter intensity stability tests. Large variations in amplitude seen during weekday tests are not present here. This implies that the problem lies with the loading on the mains circuit.

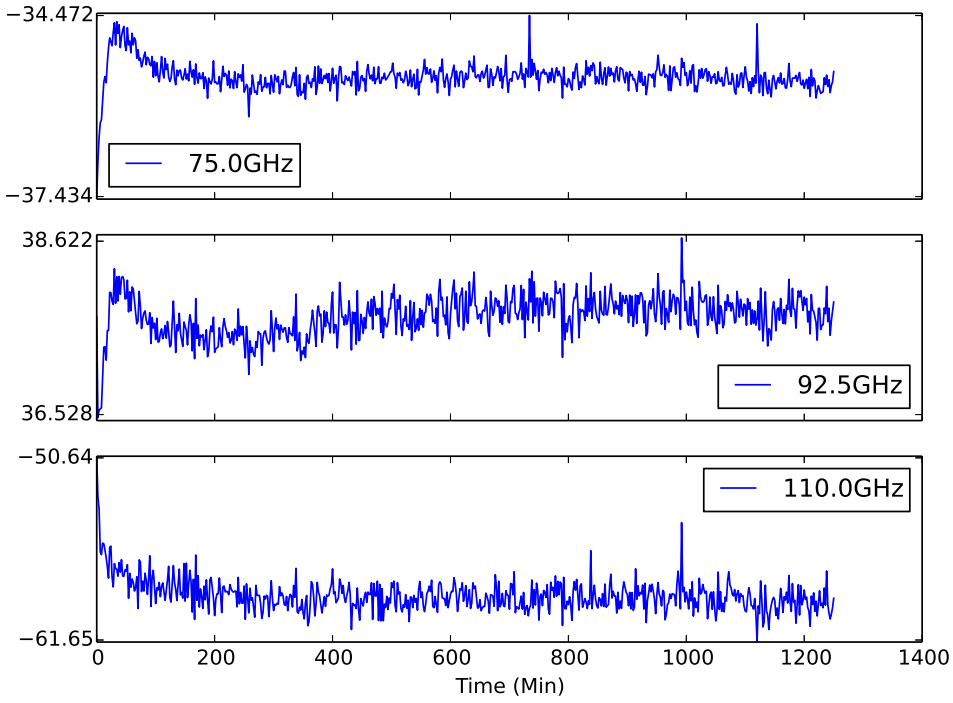

Figure 5.12: Weekend frequency converter phase stability results show no large deviations in amplitude.

Un-Shielded laboratory frequency converts in closed circuit, bench top power supply

Poor phase variation in the previous stability tests prompted a third set of tests where a separate bench top DC power supply from Rhode & Schwarz was used to power the frequency converters. However, the DC power supply itself, was powered from the building's own power supply, so the system was only partially isolated. Initial data was taken on a Sunday (15th December 2013) and into early Monday (16 December 2013) morning (Fig. 5.13 and 5.14). Intensity traces show that there is approximately a 0.176 dB, 0.166 dB and 0.407 dB peak to peak variation. Phase data shows an approximate peak to peak variation of 2.956°, 3.098° and 4.713°. There is a small visible jump in both intensity and phase around 8:00 am Monday morning.

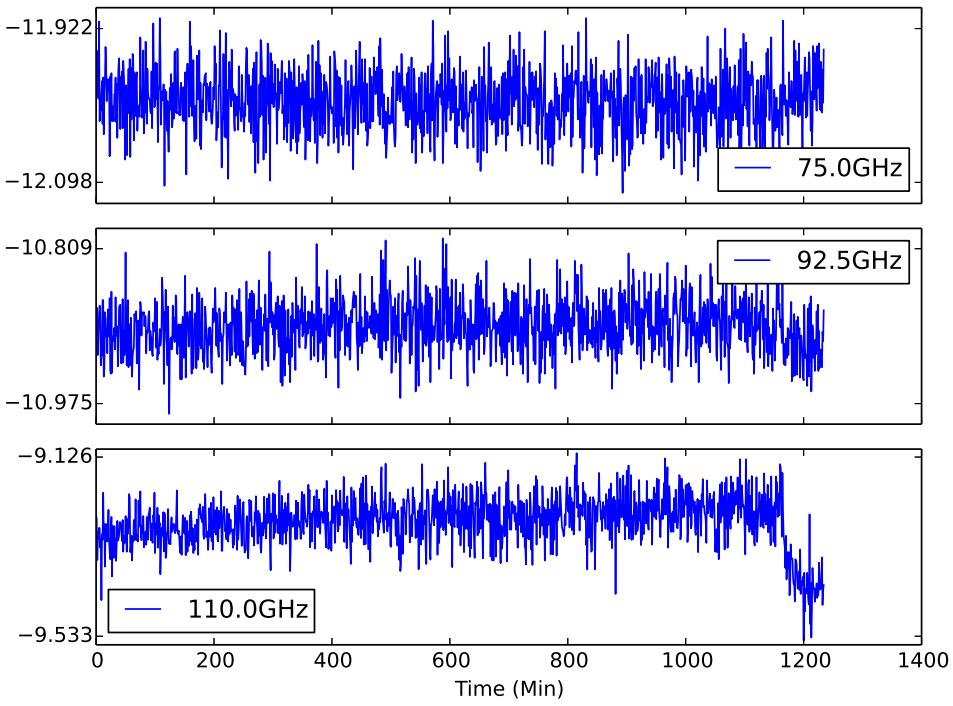

Figure 5.13: Bench top power supply intensity stability tests. These tests were conducted using a separate DC power supply. Although the amplitude variations were not completely removed, they were largely diminished.

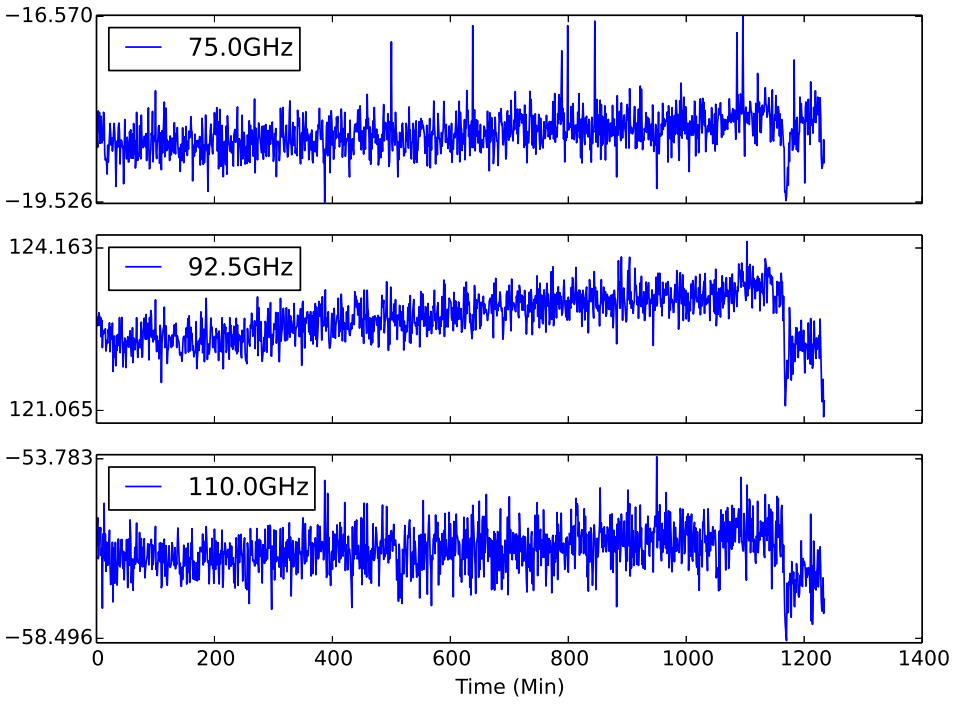

Figure 5.14: Benchtop power supply phase stability tests show minor variations in phase. However, these variations are significantly smaller then when standard power supplies are used.

Un-Shielded laboratory Port 1 short, bench top power supply

To gather a comparable set of data, S_{11} and, S_{22} intensity and phase stability tests were conducted again, on a weekday. VNA cabling was clamped down to the optical bench and the frequency converters were examined individually. This was done to asses whether there was a fault in either of the converters. For each test, a short was placed at the end of the converter's waveguide. For Port 1, S_{11} intensity and phase were measured. Since this system was not calibrated the baseline S_{11} values were not equal to zero as one might expect. However, the purpose of these measurements is to understand fluctuations in the signal with respect to the baseline. These measurements saw an approximate peak to peak variation of 0.05 dB, 0.022 dB and 0.071 dB. Compared to the set up with a standard power supply, there is a decrease in stability of the 75 GHz trace. However, There is a significant improvement in the 92.5 GHz trace, and a slight improvement in the 110 GHz trace.

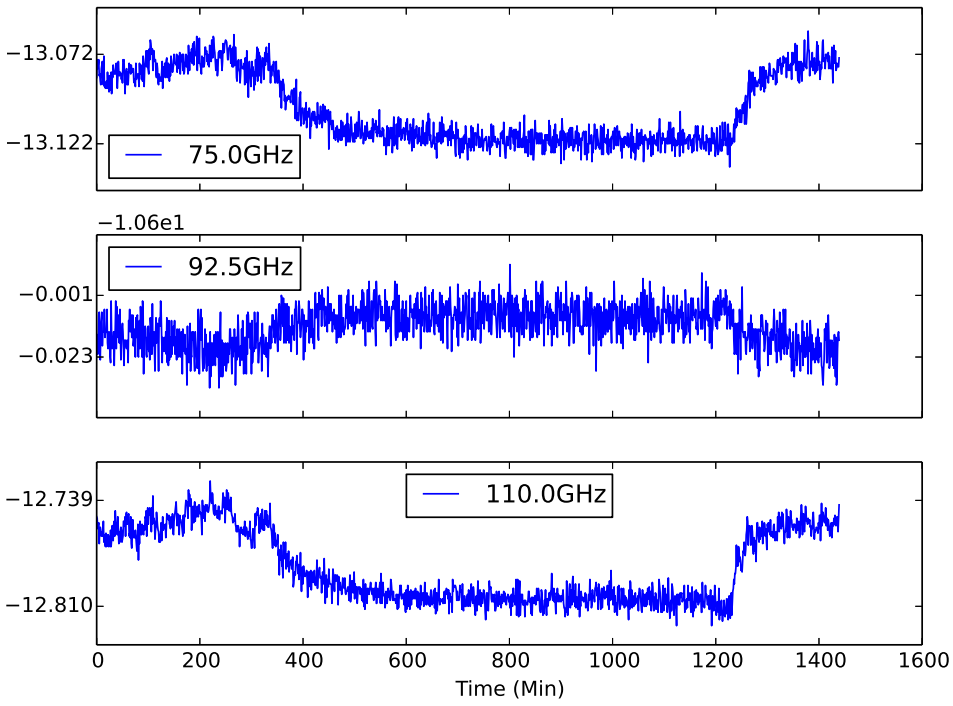

Figure 5.15: Separate power supply short Port 1 S_{11} intensity stability results. Variations in amplitude are clearly visible. Note the difference in variation amplitude and the DC offset compared to Port 2 (Fig. 5.17)

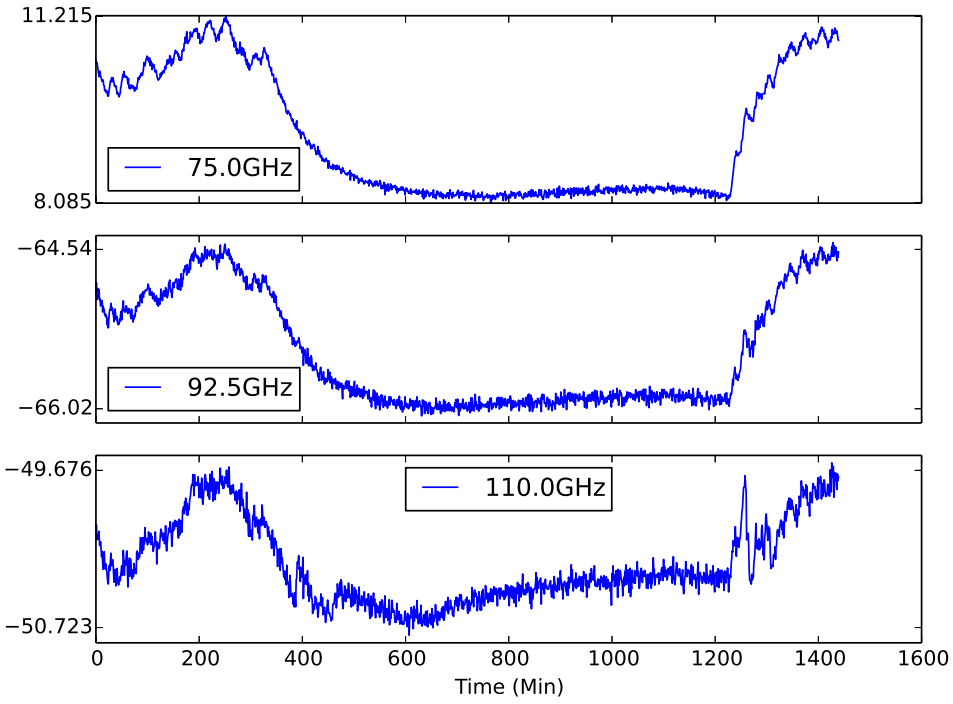

Figure 5.16: Separate power supply short Port 1 phase stability test results. Compare these results to that of Port 2 (Fig. 5.18). Note the step ascent around the $1,200\,min$ *mark.*

Un-Shielded laboratory Port 2 short, bench top power supply

The same tests were repeated on Port 2 by moving the short from Port 1 and by recording S_{22} intensity and phase data. Figure 5.17 shows that there is an approximate peak to peak variation of 0.204 dB, 0.113 dB and 0.197 dB at 75 GHz, 92.5 GHz and 110 GHz respectively. There worse results represent nearly a factor of ten decrease in stability compared to the Port 1 results. It is therefore expected that the Port 2 frequency converter amplifier is not functioning properly.

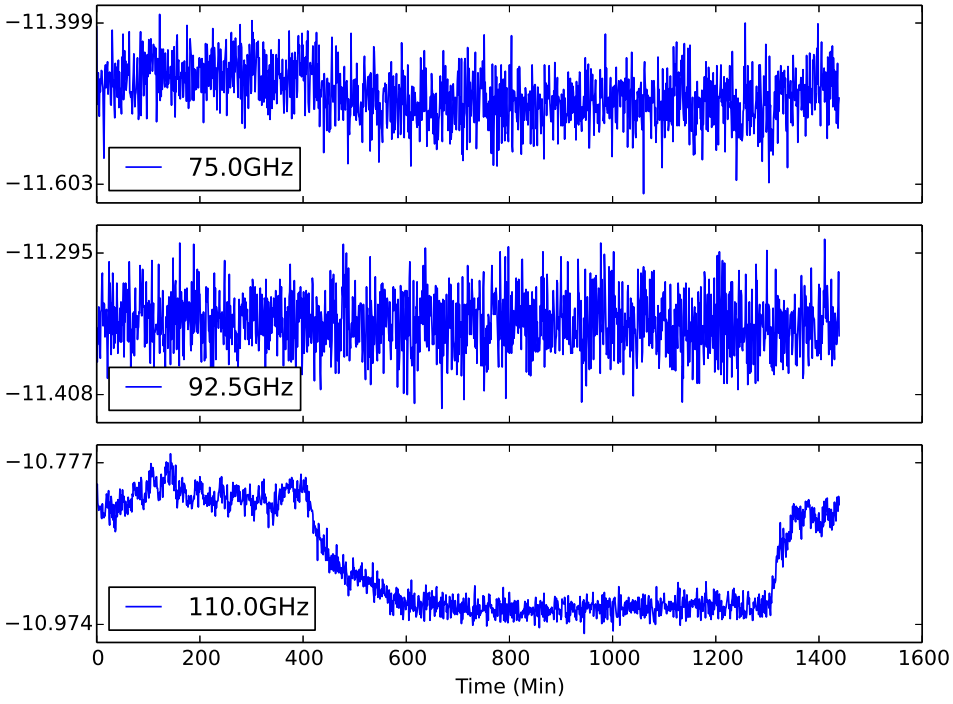

Figure 5.17: Separate power supply short Port 2 S_{22} stability. Variations in amplitude are only visible at the high end of the W-Band. There is a significant improvement compared to the Port 1 results (Fig. 5.15).

Figure 5.18 shows that there is an approximate peak to peak phase variation of 2.217°, 2.09° and 10.84° at 75 GHz, 92.5 GHz and 110 GHz respectively. There is a small improvement in phase stability at 75 GHz and 92.5 GHz, but there is a substantial decrease in phase stability at 110 GHz.

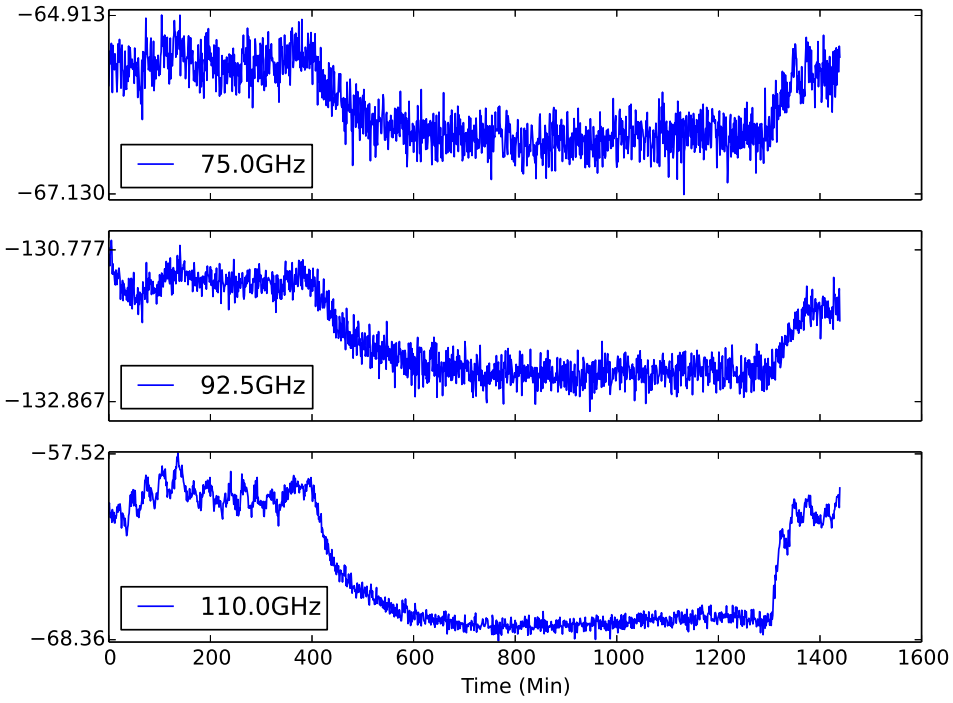

Figure 5.18: Separate power supply short Port 2 phase stability results. Comparison with (Fig. 5.16) shows DC shifts in phase and differing variations.

VNA stability conclusion and additional fixes

Further testing and adjustments to the VNA are clearly needed to improve the stability of the system. However two additional improvements have been made to help alleviate and circumvent the stability problems presented here. First, the scanner control software has been improved, which has resulted in greatly reduced scan times. Scans can now be completed inside the expected morning and afternoon jumps in intensity and phase data. Secondly, future measurements will be conducted with an increase to the VNA port power bias settings. Again, the system control software has been modified to control the port power bias remotely. This results in a higher supply power for the frequency converters, helping them to maintain proper functionality. In the future, data analysis software could be written to remove jumps in recorded data, while a directional coupler could also be used to monitor the transmitted VNA signals for later corrections.

Furthermore a truly isolated power supply known as a universal power supply (UPS), could be used. In the end, it has been decided that the VNA stability, in conjunction with the semi-isolated bench top power supply, increased Port power bias and reduced scan times, is acceptable for the future SPP measurements. Although these jumps could be present in the recorded data, the relative amplitude ($< 5^\circ$ in phase and < 1 dB in intensity [Fig. 5.13 and 5.14]) compared to the expected phase and intensity changes (360° and $\approx$ 20+ dB respectively). Furthermore, the stability of the VNA outside of these jump windows is extremely good. Therefore, no problems are anticipated if the current system, with the mentioned modifications, is used.

5.5 Probes and Corrections

Planar scanning systems are advantageous for their simple design and control, but they require corrections to be applied to measured data depending upon the measurement conducted. For far field scans, a geometrical correction must be applied to the data. This is because far field patterns are calculated on spheres of a constant radius (Fig. 5.20) from the antenna under test (AUT). Probe corrections may also be needed for near or far field scans [122–131]. Probe corrections are required when the probe is asymmetrical, has a high scattering cross section or is highly directive. Measured data represents the convolution of the AUT beam and probe pattern [108]. When the probe used has some undesirable characteristics, the probe pattern must be de-convolved out of the measured data. If a good probe is used the probe pattern will have little affect on the measured data, and no de-convolution is needed. The following system validation will determine how good the probe used is, and what probe corrections will be necessary for the following SPP measurements. The modelled probe beam pattern shown in Fig. 5.19, was achieved by using the finite element method (FEM) solver in ANSYS HFSS [132]. The modelled frequency was 100 GHz.

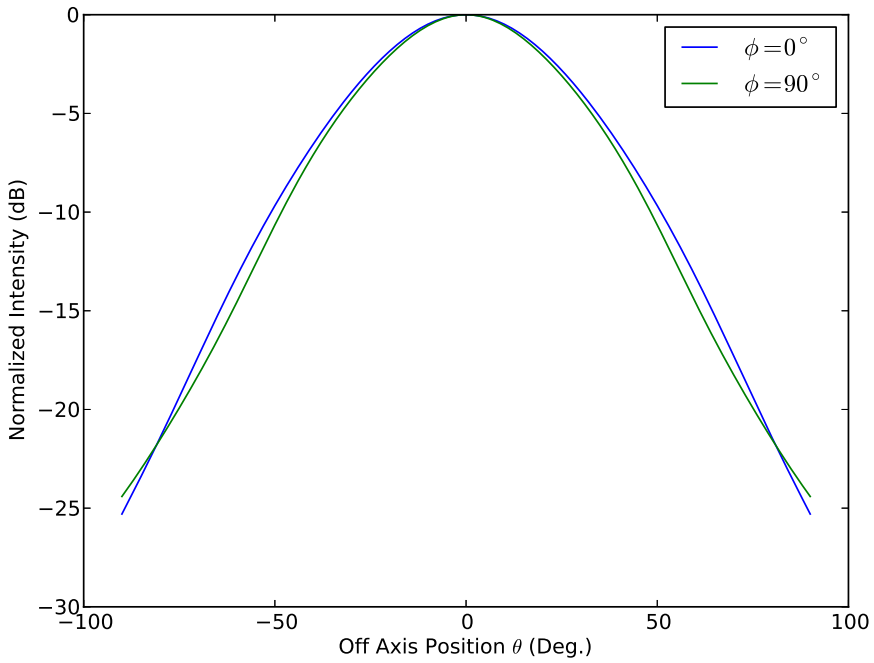

Figure 5.19: Modelled far field probe beam pattern at $\phi = 0°$ and $\phi = 90°$. The pattern is smooth, symmetrical and has poor directivity, which implies that probe corrections may not be necessary.

5.5.1 Far Field Corrections

The primary correction needed for far field scanning is geometrical in origin. Far field patterns are calculated on spheres of a constant radius from the AUT. Planar scanning systems can not easily retrieve data on a sphere. It is much more practical to measure the AUT pattern on a plane, and project that data onto a sphere. This can be done because the intensity of the field drops off as $1/(R + dR)^2$, and the phase is the product of the wavenumber k and the distance travelled, dR (Fig.5.20). To correct the planar measured data the value of dR must be calculated as a function of θ. By Fig. 5.20 the value of dR is found to be,

$$dR = R\left(\frac{1 - cos\,(\theta)}{cos\,(\theta)}\right) \tag{5.7}$$

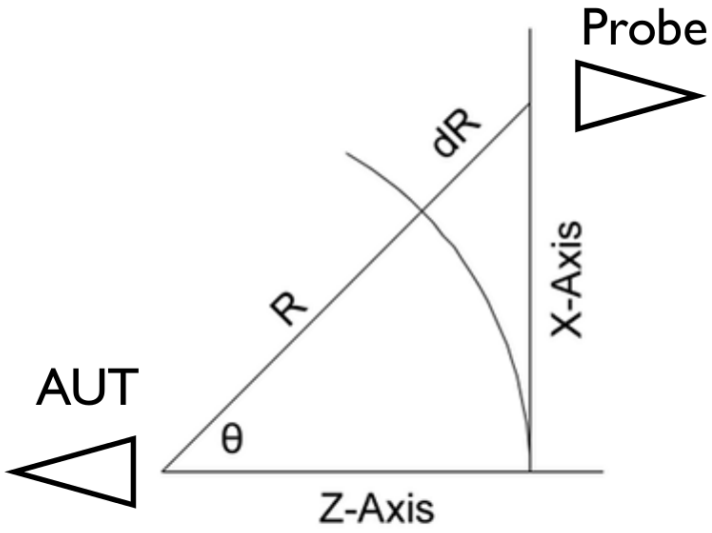

Figure 5.20: Far field probe correction geometry. The value of dR is calculated as a function of θ.

In the far field, the measured intensity pattern is the product of the AUT and probe patterns [108].

$$S_{21}^{2\,Measured}(\theta) = S_{21}^{2\,AUT}(\theta)\, S_{21}^{2\,Probe}(\theta) \tag{5.8}$$

A probe correction factor $S_{21}^{2\,C}(\theta)$ may be introduced to project the planar data onto a sphere,

$$S_{21}^{2\,Measured}(\theta)\, S_{21}^{2\,C}(\theta) = S_{21}^{2\,AUT}(\theta)\, S_{21}^{2\,Probe}(\theta) \tag{5.9}$$

The correction factor has the form,

$$S_{21}^{2\,C}(\theta) = \frac{(R+dR)^2}{R^2} = \left[1 + \left(\frac{1-cos\,(\theta)}{cos\,(\theta)}\right)\right]^2 \tag{5.10}$$

The form of $S_{21}^{2\,AUT}(\theta)$ is then,

$$S_{21}^{2\,AUT}(\theta) = S_{21}^{2\,Measured}(\theta)\, \frac{S_{21}^{2\,C}(\theta)}{S_{21}^{2\,Probe}} \tag{5.11}$$

5.5.2 Near Field Corrections

Near field corrections for planar scanning systems are well understood [122–131]. Corrections, sometimes called "probe compensations," are at times, needed in order to take into account directional dependent coupling effects between the probe and AUT. The exact form of the correction depends upon the scanning geometry. Yet, the correction is essentially a deconvolution of the probe beam pattern and measured field irrespective of the geometry. These corrections are not always needed, depending upon the required accuracy. Sec. 5.6 sets out to measure the far and near field of a corrugated horn in order to determine if the three dimensional field scanner developed here, needs near field corrections to be applied.

5.6 System Validation

Far field and near field measurements of a well known corrugated horn antenna were used to validate the measurement and correction methodology. The horn has an aperture of 17.438 mm, a total length of 75.465 mm and utilises a WR10 rectangular to circular waveguide transition to launch the field into the horn. The horn antenna was modelled using a Method of Moments (MoM) simulation by FEKO [81]. Each measurement was comprised of fifty frequency sweeps of the VNA. Presented error bars correspond to one standard deviation between the measurements. In the following plots the measurement data, model and difference between the two are plotted. The difference between the measurements and models is calculated by normalising both traces, converting to linear scaling, subtracting and then converting back to dB scaling, Eq. 5.12.

$$S^{2A}_{xx} - S^{2B}_{xx} = 10.0 \log_{10}\left(S^{2A}_{xx\,Norm.} - S^{2B}_{xx\,Norm.}\right) \tag{5.12}$$

5.6.1 Far Field

Before examining the near field, which could be overly complicated by multiple reflections and probe to source coupling, the far field was measured. The AUT and probe were separated by 314 mm. The probe was positioned so that the maximum S_{21} intensity value was achieved in both the x- and y-directions. This ensured that the probe was at the centre of the main AUT beam. To acquire data, the probe was scanned along the x-direction and y-direction. Raw data was corrected according to (5.11). The measured Co- Pol[4] intensity along $\phi = 0°$, in Fig. 5.21a, shows a maximum difference between the data and model of -12.9 dB, while the average difference across the pattern was -31.4 dB.

It should be noted that the difference between the model and measured data is a combination of errors in the manufacturing of the horn and errors induced by the scanning system. Validating the corrugated horn with just a single measurement system does not provide enough information to decouple these two contributions. Luckily, [81] has measured the same corrugated horn on a completely different system, in the far field (Utilising the same FEKO model). This far field system rotates the AUT about its phase centre and utilises a stationary horn as a probe. Although this system will also introduce some errors into the measurements, they can be assumed to be negligible especially compared to the field scanner developed here. This is a valid assumption because, in this far field system, the AUT field is always measured along the boresight of the probe. Therefore, the probe utilises the same part of it's pattern to "sense," the AUT field. Using the data in [81] and the assumption that the far field system error is negligible, the three dimensional field scanner effect can be approximated. This is best done if the differences between the measured field and model are converted to linear scaling. These linear differences will be denoted with a script $\mathcal{D}$. The difference between the measured data and model for the far field system is then,

[4]Co-Pol intensity is the intensity measured with the source and probe polarisation orientated the same way. This contrasts with Cross-Pol, or "X-Pol," which refers to the intensity measured when the source and probe polarisation vectors are at 90° to each other.

$$\mathcal{D}_1 = \mathcal{D}_{Horn} + \mathcal{D}_{FF} \tag{5.13}$$

For the field scanner it is then,

$$\mathcal{D}_2 = \mathcal{D}_{Horn} + \mathcal{D}_{NF} \tag{5.14}$$

Eq. 5.13 may be used to solve for $\mathcal{D}_{Horn}$, which is then substituted into Eq. 5.14. The difference attributed to the near field scanner is then,

$$\mathcal{D}_{NF} = \mathcal{D}_2 - \mathcal{D}_1 + \mathcal{D}_{FF} \tag{5.15}$$

but, $\mathcal{D}_{FF} = 0$. Using this, a measured beam difference of $-12.9\,\text{dB}$ in Fig. 5.21 and a measured difference of $\approx -20.0\,\text{dB}$ in [81], $\mathcal{D}_{NF}$ becomes,

$$\mathcal{D}_{NF} = 0.05 - 0.01 = 0.04. \tag{5.16}$$

The field scanner presented here introduces four times the error of the corrugated feed horn. Recall that a normalised intensity pattern in linear scaling has a maximum value of one. The field scanning system is therefore introducing an approximate 4% maximum error to measurements.

Measured Co- Pol intensity along $\phi = 90°$, in Fig. 5.21b, shows a maximum difference between data and model of $-9.4\,\text{dB}$, while the average difference across the pattern was $-24.0\,\text{dB}$. It is clear from both cuts that the data matches the model reasonably well. These measurements confirm that the measurement and correction methodology works properly for the far field. Yet, if one was attempting to make a very accurate measurement of the source horn antenna further improvements would be needed. This is mainly due to a slight misalignment between the probe and source antenna boresight. This misalignment manifests itself as a small tilt in the main beam. One way to fix this is to fit a Gaussian to the measured data, allowing the tilt angle of the Gaussian to be a free parameter. After finding the optimised tilt angle of the data, the model may be re-run using the appropriate geometry. Finally, the data may be

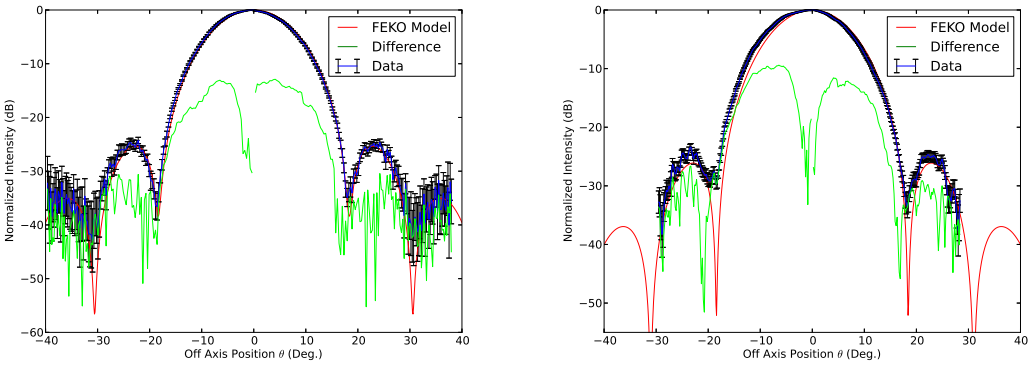

(a) Co- Pol $\phi = 0°$ *(b) Co- Pol $\phi = 90°$*

Figure 5.21: Comparison of measured and modelled far field patterns of the AUT, along $\phi = 0°$ and $\phi = 90°$. A small tilt between the probe and AUT is visible and the signal to noise ratio decreases with increased off axis position. However, the scan has largely followed the model predictions and shows that the measurement and correction methodology is sound.

compared to this altered model. This ensures that the data is compared to a model that is as close as possible to the experimental set up. Additionally, the signal to noise level decreases as the angle θ increases. This is a result of the probe scanning in a planar fashion. As the probe reaches large values of θ the visible area of the probe aperture decreases, resulting in loss of signal.

5.6.2 Near Field

The AUT field was then measured at 76 mm and 42 mm in order to validate the three dimensional scanner in the near field. Cuts of the AUT beam were taken parallel (y-direction) and perpendicular (x-direction) to the polarisation orientation of the AUT. Unlike the far field data, the near field data was left uncorrected to evaluate the difference from model predictions, thereby indicating whether corrections would be required in the future. Figures 5.22a and 5.22b display the X- and Y-Cuts conducted at a separation distance of 76 mm. In the x-direction (Fig. 5.22a), there was a maximum difference

between data and model of −12.5 dB, while the averaged difference across the beam pattern was −30.0 dB. Analysis of the plot reveals a remarkable agreement, across the main beam, between the model and experimental measurements. There appears to be hardly any tilt between the probe and boresight of the source antenna. The experimental data starts to deviate from the model around the first side lobe maxima, but rejoins the model trace approximately 10 dB further down the beam pattern. (I am lead to believe that the small deviation in the side lobes is partly to do with the lack of probe corrections, but probably more so to the actual modelling of the horn antenna. Small differences between the actual AUT and the modelled antenna could lead to the small deviations between experiment and model seen in these experiments.) Error bars on the measurements remain extremely small, down to approximately −50 dB.

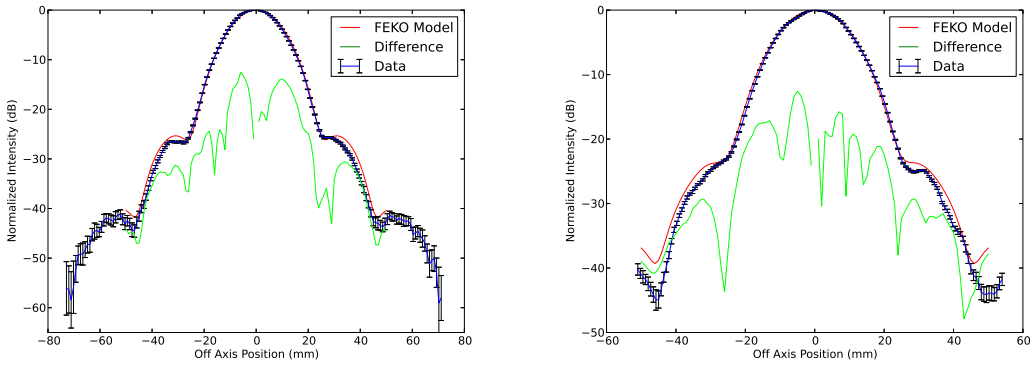

(a) Near Field X-Cut: Separation Distance 76 mm

(b) Near Field Y-Cut: Separation Distance 76 mm

Figure 5.22: X- and Y- Cuts of the AUT at a separation distance of 76 mm. There is strong agreement between model and measurement, with only slight variations in the first side lobe levels. These could be improved with minor modifications to the model.

Similarly, the measurements in the y-direction were in agreement with modelled data. There appears to be a minor tilt between the probe and AUT, indicated by the left side of the experimentally measured main beam being below the modelled data and the right side of the main beam being slightly above the modelled data. A further sign

of this small tilt can be seen in the first side lobes. The right experimental side lobe is slightly higher then the left side. This asymmetry indicates a small tilt angle. As in the far field case, if the purpose of these measurements was to measure the AUT as accurately as possible, FEKO modeling should include this tilt angle. However, this is not the case, and the results are sufficient enough to show that the scanning system is functioning properly. The maximum difference in the y-direction was -12.6 dB and the averaged difference was -34.1 dB.

To confirm that the near field measurements at 76 mm were correct, the AUT was measured again but this time at a separation distance of 42 mm. The results of these measurements are shown in Figures 5.23a and 5.23b. While the measured data in Fig. 5.22 began to deviate from the model at a intensity level of approximately -25 dB, the data in Fig. 5.23 only begins to deviate at an intensity level of approximately -35 dB. It is clear from these two measurements that near field corrections are not necessary unless accurate measurements below approximately -30 dB are required at high off axis angles. Because the SPP measurements to be conducted in this thesis are phenomenological and qualitative features of the transmitted beams, the excellent measurement accuracy achieved without near field corrections is deemed to be acceptable.

5.6.3 Dielectric Lens Measurements

To fully demonstrate the capabilities of the field scanner, a dielectric lens made from Ultra High Molecular Weight polyethylene was measured at 97 GHz. This lens was designed, manufactured and initially tested using a separate system by Fahri Ozturk [81]. The lens has a focal length of 208.5 mm, a radius of curvature of 112 mm and an index of refraction of $n = 1.517$. Each data point is comprised of ten frequency points. For these tests the lens was placed 208.5 mm from the phase centre of the feed antenna, which was the same horn used in the system characterisation tests.[5] Phase and intensity

[5]The phase centre of the horn antenna may be found by adjusting the relative position between the horn and rotation stage and measuring the far field phase pattern of the horn antenna. The correct positioning is achieved when the phase across the main beam is flat.

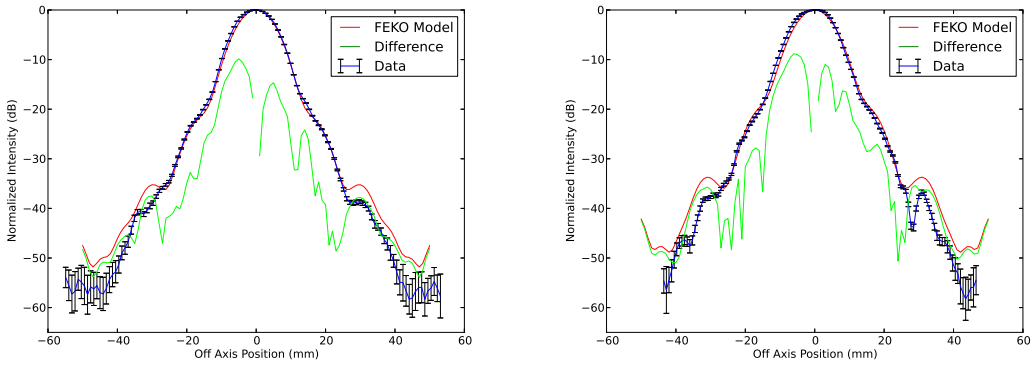

(a) Near Field X-Cut: Separation Distance 42 mm

(b) Near Field Y-Cut: Separation Distance 42 mm

Figure 5.23: X- and Y- Cuts of the AUT at a separation distance of 42 mm. Measurement data follows the model until the first primary sidelobes. This difference is expected to be produced by small differences between the modelled AUT and the actual AUT used.

data was taken for the XZ and XY planes.

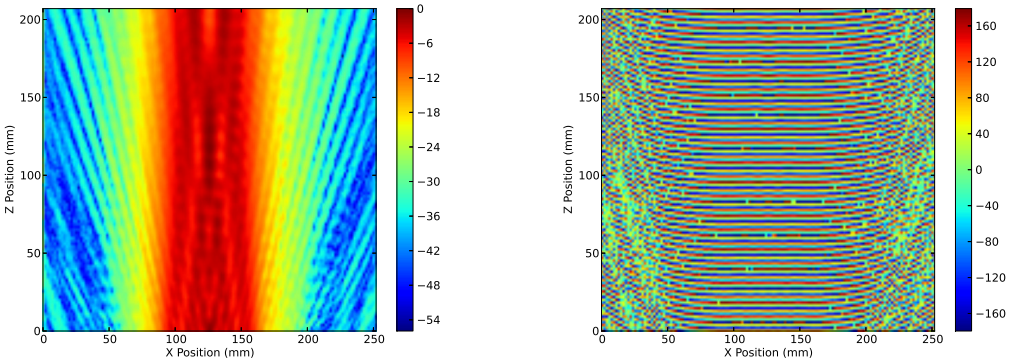

(a) Lens XZ Plane Intensity (dB)

(b) Lens XZ Plane Phase (Deg.)

Figure 5.24: Intensity and phase measurements from the dielectric lens along the XZ plane. The new beam waist is clearly visible while the phase front are flat.

Figure 5.24a shows the measured intensity values in the XZ plane. The scan started 103.75 mm from the lens' front surface and continued in the z-direction for 207.5 mm. The field was measured to 126 mm on either side of the centre of the beam propagation

axis. A resolution of 1.8 mm in the x- and z-directions was used. The scanned region reveals the new beam waist generated by the lens, visible as a high intensity region between $z = 100$ mm and $z = 130$ mm. Planar phase fronts expected from a beam emanating from a lens are visible in Fig. 5.24b.

To validate these measurements the lens beam pattern was also measured in the XY plane. Intensity measurement are displayed in Fig. 5.25a. The data in Fig. 5.25a and phase data in Fig. 5.25b were taken at a distance of 208.15 mm from the front surface of the lens, with an X and Y scan extent of 252 mm and a resolution of 1.8 mm.

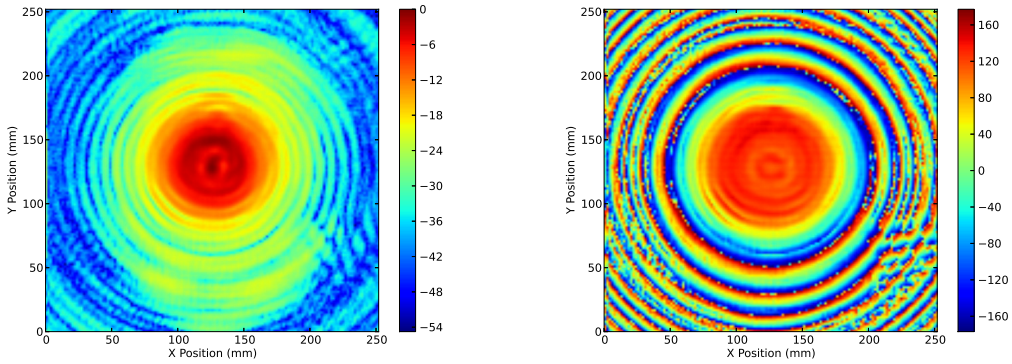

(a) Lens XY Plane Intensity (dB) *(b) Lens XY Plane Phase (Deg.)*

Figure 5.25: Intensity and phase measurements of the dielectric lens along the XY plane.

The flat phase front is visible in Fig. 5.25b. Interestingly, there are visible phase distortions that start approximately 54 mm from the centre of the lensed beam. These distortions propagate out to further radial distances. This is most likely a result of diffraction from the lens mount used, which had an inner radii of 55.6 mm and an outer radii of 65.5 mm.

A single cut form the XY intensity data was taken and compared to FEKO modelling (Fig. 5.26a). The data matches the model well across the centre portion of the beam with a maximum difference between the two of −7.9 dB. Yet, there is a clear disagreement between the model and the data at large off axis positions. This was found to be a result

of poor modelling. In the initial model the lens was surrounded by a lens mount that was smaller than what was actually used in the experimental measurements.

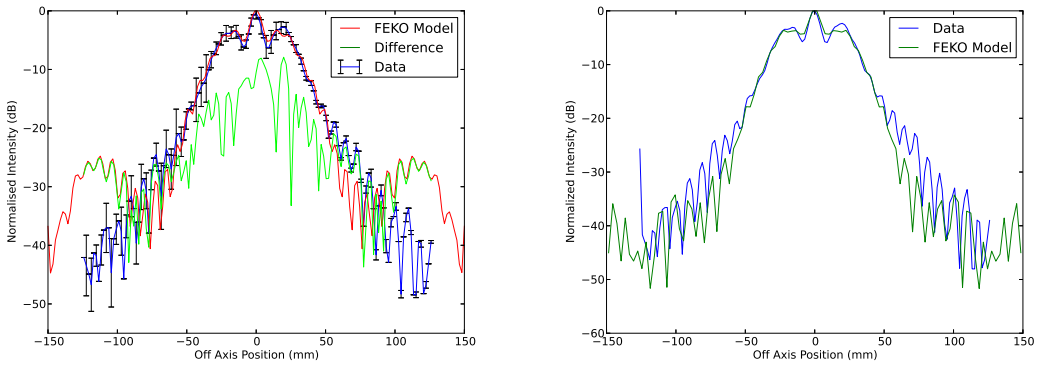

(a) Lens XY Plane Cut *(b) Lens XY Plane Cut*

Figure 5.26: The initial lens model produced large side lobes from a poor lens mount design (Fig. 5.26a). Measurements of the lens showed that the model was incorrect, the problem was fixed, and the new model was compared to the data (Fig. 5.26b).

Once this was realised, the model was adjusted to accommodate a larger lens mount. The amended results are shown in Fig. 5.26b, which shows the improved side lobe response.

To validate these measurements by a method different from FEKO modelling, the new beam waist was measured and compared to Gaussian optics predictions. Figure 5.27 shows the central cut, in the z-direction, from Fig. 5.24a. The maximum intensity value was found to have a Z-Axis scan position of 117.0 mm, which corresponded to a beam waist location of 214.75 mm, from the front lens surface, after correcting for the half thickness of the lens. Gaussian beam optics predicted that the new beam waist would be 215.0 mm from the front surface of the lens.

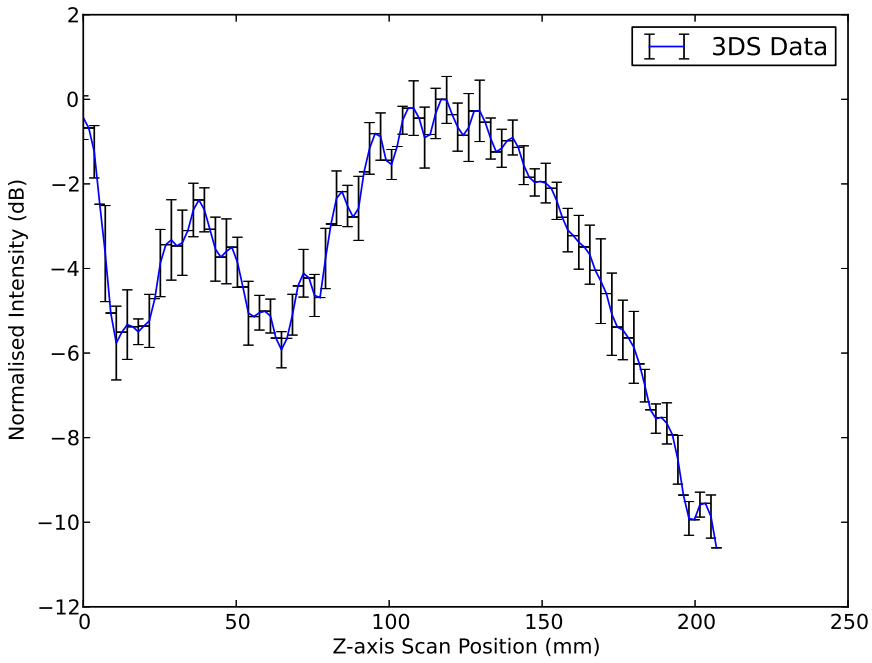

Figure 5.27: A central cut along the XZ plane, used to determine the new beam waist location.

5.7 Conclusion

These measurements, indicate that the three dimensional field scanner is functioning properly and is capable of taking highly accurate data, which can be compared to modelled data in a straightforward manner. The corrugated horn tests showed that an antenna in the far field must have a geometrical correction applied to the measured data. Comparison to near field data did not require probe corrections, however. Scans in the x- and y-direction produced similar quality results, indicating that although the scanner had two different mechanical rails, each functioned in the expected manner. Finally, the dielectric lens measurements proved that the system could measure a well known and practical DUT, accurately. For these reasons, the characterisation of the field scanner was determined to be a success, allowing the system to be used for measurement of beams with orbital angular momentum.

6

Measurements and Analysis

6.1 Introduction

Measurements of $\Delta l = \pm 1$ and $\Delta l = \pm 2$ standard and split configuration SPPs, illuminated by both the collimated beam generated by the CTRA and divergent beam generated by the same corrugated feed antenna used in Chapter 5, are presented in this chapter. Again, these three SPP configurations were chosen to firstly compare LG beams with azimuthal mode numbers of one and two and secondly to compare standard and split configuration designs. Initial proof of concept measurements of the $\Delta l = \pm 1$ SPP, illuminated by the corrugated feed antenna beam are presented in Sec. 6.3. These measurements were published in [27] (See supporting publications) and were completed using a different experimental set up than the measurements in Sec. 6.5 - 6.7. Although not shown here, all of the following measurements were highly repeatable. Both optical paths could be dismantled and reassembled without negatively affecting the measured patterns.

Table 6.1: SPP Specifications (All measurements in mm)

Configuration	SPP	Substrate Height	Total Height	Primary Step Height	Number of Steps
Standard	$\Delta l = 1$	2.17	8.11	5.94	16
Standard	$\Delta l = 2$	1.97	14.04	12.07	32
Split	$\Delta l = 2$	2.17	7.99	5.82	32

6.2 Spiral Phase Plate Design Specifications

Specifications for each measured SPP (Fig. 6.1) are listed in Table 6.1. A review of that data will show that the manufactured SPPs are not exactly matched to the design specifications. Primary step heights for each SPP should be 6 mm (12 mm for the standard $\Delta l = 2$), but actual measured primary step heights are slightly above and below this value. This is to be expected, due to the machining processes employed. The split configuration $\Delta l = \pm 2$ SPP has the largest deviation, 3% , between actual and specified step height. The diameter of each plate was 100 mm.

(a) Standard Configuration $\Delta l = \pm 1$ SPP.

(b) Split Configuration $\Delta l = \pm 2$ SPP.

(c) Standard Configuration $\Delta l = \pm 2$ SPP.

Figure 6.1: The actual SPPs used for these measurements. Note how the standard configuration $\Delta l = \pm 2$ SPP's primary step height is twice that of the $\Delta l = \pm 1$. Also note that both $\Delta l = \pm 2$ SPPs have the same number of steps per mode as the $\Delta l = \pm 1$ SPP.

6.3 Proof of Concept Measurements of a Mode One Spiral Phase Plate

In order to test the measurement system, methodology and SPP construction, the sixteen stepped polypropylene $\Delta l = \pm 1$ SPP was illuminated by a corrugated feed horn antenna and measured with the three dimensional field scanner. Measurements were conducted at 100 GHz and the horn to SPP separation distance was 66.7λ. The scanner was

placed 44.4λ behind the SPP, and scanned a volume of $88.80\lambda \times 91.60\lambda \times 1.20\lambda$ with a positioning resolution of 3.60 mm (1.20λ), 3.72 mm (1.24λ) and 0.45 mm (0.15λ) respectively. A large XY scan area was used to capture the full extent of the transmitted beam. Shifting the scan surface in the z-direction allows for a direct measurement in the shift in azimuthal position of the BC.

Two XY surfaces (the second surface, 44.7λ behind the SPP, and fifth surface, 45.15λ behind the SPP.) are presented in Fig. 6.2 for analysis. Separate surfaces were picked to show the change in position of the BC. Figures 6.2a and 6.2b show the normalised intensity and uncorrected phase on the second measurement surface. A central null in intensity is visible, producing an annular beam pattern. A spiralling BC is present in phase, and terminates with a forked BP. Figures 6.2c and 6.2d show the central section of the fifth measurement surface. Two white circles mark the locations of two prevalent intensity minima. The higher intensity minima is clearly associated with the BP located at the end of the spiralling BC. However, the second intensity minima is not clearly caused by a BP. This could be a result of too large of a distance between measurement points in the x- and y-directions. BPs are mathematical points and require a very high spatial resolution in order to isolate their true position. If a large separation distance between measurement points is used, the actual location of a BP will not be measured.

These proof of concept measurements have shown that the measurement system, methodology and SPP construction have all performed as expected. The following sections detail full measurement and analysis of a sixteen steps per mode $\Delta l = \pm 1$, a sixteen steps per mode single step configuration $\Delta l \pm 2$ SPP and a sixteen steps per mode split configuration $\Delta l = \pm 2$ SPP.

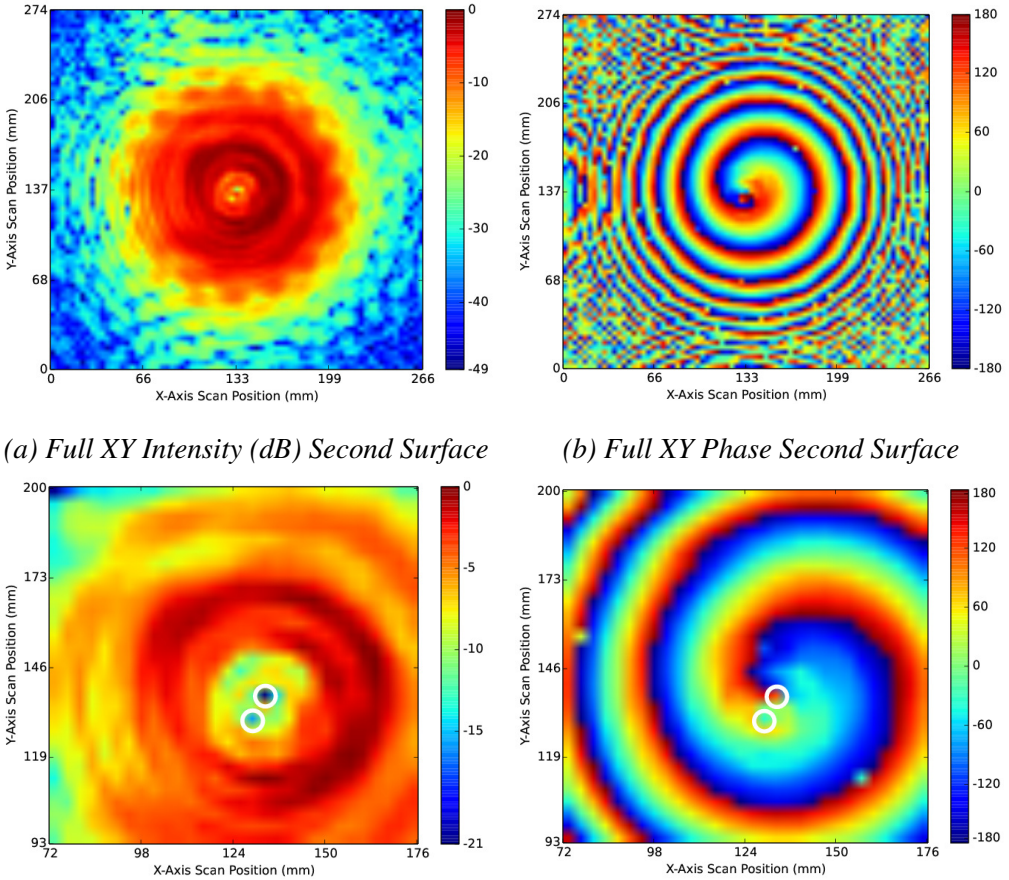

(a) Full XY Intensity (dB) Second Surface

(b) Full XY Phase Second Surface

(c) Central XY Intensity (dB) Fifth Surface

(d) Central XY Phase Fifth Surface

Figure 6.2: Proof of concept intensity and phase measurements of the $\Delta l = \pm 1$ sixteen stepped SPP. Figures 6.2a and 6.2b show the respective full intensity and phase measurements on the second measurement surface. Note the annular intensity pattern and the twisted BC. Figures 6.2c and 6.2d show the central portion of the intensity and phase measurements on the fifth surface. The white circles correspond to the positions of the two intensity minima.

6.4 Backgrounds

Two independent source beams were used to test the three separate SPPs. First, a Gaussian beam with a quasi-planar phase front was generated by a compact test range antenna (CTRA Fig. 6.3). Analysis of the generated beam at the SPP mount (Fig. 6.3b)

shows that the averaged edge taper was −4.77 dB.

Then, a compact corrugated feed horn antenna with a highly divergent beam was used (Fig. 6.4). In both cases, the SPP under test was placed inside a custom designed mount (Fig. 6.5), which was attached to a three axis positioning stage. Recall from Chapter 4 that the edge taper of this system was −40 dB. The far field beam pattern of this antenna can be seen in Chapter 5.

Absorbing material was placed around the mount and positioning stage to isolate the incident beam and the scanning system. All measurements were taken at 100 GHz. Each SPP was measured on planes perpendicular to the propagation axis. Each plane was $33.3\lambda \times 33.3\lambda$ in the x- and y-directions. Three surfaces were measured at 4.7λ, 40λ and 73.3λ behind the mount. These correspond to the modelling surfaces used in Chapter 4. A probe positioning resolution of 0.17λ was used in both x- and y-directions. Before each SPP was measured, the field generated by the illuminated SPP mount was measured at each measurement surface. These backgrounds were then used to normalise the measured phase pattern so that,

$$arg\left(E_{transmitted}\right) = arctan\left[Imag\left(\frac{E_{measured}}{E_{background}}\right), Real\left(\frac{E_{measured}}{E_{background}}\right)\right] \tag{6.1}$$

where $E_{measured}$ and $E_{background}$ are the full complex fields. Note that intensity plots are normalised so that the maximum intensity of the field is either 0.0 dB or 1.0 V/m in linear scaling.

CTRA Incident Source

Measured intensity and phase on each background surface, generated by the CTRA incident beam, are shown in Fig. 6.7. No systematic phase error is visible along the X-Axis, indicating that the CTRA is well aligned in the x-direction. However, there is a phase variation along the Y-Axis, due to a minor misalignment of one of the CTRA reflectors. This may be calculated by determining the phase shift across the beam (Fig. 6.6). Observing Fig. 6.7b, the phase at $y = 20$ mm is approximately −80° and −20° at

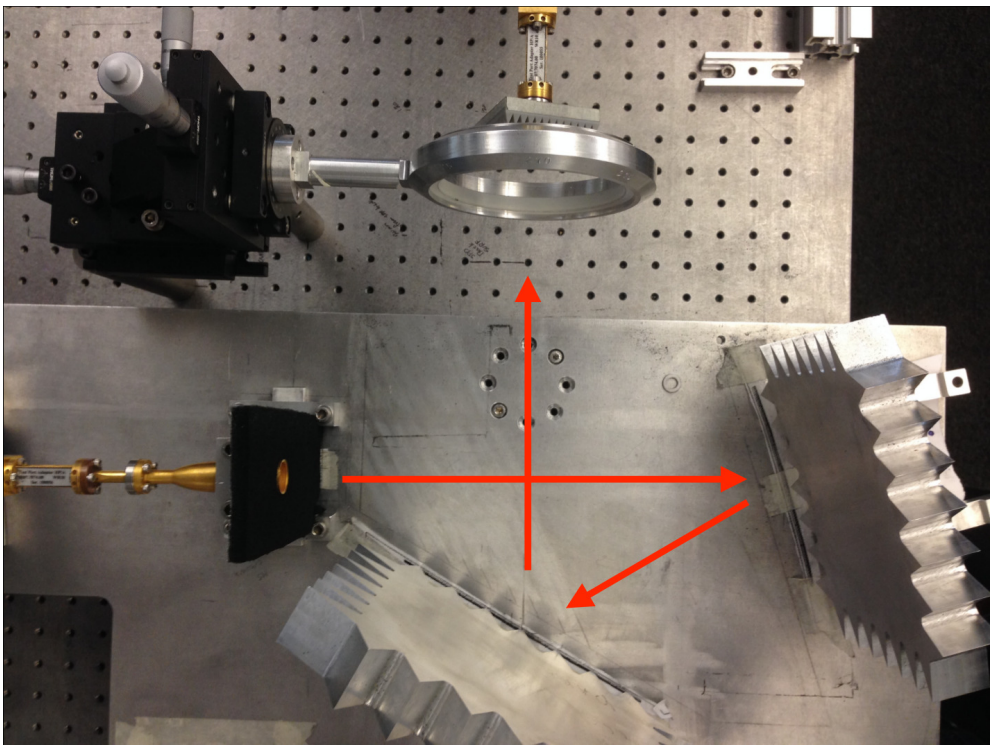

(a) Incident beam optical path.

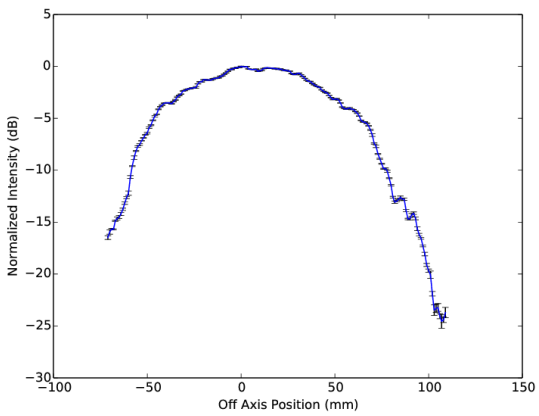

(b) Incident Intensity (dB)

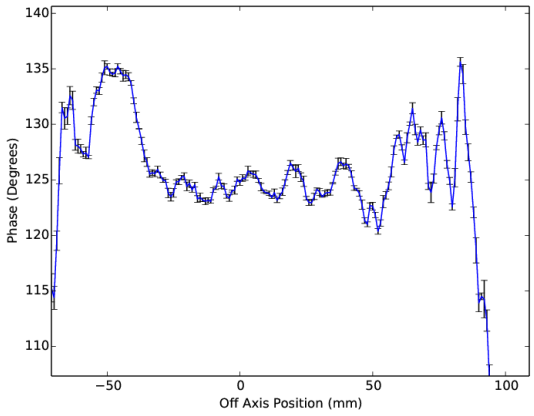

(c) Incident Phase (Degrees)

Figure 6.3: A Gaussian beam is generated by the feed horn and is reflected by both CTRA mirrors. The beam then propagates to the SPP mount and is measured by the WR-10 probe (Fig. 6.3a). The measured incident Gaussian beam created by the CTRA source with vertical error bars denoting one standard deviation of the five measurement sweeps (Fig. 6.3b). Measured near planar phase front at the beam waist created by the CTRA source with vertical error bars denoting one standard deviation of the five measurement sweeps (Fig. 6.3c). Adapted from [28].

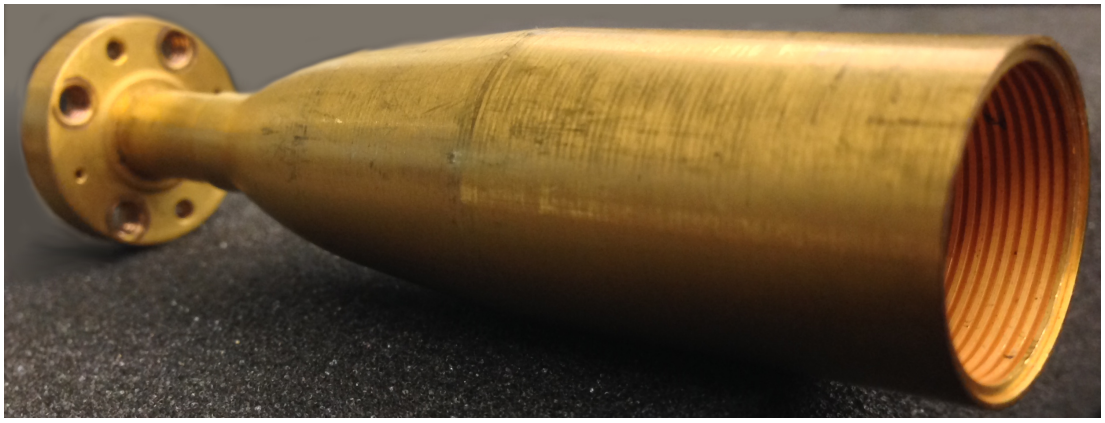

Figure 6.4: Corrugated feed antenna used to generate divergent Gaussian beams.

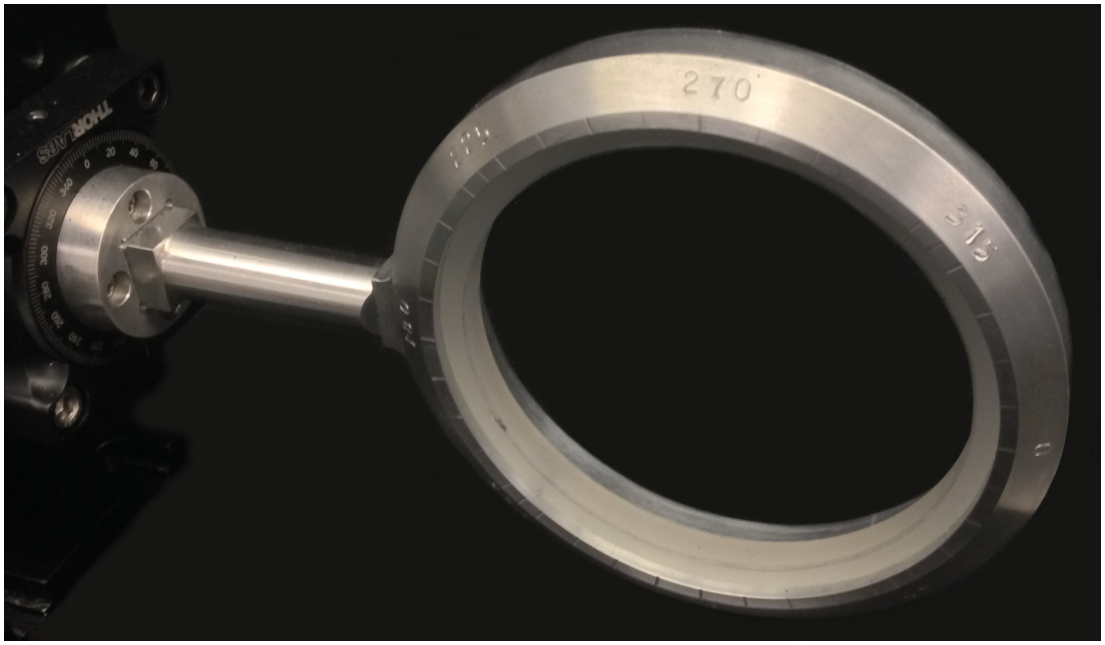

Figure 6.5: The SPP mount connected to the three axis positioning stage. A rotary stage connected to the positioning stage allows the SPP mount to be aligned perfectly vertical in relation to the propagating beam. An angular scale is visible around the outer edge of the SPP, and is used for plate positioning.

$y = 100\,\text{mm}$. Therefore there is a 60° phase shift across a vertical distance of 80 mm. Using,

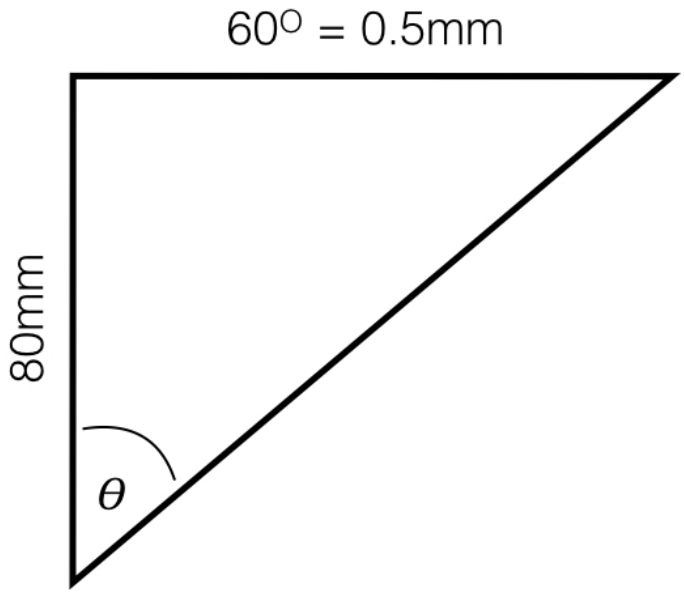

Figure 6.6: Geometry used to calculate CTRA reflector offset. Across a vertical distance of 80 *mm a phase shift of* 60° *is generated. This can be used to measure the offset angle* θ.

$$\phi = kd \tag{6.2}$$

where $\phi = 60°$ it is found that the phase shift implies a distance offset, d, of 0.5 mm. Taking the arctangent of these two distances yields the vertical angle misalignment of the reflectors.

$$\theta = tan^{-1}\left(\frac{0.5}{80}\right) = 0.385° \tag{6.3}$$

Measured background intensity on the 4.7λ surface contains rippling due to diffraction from the circular aperture. Propagation to the 40λ surface shows that a radial mode number $\rho = 3$ is present. These rings are again, due to diffraction from the circular aperture. Finally, as the beam propagates towards the far field, the intensity pattern

begins to smooth and reorganise. On the 73.3λ surface there are just two prominent annular rings. The corresponding phase at each surface is a combination of the vertical phase variation along the Y-Axis and the radial mode content of the beam. Phase on the 40λ surface clearly shows three radial nodes, while radial nodes on the 73.3λ surface are far less pronounced. Some of these aberrations and asymmetries could, in theory, be better understood by modelling the entire optical system in FEKO. However, in practice this is very difficult due to memory and CPU requirements.

Corrugated Feed Antenna Incident Source

Background intensity and phase measurements were also made for the corrugated feed horn antenna (Fig. 6.8). Because the antenna illuminated the edge of the SPP mount with the first beam pattern nulls, very few diffraction effects are visible. Intensity and phase on the 4.7λ surface show a highly symmetric Gaussian beam with a spherical and smooth phase front. Some distortions in intensity and phase are visible on the 40λ surface. A slight asymmetry in the intensity pattern is visible and is most likely due to a small misalignment between the plane perpendicular to the beam's propagation axis and the measurement surface. Additionally, there are distortions to the smooth phase front near the beam centre. These phase variations are largely removed on the 73.3λ surface. However, the minor asymmetry in intensity remains.

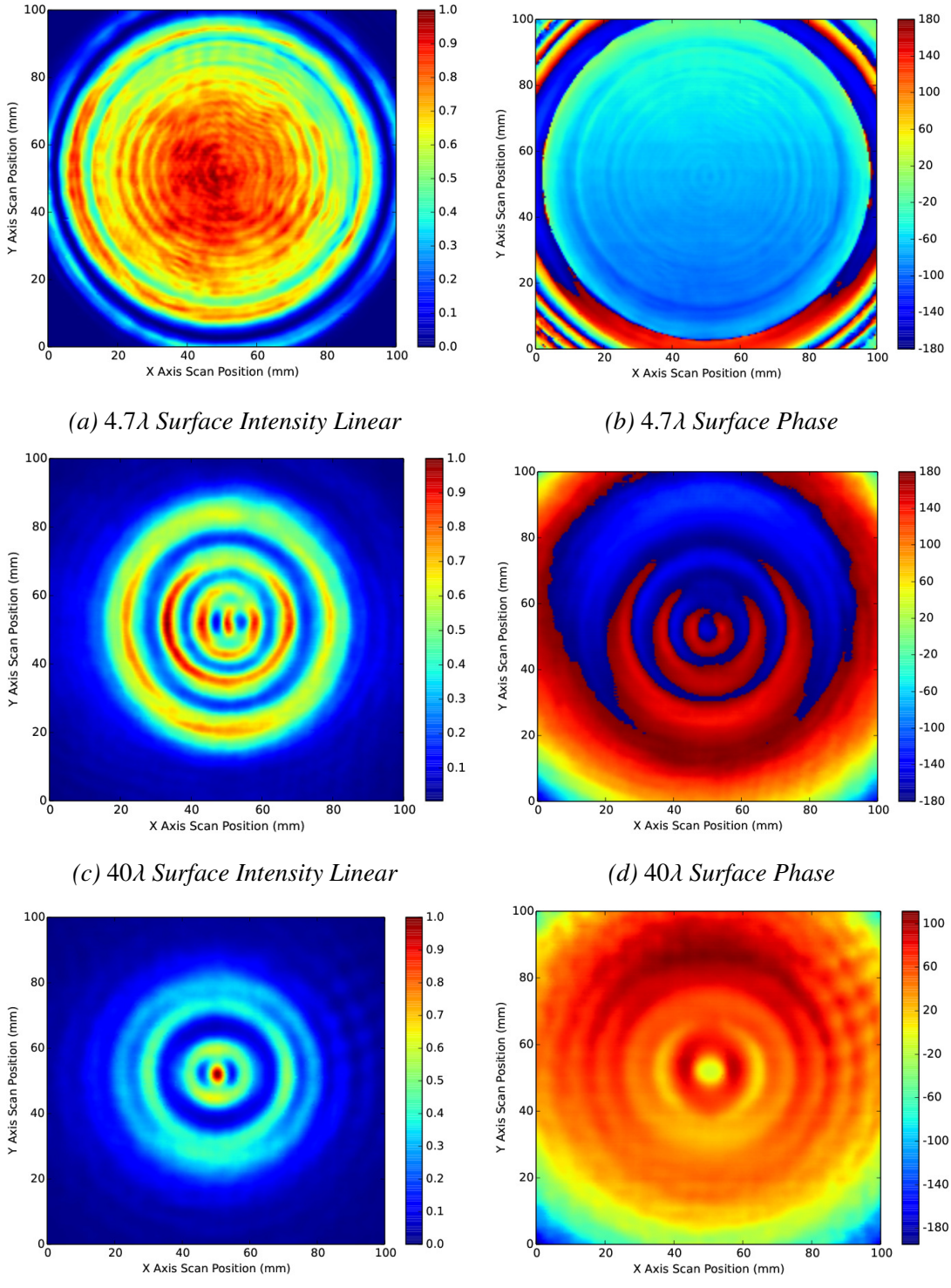

(a) 4.7λ Surface Intensity Linear

(b) 4.7λ Surface Phase

(c) 40λ Surface Intensity Linear

(d) 40λ Surface Phase

(e) 73.3λ Surface Intensity Linear

(f) 73.3λ Surface Phase

Figure 6.7: CTRA background intensity and phase measurements

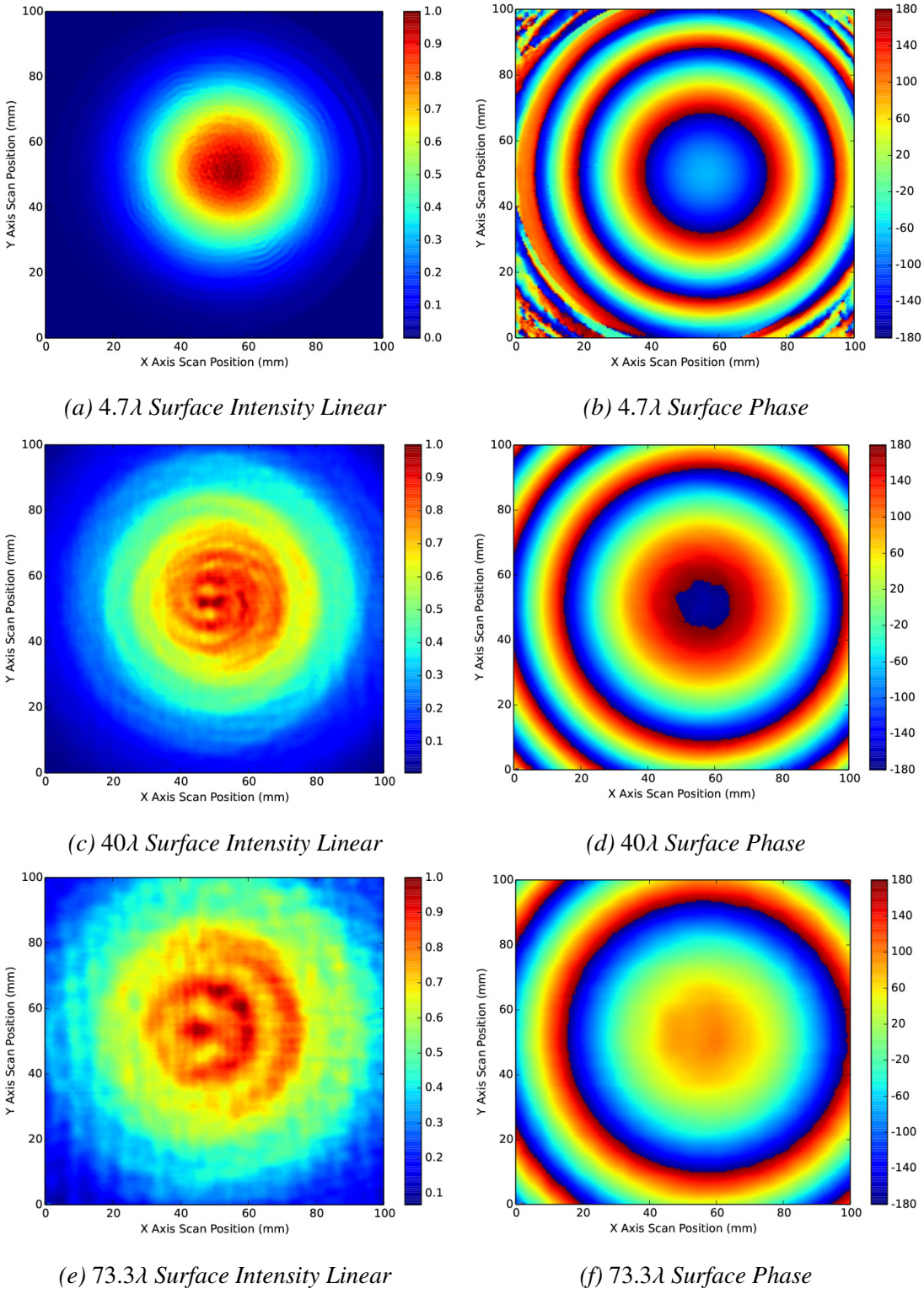

(a) 4.7λ Surface Intensity Linear

(b) 4.7λ Surface Phase

(c) 40λ Surface Intensity Linear

(d) 40λ Surface Phase

(e) 73.3λ Surface Intensity Linear

(f) 73.3λ Surface Phase

Figure 6.8: Corrugated feed horn antenna background intensity and phase measurements

6.5 Mode One Spiral Phase Plate

Normalised intensity and phase measurements generated by the polypropylene sixteen steps-per-mode $\Delta l = \pm 1$ SPP illuminated by both the CTRA and corrugated feed antenna are presented in this section.

CTRA Incident Source

A central intensity null and a single BC are clearly evident in all respective normalised intensity and phase measurements generated by the CTRA source (Fig. 6.9). Intensity measurements of the 4.7λ surface are largely dominated by dielectric transmission. This is evident from the azimuthally modulated intensity [133–135]. The primary step is clearly visible on the left side of the pattern. A discontinuity along the primary step is visible. This low intensity region is due to the boundary condition induced by the primary step. The discontinuous jump between air and polypropylene causes the field outside the step to travel faster the the field inside the SPP. This rips the field apart, at the boundary, and produces a region of very low intensity. In phase, a single BC is seen propagating away from the central BP. An annular intensity pattern forms as the beam propagates to the 40λ surface. Here, the central intensity null is surrounded by two intensity rings. Interestingly, a region of very low relative intensity, in the shape of a ribbon, is visible near the propagation axis. Phase measurements show that this unusual pattern is due to the presence of an additional BP pair. Finally, measured intensity on the 73.3λ has reorganised into a single annular intensity ring. The additional BP pair causing the strange ribbon shaped intensity null have disappeared, as the near field organises into the far field pattern.

Corrugated Feed Antenna Incident Source

Figure 6.10 presents normalised intensity and phase measurements of the $\Delta l = \pm 1$ SPP illuminated by the corrugated feed horn antenna. Just as was the case with the CTRA transmitted beam, the phase generated on the 4.7λ surface contains one BP and

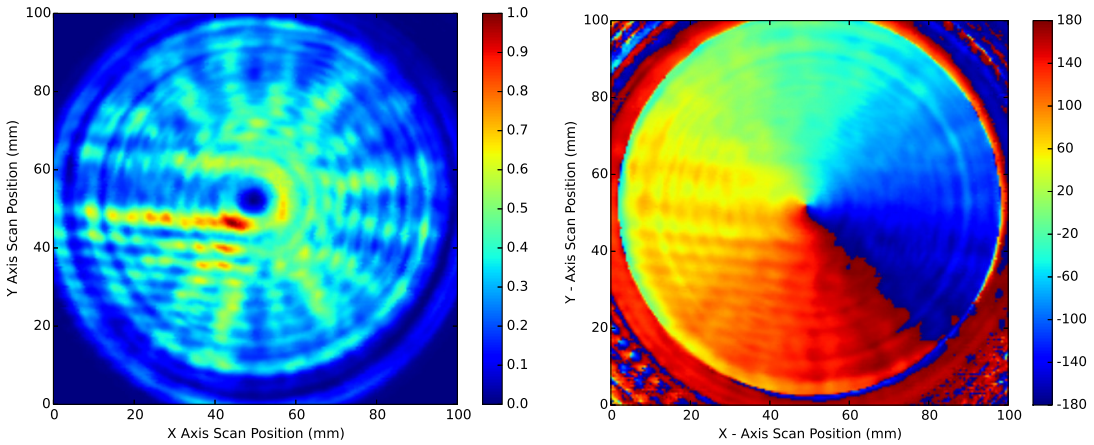

(a) Normalised Intensity 4.7λ *Surface* *(b) Normalised Phase* 4.7λ *Surface*

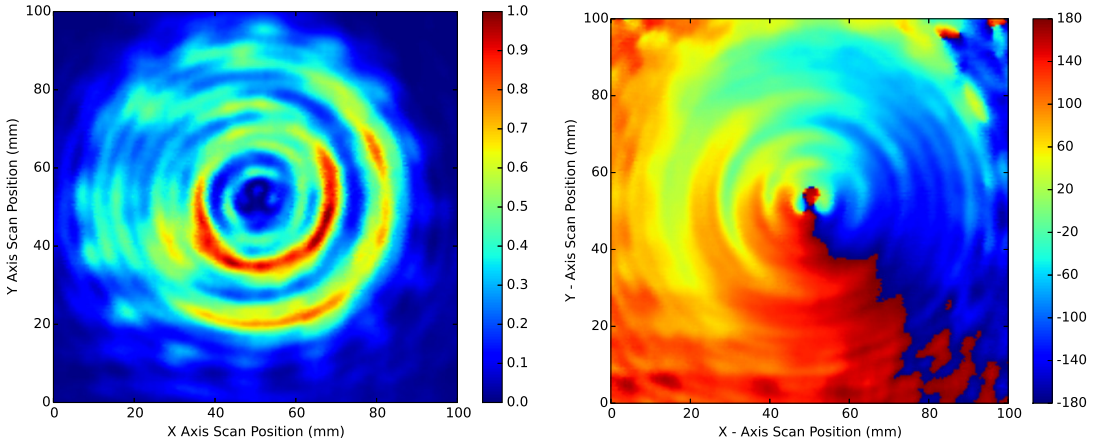

(c) Normalised Intensity 40λ *Surface* *(d) Normalised Phase* 40λ *Surface*

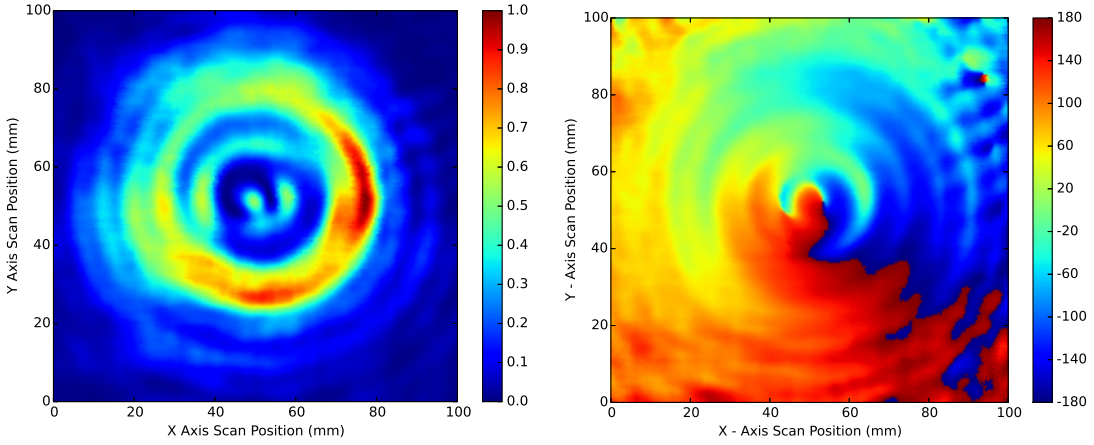

(e) Normalised Intensity 73.3λ *Surface* *(f) Normalised Phase* 73.3λ *Surface*

Figure 6.9: Normalised intensity and phase measurements on the 4.7λ, 40λ *and* 73.3λ *surfaces generated by a quasi-planar beam incident on the* $\Delta l = \pm 1$ *SPP.*

a BC. Normalised intensity measurements show a similar pattern to that created by the CTRA, however the beam pattern is modulated by the incident Gaussian pattern (Fig. 6.8a). Dielectric transmission and the primary step discontinuity dominate the beam pattern features. However, unlike the CTRA transmitted beam, the corrugated feed antenna produces a single annular intensity ring on the 40λ surface. This is due to the reduction in SPP mount diffraction. In addition, the additional BP pairs generated by the CTRA are not seen in this phase pattern (Fig. 6.10d). Additionally, few radial nodes are present, causing only minor radial variations in the BC. With further propagation to the 73.3λ surface,a small asymmetry is visible in the intensity pattern, however the beam shape remains largely unchanged compared to the 40λ surface. A single BP remains near the centre of the propagation axis, and the corresponding BC spirals around the beam centre as it proceeds towards the outer extent of the measurement surface.

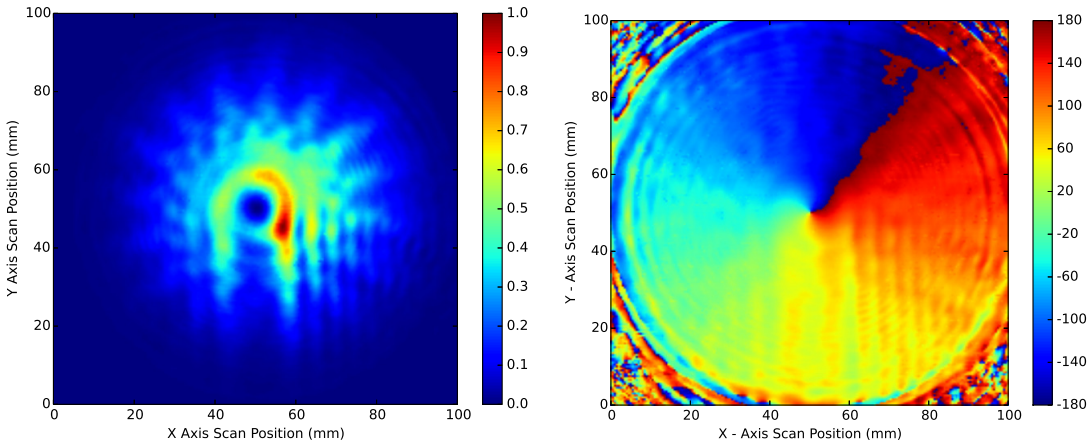

(a) Normalised Intensity 4.7λ *Surface* *(b) Normalised Phase* 4.7λ *Surface*

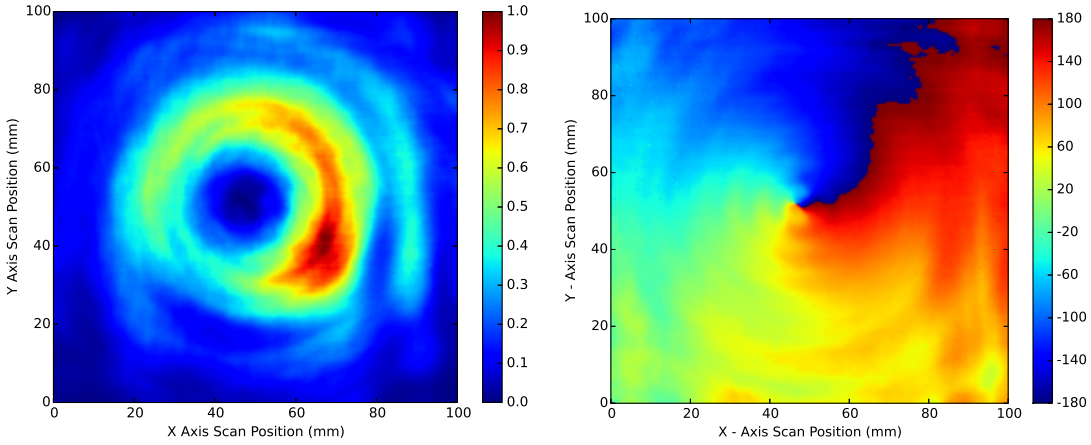

(c) Normalised Intensity 40λ *Surface* *(d) Normalised Phase* 40λ *Surface*

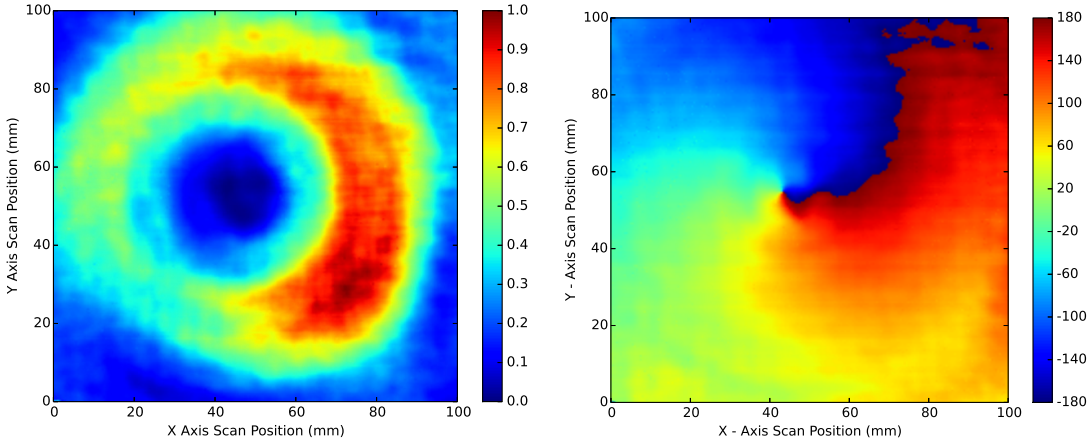

(e) Normalised Intensity 73.3λ *Surface* *(f) Normalised Phase* 73.3λ *Surface*

Figure 6.10: Normalised intensity and phase measurements on the 4.7λ, 40λ *and* 73.3λ *surfaces generated by a beam from a corrugated feed horn incident on the* $\Delta l = \pm 1$ *SPP.*

6.6 Mode Two Single Step Spiral Phase Plate

Normalised intensity and phase measurements generated by the polypropylene sixteen steps-per-mode, single step configuration, $\Delta l = \pm 2$ SPP illuminated by both the CTRA and corrugated feed antenna are presented in this section.

CTRA Incident Source

Figure 6.11 presents the normalised intensity and phase measurements generated by the CTRA incident beam. Like the previous case, intensity on the 4.7λ surface is a combination of dielectric transmission, the primary step discontinuity and central intensity null. There are two BPs and two corresponding BCs indicating that a $l = \pm 2$ beam was generated, as expected. However, unlike analytically pure beams, the BPs are separated by a finite distance. Propagation to the 40λ surface produces two annular intensity rings. A large region of relatively low intensity is present around the propagation axis. The beam pattern is symmetrical along the line $\phi = \pm 45°$. Normalised phase measurements show the creation of an additional six BPs and three BCs in conjunction to the primary two BCs. Further propagation to the 73.3λ surface shows a consolidation of the previous two annular intensity rings into one primary ring. Furthermore, the additional BCs seen in the 40λ surface have been removed by propagation to the 73.3λ.

Corrugated Feed Antenna Incident Source

Normalised intensity and phase measurements generated by the corrugated feed antenna beam incident on the $\Delta l = \pm 2$ SPP are presented in Fig. 6.12. On the 4.7λ surface, the intensity pattern is largely modulated by the incident beam pattern and primary step discontinuity. Phase on the surface shows two primary BCs with a large amount of radial modes causing rippling variations in the BC line. Propagation to the 40λ surface shows the annular intensity ring and large central intensity null. A small intensity peak, originally caused by the primary step discontinuity, is still present. Unlike the 40λ

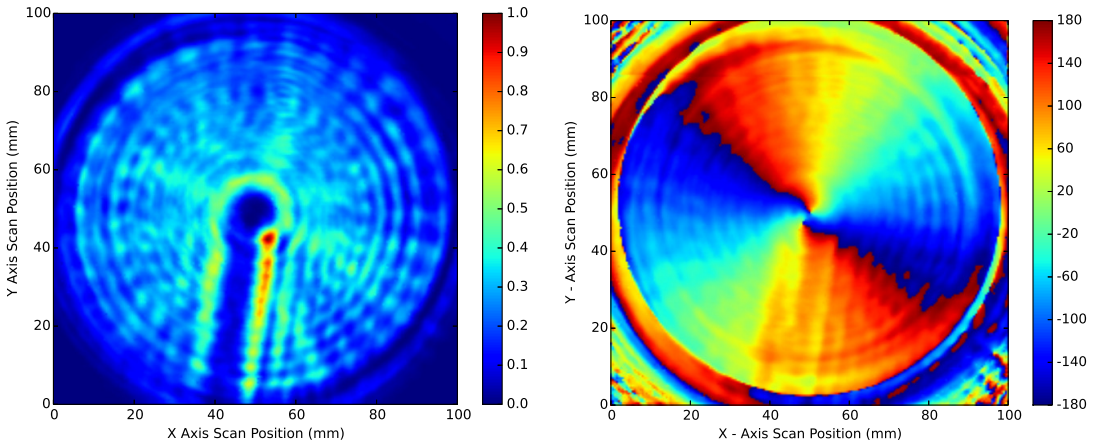

(a) Normalised Intensity 4.7λ *Surface* *(b) Normalised Phase* 4.7λ *Surface*

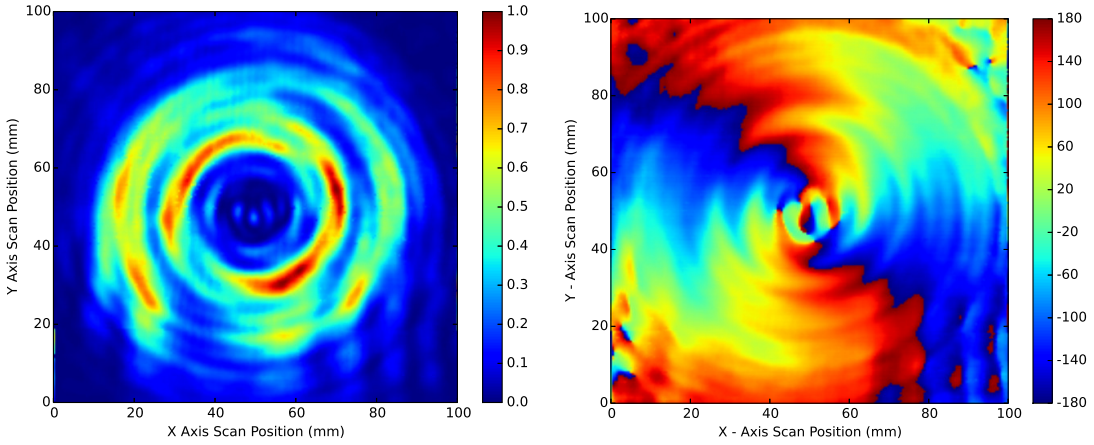

(c) Normalised Intensity 40λ *Surface* *(d) Normalised Phase* 40λ *Surface*

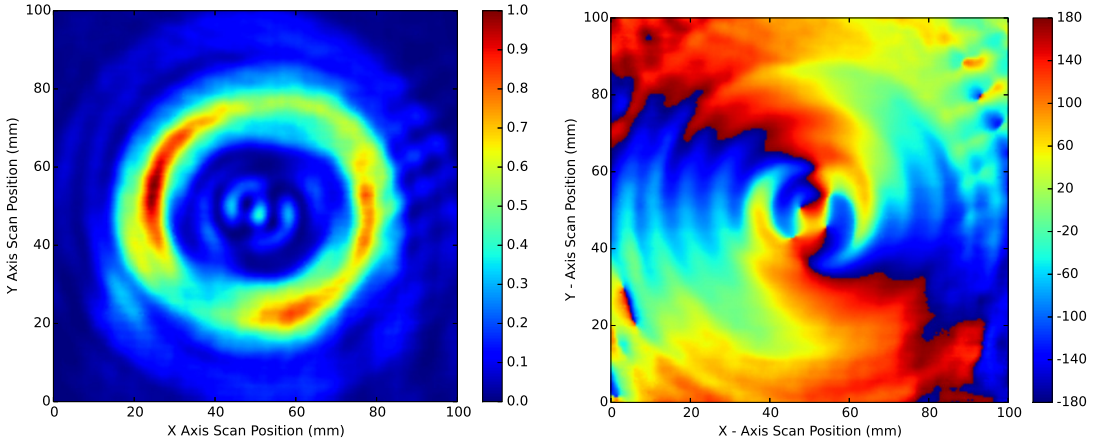

(e) Normalised Intensity 73.3λ *Surface* *(f) Normalised Phase* 73.3λ *Surface*

Figure 6.11: Normalised intensity and phase measurements on the 4.7λ, 40λ *and* 73.3λ *surfaces generated by a quasi-planar beam incident on the* $\Delta l = \pm 2$ *SPP.*

phase surface for the $\Delta l = \pm 1$ SPP (Fig. 6.10d), the $\Delta l = \pm 2$ SPP phase pattern contains one additional BC and associated pair of BPs. As the beam propagates to the 73.3λ surface a second additional BC and BP pair are generated. Unlike the CTRA generated beams, the large divergence of the corrugated feed antenna's incident beam does not allow the additional BPS to interact and annihilate. Spreading of the transmitted beam forces the additional BPs to remain in the measured phase pattern. Intensity on the 73.3λ surface is similar in features as the intensity on the 40λ surface. For example, the intensity peak and dip on the lower half of the pattern remain unchanged. However, as the beam propagates, the divergence of the beam spreads the annular ring pattern to the larger extents of the measurement surface.

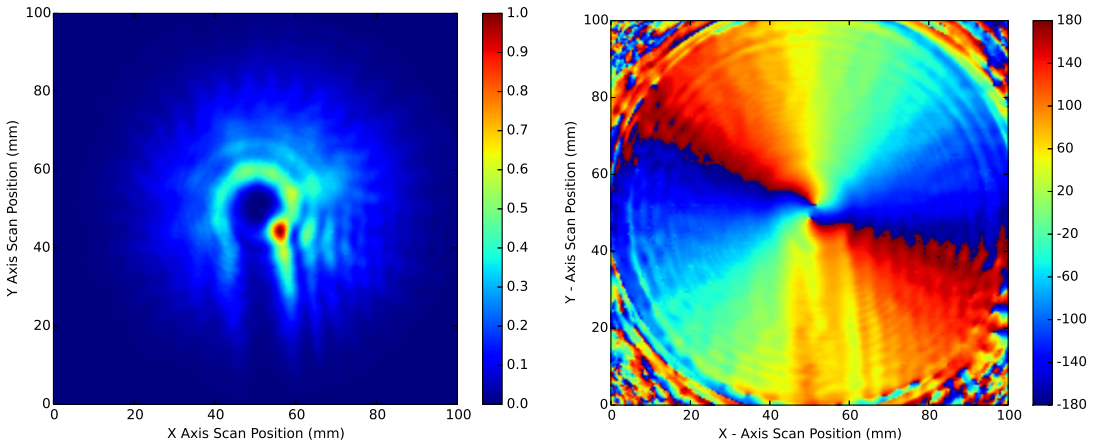

(a) Normalised Intensity 4.7λ *Surface* *(b) Normalised Phase* 4.7λ *Surface*

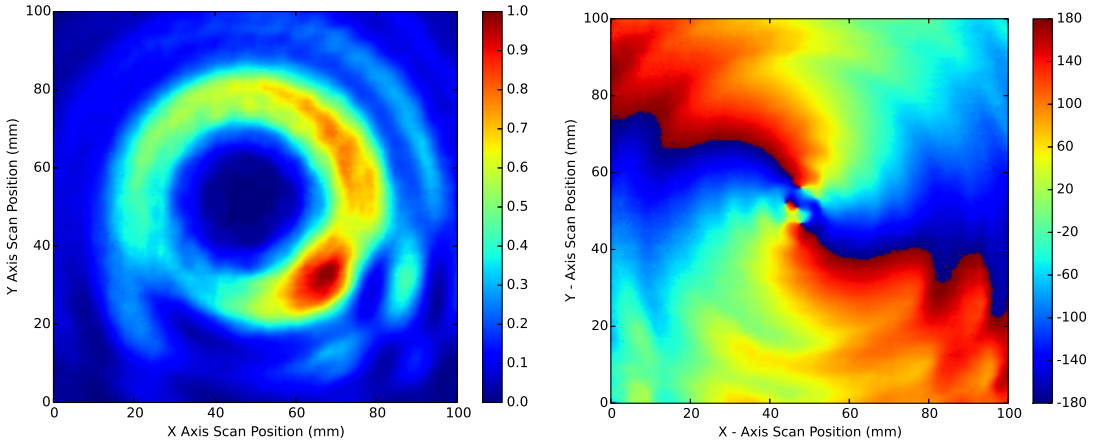

(c) Normalised Intensity 40λ *Surface* *(d) Normalised Phase* 40λ *Surface*

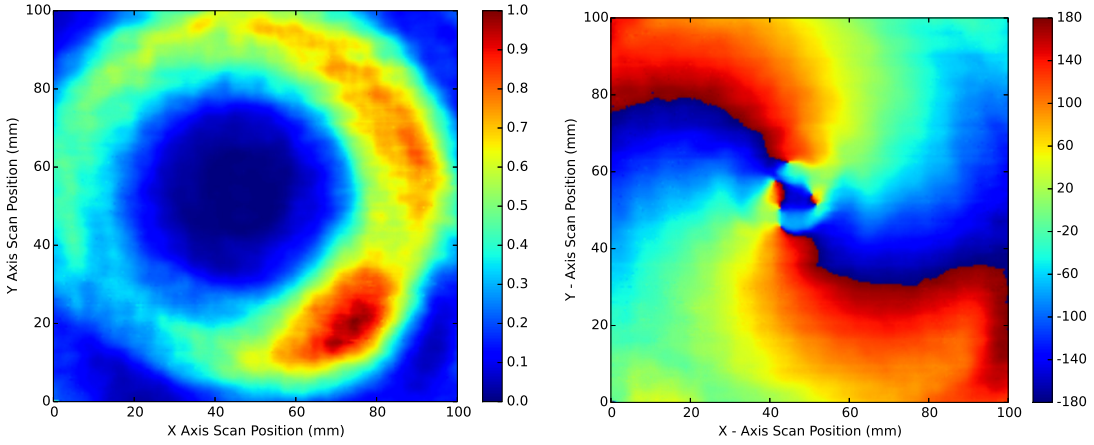

(e) Normalised Intensity 73.3λ *Surface* *(f) Normalised Phase* 73.3λ *Surface*

Figure 6.12: Normalised intensity and phase measurements on the 4.7λ, 40λ *and* 73.3λ *surfaces generated by a beam from a corrugated feed horn incident on the* $\Delta l = \pm 2$ *SPP.*

6.7 Mode Two Split Step Spiral Phase Plate

Normalised intensity and phase measurements generated by the polypropylene sixteen steps-per-mode, split step configuration, $\Delta l = \pm 2$ SPP illuminated by both the CTRA and corrugated feed antenna are presented in this section.

CTRA Incident Source

Normalised intensity on the 4.7λ surface (Fig. 6.13) shows two step discontinuities, and a beam pattern largely affected by transmission through the SPP polypropylene. Plane wave interference effects are also visible in the upper right and lower left quadrants. Corresponding normalised phase measurements show two primary BCs and two BPs separated by a finite distance. These BPs and their separation distance are responsible for the central intensity null and it's conjoined circle shape. Propagation to the 40λ surface shows an annular intensity pattern, made of a combination of individual rings which are difficult to resolve. Further propagation to the 73.3λ surface removes this ambiguity, and one annular intensity ring is clearly visible. The central intensity region on the 40λ surface is slightly elliptical and is orientated along the line $\phi = 45°$. In addition, small intensity peaks are split by lines of relatively low intensity, making a cross pattern. Phase on the 40λ surface shows two primary BCs and two BPs, but no additional BPs. However, a strong phase circulation caused by a radial node surrounds the BP pair. Normalised phase on the 73.3λ surface two BCs seem unable to penetrate the now elliptical phase circulation. Their corresponding BPs remain on the edge of the phase circulation, which is more distorted. Inside the phase circulation is a region of planar phase.

Corrugated Feed Antenna Incident Source

Figure 6.14 presents the transmitted $\Delta l = \pm 2$ field, by using the corrugated feed antenna incident beam. Intensity on the 4.7λ surface, contains two distinct intensity nulls. These are a result of the two separated BPs present in the associated phase pattern. The

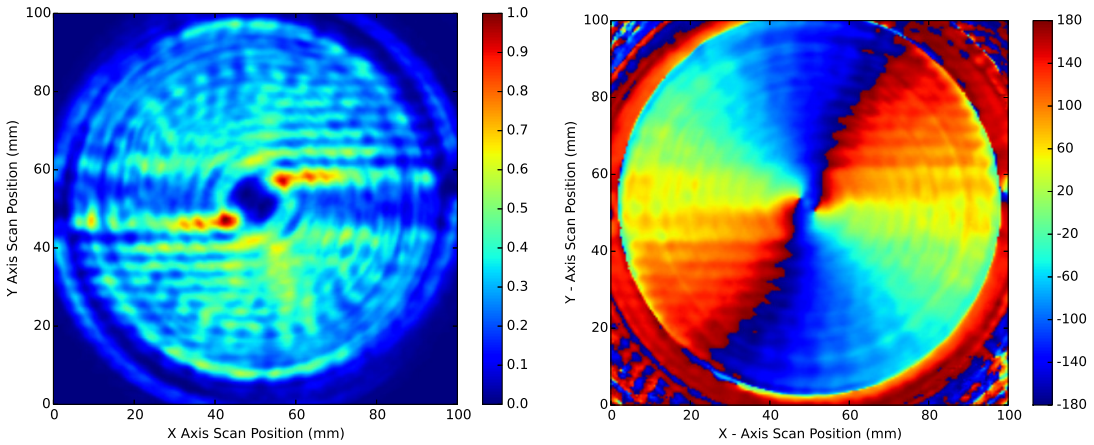

(a) Normalised Intensity 4.7λ *Surface*

(b) Normalised Phase 4.7λ *Surface*

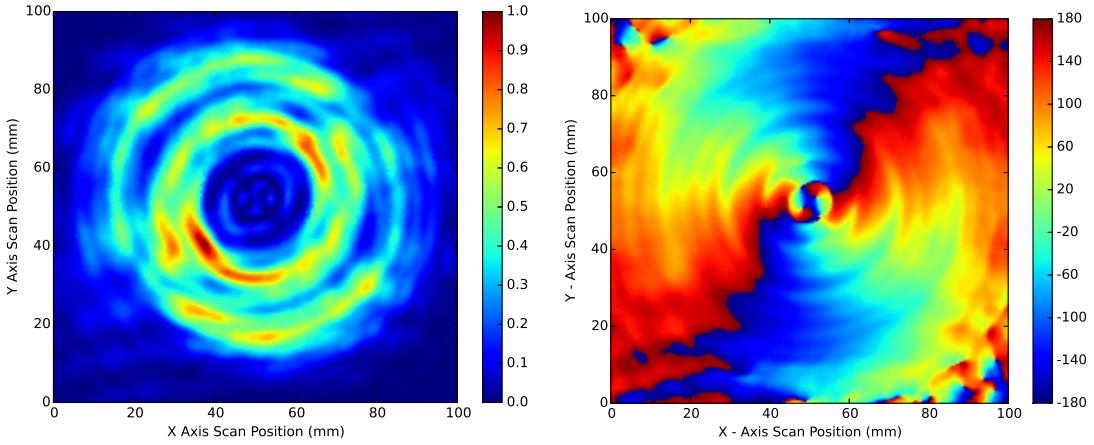

(c) Normalised Intensity 40λ *Surface*

(d) Normalised Phase 40λ *Surface*

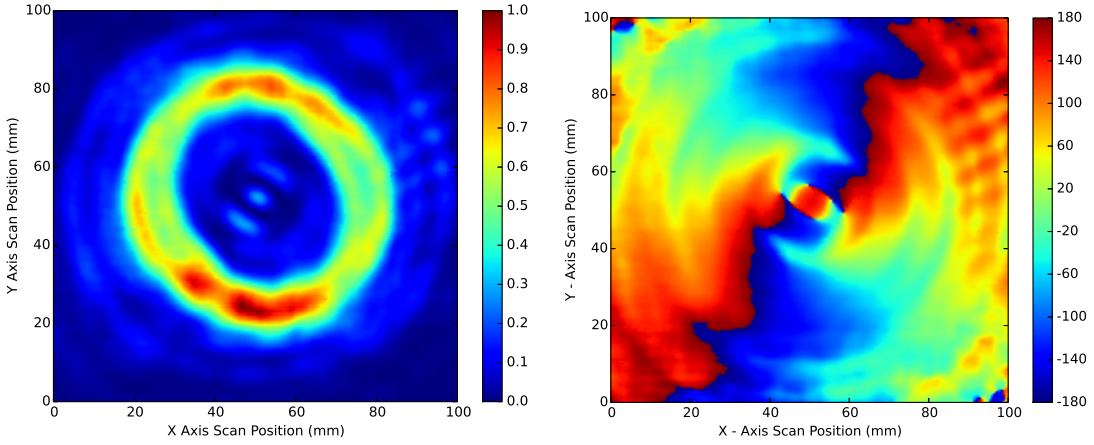

(e) Normalised Intensity 73.3λ *Surface*

(f) Normalised Phase 73.3λ *Surface*

Figure 6.13: Normalised intensity and phase measurements on the 4.7λ, 40λ *and* 73.3λ *surfaces generated by a quasi-planar beam incident on the* $\Delta l = \pm 2$ *split stepped SPP.*

intensity pattern is largely a combination of the incident beam's intensity profile, in addition to primary step discontinuities. Plane wave interference is visible in the upper right and lower left quadrants. A significant amount of phase dragging is visible in the BC lines, and is due to a large number of low power radial modes. Both intensity nulls have merged into one central intensity null by propagation to the 40λ surface. Two intensity peaks, initially generated by the primary step discontinuities remain in their initial positions, even after propagation to the 40λ surface. Phase on this surface is cleaner then the standard configuration SPP's corresponding results (Fig. 6.12d). Both BCs spiral around the propagation axis, and only a few radial node variations in the BC lines are visible. Further propagation to the 73.3λ surface shows little change in the intensity, other then the expected divergence due to the corrugated feed. Phase on the measurement surface has also smoothed, however, the BC on the left hand side of the surface has began to show some distortions close to it's BP location. It appears as if the BC as broken near the BP location, generating two new BPs and a short BC. However, the break in the BC is one to two pixels long and could indicate that this is a systematic error due to VNA noise.

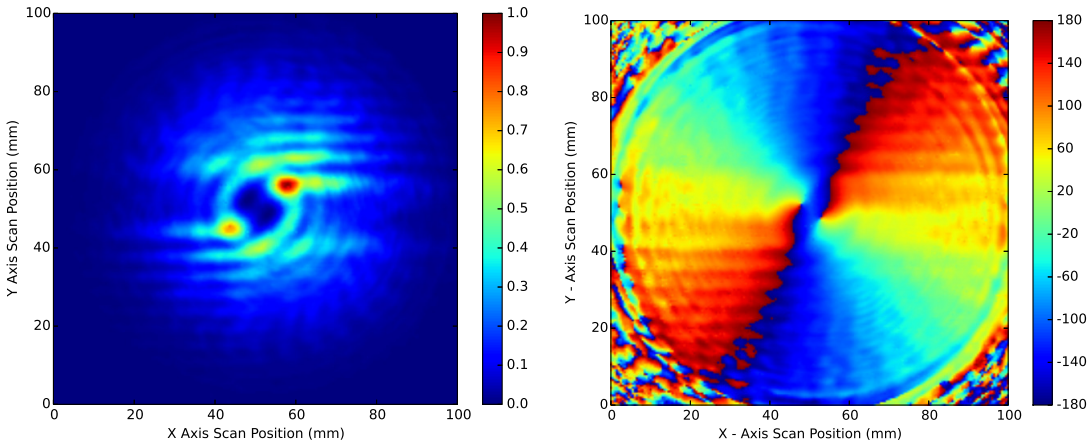

(a) Normalised Intensity 4.7λ *Surface* *(b) Normalised Phase* 4.7λ *Surface*

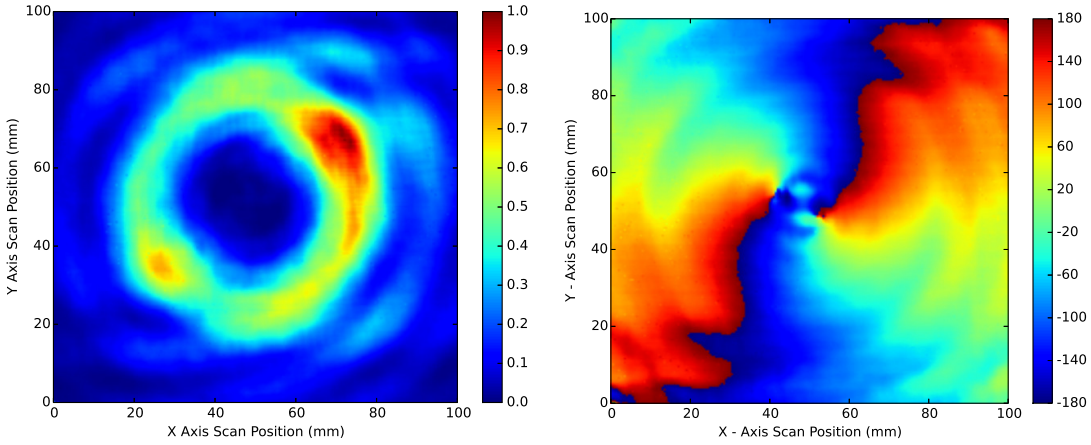

(c) Normalised Intensity 40λ *Surface* *(d) Normalised Phase* 40λ *Surface*

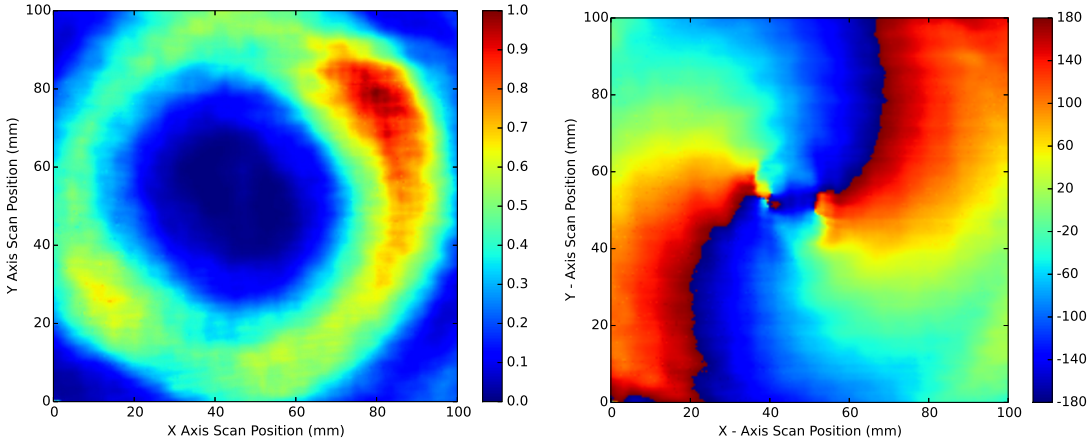

(e) Normalised Intensity 73.3λ *Surface* *(f) Normalised Phase* 73.3λ *Surface*

Figure 6.14: Normalised intensity and phase measurements on the 4.7λ, 40λ *and* 73.3λ *surfaces generated by a beam from a corrugated feed horn incident on the* $\Delta l = \pm 2$ *split stepped SPP.*

6.8 Initial Measurement and Model Comparisons

In this section, the measured intensity and phase data from the 40λ and 73.3λ surfaces are compared to the corresponding models from Chapter 4.[1] Unfortunately, both the measured and modelled data are not azimuthally symmetric in intensity or phase. Therefore it was difficult to directly calculate the difference between measured and modelled data. Work on this continues, but for now a visual comparison between data sets must suffice. A direct comparison between each SPP's 4.7λ field is omitted here because each is shows nearly identical features. For example, each 4.7λ surface is dominated by transmission through the SPP dielectric. In addition, each step produces a break in the intensity pattern, while diffracted waves from the primary step produce regions of linear linear interference.

6.8.1 Aperture Source Comparison $\Delta l = \pm 1$ SPP

40λ Surface $\Delta l = \pm 1$ SPP

Similarities and differences may be seen by comparing the measured CTRA and modelled aperture source 40λ intensity plane generated by the $\Delta l = \pm 1$ SPP (Fig. 6.15). First, the measurements show an outer ring, with faint azimuthally modulated spoke-like intensity peaks. A pair of two inner intensity rings match that of the model. Unlike the model, the measured data shows a ribbon shaped intensity vortex, while it is predicted to contain a fourth intensity ring with a central intensity null. Both phase patterns show the expected single BC with some amount of phase dragging. It is difficult to tell if the region around the measured BP resembles the clean phase circulation seen in the model, but it is certain that the modelled BC shows smoother phase dragging then its counterpart.

[1] Please be aware that the x- and y-axis of the measured data represents the scanner position and covers 0.0 to 100.0 mm while the modelled data's x- and y-axis are in respect to the propagation axis and extends from −50.0 to 50.0 mm.

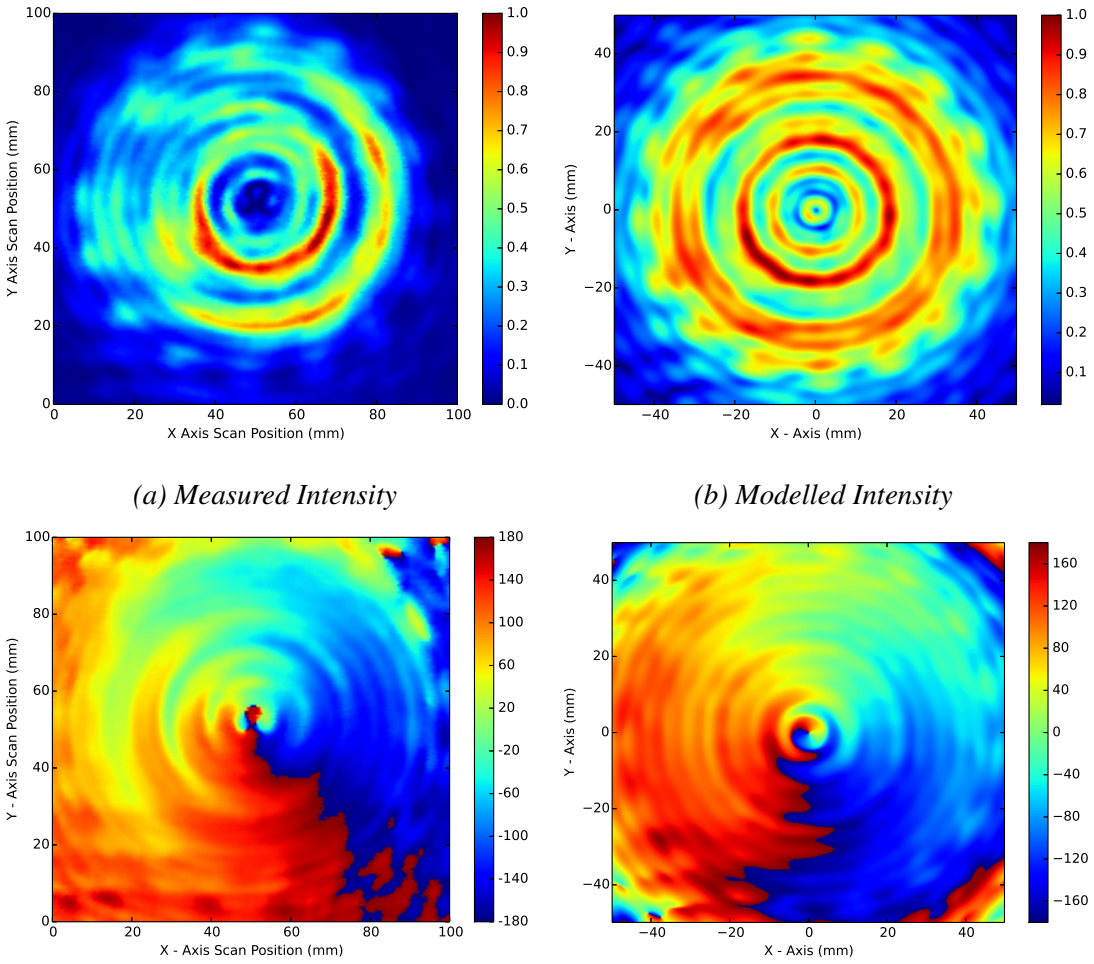

(a) Measured Intensity *(b) Modelled Intensity*

(c) Measured Phase *(d) Modelled Phase*

Figure 6.15: Intensity and phase comparison between the CTRA measured data and modelled Aperture Source of the $\Delta l = \pm 1$ *SPP on the* 40λ *surface.*

73.3λ **Surface** $\Delta l = \pm 1$ **SPP**

Similar results are obtained by comparing the measured and modelled intensity on the 73.3λ plane (Fig. 6.16). For example, the two outer most intensity rings are clearly visible. However, the measured intensity null resembles a semicircle, while the modelled intensity null is central and circular. It is evident from the measured data, that there is some intensity near the propagation axis and that the intensity semicircle is shifted off of the propagation axis. This indicates that the reason why there is no

central ring is that the mode content of the beam is made up of various azimuthal modes. Therefore, the intensity vortex is shifted off axis and distorted. If the beam had only and azimuthal mode number of one, the central ring and vortex structure seen in the model should also be seen in the measurements. Measured phase appears to match the model characteristics more so on the 73.3λ surface than on the 40λ surface. For example, the measured BC shows a straight propagation segment directly after the BP, followed by a sharp change in direction, which eventually double-backs on itself and begins to show phase dragging. This is similar to what is seen in the model. Here the BC propagates away from the BP in a straight line, reaches the phase circulation and quickly changes direction before reversing direction.

6.8.2 Plane Wave Source Comparison $\Delta l = \pm 1$ SPP

40λ Surface $\Delta l = \pm 1$ SPP

Comparing the measured CTRA generated $\Delta l = \pm 1$ SPP beam with the plane wave modelled beam (Fig. 6.17) show similar results to the comparison with the aperture source. Starting with the intensity pattern on the 40λ surface, the three annular intensity rings seen in the model are clearly present in the measurement data. Like the aperture source model, a fourth intensity ring and central intensity null are not seen in the measurements. However, the measured intensity does show a ribbon like intensity vortex, or null. The plane wave modelled phase seems to resemble the measured phase slightly better than the aperture source case. While both models show a phase circulation, the plane wave modelled phase shows a much more erratic phase dragging profile. This matches the type of phase dragging seen in the measurement data, and is the result of several radial modes.

73.3λ Surface $\Delta l = \pm 1$ SPP

The similarities between the measured CTRA beam and plane wave source modelled beam start to break down at the 73.3λ surface. While the correct number of intensity

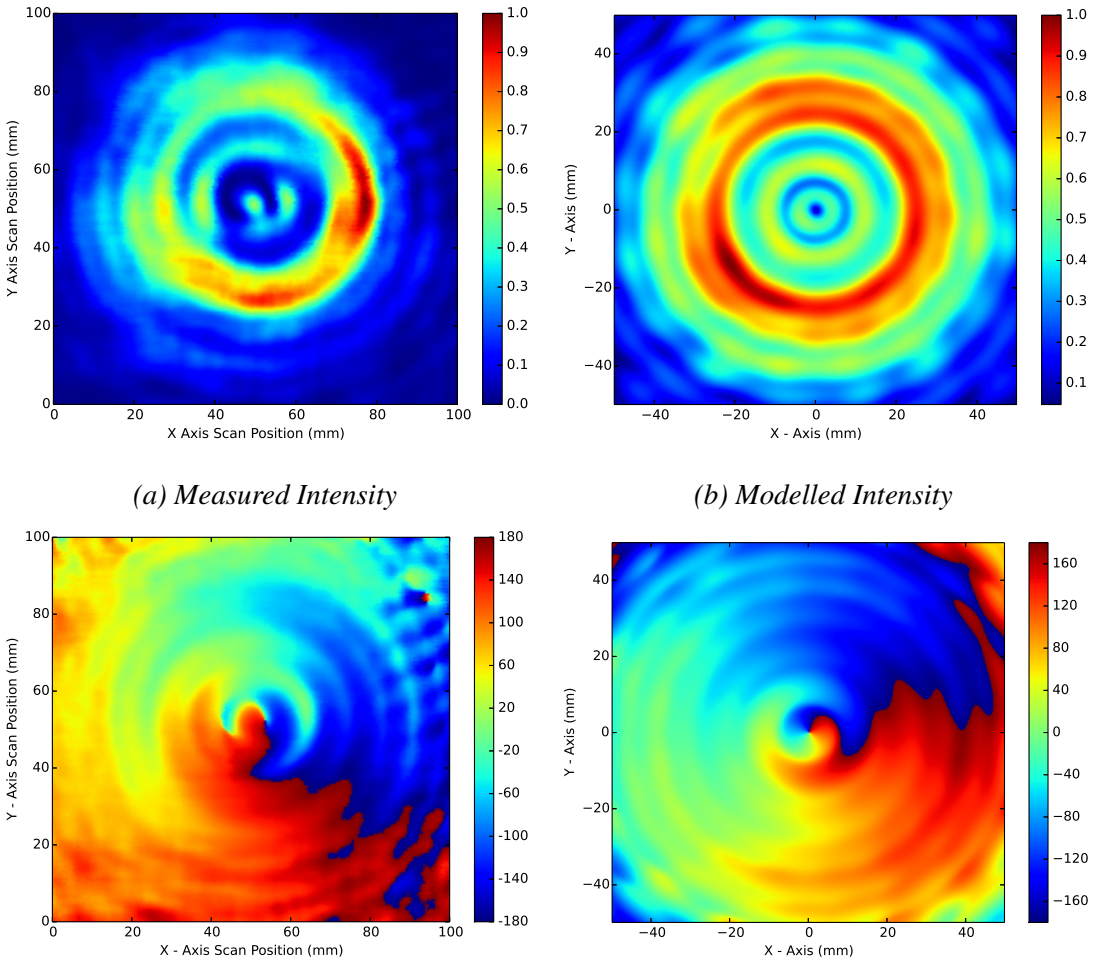

(a) Measured Intensity *(b) Modelled Intensity*

(c) Measured Phase *(d) Modelled Phase*

Figure 6.16: Intensity and phase comparison between the CTRA measured data and modelled Aperture Source of the $\Delta l = \pm 1$ SPP on the 73.3λ surface.

rings is predicted (assuming that the measured vortex was shifted back to it's proper on-axis position), the modelled intensity pattern is highly pixelated. It also predicts a higher intensity on the left hand side of the beam than on the right hand side, which is not seen in the measurements. Furthermore, phase dragging seen in the model is no predominantly perpendicular to the azimuthal direction. Again, this is not the case in the measured data.

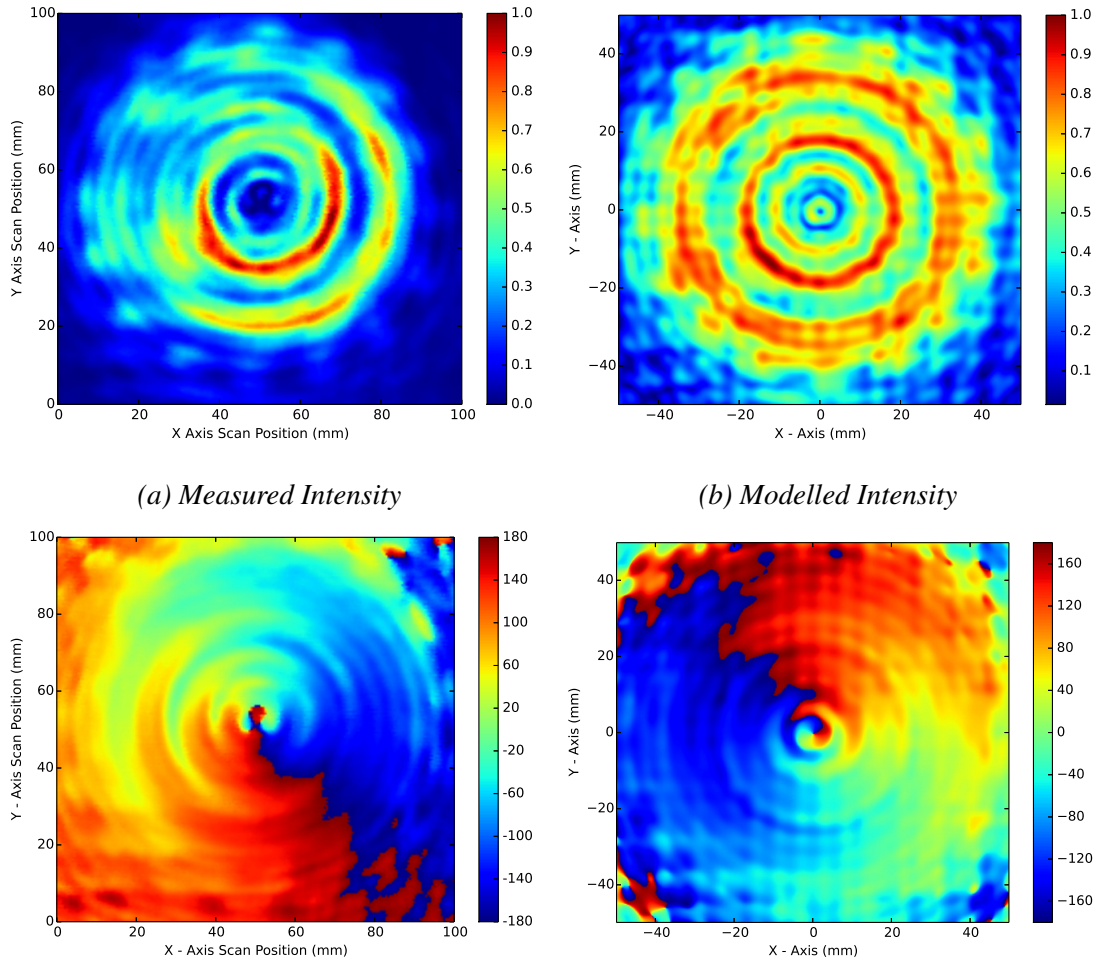

(a) Measured Intensity *(b) Modelled Intensity*

(c) Measured Phase *(d) Modelled Phase*

Figure 6.17: Intensity and phase comparison between the CTRA measured data and modelled Plane Wave Source of the $\Delta l = \pm 1$ SPP on the 40λ surface.

6.8.3 Gaussian Beam Source Comparison $\Delta l = \pm 1$ SPP

40λ Surface $\Delta l = \pm 1$ SPP

Figure 6.19 compares the Gaussian beam illuminated $\Delta l = \pm 1$ SPP measured and modelled beams on the 40λ surface. Both intensity patterns match well. Each predicts an annular intensity ring with a central intensity null. Furthermore, both predict a slightly higher region of intensity along one section of the ring. It is surprising that the intensity patterns match so well, while the phase patterns do not. Although the measured

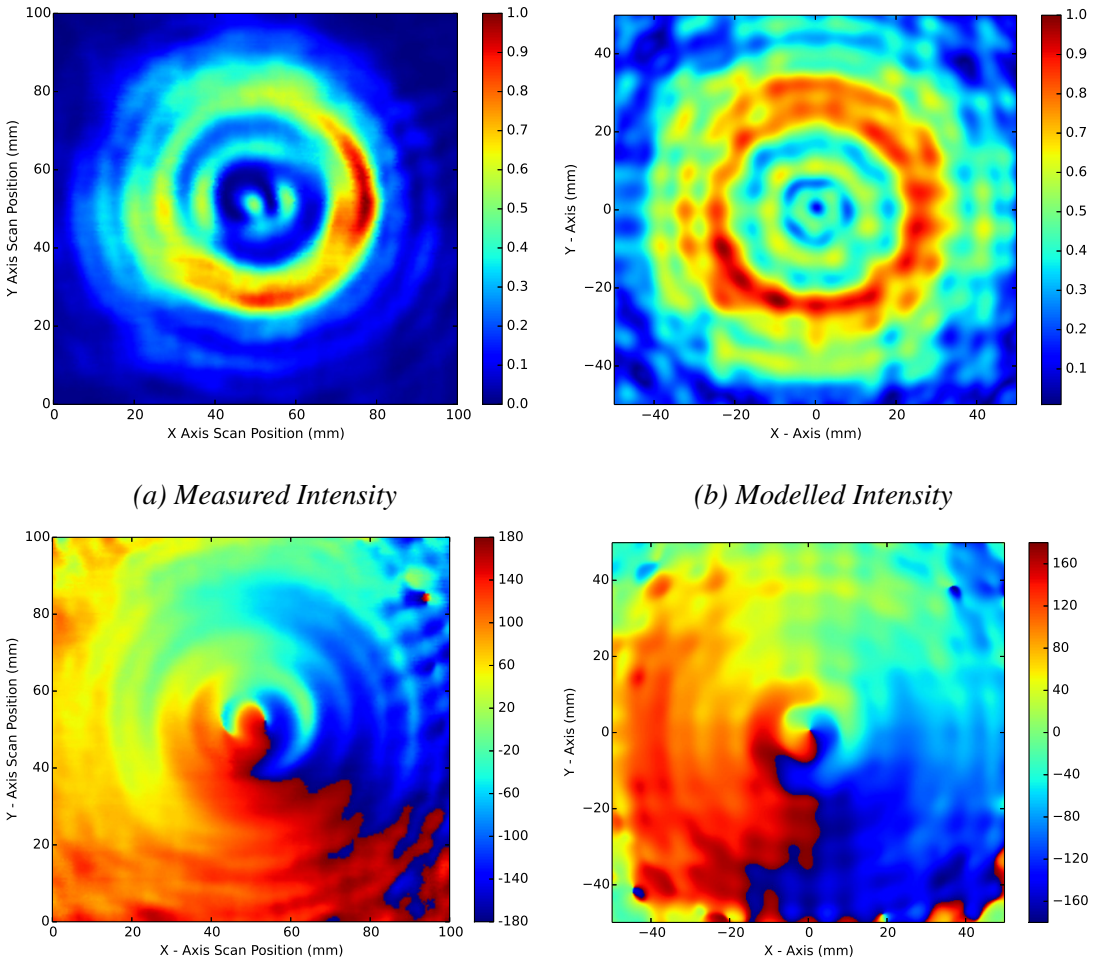

(a) Measured Intensity *(b) Modelled Intensity*

(c) Measured Phase *(d) Modelled Phase*

Figure 6.18: Intensity and phase comparison between the CTRA source measured data and modelled Plane Wave source of the $\Delta l = \pm 1$ SPP on the 73.3λ surface.

data shows the BC beginning to spiral about the propagation axis, the modelled data shows that the BC should have spiralled around the propagation axis multiple times. It is unclear as to why this is the case. It has been ensured that both model and measurement systems used the same geometrical parameters such as the source to SPP distance. Yet, it appears as if the modelled beam has propagated further then the measured beam. This could be a result of implementing the corrugated feed horn beam as a radiation source in FEKO. Since the horn and SPP can not be modelled using current computing

power, each had to be modelled separately. The feed antenna was measured first and its radiation pattern was used as an input to the SPP model. It appears that this has an impact on the modelled phase, which should be resolved in further work. Paradoxically, the modelled intensity pattern is of a similar radial size as the measured intensity pattern. If in fact the modelled beam propagated further then the measured beam, the modelled intensity should be much larger then the measured intensity due to beam divergence. Yet, this is not the case, which implies that the modelled propagation is correct.

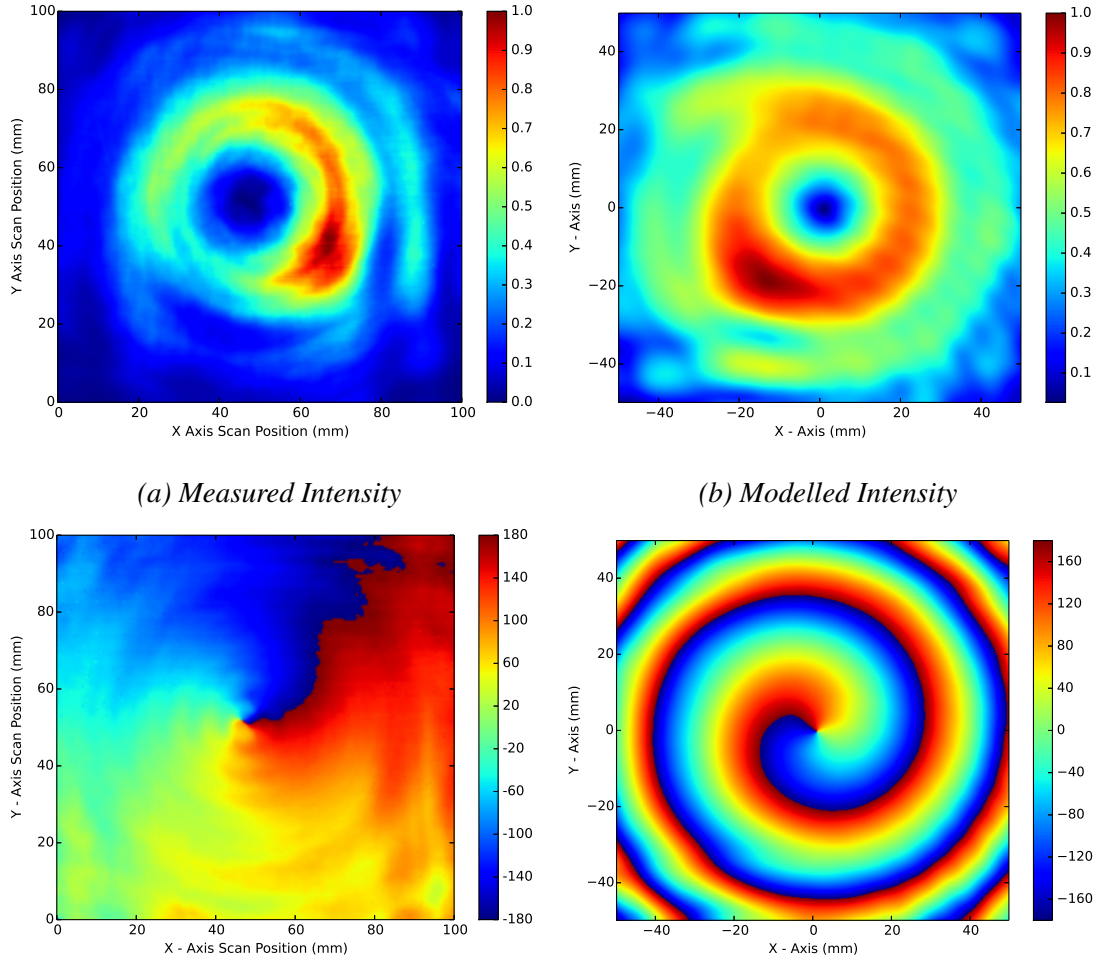

(a) Measured Intensity

(b) Modelled Intensity

(c) Measured Phase

(d) Modelled Phase

Figure 6.19: Intensity and phase comparison between the Gaussian beam measured and modelled data of the $\Delta l = \pm 1$ SPP on the 40λ surface.

73.3λ Surface $\Delta l = \pm 1$ SPP

Comparisons between the measured and modelled data show little change with propagation to the 73.3λ surface (Fig. 6.20). An annular intensity pattern is clearly visible in both, while it has grown in size due to the incident beam's divergence. A region of relatively higher intensity is visible and accompanied by a region of relatively low intensity, compared to the unaltered ring regions. Again, there is a clear mismatch between the measured and modelled phase patterns. Focusing on the measured phase, however, the expected spiralling BC is seen to be developing. The amount of curvature has certainly increased between the 40λ surface (Fig. 6.19c) and the 73.3λ surface (Fig. 6.20c).

$\Delta l = \pm 1$ SPP measurement and model review

To review, the aperture and plane wave models predicted similar features, which were confirmed by the measurement data. Both models predicted a strong phase circulation on the 40λ surface, weakening slightly at the 73.3λ surface. Measured data seems to support this by observations of the sharp change in direction of the BC. Interestingly, the measured data did not indicate a standard central intensity null. Instead, it was either ribbon-like or a semicircle. This points to either poor alignment or poor machining of the centre SPP section. In either case, an impure beam with respect to the azimuthal mode number is generated, shifting the vortex off the propagation axis. It is unclear as to how the interesting intensity null ribbon and semicircle shapes are generated, however. This is a very exciting discovery, as it is known that vortex lines can form links and knots [12, 136–142].

6.8.4 Aperture Source Comparison $\Delta l = \pm 2$ SPP

This section begins the comparison of the $\Delta l = \pm 2$ standard configuration SPP. Figure 6.21 presents the measured CTRA generated and modelled aperture source beams on the 40λ surface. Much like the $\Delta l = \pm 1$ SPP case, the measured intensity shows the

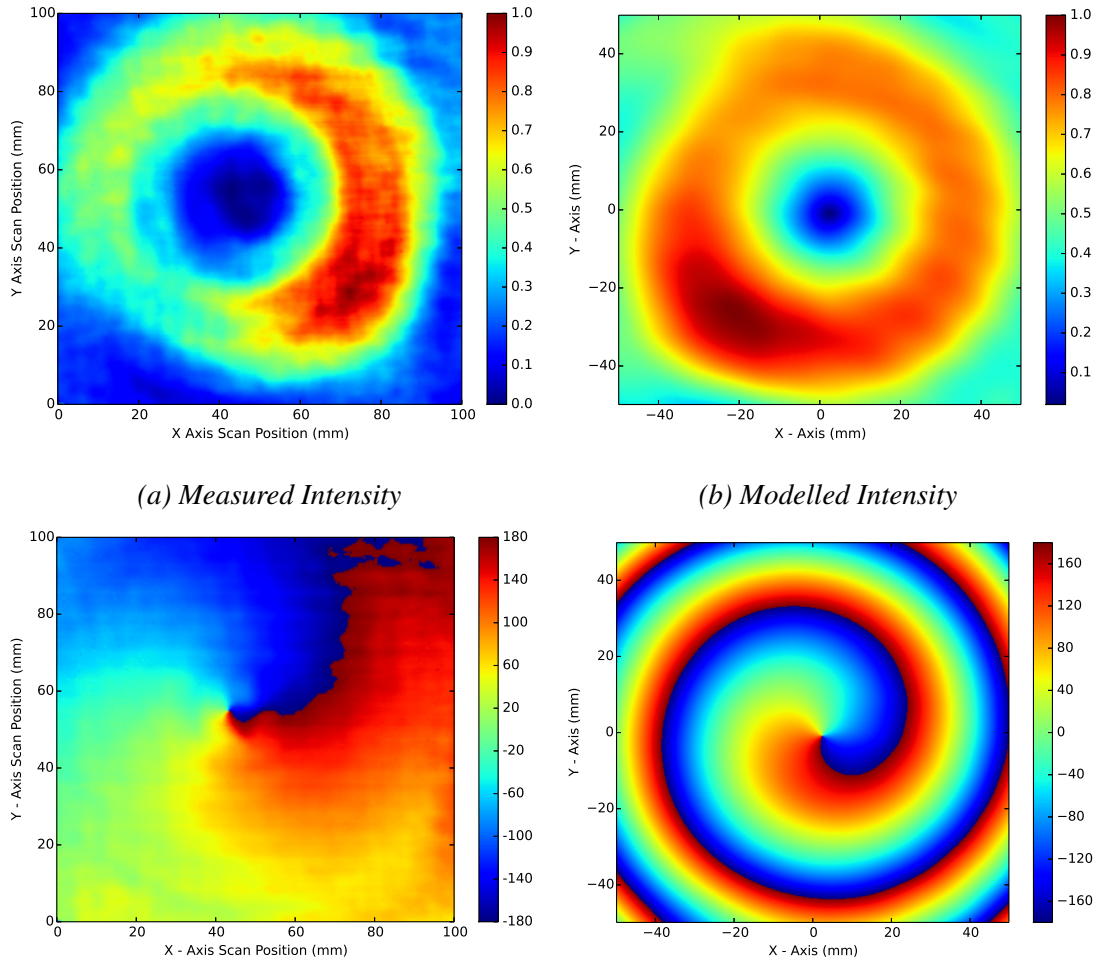

(a) Measured Intensity

(b) Modelled Intensity

(c) Measured Phase

(d) Modelled Phase

Figure 6.20: Intensity and phase comparison between the Gaussian beam measured and modelled data of the $\Delta l = \pm 1$ SPP on the 73.3λ surface.

expected outer intensity rings, but is missing the inner most ring seen in the model. Firstly, the inner measured intensity ring is stronger than the outer most ring, which is predicted by the model. There is a very faint signal inside the stronger intensity ring, seeming to indicate the possibility of a third, which again is evident in the model. Yet, the measured data does not show the inner most intensity ring. Instead an very large intensity null is present. This is probably due to the extra phase dislocation generated in the measured data. These extra dislocations are not seen in the modelled data, however

a strong phase circulation is. Also, the measured intensity pattern is slightly smaller in radial extend than the modelled pattern. Other than the extra BC and BPs present in the measured data, the model appears to predict the correct phase behaviour. For example, phase dragging near the propagation axis shows sharp changes in direction, which increase in frequency with increased propagate to the outer beam extents.

40λ **Surface** $\Delta l = \pm 2$ **SPP**

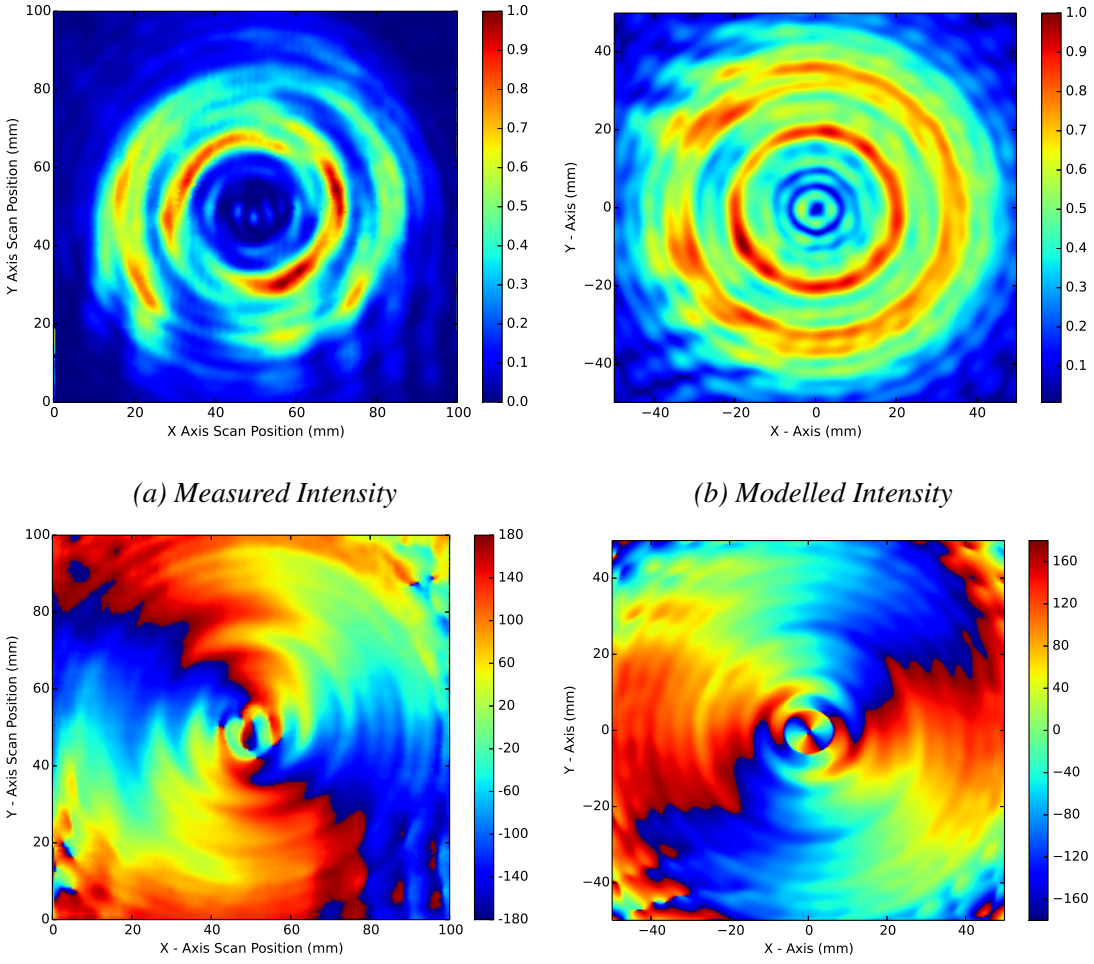

(a) Measured Intensity

(b) Modelled Intensity

(c) Measured Phase

(d) Modelled Phase

Figure 6.21: Intensity and phase comparison between the CTRA measured data and modelled Aperture Source of the $\Delta l = \pm 2$ *SPP on the* 40λ *surface.*

73.3λ Surface $\Delta l = \pm 2$ SPP

Moving on to the 73.3λ surface (Fig. 6.22), it is evident that the measured intensity pattern is still smaller in radial extent then the modelled data. An inner intensity ring is still missing from the measurements as well. Yet, the central portion of the measurement beam shows some interesting features. First, it has a small intensity peak, bordered by two intensity nulls that are surrounded by regions of high intensity. The central peak is most likely due to improper machining of the central SPP section, while the two bordering intensity nulls point towards an impure beam with various amounts of differing azimuthal mode numbers. If the beam purity could be increased, it is expected that the central intensity ring and null seen in the model would also be seen in the measurement data. Again, the extra BC and BPs seen in the measured 40λ surface have been removed with propagation to the 73.3λ surface. The higher BC contains a straight segment directly after the initial BP, indicating a phase circulation. This is confirmed by the phase circulation seen in the model. In addition, both measurement and modelled phase data show a teardrop, spiral-like pattern, directly outside the phase circulation.

6.8.5 Plane Wave Source Comparison $\Delta l = \pm 2$ SPP

40λ Surface $\Delta l = \pm 2$ SPP

Figure 6.23 shows the measured and modelled $\Delta l = \pm 2$ SPP 40λ generated surface. Similar results are apparent when compared with the aperture source models. Again, the most prominent difference is the pixelation of the plane wave generated models and what appears to be some polarisation effects (See the cross pattern in Fig. 6.23b). To review, the measured intensity pattern is smaller in radial extent than the model, while it is also missing the inner most intensity ring. However, this is primarily due to the complex phase structure near the propagation axis, which is not present in the model.

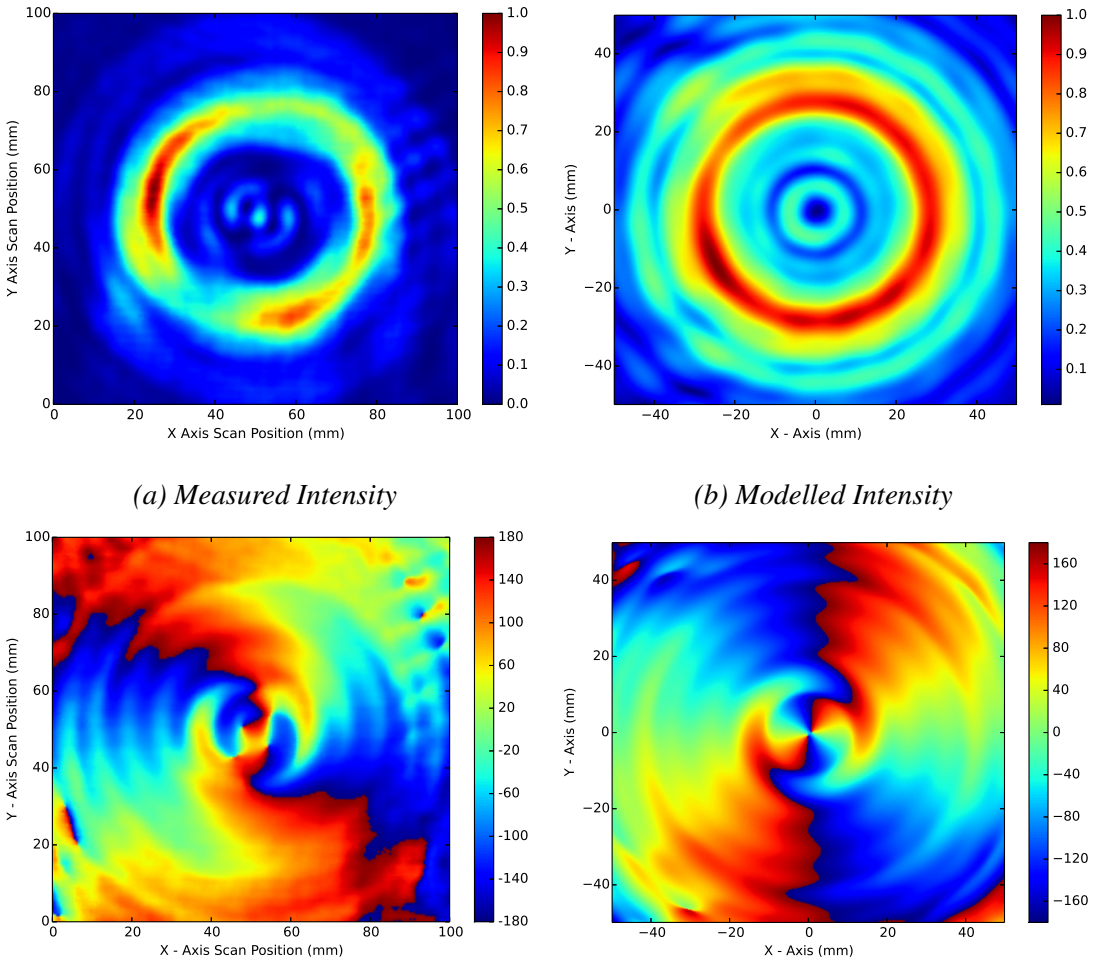

(a) Measured Intensity *(b) Modelled Intensity*

(c) Measured Phase *(d) Modelled Phase*

Figure 6.22: Intensity and phase comparison between the CTRA measured data and modelled Aperture Source of the $\Delta l = \pm 2$ SPP on the 73.3λ surface.

73.3λ Surface $\Delta l = \pm 2$ SPP

Measurement and modelled comparisons on the 73.3λ surface are shown in Fig. 6.24. Both principle intensity rings correspond nicely, while again, the central intensity ring in the model is not seen in the data. The complex phase structure seen in the measured data has begun to reorganise. While both measured and modelled phase data show the teardrop shaped extensions just outside the phase circulation, the measured data's are much stronger/longer and match the plane wave modelled phase features better.

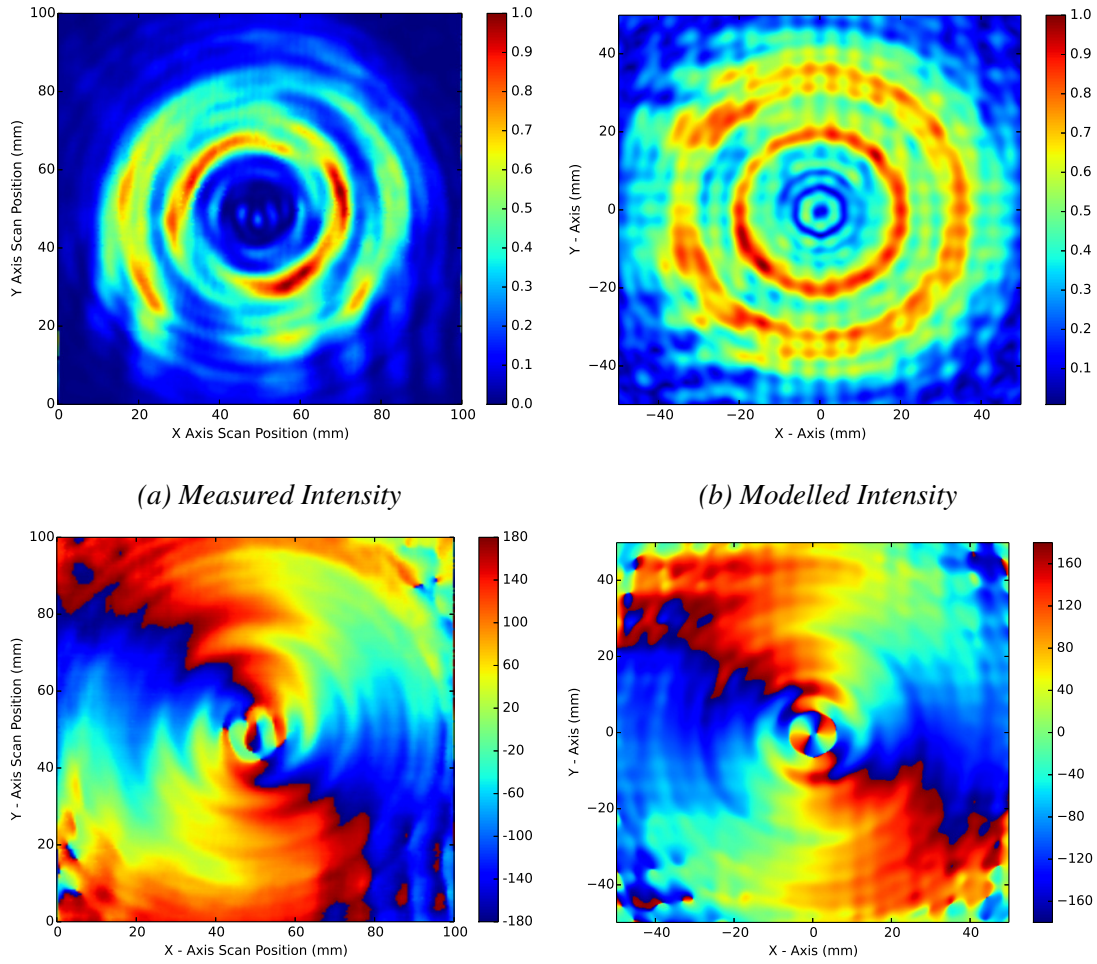

(a) Measured Intensity *(b) Modelled Intensity*

(c) Measured Phase *(d) Modelled Phase*

Figure 6.23: Intensity and phase comparison between the CTRA measured data and modelled Plane Wave Source of the $\Delta l = \pm 2$ SPP on the 40λ surface.

6.8.6 Gaussian Beam Source Comparison $\Delta l = \pm 2$ SPP

40λ Surface $\Delta l = \pm 2$ SPP

A comparison between the measured and modelled field on the 40λ surface, generated by a Gaussian beam incident on the $\Delta l = \pm 2$ SPP are show in Fig. 6.25. Again, both intensity patterns match nicely. A basic annular ring is visible, with a region of slightly higher intensity next to a region of slightly lower intensity. Recall that this feature is due to the SPP step. Both patterns show a deep intensity null, however the modelled

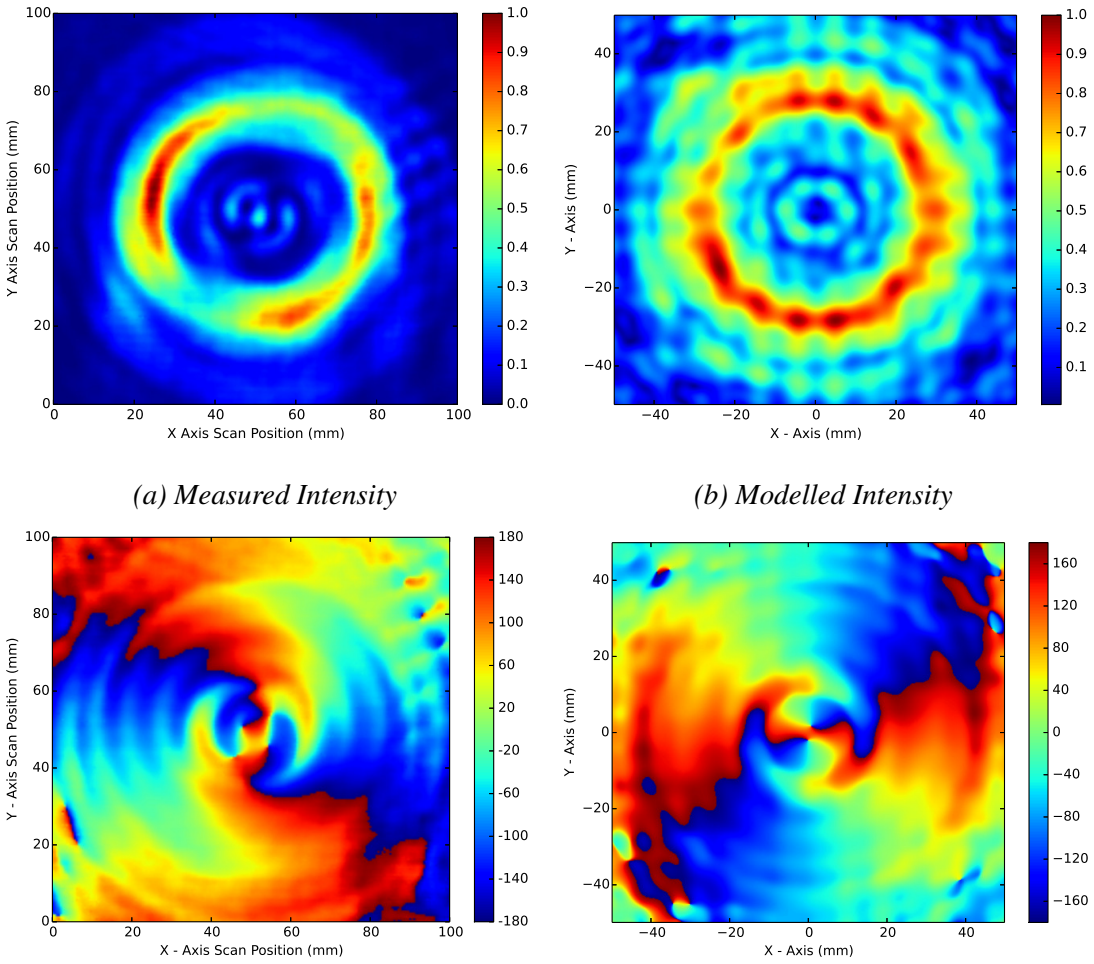

(a) Measured Intensity

(b) Modelled Intensity

(c) Measured Phase

(d) Modelled Phase

Figure 6.24: Intensity and phase comparison between the CTRA source measured data and modelled Plane Wave source of the $\Delta l = \pm 2$ SPP on the 73.3λ surface.

data has finer interior structure. For example, two prominent dips in intensity are seen to correspond to the ends of both BCs, while the measured data shows only a single intensity dip. Like the previous Gaussian illuminated case, the modelled phase spirals around the propagation axis much more then expected. Again, this is expected to be due to some propagation distance error induced by being forced to model the horn and SPP separately. In addition, the measured phase shows the presence of a third BC, although it is very small in extent.

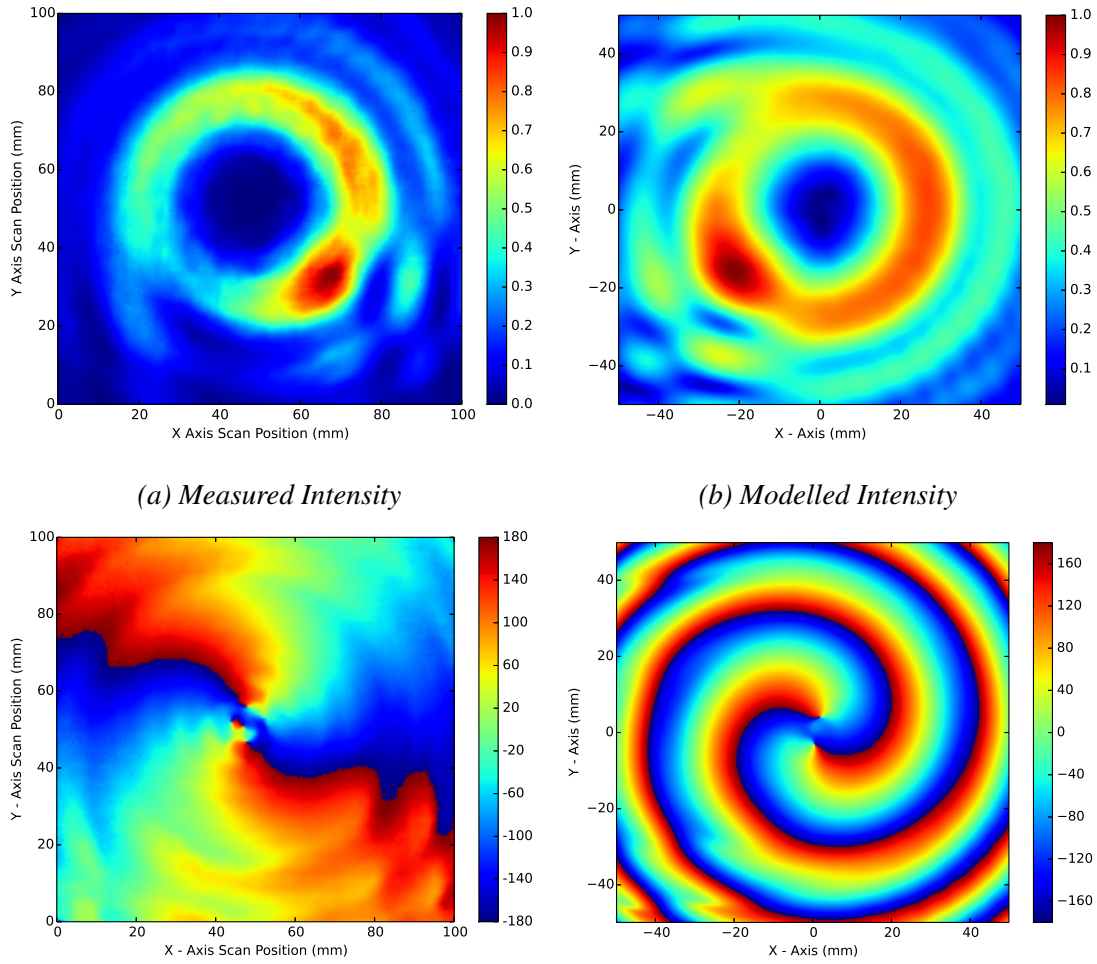

(a) Measured Intensity

(b) Modelled Intensity

(c) Measured Phase

(d) Modelled Phase

Figure 6.25: Intensity and phase comparison between the Gaussian beam measured and modelled data of the $\Delta l = \pm 2$ SPP on the 40λ surface.

73.3λ Surface $\Delta l = \pm 2$ SPP

Propagation to the 73.3λ surface (Fig. 6.26) shows some addition interesting comparisons between the measured and modelled data. Firstly, the intensity patterns are extremely similar, aside from the finer detail in the modelled data. Again, the basic annular ring pattern is visible, with the relatively high and low regions cause by the SPP step discontinuity. In the measured phase, a second additional BC and BP pair have developed. This is due to the beam's divergence not allowing the BPs to re-annihilate.

These extra BCs are not visible in the modelled data. This indicates that they are caused by improper phase shifting of the incident beam. This can either be due to improper machining of the SPP surface, or improper step heights for the desired frequency.

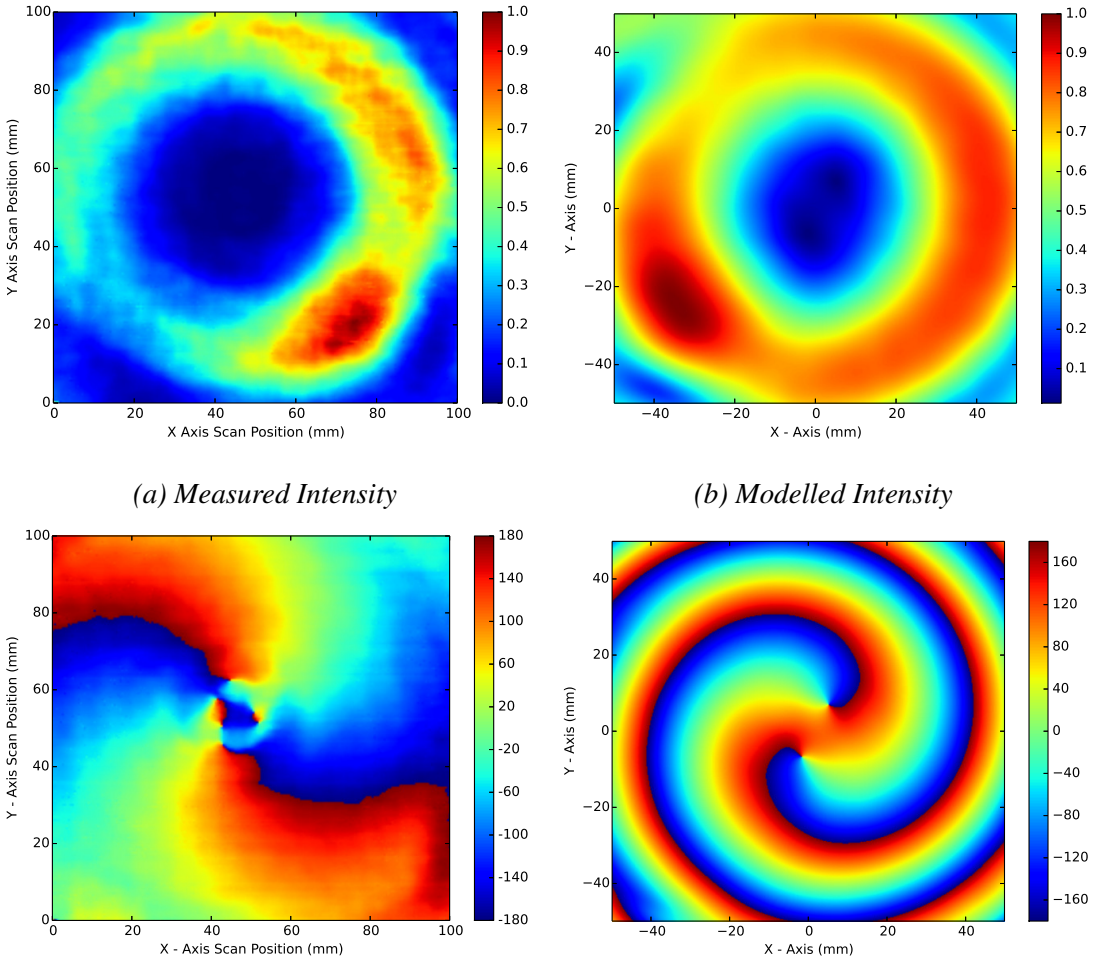

(a) Measured Intensity *(b) Modelled Intensity*

(c) Measured Phase *(d) Modelled Phase*

Figure 6.26: Intensity and phase comparison between the Gaussian beam measured and modelled data of the $\Delta l = \pm 2$ SPP on the 73.3λ surface.

$\Delta l = \pm 2$ SPP measurement and model review

To conclude, measured and modelled data for the $\Delta l = \pm 2$ SPP were compared. The aperture and plane wave illuminated cases produced similar results. Yet, upon closer

examination it was discovered that the aperture source illuminated SPP data was more in line with what was measured. This is to be expected, since the measurement system could not produce a perfect plane wave. However, it is insightful to see that the plane wave illuminated case produces very similar features. This is advantageous for a few reasons. Firstly, modelling with a plane wave is slightly faster then modelling other incident beams. Secondly, modelling with a plane wave reduces the complexity of the model, helping to isolate certain SPP characteristics. Now it is clear that comparing plane wave modelled data to CTRA measured data is probably not ideal. Yet, for practical reasons, it can be used in the initial modelling stages to give the experimenter an approximate idea of what the resulting beam will be, while also decreasing model complexity and computation time.

6.8.7 Aperture Source Comparison $\Delta l = \pm 2$ split configuration SPP

40λ Surface $\Delta l = \pm 2$ split configuration SPP

Figure 6.27 shows the measured and modelled data on the 40λ surface generated by an aperture source illuminated $\Delta l = \pm 2$ split configuration SPP. Unlike the $\Delta l = \pm 1$ and $\Delta l = \pm 2$ SPP cases where the measured and modelled intensities were very similar, the intensities patterns in Fig. 6.27 are very different. While the measured data does show two annular intensity rings, they are significantly closer to each other than the intensity rings in the modelled data. As a result, the measured beam pattern is notable smaller in radial extent then the modelled data. However, like the previous SPP comparisons, the measured data is still missing a clear inner intensity ring and central intensity null. However, the measured $\Delta l = \pm 2$ split configuration SPP case shows some interesting features. Firstly, there appears to be two extremely faint inner intensity rings. Yet, the inner most ring is split by a cross pattern, while the second intensity ring is split across the diagonal. Both measured and modelled phase patterns show a strong phase circulation with two BCs. As expected, the BC segments inside the phase circulation

are straight, then as the BC passes through the circulation boundary it sharply changes propagation direction. Finally, the frequency of phase dragging increases towards the outer beam extents.

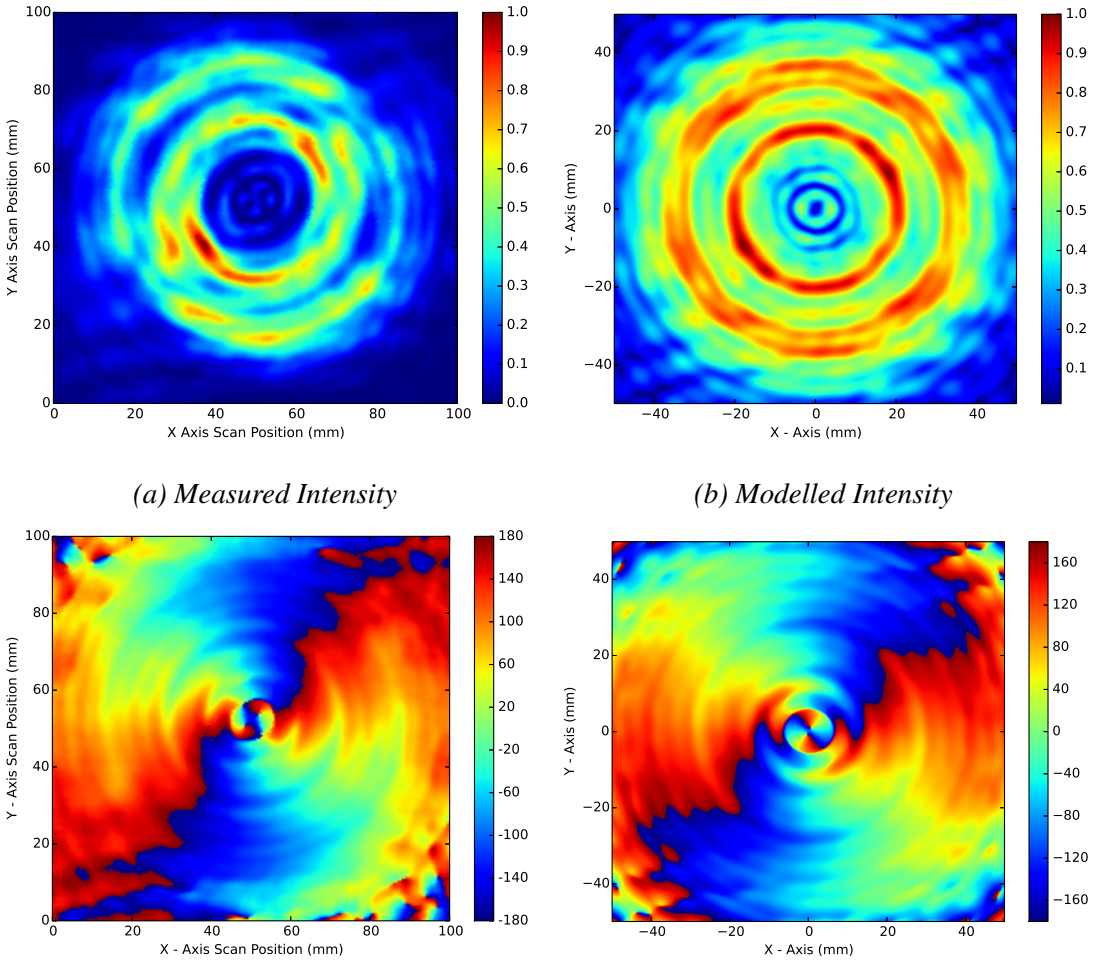

(a) Measured Intensity *(b) Modelled Intensity*

(c) Measured Phase *(d) Modelled Phase*

Figure 6.27: Intensity and phase comparison between the CTRA measured data and modelled Aperture Source of the $\Delta l = \pm 2$ split configuration SPP on the 40λ surface.

73.3λ Surface $\Delta l = \pm 2$ split configuration SPP

The discrepancy between measured and modelled intensity patterns continues with propagation to the 73.3λ surface (Fig. 6.28). While the measured intensity on the 40λ

surface showed two closely placed intensity rings, the 73.3λ surface indicates that the rings have merged into one. Again, this is not present on the modelled surface. There, both intensity rings remain largely distinct. Furthermore, the central portion of the measured intensity shows a very faint on-axis intensity peak and corresponding ring. Both measured and modelled phase surfaces show a phase circulation.

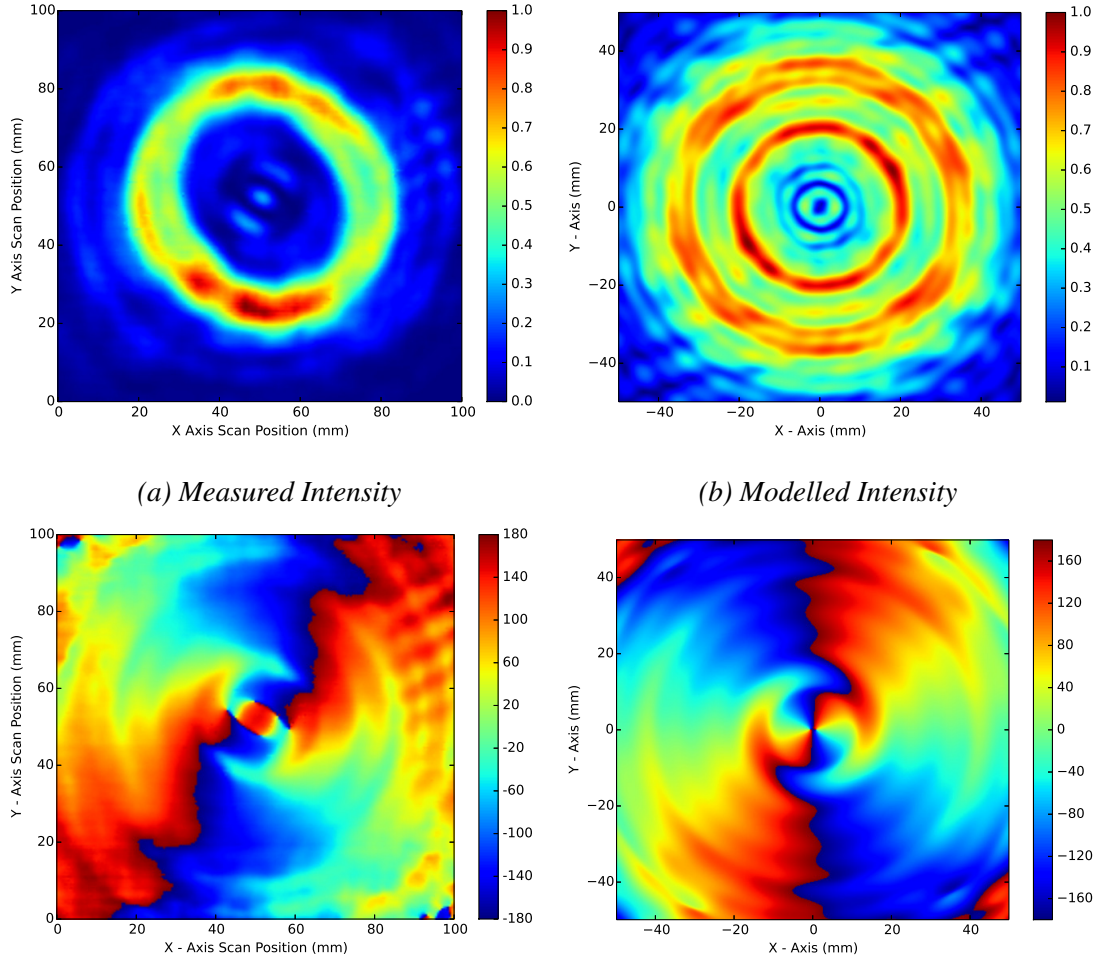

(a) Measured Intensity

(b) Modelled Intensity

(c) Measured Phase

(d) Modelled Phase

Figure 6.28: Intensity and phase comparison between the CTRA measured data and modelled Aperture Source $\Delta l = \pm 2$ split configuration SPP on the 73.3λ surface.

6.8.8 Plane Wave Source Comparison $\Delta l = \pm 2$ split configuration SPP

40λ Surface $\Delta l = \pm 2$ split configuration SPP

Much like the previous aperture source illuminated case, the plane wave illuminated case on the 40λ surface (Fig. 6.29) shows several differences between the measured and modelled data. To start, the measured data was made up of two very closely placed intensity rings, while on the other hand the modelled data shows two relatively largely spaced intensity rings. Secondly, the measured data shows a complex central intensity region, while the modelled data shows a central intensity null surrounded by an annular ring. Both measured and modelled phase surfaces show a strong phase circulation and phase dragging of the BC. Again, the plane wave model shows a large amount of pixelation.

73.3λ Surface $\Delta l = \pm 2$ split configuration SPP

Figure 6.30 shows an interesting intensity pattern difference compared to the aperture illuminated 73.3λ surface. This major difference is that the modelled intensity data shows a single primary intensity ring, with a relatively low intensity centre ring around the central intensity null. This matches the measured data, which is also made up of just a single primary intensity ring. A faint inner ring is partly visible, but appears to be broken up by the complex phase structure. There, both BCs are forced away from the propagation axis by the phase circulation. Interestingly, this presents a case where plane wave illumination has produced a more accurate beam compared to the aperture illuminated cases.

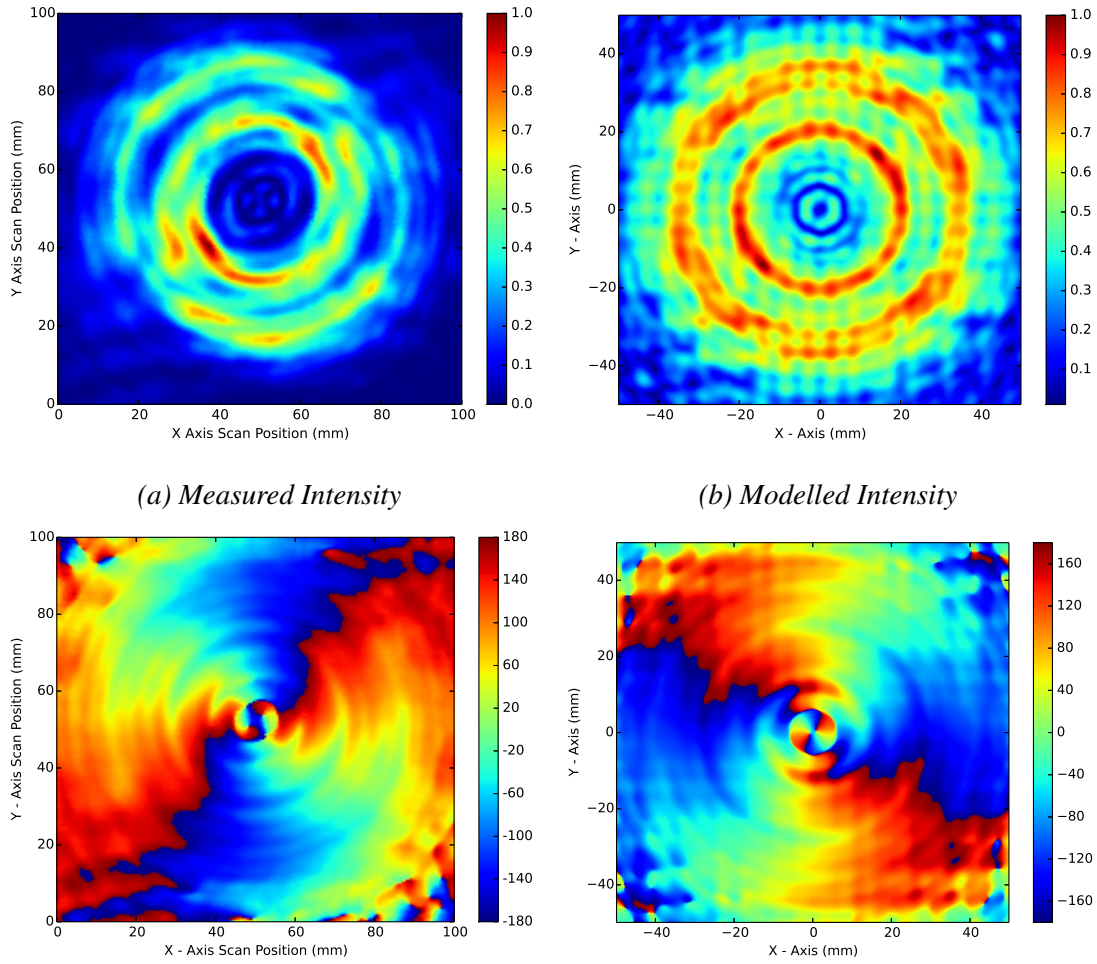

(a) Measured Intensity *(b) Modelled Intensity*

(c) Measured Phase *(d) Modelled Phase*

Figure 6.29: Intensity and phase comparison between the CTRA measured data and modelled Plane Wave Source $\Delta l = \pm 2$ split configuration SPP on the 40λ surface.

6.8.9 Gaussian Beam Source Comparison $\Delta l = \pm 2$ split configuration SPP

40λ Surface $\Delta l = \pm 2$ split configuration SPP

Measured and modelled data on the 40λ surface, generated by a Gaussian beam incident on the $\Delta l = \pm 2$ split configuration SPP, is compared in Fig. 6.31. Both measured and modelled intensity patterns are very similar. Both show a elliptical central intensity

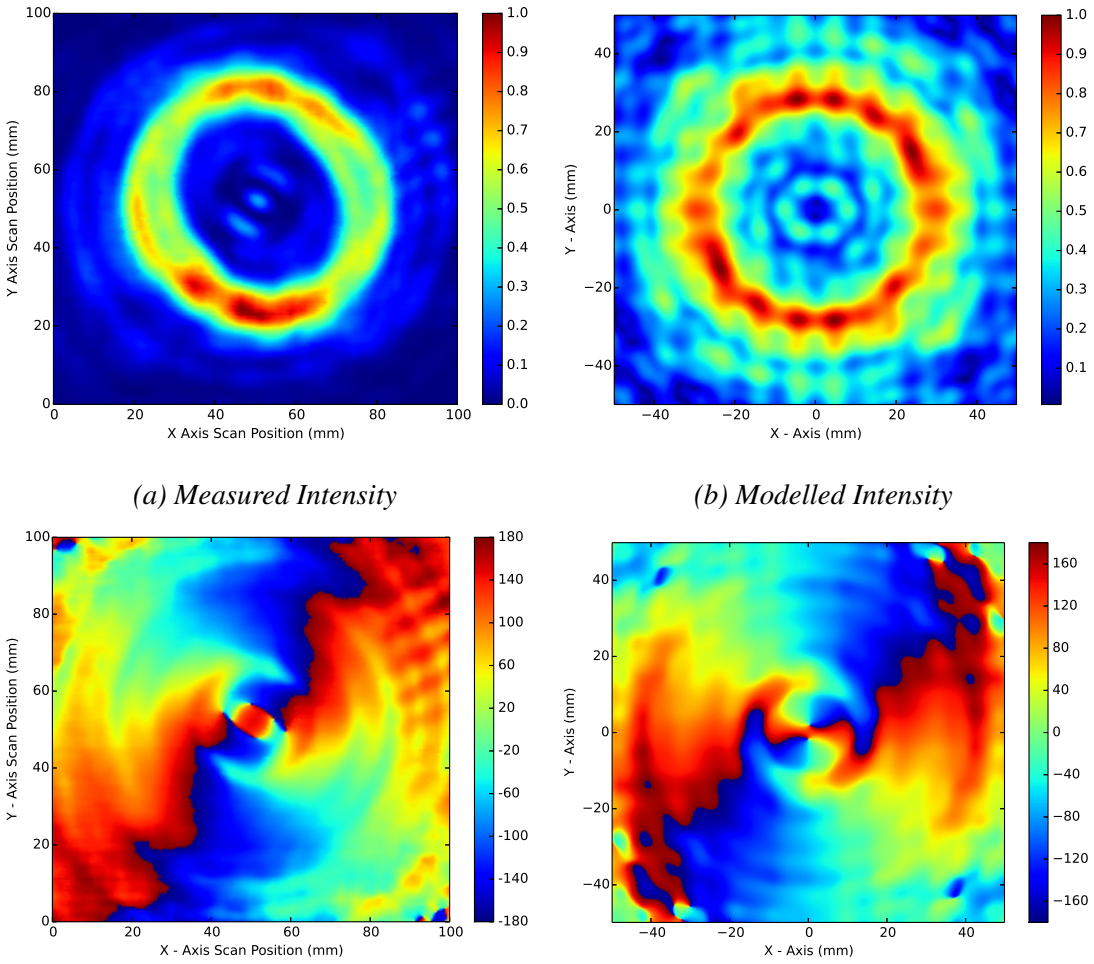

(a) Measured Intensity

(b) Modelled Intensity

(c) Measured Phase

(d) Modelled Phase

Figure 6.30: Intensity and phase comparison between the CTRA source measured data and modelled Plane Wave source $\Delta l = \pm 2$ split configuration SPP on the 73.3λ surface.

null, while the modelled null shows finer detail. Both intensity patterns also show a distorted annular intensity ring with two regions of relatively high intensity and two regions of relatively low intensity. These regions are due to the two primary steps of the split configuration SPP. Finally, both intensity patterns are comparable in size. Again, the modelled phase for the Gaussian illuminated case spirals about the propagation axis much more then the measured data indicates. Very little phase dragging is visible in either case, showing that few radial modes are present.

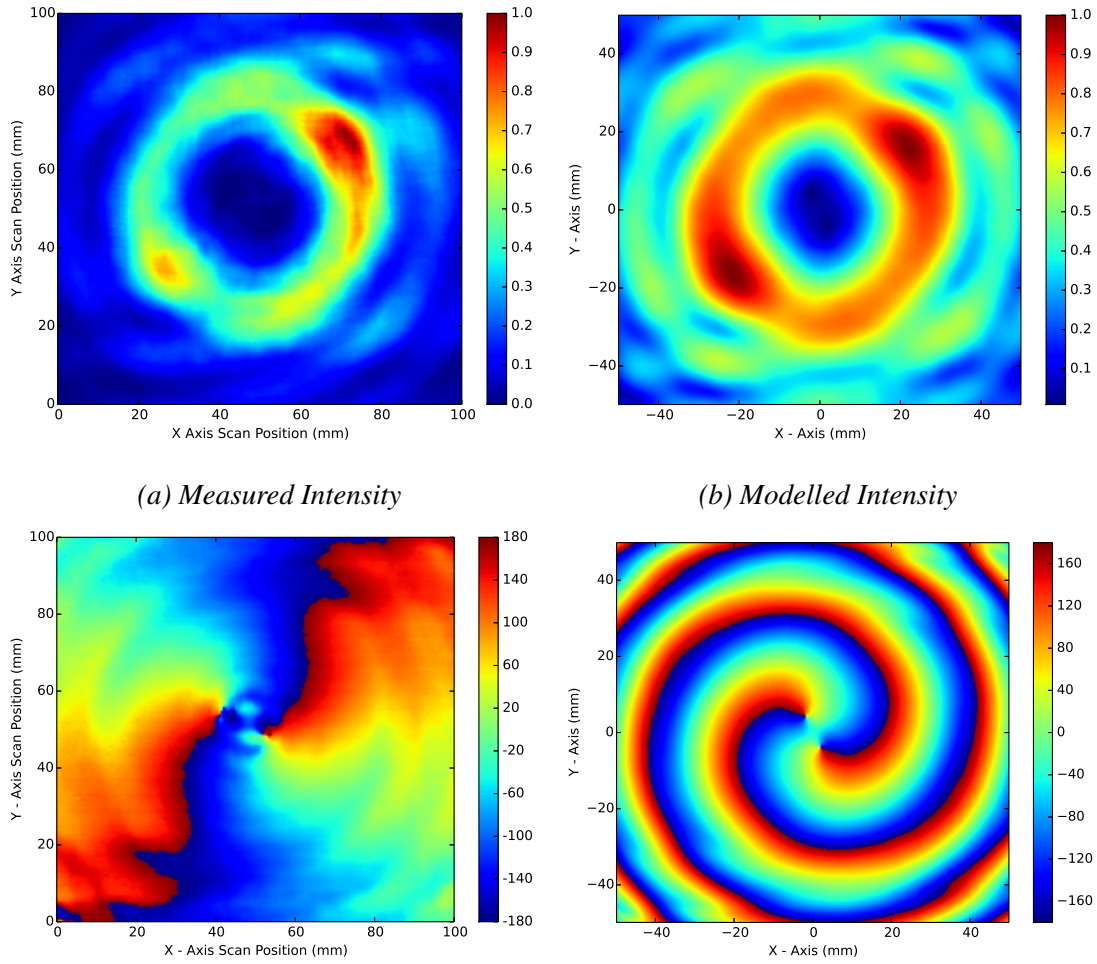

(a) Measured Intensity

(b) Modelled Intensity

(c) Measured Phase

(d) Modelled Phase

Figure 6.31: Intensity and phase comparison between the Gaussian beam measured and modelled data $\Delta l = \pm 2$ split configuration SPP on the 40λ surface.

73.3λ Surface $\Delta l = \pm 2$ split configuration SPP

Figure 6.32 shows the measured and modelled data on the 73.3λ surface generated by the $\Delta l = \pm 2$ split configuration SPP. Both intensity patterns have grown in radial size, which is due to the level of divergence of the incident Gaussian beam. Both regions of relatively high and low intensity are still visible. The modelled central intensity null shows finer detail then is seen in the measured data. This could be due to the available dynamic range of the VNA at such low signal levels. Finally, the measured

phase pattern shows increased BC curvature compared to the 40λ surface. Again, this is expected with increased propagation distance. Yet, the measured BCs do not spiral about the propagation axis as much as the modelled BC data.

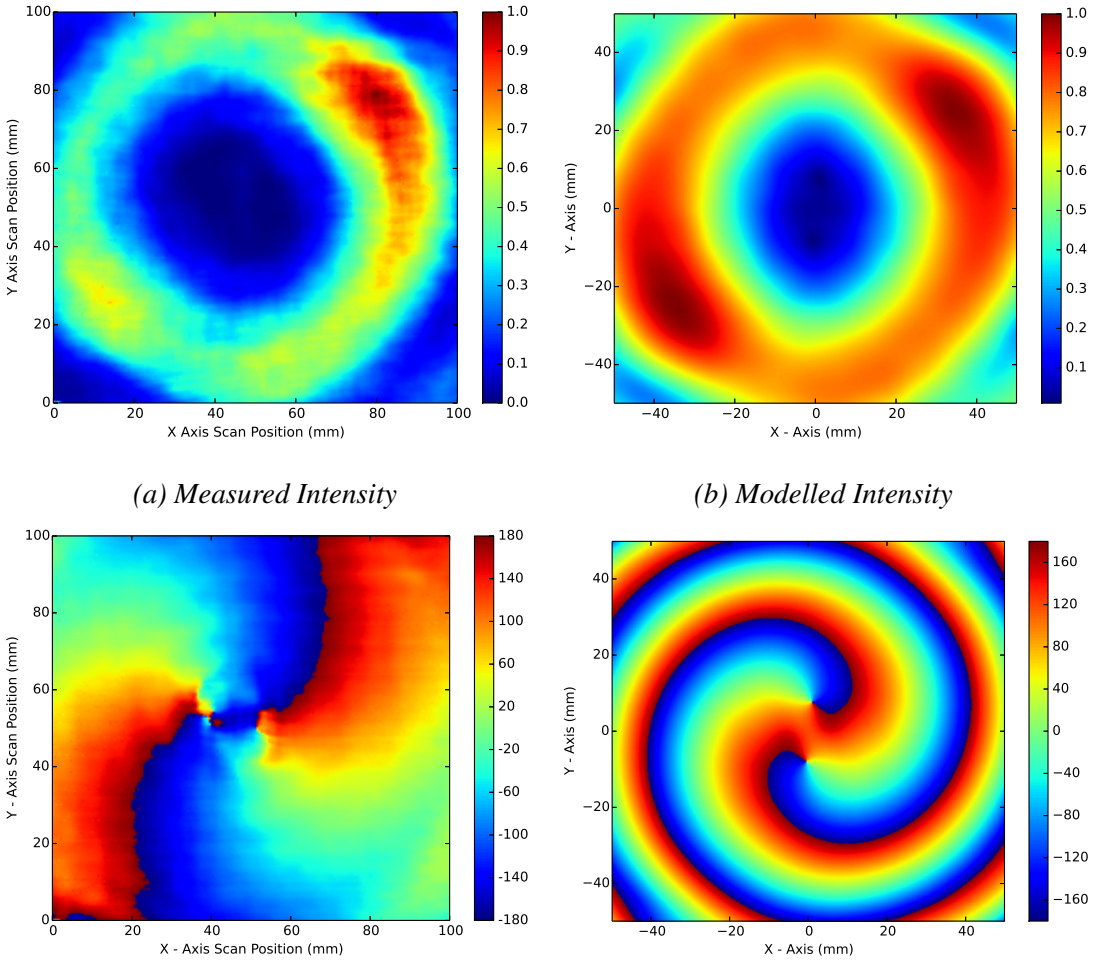

(a) Measured Intensity *(b) Modelled Intensity*

(c) Measured Phase *(d) Modelled Phase*

Figure 6.32: Intensity and phase comparison between the Gaussian beam measured and modelled data $\Delta l = \pm 2$ split configuration SPP on the 73.3λ surface.

$\Delta l = \pm 2$ split configuration SPP measurement and model review

The $\Delta l = \pm 2$ split configuration SPP shows some interesting features not seen in the other SPP designs. Surprisingly, the modelled plane wave illuminated case on the 73.3λ

surface (Fig. 6.30), showed a better match to the measured data then the aperture source case (Fig. 6.28). This was an unexpected result since all previous cases showed that while the plane wave and aperture sources produced similar patterns, the aperture source was slightly closer to measurements. In either case, both the plane wave and aperture illuminated models properly predicted phase circulations on both the 40λ and 73.3λ surface. Gaussian illuminated models predicted the measured intensity patterns very well. Regions of high and low intensity due to both primary SPP steps were predicted in addition to the elliptical central intensity nulls. Furthermore, the radial extent of the measured and modelled intensity patterns matched at both propagation distances. However, the Gaussian illuminated models continued to predict more BC spiralling about the propagation axis, not seen in the measured data.

6.9 Conclusion

This chapter has presented normalised intensity and phase data for a sixteen steps-per-mode $\Delta l = \pm 1$, a sixteen steps-per-mode standard configuration $\Delta l = \pm 2$ and a sixteen steps-per-mode split configuration $\Delta l = \pm 2$ SPPs. Measurements of each plate were conducted using a CTRA producing a low divergent Gaussian beam with a quasi-planar phase front, and a corrugated feed horn antenna with a spherical phase front and high divergent Gaussian intensity profile. Both sources had advantages and drawbacks. For example, the CTRA source suffered from mount induced diffraction. However, the quasi-planar phase front illuminated the SPP evenly and ensured that the small angle approximation used in the analytical theories was achieved. On the other hand, the corrugated feed antenna had a highly divergent beam and a spherical phase front. The small angle approximation may not have been as valid over the entire range of this set up, and the SPP was not illuminated uniformly across the diameter. However, the beam did not suffer from mount induced diffraction, which resulted in purer transmission. Background measurements were taken for each incident beam, and were used to normalise the phase patterns.

Measurements of the SPPs illuminated by the CTRA showed similar features. For example, additional BC and BPs were generated on the 40λ surface. These are due to a non-integer azimuthal mode number. Such modes can not exist, and therefore the SPP generates a finite number of additional BPs. As the beam propagates closer to the far field, these additional BPs annihilate. This was experimentally proven by observation of the 73.3λ surface, where the additional BPs often were not present or, at a minima, decreased in strength. Measurements generated by the corrugated feed antenna showed fewer diffraction features, and did not always have these additional BPs. This is due to a more purely transmitted beam. In addition, the high divergence of the incident beam pulled the BPs apart. As the BPs pulled apart they were not able to annihilate with a BP of opposite helicity, and therefore survived. A comparison of the standard and split configuration $\Delta l = \pm 2$ SPPs indicated that in both the CTRA and the corrugated feed antenna cases, the split configuration was more symmetrical and had fewer deformities. This is expected due to the decrease in the primary step height, resulting in a closer approximation to the analytical expectation that the SPP is only a phase modulating and not an amplitude modulating device as well.

The following chapter details the development of a new modular SPP design. This modular design was used to make a $\Delta l = \pm 10$ SPP, and was measured using the same systems as was used here.

7

Modular Spiral Phase Plate

A significant majority of this work was published in [28]. For brevity, further in-text citations of this paper are omitted from this Chapter.

7.1 Introduction and Motivation

As the desire to build more sophisticated OAM sensitive equipment increases, so does the need to manipulate large numbers of OAM modes. In the visible regime, where wavelengths are measured in nanometers, this is easily accomplished by the use of a spatial light modulator (SLM). SLMs are programable liquid crystal displays. In visible wavelength experiments, diffractive holograms are routinely programmed onto SLM displays in order to manipulate OAM states. Since these systems are programable, the displayed hologram profile can be changed rapidly. Unfortunately, there is no readily available counterpart to SLMs at millimetre or radio wavelengths due to the inability to make adjustable microwave holograms. Therefore, individual OAM states must be handled by separate devices independently [69, 70].

Perhaps the simplest method for multiple state manipulation is achieved by using several interchangeable SPPs, where each SPP is designed for one specific OAM state. This requires the development of large Δl SPPs. The standard approach for manufacturing millimetre wave SPPs is to machine the SPP surface geometry into a

single slab of dielectric. Manufacturing SPPs with $\Delta l > \pm 2$ becomes extremely difficult due to the finite size of the available tooling. SPP sections not machined to the proper height introduce a non-integer azimuthal phase shift to the transmitted beam. However, such beams can not exist, as the OAM of the transmitted beam must be quantised [1]. Therefore, pairs of phase vortices are created and annihilated inside the transmitted beam's near field [143].

Two primary designs for $|\Delta l| > 1$ SPPs exist. The simplest method to design high mode plates is to increase the primary step height h. However, as Δl increases, this creates a large discontinuity at the primary step, between the thickest and thinnest part of the SPP. This discontinuity manifests itself as a discontinuity in the transmitted field, and introduces unwanted phase and intensity aberrations. A more advanced approach is the 'split," configuration (Fig. 7.1). Here, the behaviour of some number of $l = 1$ SPPs (specifically a number $b = |l|$) are compressed into a specified angular region $\Theta_b = 2\pi/b$.

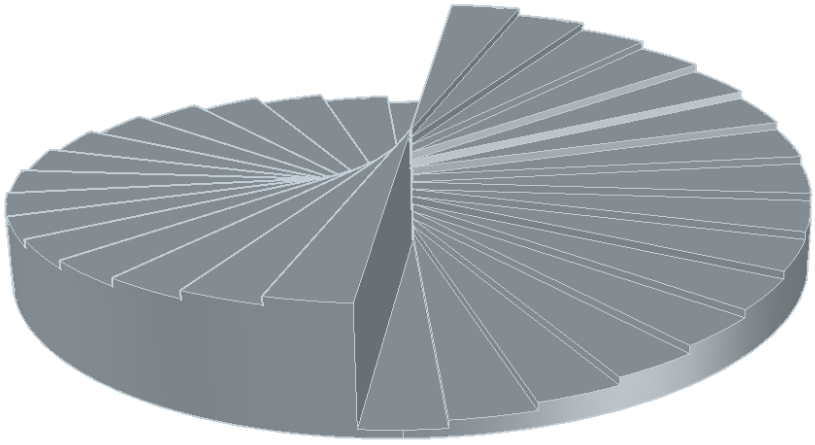

Figure 7.1: A CAD model of a "split stepped," SPP. Here two $\Delta l = \pm 1$ SPPs were compressed from an angular range of $[0, 2\pi]$ to $[0, \pi]$ in order to generate an $l = \pm 2$ LG beam. Adapted from [28].

A solution to high mode number manipulation is to design a "modular," SPP in a split configuration. In such a design, each individual $|l| = 1$ section of the SPP is

machined individually with an additional tongue and groove. This allows each section to be machined to exact height specifications. Afterwards, the modules are assembled into the full SPP. To test this concept a modular $\Delta l = \pm 10$ split configuration SPP was manufactured from polypropylene (index of refraction $n \approx 1.5$), for use at 100 GHz ($\lambda = 3.00$ mm) (Fig. 7.2).

(a) Full $\Delta l = \pm 10$ SPP

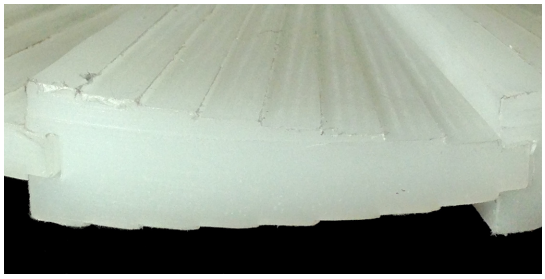

(b) A single module of the full SPP

Figure 7.2: A full $\Delta l = \pm 10$ SPP (a). A single module from the full SPP showing the interlocking tongue and groove system (b). Adapted from [28].

Figure 7.3 shows the soft jaws used to manufacture each modular SPP wedge. This device was used to hold each modular section as in place as a CNC machine was used to shape the top face. A small tongue is visible on the upper right side of the jaws. This was inserted into the machined groove of the modular section. A corresponding groove (not visible in image) on the left side of the jaws is used to position the modular SPP's protruding tongue.

The remaining sections of the chapter detail numerical simulations of the modular SPP, a description of two measurement systems used to test the SPP design and measured results.

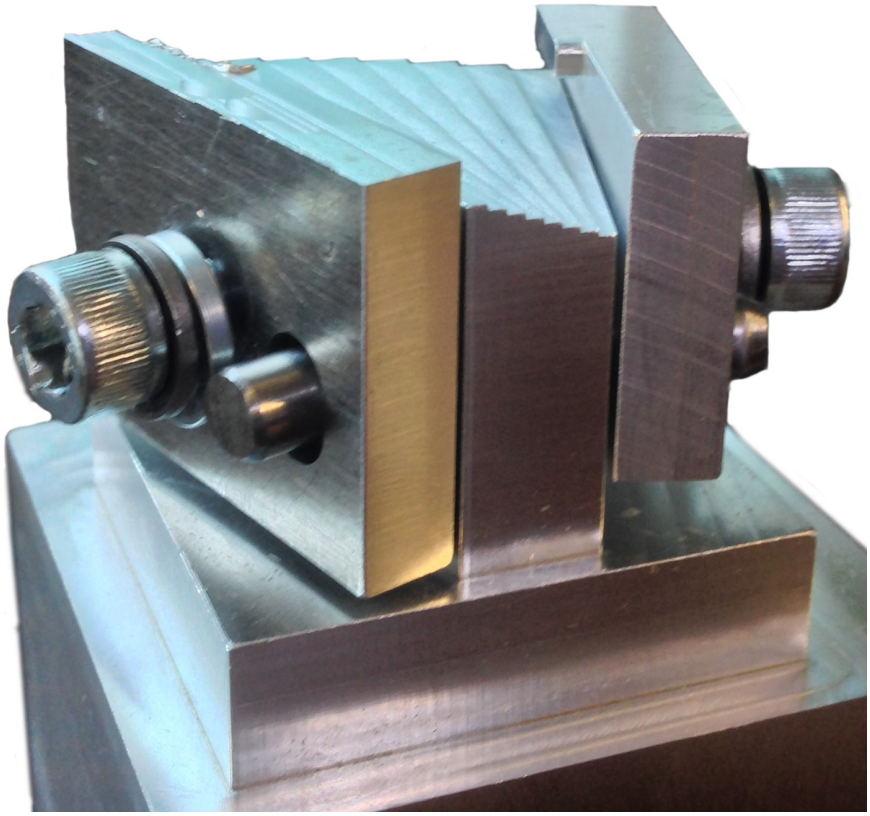

Figure 7.3: Soft Jaws used in the manufacture of the modular SPP wedges.

7.2 Numerical Simulations

Gaussian beam mode analysis (GBMA) was covered in detail in Sec. 3.3.3, and is an important tool for understanding how a SPP will function. To quickly review, GBMA uses a basis set of high order Gaussian modes to describe propagating EM fields. In addition, GBMA may be used to determine the effect of arbitrary phase shifts imposed on propagating beams. This makes it a reasonable choice for SPP analysis. The output of GBMA is a mode spectrum, or the fractional amount of power in a specific Gaussian mode contained in the propagating beam. Standard GBMA techniques may be modified in order to account for the discrete stepped surface of SPPs, split configurations and machining errors. It should be noted that while antireflection coatings and a properly machined SPP surface will produce pure beams with respect to the azimuthal mode number, a superposition of radial modes will remain.

Table 7.1: Mode content, in percentages, of a U_0^0 beam passed through a smooth and an eight-steps-per-mode $\Delta l = 10$ SPP.

Smooth	$l = 10$	0.40	0.90	1.35	1.70	1.94	2.10	2.19	2.22
Stepped	$l = 10$	0.35	0.80	1.20	1.51	1.73	1.87	1.95	1.99
	$\rho =$	0	1	2	3	4	5	6	7

Numerical GBMA simulations of the modular $\Delta l = \pm 10$ SPP were conducted on a field eight times the input beam width (for convergence purposes) comprised of 200×200 points. The decomposition was completed with modes ranging between $-40 \leq l \leq 40$ and $0 \leq \rho \leq 40$. Remember that the number of modes decomposed over does not affect the numerical results (See Section 3.3.6). Recall that SPPs are impure mode converters due to a mismatch between the azimuthal mode number in the phase and complex amplitude terms. Only the azimuthal mode number in the phase term is modified by the SPP, while the complex amplitude is left unchanged. This results in a transmitted beam with a slightly smaller radius then the pure beam modes used for decomposition. For a $\Delta l = \pm 10$ SPP, the difference between the transmitted and pure beam size is large, resulting in very low mode spectrum coefficients and a large number of required decomposition modes (Table 7.1).

However, the decomposition mode beam waist may be optimised since it is a free parameter [19, 76]. Doing this is advantageous because it concentrates a large amount of the mode content into a single Gaussian beam mode, which decreases the number of required decomposition modes and speeds up computation time. To find the optimised decomposition beam waist, several numerical simulations were run using a smooth $\Delta l = 10$ SPP (Fig. 7.4).

These calculations showed that the mode content of a U_0^0 Gaussian beam passed through a $\Delta l = 10$ SPP was maximised when the decomposition beam waist was 7.5 mm. Using this optimised decomposition beam waist, a new mode spectrum may be calculated (Table 7.2).

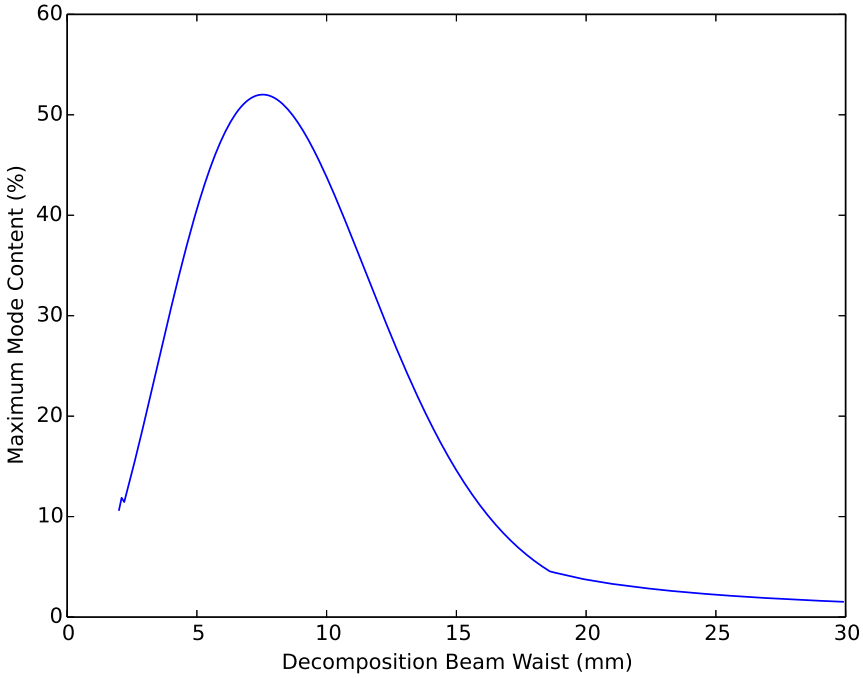

Figure 7.4: Maximum mode content as a function of the decomposition beam waist has a maximum of 52.01% *at* 7.5 *mm. Adapted from [28].*

Table 7.2: Mode content, in percentages, of a U_0^0 *beam passed through a smooth and an eight-steps-per-mode* $\Delta l = 10$ *SPP, with an optimised decomposition mode beamwaist of* 7.5 *mm.*

Smooth	$l = 10$	52.01	0.00	16.61	0.04	8.14	0.13	4.56	0.21
Stepped	$l = 10$	45.40	1.40	15.09	1.71	7.27	1.71	4.31	1.45
	$\rho =$	0	1	2	3	4	5	6	7

A superposition of the calculated mode spectra components of the smooth $\Delta l = 10$ SPP are then used to calculate the final propagated field (Fig. 7.5). The superimposed fields were calculated at a propagation distance of 40λ (120 mm) and 73.3λ (220 mm). Simulations of the intensity (Fig. 7.5a and 7.5c) show a smooth and continuous annular beam pattern. Phase simulations (Fig. 7.5b and 7.5d) show ten spiral phase dislocations or branch cuts (BCs), which surround a small radial node. Curiously, only two BCs are

present inside the radial node, where one would expect to see all ten.

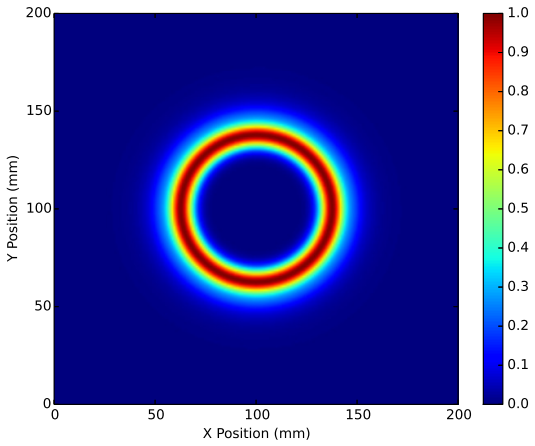

(a) Normalised intensity on the 40λ *(*$120\,mm$*) surface.*

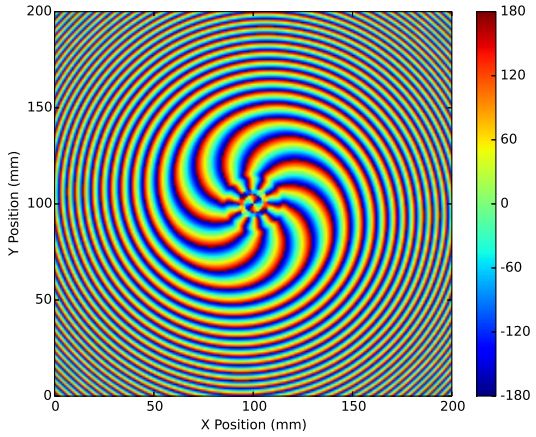

(b) Phase (Degrees) on the 40λ *(*$120\,mm$*) surface.*

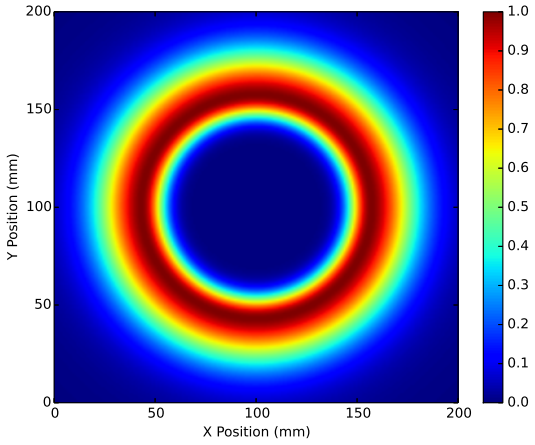

(c) Normalised intensity on the 73.3λ *(*$220\,mm$*) surface.*

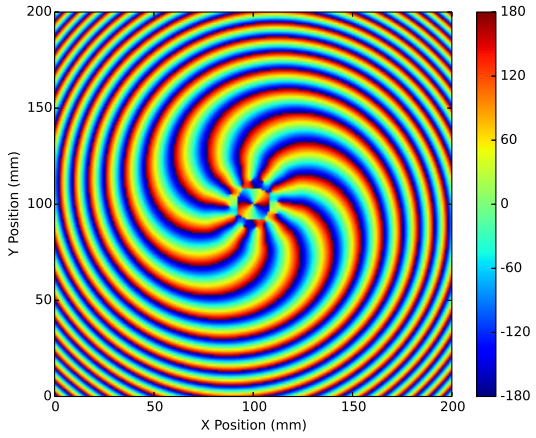

(d) Phase (Degrees) on the 73.3λ *(*$220\,mm$*) surface.*

Figure 7.5: Numerical simulations of a smooth $\Delta l = 10$ *SPP. Normalised linear intensity on both the* 40λ *(*$120\,mm$*) Fig. 7.5a and* 73.3λ *(*$220\,mm$*) Fig. 7.5c measurement surfaces display a continuous annular intensity pattern. A radial node is present in both phase planes (Fig. 7.5b and 7.5d), which bisects each BC. Adapted from [28]. (Note the x- and y-axis extended from* $0.0\,mm$ *to* $200\,mm$ *in order to show the large beam structure on the* 73.3λ *surface.)*

Slightly different intensity (Fig. 7.6a and 7.6c) and phase (Fig. 7.6b and 7.6d) patterns are generated by using the modular SPP mode spectrum. The superimposed fields were calculated at a propagation distance of 40λ (120 mm) and 73.3λ (220 mm). Both intensity patterns are no longer continuous. Instead, each pattern is made up of ten high intensity peaks. Inside the annular intensity pattern is a gear shaped island representing a small increase in intensity. As the beam propagates to 73.3λ the gear shaped island remains roughly the same size. Comparing this to the phase patterns, it is clear that BPs are creating an intensity trough and not the singularity as expected of a pure mode. Further examination of the phase patterns shows ten primary BCs with minor radial nodes breaking off the ends of the BCs. This radial node interference generates ten new BP pairs on the 40λ plane. A second radial node is generated as the beam propagates to the 73.3λ plane, and ten more BP pairs are created.

As useful as standard GBMA can be, it leaves out significant contributions from transmission loss through a dielectric. Dielectric transmission can be studied through simple transmission line modelling. Typically, transmission coefficients for a dielectric slab are calculated as a function of frequency. Because SPPs are designed to work at a single frequency, but vary in thickness, the transmission through each step will instead be calculated as a function of step height. The elementary reflection coefficients needed to calculate the transmission are [18],

$$\rho_1 = \frac{n_{spp} - n_f}{n_{spp} + n_f} \tag{7.1}$$

$$\rho_2 = \frac{n_f - n_{spp}}{n_{spp} + n_f} \tag{7.2}$$

where n_{spp} and n_f are the respective indices of refraction for the SPP dielectric and free space. Using these, the reflectance as a function of SPP thickness (h_{spp}) is,

$$R = \frac{\rho_1 + \rho_2\, exp\left(-2\, i\, k_{spp}\, h_{spp}\right)}{1 + \rho_1\rho_2\, exp\left(-2\, i\, k_{spp}\, h_{spp}\right)} \tag{7.3}$$

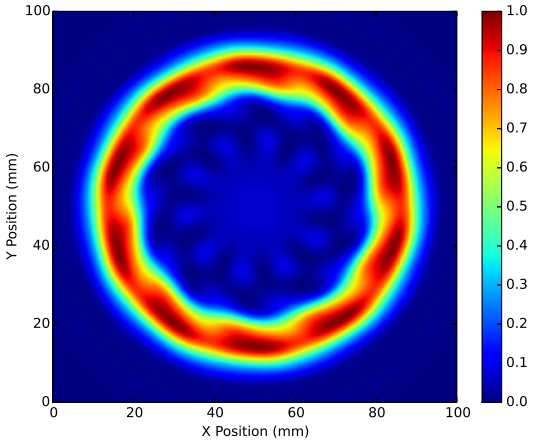

(a) Normalised intensity on the 40λ *(*$120\,mm$*)*

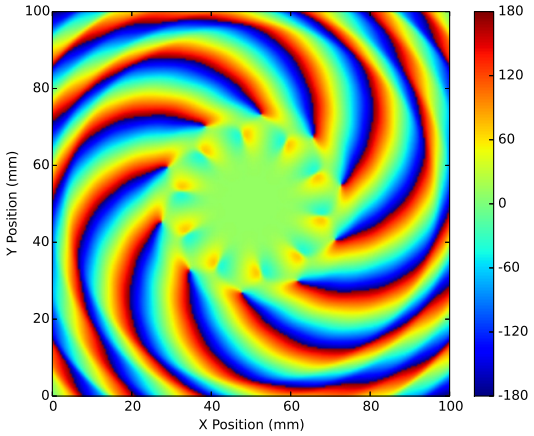

(b) Phase (Degrees) on the 40λ *(*$120\,mm$*) surface.*

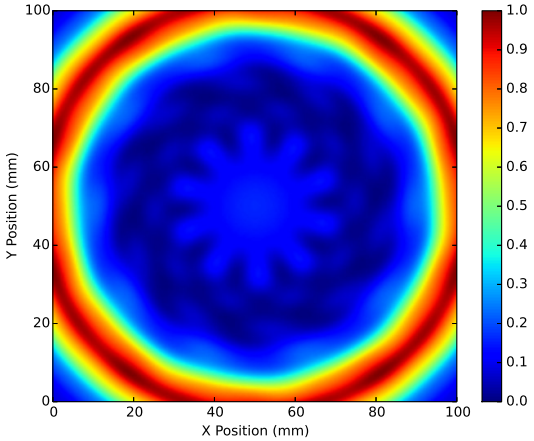

(c) Normalised intensity on the 73.3λ *(*$220\,mm$*)*

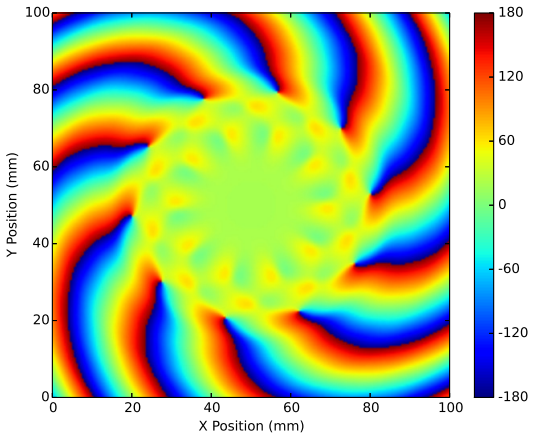

(d) Phase (Degrees) on the 73.3λ *(*$220\,mm$*) surface.*

Figure 7.6: Numerical simulations of a $\Delta l = 10$ *stepped SPP in a split configuration. The normalised linear intensity on both the* 40λ *(*$120\,mm$*) Fig. 7.6a and* 73.3λ *(*$220\,mm$*) Fig. 7.6c measurement surfaces display a discontinuous intensity ring. In both Fig. 7.6b and Fig. 7.6d radial modes generate discontinuities in the phase dislocation lines. Adapted from [28].*

Table 7.3: Measured average and standard deviation step heights for the manufactured $\Delta l = \pm 10$ modular split stepped SPP.

Step Number	1	2	3	4	5	6	7	8
Average Height (mm)	9.88	9.13	8.26	7.45	6.63	5.85	4.99	4.10
Standard Deviation (±mm)	0.12	0.14	0.23	0.21	0.21	0.21	0.20	0.22

where $k_{spp} = 2\pi\, n_{spp}/\lambda_{freespace}$ is the wavenumber inside the dielectric. Finally, the transmission is,

$$T = 1 - R \tag{7.4}$$

Actual averaged individual step heights for each module, and the respective standard deviations, are presented in Table 7.3. These values are used to measure the expected transmission for each step.

Figure 7.7 shows the transmission through each modular SPP step. Each black dot corresponds to the eight discrete SPP step heights (Table 7.3). Transmission is nearly 100% through the thinnest and thickest steps and drops to nearly 86% for the middle two steps.

To conclude this section, the RMS error between intensity patterns generated by smooth and modular $\Delta l = \pm 10$ SPPs has been calculated in order to justify the use of eight steps-per-mode (Table 7.4). It has been shown that discretising SPPs with too few steps leads to azimuthal intensity modulations, while a RMS error below 2% is deemed acceptable [100].

Using eight-steps-per-mode, or a total of eighty steps, results in a 1.37% RMS error between intensity patterns, and is therefore an acceptable deviation from a beam generated by a SPP with a smooth surface (Table 7.4).

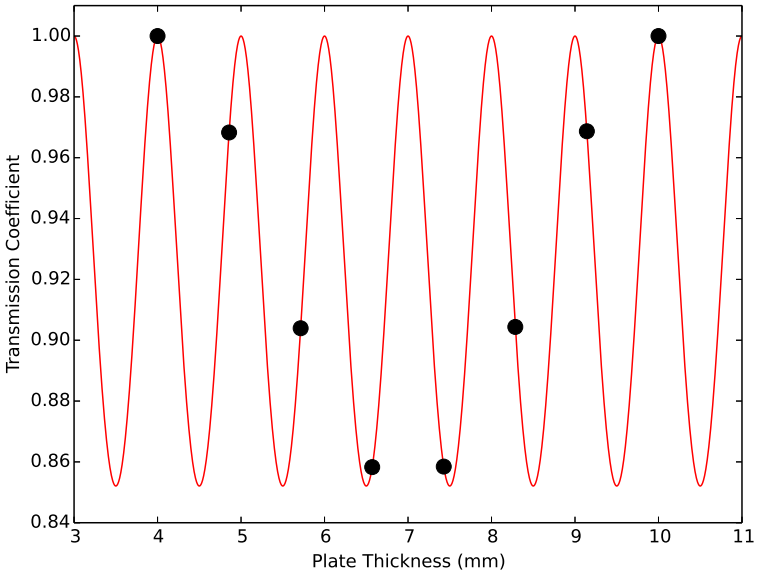

Figure 7.7: Transmission coefficients calculated as a function of SPP thickness (red line). Black dots indicate the eight individual step heights that make up the modular SPP. Adapted from [28].

Table 7.4: RMS intensity pattern error as a function of the number of steps per mode between a perfect and modular split stepped $\Delta l = \pm 10$ *SPP.*

Steps per mode	RMS (%)
4	12.02
5	5.01
6	2.93
7	1.98
8	1.37
9	1.01
10	0.80

7.3 Measurement System

Both measurement systems used in Chapter 6 were reused to measure the modular SPP. A quick review is presented here. A corrugated feed horn antenna [116] and a quasi-planar Gaussian beam from a compact test range antenna (CTRA) [81, 144] were used to illuminate the modular SPP. The three dimensional field scanner detailed in Chapter 5 was used to measure the transmitted field parameters. Measurements for both sources were taken at 100 GHz. Measurements of the field were conducted on three surfaces perpendicular to the propagation axis. These surfaces were located 4.7λ, 40λ and 73.3λ (20 mm, 120 mm and 220 mm) behind the SPP centre. Each surface was $33.3\lambda \times 33.3\lambda$ (100 mm $\times$ 100 mm) and was measured with a positioning resolution of 0.17λ or 0.5 mm.

Figure 7.8: CAD renderings of the SPP mount designed for these experiments. A slotted base is used to position the mount on an optical bench or three-axis positioning stage. The mount surface and support are angled to minimise reflections and reduce standing waves. A SPP is placed inside the mount and secured with a threaded backing ring.

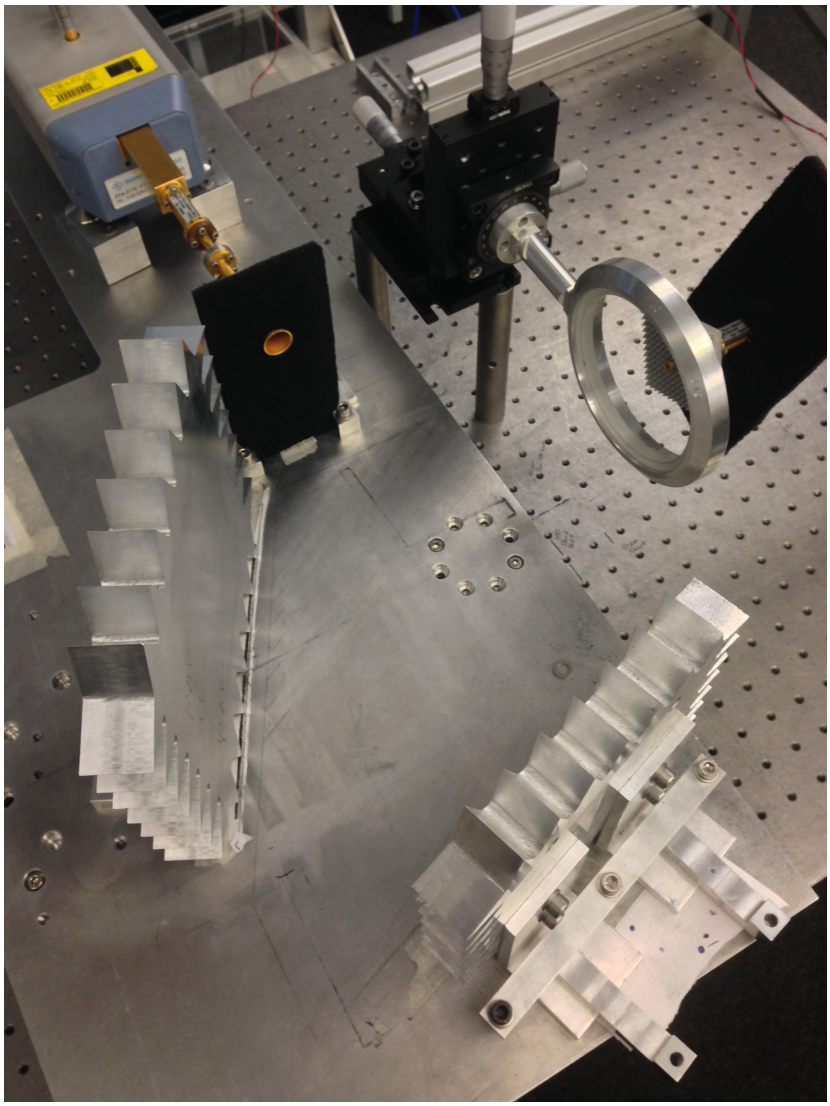

Figure 7.9: A Gaussian beam is generated by the feed horn and is reflected by both CTRA mirrors. The beam then propagates to the SPP mount and is measured by the WR-10 probe (Fig. 7.9). (Not pictured is the absorbing material surrounding the mounting structure.

7.3.1 CTRA

A low divergent Gaussian beam with quasi-planar phase fronts and a large beam waist was generated by the CTRA by reflecting a Gaussian beam from a corrugated feed horn antenna using a main and sub reflector (Fig. 7.9). A new beam waist, approximately 25 mm, is generated 265 mm from the main reflector (Fig. 6.3b and 6.3c). A custom designed SPP mount (Fig. 7.8) was centred on the generated beam waist.

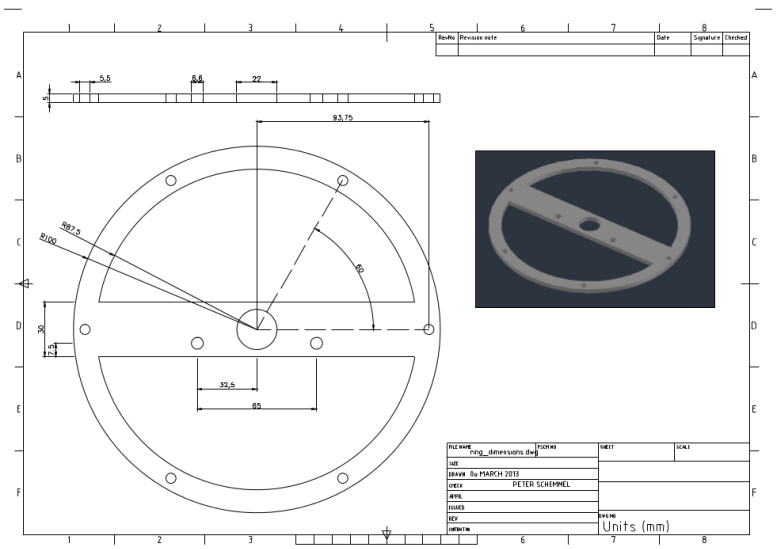

Figure 7.10: Technical dimensioned drawing for the custom designed ring mount for the corrugated feed antenna. Six M5 bolts secure the ring to the azimuthal rotation stage, while two M6 bolts attached the antenna clamp (Fig. 7.11).

7.3.2 Corrugated Feed Antenna

A corrugated feed antenna was also used to illuminate the modular SPP. The antenna operates in the W-band (75 − 110 GHz) and has a beam waist of roughly 4.0 mm at the 100 GHz measurement frequency. It was mounted in an azimuthal rotation stage with a custom designed ring mount. This ring mount (Fig. 7.10 and 7.11) is used to ensure that the antenna is properly aligned to the rotation stage and SPP, while also providing a support for a 3D printed absorber panel used to minimise standing waves between

mounting surfaces. To minimise mount induced diffraction effects, the antenna was placed 150 mm from the SPP. This illuminated the mount edges with the first beam nulls at roughly −40 dB.

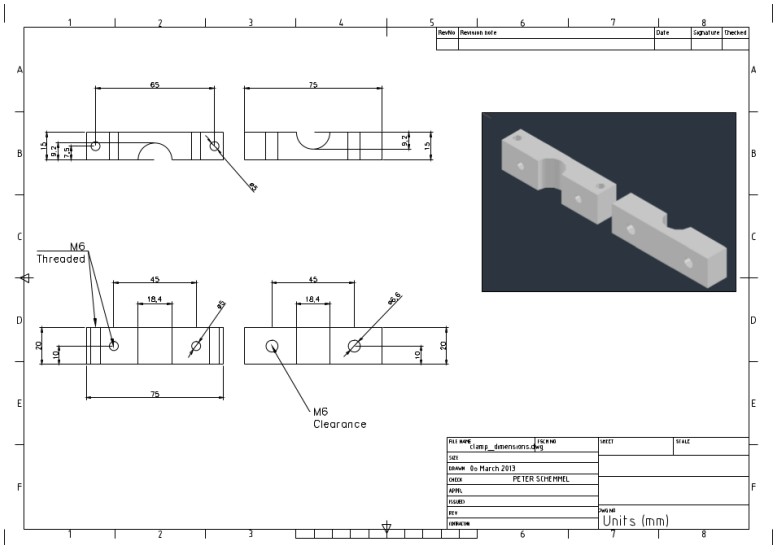

Figure 7.11: Technical dimensioned drawing for the custom designed antenna clamp used in conjunction with the ring mount (Fig. 7.11). A bottom clamping block is secured to the ring mount via two M6 bolts. The antenna feed horn is placed in the bottom clamping block and secured with a top clamping block, secured to two additional M6 bolts.

7.4 Measurements

Before the modular SPP was measured with either source type, background measurement were taken. These results have already been presented in Sec. 6.4. Recall that the averaged edge taper of the CTRA and corrugated feed systems was −4.7 dB and −40 dB respectively. Also note, that the phase backgrounds indicated that there was a $\theta = 0.358°$ tilt in one of the CTRA's reflectors. In the following measurements, the intensity was normalised to the maximum obtained value, while the phase was normalised to the background by

$$arg\left(E_{transmitted}\right) = arctan\left[Imag\left(\frac{E_{measured}}{E_{background}}\right), Real\left(\frac{E_{measured}}{E_{background}}\right)\right] \tag{7.5}$$

where $E_{measured}$ and $E_{background}$ are the full complex fields.

7.4.1 CTRA Measurements

Figure 7.12a and Fig. 7.12b show the normalised intensity and phase of the first measurement surface, 4.7λ (20 mm) from the SPP centre. Due to the close proximity of the probe to the SPP, the intensity pattern is dominated by dielectric transmission (Fig. 7.7) [133–135]. Note how there are ten pairs of high intensity radial lines. These correspond to the thinnest and thickest step, each having nearly 100% transmission. Between each of these pairs is a thin line of relatively lower intensity, cause by the field discontinuity introduced by the large step between the thickest and thinnest SPP steps. Transmission through the middle of each module should lower to a minimum of 86%, however the measured intensity drops to nearly 20% in some regions. Clearly dielectric transmission alone can not account for this feature, and further analysis must be conducted. Measured, background normalised phase indicates that there are ten BCs, each terminating at a BP near the centre of the beam. However, there is a large region of planar phase, which is a result of the large number of radial modes present in the superimposed field. Additionally, the outer circumference of the SPP is clearly visible in the phase pattern.

Propagation to the second measurement surface (40λ from the SPP) shows that the field has matured into a more recognisable LG beam. Dielectric transmission effects can still be seen in the intensity pattern, which is now an annular ring. A small central intensity peak is also visible, and is due to a small misalignment between the central portion of the ten individual modules. Ten BCs are still visible in the background normalise phase pattern. However, the presence of radial modes has split the inner BC segments. Some of the segment ends are still visible as a new BC with an associated pair of BPs. There are three rings of segmented BCs, indicating that there are three

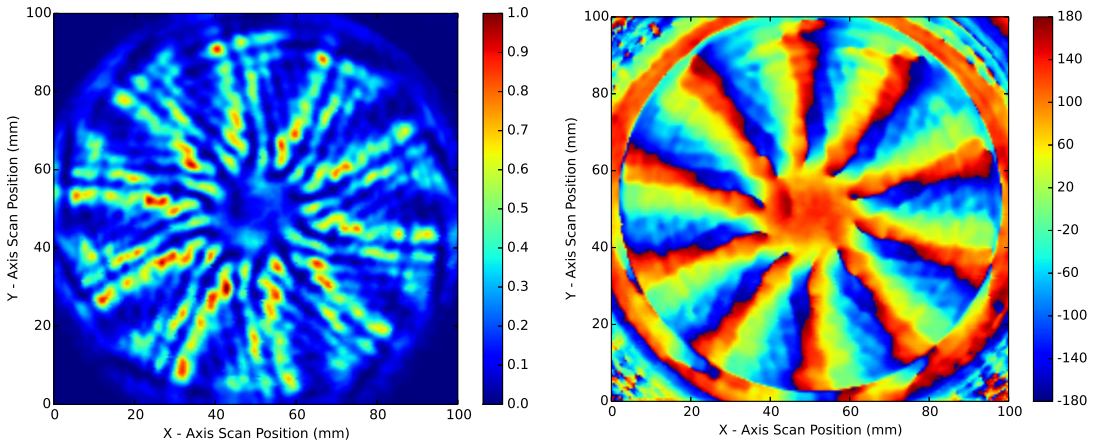

(a) Normalised Intensity *(b) Background Normalised Phase*

Figure 7.12: Normalised intensity and phase of the modular SPP illuminated by the CTRA, on the 4.7λ *measurement surface. A near field "image," of the SPP is seen in the intensity patter, while ten BCs are visible in the measured phase.*

primary radial modes. Several similarities may be seen by comparing the measured intensity and phase to the analytically modelled intensity (Fig. 7.6a) and phase (Fig. 7.6b). First the segmentation of the annular intensity pattern is visible in both fields. While, the transmission losses are much higher then expected in the measured data, the breaking of the annular ring is predicted by the model. Further more, the extra BCs in the measured phase are also seen in the analytical model. As one might expect however, the analytically modelled phase does not show as much detail as is seen in the measured phase.

Low divergence of the incident beam has allowed the generated LG beam to remain highly collimated, even at a distance of 73.3λ (Fig. 7.14a). Dielectric transmission variations modulate the annular intensity pattern, while the central intensity peak due to a misalignment between several modules remains present. Interestingly, the phase pattern has largely smoothed itself into ten primary BCs with one nearly full ring of bisected BCs. There also appears to be a second ring of bisected BCS, however their lengths seem to be too small to be visible with 0.5 mm resolution. It is evident that the

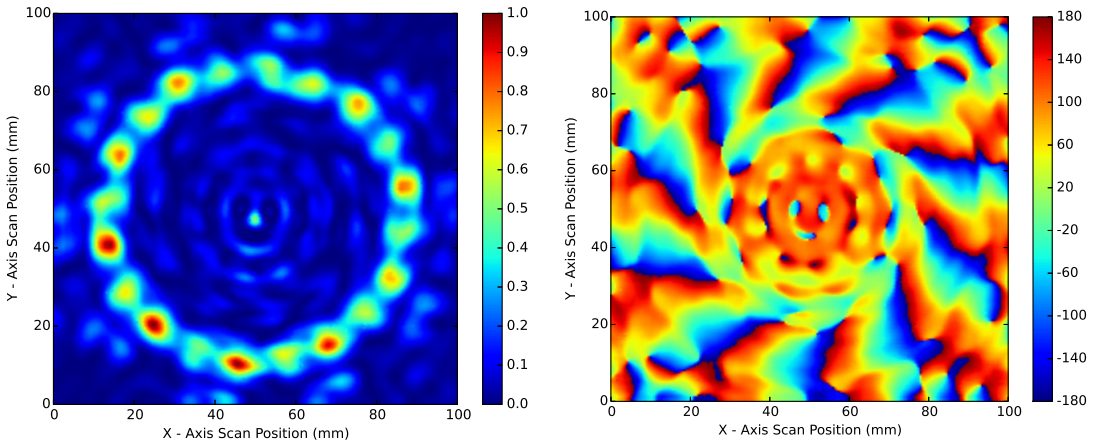

(a) Normalised Intensity *(b) Background Normalised Phase*

Figure 7.13: Normalised intensity and phase of the modular SPP illuminated by the CTRA, on the 40λ *measurement surface. Ten pairs of high intensity regions make up the intensity pattern, while the phase is largely distorted due to a high number of radial modes.*

SPP is behaving as expected by comparing these results to the analytically modelled intensity (Fig. 7.6c) and phase (Fig. 7.6d). First, the radial extent of both the measured and modelled annular intensity rings is very similar. A small disagreement between the two indicates a slightly different beam waist size or location. Segmentation of the annular ring pattern has decreased in both. At the same time, the BP locations have moved to a slightly larger radius. In addition, two breaks in the ten BCs are present in both, while the chaotic central region of the measured phase begins to smooth.

7.4.2 Corrugated Feed Antenna Measurements

Analysis of the intensity (Fig. 7.15a) generated by the modular SPP on the 4.7λ measurement surface shows that transmission through the SPP dielectric (Fig. 7.7) and dominates the beam pattern. Quasi-planar phase in the centre of the beam (Fig. 7.15b) gives rise to a relatively flat central intensity. Ten intensity nulls can be seen, and are associated with the ten BPs. Radial lines of high intensity propagate from the beam's

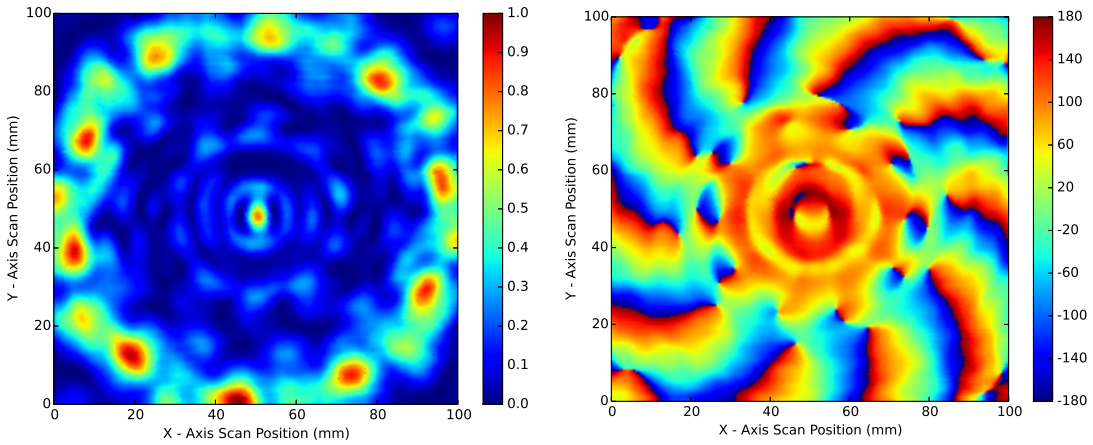

(a) Normalised Intensity *(b) Background Normalised Phase*

Figure 7.14: Normalised intensity and phase of the modular SPP illuminated by the CTRA, on the 73.3λ measurement surface. Large phase distortions seen in Fig. 7.13b have been smoothed out as the beam propagates towards the far field. A small intensity peak is present in the middle of the pattern, and is due to a misalignment between the individual SPP models.

centre towards the beam edge, and are separated by regions of relatively low intensity caused by multiple internal reflections.

Due to the divergence of the incident beam, the intensity pattern generated by the modular SPP reaches the far extents of the 40λ measurement surface (Fig. 7.16). Central intensity rippling is visible, and are remnants of minor mount diffraction effects. Regions of near zero intensity are visible just inside the main intensity ring. These are associated with the ten BPs seen in the background normalised phase pattern (Fig. 7.16b). Unwanted radial modes, present in the mode spectrum, push the BPs radially outward from the propagation axis. This creates a large quasi-planar phase front in the beam centre.

A combination of high mode number ($l = 10$) and high incident beam divergence has caused the propagating beam's annular intensity ring to have a larger radius than the extents of the 73.3λ measurement surface (Fig. 7.17). However, small interference

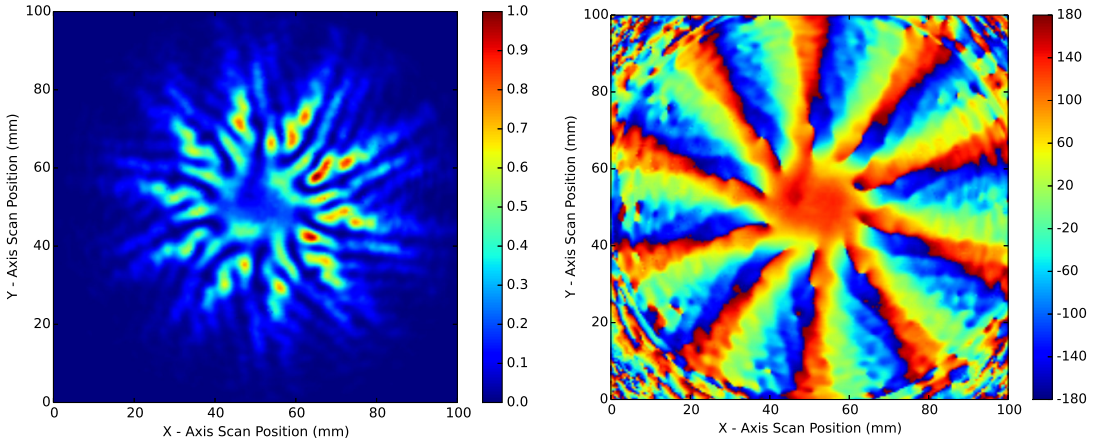

(a) Normalised Intensity *(b) Background Normalised Phase*

Figure 7.15: Normalised intensity and phase of the modular SPP illuminated by the corrugated feed antenna, on the 4.7λ *measurement surface. A near field "image," of the SPP is superimposed onto a Gaussian distribution. Ten BCs are visible in the measured phase data.*

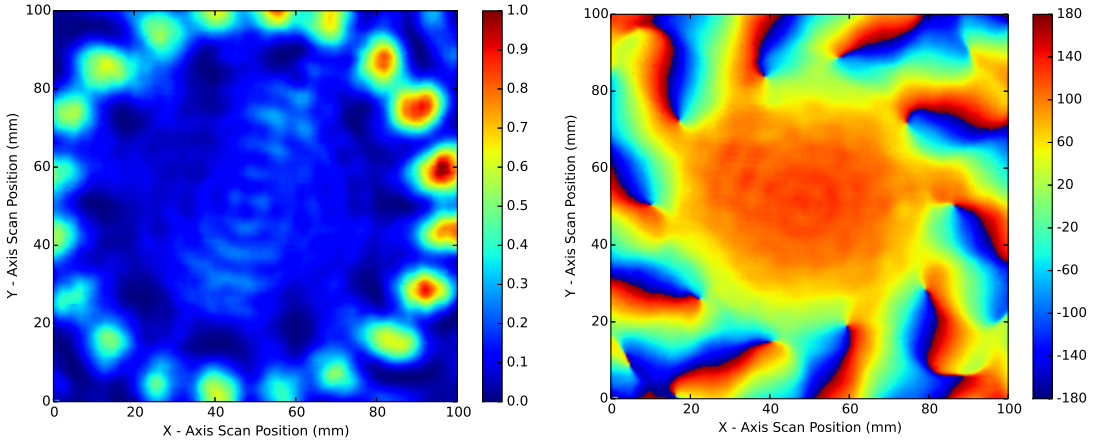

(a) Normalised Intensity *(b) Background Normalised Phase*

Figure 7.16: Normalised intensity and phase of the modular SPP illuminated by the corrugated feed antenna, on the 40λ *measurement surface. Due to the relatively large divergence of the corrugated feed's beam pattern and the large azimuthal mode number of the SPP, the intensity pattern extends to the edges of the measurement surface. Phase measurements show ten BCs, and a central planar phase region.*

fringes from the SPP mount are visible in the beam centre. Additionally, the phase pattern resembles a propagating Gaussian beam.

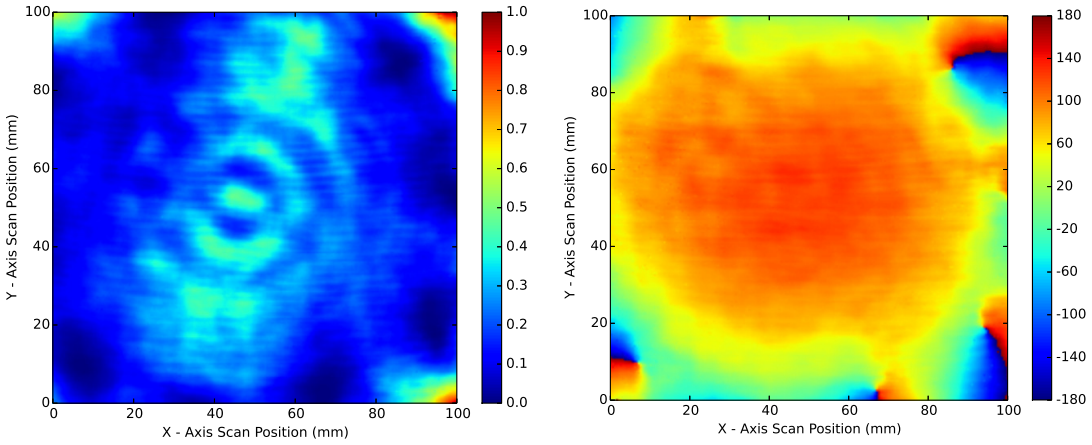

(a) Normalised Intensity

(b) Background Normalised Phase

Figure 7.17: Normalised intensity and phase of the modular SPP illuminated by the corrugated feed antenna, on the 73.3λ *measurement surface. The intensity pattern has diverged past the extend of the measurement surface. However, this yields a detailed analysis of the central portion of the beam. Phase measurements show ten BCs, and a central planar phase region.*

7.5 Conclusion

This chapter has addressed the need for SPPs capable of handling large OAM mode numbers by designing, manufacturing and testing a $\Delta l = \pm 10$ modular SPP. Modular SPP designs help improve machining accuracy by eliminating the need for infinitesimally small tooling. Typical split and stepped SPP configurations were combined, and each $\Delta l = \pm 1$ section of the SPP was manufactured individually. Finally, each modular section as assembled into the full SPP. Numerical GBMA simulations were conducted to model the generated beam. Due to the large mode number, a non-optimised decomposition beam waist resulted in a high number of required decomposition modes, each

contributing only a small amount of power to the final field. To resolve this issue, and speed up computation time, the decomposition beam waist was optimised. Final field superpositions were calculated using the optimised beam waist. Transmission characteristics were also modelled with simple transmission line codes. Finally, the modular SPP was tested using a Gaussian beam with a quasi-planar and spherical phase front. Results showed that the beam pattern was largely dominated by the SPP transmission function, and multiple reflections inside the SPP surface. Radial modes were also shown to bisect sections of the ten primary BCs, thereby creating new BP pairs. As the beam propagated further into the far field these distortions were minimised.

8

Conclusions and Future Work

8.1 Introduction

Presented here is a short review of each chapter's contents, followed by my thoughts on the work yet to be done on millimetre orbital angular momentum studies Specific interest was placed on phase modulating devices known as spiral phase plates. Analytical simulations and computational modelling of spiral phase plates using FEKO was carried out for three spiral phase plate designs in Chapter 4. A three dimensional field scanner was developed in Chapter 5, and was used to measure the three SPPs in Chapter 6. A unique modular spiral phase plate was designed, fabricated and tested in Chapter 7.

8.1.1 Chapter 3

Chapter 3 explored various ways that beams with OAM may be generated. These included natural mechanisms and so called synthetic, or laboratory made, OAM. Following this, a review of several phase modulating devices was conducted. First, the hologram, or a diffraction grating containing a singularity was discussed. Following this was the Q-Plate. This device interchanges spin angular momentum states and in turn generates OAM. A large section of work was completed on spiral phase plates. SPPs are the simplest and most versatile type of OAM manipulating device for millimetre and

radio wavelengths. SPPs have a helical surface geometry and may be easily machined. The equation relating the primary step height, index of redaction, mode number and incident wavelength was derived from simple optics expressions. In addition, a simple ray optics model and Snell's Law was used to show how SPPs can generate quantised OAM. Gaussian beam mode analysis for SPP use was also discussed. Then, several SPP designs were reviewed. These included smooth versus stepped SPPS, standard versus split configurations and even modular designs. Concluding the chapter was a review of OAM applications. These included OAM coronagraphy, OAM based communications, and spiral imaging.

8.1.2 Chapter 4

Analytical and computational modelling of a $\Delta l = \pm 1$, a standard configuration $\Delta l = \pm 2$ and a split configuration $\Delta l = \pm 2$ SPP were conducted in Chapter 3. Work began by using a self written GBMA code to determine the mode content of transmitted beams through each SPP. The GBMA code also allowed for modified configurations, such as smooth, stepped, split and modular. Mode spectra for each design was analysed. In addition to this, the mode spectra were used to recreate the superimposed field. From these generated fields, various features of SPP generated beams were understood. These features included an annular intensity pattern, a spiralling BC in phase and termination point (BPs). In addition, phase circulations and radial nodes were visible.

After this, computational models of each plate were developed using FEKO. All three SPP designs were tested using a plane wave, aperture source plane wave and corrugated feed antenna as incident fields. This would allow for a comparison of SPP functionality under different initial conditions. It also lead to the ability to analyse different aspects of OAM generation. Transmitted fields were modelled on three different planes, each corresponding to the three measurement planes used in Chapter 5 and Chapter 6. All modelling was conducted at 100 GHz. This modelling analysis was done in three successive stages. First, the incident beams were modeled free from any

other component or device. Secondly, the incident wave was analysed with only the SPP mounting structure. This allowed for insight into how the SPP mounting structure would impact measurements. It was found that the plane wave and aperture sources produced mount induced diffraction effects in the transmitted beams, but illuminated the SPPs evenly. On the other hand, the corrugated feed antenna did not illuminate the SPP evenly, but did not produce undesirable diffraction. Finally, each incident beam was tested in conjunction with each SPP design, on each of the three measurement planes and in linear intensity, dB intensity and phase.

8.1.3 Chapter 5

Characterisation of the three dimensional field scanner, used to measure beams generated by the SPPs, was conducted in Chapter 4. A VNA frequency converter is used to reach the W-Band. One of these converters is connected to the source antenna, while the other one powers the probe. The probe is placed on the three dimensional field scanner carriage.

A significant amount of time was spent reviewing the stability of the VNA. For long scans, stability becomes an issue. The stability of our system was not desirable. Improvements were attempted, but none had the expected effect. Instead, improvements to the control software allowed for much faster scanning (6 hour scans were cut down to 1 hour). This reduction is scanning time meant that the long term stability issues were no longer a major concern. A review of probe and planar scanning planar scanning corrections are reviewed. Correction for the probe beam pattern adjust for the probe "seeing," the measured field at various levels. Geometrical corrections are required to compare planar scanned data and far field models.

A validation of the scanning system and methodology were conducted by scanning the far and near field of a corrugated feed horn antenna. Far field measurements were compared to previous measurements and validated models. Cuts in both the x- and y- directions were taken. Results showed very little difference between the model

and measurement. After this success, the near field of the antenna was measured and compared to previously un-validated modes. Measurements at three different distances were conducted and all resulted in a good agreement to the models. To show that this system could also measure compound devices, two dimensional planes of a dielectric lens were measured.

8.1.4 Chapter 6

Detailed measurements of the three SPP designs were carried out in Chapter 5. Initial proof of concept measurements were conducted on the $\Delta l = \pm 1$ SPP. These measurements proved the SPP manufacture, the measurement system and methodology worked as expected.

Following these proof of concept measurements, background data was taken. These backgrounds were used to normalise the measured phase. Features seen in the modelling, such as radial nodes, phase circulations, breaking of the BC and lack of diffraction distortions in the corrugated feed antenna patterns were also seen in the measurements.

8.1.5 Chapter 7

Due the success of the previous SPP designs, a unique modular SPP designed to generated a $l = \pm 10$ was then developed. This design has possible applications to OAM based communications and OAM astrophysics.

Analytical simulations of the SPP design was compared to smooth and stepped configurations. It was shown that the mode content of the GBMA results were extremely small. This is due to a mismatch between the pure decomposition modes and the actual field. To fix this problem, the decomposition beamwaist was optimised, and the mode decomposition and final field calculations were recalculated. The modular SPP was then measured using the corrugated feed horn antenna and CTRA sources. Impressive results were achieved in both cases.

8.2 Achievements of the Thesis

This thesis has produced multiple advances in the field of millimetre wavelength OAM research. At the beginning of this work, publications on millimetre wavelength OAM were extremely rare. Two first authored peer-revised papers, one first authored conference paper and a conference poster were produced from the work encapsulated in this thesis. It is hoped that this will help to spur additional research into millimetre wavelength OAM. In addition to these deliverables, multiple scientific advances have been accomplished. First, analytical GBMA analysis was applied to several SPP designs. These models were compared and showed differences between each SPP design. Computational electromagnetic modelling was also conducted on several SPP designs for the first time. A three dimensional field scanner was developed to measure OAM beams. Both the control software, written in labview, and the analysis software, written in Python, were developed by the author. Exceptional accuracy has been achieved and the creation and annihilation of vortices may have been observed. This system is now being used in several other research projects. Finally, a new SPP design, the modular SPP, was developed especially for this thesis. Again, it is hoped that these achievements will help promote millimetre OAM research and lead to additional developments in the field.

8.3 Future Work on OAM

I would like to end this thesis with a short exploration into the future work on OAM I plan to undertake. Some of this work is already under progress, or was first investigated before but did not make it into this thesis. Most of this future work is focused on the further development of PMTs for astrophysical observations of OAM. Yet, some of these future works explore new applications for OAM research.

Currently under study is the development of 10 GHz OAM reflecting dish receiving system. The intent is to use this system to simulate measurements of astrophysical

OAM. This system utilises a 110 cm diameter commercial satellite dish and a modified commercial feed antenna. A SPP was designed to generate a $\Delta l = \pm 1$ beam at 10 GHz, and is connected to the feed support arm via a custom designed 3D printed mounting system. This system utilises the simplest PMT design, and places the SPP in between the feed antenna and reflecting dish.

Some other future works intended to extend PMT develop include the design of mesh grid (or meta-material) SPPs. These are SPPs, which use stacks of metal grids to induce an azimuthal phase shift. This approach was used to develop a mesh grid lens [112]. The advantage of this system is that mesh SPPs do not have an azimuthally varying thickness and therefore diffraction contamination is minimised. Mode conversion efficiency for several SPP designs must be measured as well. Equations to describe and measurements to extract the pertinent parameters were derived in unpublished work. A calculation of the mode conversion efficiency for a specific SPP design is necessary for PMTs because this efficiency must be used to determine the minimum signal level required to declare an OAM detection. A third future project relevant to PMT design is the measurement of SPP systematics. Specifically, reduced SPP performance as a function of SPP position offsets from and rotations about the feed antenna propagation axis must be measured. Finally, OAM spiral imaging systems should be developed. These systems are in essence a PMT, but are designed for image retrieval at relatively short terrestrial propagation distances. However, developing the small scale OAM telescopes is essential to developing a firm understanding of PMT operation. In addition to a pure OAM imaging system, it would be very interesting to develop and OAM based radar system. Such a system is another step towards full scale PMTs, and could also become a new practical OAM application.

Appendix A

From Electro- and Magnetostatics to the Helmholtz Wave Equation

A.1 Introduction

Classical electrodynamics is described by the four Maxwell equations. These equations show how electric and magnetic fields are generated and propagate. Since Maxwell's equations form the basis of electromagnetic fields, it is important to understand where these equations come from and how the describe propagating fields, before a discussion of the OAM of these fields takes place. Maxwell's equations can be found in numerous textbooks, however a rigorous derivation is not typically included. Therefore, this appendix starts with electro- and magnetostatics, develops the Maxwell equations and finally derives the Helmholtz wave equation. For more information on the subject the reader is referred to [16–18].

A.2 Electrostatics

It has been experimentally shown that the force on a test charge q' due to a stationary source charge q is known as Coulomb's Law,

$$\boldsymbol{F}(\boldsymbol{r}) = \frac{qq'}{4\pi\epsilon_0}\frac{\boldsymbol{x}-\boldsymbol{x'}}{|\boldsymbol{x}-\boldsymbol{x'}|^3} = \frac{qq'}{4\pi\epsilon_0}\frac{\hat{r}}{r^2} = \frac{-qq'}{4\pi\epsilon_0}\nabla\left(\frac{1}{|\boldsymbol{r}|}\right) \tag{A.1}$$

since,

$$-\nabla\left(\frac{1}{|\boldsymbol{r}|}\right) = \frac{-d}{dr}\left(\frac{1}{|\boldsymbol{r}|}\right)\hat{r} = \frac{\hat{r}}{r^2} \tag{A.2}$$

where ϵ_0 is the permitivity of free space, $\boldsymbol{r} = |\boldsymbol{r}|\,\hat{r}$. The electric field is then defined as,

$$\boldsymbol{E}(\boldsymbol{r}) = \frac{\boldsymbol{F}(\boldsymbol{r})}{q'} = \frac{q}{4\pi\epsilon_0}\frac{\hat{r}}{r^2} = \frac{-q}{4\pi\epsilon_0}\nabla\left(\frac{1}{|\boldsymbol{r}|}\right) \tag{A.3}$$

or,

$$\boldsymbol{E}(\boldsymbol{x}) = \frac{-q}{4\pi\epsilon_0}\nabla\left(\frac{1}{|\boldsymbol{x}-\boldsymbol{x'}|}\right) \tag{A.4}$$

Coulomb's law holds even if the charges are not discrete, but form a continuous distribution. In this case the elemental charge dq is equal to the product of the charge density ρ and the differential volume element.

$$dq = d^3x'\rho(\boldsymbol{x'}) \tag{A.5}$$

Equation (A.4) then becomes,

$$\boldsymbol{E}(\boldsymbol{x}) = \frac{-1}{4\pi\epsilon_0}\int_V \rho(\boldsymbol{x'})\,\nabla\left(\frac{1}{|\boldsymbol{x}-\boldsymbol{x'}|}\right)d^3x' \tag{A.6}$$

In order to know everything thing about the electric field the divergence and curl of the field must be found [16]. The partial integration identity [20] may be used to find the divergence of the electric field.

$$\nabla\cdot\nabla\int_{V'} d^3x'\frac{A(\boldsymbol{x'})}{|\boldsymbol{x}-\boldsymbol{x'}|} = \int_{V'} d^3x' A(\boldsymbol{x'})\,\nabla^2\left(\frac{1}{|\boldsymbol{x}-\boldsymbol{x'}|}\right) = -4\pi A(\boldsymbol{x}) \tag{A.7}$$

Applying this to (A.6) we find,

$$\nabla \cdot \boldsymbol{E}(\boldsymbol{x}) = \frac{-1}{4\pi\epsilon_0}\nabla \cdot \nabla \int_{V'} d^3x' \frac{\rho(\boldsymbol{x}')}{|\boldsymbol{x}-\boldsymbol{x}'|} = \frac{-4\pi\rho(\boldsymbol{x}')}{-4\pi\epsilon_0} = \frac{\rho(\boldsymbol{x})}{\epsilon_0} \tag{A.8}$$

leaving,

$$\boxed{\nabla \cdot \boldsymbol{E}(\boldsymbol{x}) = \frac{\rho(\boldsymbol{x})}{\epsilon_0}} \tag{A.9}$$

To find the curl of the electric field it is noted that the curl of the gradient of a scalar function is equal to zero.

$$\nabla \times \nabla\alpha(x) = 0 \tag{A.10}$$

Taking the curl of the electric field from (A.6) we see that,

$$\nabla \times \boldsymbol{E}(\boldsymbol{x}) = \frac{-1}{4\pi\epsilon_0}\nabla \times \nabla \int_{V'} d^3x' \frac{\rho(\boldsymbol{x}')}{|\boldsymbol{x}-\boldsymbol{x}'|} = 0 \tag{A.11}$$

$$\boxed{\nabla \times \boldsymbol{E}(\boldsymbol{x}) = 0} \tag{A.12}$$

Equations (A.9) and (A.12) define electrostatics.

A.3 Magnetostatics

While electrostatics describes the electric field due to stationary charges, magnetostatics describes the magnetic field due to stationary, or steady, currents. The magnetic field of a steady current is given by the Biot-Savart law,

$$\begin{aligned}
\boldsymbol{B}(\boldsymbol{x}) &= \frac{\mu_0}{4\pi}\int_V \boldsymbol{J}(\boldsymbol{x}') \times \left(\frac{\boldsymbol{x}-\boldsymbol{x}'}{|\boldsymbol{x}-\boldsymbol{x}'|^3}\right) d^3x' \\
&= \frac{-\mu_0}{4\pi}\int_V \boldsymbol{J}(\boldsymbol{x}') \times \nabla\left(\frac{1}{|\boldsymbol{x}-\boldsymbol{x}'|}\right) d^3x' \\
&= \frac{\mu_0}{4\pi}\nabla \times \int_V \frac{\boldsymbol{J}(\boldsymbol{x}')}{|\boldsymbol{x}-\boldsymbol{x}'|} d^3x'
\end{aligned} \tag{A.13}$$

where $\boldsymbol{J}(\boldsymbol{x}')$ is a current density and μ_0 is the permeability of free space. Using, the knowledge that the divergence of the curl of a scalar function is equal to zero,

$$\nabla \cdot (\nabla \times \boldsymbol{a}(\boldsymbol{x})) = 0 \tag{A.14}$$

the divergence of the magnetic field is,

$$\nabla \cdot \boldsymbol{B}(\boldsymbol{x}) = \frac{\mu_0}{4\pi} \nabla \cdot \nabla \times \int_V \frac{\boldsymbol{J}(\boldsymbol{x}')}{|\boldsymbol{x} - \boldsymbol{x}'|} d^3x' = 0 \tag{A.15}$$

$$\boxed{\nabla \cdot \boldsymbol{B}(\boldsymbol{x}) = 0} \tag{A.16}$$

To find the curl of the magnetic field the following identity is needed [20],

$$\nabla \times \left(\nabla \times \int_V \frac{\boldsymbol{a}(\boldsymbol{x}')}{|\boldsymbol{x} - \boldsymbol{x}'|} d^3x' \right) = \nabla \nabla \cdot \int_V \frac{\boldsymbol{a}((\boldsymbol{x}')}{|\boldsymbol{x} - \boldsymbol{x}'|} d^3x'$$

$$= -\nabla \cdot \nabla \int_V \frac{\boldsymbol{a}(\boldsymbol{x}')}{|\boldsymbol{x} - \boldsymbol{x}'|} d^3x'$$

$$= 4\pi \boldsymbol{a}(\boldsymbol{x}) - \int_V (\nabla' \cdot \boldsymbol{a}(\boldsymbol{x}')) \nabla' \left(\frac{1}{|x - x'|} \right) d^3x' + \oint_{S'} \hat{n}' \cdot \left(\frac{\boldsymbol{a}(\boldsymbol{x}')(\boldsymbol{x} - \boldsymbol{x}')}{|\boldsymbol{x} - \boldsymbol{x}'|^3} \right) d^2x' \tag{A.17}$$

Applying this to the magnetic field,

$$\begin{aligned} \nabla \times \boldsymbol{B} &= \frac{\mu}{4\pi} \nabla \times \nabla \times \int_{V'} \frac{\boldsymbol{J}(\boldsymbol{x}')}{|x - x'|} d^3x' \\ &= \mu_0 \boldsymbol{J}(\boldsymbol{x}) - \frac{\mu_0}{4\pi} \int_{V'} (\nabla \cdot \boldsymbol{J}(\boldsymbol{x}')) \nabla' \left(\frac{1}{|\boldsymbol{x} - \boldsymbol{x}'|} \right) d^3x' \end{aligned} \tag{A.18}$$

Since magnetostatics requires steady currents the divergence of the current must be equal to zero.

$$\nabla \cdot \boldsymbol{J}(\boldsymbol{x}) = 0 \tag{A.19}$$

Therefore the right side of (A.18) is equal to zero leaving,

$$\nabla \times \boldsymbol{B}\left(\boldsymbol{x}\right) = \mu_0 \boldsymbol{J}\left(\boldsymbol{x}\right) \tag{A.20}$$

Equations (A.16) and (A.20) define magnetostatics.

A.4 Maxwell's Equations

Some corrections to the divergence and curl of the electric and magnetic fields must be applied in order to move from static to dynamic situations. Firstly, the assumption that the divergence of the current is zero is not true in electrodynamics. In general, the divergence of current is,

$$\nabla \cdot \boldsymbol{J}\left(t, \boldsymbol{x}\right) = \frac{-\partial \rho\left(t, \boldsymbol{x}\right)}{\partial t} \tag{A.21}$$

Then,

$$\begin{aligned}
\nabla \times \boldsymbol{B} &= \mu_0 \boldsymbol{J}\left(t, \boldsymbol{x}\right) - \frac{\mu_0}{4\pi} \int_{V'} \left(\nabla \cdot \boldsymbol{J}\left(t, \boldsymbol{x'}\right)\right) \nabla' \left(\frac{1}{|\boldsymbol{x} - \boldsymbol{x'}|}\right) d^3 x' \\
&= \mu_0 \boldsymbol{J}\left(t, \boldsymbol{x}\right) + \frac{\mu_0}{4\pi} \int_{V'} \left(\frac{\partial \rho\left(t, \boldsymbol{x}\right)}{\partial t}\right) \nabla' \left(\frac{1}{|\boldsymbol{x} - \boldsymbol{x'}|}\right) d^3 x' \\
&= \mu_0 \boldsymbol{J}\left(t, \boldsymbol{x}\right) + \mu_0 \epsilon_0 \frac{1}{4\pi\epsilon_0} \frac{\partial}{\partial t} \int_{V'} \rho\left(t, \boldsymbol{x'}\right) \nabla' \left(\frac{1}{|\boldsymbol{x} - \boldsymbol{x'}|}\right) d^3 x' \qquad \text{(A.22)} \\
&= \mu_0 \boldsymbol{J}\left(t, \boldsymbol{x}\right) + \mu_0 \epsilon_0 \frac{\partial}{\partial t} \left[\frac{-1}{4\pi\epsilon_0} \nabla' \int_{V'} \frac{\rho\left(t, \boldsymbol{x'}\right)}{|\boldsymbol{x} - \boldsymbol{x'}|} d^3 x'\right] \\
&= \mu_0 \boldsymbol{J}\left(t, \boldsymbol{x}\right) + \mu_0 \epsilon_0 \frac{\partial}{\partial t} \boldsymbol{E}\left(t, \boldsymbol{x}\right) \\
&\boxed{\nabla \times \boldsymbol{B} - \frac{1}{c^2} \frac{\partial \boldsymbol{E}}{\partial t} = \mu_0 \boldsymbol{J}} \qquad \text{(A.23)}
\end{aligned}$$

A.4.1 Electromotive Force

For linear systems the current density $\boldsymbol{J}$ is proportional to the force per unit charge $\boldsymbol{f}$ such that,

$$\boldsymbol{J} = \sigma \boldsymbol{f} \tag{A.24}$$

where σ is the conductivity of the material. If the force on each charge is electromagnetic in nature $\boldsymbol{f}$ can be replaced by,

$$\boldsymbol{J} = \sigma \left(\boldsymbol{E} + \boldsymbol{v} \times \boldsymbol{B}\right) \tag{A.25}$$

If $\boldsymbol{v} \times \boldsymbol{B} \ll \boldsymbol{E}$ then (A.25) may be simplified to,

$$\boldsymbol{J}\left(t, \boldsymbol{x}\right) \approx \sigma \boldsymbol{E}\left(t, \boldsymbol{x}\right) \tag{A.26}$$

In real systems, a static electric field is not enough to maintain a steady current due to energy loss in the medium. Therefore, the electric field is split into a static component E_s and a second component due to some electromagnetic force E_f.

$$\boldsymbol{J}\left(t, \boldsymbol{x}\right) = \sigma \left(E_s + E_f\right) \tag{A.27}$$

The electromagnetic force can then be defined as,

$$\mathcal{E} = \oint_C \left(E_s + E_f\right) dl = \oint E_s dl + \oint E_f dl \tag{A.28}$$

From equation (A.10), it is known that the curl of the gradient of a scalar function is equal to zero. Since,

$$\nabla \times \boldsymbol{E} = 0 \tag{A.29}$$

the electric field can be rewritten as the gradient of a scalar function ϕ,

$$\boldsymbol{E} = \nabla \phi \tag{A.30}$$

Using the identity that the integral of the gradient of a scalar function over a closed path is equal to zero,

$$\oint \nabla \phi dl = 0 \tag{A.31}$$

and the curl theorem,

$$\int (\nabla \times \boldsymbol{A}) \cdot da = \oint \boldsymbol{A} \cdot dl \tag{A.32}$$

The static electric field is shown to be,

$$\oint \boldsymbol{E_S} \cdot dl = \int (\nabla \times \boldsymbol{E_S}) \cdot da = 0 \tag{A.33}$$

The electromotive force is then,

$$\begin{aligned} \mathcal{E} &= \oint \boldsymbol{E_S} \cdot dl + \oint \boldsymbol{E_F} \cdot dl = 0 + \oint \boldsymbol{E_F} \cdot dl = -\frac{d}{dt}\Phi_M \\ &= -\frac{d}{dt} \int \hat{n} \cdot \boldsymbol{B}\,(t, \boldsymbol{x})\, d^2x \\ &= -\int \hat{n} \cdot \frac{\partial}{\partial t} \boldsymbol{B}\,(t, \boldsymbol{x})\, d^2x \end{aligned} \tag{A.34}$$

where Φ_M is the magnetic field flux. Using the curl theorem again,

$$\oint \boldsymbol{E_F} \cdot dl = \int (\nabla \times \boldsymbol{E_F})\, d^2x \tag{A.35}$$

Setting (A.34) and (A.35) equal to each other gives,

$$\begin{aligned} \int (\nabla \times \boldsymbol{E_F})\, d^2x &= -\int \hat{n} \frac{\partial \boldsymbol{B}\,(t, \boldsymbol{x})}{\partial t} d^2x \\ \int \left(\nabla \times \boldsymbol{E} - \frac{\partial \boldsymbol{B}\,(t, \boldsymbol{x})}{\partial t} \right) \cdot \hat{n} da &= 0 \end{aligned} \tag{A.36}$$

The only way (A.36) may be satisfied is if,

$$\boxed{\nabla \times \boldsymbol{E} + \frac{\partial \boldsymbol{B}\,(t, \boldsymbol{x})}{\partial t} = 0} \tag{A.37}$$

The set of four Maxwell Equations are then,

$$\boxed{\nabla \cdot \boldsymbol{E} = \frac{\rho}{\epsilon_0}} \tag{A.38}$$

$$\boxed{\nabla \cdot \boldsymbol{B} = 0} \tag{A.39}$$

$$\boxed{\nabla \times \boldsymbol{E} + \frac{\partial \boldsymbol{B}}{\partial t} = 0} \tag{A.40}$$

$$\boxed{\nabla \times \boldsymbol{B} - \frac{1}{c^2}\frac{\partial \boldsymbol{E}}{\partial t} = \mu_0 \boldsymbol{j}} \tag{A.41}$$

A.5 The Helmholtz Wave Equation

Taking the curl of (*A*.40) and (*A*.41) we see that the solutions to $\boldsymbol{E}$ and $\boldsymbol{B}$ are found by solving wave equations.

$$\nabla \times \left[(\nabla \times \boldsymbol{E}) + \frac{\partial \boldsymbol{B}}{\partial t} \right] = 0$$

$$\nabla \times \nabla \times \boldsymbol{E} + \nabla \times \frac{\partial \boldsymbol{B}}{\partial t} = \nabla \times \nabla \times \boldsymbol{E} + \frac{\partial}{\partial t} (\nabla \times \boldsymbol{B}) = 0$$

$$\nabla \times \nabla \times \boldsymbol{E} + \frac{\partial}{\partial t} \left[\mu_0 \boldsymbol{J} + \frac{1}{c^2} \frac{\partial \boldsymbol{E}}{\partial t} \right] = 0 \tag{A.42}$$

$$\nabla \times \nabla \times \boldsymbol{E} = -\frac{\partial}{\partial t} \mu_0 \boldsymbol{J} - \frac{1}{c^2} \frac{\partial^2 \boldsymbol{E}}{\partial t^2}$$

$$= \nabla (\nabla \cdot \boldsymbol{E}) - \nabla^2 \boldsymbol{E}$$

$$\frac{1}{c^2} \frac{\partial^2 \boldsymbol{E}}{\partial t^2} - \nabla^2 \boldsymbol{E} = \nabla (\nabla \cdot \boldsymbol{E}) - \mu_0 \frac{\partial \boldsymbol{J}}{\partial t}$$

Using (A.9) and setting $\boldsymbol{J} = 0$ for regions away from the source current the wave equation for the electric field is found to be,

$$\frac{1}{c^2} \frac{\partial^2 \boldsymbol{E}}{\partial t^2} - \nabla^2 \boldsymbol{E} = 0 \tag{A.43}$$

The wave equation for the magnetic field can be found by repeating the steps completed for the electric field.

$$\nabla \times \left[(\nabla \times \boldsymbol{B}) - \frac{1}{c^2} \frac{\partial \boldsymbol{E}}{\partial t} - \mu_0 \boldsymbol{J} \right] = 0$$

$$\nabla \times \nabla \times \boldsymbol{B} - \frac{1}{c^2} \frac{\partial}{\partial t} \nabla \times \boldsymbol{E} - \mu_0 \nabla \times \boldsymbol{J} = 0$$

$$\nabla \times \nabla \times \boldsymbol{B} + \frac{1}{c^2} \frac{\partial^2 \boldsymbol{B}}{\partial t^2} \nabla \times \boldsymbol{E} - \mu_0 \nabla \times \boldsymbol{J} = 0 \tag{A.44}$$

$$\nabla \times \nabla \times \boldsymbol{B} = \nabla (\nabla \cdot \boldsymbol{B}) - \nabla^2 \boldsymbol{B}$$

Since,

$$\nabla (\nabla \cdot \boldsymbol{B}) = 0 \tag{A.45}$$

Again, $\boldsymbol{J} = 0$ in regions away from the source current so,

$$\frac{1}{c^2} \frac{\partial^2 \boldsymbol{B}}{\partial t^2} - \nabla^2 \boldsymbol{B} = \mu_0 \nabla \times \boldsymbol{J} = 0 \tag{A.46}$$

The wave equation for the magnetic field is then,

$$\frac{1}{c^2} \frac{\partial^2 \boldsymbol{B}}{\partial t^2} - \nabla^2 \boldsymbol{B} = 0 \tag{A.47}$$

Equations (A.43) and (A.47) can be compacted into the Helmholtz equation, where Ψ takes the place of either $\boldsymbol{E}$ or $\boldsymbol{B}$.

$$\left(\nabla^2 + k^2 \right) \Psi = 0 \tag{A.48}$$

where $k = 2\pi/\lambda$ is known as the wave number, and λ is the wavelength.

A.6 Conclusion

In this appendix, the empirical laws of electro- and magnetostatics were used to develop the four Maxwell equations. Corrections to the Maxwell equations were found by removing assumptions of static charge. Non-static charge, or current, was found to couple the electric and magnetic fields. Finally, it was shown that the solution to the electric and magnetic fields of Maxwell's equations is an electromagnetic wave, described by the Helmholtz wave equation.

Appendix B

Expansions with Orthonormal Functions

B.1 Introduction

Electromagnetic fields are often described by superpositions of orthonormal functions. For example, solutions to electromagnetic fields inside a rectangular waveguide are formulated in terms of sines and cosines. Which set of orthonormal functions to use depends upon the symmetry and geometry of the problem at hand. In this appendix, the mathematics behind orthonormal expansions of arbitrary functions is reviewed. The reader is referred to [16, 19] for additional information on this topic.

B.2 Orthonormal Expansions

Orthonormal functions are normalised orthogonal functions. The function $U(x)$ is an orthogonal function on the interval (a, b) if it satisfies the condition,

$$\int_a^b U_n^*(x)\, U_n(x)\, dx = \delta_{n,m} \tag{B.1}$$

Where $\delta_{n,m}$ is the Kronecker delta,

$$\delta_{n,m} = \begin{cases} 1 & m = n \\ 0 & m \neq n \end{cases} \tag{B.2}$$

Any arbitrary, square integrable[1] equation $f(x)$ on the interval (a, b) can be described by a superposition of orthonormal functions.

$$f(x) = \sum_n a_n U_n(x) \tag{B.3}$$

where, a_n are the "expansion," or "mode," coefficients. The coefficients are found by,

$$a_n = \int_a^b U_n^*(x) f(x) \, dx \tag{B.4}$$

The relative weight of the coefficient is then,

$$C_n = |a_n|^2 \tag{B.5}$$

The choice of orthonormal function to use for the expansion depends on the geometry of the problem.

Geometry	Orthonormal Function
Spherical	Spherical Harmonics
Cylindrical	Laguerre Polynomials
Planar	Hermite Polynomials
One Dimensional	Sines and Cosines

Table B.1: Typically used orthonormal functions for several geometries

[1] A square integrable function is a function whose integral of the absolute value squared of said function is less then infinity.

B.3 Conclusion

In this appendix, it was shown that an arbitrary square integrable function on some interval may be described by a superposition of orthonormal functions. Each orthonormal function used in the expansion has some mode coefficient, representing the fractional amount of power of that specific function in the arbitrary function. Several orthonormal functions exists, but the choice of which one to utilise depends on the geometry of the initial problem.

Appendix C

Useful Terms, Definitions and Field Features

C.1 Introduction

This appendix defines some commonly used, or obscure, terms and definitions, which the reader may find helpful. Some common features of the electromagnetic fields presented in this thesis are highlighted in Sec. C.3.

C.2 Terms and Definitions

1. SAM - Spin angular momentum.
2. OAM - Orbital angular momentum.
3. PMD - Phase modulated device.
4. PMT - Phase modulating telescope.
5. Q - Plate - A device that alters SAM states in order to generated OAM sates.
6. SPP - Spiral phase plate.

7. TAMA - Turbulent assemblages of molecules or atoms.

8. GBMA - Gaussian beam mode analysis

9. CTRA - Compact test range antenna.

10. FEKO - A computational electromagnetic software package.

11. MFLMM - Multi-Level Multipole Method, a computational electromagnetic solver algorithm.

12. Central Intensity Null / Intensity Vortex - The location of zero field intensity produced by the undefined phase along the propagation axis, of a LG beam (Fig. C.1).

13. Phase Dislocation (Branch Cut) - A line in phase, where the value of the phase changes from $\pm 180^\circ$ to $\mp 180^\circ$ and ends/starts in a termination point (Fig. C.2).

14. Termination Point (Branch Point) - The ending/starting point of the phase dislocation. The termination point has an undefined phase, and therefore results in an undefined electromagnetic field (Fig. C.2).

15. Phase Dragging - A phenomena cause by several low power radial modes, which causes the propagating phase dislocation to wiggle back and forth (Fig. C.3).

16. Phase Cusp - A region where the spherical phase front of a beam begins to break apart and form a phase dislocation (Fig. C.4).

17. Linear Step Interference - Interference pattern caused by reflections of the field off of the SPP steps (Fig. C.5).

18. Phase Circulation - A strong radial mode that generates a phase boundary, where the direction of propagating phase dislocations change abruptly (Fig. C.6).

C.3 Electromagnetic field features

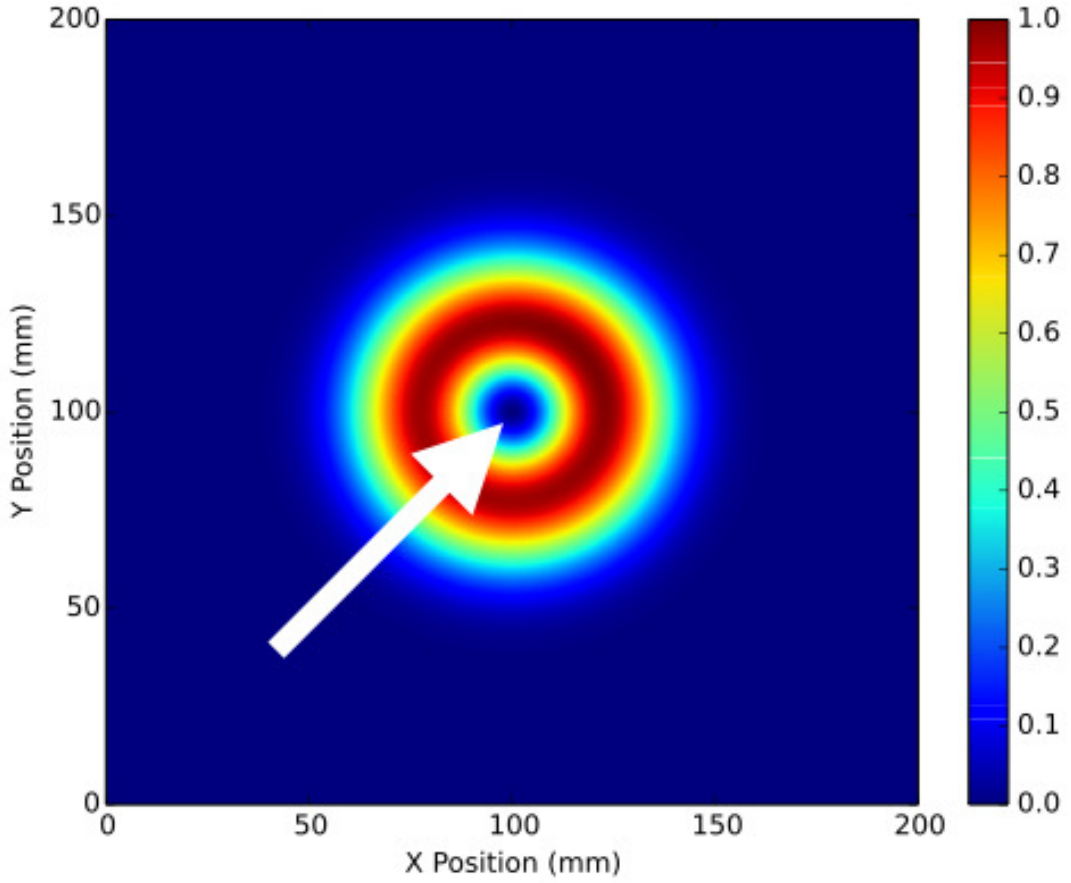

Figure C.1: Central Intensity Null or Intensity Vortex.

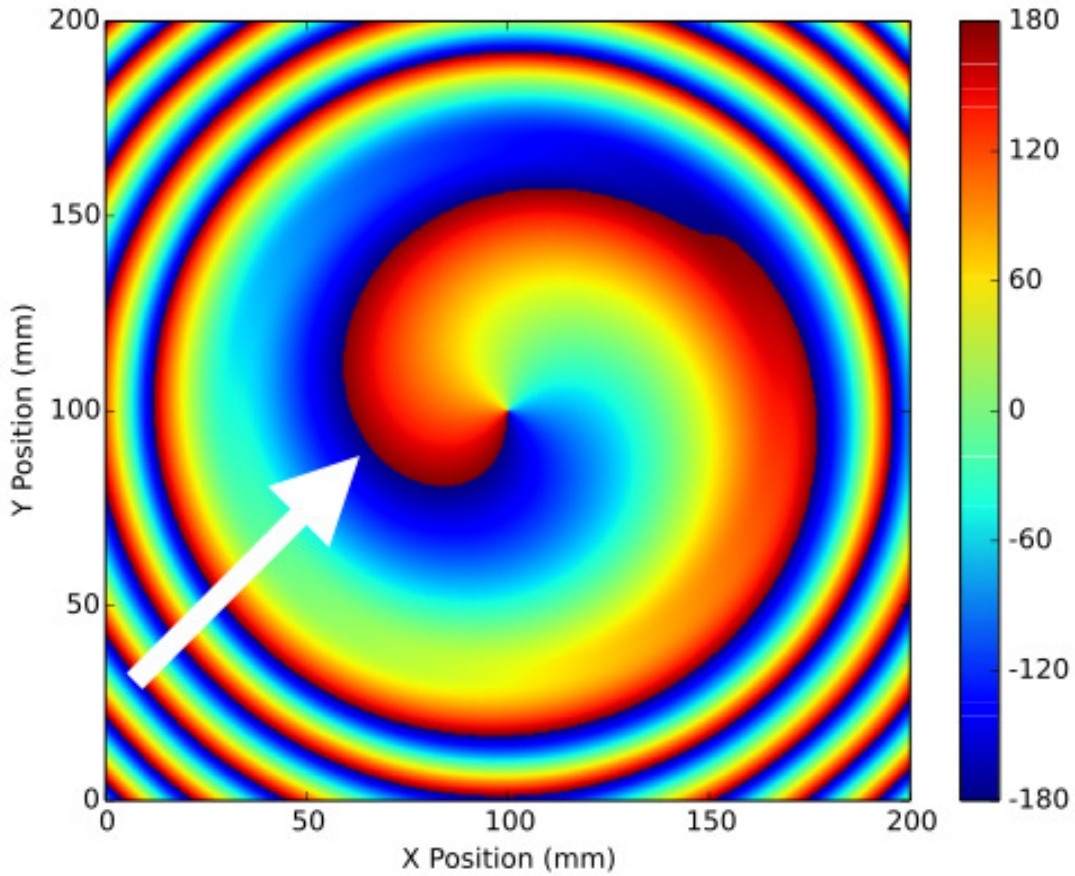

Figure C.2: Phase Dislocation (Branch Cut) with a Termination Point (Branch Point).

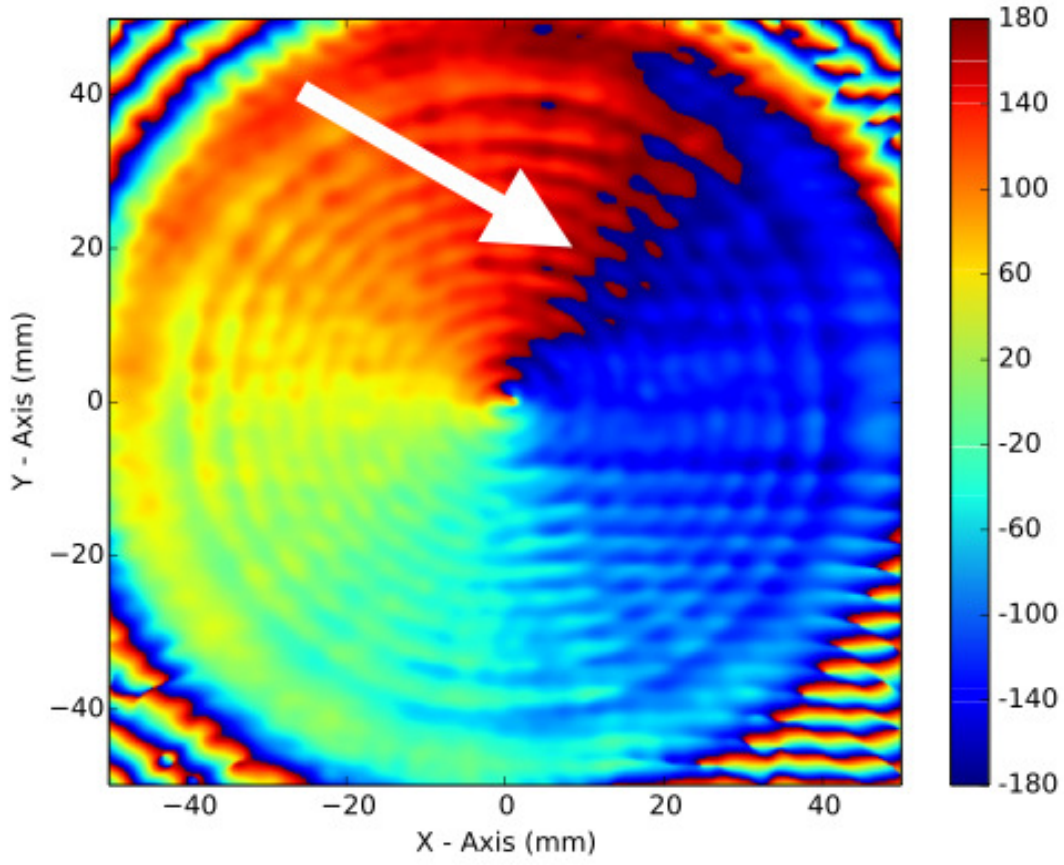

Figure C.3: Phase Dragging.

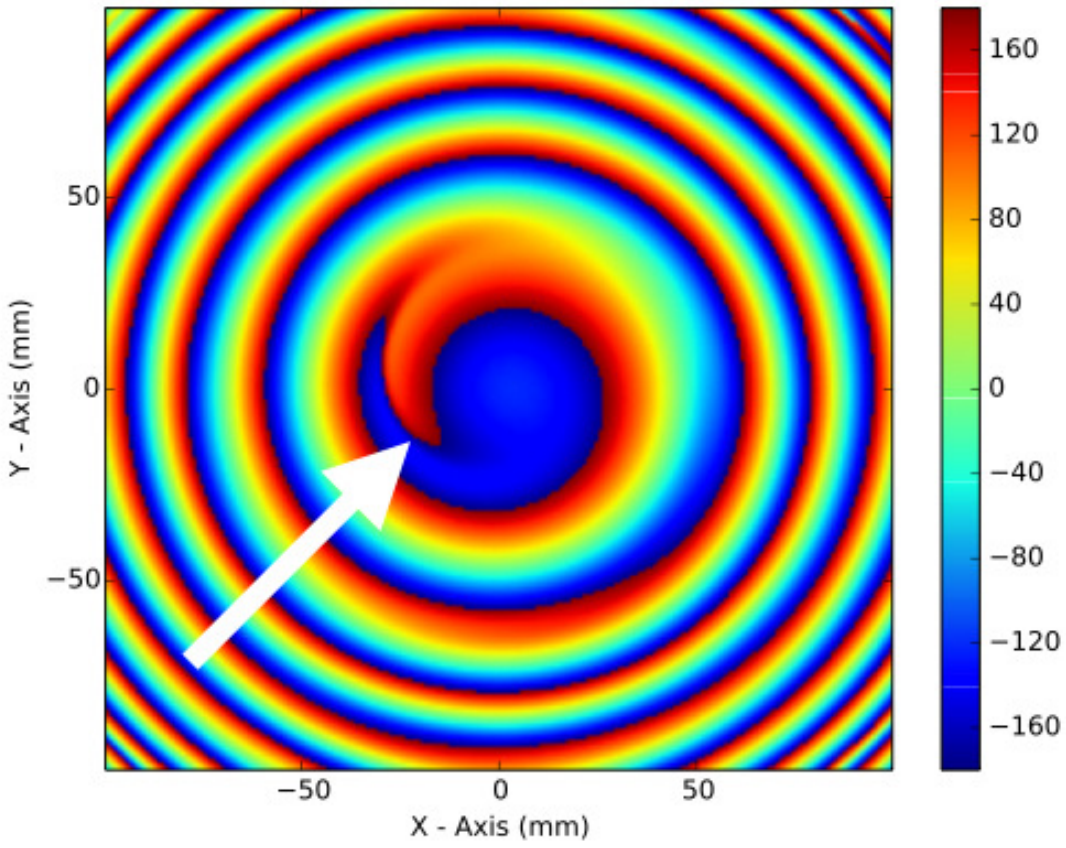

Figure C.4: Phase Cusp.

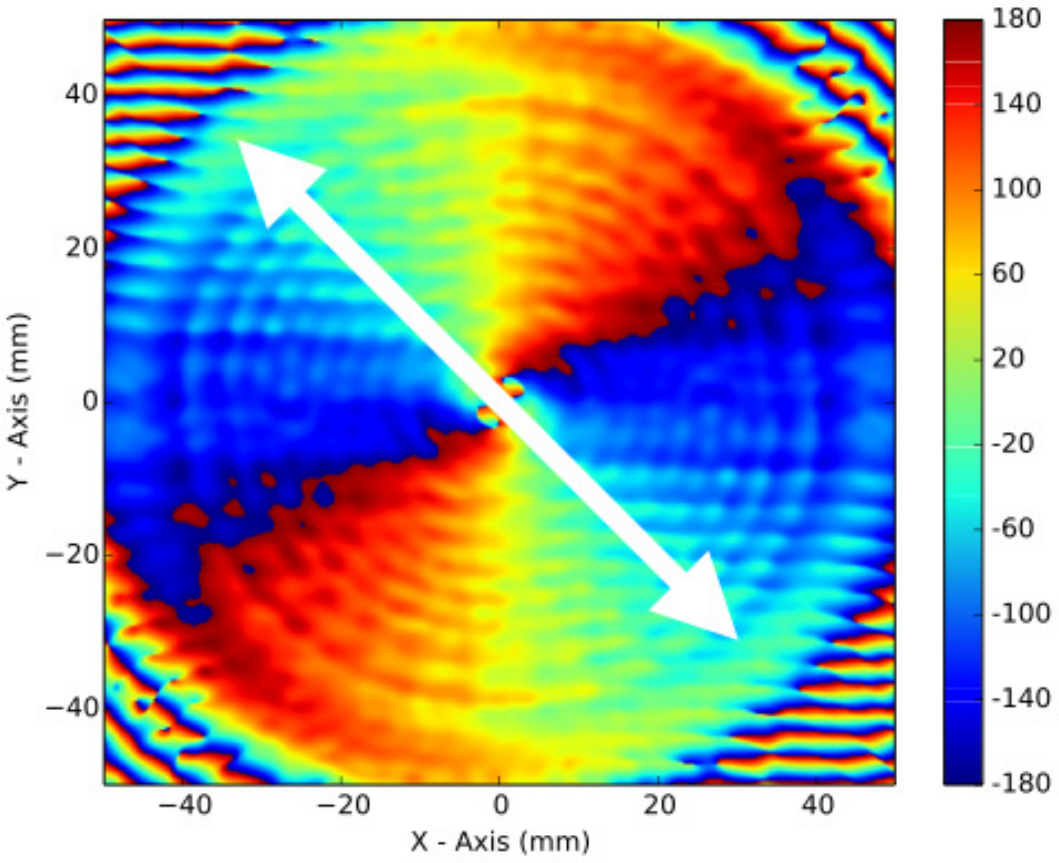

Figure C.5: Linear Step Interference

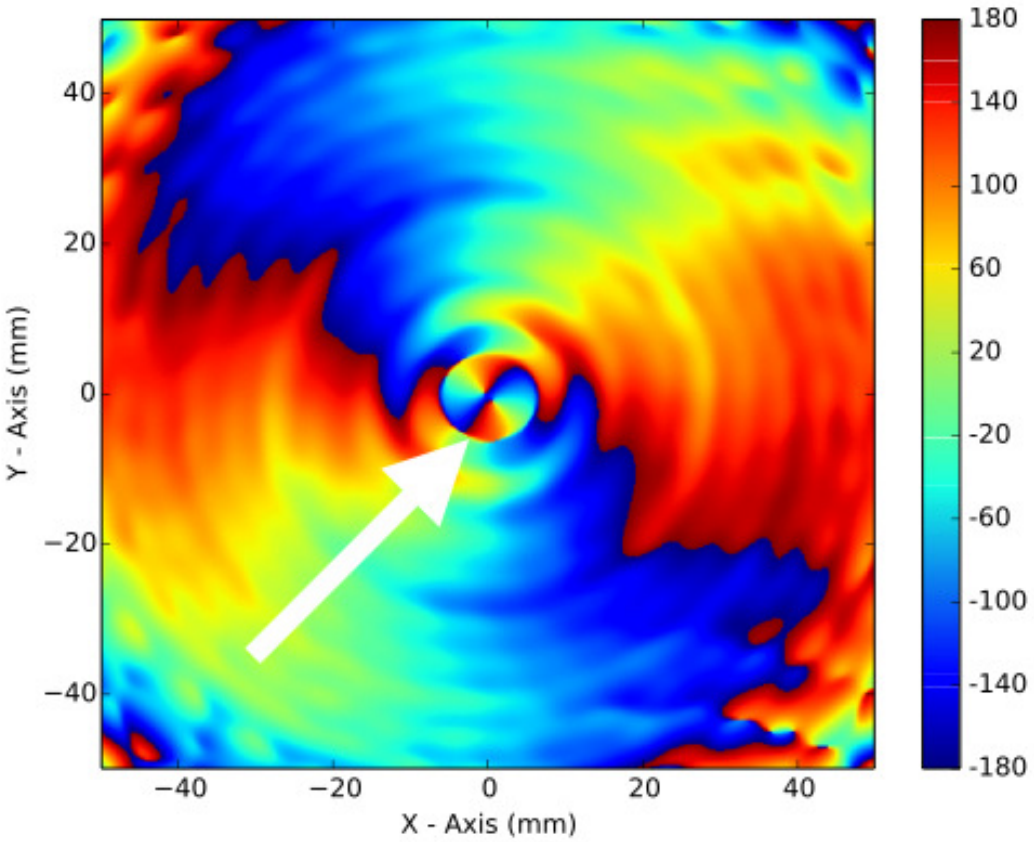

Figure C.6: Phase Circulation

A modular spiral phase plate design for orbital angular momentum generation at millimetre wavelengths

Peter Schemmel,* Giampaolo Pisano, and Bruno Maffei

Jodrell Bank Centre for Astrophysics, School of Physics and Astronomy, University of Manchester, Oxford Road, Manchester M13 9PL, UK

*peter.schemmel@postgrad.manchester.ac.uk

Abstract: Proof of concept measurements of a modular spiral phase plate design able to generate millimetre wavelength beams with an azimuthal mode number of $l = \pm 10$ are presented. The plate is comprised of ten single modules that interlock to create the full plate assembly, allowing improved machining accuracy compared to standard techniques. Therefore, this design could be used in millimetre wavelength systems that require the manipulation of large OAM modes. The plate was manufactured from polypropylene (index of refraction $n \approx 1.5$), and was measured at 100 GHz. A three dimensional field scanner was used to measure three near field surfaces behind the plate. Intensity measurements showed the expected OAM intensity ring, and phase measurements showed ten phase dislocations, implying proper functionality.

OCIS codes: (120.5050) Phase measurements; (120.5060) Phase modulation; (120.5800) Scanners; (350.5500) Propagation; (350.5030) Phase; (350.4010) Microwaves.

References and links

1. J. Wang, J. Yang, I.M. Frazal, N. Ahmed, Y. Yan, H. Huang, Y. Ren, Y. Yue, S. Dolinar, M. Tur, and A.E. Willner, "Terabit free-space data transmission employing orbital angular momentum multiplexing," Nature Photon. **6**, 488-496 (2012).
2. H. Huang, G. Xie, Y. Yan, N. Ahmed, Y. Ren, Y. Yue, D. Rogawski, M. J. Willner, B. I. Erkmen, K. M. Birnbaum, S. J. Dolinar, M. P. J. Lavery, M. J. Padgett, M. Tur and A. E. Willner, "100 Tbit/s free-space data link enabled by three-dimensional multiplexing of orbital angular momentum, polarization and wavelength," Opt. Lett. **39**, 197-200 (2014).
3. I. M. Frazal, N. Ahmed, J. Wang, J. Y. Yang, Y. Yan, B. Shamee, H. Huang, Y. Yue, S. Dolinar, M. Tur, and A. E. Willner, "2 Tbit/s free-space data transmission on two orthogonal orbital-angular-momentum beams each carrying 25 WDM channels," Opt. Lett. **37**, 4753-4755 (2012).
4. F. Tamburini, E. Mari, A. Sponselli, B. Thidé, A. Bianchini, and F. Romanato, "Encoding many channels on the same frequency through radio vorticity: first experimental test," New J. Phys. **14**, 033001 (2012).
5. D. J. Sanchez, D. W. Oesch and O. R. Reynolds, "The creation of photonic orbital angular momentum in electromagnetic waves propagating through turbulence," Astron. Astrophys. **556**, A130 (2013).
6. M. Harwit, "Photon Orbital Angular Momentum in Astrophysics," Astrophys. J. **597**, 1266 (2003).
7. M. Gray, Jodrell Bank Centre for Astrophysics, School of Physics and Astronomy, University of Manchester, Oxford Road, Manchester M13 9PL, UK, is preparing a manuscript to be called "A photon orbital angular momentum model in an astrophysical maser."
8. B. Thidé, H. Then, J. Sjöholm, K. Palmer, J. Bergman, T.D. Carozzi, Ya. N. Istomin, N.H. Ibragimov, and R. Khamitova, "Utilization of Photon Orbital Angular Momentum in the Low-Frequency Radio Domain," Phys. Rev. Lett. **99**, 087701 (2007).
9. F. Tamburini, B. Thidé, G Molina-Terriza, and G. Anzolin, "Twisting of light around rotating black holes," Nature Phys. **7**, 195-7 (2011).

10. L. Allen, M. W. Beijersbergen, R. J. C. Spreeuw, and J. P. Woerdman, “Orbital angular momentum of light and the transformation of Laguerre-Gaussian laser modes,” Phys. Rev. A. **45**, 8185-8189 (1992).
11. M.J. Padgett and L. Allen, “The Poynting vector in Laguerre-Gaussian laser modes,” Optics Commun. **121**, 36 - 40 (1995).
12. A. V. Carpentier, H. Michinel and J. R. Salgueiro, “Making optical vortices with computer-generated holograms,” Am. J. Phys. **76**, 916-921 (2008).
13. P. Schemmel, S. Maccalli, G. Pisano and B. Maffei, “Three dimensional measurements of a millimetre wave orbital angular momentum vortex,” Opt. Lett. **39**, 626-629 (2014).
14. G.A. Turnbull, D.A. Robertson, G.M. Smith, L. Allen, and M.J. Padgett, “The generation of free-space Laguerre-Gaussian modes at millimetre-wave frequencies by use of a spiral phaseplate,” Opt. Commun. **127**, 183-188 (1996).
15. M.W. Beijersbergen, R.P.C. Coerwinkel, M. Kristensen, J.P. Woerdman, “Helical-wavefront laser beams produced with a spiral phaseplate,” Opt. Commun. **112**, 321-327 (1994).
16. M.V. Berry, “Optical vortices evolving from helicoidal integer and fractional phase steps,” J. Opt. A: Pure Appl. Opt. **6**, 259-268 (2004).
17. D. Martin and J. Bowen, “Long-Wave Optics,” IEEE Trans. Microw. Theory Tech. **41**, 1676-89 (1993).
18. P. Goldsmith, *Quasioptical Systems: Gaussian Beam Quasioptical Propagation and Applications* , (IEEE Press, 1998).
19. J. D. Jackson, *Classical Electrodynamics Third Edition*, (John Wiley and Sons, Inc., 1998).
20. N. Trappe, J. A. Murphy and S. Withington, “The Gaussian beam mode analysis of classical phase aberrations in diffraction-limited optical systems,” Eur. J. Phys. **24**, 403 - 412 (2003).
21. Y.S. Rumala and A.E. Leanhardt, “Multiple-beam interference in a spiral phase plate,” J. Opt. Soc. Am. B. **30**, 615-621 (2013).
22. Y.S. Rumala, “Interference theory of multiple optical vortex states in spiral phase plate etalon: thick-plate and thin-plate approximation,” J. Opt. Soc. Am. B. **31**, 615-621 (2013).
23. Y.S. Rumala, “Structured light interference due to multiple reflections in a spiral phase plate device and its propagation,” Proc. SPIE **8999**, 899912 (2014).
24. R. L. Phillips and L. C. Andrews, “Spot size and divergence for Laguerre Gaussian beams of any order,” Appl. Opt. **22**, 643 (1982).
25. V. Kotlyar and A. Kovalev, “Fraunhofer diffraction of the plane wave by a multilevel (quantised) spiral phase plate,” Opt. Lett. **33**, 189-191 (2008).
26. P. Schemmel, S. Maccalli, B. Maffei, F. Ozturk, G. Pisano and M.W. Ng, “A Near Field 3D Scanner for Millimetre Wavelengths,” in Proceedings of the 35th ESA Antenna Workshop on Antenna and Free Space RF Measurements, 10 - 13 September (2013), ESTEC, Noordwijk, The Netherlands.
27. F. Ozturk, B. Maffei and M. W. Ng, “A quasi-optical free-space s-parameters measurement system for material characterisation in W and Ka bands,” in Proceedings of the 33rd ESA Antenna Workshop on Antenna and Free Space RF Measurements, 18 - 21 October (2011), ESTEC, Noordwijk, The Netherlands.
28. B. Maffei, S. Legg, M. Robinson, F. Ozturk, M. W. Ng, P. Schemmel and G. Pisano, “Implementation of a quasi-optical free-space s-parameter measurement system,” in Proceedings of the 35th ESA Antenna Workshop on Antenna and Free Space RF Measurements, 10 - 13 September (2013), ESTEC, Noordwijk, The Netherlands.
29. P. Schemmel, Jodrell Bank Centre for Astrophysics, School of Physics and Astronomy, University of Manchester, Oxford Road, Manchester M13 9PL, UK, is preparing a manuscript to be called “Systematics Study of Spiral Phase Plate Designs for Millimetre Wave Orbital Angular Momentum State Manipulation.”
30. M.S. Soskin, V. N. Gorshkov, M. V. Vasnetsov, J. T. Malos and N. R. Heckenberg, “Topological charge and angular momentum of light beams carrying optical vortices,” Phys. Rev. A. **56**, 4064 (1997).

1. Introduction

Recently, there has been an increasing interest in the desire to use orbital angular momentum (OAM) states in communication systems [1]. Such systems promise high data transfer rates over a single frequency. Proof of concept experiments have shown such OAM based communication systems to be possible over optical [2,3] and radio frequencies [4]. However, in order to become practical, these systems must handle a large number of OAM modes.

There is additional interest in trying to observe OAM modes from astrophysical sources [5–9]. Ideal astrophysical OAM observations would require the acquisition of an OAM mode spectrum, or a measure of the amount of power in each OAM mode emitted by a source. In order to accomplish this a telescope should be sensitive to multiple OAM modes.

In cylindrical coordinates, OAM beams are typically described by Laguerre Gaussian (LG) modes [10]. A single LG mode has the following form,

$$U_\rho^l(r,\phi,z) = A_\rho^l(r,z) L_\rho^{|l|}\left(\frac{2r^2}{w^2(z)}\right)\exp(il\phi)\exp\left[\left(\frac{ik_0 r^2 z}{2(z^2+z_R^2)}\right) - i(2\rho+|l|+1)\phi_0(z)\right] \quad (1)$$

where $A_\rho^l(r,z)$ is a complex amplitude, ρ is the radial mode number, l is the azimuthal mode number, $w(z)$ is the beam radius, k_0 is the free space wave number, z_r is the Rayleigh range, $\phi_0(z)$ is the Gaussian beam phase shift and $L_\rho^{|l|}(x)$ is the generalised Laguerre polynomial.

LG modes with a non-zero azimuthal mode number l contain phase discontinuities [Fig. 1(a)]. These discontinuities propagate outwardly from the centre of, and rotate around, the propagation axis. For this reason, LG modes with non-zero azimuthal mode numbers are said to contain a "phase vortex." The phase value at the "termination point," or origin of the dislocation, is undefined [Fig. 1(a)]. This undefined phase leads to a null in the intensity pattern [Fig. 1(b)], producing an annular ring shape [Fig. 1(c)].

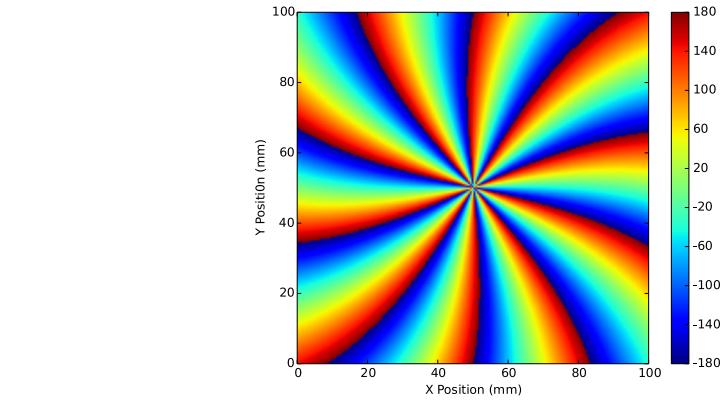

(a) Phase (Degrees)

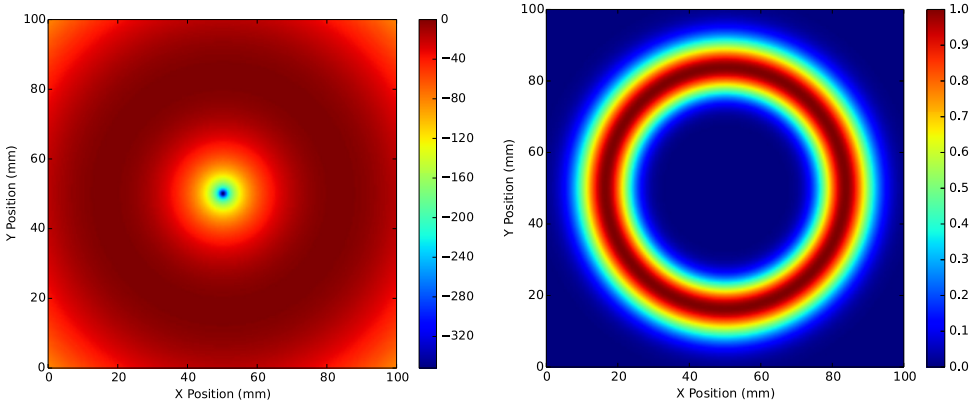

(b) Normalised Intensity (dB)

(c) Normalised Linear Intensity

Fig. 1. Expected phase (a), dB intensity (b) and linear intensity (b) patterns of a numerically generated LG beam with $l = 10$ and $\rho = 0$. The central intensity null is caused by the undefined phase at the end of each phase dislocation. Each dislocation is curved because the LG mode was plotted away from the beam waist.

For a beam with $\rho = 0$ the radius of maximum intensity is [11],

$$r_{max} = w(z)\sqrt{\frac{l}{2}} \tag{2}$$

In optical systems, large numbers of OAM modes are typically manipulated with a diffractive hologram [12] displayed on spatial light modulator, but similar systems do not exist for millimetre and radio frequencies due to the relatively large wavelengths.

The simplest device to manipulate OAM modes at millimetre frequencies is a spiral phase plate (SPP) [13–15]. A SPP is a dielectric slab of material with an azimuthally dependent thickness that imparts an azimuthal phase shift onto incident radiation (Fig. 2). The total step height, h of the SPP is chosen so that the total phase shift around the centre of the SPP is an integer multiple of $2\pi l$, where l is an integer. This imparts a change to the incident radiation's azimuthal mode number l, such that,

$$\Delta l = \frac{h\Delta n}{\lambda} \tag{3}$$

where Δn is the change in the refractive index between the dielectric material and the surrounding medium, and λ is the incident wavelength.

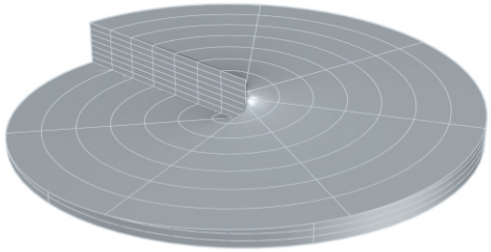

Fig. 2. A CAD model of a smooth surfaced $\Delta l = \pm 1$ SPP.

One can envision that future millimetre and radio OAM sensitive systems will manipulate the large number of modes required by using several interchangeable SPPs with $\Delta l = \pm 1, \pm 2, \ldots \pm N$ where N is some integer. There are two standard approaches to manufacture SPPs with $|\Delta l| > 1$. The first is to simply increase the step height h. The second approach is to compress the behaviour of an $l = 1$ SPP into a specified angular region, a "split," configuration. To accomplish this, a certain number of $\Delta l = \pm 1$ SPPs (specifically a number $b = |l|$) can be restricted to angular regions of $\theta_b = 2\pi/b$. Additionally, the smooth SPP surface may be approximated by a series of discrete steps. Figure 3 shows a $\Delta l = \pm 2$ ($\theta_b = \pi$) SPP model with a stepped surface in a split configuration.

Dielectric SPPs are typically machined from a single piece of material. Although this is a simple process, accuracy near the centre region of the plate has to be compromised due to the finite size of the milling tools. This leaves some sections of the SPP cut to an improper height. This results in fractional step heights and the subsequent generation of a non-integer Δl Eq. (3). Fractional step heights force the creation and annihilation of additional vortices [16], resulting in a beam with an undesired mode content.

A solution to the problem is to machine each SPP section, or module, individually and assemble them into the full plate afterwards. Doing so allows each section to be machined to the proper height, limiting mode contamination. To test this concept a modular split stepped $\Delta l = \pm 10$ SPP was designed and manufactured [Fig. 4(a)] from polypropylene ($n \approx 1.50$) for use at 100 GHz ($\lambda = 3$ mm).

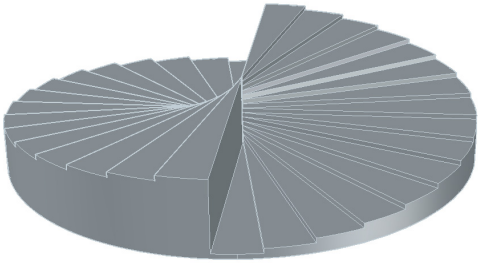

Fig. 3. A CAD model of a "split stepped," SPP. Here two $\Delta l = \pm 1$ SPPs were compressed from an angular range of $[0, 2\pi]$ to $[0, \pi]$ and pushed together in order to generate an $l = \pm 2$ LG beam.

The full spiral is comprised of ten individual modules [Fig. 4(b)], which have machined steps on the top and bottom to minimise the height change between the largest and smallest steps. Each module has an additional tongue and groove on the surfaces parallel to the beam propagation. These are used to attach each module together and to insure proper alignment between them.

(a) Full $\Delta l = \pm 10$ SPP

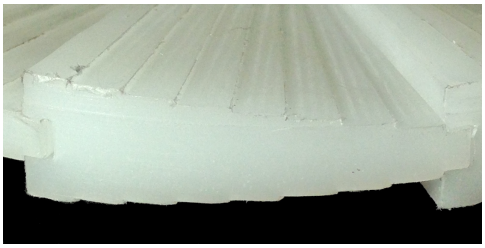

(b) A single module of the full SPP

Fig. 4. A full $\Delta l = \pm 10$ SPP (a). A single module from the full SPP showing the tongue and groove interlocking system (b).

2. Gaussian beam mode analysis

In general, SPPs are not pure mode converters, but instead produce a superposition of LG modes [15]. Multiplying a pure LG mode by $exp(-i\Delta l\phi)$ alters the incident mode number l so that the transmitted beam has an azimuthal phase term $exp(-il'\phi)$, where $l' = l_{in} + \Delta l$. However, the azimuthal mode numbers in the complex amplitude $A_p^l(r,z)$ remain unchanged. Therefore, the complex amplitude term utilises l_{in}, while the azimuthal phase shift term contains l'. This results in an impure LG mode, which must be described as a superposition of pure LG modes. It should be noted that while a perfectly manufactured SPP with antireflection coatings will produce perfect LG beams with respect to the azimuthal mode number, a superposition of radial modes will always exist. The modal description of SPPs may be found by using Gaussian Beam Mode Analysis (GBMA) [17, 18], when the input beam divergence and SPP step height h, are small [15]. In GBMA, any arbitrary square integrable function on the interval (a,b) can

be described by a superposition of orthonormal functions [19].

$$U_m^n(r,\phi,z) = \sum_{l=-\infty}^{\infty} \sum_{\rho=0}^{\infty} a_{\rho,m}^{l,n} U_\rho^l(r,\phi,z) \tag{4}$$

where, U_ρ^l are the LG modes if a cylindrical coordinate system is adopted. The mode coefficients $a_{\rho,m}^{l,n}$ are found by [15],

$$a_{\rho,m}^{l,n} = \left\langle U_\rho^l | U_m^n \right\rangle \tag{5}$$

Here the brackets denote an integration on the plane perpendicular to the propagation axis z (this is the (r,ϕ) plane in cylindrical coordinates). An arbitrary phase shift may be introduced into the system by multiplying the input field by $exp(-i\Phi)$ [20]. For SPPs, the function Φ is required to induce an azimuthal phase shift of Δl, found using Eq. (3). Therefore, the phase shift term for a SPP is $exp(-i\Delta l\phi)$ [15]. Introducing the phase shift term to Eq. (4) gives,

$$U_m^n(r,\phi,z) = \sum_{l=-\infty}^{\infty} \sum_{\rho=0}^{\infty} a_{\rho,m}^{l,n} U_\rho^l(r,\phi,z)\, exp(-i\Delta l\phi) \tag{6}$$

which then implies that,

$$a_{\rho,m}^{l,n} = \left\langle U_\rho^l | exp(-i\Delta l\phi) | U_m^n \right\rangle \tag{7}$$

Finally, the mode spectrum, or fraction of power of the input field U_ρ^l contained in each mode U_m^n is found by calculating the normalised coupling coefficient for each mode.

$$\left| C_{\rho,m}^{l,n} \right|^2 = \frac{\left| \left\langle U_\rho^l | exp(-i\Delta l\phi) | U_m^n \right\rangle \right|^2}{|\langle U_m^n | U_m^n \rangle|^2} \tag{8}$$

3. Numerical simulations

Mode spectra [Eq. (8)] for various SPP designs may be calculated numerically. Additionally, the phase shift function Φ, which is normally smooth and continuos, may be discretised to mimic stepped SPP designs. Machining tolerances may also be accounted for by allowing each SPP step to vary from the designed thickness by some small random amount. It should be noted that multiple reflections are a significant effect and are not taken into account by the model in Sec. 2 [21–23]. In addition, other factors could also be taken into consideration, such as machining errors as a function of radius, the effects of transmission through the dielectric, inhomogeneities of the index of refraction or the finite size of the SPP.

To compare the effect of a stepped to a smooth SPP, numerical simulations of a $\Delta l = 1$ SPP illuminated with a U_0^0 Gaussian beam were conducted on a field eight times the input beam width (to ensure proper convergence) on a grid of 200×200 points. The stepped SPP was comprised of sixteen steps without random variations in thickness. The decomposition results (Table 1) for both the smooth and stepped SPP show that all of the initial Gaussian power was converted into a LG beam with $l = 1$. However, since the SPP is not a pure mode converter, radial modes with $\rho \neq 0$ are also present. It should also be noted that the mode content for each (l,ρ) pair generated by the sixteen stepped SPP is lower than for the smooth SPP. This is a result of leakage from modes containing a large fraction of the incident power, to modes containing less power. Analysis of each mode in Table 1 shows that there is roughly a 2.7 percent drop in power in the first six modes.

Table 1. Mode content, in percentages, of a U_0^0 beam passed through a smooth and a sixteen stepped $\Delta l = 1$ SPP.

Smooth	$l = 1$	78.56	9.82	3.68	1.92	1.18	0.79
Stepped	$l = 1$	76.35	9.54	3.58	1.86	1.14	0.77
	$\rho =$	0	1	2	3	4	5

These numerical simulations can be repeated for the modular $\Delta l = \pm 10$ SPP. Table 2 shows the first eight radial modes of the decomposition of a smooth and an eight-steps-per-mode split configuration $\Delta l = 10$ SPP. Immediately obvious are the extremely low mode contents.

Table 2. Mode content, in percentages, of a U_0^0 beam passed through a smooth and an eight-steps-per-mode $\Delta l = 10$ SPP.

Smooth	$l = 10$	0.40	0.90	1.35	1.70	1.94	2.10	2.19	2.22
Stepped	$l = 10$	0.35	0.80	1.20	1.51	1.73	1.87	1.95	1.99
	$\rho =$	0	1	2	3	4	5	6	7

This is due to a mismatch between the generated beam's and decomposition mode's azimuthal mode numbers in the complex amplitude term $A_\rho^l(r,z)$ and azimuthal phase term $exp(-il'\phi)$. While the decomposition modes use the same azimuthal mode number in both the complex amplitude and azimuthal phase term, the generated beam does not. Here, the complex amplitude utilises an azimuthal mode number of $l_{in} = 0$, yet the azimuthal phase term uses $l' = \Delta l$. Since the spot size of an LG mode is dependent on both ρ and l [24], the generated beam will have a smaller radius then the decomposition modes. Therefore, a higher number of radial modes must be included in the decomposition in order to describe the generated beam. Alternatively, the beam waist of the decomposition modes may be optimised in order to concentrate the mode spectra into a primary mode [18, 20]. This has the advantage of reducing the number of modes needed to describe the generated beam, thereby speeding up computation time. Several mode spectra were calculated to determine the optimal decomposition beam waist. Figure 5 shows the maximum mode coefficient as a function the decomposition beam waist. The mode content is maximised in a primary mode when the decomposition beam waist is 7.5 mm. Optimised mode spectra for a smooth and split stepped configurations are shown in Table 3.

Table 3. Mode content, in percentages, of a U_0^0 beam passed through a smooth and an eight-steps-per-mode $\Delta l = 10$ SPP, with an optimised decomposition mode beamwaist of 7.5 mm.

Smooth	$l = 10$	52.01	0.00	16.61	0.04	8.14	0.13	4.56	0.21
Stepped	$l = 10$	45.38	1.40	15.09	1.71	7.27	1.71	4.31	1.45
	$\rho =$	0	1	2	3	4	5	6	7

Now that the mode coefficients for the modular $\Delta l = \pm 10$ SPP are known, Eq. (4) may be used to propagate and reconstruct the final field as a mode superposition. Using a wavelength of $\lambda = 3$ mm, a beam waist, $\omega_0 = 25$ mm (this is representative of the beam waist used in the experimental setup. See Sec. 4) and a propagation distance of 40λ (120 mm) and 73.3λ (220 mm) respectively, the expected beam intensity and phase may be plotted (Fig. 6). These simulations

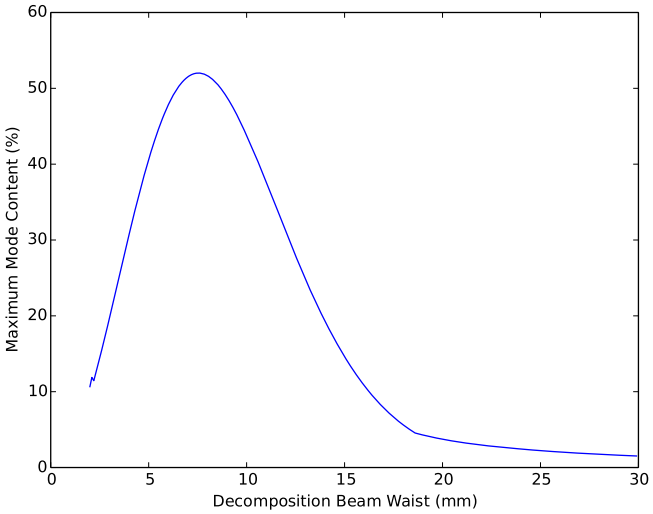

Fig. 5. Maximum mode content as a function of the decomposition beam waist has a maximum of 52.01% at 7.5 mm.

were done on a grid 100 mm $\times$ 100 mm with a resolution of 0.5 mm in either direction and decomposed over the modes $-40 \leq l \leq 40$ and $0 \leq \rho \leq 40$ in order to ensure proper convergence.

Both intensity simulations [Fig. 6(a) and Fig. 6(c)] show a pattern comprised of a semi-discrete ring with a shallow inner intensity island surrounded by a deep intensity trough. Ten intensity peaks make up the semi-discrete ring, which is a result of the ten singular modules of the SPP model. Phase calculations on the 40λ (120 mm) surface [Fig. 6(b)] show ten primary dislocation lines broken by a radial node, leaving ten smaller dislocations inside the radial break. A further break in the dislocation lines is visible in the 73.3λ (220 mm) phase pattern [Fig. 6(d)]. Note that the dislocation lines do not meet in the centre of the propagation axis, as is the case for the pure $l = 10$ LG mode in Fig. 1(a). This is due to the increase of non-zero radial modes in the mode spectrum generated by the SPP.

Although the GBMA model presented did not take into account thickness dependent reflection losses in a dielectric slab, such effects are known to be pronounced in typical dielectric etalons. Therefore, losses for each step height (Table 5) of the modular SPP were calculated using a simple transmission line code (Fig. 7). Maximum transmission was near 100% while the minimum transmission was 85.2%. Specifically, the simple transmission line code predicted a minimum transmission of 85.2071%, which may be compared to the multiple reflections, thin plate approximation [21] predicted value of 85.2074%. It is clear that transmission modulation due to multiple reflections inside the dielectric is a small effect. However, multiple reflections in a dielectric SPP also introduce unwanted azimuthal modes, which may lead to azimuthal modulations in intensity [21–23]. Furthermore, standing waves inside the dielectric may also affect transmission. For example, the second and sixth largest step heights are on average 3.04λ and 1.95λ tall. Since these steps are nearly integer multiples of the incident wavelength standing waves could be produced.

Finally, it is known that discretising a SPP with too few steps will induce azimuthal intensity modulations [25]. Therefore, the RMS error between the intensity patterns of a perfectly smooth $\Delta l = \pm 10$ SPP and modular split stepped $\Delta l = \pm 10$ SPP, as a function of the number of total steps was calculated (Table 4). Using eight-steps-per-mode, or a total of eighty steps, results in

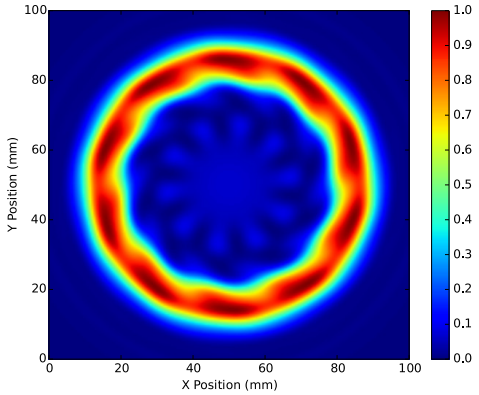

(a) Normalised intensity on the 40λ (120 mm) surface.

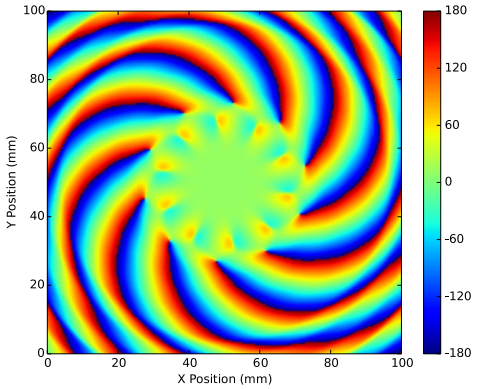

(b) Phase (Degrees) on the 40λ (120 mm) surface.

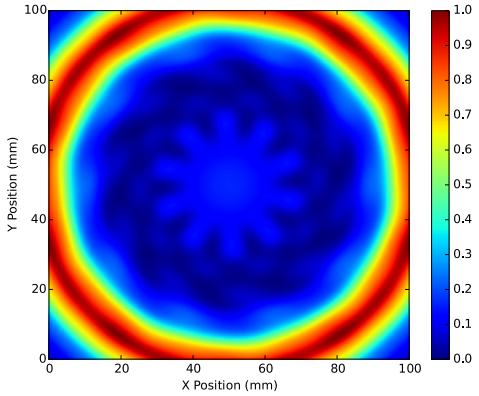

(c) Normalised intensity on the 73.3λ (220 mm) surface.

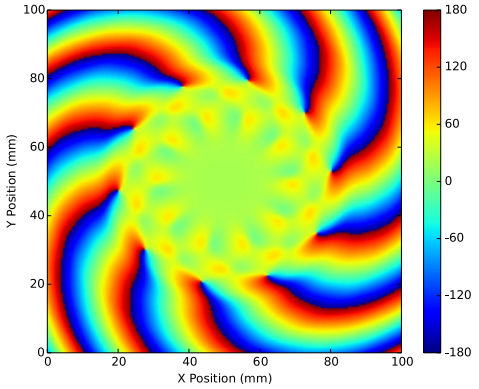

(d) Phase (Degrees) on the 73.3λ (220 mm) surface.

Fig. 6. Numerical simulations of a $\Delta l = 10$ stepped SPP in a split configuration. The normalised linear intensity on both the 40λ (120 mm) [Fig. 6(a)] and 73.3λ (220 mm) [Fig. 6(c)] measurement surfaces display a discontinuous intensity ring when compared with Fig. 1(c). The calculated phase on both surfaces also differs from the pure $(l = 10, \rho = 0)$ pattern [Fig. 1(a)]. In both Fig. 6(b) and Fig. 6(d) radial modes generate discontinuities in the phase dislocation lines.

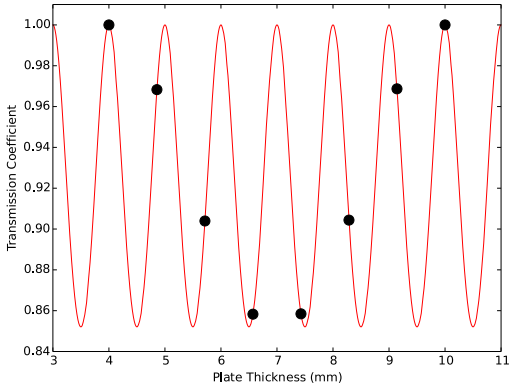

Fig. 7. Transmission coefficients calculated as a function of SPP thickness (red line). Black dots indicate the eight individual step heights that make up the modular SPP.

a 1.37% RMS error in the intensity pattern. Following the criteria set out in [25] where an RMS error of less then 2% is acceptable, a polypropylene $\Delta l = \pm 10$ modular split stepped SPP for use at 100 GHz should have at least seven-steps-per-mode.

Table 4. RMS intensity pattern error as a function of the number of steps per mode between a perfect and modular split stepped $\Delta l = \pm 10$ SPP.

Steps per mode	RMS (%)
4	12.02
5	5.01
6	2.93
7	1.98
8	1.37
9	1.01
10	0.80

4. Measurement system and SPP parameters

A three dimensional W-band ($75 - 100$ GHz) scanning system was used to record the data [13, 26]. The scanner has a 50 cm $\times$ 50 cm $\times$ 50 cm working volume, and uses a WR-10 rectangular to circular waveguide transition with a 3.0 mm opening diameter as a field probe. To minimise reflections between the probe and SPP, a 3D printed pyramidal absorber was placed around the probe opening. The modular SPP was illuminated with a quasi-planar Gaussian beam created with a compact test range antenna (CTRA) [Fig. 8(a)] designed for material characterisation [27, 28]. The CTRA section is comprised of a source antenna, sub reflector and main reflector, which generates a Gaussian beam [Fig. 8(b)] profile with planar phase fronts [Fig. 8(c)] approximately 265 mm from the main reflector. A horizontal cut was taken through the centre of the beam with a positioning resolution of 0.5 mm and utilised five measurement sweeps.

The SPP was placed in a custom designed mount and centred on the CTRA beam. The surrounding area was covered with radiation absorbing material. Measurements across three surfaces perpendicular to the propagation axis were carried out at distances of 6.7λ, 40λ and 73.3λ (20 mm, 120 mm and 220 mm, Figs. 9 - 11) behind the modular SPP. As the far field

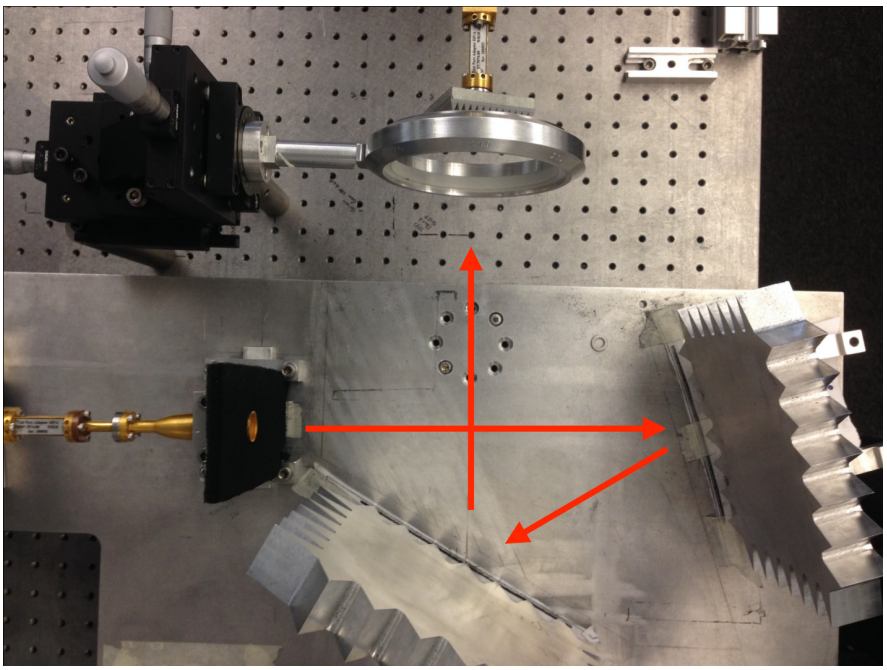

(a) Incident beam optical path.

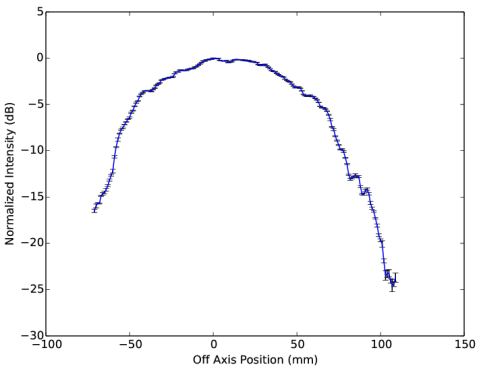

(b) Incident Intensity (dB)

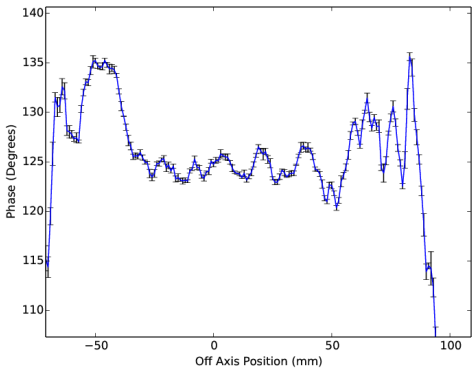

(c) Incident Phase (Degrees)

Fig. 8. A Gaussian beam is generated by the feed horn and is reflected by both CTRA mirrors. The beam then propagates to the SPP mount and is measured by the WR-10 probe [Fig. 8(a)]. (Not pictured is the absorbing material surrounding the mounting structure.) The measured incident Gaussian beam created by the CTRA source with vertical error bars denoting one standard deviation of the five measurement sweeps [Fig. 8(b)]. Measured near planar phase front at the beam waist created by the CTRA source with vertical error bars denoting one standard deviation of the five measurement sweeps [Fig. 8(c)].

of this system is greater then one metre, each surface cut is well within the near field of the SPP. Each surface cut was centred on the propagation axis, comprising of a $33.3\lambda \times 33.3\lambda$ (100 mm $\times$ 100 mm) scan area, while the probe had a mechanical positioning resolution of 0.17λ (0.5 mm) in both directions. Due to the presence of phase fluctuations [Fig. 8(c)] in combination with diffraction effects generated by the SPP mount, background measurements were taken without the modular SPP and were used to correct the SPP measurements. Background phase data was subtracted from the SPP generated phase in order to produce normalised phase patterns. The incident beam waist was 41 mm while the averaged edge taper at the SPP mount inner edge was -4.77 dB. Additionally, measured background intensity on each plane (not presented here) did not indicate any azimuthal intensity modulations.

Table 5 shows the measured average height and standard deviation for each SPP step. Additionally, the measured average difference from the expected $\Delta h = 6.00$ mm primary step height was 0.07λ with a standard deviation of 0.06λ.

Table 5. Measured average and standard deviation step heights for the manufactured $\Delta l = \pm 10$ modular split stepped SPP.

Step Number	1	2	3	4	5	6	7	8
Average Height (mm)	9.88	9.13	8.26	7.45	6.63	5.85	4.99	4.10
Standard Deviation (mm)	0.12	0.14	0.23	0.21	0.21	0.21	0.20	0.22

5. Results

Measured normalised intensity and phase results on the 6.7λ (20 mm) surface cuts are presented in Fig. 9(a) and Fig. 9(b) respectively. Due to the close proximity of the probe to the plate, the intensity pattern is dominated by the varying transmission (Fig. 7) of the incident beam through the individual SPP steps. Each of the ten modules, or sections, are visibly separated by a pair of radial lines of high intensity. Each radial line of high intensity corresponds to the thickest and thinnest section of the SPP, respectively. A small line of lower intensity separates the two high intensity lines and is the result of a boundary condition mismatch between the field inside and outside the largest modular SPP step. It is clear from the intensity data (Fig. 9) that variations larger than the $\approx 15\%$ predicted by simple transmission line or multiple reflection codes (Sec. 3) exist. This is currently under study [29]. Therefore, we must conclude that there is some other effect creating the observed larger variations. Background normalised phase in Fig. 9(b) indicates that the modular SPP functioned properly, and generated the desired $\Delta l = \pm 10$ change in mode number. Ten dislocation lines are clearly visible, radiating outwards, from the centre of the beam. Each dislocation line abruptly ends at a "termination point," resulting in a "phase vortex." The exact value of the phase at the termination point is undefined, resulting in an intensity null. Additionally, the phase circulates by an amount of 2π around each termination point. The integrated phase shift around the beam is $2\pi l$, in this case 20π.

Normalised linear intensity of the 40λ (120 mm) surface is presented in Fig. 10(a). The intensity ring expected in beams with a non-zero azimuthal mode number is clearly visible. However, it is not continuous, but is instead broken into ten pairs of high intensity regions.

Transmission through each SPP step alone can not entirely account for the intensity pattern produced. Diffraction from the largest SPP steps introduces discontinuities between each pair of high intensity peaks. In addition, individual steps form a triangular aperture, which introduces additional diffractive effects. A study comparing several SPP configurations, utilising different source configurations, and finite element analysis modelling is being conducted to further understand how these additional effects interact to produce the generated SPP beams [29].

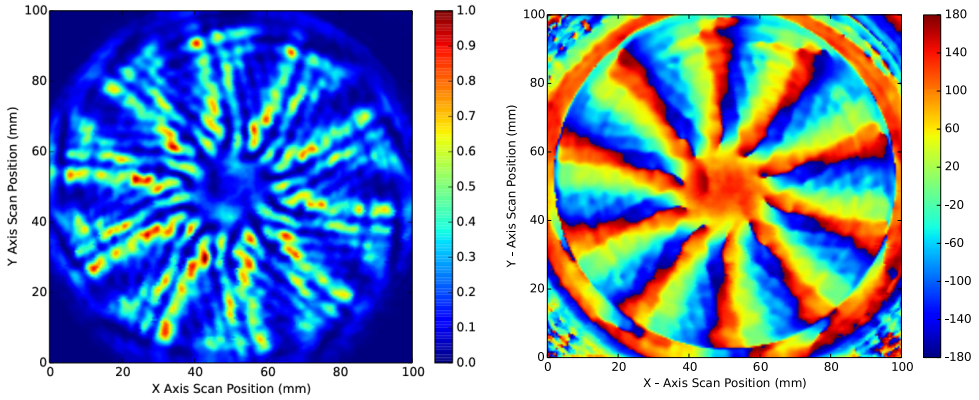

(a) Normalised Intensity

(b) Background Normalised Phase

Fig. 9. Measured 6.7λ (20 mm) surface normalised intensity pattern (Units in (V/m)) [Fig.9(a)] shows a near field "image," of the modular SPP is a result of the variable transmission through the SPP dielectric. Background normalised phase data (Units in degrees) for the 6.7λ (20 mm) surface [Fig.9(b)] contains ten phase dislocations, indicating that the modular SPP imparts a change in mode number of $\Delta l = \pm 10$.

Intensity peak splitting could either be due to the added surface boundaries between the tongue and groove regions, or further machining imperfections. This splitting could be lessened, or perhaps removed entirely, with improvements to the interfacing between the modules while the continuity of the intensity ring could be improved by using more steps-per-mode.

Figure 10(b) shows the phase results for the 40λ (120 mm) surface. Ten phase dislocations are visible at a radial distance of approximately 30 mm from the centre of the beam. Inside this radial distance the phase is distorted. Recalling the phase results in Fig. 6, the first ring of broken dislocations may be attributed to the increase of radial mode strength resulting from the discrete SPP surface. Additional inner dislocation pairs are produced by complex interference between each step of an individual module. The interference becomes more pronounced as the width of each step decreases. This effect in combination with machining imperfections produce a beam with a fractional mode number [16].

Intensity and phase results for the 73.3λ (220 mm) surface are presented in Fig. 11. Still visible is the primary intensity ring, which has diverged as expected according to Gaussian beam propagation [18]. The central intensity peak is still visible in Fig. 11(a).

More interesting is the phase pattern. Whereas the phase in the centre of Fig. 10 was distorted and included additional dislocations, the phase in Fig. 11(b) is smoother. There are still ten outer dislocation lines, indicating that the beam has an azimuthal mode number of $l = 10$. Eight of the outer phase dislocations are also associated with a smaller dislocation pair at a small radii. These are due to radial modes generated by the SPP breaking the phase dislocation lines. However, the additional dislocations in the centre of Fig. 10(b) have largely disappeared. This appears to be evidence of the annihilation of phase vortices as described by [16]. The annihilation of phase vortices is not unexpected, and has been discussed in theory and experiments of the free-space propagation of light waves [30].

6. Conclusions

There is a growing interest in manipulating OAM modes for use in millimetre and radio wave communication and astronomical observing systems. One of the simplest ways to manipulate

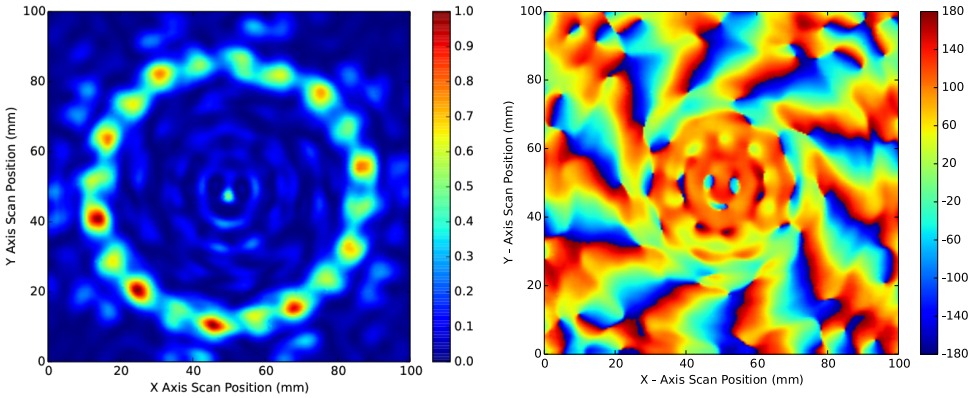

(a) Normalised Intensity (b) Background Normalised Phase

Fig. 10. Normalised linear intensity pattern (Units in V/m) for the 40λ (120 mm) surface [Fig. 10(a)]. The expected intensity ring has developed and is clearly visible, although it remains discontinuous. Phase (Units in degrees) measured on the 40λ (120 mm) surface [Fig. 10(b)] shows ten outer phase dislocations and a largely distorted centre. Phase distortions in the centre of the pattern are produced by complex interference as the width of each SPP step decreases with a decreasing radius and machining imperfections.

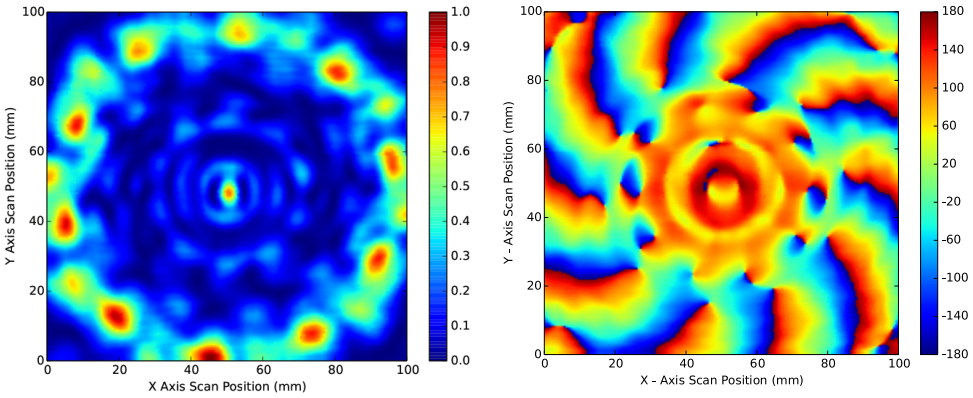

(a) Normalised Intensity (b) Background Normalised Phase

Fig. 11. Measured normalised linear intensity (Units in V/m) of the 73.3λ (220 mm) surface [Fig. 11(a)], showing the OAM intensity ring resulting from the undefined phase at the termination point of the dislocation lines. Background normalised phase (Units in degrees) on the 73.3λ (220 mm) surface [Fig. 11(b)] contains ten outer phase dislocations at radial distances greater then 30 mm. The clean central region, especially compared to that in Fig. 10, indicates the possible annihilation of phase vortices.

OAM modes is through the use of a SPP. Using several interchangeable SPPs, one for each specific mode, may be one way to handle a large set of OAM modes with future radio communication and astronomy systems. Manufacturing SPPs for large mode numbers becomes difficult using standard techniques. To alleviate this problem, a proof of concept, modular stepped SPP was design, manufactured and tested at 100 GHz. The modular SPP consists of ten separate sections that interlock to create the full $\Delta l = \pm 10$ plate assembly. The near field intensity and phase of the full SPP was measured in 100 mm $\times$ 100 mm surface cuts perpendicular to the propagation axis at 6.7λ, 40λ and 73.3λ (20 mm, 120 mm and 220 mm) from the SPP. Phase results showed that the modular SPP induced an azimuthal mode number change of $\Delta l = \pm 10$. The 40λ (120 mm) and 73.3λ (220 mm) intensity patterns indicated that the modular interlocking method and stepped surface were causing some discontinuities in the expected intensity ring pattern. These systematics can be improved with modified plate designs. However, the modular SPP concept was proven to function properly.

Phase results did show some additional interesting properties. Initial and final near field surfaces showed that there were ten phase dislocations indicating a $|l| = 10$ beam. Yet, the 40λ (120 mm) surface showed that the phase at the centre of the beam was largely distorted. The large number of extra dislocations seem to point at the creation and annihilation of phase vortices. These effect are currently under study using other plate designs and incident source beam configurations in order to isolate them in future analysis.

Acknowledgments

The authors would like to thank Mr. Saul Beeson for his outstanding dedication and craftsmanship in creating the modular SPP used for this paper. The authors also acknowledge support from the Science Technology Facilities Council (STFC).

Three-dimensional measurements of a millimeter wave orbital angular momentum vortex

Peter Schemmel,* Stefania Maccalli, Giampaolo Pisano, Bruno Maffei, and Ming Wah Richard Ng

Jodrell Bank Centre for Astrophysics, School of Physics and Astronomy, University of Manchester, Oxford Road, Manchester M13 9PL, UK
**Corresponding author: peter.schemmel@postgrad.manchester.ac.uk*

Received November 4, 2013; accepted December 13, 2013;
posted December 23, 2013 (Doc. ID 200611); published January 28, 2014

Initial three-dimensional phase and intensity measurements of a 100 GHz $l = \pm 1$ orbital angular momentum (OAM) vortex are presented. The vortex was generated by illuminating a polypropylene spiral phase plate. Measurements were taken with a three-dimensional field scanner operating in the W-band (75–100 GHz). Early analysis shows splitting of the OAM phase dislocation at the vortex center, resulting in a complex inner vortex intensity pattern.

OCIS codes: (120.5060) Phase modulation; (350.4010) Microwaves; (120.5050) Phase measurement; (120.5800) Scanners; (350.5030) Phase.
http://dx.doi.org/10.1364/OL.39.000626

It has recently been established that manipulation of electromagnetic (EM) fields carrying orbital angular momentum (OAM) can provide new information for astronomical observations [1–4] and advances in telecommunications [5,6]. Previously, these applications were limited to using either one or a combination of two possible orthogonal linear and two orthogonal circular polarizations. However, it has been shown that EM fields can also occupy a theoretically unlimited number of OAM states. EM fields with OAM exhibit an azimuthal phase variation of $2\pi l$ about the propagation axis, with l phase dislocations in the plane perpendicular to the propagation axis [7]. Here l is the azimuthal OAM mode number, which is an integer ranging between $-\infty$ and ∞. The three-dimensional phase structure of an EM field with OAM resembles l intertwined helical planes. Additionally, the phase along the propagation axis is undefined, causing the EM field to have a central intensity null. This results in annular intensity patterns. The central intensity null and twisted helical phase have led these beams to be called "optical vortices" [8].

Importantly, it has been shown that OAM fields can be created by natural mechanisms. The recognition that branch points in wavefront sensor data are actually EM fields with OAM induced by turbulent atmospheric layers is such an example [9]. These measurements have allowed for the calculation of the number of turbulent layers in the atmosphere and their relative velocities [10]. This clearly shows that OAM measurements can be used to gather valuable scientific information.

Unfortunately, studies of OAM at millimeter and radio wavelengths have been less popular, despite showing great potential. Radio frequency OAM fields have been used to transmit information from point-to-point over a single frequency [5,6]. It has also been suggested that OAM fields could be detected in millimeter and radio wave astrophysical sources, such as rotating black holes [3], masers, and possibly the cosmic microwave background radiation [1].

Millimeter wave studies of OAM fields provide the distinct advantage of being able to conduct accurate direct complex field measurements. This is advantageous for two reasons. First, analysis of the complex field structure of millimeter OAM beams can provide insight into how superpositions of OAM waves are created. This is extremely important for understanding the leakage between modes in OAM based communication systems. Secondly, large near field distances can be easily created using quasi optical—millimeter wave devices, providing ample space to probe the transition to the far field. Therefore, we have developed a polypropylene spiral phase plate (SPP) to generate, and a three dimensional field scanner to take measurements of, millimeter wave OAM vortices.

Holographic diffraction gratings [11], q-plates [12,13], and SPPs [14–16] are the three main categories of phase modulating devices (PMDs) used to generate OAM. At millimeter wavelengths, the required hologram dimensions are unfeasibly large and are, therefore, impractical. Q-plates have been used to generate OAM at millimeter wavelengths before [12], but they require circularly polarized input radiation and complex surface geometries. This limits their usability. On the other hand, SPPs can be used with any polarization and have a simple structure that may be machined more easily. For these reasons, SPPs are the preferred method for OAM generation at millimeter wavelengths. SPPs are dielectric components that vary in thickness azimuthally around the plate surface. The continuously changing plate thickness imparts an azimuthal phase shift to an incident EM field. Considering optical path delays in a dielectric shows that the step height h of the SPP is dependent on the incident wavelength λ and change in refractive index Δn between the SPP and the surrounding medium such that [14,15]

$$h = \frac{\Delta l \lambda}{\Delta n}, \tag{1}$$

where Δl is the change in mode number between the incident and transmitted EM fields. The only physical SPP dimension dependent on the wavelength is the step height h.

There are several possible functional descriptions of OAM modes, but the most often used are the Laguerre–Gaussian (LG) modes [7]. In cylindrical coordinates the LG modes are described by

$$u_\rho^l = A_\rho^l(r,z)L_\rho^{|l|}\left(\frac{2r^2}{w^2(z)}\right)\exp(il\phi)\exp\left(\frac{ik_0r^2z}{2(z^2+z_R^2)}\right)$$
$$\times\exp\left[-i(2\rho+|l|+1)\tan^{-1}\left(\frac{z}{z_R}\right)\right], \quad (2)$$

where $A_\rho^l(r,z)$ is a complex amplitude, ρ is the radial mode number, $\omega(z)$ is the beam radius, k_0 is the free space wave number, z_r is the Rayleigh range, and $L_\rho^{|l|}(x)$ is the generalized Laguerre polynomial.

LG modes form a complete orthogonal basis set. Any singular or combination of OAM mode(s) may be described by some superposition of LG modes. The relative weights of the modes of an OAM beam generated by a SPP are found from the expansion coefficients by [15]

$$I_{lp,l'p'} = |\langle u_{p'}^{l'}|e^{-i\Delta l\phi}|u_p^l\rangle|^2, \quad (3)$$

where the brackets indicate an integral over the (r,ϕ) surface and Δl is derived from Eq. (1).

The spiral surface of SPPs can either be machined to a smooth finish, or it can be approximated by a series of steps. Trying to obtain a smooth surface while also maintaining the critical geometry near the center of the plate proved difficult due to the finite size of the machining tools. Therefore, a 16-stepped polypropylene ($n = 1.53$) SPP was designed to generate an EM field with $l = \pm 1$ at 100 GHz ($\lambda = 3$ mm) (Fig. 1). The stepped design allows a more accurate center section of the SPP [Fig. 1 (highlighted)], compared to the initial smooth SPP prototype. Flipping the SPP so that the stepped face is pointed toward or away from the source alters the sense of phase rotation. We adopt the convention that a right-handed phase rotation, viewed along the Poynting vector corresponds to $l = +1$ and a left handed phase rotation corresponds to $l = -1$. The SPP has a final machined diameter of 100 mm and a step height of 5.94 mm.

To generate a millimeter wave beam with OAM, the $\Delta l = \pm 1$ SPP was illuminated by a well-known circular corrugated horn antenna [17]. The SPP-to-horn separation distance was 66.7λ. A three-dimensional W-band (75–110 GHz) scanning system has been employed to measure the resulting fields [Fig. 2 (inset)]. The scanner

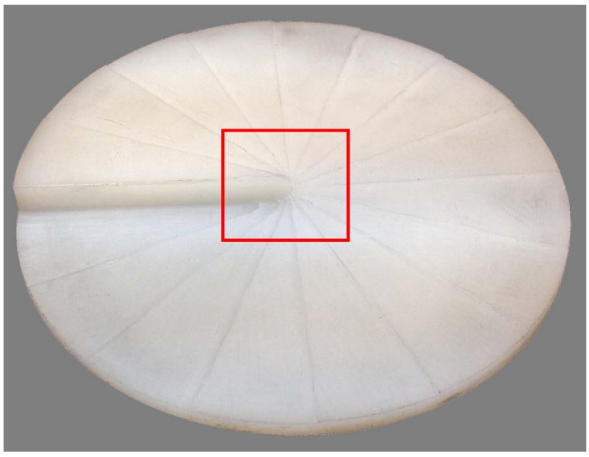

Fig. 1. $l = \pm 1$ polypropylene SPP, with improved center geometry (highlighted).

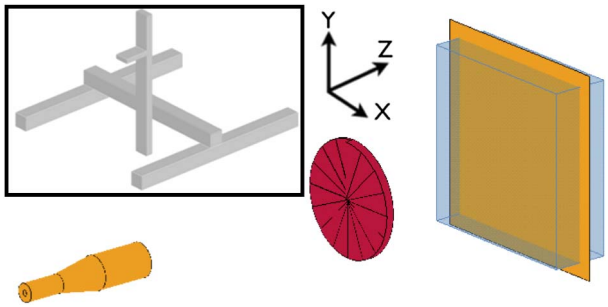

Fig. 2. Measurement setup with source horn (left), SPP (middle), data cube (right), and a CAD schematic of the three-dimensional field scanner (inset).

has a 50 cm × 50 cm × 50 cm working volume, with a mechanical positioning accuracy better than 0.1 mm. System characterization [18] and further studies have shown that probe corrections to remove the effect of the probe beam pattern are not necessary for these measurements.

The horn was centered in a two-axis rotary stage, which could be translated along an optical bench for alignment purposes. Before measurements could be taken, probe-to-horn alignment had to be checked by taking one-dimensional near-field beam cuts and comparing the results to previously validated models. These alignment measurements were taken at a probe-to-horn separation distance of 25.3λ. The near-field model was obtained by using the computational EM software package FEKO [19]. A specifically designed SPP mount was then placed on a three-axis positioning and rotation stage, located between the source and the probe.

With the probe along the boresight of the source, the SPP was positioned so that the probe recorded the minimum transmitted intensity. This corresponds to the center of the vortex, not necessarily the geometrical center of the SPP itself. This is because impure OAM modes are not perfectly circularly symmetric [20]. Once the SPP was positioned, absorbing material was placed around the mounting surfaces.

The scanner was positioned 44.4λ behind the SPP surface. A volume of $88.80\lambda \times 91.60\lambda \times 1.2\lambda$ was scanned with spatial positioning between measurement points of 3.60 mm (1.20λ), 3.72 mm (1.24λ), and 0.45 mm (0.15λ), along the X, Y, and Z axis respectively. The discrepency

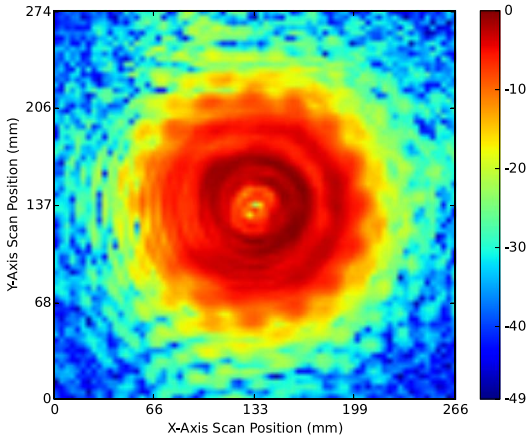

Fig. 3. Second X–Y plane annular intensity (decibel) pattern.

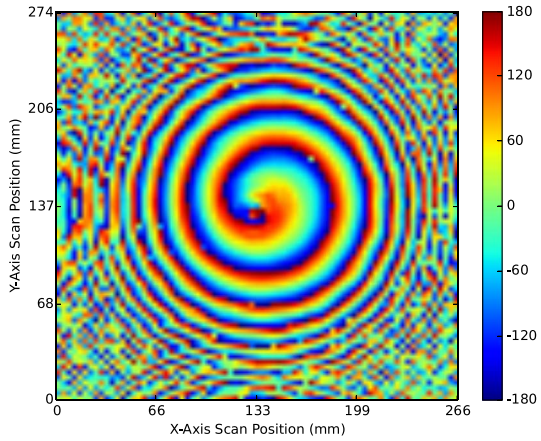

Fig. 4. Second X–Y plane with twisted phase (degrees) dislocation and forked termination point.

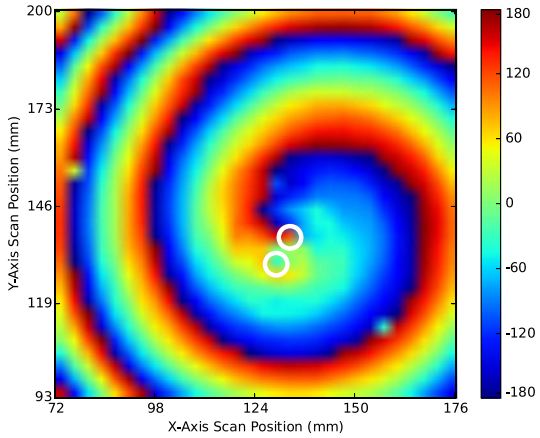

Fig. 6. Central section of the fifth X–Y phase plane. The white circles indicate the position of the two intensity minima, which do not change between plane cuts.

in X and Y position spacing is due to a difference in gear ratio between the two scanner axes.

For analysis, several X–Y planes were extracted from the three-dimensional data cube (Fig. 2). Normalized intensity (decibels) and phase (degrees), from the second X–Y plane can be seen in Figs. 3 and 4, respectively. The plane numbering follows the order that each plane was measured. Therefore, the first plane is closest to the SPP, while the second plane is 0.15λ farther away from the SPP, in the Z direction. The annular intensity ring is clearly visible, while the phase exhibits the expected twisting dislocation. The center of the intensity vortex clearly has some internal structure, while the phase dislocation forks into two minor dislocations.

To understand these unexpected results, the center of each X–Y surface was isolated. Figure 5 shows the isolated section of the fifth X–Y intensity plane. The vortex has two important visible features. First, there is a large, shallow intensity region approximately −8.0 to −10.0 dB directly inside the annular intensity ring. Second, there are a further two intensity minima, approximately −19.0 dB inside the shallow intensity region. These are pointed out in Fig. 5 by the white outline and seem to indicate a splitting of the central vortex structure. Even more surprisingly, the position of these two intensity minima did not change with changes in the Z-axis scan position. We expect this to be true only in the far-field however.

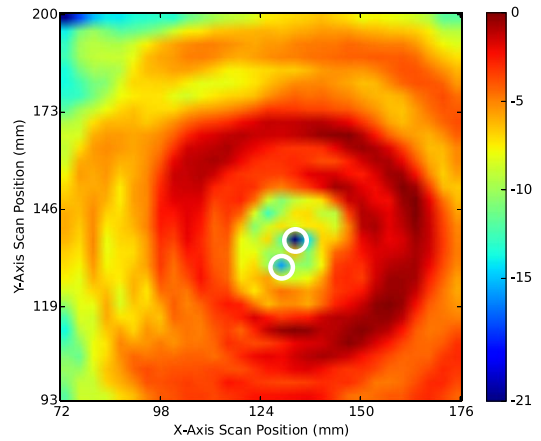

Fig. 5. Central section of the fifth X–Y intensity plane. The white circles highlight the two intensity minima.

The position of the two intensity minima are also outlined in the corresponding phase plane (Fig. 6). It is clear that the upper right minima is caused by the undefined phase at the termination point of the dislocation. As the wave propagates, the phase dislocation rotates about this point. The lower left minima is not directly associated with the phase dislocation, despite some phase planes exhibiting a forking of the dislocation, as in Fig. 4. This second minima resides near the forked, secondary phase dislocation, but is not directly at its termination point. The exact cause of the phase splitting, and the relation between it and the second intensity minima, should be investigated further, though we believe it is related to the fractional wavelength value of the step height h.

In this paper, three-dimensional phase and intensity data were taken of an $l = +1$ 100 GHz millimeter wave vortex beam. From the resulting data cube, several X–Y planes were extracted. Two separate planes were highlighted with the annular intensity pattern clearly visible, along with the twisting phase dislocation terminating in the center of the intensity pattern. Close examination of the intensity vortex showed that there were two intensity minima, not one as expected. The location of these two intensity minima surprisingly did not change with the Z-axis scan position. One of these intensity minima was shown to be associated with the termination point of the twisted phase dislocation, which indicates that it is the primary vortex. The second intensity minima was not directly associated with the phase dislocation termination point, despite some of the plane cuts showing a fork in the end of the phase dislocation. The exact source of this second intensity minima is still undetermined, but is believed to be related to the fractional wavelength value of the SPP step height h. Expanding on this, we are currently comparing vortex beams generated by several different SPPs. The resulting beams are measured from the SPP surface through the near field and into the far field, showing the creation of millimeter wave vortices. We intend to complete a thorough device study in order to insert SPPs into millimeter wave astronomical and

communication systems. Our ultimate goal is to conduct high-precision millimeter wave astronomical measurements and to explore the concept of using SPPs to expand upon the current OAM-based communication systems.

References

1. M. Harwit, Astrophys. J. **597**, 1266 (2003).
2. B. Thidé, H. Then, J. Sjöholm, K. Palmer, J. Bergman, T. D. Carozzi, Y. N. Istomin, N. H. Ibragimov, and R. Khamitova, Phys. Rev. Lett. **99**, 087701 (2007).
3. F. Tamburini, B. Thidé, G. Molina-Terriza, and G. Anzolin, Nat. Phys. **7**, 195 (2011).
4. G. Anzolin, F. Tamburini, A. Bianchini, G. Umbriaco, and C. Barbieri, Astron. Astrophys. **488**, 1159 (2008).
5. J. Wang, J. Yang, I. M. Frazal, N. Ahmed, Y. Yan, H. Huang, Y. Ren, Y. Yue, S. Dolinar, M. Tur, and A. E. Willner, Nat. Photonics **6**, 488 (2012).
6. F. Tamburini, E. Mari, A. Sponselli, B. Thidé, A. Bianchini, and F. Romanato, New J. Phys. **14**, 033001 (2012).
7. L. Allen, M. W. Beijersbergen, R. J. C. Spreeuw, and J. P. Woerdman, Phys. Rev. A **45**, 8185 (1992).
8. P. Coullet, L. Gil, and F. Rocca, Opt. Commun. **73**, 403 (1989).
9. D. Sanchez and D. Oesch, Opt. Express **19**, 24596 (2011).
10. D. Oesch, D. Sanchez, and C. Matson, Opt. Express **18**, 22377 (2010).
11. A. Carpentier, H. Michinel, and J. Salgueiro, Am. J. Phys. **76**, 916 (2008).
12. S. Maccalli, G. Pisano, S. Colafrancesco, B. Maffei, M. W. Ng, and M. Gray, Appl. Opt. **52**, 635 (2013).
13. L. Marrucci, C. Manzo, and D. Paparo, Phys. Rev. Lett. **96**, 163905 (2006).
14. G. A. Turnbull, D. A. Robertson, G. M. Smith, L. Allen, and M. J. Padgett, Opt. Commun. **127**, 183 (1996).
15. M. W. Beijersbergen, R. P. C. Coerwinkel, M. Kristensen, and J. P. Woerdman, Opt. Commun. **112**, 321 (1994).
16. F. Tamburini, E. Mari, B. Thidé, C. Barbieri, and F. Romanato, Appl. Phys. Lett. **99**, 204102 (2011).
17. B. Maffei, Jodrell Bank Centre for Astrophysics, School of Physics and Astronomy, University of Manchester, Oxford Road, Manchester M13 9PL, UK, is preparing a manuscript to be called "A compact Gaussian feedhorn for large arrays."
18. P. Schemmel, S. Maccalli, B. Maffei, F. Ozturk, G. Pisano, and M. W. Ng, "A near field 3D scanner for millimetre wavelengths," in *Proceedings of the 35th European Space Agency Antenna Workshop on Antenna and Free Space RF Measurements*, The Netherlands, September 10–13, 2013.
19. FEKO Comprehensive Electromagnetic Solutions, http://www.feko.info.
20. M. V. Berry, J. Opt. A **6**, 259 (2004).

IMPLEMENTATION OF A QUASI-OPTICAL FREE-SPACE S-PARAMETERS MEASUREMENT SYSTEM

B. Maffei, S. Legg, M. Robinson, F. Ozturk, M. W. Ng, P. Schemmel and G. Pisano.

JBCA, School of Physics and Astronomy, The University of Manchester, UK

ABSTRACT

A quasi-optical (QO) free-space test bench, based on two dual reflector Compact Test Range (CTR) systems, has been developed to characterise the RF properties of materials and QO components used in mm-wave astronomical instrumentation. While this facility has been designed to operate for several spectral bandwidths, in the first instance measurements have been performed in the W-band (75-110 GHz). We present the modelled and measured performance of the test bench and the procedure for calibrating and measuring samples under test. First measured results of the field across a 10 cm quiet zone indicate a maximum intensity variation of -4.5 dB and a maximum phase variation of 7°. Measurements of the cross-polarisation indicate higher levels than were predicted. A free-space calibration method has been developed based on the use of 3 calibration standards (Thru-Reflect-Line). Initial measurements of the reflectivity and transmittance for a range of materials have been performed, allowing the deduction of the refractive index.

1. INTRODUCTION

Measuring the Cosmic Microwave Background (CMB) polarisation is a powerful tool for testing cosmological models. Several present and future projects aiming at measuring this polarisation are based on the use of cold detectors coupled to microwave waveguide components and quasi-optical (QO) components. Some of them will contain interference filters, dewar windows and lenses for instance. The signal from the B-mode CMB polarisation is predicted to be extremely faint. Therefore these instruments require highly sensitive detectors and receiver components with well-known and characterised systematic effects that they will inevitably introduce in the measured signal.

A test set-up has been constructed to accurately test the RF and optical properties of quasi-optical components that are being developed, and to study their systematic effects. Components such as interference filters, half-wave plates and polarisers are all under study. This test bench will also allow the RF characterisation of materials from which these quasi-optical components are constructed. For instance, the accurate modelling and performance prediction of the QO components that are being developed are highly sensitive to the refractive index of the material being used. For the same material, the refractive index could vary from one supplier to another.

In order to retrieve the most accurate performance, these measurements must be performed in a collimated beam, to disentangle systematic effects that might arise from an oblique incidence on the sample under test. Moreover, since the QO components will be used in instruments dedicated to the study of the CMB, it is vital that they are tested within a zone with low aberrations and a low cross-polarisation [1] and where the electro-magnetic field is well controlled and known (referred as the Quiet Zone).

The CMB is best studied in the frequency domain comprised between 40 to 300 GHz. While this range could be covered in principle, our test set-up has been optimised for W-band to be used with our Vector Network Analyser in order to reach a typical maximum cross-polarisation of -40 dB [2].

2. SYSTEM DESIGN AND MANUFACTURE

The optical design of the test set-up coupled to a Vector Network Analyser (Rohde & Schwarz ZVNA-40) is detailed in a previous article [1]. It is based on two dual reflector Compact Test Ranges (CTR), each comprising a parabolic and a hyperbolic mirror (Fig. 1). Each CTR has a VNA converter head located at its focus acting both as a receiver and emitter. For these tests, the converters are operating in the W-band (75 – 110 GHz). However the corrugated horns that have been used on the converter waveguide outputs only transmit above 82 GHz. The combination of the converter, horn and CTR is creating a collimated beam where the EM field is pseudo-planar where the samples under test can be located. This cylindrical Quiet Zone (QZ) region has

low intensity and phase variations. The beam is then refocused on the horn aperture of the second VNA converter located at the focus of the second CTR. The mirrors have serrated edges in order to minimise the phase and amplitude variations across the QZ [1].

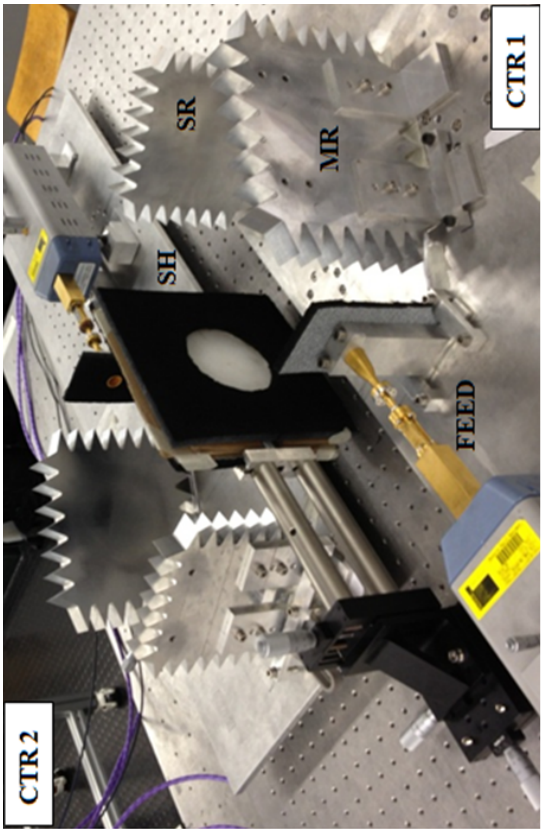

Figure 1. Test set-up. Each Compact Test Range (CTR) consists of a corrugated feed horn (Feed), a hyperbolic Sub-Reflector (SR) of size 17 cm and a parabolic Main-Reflector (MR) of 20 cm aperture, creating a central cylindrical Quiet Zone (QZ) region of 10 cm diameter, extending axially 5 cm towards each MR. Samples under test (SUT) are placed within this QZ, positioned such that the centre of the SUT lies coplanar to a reference plane, which is defined to be halfway between the two main reflectors. A Sample Holder (SH) secures an 11 cm diameter SUT and absorbs unwanted radiation from outside the QZ using a piece of RF absorber. The sample holder has been connected to a 3-axis positioning stage to allow accurate positioning.

3. ALIGNMENT

Each component has several degrees of freedom, making the alignment procedure difficult. To reduce the number of alignment parameters associated with the system, the feed horn is located in a fixed position. The reflectors (Main parabolic and Secondary hyperbolic) are positioned geometrically according to the CTR design parameters, with the feed horn acting as the point of origin. Each mirror is then roughly adjusted in order to maximise the signal between the emitter and the receiver. The CTR systems are then aligned independently to each other. A reflector is inserted in the QZ region and the Return Loss (RL) is optimised to be as close as possible to 0 dB (S parameter maximised close to 1) for each CTR individually by adjusting the position and tilt of the sub-reflector and the tilt of the main-reflector. Each component is repositioned in an iterative fashion until the optimum RL is reached.

The beam of each CTR is then investigated to ensure that it is at normal incidence to the QZ by scanning the phase across the reference plane using a 3D scanning system [3]. For these measurements the field probe consists of a circular to rectangular waveguide transition matched to free space and surrounded by absorber to eliminate reflections as shown in Fig. 2. Any misalignment would introduce a phase gradient over the scanned region. Adjusting the tilt of the main reflector accordingly can counteract this gradient. To achieve the optimal alignment the whole process is repeated iteratively, optimising the RL and correcting the phase gradient each time until no further improvement can be achieved.

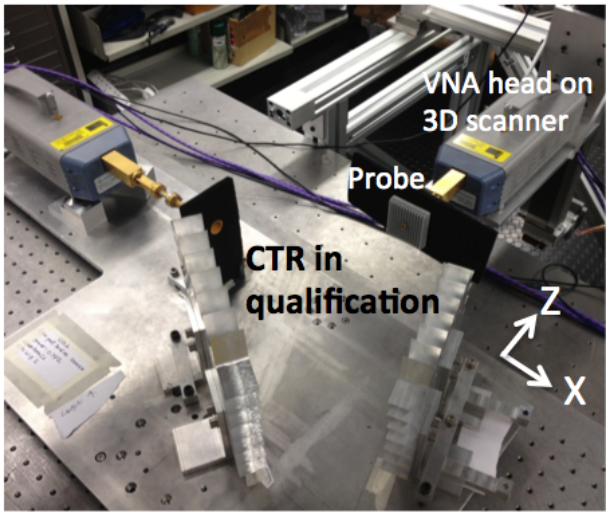

Figure 2. Image of the system configured to enable measurements of the QZ field in 3-dimensions using a circular to rectangular waveguide transition as the field probe.

Once each CTR is aligned, both are assembled together and the signal between the two converters maximised. When the free-space S-parameter system is in place, a loss of less than 1dB between the two VNA converters is observed.

4. CALIBRATION

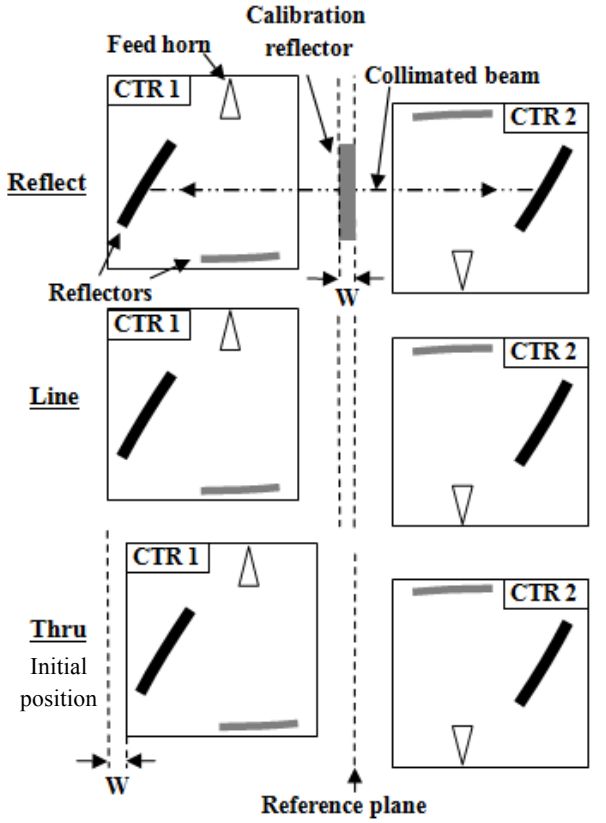

Figure 3. TRL calibration method of the set-up adapted from [5]. The initial position of the set-up is shown as the Thru standard, where the reference plane lies halfway between the two CTRs. The Reflect standard is taken by placing a calibration reflector of thickness W between the CTRs and moving CTR 1 back by a corresponding distance W. The Line standard is taken by removing the calibration reflector whilst keeping the separation distance between the two CTRs unchanged. The Thru standard is taken by moving CTR 1 back to its original position.

The set-up needs to be calibrated to remove systematic errors caused by transmission losses in the CTR components and the cables of the VNA. A well-established calibration method known as Thru-Reflect-Line [4] (TRL) is appropriate for this free-space set-up. This method requires the propagation distance between the two feed horns to be increased by a pre-determined precise amount when taking the Thru standard, therefore one CTR has been mounted on a micrometre controlled sliding platform. The TRL method is performed using the following procedure [5] (see Fig. 3):

1) Starting with the set-up initially in the Thru position, the Reflect standard is taken by placing a reflector of thickness W between the two CTRs, with one of the reflector faces aligned collinear to the reference plane, then moving CTR 1 back by a corresponding distance W.
2) The Line standard is obtained by removing the calibration reflector whilst keeping the separation distance between the two CTRs unchanged. The line length must satisfy: $10^\circ < k \cdot W < 170^\circ$ over the spectral band, where $k = 2\pi / \lambda$ and λ is the free-space wavelength. The restriction is to ensure that any phase ambiguity is avoided.
3) The Thru standard is taken by moving CTR 1 back to its initial position.

5. SYSTEM VERIFICATION

5.1 Simulation and measurement procedure

The free-space measurement system is modelled in GRASP [6]. Physical Optics (PO) calculations are conducted to simulate the properties of the RF field produced in the QZ. Further to simulation work conducted previously [1], the simulated far field radiation pattern of the corrugated feed horn is inputted as the radiation source instead of a simple linearly polarised Gaussian beam.

The intensity and phase of the field produced by the CTR system in the QZ region is sampled along the x-axis (as defined in Fig. 2) using the 3D scanning system described in section 3. In order to verify the performance of the system both GRASP simulations and the measured data are presented in the following two sections.

5.2 Intensity and phase measurements

As demonstrated in Fig. 4, the beam intensity observed across the QZ agrees well with the simulation over a 7.5 cm radius with increasing deviations from the model at larger radii. However, upon closer inspection over a 5 cm radius, deviations from the simulation in excess of 0.5 dB are observed. Over this 5 cm radius QZ, the

intensities observed have a range of 4.5 dB; 1 dB larger than predicted using the GRASP model.

The general phase evolution over a 10 cm diameter QZ matches that of the model, however larger oscillations are observed over the plateau region as shown in Fig. 5. Deviations from the model are typically less than 5° and the maximum phase variation over this 10 cm QZ is 7°. Further agreement with the model is likely to be hindered by component inefficiencies such as in the VNA cables and imperfections on the reflector surfaces.

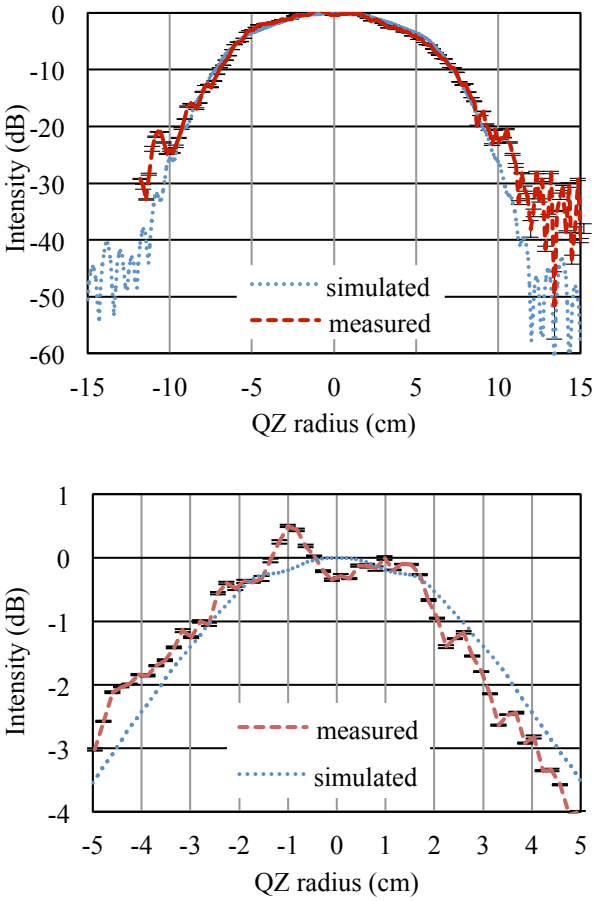

Figure 4. Comparison of the simulated field intensities across the QZ and the intensities measured using a circular to rectangular waveguide transition as a field probe. Data has been normalised using the maximum intensity of the model as the definition for the zero point. Top: comparison over a 30 cm diameter QZ. Bottom: comparison over a 10 cm diameter QZ.

5.3 Cross-polarisation measurements

It is predicted that the maximum cross-polarisation produced by the CTR system is in a diagonal cut through the QZ orientated at an angle of ϕ=45° to the test bench. In order to measure the field in this cut along the x-axis of the laboratory system, an additional waveguide was used, which rotated the beam pattern through an angle of 45°. The field could then be measured using the 3D scanning system.

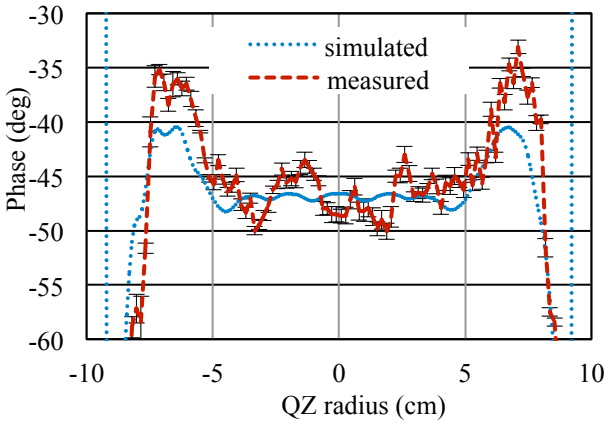

Figure 5. Comparison of the phase of the QZ field predicted by the GRASP simulation with the phase measured in the laboratory system over a 20 cm diameter QZ.

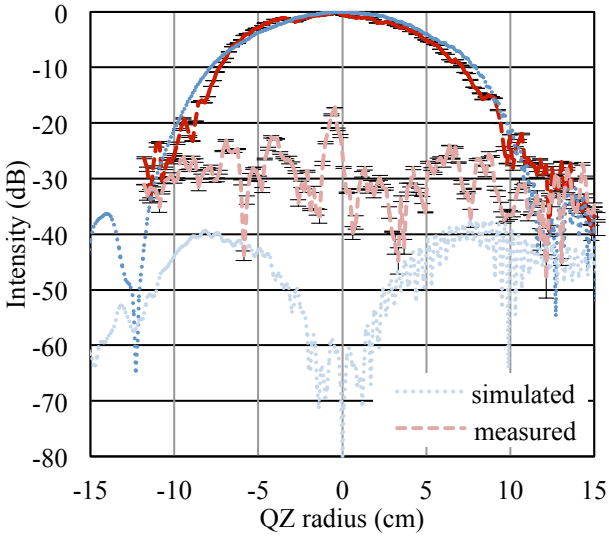

Figure 6. Measurements of the co-polarised intensity and cross-polarisation of the QZ field over a 30 cm diameter scan compared with the model prediction. Data is normalised so that the maximum intensity of the co-polarised field in the model is at zero.

Fig. 6 shows that the diagonal co-polarised intensity exhibits larger deviations from the model when compared with Fig. 4 (ϕ=0°), particularly at radii greater

than 5 cm. The measured cross-polarisation is also significantly higher than predicted across the entire 30 cm diameter scan zone. Most noticeable is the lack of a dip near zero. It is expected that this high cross-polarisation can be in part attributed to the field probe used for data collection and part to the manufacture error of the corrugated horn.

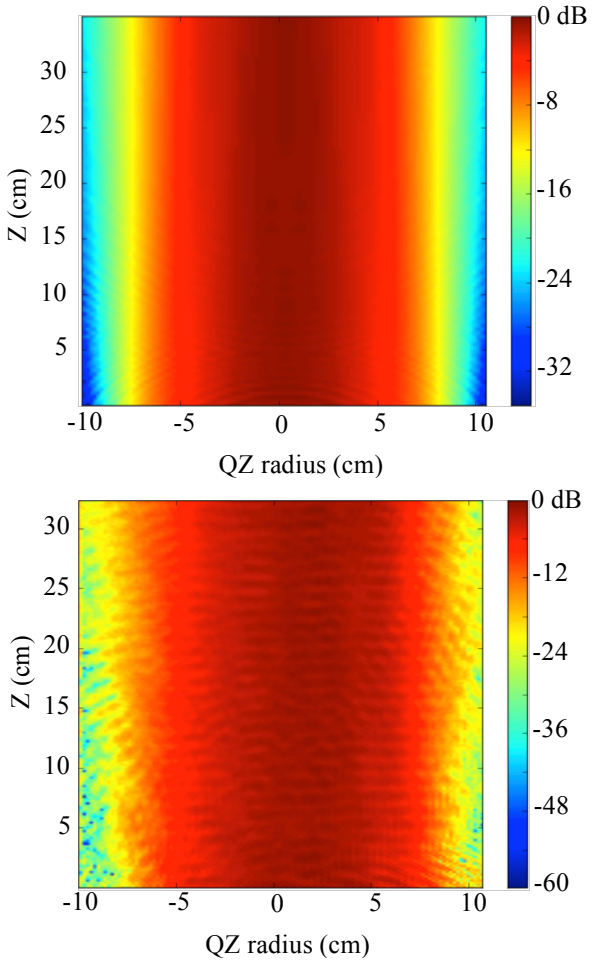

Figure 7: Top: Beam evolution predicted from the GRASP model. Bottom: Evolution of the beam measured from the CTR system using a circular to rectangular waveguide transition as a field probe.

5.4 Beam evolution

In order to further test the alignment of this measurement system, further field scans were conducted at increasing distances from the main-reflector along the z-axis. Fig. 7 illustrates how the QZ beam evolves along the z-axis. Both model simulations and the laboratory measurements are shown. The measured field exhibits ripples associated with the performances of the feed pattern and diffraction effects [1]. Artefacts in the outer beam region are also observed due to reflections from the edge of the sub- reflector.

6. COMPONENT CHARACTERISATION

6.1 RF properties of materials

A useful parameter when describing a dielectric is its permittivity (or refractive index). The knowledge of a material's refractive index is important as it describes how the material will interact with an external electric field and will be crucial to model the RF properties of the QO components that we are developing.

When a SUT is placed in the set-up, the resulting S-parameter, corresponding to reflections, has a series of troughs at specific frequencies due to destructive interference within the sample, as shown in Fig. 8.

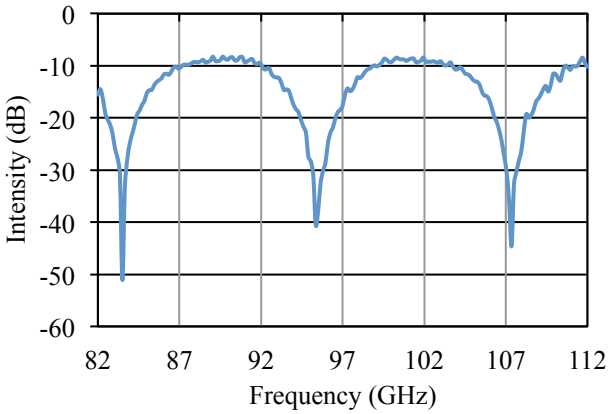

Figure 8. Illustration of the measured pattern in reflected power due to destructive interference within a 2.8 mm thick sample of Ultra-High-Molecular-Weight-Polyethylene (UHMWPE).

The position of the troughs is given by Eq. 1.

$$\alpha \frac{\lambda_0}{2n} = d \qquad (1)$$

where α is an unknown integer corresponding to the number of half-wavelengths in the sample, λ_0 is the free-space wavelength, n is the refractive index of the sample and d is the sample thickness. Using an initial guess for the refractive index that is close to its true value, the integer, α, can be found for the first trough in

the series. For each consecutive trough the value of α simply increases by 1.

Samples of 8.3mm thick Ultra-High-Molecular-Weight Polyethylene (UHMWPE) and 2.8 mm thick Polypropylene (PP) were both characterised using an initial guess for the refractive index of 1.5. The results are shown in Table 1 and 2 respectively. The two main sources of error are identified to be due to inhomogeneities in the sample thickness and sample positioning errors during the characterisation process. The later error can be determined by repeating the procedure multiple times to determine a statistical error. For each result only the most dominant error has been quoted, and this varied between individual measurements.

Table 1. Measurements of the refractive index of Ultra-High-Molecular-Weight Polyethylene.

Frequency (GHz)	Refractive index
≈83.5	1.518±0.002
≈95.5	1.517±0.001
≈107.5	1.5178±0.0007

Table 2. Measurements of the refractive index of Polypropylene.

Frequency (GHz)	Refractive index
≈108.0	1.506±0.001

7. CONCLUSION

In this paper, the alignment techniques and TRL calibration for the CTR system operating in the W-band have been discussed. In addition, the QZ field has been measured and it has been compared against a model created in GRASP. The measured field characteristics exhibit a maximum intensity variation of 4.5 dB and maximum phase variation of 7° over a 10 cm diameter QZ. Measurements of the cross-polarisation indicate higher levels than were predicted however further work needs to be done in this area in terms of limiting the effects of the field probe on these measurements. First measurements of materials have also been conducted in the system. The refractive index of UHMWPE and PP was extracted from the s-parameters to be 1.517±0.001 at 95.5 GHz and 1.506±0.001 at 108 GHz respectively. Improvements of this system need to be performed in order to limit the standing waves created by reflections of the SUTs, which can impact their measured RF performance. The use of the time domain gating function of the VNA can limit their effects. Another solution would be to perform an average across the spectral bandwidth.

REFERENCES

[1] F. Ozturk, B. Maffei, and M.W. Ng, "A quasi-optical free-space s-parameters measurement system for material characterization in W and Ka bands", Proceedings of the 33rd ESA Antenna Workshop on Challenges for Space Antenna Systems, ser. ESA Special Publication, 2011

[2] B. Maffei, et. al., "Effects of quasi-optical components on feed-horn co- and cross-polarisation radiation patterns," Proc. of SPIE, Vol. 7020, 70202H-1, 2008

[3] P. Schemmel et al, "A near field 3D scanner for millimeter wavelegths", these proceedings

[4] G. F. Engen and C. A. Hoer, "Thru-reflect-line: An improved technique for calibrating the dual six port automatic network analyzer," IEEE Trans. Microw. Theory Tech., vol. MTT-27, no. 12, pp. 987–993, Dec. 1979

[5] D. Bourreau, A. Péden, and S. L. Maguer, "A Quasi-Optical Free-Space Measurement Setup Without Time-Domain Gating for Material Characterization in the W-Band", IEEE Transactions on instrumentation and measurement, vol. 55, no. 6, December 2006

[6] GRASP available online at the web address: http://www.ticra.com

A NEAR FIELD 3D SCANNER FOR MILLIMETRE WAVELENGTHS

P. Schemmel, S. Maccalli, B. Maffei, F. Ozturk, G. Pisano, and M.W. Ng

Jodrell Bank Centre for Astrophysics, School of Physics and Astronomy, University of Manchester, Oxford Road, Manchester M13 9PL, UK
E-mail: peter.schemmel@postgrad.manchester.ac.uk

ABSTRACT

Typical millimetre wave astronomical receiver systems make use of quasi-optical (QO) components such as lenses, interference filters, polarisers, or polarisation modulators. Each of these may be located in the near field of additional components. Combinations of these components lead to standing waves and reflections, which degrade the overall RF performance. Therefore, it is important to characterise the near field of QO components and QO systems, as well as the evolution of the near field along the propagation axis. Additionally, it is not always feasible to measure the far-field of large systems. This limitation may be overcome by using analytic methods to transform near field measurements into far field radiation patterns.

We have developed a 3D near field scanner for millimetre wavelengths. The scanner has a working volume of 50 cm $\times$ 50 cm $\times$ 50 cm and is coupled to a vector network analyser (VNA) operated in the W-band (75-110 GHz). Volumetric scanning provides the advantage of being able to directly measure field parameters at all positions in the optical path and to map the evolution of the near field.

We present the design and performance of this facility together with the initial near field characterisation of some QO components that are also compared to RF simulations.

1. INTRODUCTION

Electromagnetic fields generated by radiating antenna are typically divided into three sections, the reactive near field, radiating near field (or Fresnel Region) and the far field (Fraunhofer Region). Although the accepted region definitions have discrete boundaries, the actual fields vary smoothly as they propagate and the distinction between near field and far field regions is not always clear. The reactive near field is defined as the region within a distance of one wavelength (λ) from the antenna. The minimum radial distance from the antenna, at which a wave can be considered in the far field is,

$$r_{min} = \frac{2D^2}{\lambda} + \lambda \tag{1}$$

where D is the largest cross sectional dimension of the antenna [1]. The radiating near field occupies the region between these two boundaries. The composition and form of the radiated field varies significantly between regions. The reactive near field is comprised of several plane wave modes in addition to evanescent modes, while the far field is primarily a single plane wave mode [2]. Alternatively, the radiating near field is free from evanescent modes, but a superposition of plane wave modes are required to describe the field accurately.

If a QO component is introduced into the near field of another component, antenna or otherwise, the interaction of the component and radiated field can result in spurious reflections and standing waves, which reduce the overall RF performance. Additionally, the several plane wave modes of the near field, interact with the QO components at various oblique incidence angles [4, 5]. These effects might not be included in some RF models, which can result in significant discrepancies between modelled and measured data.

2. CONCEPT

The 3D near field scanner consists of two parallel Z axis and one X axis belt driven rails supported by a 1.0 metre high aluminum frame. A movable carriage is allowed to translate along a Y axis screw driven rail that is mounted to the X axis (Fig. 1). Stepper motors are used to drive the translating rails. The total scanning volume is 50 cm $\times$ 50 cm $\times$ 50 cm. The scanner has a mechanical positioning accuracy better then 0.1 mm.

A Rohde & Schwarz RS ZVA-110 converter, used for the probe, is mounted to the Y axis carriage while a second converter used for the antenna under test (AUT) is mounted on a separate frame. A RS ZVA-40 VNA is used to measure the S-parameters of the AUT, across the W-Band. Although data is recorded across the entire W-Band, the data in section 4 is comprised of only the

100 GHz trace. Motor control and VNA data acquisition is carried out by custom Labview programming.

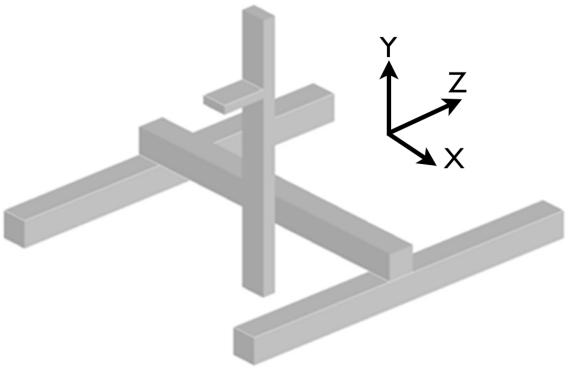

Figure 1. 3D Near Field Scanner

A WR-10 rectangular to circular transition waveguide, matched to free space, is used as the receiving probe. The probe has an opening diameter of 3 mm, a measured return loss of -34.4 dB at 100 GHz and is surrounded by 3D printed plastic absorber with a pyramidal shaped front face, to minimize reflections. For pattern corrections the probe beam pattern is modelled by HFSS, a finite element method solver from ANSYS.

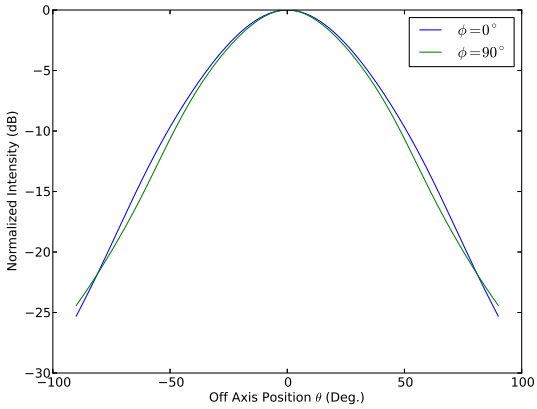

Figure 2. Far Field Probe Beam Pattern

2.1. VNA Stability

Large volume scans can take many hours to complete, which means VNA stability can become a limiting factor in the precision of the field measurements. To assess the stability of our VNA, the probe and AUT were aligned on the near field scanner and were separated by 300 mm. For eighteen hours, S_{21} and phase data was taken at one minute intervals, where the S-parameters are in intensity as opposed to amplitude.

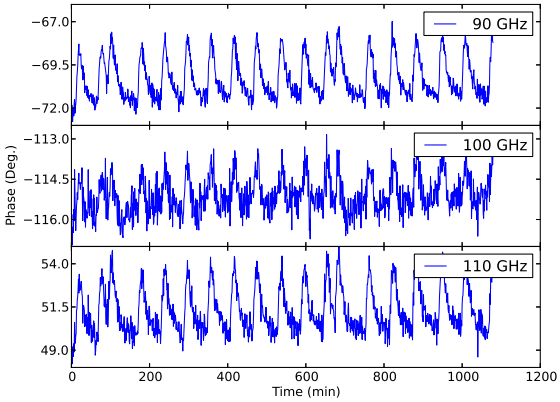

Figure 3. Phase Stability

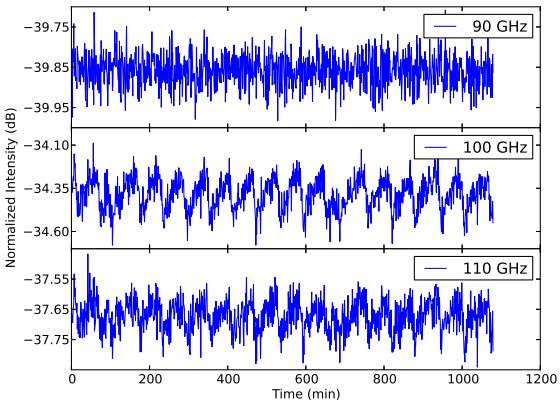

Figure 4. S_{21} Stability

The VNA stability tests show a S_{21} peak to peak variation of approximately 0.6 dB and a peak to peak phase variation of 4.5° at 100 GHz (See Figures 3 and 4). For the three frequencies measured, a cycle period of approximately one hour was observed. In the future, a directional coupler will be used to monitor VNA stability during scans for accurate data correction.

3. MEASUREMENT CORRECTIONS

3.1. Far Field Corrections

When measuring the co-polar far field of a radiating antenna with a planar scanning system, two corrections must be applied to reconstruct the field. The first correction is geometrical. Typically, far fields are calculated on a sphere of constant radius from the origin of the optical system. This condition is not met when scanning along a linear axis (Fig. 5). For increased values of θ

the difference in distance between the probe position and calculation differs by

$$dR = R\left(\frac{1-\cos(\theta)}{\cos(\theta)}\right) \tag{2}$$

The intensity of the field, S_{21}^2 drops off as $\frac{1}{(R+dR)^2}$ while the phase changes linearly with dR.

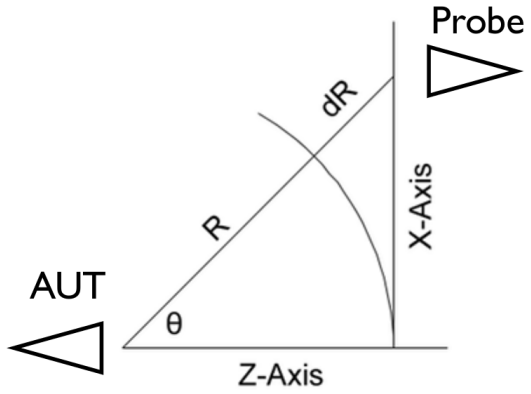

Figure 5. Correction Geometry

The S_{21} correction factor is then,

$$S_C(\theta) = \frac{(R+dR)^2}{R^2} = \left(1+\left(\frac{1-\cos(\theta)}{\cos(\theta)}\right)\right)^2 \tag{3}$$

The second correction required compensates the measured data for the probe beam pattern. As the scanner moves to larger values of θ, the response of the probe to the AUT field changes (Fig. 2). The measured field is the product of the probe pattern and AUT pattern [6],

$$S_{21}^{Measured}(\theta) = S_{21}^{AUT}(\theta)S_{21}^{Probe}(\theta) \tag{4}$$

The actual AUT co-polar field is then

$$S_{21}^{AUT}(\theta) = S_{21}^{Measured}(\theta)\frac{S_C(\theta)}{S_{21}^{Probe}(\theta)} \tag{5}$$

3.2. Near Field Corrections

Since the probe used in these experiments meets all the criteria (low-directivity, small return loss, etc.) for a desirable planar scanning probe according to [6] and [8], near field probe corrections are not included here. However, the close proximity of the probe and AUT could result in large standing wave effects. As stated earlier, 3D printed plastic absorber with a pyramidal front surface, backed with copper foil surrounded the AUT and probe to minimize reflections. Another way to minimize the effect of standing waves is by time domain gating the VNA signal.

3.3. Time Domain Gating

Time domain gating is used to remove standing wave effects from the recovered field parameters. This is accomplished by Fourier transforming the VNA frequency sweep data. The main signal appears as a large peak in the time domain. Since reflections travel a greater distance then the main signal they appear after it in the time domain. The VNA can be instructed to only accept the main signal, rejecting the reflections and improving the recorded data. In these initial tests the time domain gate was set by scanning the probe along each axis and recording the global minimum and maximum of the main signal. In the future the time domain gating will be set automatically by the control software during the scan.

For each measurement position, three scans were taken with varying degrees of time domain gating: no time domain gating, weak time domain gating and strong time domain gating. The absolute amount of time gating was dependent on the Z axis position of the probe relative to the AUT. However, strong time domain gating greatly constrained the peak signal, while weak time domain gating allowed more signal to pass through. The time domain gating results are detailed in section 4.3.

4. SYSTEM VALIDATION

4.1. Far Field Measurements

Measurement and correction methodology were validated by measuring the far and near field beam pattern of a well known corrugated horn [7], which was modeled using a Method of Moments (MOM) simulation by FEKO. Each data point is comprised of 50 frequency sweeps of the VNA, and the error bars correspond to one standard deviation of the sweep data. In the following sections, the difference between the modelled and measured data is calculated by taking the difference between the normalized modelled and measured data in linear scaling. The difference is then converted into dB scaling for comparison purposes.

Figures 6 and 7 show the co-polar far field $\phi = 0°$ and $\phi = 90°$ modelled beam cut, data and difference. The data is corrected according to equation (5). The maximum difference between the model and the data in the $\phi = 90°$ cut is -12.9 dB while the averaged difference across the pattern is -31.4 dB. Along the $\phi = 0°$ cut, the

maximum difference is -9.4 dB and the averaged difference is -24.0 dB. This indicates that the data for both cut directions matches the modell well. However, the signal to noise ratio decreases with increasing θ. This is due to the probe boresight not being aligned with the phase center of the AUT. Additionally, planar scanning is limited in accessible values of θ, where a cylindrical system has no such limitation. For these reasons, planar scanning is not optimal for far field scanning. Yet, these measurements prove that the planar scanning system and correction methodologies are working properly.

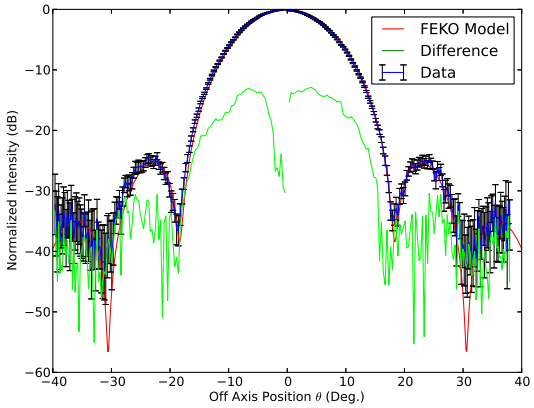

Figure 6. Co- Pol $\phi = 0°$

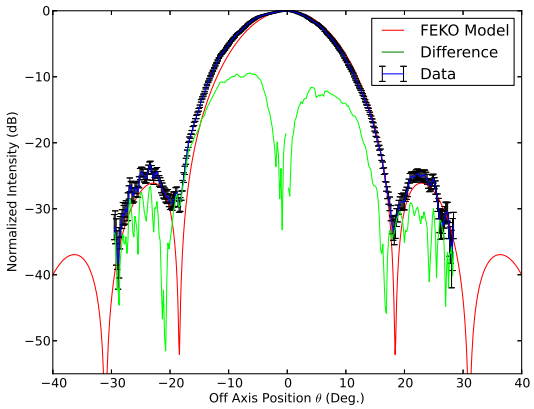

Figure 7. Co- Pol $\phi = 90°$

4.2. Near Field Measurements

The corrugated horn was also used to validate the near field capabilities of the 3D scanner. Near field cuts parallel and perpendicular to the polarization direction of the horn were taken at horn to probe separation distances of 76 mm and 42 mm. All near field data was left uncorrected for probe effects. Figures 8 and 9 show the near field data, model and difference for the near field X axis and Y axis cuts at a probe to horn separation distance of 76 mm. In the X cut, the maximum difference between the model and data is -12.5 dB, while the averaged difference across the beam is -30.0 dB. The results in the Y cut direction are similar. The maximum difference is -12.6 dB and the averaged difference is -34.1 dB.

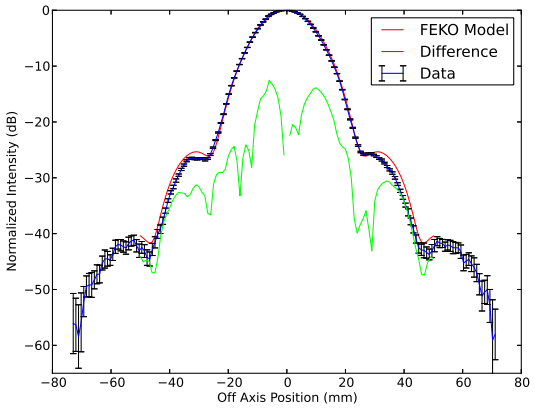

Figure 8. Near Field X Cut: Separation Distance 76 mm

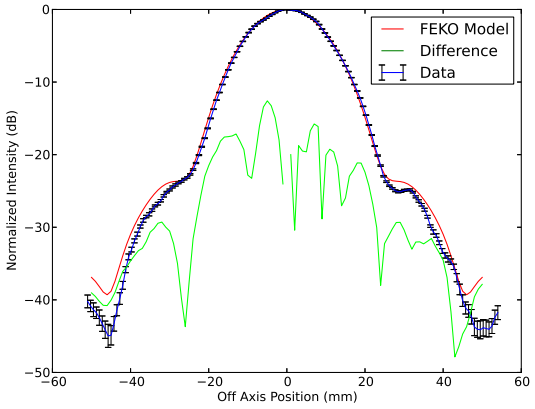

Figure 9. Near Field Y Cut: Separation Distance 76 mm

Figures 10 and 11 show the data, model and difference for a probe to horn separation distance of 42 mm. Along the X axis cut the maximum difference between the data and model, in the main lobe is -9.9 dB and the averaged difference is -36.6 dB. As expected, the uncorrected near field data fails to match the modelled data at large distances from the center of the main beam. The near field Y axis data matches well across the main beam, but has asymmetrical side lobes. This could be due to a small misalignment between the AUT and probe. The maximum difference across the main beam of the Y axis cut is -8.8 dB and the averaged difference is -34.1 dB.

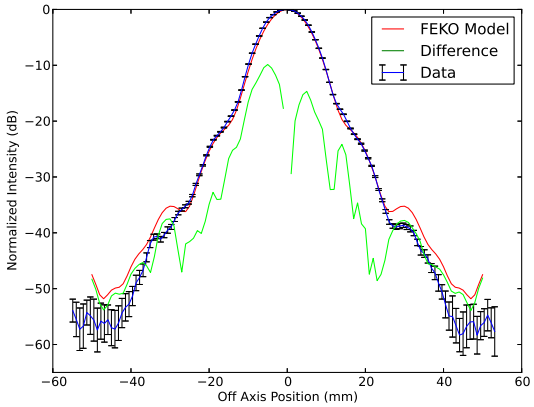

Figure 10. Near Field X Cut: Separation Distance 42 mm

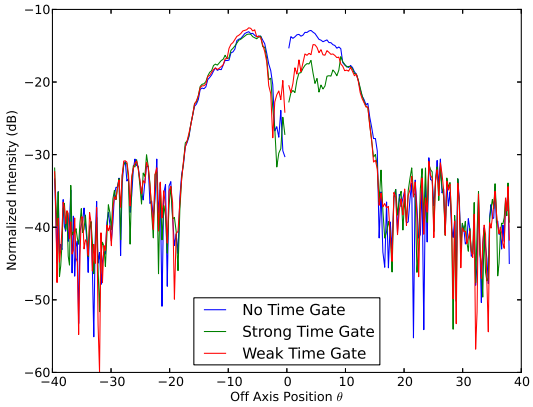

Figure 12. Far Field $\phi = 0°$ Time Gate Test

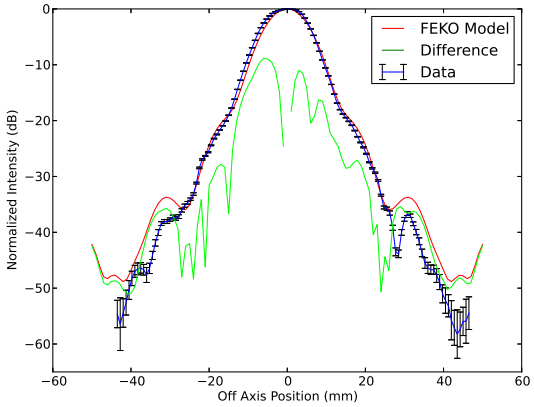

Figure 11. Near Field Y Cut: Separation Distance 42 mm

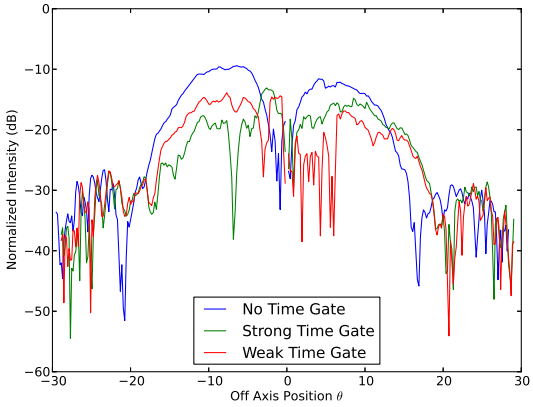

Figure 13. Far Field $\phi = 90°$ Time Gate Test

4.3. Time Domain Gating Results

Figures 12 and 13 show the time domain gating results in the far field of the AUT. The strong time domain gate had a width of 0.45 ns centred on the main signal, and the weak time domain gate had a width of 1.05 ns. The effectiveness of time domain gating in the far field was inconclusive. The averaged difference across the pattern between the best time gate state and no time gating was 0.3 dB for the $\phi = 90°$ cut, and 0.6 dB for the $\phi = 0°$ cut. Strong time domain gating showed the best results for $\phi = 90°$, but weak time domain gating was most effective along the $\phi = 0°$ cut.

Figures 14 and 15 show the time domain gating data for the near field of the AUT at a distance of 76 mm. The strong gate had a width of 0.45 ns, while the weak gate had a width of 1.1 ns. The averaged difference between strong time gating and no time gating was 2.1 dB along the X cut, and was 0.6 dB along the Y cut. Along the X cut direction, strong time domain gating performed the best. Strong and weak time domain gating performed equally well along the Y cut. However, the discrepancy between X and Y cuts is most likely due to misalignment of the system rather then suppression of standing waves.

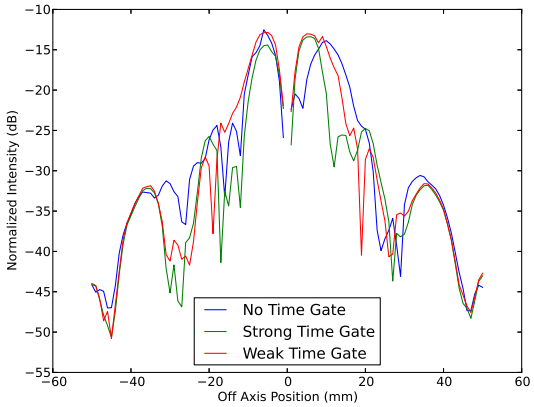

Figure 14. Near Field X Cut: Separation Distance 76 mm - Time Gate Test

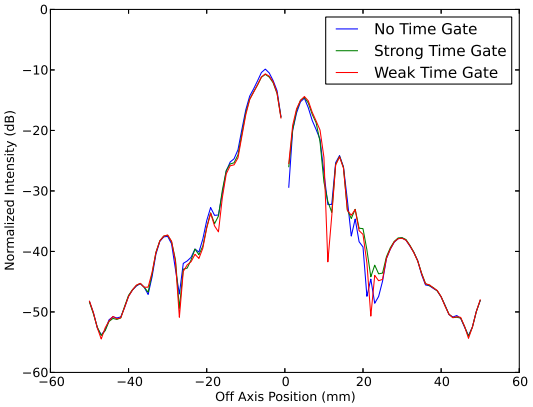

Figure 16. Near Field X Cut: Separation Distance 42 mm - Time Gate Test

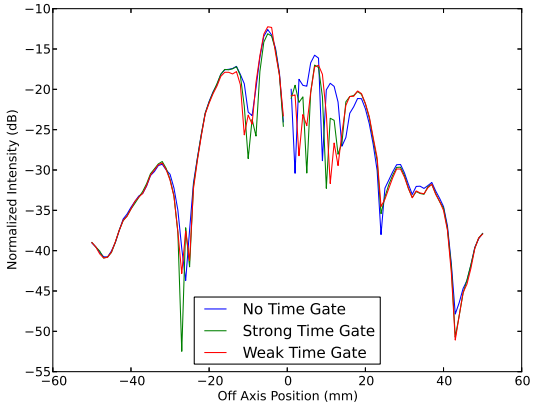

Figure 15. Near Field Y Cut: Separation Distance 76 mm - Time Gate Test

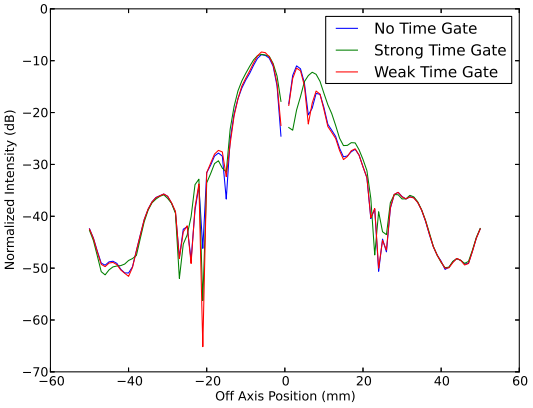

Figure 17. Near Field Y Cut: Separation Distance 42 mm - Time Gate Test

Finally, Figures 16 and 17 show the time domain gating data for the near field of the AUT at a distance of 42 mm. The strong gate had a width of 0.45 ns, while the weak gate had a width of 0.9 ns. Like the previous cases, time domain gating had little impact on the recorded signals at the 42 mm separation distance. Along the X axis, weak time domain gating provided a 0.1 dB decrease in the averaged difference between the model and data. Along the Y cut, strong time domain gating actually increased the averaged different between data and model by 0.4 dB, while weak time gating provided a decrease in the averaged difference of 0.1 dB.

For the six measurement positions, strong and weak time domain gating produced the best averaged difference value three times respectively. Yet, strong time domain gating produced the worst values at the 42 mm separation distance. It is also unclear as to how much the AUT and probe alignment affected the results. For these reasons the best time gating parameters to use are unclear. The time domain gating analysis has shown that for this specific set up, any AUT to probe separation distance equal to or greater then 42 mm, has a minimal affect on the measured data. This is due to the small cross sectional area of both the AUT and the probe, in conjunction with the 3D printed absorber panels used to surround both antenna. However, other systems could have a configuration that would render time domain gating extremely important.

5. LENS MEASUREMENTS

To demonstrate the 3D scanning capabilities of this near field scanning system we have measured the XZ and XY plane of a dielectric Ultra High Molecular Weight polyethylene lens at 97 GHz, with 10 frequency sweeps per point. The lens has a focal length of 208.5 mm, radius of curvature of 112 mm and a measured index of refraction $n = 1.517$. The lens was placed 208.5 mm from the phase center of the corrugated horn used in the previous sections.

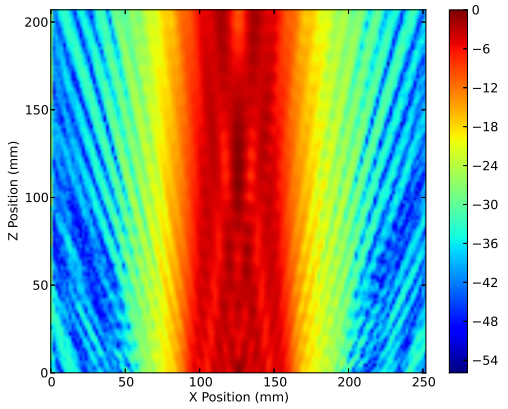

Figure 18. Lens XZ Plane S_{21} (dB)

Figure 18 shows S_{21} in the XZ plane. The scan was started 103.75 mm from the front surface of the lens, and scanned along the Z axis for 207.5 mm. Along the X axis, the scanner measured the field, up to 126 mm to either side of the centre of the propagated beam. A resolution of 1.8 mm was used for both the Z and X axis.The beam waist is visible as a high intensity region approximately between $z = 100$ mm and $z = 130$ mm. Figure 19 displays the phase of the lensed beam, in the XZ plane. The flat phase fronts are clearly visible across the beam.

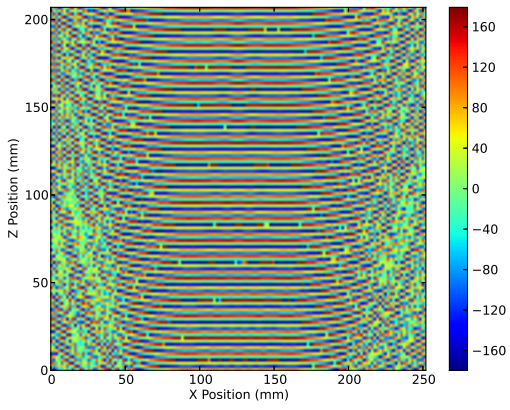

Figure 19. Lens XZ Plane Phase (Deg.)

Figure 20 shows the measured S_{21} values of the lensed beam in the XY plane. The XY plane was taken at a distance of 208.15 mm from the front surface of the lens, with a range of 252 mm and resolution of 1.8 mm in both the X and Y axis directions.

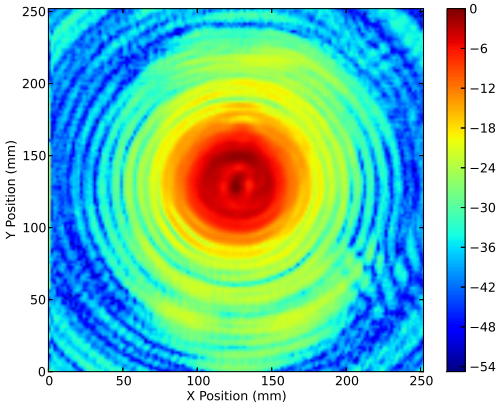

Figure 20. Lens XY Plane S_{21} (dB)

Figure 21 shows the flat phase front of the lensed beam in the XY plane. There are visible phase distortions which start approximately 54 mm from the centre of the main beam, and continue to propagate to larger radial distances. These are most likely caused by diffraction from the aluminum lens mount, which has an inner radius of 55.6 mm and an outer radius of 65.5 mm.

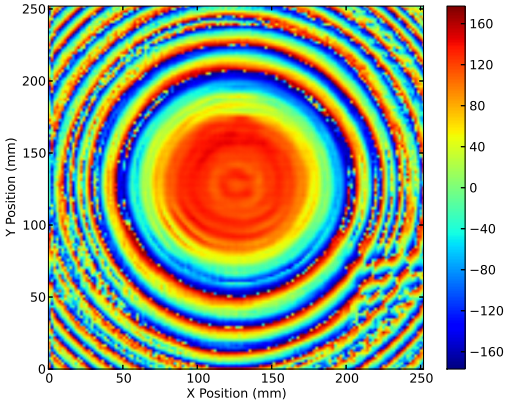

Figure 21. Lens XY Plane Phase (Deg.)

A cut was taken from the centre of the XY plane data, and was compared to a FEKO model in order to validate these measurements (Fig. 22). The data matches the model well across the center portion of the beam, with a maximum difference between model and data of -7.9 dB. However, the lack of probe corrections have resulted in severe side lobe suppression.

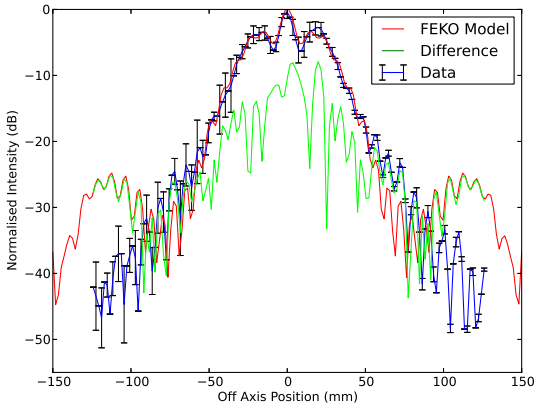

Figure 22. Lens XY Plane Cut

Figure 23 shows the centre cut of the XZ plane, used to accurately determine the measured new beam waist position. The maximum of the XZ plane cut was found to be 117.0 mm from the initial scan Z axis position. This corresponds to a beam waist position of 214.75 mm, after correcting for the lens half thickness. Gaussian beam optics calculations predict a beam waist position of 215.0 mm.

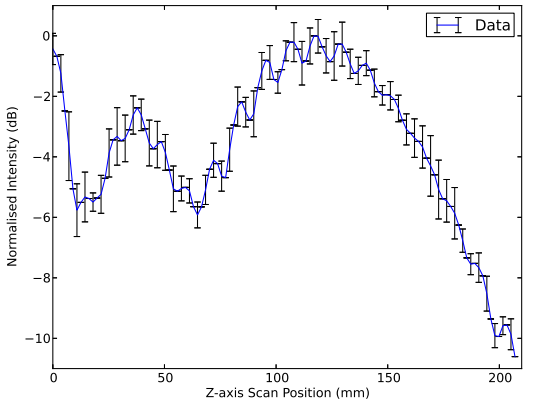

Figure 23. Lens XZ Focal Point Cut

6. CONCLUSIONS

To review, this paper has demonstrated the capabilities of a new 3D field scanner for millimetre wave antenna measurements. It has been shown that for scans greater than one hour, our VNA stability is a significant source of variation in the measured data. A well known corrugated horn was used to characterize the system in the far- and near field. Geometrical and probe beam pattern corrections were applied to the far field data, while the near field data was left uncorrected. Time domain gating was tested to see the effect of reflections between the AUT and probe. Yet, no significant variation in the beam cuts were seen. The AUT was measured in the far field along the $\phi = 0°$ and $\phi = 90°$ planes, and matched the modelled data well. Due to the off-boresight angle between the probe and AUT, the signal to noise level began to drop at large scan angles. The near field of the AUT was measured along the X and Y axis, at two different separation distances. The main beam for each near field cut matched the model well, with the side lobes being slightly lower then expected due to the lack of near field probe correction. Finally, to demonstrate the full 3D capabilities of this system, an Ultra High Molecular Weight polyethylene lens was measured in the XZ and XY planes. The new beam waist was measured to be within 0.5 mm of the predicted value and the field intensity matches the model predictions well.

Our continued work on this scanning system includes improvements to the scanning speed, signal to noise levels and programming optimization. We also plan to include near field probe corrections and to measure components which have significant variations in the beam along the propagation axis. Additionally, we intend to measure 3D x-pol patterns of several different antenna and QO components.

REFERENCES

[1] A. Yaghjian, *"An Overview of Near Field Antenna Measurements,"* IEEE Trans. Antennas Propagat., vol. AP-34, pp. 3–44, Jan. 1986.

[2] R.H. Clarke and J. Brown, *"Diffraction Theory and Antennas,"* Chichester, United Kingdom. John Wiley & Sons, 1980.

[3] D.M. Kerns, *"Plane-Wave Scattering-marix Theory of Antennas and Antenna-Antenna Interactions,"* Nat. Bureau of Standards, Monograph 162, June 1981.

[4] J. Anthony Murphy, *"Gaussian beam mode analysis of partial reflections in simple quasi-optical systems fed by horn antennas,"* Infrared Physics and Technology 44 (2003) 289 - 297.

[5] B. Maffei, G. Pisano, M.W. Ng, V.C. Haynes, *"Di-electrically embedded mesh half wave plate beam impact studies,"* Proc. SPIE 8452, 84520K (2012).

[6] S. Gregson, J. McCormick and C. Parini, *"Principles of Planar Near-Field Antenna Measurements,"* Stevenage, United Kingdom. Michael Faraday House, 2007.

[7] B. Maffei, E. Gleeson, J.A. Murphy, G. Pisano, *"Study of corrugated Winston horns,"* Astronomical Structures and Mechanisms Technology. Proceedings of the SPIE, Volume 5498, pp. 812-817 (2004).

[8] J. Wang, *"An Examination of the Theory and Practices of Planar Near-Field Measurement,* IEEE Trans. Antennas Propagat., vol. 36, No. 6, pp. 746-753, June. 1988.

References

[1] L. Allen, M. Beijersbergen, R. Spreeuw, and J. Woerdman, Physical Review A, **45**, 8185 (1992).

[2] M. Padgett, J. Courtial, and L. Allen, Physics Today, **57**, 35 (2004).

[3] J. Leach, M. Padgett, S. Barnett, S. Franke-Arnold, and J. Courtial, Physical Review Letters, **88**, 257901 (2002).

[4] M. Uchida and A. Tonomura, Nature, **464**, 737 (2010).

[5] B. McMorran *et al.*, Science, **331**, 192 (2011).

[6] R. Beth, Physical Review, **50**, 115 (1936).

[7] O. Emile *et al.*, Physical Review Letters, **112**, 053902 (2014).

[8] S. Franke-Arnold, L. Allen, and M. Padgett, Laser & Photonics Reviews, **2**, 299 (2008).

[9] A. Yao and M. Padgett, Advances in Optics and Photonics, **3**, 161 (2011).

[10] K. O'Holleran, M. Dennis, and M. Padgett, Physical Review Letters, **102**, 143902 (2009).

[11] K. O'Holleran, M. Dennis, F. Flossmann, and M. Padgett, Physical Review Letters, **100**, 053902 (2008).

[12] J. Leach, M. Dennis, J. Courtial, and M. Padgett, New Journal of Physics, **7**, 55 (2005).

[13] J. Nye, Journal of Optics A: Pure and Applied Optics, **6**, S251 (2004).

[14] M. Harwit, The Astrophysical Journal, **597**, 1266 (2003).

[15] D. Sanchez, D. Oesch, and O. Reynolds, Astronomy & Astrophysics, **556**, A130 (2013).

[16] J. Jackson, Classical Electrodynamics, 3rd Edition (1998).

[17] D. Griffiths, Introduction to Electrodynamics, 3rd Edition (1999).

[18] G. Fowles, Introduction to Modern Optics, (1975).

[19] P. Goldsmith, Quasioptical systems (1998).

[20] B. Thidé, Electromagnetic Field Theory (2014).

[21] Arnoldsat, http://www.arnoldsat.com, 2014.

[22] J. Alda, Encyclopaedia of Optical Engineering , 999 (2003).

[23] A. O'Neil, I. MacVicar, L. Allen, and M. Padgett, Physical Review Letters, **88**, 053601 (2002).

[24] M. Beijersbergen, R. Coerwinkel, M. Kristensen, and J. Woerdman, Optics Communications, **112**, 321 (1994).

[25] G. Turnbull, D. Robertson, G. Smith, L. Allen, and M. Padgett, Optics Communications, **127**, 183 (1996).

[26] K. Sueda, G. Miyaji, N. Miyanaga, and M. Nakatsuka, Optics Express, **12**, 3548 (2004).

[27] P. Schemmel, S. Maccalli, G. Pisano, B. Maffei, and M. Ng, Optics Letters, **39**, 626 (2014).

[28] P. Schemmel, G. Pisano, and B. Maffei, Optics Express, **Submitted** (2014).

[29] D. Sanchez and D. Oesch, The aggregate behavior of branch points: the creation and evolution of branch points, 2009.

[30] D. Oesch, D. Sanchez, C. Tewksbury-Christle, and P. Kelly, The aggregate behaviour of branch points: branch point density as a characteristic of an atmospheric turbulence simulator, 2009.

[31] C. Tewksbury-Christle, D. Oesch, D. Sanchez, and P. Kelly, The aggregate behavior of branch points: the use of branch point pairing to generate a hidden phase for closed-loop ao, 2009.

[32] D. Sanchez, D. Oesch, C. Tewksbury-Christle, and P. Kelly, The aggregate behavior of branch points: a proposal for an atmospheric turbulence layer sensor, 2010.

[33] D. Oesch, D. Sanchez, C. Tewksbury-Christle, and P. Kelly, The aggregate behavior of branch points: altitude and strength of atmospheric turbulence layers, 2010.

[34] D. Oesch, D. Sanchez, and C. Matson, Optics Express, **18**, 22377 (2010).

[35] D. Sanchez and D. Oesch, Optics Express, **19**, 25388 (2011).

[36] D. Sanchez and D. Oesch, Optics Express, **19**, 24596 (2011).

[37] D. Sanchez and D. Oesch, Hiding the phase: the filling of the slope discrepancy hilbert space, 2012.

[38] D. Sanchez, D. Oesch, and P. Kelly, The aggregate behaviour of branch points: theoretical calculation of branch point velocity, 2012.

[39] D. Oesch, C. Tewksbury-Christle, D. Sanchez, and P. Kelly, The aggregate behaviour of branch points: verification in wave optical simulation ii, 2012.

[40] D. Oesch, C. Tewksbury-Christle, D. Sanchez, and P. Kelly, The aggregate behaviour of branch points: verification in wave optical simulation i.

[41] D. Oesch and D. Sanchez, Optics Express, **20**, 12292 (2012).

[42] D. Oesch, D. Sanchez, and C. Tewksbury-Christle, Optics Express, **20**, 1046 (2012).

[43] B. Sickmiller, D. Oesch, D. Sanchez, and P. Kelly, High contrast imaging in the presence of turbulence, 2012.

[44] D. Oesch *et al.*, Optics Express, **21**, 5440 (2013).

[45] L. Marrucci, C. Manzo, and D. Paparo, Physical Review Letters, **96**, 163905 (2006).

[46] S. Maccalli *et al.*, Applied Optics, **52**, 635 (2013).

[47] S. Li and Z. Wang, Applied Physics Letters, **103** (2013).

[48] Q. Bai, A. Tennant, B. Allen, and M. Rehman, Generation of orbital angular momentum (oam) radio beams with phased patch array, 2013.

[49] B. Thidé *et al.*, Physical Review Letters, **99**, 087701 (2007).

[50] S. Vyas and P. Senthilkumaran, Applied Optics, **46**, 7862 (2007).

[51] L. Wang, L. Wang, and S. Zhu, Optics Communications, **282**, 1088 (2009).

[52] M. Gray, G. Pisano, S. Maccalli, and P. Schemmel, A Model of an Orbital Angular Momentum Signal in an Astrophysical Maser, In Preparation (2014).

[53] M. Gray, G. Pisano, S. Maccalli, and P. Schemmel, OAM amplification in a Maser, In Preparation (2014).

[54] F. Tamburini, B. Thidé, G. Molina-Terriza, and G. Anzolin, Nature Physics, **7**, 195 (2011).

[55] D. Akamatsu and M. Kozuma, Physical Review A, **67**, 023803 (2003).

[56] Y. Ueno, Y. Toda, S. Adachi, R. Morita, and T. Tawara, Optics Express, **17**, 20567 (2009).

[57] W. Jiang, Q. Chen, Y. Zhang, and G. Guo, Physical Review A, **74**, 043811 (2006).

[58] S. Barreiro, J. Tabosa, J. Torres, Y. Deyanova, and L. Torner, Optics Letters, **29**, 1515 (2004).

[59] J. Mendonça *et al.*, arXiv preprint arXiv:0804.3221 (2008).

[60] U. Jentschura and V. Serbo, The European Physical Journal C, **71**, 1 (2011).

[61] U. Jentschura and V. Serbo, Physical Review Letters, **106**, 013001 (2011).

[62] I. Ivanov and V. Serbo, Physical Review A, **84**, 033804 (2011).

[63] I. Ivanov, Physical Review D, **83**, 093001 (2011).

[64] P. Bandyopadhyay, B. Basu, and D. Chowdhury, Proceedings of the Royal Society A: Mathematical, Physical and Engineering Science, **470**, 20130525 (2014).

[65] A. Carpentier, H. Michinel, J. Salgueiro, and D. Olivieri, American Journal of Physics, **76**, 916 (2008).

[66] M. Malik *et al.*, Nature communications **5** (2014).

[67] M. N. OSullivan, M. Mirhosseini, M. Malik, and R. W. Boyd, Optics express **20**, 24444 (2012).

[68] R. Neo *et al.*, Optics Express **22**, 9920 (2014).

[69] J. Salo *et al.*, Journal of Optics A: Pure and Applied Optics **4**, S161 (2002).

[70] J. Meltaus *et al.*, Microwave Theory and Techniques, IEEE Transactions on **51**, 1274 (2003).

[71] D. C. Flanders, Applied Physics Letters **42**, 492 (1983).

[72] S. Oemrawsingh *et al.*, Applied Optics, **43**, 688 (2004).

[73] F. Tamburini, E. Mari, B. Thidé, C. Barbieri, and F. Romanato, Applied Physics Letters, **99**, 204102 (2011).

[74] D. Martin and J. Bowen, Microwave Theory and Techniques, IEEE Transactions, **41**, 1676 (1993).

[75] J. Murphy, M. McCabe, and S. Withington, International journal of infrared and millimeter waves **18**, 501 (1997).

[76] N. Trappe, J. Murphy, and S. Withington, European Journal of Physics, **24**, 403 (2003).

[77] F. Tamburini, E. Mari, B. Thidé, C. Barbieri, and F. Romanato, Applied Physics Letters, **99**, 204102 (2011).

[78] A. Beniss *et al.*, Flat plate for OAM generation in the millimeter band, In Proceedings of EuCAP, (2013).

[79] J. Leach and M. Padgett, New Journal of Physics, **5**, 154 (2003).

[80] FEKO, http://www.feko.info, 2014.

[81] F. Ozturk, *Modelling and experimental study of millimetre wave refractive systems*, PhD thesis, The University of Manchester, 2013.

[82] J. Lee, G. Foo, E. Johnson, and G. Swartzlander, Physical Review Letters, **97**, 053901 (2006).

[83] J. Grover Swartzlander *et al.*, Optics Express, **16**, 10200 (2008).

[84] E. Serabyn, D. Mawet, and R. Burruss, Nature, **464**, 1018 (2010).

[85] C. Jenkins, Monthly Notices of the Royal Astronomical Society, **384**, 515 (2008).

[86] F. Tamburini, G. Anzolin, G. Umbriaco, A. Bianchini, and C. Barbieri, Physical Review Letters, **97**, 163903 (2006).

[87] G. Anzolin, F. Tamburini, A. Bianchini, and C. Barbieri, Physical Review A, **79**, 033845 (2009).

[88] B. Guan *et al.*, Optics Express, **22**, 145 (2014).

[89] I. Fazal *et al.*, Optics Letters, **37**, 4753 (2012).

[90] P. Jia, Y. Yang, C. Min, H. Fang, and X. Yuan, Optics Letters, **38**, 588 (2013).

[91] H. Huang *et al.*, Optics Letters, **39**, 197 (2014).

[92] J. Wang *et al.*, Nature Photonics, **6**, 488 (2012).

[93] Y. Liu, C. Gao, X. Qi, and H. Weber, Optics Express, **16**, 7091 (2008).

[94] F. Tamburini *et al.*, New Journal of Physics, **14**, 033001 (2012).

[95] F. Mahmouli and S. Walker, IEEE Telecommunications Forum (TELFOR), 2012 20th , 315 (2012).

[96] L. Torner, J. Torres, and S. Carrasco, Optics Express, **13**, 873 (2005).

[97] D. Petrov, N. Rahuel, G. Molina-Terriza, and L. Torner, Optics Letters, **37**, 869 (2012).

[98] G. Molina-Terriza, L. Rebane, J. Torres, L. Torner, and S. Carrasco, Journal of the European Optical Society, **2** (2007).

[99] S. Maccalli, *Stefania's Thesis*, PhD thesis, The University of Manchester, 2014.

[100] V. V. Kotlyar and A. A. Kovalev, Optics letters **33**, 189 (2008).

[101] P. Schemmel *et al.*, A near field 3d scanner for millimetre wavelengths, 2013.

[102] S. Nakazawa, M. Nagasaka, M. Kamei, S. Tanaka, and Y. Ito, Near field measurement of radiation pattern configured by an array-fed imaging reflector antenna for 21-ghz band broadcasting satellite, 2013.

[103] A. Montesano *et al.*, Hag1 dra-elsa active antenna: Rf and electrical measurements, 2013.

[104] F. Beckers, Minimum weight transportable spherical near field scanner, 2013.

[105] T. Fritzel *et al.*, Concept of a portable antenna measurement system for large scale and multi contour near fields, 2013.

[106] F. L. Fur *et al.*, Spherical near field antenna measurement facility in vhf range - investigation on system design, 2013.

[107] S. Burgos *et al.*, Hybrid test range in the estec compact payload test range, 2013.

[108] S. Gregson, J. McCormick, and C. Parini, Principles of planar near-field antenna measurements **53** (2007).

[109] G. Savini, G. Pisano, and P. A. R. Ade, Appl. Opt. **45**, 8907 (2006).

[110] G. Pisano *et al.*, Appl. Opt. **44**, 3208 (2005).

[111] G. Pisano, G. Savini, P. A. R. Ade, and V. Haynes, Appl. Opt. **47**, 6251 (2008).

[112] G. Pisano, M. W. Ng, F. Ozturk, B. Maffei, and V. Haynes, Appl. Opt. **52**, 2218 (2013).

[113] J. A. Murphy, N. Trappe, and S. Withington, Infrared physics & technology **44**, 289 (2003).

[114] T. J. Finn, N. A. Trappe, and J. A. Murphy, JOSA A **25**, 80 (2008).

[115] ondrives, http://www.ondrives.com, 2014.

[116] B. Maffei, In Preparation (2014).

[117] Swissto12, http://www.swissto12.com, 2014.

[118] Agilent, Network analyser basics, http://www.home.agilent.com, 2014.

[119] N. Instruments, Fundamentals of network analysers, http://www.ni.com, 2014.

[120] R. Collins, Foundations for Microwave Engineering, 2nd Edition (2001).

[121] P. Schemmel and J. Lunn, Vna port power bias, Private Correspondence, 2014.

[122] S. Pivnenko, J. Nielsen, O. Breinbjerg, T. Laitinen, and T. Hansen, Comparison of the fft/matrix inversion and system matrix techniques for higher order probe corrections in spherical near field antenna measurements, 2011.

[123] C. van't Klooster, On probes for planar near field measurements, 2011.

[124] A. G. Repjar, A. C. Newell, and M. H. Francis, Antennas and Propagation, IEEE Transactions on **36**, 855 (1988).

[125] T. B. Hansen and A. D. Yaghjian, Antennas and Propagation, IEEE Transactions on **43**, 569 (1995).

[126] E. Joy, W. Leach Jr, and G. Rodrigue, Antennas and Propagation, IEEE Transactions on **26**, 379 (1978).

[127] D. Paris, W. Leach Jr, and E. Joy, Antennas and Propagation, IEEE Transactions on **26**, 373 (1978).

[128] A. C. Newell, Antennas and Propagation, IEEE Transactions on **36**, 754 (1988).

[129] A. D. Yaghjian, Antennas and Propagation, IEEE Transactions on **34**, 30 (1986).

[130] J. J. Wang, Antennas and Propagation, IEEE Transactions on **36**, 746 (1988).

[131] D. M. Kerns, Journal of Research Section B Mathematical Sciences B **80**, 5 (1976).

[132] HFSS, http://www.ansys.com, 2014.

[133] Y. Rumala and A. Leanhardt, Journal of Optical Society of America B, **30**, 615 (2013).

[134] Y. S. Rumala, JOSA B **31**, A6 (2014).

[135] Y. S. Rumala, Structured light interference due to multiple reflections in a spiral phase plate device and its propagation, in *SPIE OPTO*, pp. 899912–899912, International Society for Optics and Photonics, 2014.

[136] M. Berry and M. Dennis, Journal of Physics A: Mathematical and General **34**, 8877 (2001).

[137] M. R. Dennis, R. P. King, B. Jack, K. OHolleran, and M. J. Padgett, Nature Physics **6**, 118 (2010).

[138] W. T. Irvine and D. Bouwmeester, Nature Physics **4**, 716 (2008).

[139] J. Leach, M. R. Dennis, J. Courtial, and M. J. Padgett, Nature **432**, 165 (2004).

[140] M. Berry and M. Dennis, Proceedings of the Royal Society of London. Series A: Mathematical, Physical and Engineering Sciences **457**, 2251 (2001).

[141] A. S. Desyatnikov, D. Buccoliero, M. R. Dennis, and Y. S. Kivshar, Scientific reports **2** (2012).

[142] D. Proment, M. Onorato, and C. F. Barenghi, Physical Review E **85**, 036306 (2012).

[143] M. Berry, Journal of Optics A: Pure and Applied Optics, **6**, 259 (2004).

[144] B. Maffei *et al.*, Implementation of a quasi-optical free-space s-parameters measurement system, 2013.